VORTEX-LATTICE

UTILIZATION

A workshop held at
LANGLEY RESEARCH CENTER
Hampton, Virginia
May 17–18, 1976

NATIONAL AERONAUTICS AND SPACE ADMINISTRATION

ERRATA

NASA SP-405

VORTEX-LATTICE UTILIZATION

Page 231:   Figure 6 is in error.   Replace figure 6 with the following
corrected version.
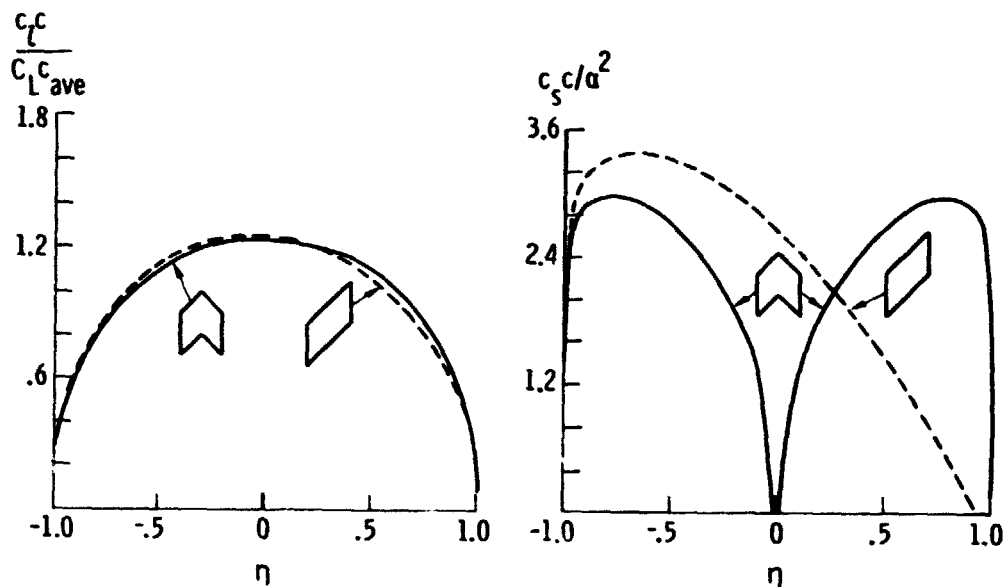
Figure 6.- Span load and section suction distributions on a swept and
skewed wing. $\Lambda = 45^o$;   A = 1;   M = 0.

VORTEX-LATTICE

UTILIZATION

A workshop held at Langley Research Center,
Hampton, Virginia, on May 17–18, 1976

Prepared by Langley Research Center

CONTENTS

HISTORICAL EVOLUTION OF VORTEX-LATTICE METHODS

John DeYoung
Vought Corporation Hampton Technical Center

Good morning. In this short talk I will give a review of the beginnings and some orientation of the vortex-lattice method. The vortex-lattice method is a discrete vortex colocation method for obtaining numerical solutions to the loading integral equation relating normal velocity an' wing loading. It is a branch of computer fluid dynamics which in turn is mathcmatically descended from finite-difference concepts. Finite-difference concepts had been applied to the development of calculus which dates it a relatively long time ago. For our subject the beginning is much more current. Here for orientation we will follow the historical course of the vortex-lattice method in conjunction with its field of computational fluid dynamics. An outline of the concurrent development of computer fluid dynamics and vortex-lattice methods is as follows:

L.F. RICHARDSON (1910)

L. PRANDTL (1918, 1921)

H. LIEPMANN (1918)

R. COURANT, K. FRIEDRICHS, AND H. LEWY (1928) ELLIPTIC AND HYPERBOLIC EQUATIONS

A. THOM (1928) FIRST NUMEPICAL SOLUTION OF VISCOUS FLUID-DYNAMICS PROBLEM

1/4 - 3/4 RULE CHORD CONCEPT (1937)

G. H. SHORTLEY, AND R. WELLER (1938)

LOS ALAMOS SCIENTIFIC LABORATORY (WORLD WAR II)

V.M. FALKNER (1943) FIRST USE OF NAME VORTEX-LATTICE THEORY

R. V. SOUTHWELL (1946)

C.M. TYLER, JR. (1949)

D. N. DeG. ALLEN, AND S.C.R. DENNIS (1951)

D. N. DeG. ALLEN, AND R.V. SOUTHWELL (1955)

F. H. HARLOW, AND J. E. FROMM (1965)

AERODYNAMIC ANALYSIS REQUIRING ADVANCED COMPUTERS, NASA SP347 (1975)

Since many mathematical models of fluid dynamics can be expressed as partial differential equations then, historically, computer fluid dynamics can be said to start with L. F. Richardson's paper. Some consider this paper as the foundation of modern numerical analysis of partial differential equations. He applied his methods to the engineering problem of determining stresses in a masonry dam. In 1918 Prandtl formulated the lifting-line theory. The chord loading is concentrated into a single load vortex, thus it is a one panel chord-wise vortex lattice with flow conditions satisfied at the load line. In 1938 Prandtl proposed an explicit finite-difference method for solving boundary-layer equations. Liepmann showed how to improve the convergence rate of

Richardson's procedure. In later years Liepmann's method was found very compatible with electronic computers and has been further developed. The classic paper of Courant, Friedrichs, and Levy has become a guide for practical fluid flow computational solutions. A. Thomm did early computational work in fluid flow, two-dimensional and flow past circular cylinders.

The 1/4-3/4 rule has a fundamental role in vortex-lattice methods. This concept first appeared in a paper by E. Pistolesi in 1937. He in effect did a single panel vortex-lattice solution for a two-dimensional wing and found that with the load vortex at the 1/4 chord line and downwash or normal wash point (no-flow through condition) at 3/4 chord, the section lift and moment for constant angle of attack is exactly that of thin wing theory. And lift is predicted exactly for wing with parabolic camber. This rule was first applied to wings of finite aspect ratio by W. Mutterperl (1941) and J. Weissinger (1942) and very often since by others. P.A. Byrd (Ing.-Arch. 19, 321-323, 1951) expanded Pistolesi's work for sections divided into more than one panel on the chord and with the 1/4-3/4 rule applied for each panel found that lift and moment are predicted exactly. In later years this chordwise rule received further mathematical attention. Shortley and Weller developed block relaxation-a developed version of Liepmann's method. It was this work from Ohio State University I had used in a graduate course at Washington State in 1943 to numerically solve the Laplace equation for determining the stress pattern in a twisted grooved rod. Work at the Los Alamos Scientific Laboratory has contributed much to the advancement of computer fluid dynamics. This includes the work of J. von Neumann, J. Fromm, and F. Harlow. From Los Alamos a graphics fluid dynamics motion picture was circulated in this country in the 1960's. It showed a computer fluid dynamics flow prediction of a dam bursting and the water cascading down a gorge. V. Falkner covered the wing with a grid of straight horseshoe vortices. Wing surface loadings were predicted. In one report he uses the title, "The Solution of Lifting Plane Problems by Vortex Lattice Theory," A.R.C.R.& M. 2591, 1947, which is a first use of this name. Faulkner's method and variations were tried extensively throughout the industry during the 1950's. However, the calculation effect was large which limited the number of panels then accuracy became questionable for some configuration designs. The vortex-lattice method had to await computer capability. Southwell improved the relaxation procedure by scanning the mesh for larger residuals for new values calculation. This scanning procedure is not so suitable for electronic computers. Tyler, in a Ph.D. dissertation, and Allen and Dennis developed relaxation method solutions for computing wing lifting surface loading. Using Southwell's relaxation method, Allen and Southwell did a solution for the viscous imcompressible flow over a cylinder. The year 1965 is considered by some as a modern start to computer or computational fluid dynamics. Harlow and Fromm provided stimulus and awareness in a Scientific American paper entitled, "Computer Experiments in Fluid Dynamics" which includes the concept of numerical simulation. It has been observed that the percentage of published scientific engineering numerical methods papers to total papers has increased twenty fold in the decade of 1963 to 1973. The year 1965 can be considered as the start of the computational vortex-lattice method. It has had a many fold growth in applications and development during the last decade. It was certainly influenced by the stimulus and awareness of the potential of the scientific computer occurring throughout the field of

2

computational fluid dynamics. In the mid 1960's four independent papers appeared on vortex-lattice methods, respectively by Rubbert, Dulmovits, Hedman, and Belotserkovskii. These were extensions of Faulkner's method and adapted to electronic computers. For the reported work of the 1960's and 70's reference can be made to the bibliography list of this workshop. The state of the art in general computational fluid dynamics is demonstrated in the volumes of NASA SP-347 which is the result of a March 4-6, 1975 NASA conference at Langley.

Computer capacity is developing rapidly. Computational speed has been increased by a factor of 2.5 each year. The application of the vortex-lattice method is being made to increasingly complex configuration designs such as multi-planes, nonplanar wings, interference, and wing tip. It is a powerful tool as an aid in parameter study and optimization. Currently attention is being directed toward further improving the vortex-lattice representation by lattice arrangement, panel geometry, and by better mathematical modeling of the flow in the panel region. These have been referred to as advanced panel methods. However, in some of these developments the simplicity of an elemental vortex representation is lessened and leads to greater mathematical model complexity of the panel flow, but computational efficiency may be increased. In summary, this is computationally a new technology field only about 10 years old. It is computer oriented with numerical simulation of the physical laws governing the problem. It is a supplement to the two disciplines of theory and experiment. It can logically be extended to find answers of complex flow impractical to measure experimentally. In this workshop we will learn of many unique utilizations of the vortex-lattice method, of lattice analytical advancements, and the power and nature of this new discipline. Thank you.

3

BIBLIOGRAPHY

Pistolesi, E.: Betrachtungen über die gegenseitige Beeinflussung von Trag-flügelsystemen (Considerations on the Mutual Interference of Aerofoil Systems). L.G.L. Rep., 1937, pp. 214-219.

Falkner, V. M.: The Calculation of Aerodynamic Loading on Surfaces of Any Shape. R. & M. No. 1910, British A.R.C., 1943.

Falkner, V. M.: The Accuracy of Calculations Based on Vortex Lattice Theory. Rep. No. 9621, British A.R.C., 1946.

Falkner, V. M.: Calculations of the Aerodynamic Loading of a Delta Wing. Rep. No. 9830, British A.R.C., 1946.

Falkner, V. M.: The Effect of Pointed Tips on Wing Loading Calculations. R. & M. No. 2483, British A.R.C., 1946.

Falkner, V. M.: A Note on the Present Position of Calculations by Vortex Lattice Theory. Rep. No. 9637, British A.R.C., 1946.

Falkner, V. M.: The Use of Equivalent Slopes in Vortex Lattice Theory. R. & M. No. 2293, British A.R.C., 1946.

Jones, W. P.: The Calculation of Aerodynamic Derivative Coefficients for Wings of Any Plan Form in Non-Uniform Motion. R. & M. No. 2470, British A.R.C., 1946.

Schlichting, H.; and Thomas, H. H. B. M.: Note on the Calculation of the Lift Distribution of Swept Wings. Rep. No. Aero. 2236, British R.A.E., Dec. 1947.

Van Dorn, Nicholas H.; and DeYoung, John: A Comparison of Three Theoretical Methods of Calculating Span Load Distribution on Swept Wings. NACA TN 1476, 1947. (Supersedes NACA RM A7C31.)

Berndt, Sune B.; and Orlik-Rückemann, Kazimierz: Comparison Between Theoretical and Experimental Lift Distributions of Plane Delta Wings at Low Speeds and Zero Yaw. KTH-Aero TN 10, Div. Aeronaut., Roy. Inst. Technol. (Stockholm), 1948.

Garner, H. C.: Methods of Approaching an Accurate Three-Dimensional Potential Solution for a Wing. R. & M. No. 2721, British A.R.C., 1948.

Jones, Arthur L., and Sluder, Loma: An Application of Falkner's Surface-Loading Method to Predictions of Hinge-Moment Parameters for Swept-Back Wings. NACA TN 1506, 1948.

Falkner, V. M.: A Comparison of Two Methods of Calculating Wing Loading With Allowance for Compressibility. R. & M. No. 2685, British A.R.C., 1949

4

Falkner, V. M.: The Scope and Accuracy of Vortex Lattice Theory. R. & M. No. 2740, British A.R.C., 1949.

Garner, H. C.: The Evaluation of Downwash at Large Spanwise Distances From a Vortex Lattice. R. & M. No. 2808, British A.R.C., 1950.

Byrd, P. F.: Ergänzung zu dem Aufsatz von N. Scholz, Beiträge zur Theorie der tragenden Fläche. Ing.-Arch., Bd. XIX, Heft 6, 1951, pp. 321-323.

Campbell, George S.: A Finite-Step Method for the C culation of Span Loadings of Unusual Plan Forms. NACA RM L50L13, 1951.

Falkner, V. M: Calculation by Lifting Plane Theory of the Rolling and Yawing Moments of a Wing Due to Rotary Motion in Yaw. Aircraft Eng., vol. XXIII, no. 264, Feb. 1951, pp. 44-50, 54.

Garner, H. C.: Swept-Wing Loading. A Critical Comparison of Four Subsonic Vortex Sheet Theories. C.P. No. 102, British A.R.C., Oct. 11, 1951.

Lehrian, Doris E.: Aerodynamic Coefficients for an Oscillating Delta Wing. R. & M. No. 2841, British A.R.C., 1951.

Falkner, V. M.: The Solution of Lifting-Plane Problems by Vortex-Lattice Theory. R. & M. No. 2591, British A.R.C., 1953.

Lehrian, Doris E.: Calculation of Stability Derivatives for Oscillating Wings. R. & M. No. 2922, British A.R.C., 1953.

Schneider, William C.: A Comparison of the Spanwise Loading Calculated by Various Methods With Experimental Loadings Obtained on a 45° Sweptback Wing of Aspect Ratio 8.02 at a Reynolds Number of 4.0×10^6. NACA Rep. 1208, 1954. (Supersedes NACA RM L51G30.)

Ward, G. N.: Linearized Theory of Steady High-Speed Flow. Cambridge Univ. Press, 1955.

Lehrian, Doris E.: Calculated Derivatives for Rectangular Wings Oscillating in Compressible Subsonic Flow. R. & M. No. 3068, British A.R.C., 1956.

Lehrian, Doris E.: Vortex-Lattice Treatment of Rectangular Wings With Oscillating Control Surfaces. R. & M. No. 3182, British A.R.C., 1957.

Carlson, Harry W.; and Middleton, Wilbur D.: A Numerical Method for the Design of Camber Surfaces of Supersonic Wings With Arbitrary Planforms. NASA TN D-2341, 1964.

Rubbert, Paul E.: Theoretical Characteristics of Arbitrary Wings by a Non-Planar Vortex Lattice Method. Doc. No. D6-9244, Boeing Co., Feb. 1964.

Ashley, Holt; and Landahl, Marten: Aerodynamics of Wings and Bodies. Addison-Wesley Pub. Co., Inc., c.1965.

Middleton, Wilbur D.; and Carlson, Harry W.: A Numerical Method for Calculating the Flat-Plate Pressure Distributions on Supersonic Wings of Arbitrary Planform. NASA TN D-2570, 1965.

Blackwell, James A., Jr.: Numerical Method for the Design of Warped Surfaces for Subsonic Wings With Arbitrary Planform. M. S. Thesis, Univ. of Virginia, 1966. (Available as NASA TM X-57857.)

Hedman, Sven G.: Vortex Lattice Method for Calculation of Quasi Steady State Loadings on Thin Elastic Wings in Subsonic Flow. FFA Rep. 105, Aeronaut. Res. Inst. of Sweden, 1966.

Kfoury, Denis J.: A Routine Method for the Calculation of Aerodynamic Loads on a Wing in the Vicinity of Infinite Vortices. Tech. Rep. 133-2 (Contract NOw 65-0139-d), Massachusetts Inst. Technol., May 1966.

Belotserkovskii, Sergei Mikhailovich (Maurice Holt, transl. ed.): The Theory of Thin Wings in Subsonic Flow. Plenum Press, 1967.

Joppa, Robert G.: A Method of Calculating Wind Tunnel Interference Factors for Tunnels of Arbitrary Cross Section. NASA CR-845, 1967.

Mirokhin, B. V.: Design V-Shaped Foils of Small Aspect Ratio by the Method of Horseshoe Vortices. News of Institutions of Higher Learning - Aeronautical Engineering, FTD-TT-67-6235-0 (MT-64-288), U.S. Air Force, Apr. 27, 1967, pp. 23-35. (Available from DDC as AD 655 358.)

Albano, E.; and Rodden, W. P.: A Doublet Lattice Method for Calculating Lift Distributions on Oscillating Surfaces in Subsonic Flows. AIAA Paper No. 68-73, Jan. 1968.

Bukhovtsev, B. B.; and Stepanova, N. V.: The Non-Stationary Calculation of Flow Past a Rectangular Wing of Low Aspect Ratio. NASA TT F-11, 823, 1968.

Giesing, Joseph P.: Lifting Surface Theory for Wing-Fuselage Combinations. Rep. DAC-67212, Vol. I, McDonnell Douglas, Aug. 1, 1968.

Landahl, Marten T.; and Stark, Valter J. E.: Numerical Lifting-Surface Theory - Problems and Progress. AIAA J., vol. 6, no. 11, Nov. 1968, pp. 2049-2060.

Stahl, B.; Kálmán, T. P.; Giesing, J. P.; and Rodden, W. P.: Aerodynamic Influence Coefficients for Oscillating Planar Lifting Surfaces by the Doublet Lattice Method for Subsonic Flows Including Quasi-Steady Fuselage Interference - Part I. Rep. No. DAC-67201, McDonnell Douglas Corp., 1968. (Available from DDC as AD 903 874.)

Belotserkovskiy, S. M.: Calculation of the Flow Around Wings of Arbitrary Planform in a Wide Range of Angles of Attack. NASA TT F-12,291, 1969.

Blackwell, James A., Jr.: A Finite-Step Method for Calculation of Theoretical Load Distributions for Arbitrary Lifting-Surface Arrangements at Subsonic Speeds. NASA TN D-5335, 1969.

6

Houbolt, John C.: Some New Concepts in Oscillatory Lifting Surface Theory. AFFDL-TR-69-2, U.S. Air Force, June 1969. (Available from DDC as AD 857 522.)

James, R. M.: On the Remarkable Accuracy of the Vortex Lattice Discretization in Thin Wing Theory. Rep. No. DAC 67211, McDonnell Douglas, Feb. 1969.

Kálmán, T. P.; Rodden, W. P.; and Giesing, J. P.: Aerodynamic Influence Coefficients by the Doublet Lattice Method for Interfering Nonplanar Lifting Surfaces Oscillating in a Subsonic Flow - Part I. Rep. No. DAC-67977, McDonnell Douglas Corp., 1969.

Rodden, William P.; and Liu, David T.: Correlation of the Vortex Lattice Method on Rotor/Wing Configurations. J. Aircr., vol. 6, no. 4, July-Aug. 1969, p. 375.

Brebner, G. G.; and Wyatt, L. A.: The Velocities Induced by Distributions of Infinite Kinked Source and the Vortex Lines Representing Wings With Sweep and Dihedral in Incompressible Flow. R. & M. No. 3667, British A.R.C., 1970.

Kálmán, T. P.; Giesing, J. P.; and Rodden, W. P.: Spanwise Distribution of Induced Drag in Subsonic Flow by the Vortex Lattice Method. J. Aircr., vol. 7, no. 6, Nov.-Dec. 1970, pp. 574-576.

Maskew, B.: Calculation of the Three-Dimensional Potential Flow Around Lifting Non-Planar Wings and Wing-Bodies Using a Surface Distribution of Quadrilateral Vortex-Rings. TT 7009, Loughborough Univ. Technol., Sept. 1970.

Rodden, William P.; and Giesing, Joseph P.: Application of Oscillatory Aerodynamic Theory to Estimation of Dynamic Stability Derivatives. J. Aircr., vol. 7, no. 3, May-June 1970, pp. 272-275.

Giesing, J. P.; Kálmán, T. P.; and Rodden, W. P.: Subsonic Unsteady Aerodynamics for General Configurations. Part I, Vol. I - Direct Application of the Nonplanar Doublet-Lattice Method. AFFDL-TR-71-5, Pt. I, Vol. I, U.S. Air Force, Nov. 1971.

Kálmán, T. P.; Rodden, W. P.; and Giesing, J. P.: Application of the Doublet-Lattice Method to Nonplanar Configurations in Subsonic Flow. J. Aircr., vol. 8, no. 6, June 1971, pp. 406-413.

Margason, Richard J.; and Lamar, John E.: Vortex-Lattice FORTRAN Program for Estimating Subsonic Aerodynamic Characteristics of Complex Planforms. NASA TN D-6142, 1971.

Rodden, W. P.; Giesing, J. P.; and Kálmán, T. P.: New Developments and Applications of the Subsonic Doublet-Lattice Method for Nonplanar Configurations. Symposium on Unsteady Aerodynamics for Aeroelastic Analyses of Interfering Surfaces, Part II, AGARD CP No. 80, Apr. 1971, pp. 4-1—4-27.

Ashley, Holt; and Rodden, William P.: Wing-Body Aerodynamic Interaction. Annual Review of Fluid Mechanics, Vol. 4, M. Van Dyke, W. G. Vincenti, and J. V. Wehausen, eds., Annual Rev., Inc., 1972, pp. 431-472.

Giesing, J. P.; Kálmán, T. P.; and Rodden, W. P.: Subsonic Steady and Oscillatory Aerodynamics for Multiple Interfering Wings and Bodies. J. Aircr., vol. 9, no. 10, Oct. 1972, pp. 693-702.

Giesing, J. P.: Subsonic Unsteady Aerodynamics for General Configurations. Part 2, Vol. I - Application of the Doublet-Lattice Method and the Method of Images to Lifting Surface Body Interference. AFFDL-TR-71-5, Pt. II, Vol. I, U.S. Air Force, Apr. 1972. (Available from DDC as AD 893 825L.)

Giesing, J. P.; Kálmán, T. P.; and Rodden W. P.: Subsonic Unsteady Aerodynamics for General Configurations. AIAA Paper No. 72-26, Jan. 1972.

Gomez, Antulio V.: TRW Vortex-Lattice Method Subsonic Aerodynamic Analysis for Multiple-Lifting-Surfaces (N. Surface) TRW Program Number HA010B. 20029-H110-RO-00 (Contract NAS9-12330), TRW Syst., Sept. 1, 1972. (Available as NASA CR-128588.)

James, Richard M.: On the Remarkable Accuracy of the Vortex Lattice Method. Comput. Methods Appl. Mech. & Eng., vol. 1, no. 1, June 1972, pp. 59-79.

Rodden, W. P.; Giesing, J. P.; and Kálmán, T. P.: Refinement of the Nonplanar Aspects of the Subsonic Doublet-Lattice Lifting Surface Method. J. Aircr., vol. 9, no. 1, Jan. 1972, pp. 69-73.

Sorrells, Russell B.; and Miller, David S.: Numerical Method for Design of Minimum-Drag Supersonic Wing Camber With Constraints on Pitching Moment and Surface Deformation. NASA TN D-7097, 1972.

Tulinius, J.: Unified Subsonic, Transonic, and Supersonic NAR Vortex Lattice. TFD-72-523, Los Angeles Div., North American Rockwell, Apr. 27, 1972.

Clever, W. C.: A Vortex Lattice Program for Jet Flapped Airfoils. TFD-73-70, Los Angeles Div., North American Rockwell, Jan. 26, 1973.

Hedman, Sven G.: Computation of Vortex Models for Wings at High Angle of Attack in Incompressible Flow. Tech. Note FFA AU-653, Aeronaut. Res. Inst. of Sweden, 1973.

Hough, Gary R.: Remarks on Vortex-Lattice Methods. J. Aircr., vol. 10, no. 5, May 1973, pp. 314-317.

McCormick, Barnes W.: Final Report to Close Out NASA Grant NGR-39-009-111 [Rotor Blade-Vortex Interaction]. NASA CR-139594, 1973.

Carlson, Harry W.; and Miller, David S.: Numerical Methods for the Design and Analysis of Wings at Supersonic Speeds. NASA TN D-7713, 1974.

8

Lan, C. Edward: An Analytical Investigation of Wing-Jet-Interaction.
CRINC-FRL 74-001 (NASA Grant NGR 17-002-107), Univ. of Kansas, Apr. 1974.
(Available as NASA CR-138140.)

Lan, C. Edward: A Quasi-Vortex-Lattice Method in Thin Wing Theory. J. Aircr.,
vol. 11, no. 9, Sept. 1974, pp. 518-527.

Mook, D. T.; and Maddox, S. A.: Extension of a Vortex-Lattice Method to Include
the Effects of Leading-Edge Separation. J. Aircr., vol. 11, no. 2, Feb. 1974,
pp. 127-128.

Rodden, William P.; Giesing, Joseph P.; Kálmán, Terez P; and Rowan, Jack C.:
Comment on "A Finite-Element Method for Calculating Aerodynamic Coefficients
of a Subsonic Airplane.' J. Aircr., vol. 11, no. 6, June 1974, pp. 366-368.

Aerodynamic Analyses Requiring Advanced Computers - Parts I and II. NASA SP-347,
1975.

Lamar, John E.; and Gloss, Blair B.: Subsonic Aerodynamic Characteristics of
Interacting Lifting Surfaces With Separated Flow Around Sharp Edges Predicted
by a Vortex-Lattice Method. NASA TN D-7921, 1975.

Tulinius, J.; Clever, W.; Niemann, A.; Dunn, K.; and Gaither, B.: Theoretical
Prediction of Airplane Stability Derivatives at Subcritical Speeds.
NASA CR-132681, 1975.

Lamar, John E.: A Vortex-Lattice Method for the Mean Camber Shapes of Trimmed
Noncoplanar Planforms With Minimum Vortex Drag. NASA TN D-8090, 1976.

Rodden, W. P.: A Comparison of Methods Used in Interfering Lifting Surface
Theory. AGARD Rep. No. 643, Feb. 1976.

Tulinius, Jan R.; and Margason, Richard J.: Aircraft Aerodynamic Design and
Evaluation Methods. AIAA Paper No. 76-15, Jan. 1976.

SUBSONIC FINITE ELEMENTS FOR WING-BODY COMBINATIONS

James L. Thomas
NASA Langley Research Center

SUMMARY

Capabilities, limitations, and applications of various theories for the prediction of wing-body aerodynamics are reviewed. The methods range from approximate planar representations applicable in preliminary design to surface singularity approaches applicable in the later stages of detail design. The available methods for three-dimensional configurations are limited as inviscid solutions with viscous effects included on an empirical or strip basis.

INTRODUCTION

Current research efforts directed toward the design of fuel-efficient aircraft dictate that adequate tools be available for the assessment of aerodynamic loads across the expected speed envelope. Ashley and Rodden (ref. 1) have summarized the available methods for aerodynamic analyses of wings and bodies in steady and oscillatory motion at both subsonic and supersonic speeds. The analytical methods applicable to generalized configurations vary over a range of sophistication, accuracy, and computer times required but are generally limited as inviscid solutions. Some inviscid-viscid coupling techniques in two dimensions have yielded good results (refs. 2 and 3), and their inclusion on a strip basis into three-dimensional inviscid solutions may serve as a near-term solution. The inclusion of viscous effects for generalized configurations across the Mach number range remains a far-term solution requiring extensive computer resources and advances in turbulence modeling (ref. 4). Immediate design and verification methods are thus a combination of experimental and analytical techniques. The analytical methods largely remain inviscid solutions guided by the inclusion of viscous effects on a semiempirical or strip basis.

The purpose of this paper is to summarize the capabilities and limitations of the existing methods for the steady subsonic analysis of wing-body combinations. Solutions to the linearized perturbation potential equation (Laplace's equation), with Mach number effects included by the Prandtl-Glauert transformation, are considered. Since the governing partial differential equation is linear, the solutions may be approximated by distributing a finite number of elemental solutions over the body and solving for their relative strengths by imposing proper boundary conditions; for example, the flow field must satisfy the tangential requirement on the body surface and the Kutta condition at subsonic trailing edges. Such finite-element solutions have proven to be most useful and versatile at subsonic as well as supersonic speeds. The quality of the resulting solution is, however, a function of the type, distribution, and number of elemental solutions assumed. They require considerably less computer resources than the equivalent three-dimensional finite-difference solutions required at transonic speeds where the governing equations are nonlinear (ref. 5).

11

SYMBOLS

A	aspect ratio, b^2/S
b	wing span
C_L	lift coefficient
C_p	pressure coefficient
c	chord
c_l	section lift coefficient
d	body diameter
L	body length
M	Mach number
r	body radius
S	wing area
X,Y,Z	axis system
x,z	distances along X- and Z-axes
α	angle of attack
η	distance along semispan
Λ	sweep angle
λ	taper ratio

Subscripts:

av	average
max	maximum
∞	free stream
f	fuselage

GENERAL SLENDER BODY AND PLANAR WING SOLUTION

A large number of methods exist for the analysis of planar lifting surfaces which account approximately for the presence of bodies. Generally, the methods

12

treat the body separately in an initial analysis and then modify the analysis of the lifting surface such that the normal wash on the wing from the body is included and the flow is diverted around the body.

Slender body theory is used in the initial analysis of the body since its accuracy is consistent with the assumptions to be made in the wing-body interactions. Slender body theory assumes the total potential can be composed of a far-field potential dependent only on the area distribution and the Mach number and a near-field constant-density cross-flow potential solved subject to the three-dimensional boundary conditions of flow tangency at the surface (refs. 6 and 7). The equivalence rule extends the formulation to bodies of general cross section as indicated in figure 1. The flow around the actual body differs from that of the equivalent body of revolution by only a two-dimensional constant-density cross-flow potential that satisfies the flow tangency condition at the surface.

The constant-density cross-flow potential can be solved by any two-dimensional method. Dillenius, Goodwin, and Nielsen (ref. 8) have developed a solution applicable to noncircular fuselages composed of polar harmonic and two-dimensional source-sink terms. A conformal transformation and a distributed singularity approach are shown in figure 2. The conformal transformation is an adaption of the Theodorsen technique for airfoil design and was developed by Bonner of Rockwell International (ref. 9). The actual body is mapped into a circle and the potential for a source or doublet satisfying the boundary conditions for the equivalent body is transformed back to the physical plane. The method is very fast and simple but is limited to bodies in uniform flow fields that can be described in polar coordinates as a single-valued function of radius versus subtended angle. The distributed singularities approach was developed by J. Werner and A. R. Krenkel of Polytechnic Institute of New York and solves for the strengths of constant-strength source segments around the body by satisfying the flow tangency requirement. The method is applicable to very arbitrary bodies in nonuniform flow fields. Comparison of the conformal transformation technique of Bonner with experiment (ref. 10) for a parabolic body of revolution of fineness ratio 12 and elliptic cross section is shown in figure 3. The agreement at this high subsonic Mach number at angles of attack of 0° and 4° is generally very good.

Giesing, Kálmán, and Rodden (ref. 11) and Dillenius, Goodwin, and Nielsen (ref. 8) have developed methods based on general slender body theory in combination with vortex-lattice theory and the method of images. In both methods, the influence of the body on the lifting surface is accounted for by including the normal wash exterior to the body and then imaging the external singularities inside the body. Since the method of images is based on a two-dimensional analysis, it does not entirely negate the normal wash from the wing onto the body. Thus, the body loading in the nonuniform flow field of the lifting surface and image system must be recalculated to solve for this residual potential. The complete solution is an iterative process in which the continued interaction between the body and the lifting surface needs to be computed. However, reference 8 has indicated the method is strongly convergent and most of the effects are included after the first iteration. The method of images is very attractive in that no new unknowns are introduced into the solutions since the image strength and location are directly related to the external singularity strengths and the geometry of the body cross section.

13

An alternate approach has been used by Spangler, Mendenhall, and Dillenius (ref. 12) and Woodward (ref. 13) to approximately account for interference effects. In their analysis, interference panels are placed on constant-section stream tubes of the body. The normal wash from the body is included on the lifting surface exterior to the body and the interference panels exist to cancel the normal wash induced on the surface of the body. The net result is exactly the same as that using the method of images in that the initial influence of the body on the wing is included and the normal wash onto the body from the wing is negated. However, there are more equations to solve when the interference panels are used, although the region of influence of the wing on the body can generally be assumed to be within a couple of chord lengths of the wing root. A schematic of the utilization of general slender body theory with a traditional vortex-lattice system is shown in figure 4.

The methods of images (ref. 14) and interference paneling in combination with a vortex lattice are compared with an earlier modified Multhopp lifting-line approach (ref. 15) for a high-aspect-ratio wing-body combination in figure 5. Both the method of images and the method of interference panels give similar results and give lower results for the loadings than the earlier Multhopp results. Reference 11 has compared the method of images with the interference paneling used by Woodward and the agreement is excellent.

The assumption with either approach is that the flow field around the body in the presence of the wing is the same as that for the body alone. Thin-wing assumptions are used which do not account for the finite regions of intersection between a wing and a body or the longitudinal acceleration of flow over the body on the wing. Because of the singularities trailing downstream with either images or interference paneling in accounting for interference effects, the body representation is restricted to constant-section cylinders. The methods thus give identical results for equivalent positions of the wing above or below the midwing position as indicated in figure 6. The results presented are for a high-aspect-ratio wing-body combination using a vortex lattice with interference paneling.

A comparison of the theoretical and experimental (ref. 16) span loads for a wing-body combination is given in figure 7. All the theoretical methods over-estimate the span loading because of the low Reynolds number of the experiment (0.3×10^6). The more approximate theories, however, agree well in the loading prediction with the more exact surface singularity representations, such as those of Labrujere (ref. 17) or Hess (ref. 18), and, in general, adequate predictions of lift and moment are possible with the approximate theories.

The assumptions of the methods which limit their applicability to generalized configurations also enhance their capability as a preliminary design tool. Most of the wing-body interactions are handled and the computer resources required are small because of the relatively small number of unknowns. Since planar representations are used, the intersection of the wing and body is a line and the geometry can be input rapidly. The capability is provided to predict quickly and accurately overall lift, moment, and induced drag for complete configurations at the early design stage, such as in the store separation studies of reference 8. The prediction of optimum trimmed loadings subject to lift and moment constraints are also possible from a far-field equivalent-horseshoe-vortex Trefftz plane analysis such as in references 19 and 20.

14

QUADRILATERAL VORTEX AND SOURCE LATTICE SOLUTION

A method which computes the interfering flow fields of both wing and body simultaneously while still retaining the linearized boundary condition is that of Tulinius (ref. 21). The method distributes a series of constant-strength quadrilateral vortices over the surface of the body and in the region of the wing near the wing-body intersection region as shown in figure 8. Horseshoe vortices are used in regions of the wing away from the wing-body intersection region. A source lattice is distributed over the surface of the wing at the quarter-chord and three-quarter-chord of each panel, and the source strengths are defined as the local slopes of the thickness distribution independent of the wing lift. The influence of the quadrilateral vortex dies off rapidly at points away from the quadrilateral because of the canceling effects of adjacent sides. Hence, the panels can be extended over the fore and aft regions of the body. The analysis has been extended to predict thick wing and pylon-fuselage-fanpod-nacelle characteristics at subsonic speeds by placing the vortices along the mean camber line of the wing (ref. 22).

Results of the Tulinius wing-body program are compared with experiment in figures 9, 10, and 11 for a swept wing-body combination at a Mach number of 0.60 and an angle of attack of 4°. The unit span load $c_l c / C_L c_{av}$ and the longitudinal distribution of fuselage lift $c_{l,f} d/d_{max}$ are predicted very well by the theory (fig. 9); the fuselage lift increases rapidly in the region of the wing root. The pressure coefficients on the wing at two spanwise stations in figure 10 and the pressure coefficients on the body at longitudinal stations just above and below the wing in figure 11 are also predicted well. The body pressures are influenced by the wing primarily in the wing root region, and the pressures over the aft end of the body are not predicted because of viscous and separation effects. The agreement with theory is expected since the wing is relatively thin and attached in the midwing position.

The method cannot account for the longitudinal acceleration of flow over the body on the wing (speed bump effect) or equivalent high and low positions of the wing because of the linearized planar boundary conditions. The pressure coefficients and not just loadings are predicted so that streamlining and contouring of adjacent surfaces at high subsonic Mach numbers can be accomplished. Regions of intersecting surfaces are lines so that geometry description is relatively easy. The number of equations to solve for the simultaneous quadrilateral and horseshoe vortex strength increases in comparison with the slender body and planar wing analyses but the quality of the aerodynamic solution is higher since the body and wing flow fields are solved simultaneously.

SURFACE SINGULARITY POTENTIAL FLOW

In order to account for the full potential interactions between the wing and body, a surface singularity technique such as that in references 17, 18, 23, 24, or 25 must be used. In such a method, the singularities are placed on the surface of the wing and body such that the tangency and Kutta conditions are satisfied. The type of finite-element modeling used for the lifting surfaces has been varied, including (1) constant-strength surface source panels with a constant-strength vortex sheet on the surface (ref. 18), (2) constant-strength

15

source panels on the surface with interior vortex sheet (ref. 17), or (3) linearly varying source and quadratically varying doublet distributions on curved surface panels (ref. 25). Constant-strength source panels have been generally used to model the body with the lifting surface carried through the body in order to approximately account for the wing carry-throug' 'ift.

Such a surface singularity approach accounts for the finite intersection region of a wing and body as well as the longitudinal velocity perturbations of the body on the wing. However, the method requires a considerable amount of geometry specification to panel a complete configuration as shown in figure 12. The quality of the resulting aerodynamic solutions are a function of the particular finite elements chosen, their placement on the body, and the number chosen. Since matrix solution times are a function of the number of elements cubed, the paneling of complete configurations with a minimum of computer time while retaining desired accuracy is a difficult task. Recent advances to relieve the dependence of the resulting solution on the aerodynamic paneling chosen and to reduce the number of unknowns required have been made in references 25 to 27.

Results for the Hess surface singularity approach (ref. 18) are presented in figure 13 for the $A = 6$ untapered unswept wing attached in intermediate, high, and low positions to an infinite circular-cylinder body - the case considered earlier with the approximate theory. The local span loading and total lift vary with the relative placement of the wing on the body; the body loads are shown as average values since the available version of the computer program only outputs pressures and integrated loads for the body. The intersection of the wing section with the curved body is another curved region that tends to accelerate the flow under the wing in a high wing position and above the wing in a low wing position. Since the singularities are on the surface, the local velocity increase on the lower surface of the high wing decreases the local loading and vice versa. Thus, the surface singularity approach yields differences in potential theory for high and low wing placement, whereas, the linearized planar lifting surface theories do not. However, the integrated values of lift differ very little with wing placement, indicating again that the approximate theories are able to give reasonable estimates of the total forces and moments.

The surface singularity approach is a detail design tool applicable in the later stages of design after the initial planform sizes and locations have been determined, such as in the design of cruise overwing nacelle configurations in reference 28. The inverse design for the surface singularity approach has been completed in reference 24, but the procedure for generalized configurations is necessarily lengthy and difficult. The surface singularity approach allows the calculation of detailed pressure distributions in regions of adjacent surfaces (wing fillets, nacelle-strut intersections, etc.) so that contouring and streamlining for minimum adverse pressure and viscous drag can be accomplished.

CONCLUDING REMARKS

Various approximate methods utilizing some variation of general slender body theory in combination with a planar lifting-surface representation, such as the vortex-lattice method or the constant-pressure panel of Woodward, are adequate to estimate the loads, moments, and pressures in preliminary design

applications. Such methods require limited computer resources and simple geometry input specifications and are well suited to inverse design procedures since the number of unknowns are small and the planar boundary conditions are retained. The methods are most applicable to midwing cases with constant-section cylindrical bodies.

An extension of the vortex-lattice method to include a quadrilateral vortex representation of the body solves for the wing and body loads simultaneously. No restrictions on body shape or wing shape in the intersection regions are made although the thin-wing representation is retained. Regions of intersecting surfaces are curved lines and the geometry input remains relatively simple. With the method, pressures in regions of adjacent surfaces are predicted to allow contouring and streamlining. The method is also well suited to inverse design procedures for the wing in the presence of the body since the camber and thickness solutions are separate.

In order to accurately predict the correct potential flow pressures in areas of intersecting wings and bodies, a surface singularity approach is needed. The surface singularity approach removes all thin-wing and linearized-boundary-condition assumptions but more than doubles the number of unknowns to be solved and the geometry definition required. The detail pressure distributions in regions of intersecting surfaces are available so that adverse viscous effects can be minimized.

Viscous effects are not predicted in any of the methods. For the present, empirical or strip analyses must be used, such as in the prediction of viscous effects using an infinite yawed-wing analogy in two-dimensional strips along a swept wing. The usefulness of all the wing-body theories depend on how well the theoretical loadings or pressures can be related to the actual physical situation. The nonlinear and viscous effects, such as vortex formation near the wing-body juncture or separated flow at higher angles of attack, remains untractable computationally. The viscous calculation for generalized configurations across the Mach number range remains a far-term solution.

17

REFERENCES

1. Ashley, Holt; and Rodden, William P.: Wing-Body Aerodynamic Interaction. Annual Review of Fluid Mechanics, Vol. 4, M. Van Dyke, W. G. Vincenti, and J. V. Wehausen, eds., Annual Rev., Inc., 1972, pp. 431-472.

2. Morgan, Harry L., Jr.: A Computer Program for the Analysis of Multielement Airfoils in Two-Dimensional Subsonic, Viscous Flow. Aerodynamic Analyses Requiring Advanced Computers, Part II, NASA SP-347, 1975, pp. 713-747.

3. Garabedian, Paul R.: Computational Transonics. Aerodynamic Analyses Requiring Advanced Computers, Part II, NASA SP-347, 1975, pp. 1269-1280.

4. Chapman, Dean R.; Mark, Hans; and Pirtle, Melvin W.: Computer vs. Wind Tunnels for Aerodynamic Flow Simulations. Astronaut. & Aeronaut., 13, no. 4, Apr. 1975, pp. 22-35.

5. Bailey, F. R.; and Ballhaus, W. F.: Comparisons of Computed and Experimental Pressures for Transonic Flows About Isolated Wings and Wing-Fuselage Configurations. Aerodynamic Analyses Requiring Advanced Computers, Part II, NASA SP-347, 1975, pp. 1213-1231.

6. Adams, Mac C.; and Sears, W. R.: Slender Body Theory - Review and Extension. J. Aeronaut. Sci., vol. 20, no. 2, Feb. 1953, pp. 85-98.

7. Ashley, Holt; and Landahl, Marten: Aerodynamics of Wings and Bodies. Addison-Wesley Pub. Co., Inc., c.1965.

8. Dillenius, Marnix F. E.; Goodwin, Frederick K.; and Nielsen, Jack N.: Analytical Prediction of Store Separation Characteristics From Subsonic Aircraft. J. Aircr., vol. 12, no. 10, Oct. 1975, pp. 812-818.

9. Bonner, E.: Theoretical Prediction of Inviscid Three Dimensional Slender Body Flows. Report No. NA-74-687, Los Angeles Aircraft Div., Rockwell International Corp., 1974.

10. McDevitt, John B; and Taylor, Robert A.: Force and Pressure Measurements at Transonic Speeds for Several Bodies Having Elliptical Cross Sections. NACA TN 4362, 1958.

11. Giesing, J. P.; Kálmán, T. P.; and Rodden, W. P.: Subsonic Steady and Oscillatory Aerodynamics for Multiple Interfering Wings and Bodies. J. Aircr., vol. 9, no. 10, Oct. 1972, pp. 693-702.

12. Spangler, S. B.; Mendenhall, M. R.; and Dillenius, M. F. E.: Theoretical Investigation of Ducted Fan Interference for Transport-Type Aircraft. Analytic Methods in Aircraft Aerodynamics, NASA SP-228, 1970, pp. 703-719.

13. Woodward, Frank A.: Analysis and Design of Wing-Body Combinations at Subsonic and Supersonic Speeds. J. Aircr., vol. 5, no. 6, Nov.-Dec. 1968, pp. 528-534.

14. Giesing, Joseph P.: Lifting Surface Theory for Wing-Fuselage Combinations. Rep. DAC-67212, Vol. I, McDonnell Douglas, Aug. 1, 1968.

15. Weber, J.; Kirby, D. A.; and Kettle, D. J.: An Extension of Multhopp's Method of Calculating the Spanwise Loading of Wing-Fuselage Combinations. R. & M. No. 2872, British A.R.C., 1956.

16. Körner, H.: Untersuchungen zur Bestimmung der Druckverteilung a.. Flügel-Rumpf-Kombinationen - Teil I: MeBergebnisse für Mitteldeckeranordnung aus dem 1,3 m-Windkanal. DFVLR-Ber, Nr. 0562, 1969.

17. Labrujere, Th. E.; Loeve, W.; and Slooff, J. W.: An Approximate Method for the Calculation of the Pressure Distribution on Wing-Body Combinations at Subcritical Speeds. Aerodynamic Interference, AGARD CP No. 71, Jan. 1971, pp. 11-1 - 11-15.

18. Hess, John L.: Calculation of Potential Flow About Arbitrary Three-Dimensional Lifting Bodies. Rep. No. MDC J5679-01 (Contract NOC019-71-C-0524), McDonnell Douglas Corp., Oct. 1972.

19. Paulson, John W.: Applications of Vortex-Lattice Theory to Preliminary Aerodynamic Design. Vortex-Lattice Utilization, NASA SP-405, 1976. (Paper no. 7 of this compilation.)

20. Tulinius, J. R.; and Margason, Richard J.: Aircraft Aerodynamic Design and Evaluation Methods. AIAA Paper No. 76-15, Jan. 1976.

21. Tulinius, J.: Theoretical Prediction of Wing-Fuselage Aerodynamic Ch acteristics at Subsonic Speeds. Rep. No. NA-69-789, Los Angeles Div., North American Rockwell Corp., 1969.

22. Tulinius, J. R.: Theoretical Prediction of Thick Wing and Pylon-Fuselage-Fanpod-Nacelle Aerodynamic Characteristics at Subcritical Speeds - Part I: Theory and Results. NASA CR-137578, 1974.

23. Woodward, F. A.; Dvorak, F. A.; and Geller, E. W.: A Computer Program for Three-Dimensional Lifting Bodies in Subsonic Inviscid Flow. Rep. No. USAAMRDL-TR-74-18, U.S. Army, Apr. 1974. (Available from DDC as AD 782 202.)

24. Chen, Lee-Tzong, Suciu, Emil O.; and Morino, Luigi: A Finite Element Method for Potential Aerodynamics Around Complex Configurations. AIAA Paper No. 74-107, Jan.-Feb. 1974.

25. Ehlers, F. Edward; Johnson, Forrester T.; and Rubbert, Paul E.: Advanced Panel-Type Influence Coefficient Methods Applied to Subsonic and Supersonic Flows. Aerodynamic Analyses Requiring Advanced Computers, Part II, NASA SP-347, 1975, pp. 939-984.

26. Hess, John L.: The Use of Higher-Order Surface Singularity Distributions to Obtain Improved Potential Flow Solutions for Two-Dimensional Lifting Airfoils. Comput. Methods Appl. Mech. & Eng., vol. 5, no. 1, Jan. 1975, pp. 11-35.

27. Bristow, D. R.: A New Surface Singularity Approach for Multi-Element Airfoil Analysis and Design. AIAA Paper No. 76-20, Jan. 1976.

28. Mohn, L. W.: Comparison of Wind-Tunnel Test Results at $M_\infty = 0.7$ With Results From the Boeing TEA-230 Subsonic Flow Method. NASA CR-2554, 1975.

FLOW FIELD AT ANY POINT DUE TO AN ARBITRARY BODY IS GIVEN BY EQUIVALENCE RULE:

| FLOW FIELD DUE TO ACTUAL BODY | = | SOLUTION FOR EQUIVALENT BODY OF REVOLUTION | + | 2-D SOLUTION FOR ACTUAL BODY CROSS-SECTION A-A | − | 2-D SOLUTION FOR EQUIVALENT CROSS-SECTION A-A |

3-D BOUNDARY CONDITIONS ARE SATISFIED IN THESE 2-D SOLUTIONS
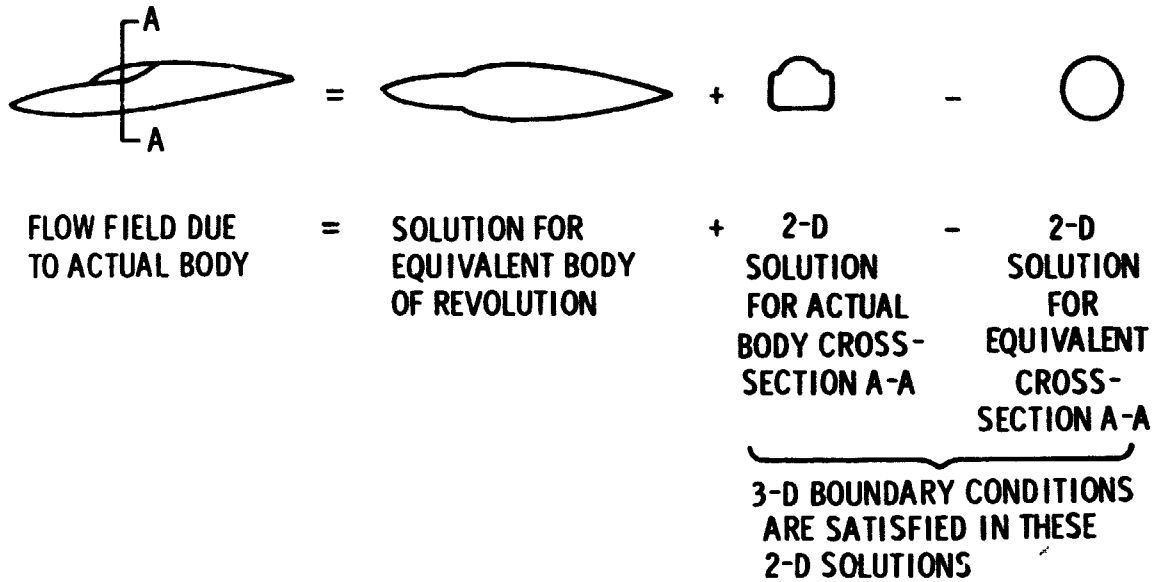
Figure 1.- General slender body theory.

u-PLANE   ū-PLANE

CONFORMAL TRANSFORMATION   DISTRIBUTED SINGULARITIES
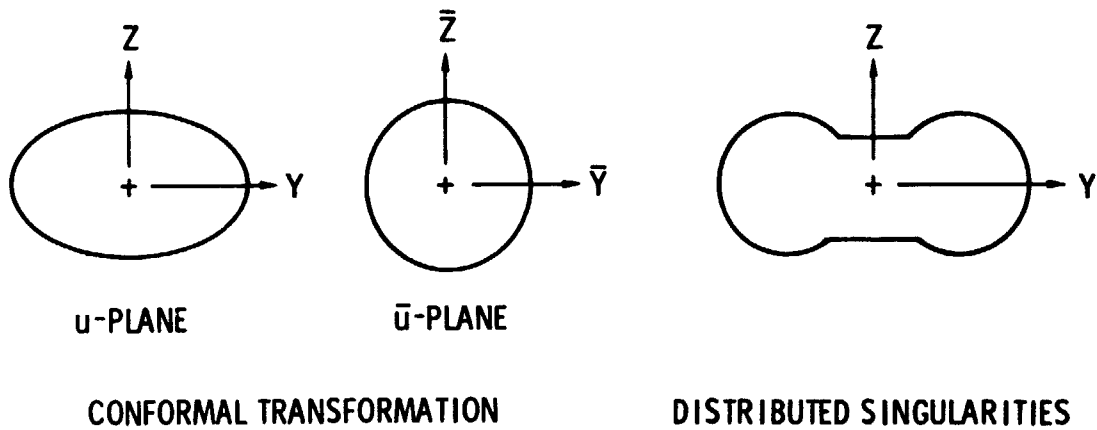
Figure 2.- Methods for solving two-dimensional cross-flow potential for arbitrary cross sections.
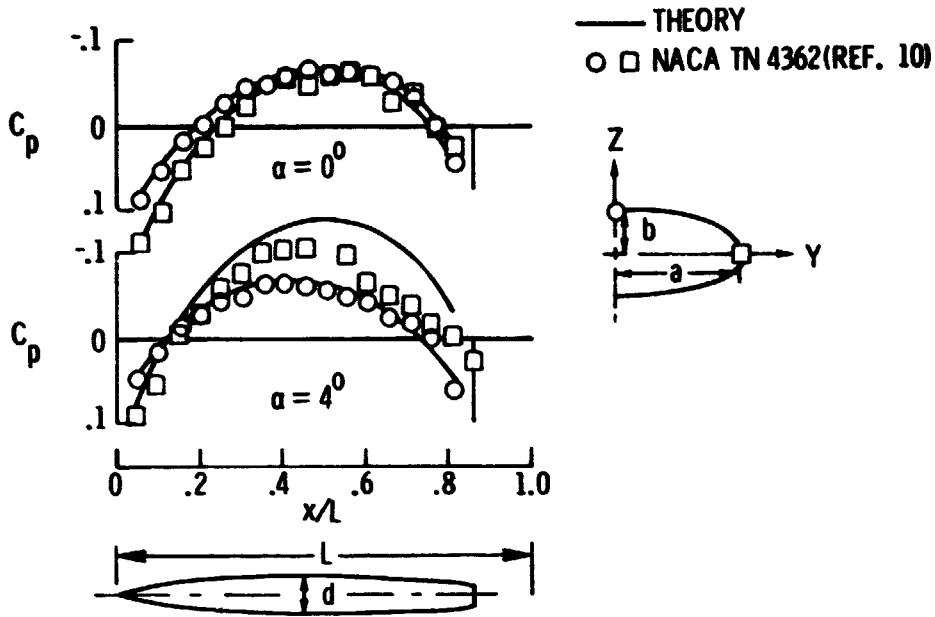
Figure 3.- Comparison of slender body theory and experiment.
L/d = 12; M_∞ = 0.9;   a/b = 3.
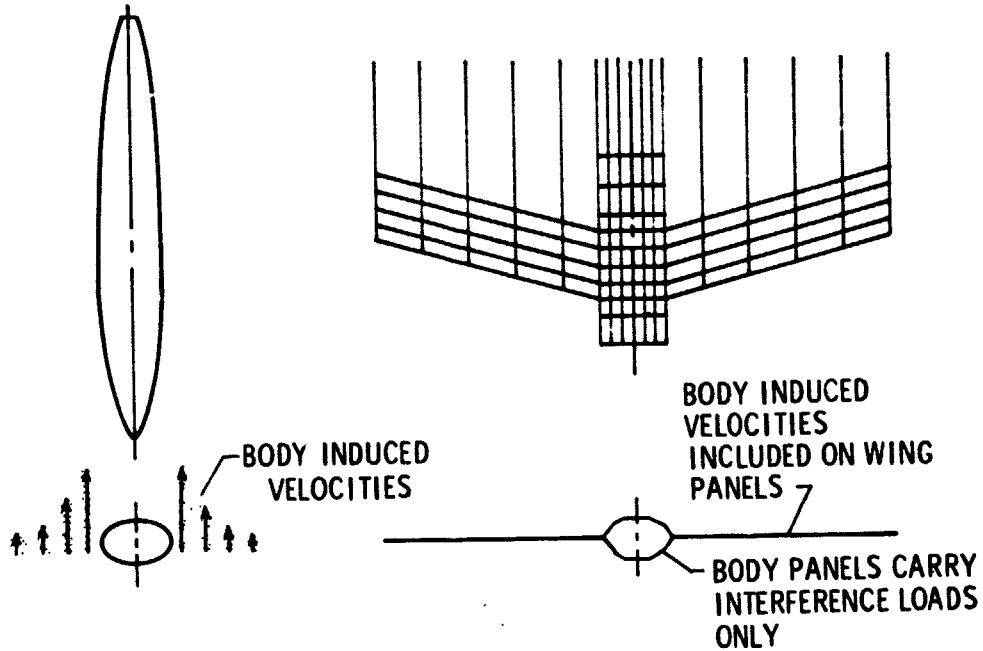
Figure 4.- Schematic of utilization of general slender body in
vortex-lattice theory.
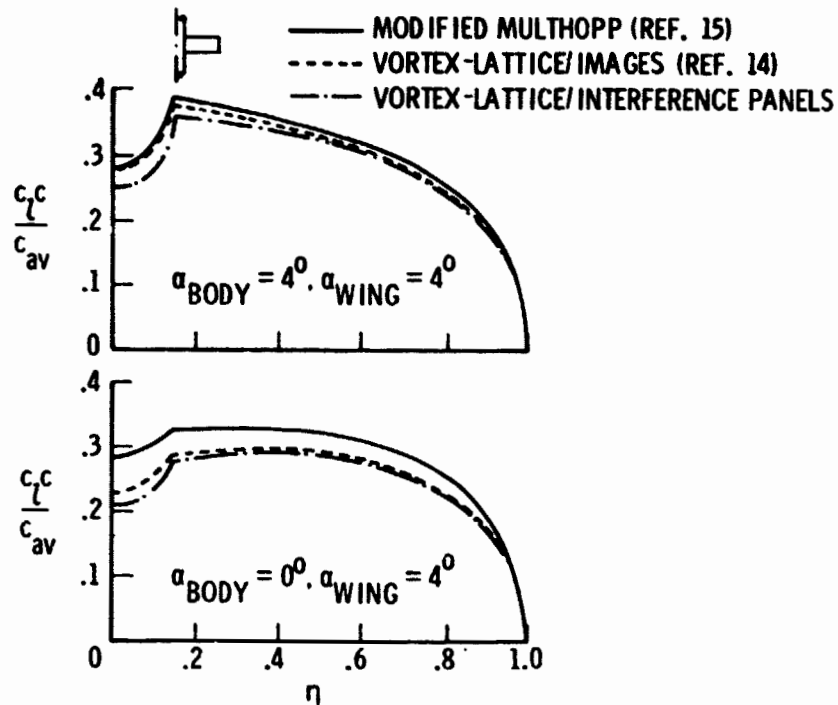
Figure 5.- Spanwise load calculation for wing-body combination.
$M_\infty = 0$; $A = 5$; $d/c = 0.72$; $\Lambda = 0$; $\lambda = 1$.
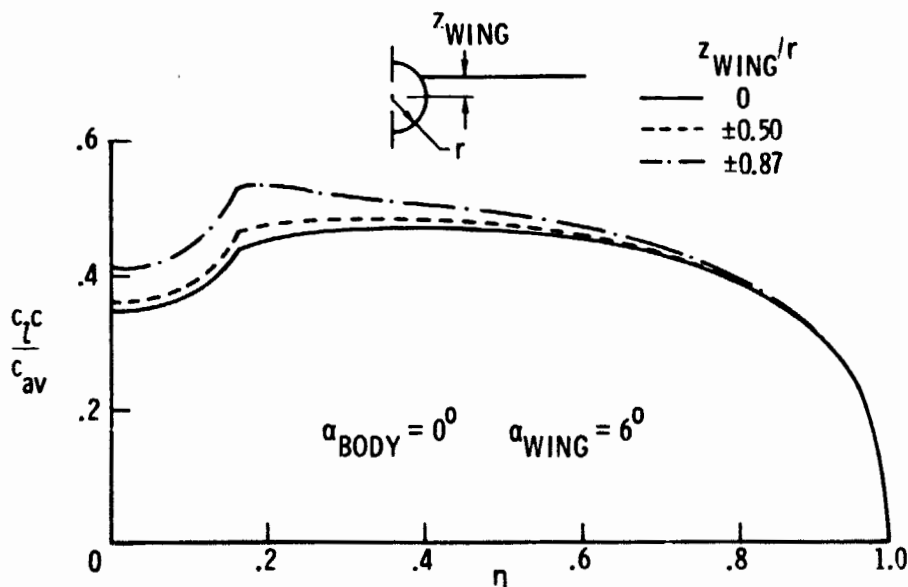
Figure 6.- Variation of wing placement for $A = 6$ wing and infinite circular-cylinder combination using vortex lattice with interference paneling. $M_\infty = 0$; $d/c = 1$; $\Lambda = 0$; $\lambda = 1$.

22
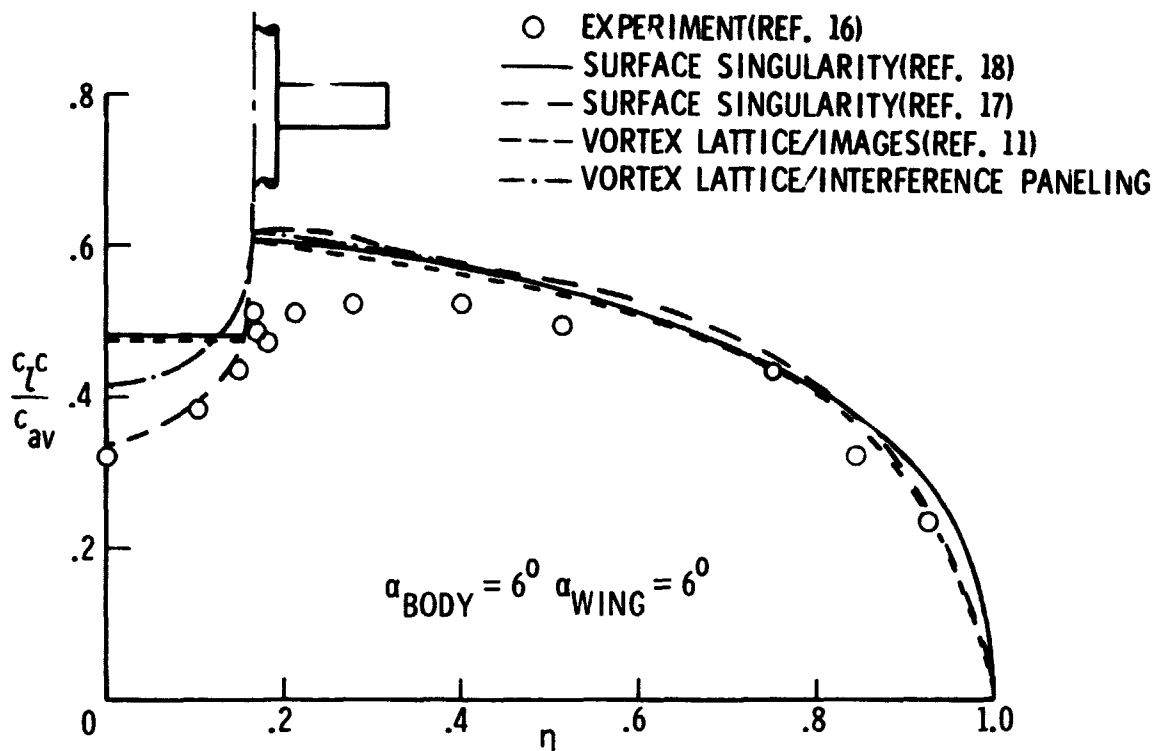
Figure 7.- Comparison of theory and experiment for $A = 6$ wing and infinite circular-cylinder combination. RAE 101 section; $M_\infty = 0$; $d/c = 1$; $\Lambda = 0$; $\lambda = 1$.
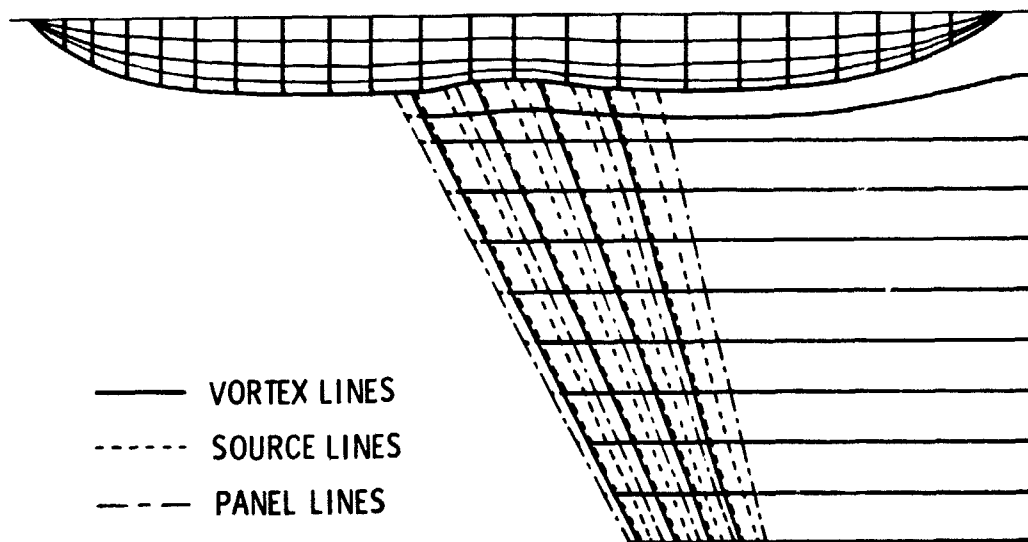
Figure 8.- Quadrilateral vortex and source lattice analysis and design.
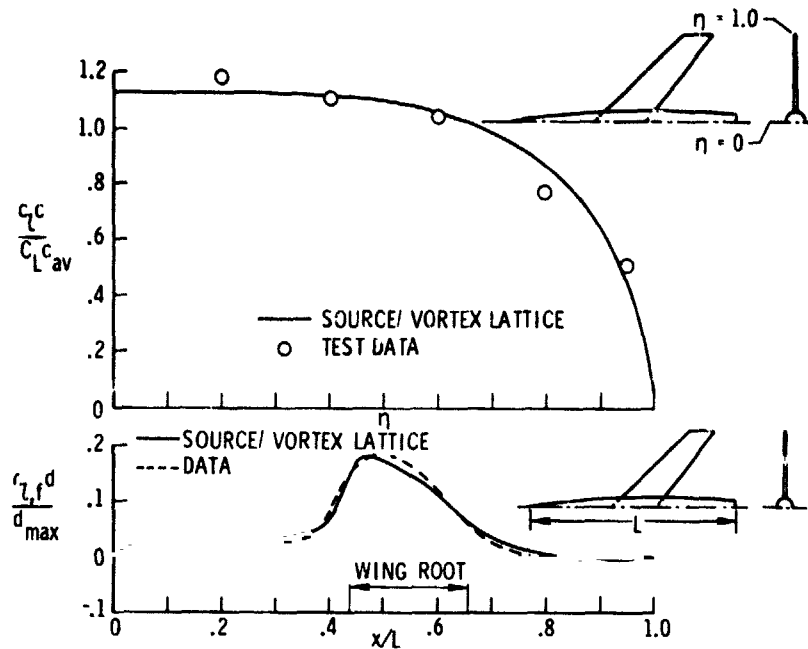
Figure 9.- Quadrilateral vortex and source lattice results for a wing-body combination. $M_\infty = 0.6$; $\alpha = 4^\circ$.
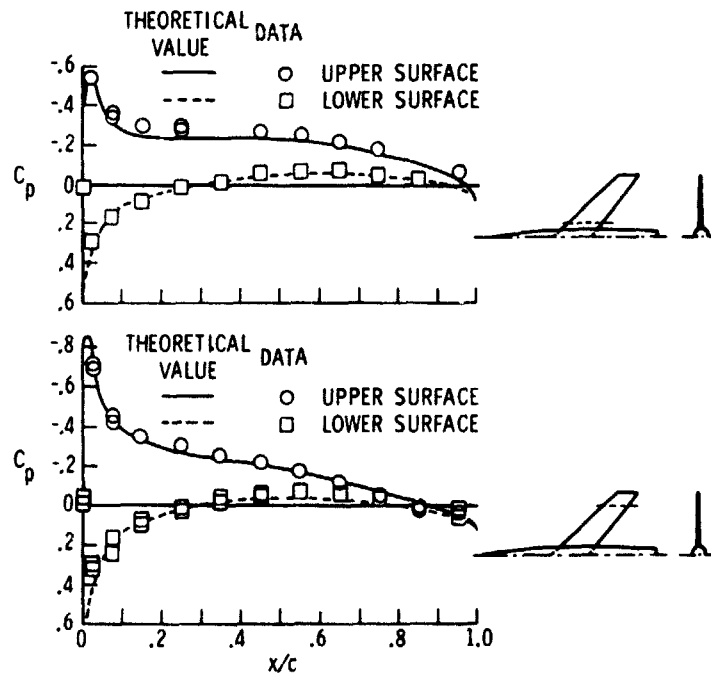
Figure 10.- Quadrilateral vortex and source lattice wing-surface pressure coefficients. $M_\infty = 0.6$; $\alpha = 4^\circ$.

24
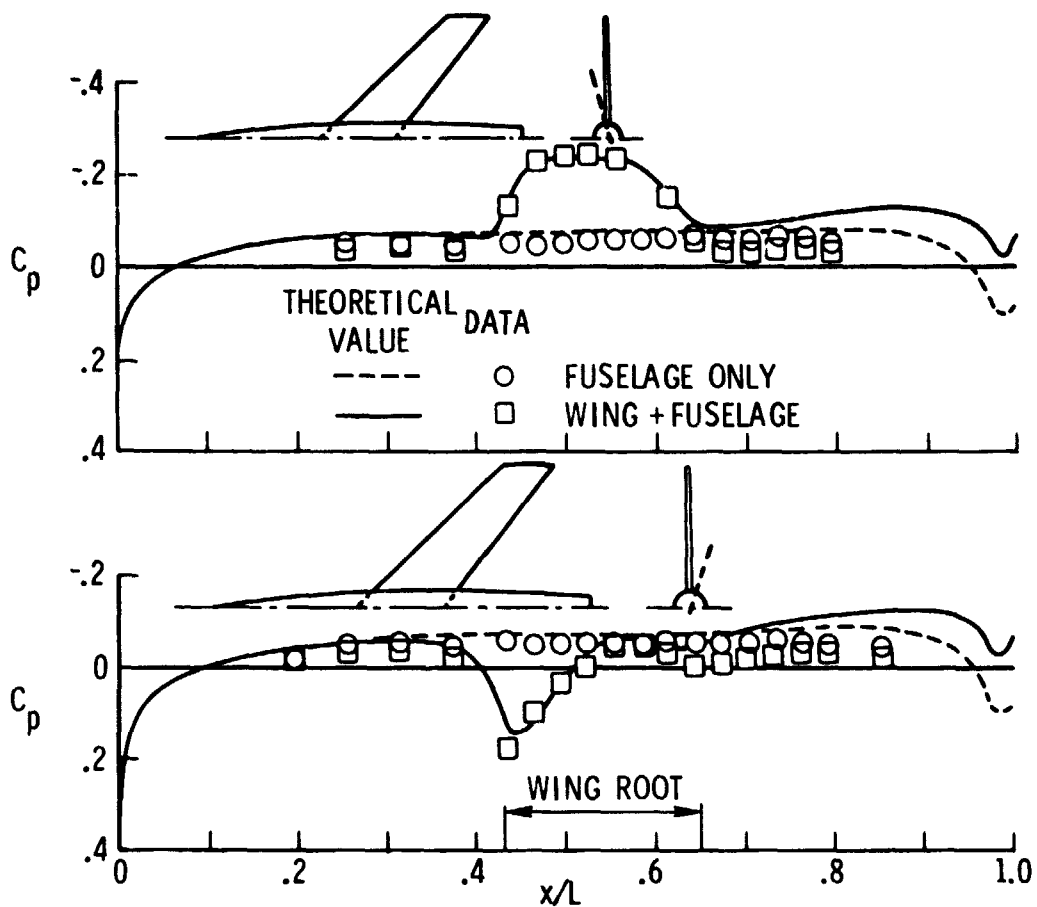
Figure 11.- Quadrilateral vortex and source lattice body-surface pressure coefficients. $M_\infty = 0.6$; $\alpha = 4^\circ$.
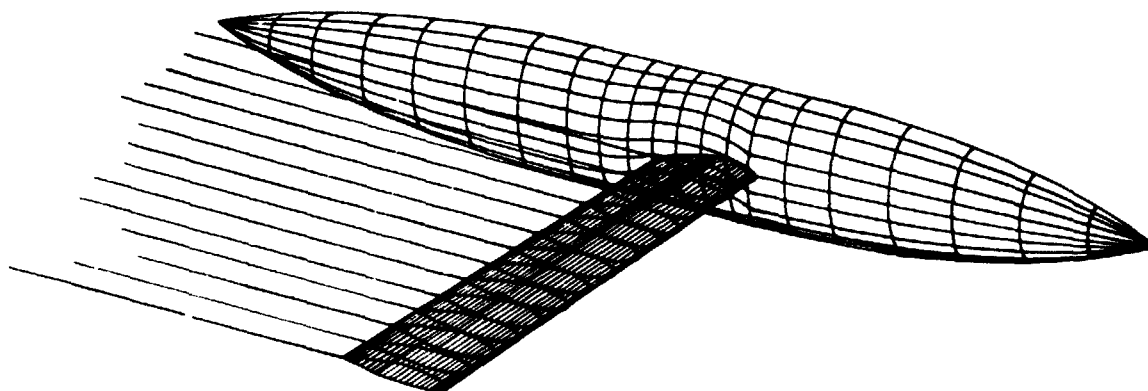
Figure 12.- Representative paneling for three-dimensional surface singularity approach.
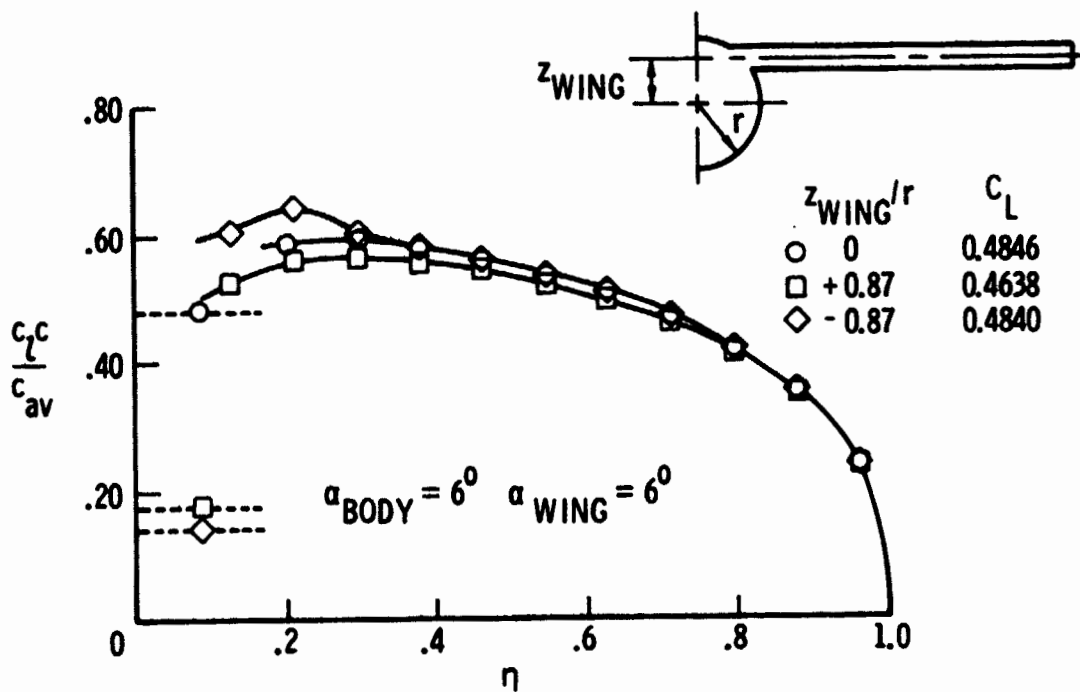
Figure 13.- Variation of wing placement for $A = 6$ wing and infinite circular-cylinder combination using Hess surface singularity approach (ref. 18). RAE 101 section (thickness = 0.09c); $M_\infty = 0$; d/c = 1; $\Lambda = 0$; $\lambda = 1$.

EXTENDED APPLICATIONS OF THE VORTEX LATTICE METHOD

Luis R. Miranda
Lockheed-California Company

SUMMARY

The application of the vortex lattice method to problems not usually dealt with by this technique is considered. It is shown that if the discrete vortex lattice is considered as an approximation to surface-distributed vorticity, then the concept of the generalized principal part of an integral yields a residual term to the vortex-induced velocity that renders the vortex lattice method valid for supersonic flow. Special schemes for simulating non-zero thickness lifting surfaces and fusiform bodies with vortex lattice elements are presented. Thickness effects of wing-like components are simulated by a double vortex lattice layer, and fusiform bodies are represented by a vortex grid arranged on a series of concentrical cylindrical surfaces. Numerical considerations peculiar to the application of these techniques are briefly discussed.

INTRODUCTION

The several versions or variations of the vortex lattice method that are presently available have proven to be very practical and versatile theoretical tools for the aerodynamic analysis and design of planar and non-planar configurations. The success of the method is due in great part to the relative simplicity of the numerical techniques involved, and to the high accuracy, within the limitations of the basic theory, of the results obtained. But most of the work on vortex lattice methods appears to have concentrated on subsonic flow application. The applicability of the basic techniques of vortex lattice theory to supersonic flow has been largely ignored. It is one of the objectives of this paper to show how the vortex lattice method can be easily extended to deal with problems at supersonic Mach numbers with the same degree of success that it enjoys in subsonic flow.

The other objective of this paper is to discuss a couple of schemes by which it is possible to simulate thickness and volume effects by using vortex lattice elements only. This represents an alternative, with somewhat reduced computational requirements, to the method of quadrilateral vortex rings (refs. 1 and 2). The simulation of thickness and volume effects makes possible the computation of the surface pressure distribution on wing-body configurations. The fact that this can be done without having to resort to additional types of singularities, such as sources, results in a simpler digital computer code.

THE BASIC EQUATIONS

Ward has shown, (ref. 3), that the small-perturbation, linearized flow of an inviscid compressible fluid is governed by the three first order vector equations:

$$\nabla \times \overline{v} = \overline{\omega}, \qquad \nabla \cdot \overline{w} = Q, \qquad \overline{w} = \Psi \cdot \overline{v} \qquad (1)$$

on the assumption that the vorticity $\overline{\omega}$ and the source intensity Q are known functions of the point whose position vector is $\overline{R}$. The vector $\overline{v}$ is the perturbation velocity with orthogonal cartesian components u, v, and w, and Ψ is a constant symmetrical tensor that for orthogonal cartesian coordinates with the x-axis aligned with the freestream direction has the form

$$\Psi = \begin{bmatrix} 1 - M_\infty^2 & 0 & 0 \\ 0 & 1 & 0 \\ 0 & 0 & 1 \end{bmatrix} \qquad (2)$$

where M_∞ is the freestream Mach number. If $\beta^2 = 1-M_\infty^2$, then the vector $\overline{w}$ has the components $\overline{w} = \beta^2 u \, \overline{I} + v \, \overline{J} + w \, \overline{k}$. This vector was first introduced by Robinson (ref. 4), who called it the "reduced current velocity". If $\overline{u}$ denotes the total velocity vector, i.e., $\overline{u} = (u_\infty + u) \, \overline{I} + v \, \overline{J} + w \, \overline{k}$, and ρ the fluid density, then it can be shown that for irrotational and homentropic flow

$$\rho \, \overline{u} = \rho_\infty \, \overline{u}_\infty + \rho_\infty \, \overline{w} + \text{higher order terms} \qquad (3)$$

where the subscript ∞ indicates the value of the quantity at upstream infinity, e.g., $\overline{u}_\infty = u_\infty \, \overline{I}$. Therefore, to a linear approximation, the vector $\overline{w}$ is directly related to the perturbation mass flux as follows:

$$\overline{w} = (\rho \, \overline{u} - \rho_\infty \, \overline{u}_\infty) / \rho_\infty \qquad (4)$$

The second equation of (1), i.e., the continuity condition, shows that for source-free flows (Q = 0), w is a conserved quantity.

Ward has integrated the three first order vector equations directly without having to resort to an auxiliary potential function. He obtained two different solutions for $\overline{v}$ ($\overline{R}$), depending on whether β^2 is positive (subsonic flow), or negative (supersonic flow). These two solutions can be combined formally into a single expression if the following convention is used:

$$K = 2 \quad \text{for} \quad \beta^2 > 0$$
$$K = 1 \quad \text{for} \quad \beta^2 < 0$$
$$R_\beta = \text{Real part of} \left\{ (x-x_1)^2 + \beta^2 \left[(y-y_1)^2 + (z-z_1)^2 \right] \right\}^{1/2}$$

28

$\displaystyle\oint$ = Finite part of integral as defined by Hadamard (refs. 5 and 6).

The resulting solution for the perturbation velocity $\bar{v}$ at the point whose position vector is $\bar{R}_1 = x_1\,\bar{i} + y_1\,\bar{j} + z_1\,\bar{k}$, is given by

$$\bar{v}\,(\bar{R}_1) = -\frac{1}{2\pi K}\oint_3 \bar{n}\cdot\bar{w}\,(\bar{R})\,\nabla\frac{1}{R_\beta}\quad dS$$

$$+\frac{\beta^2}{2\pi K}\oint_S \{\bar{n}\times\bar{v}\,(\bar{R})\}\times\frac{\bar{R}-\bar{R}_1}{R_\beta^3}\quad dS$$

$$+\frac{1}{2\pi K}\oint_V Q(\bar{R})\,\nabla\frac{1}{R_\beta}\,dV +\frac{\beta^2}{2\pi K}\oint_V\frac{\bar{R}-\bar{R}_1}{R_\beta^3}\times\bar{w}(\bar{R})\,dV \quad (5)$$

This formula determines the value of $\bar{v}$ within the region V bounded by the surface S. The vector $\bar{n}$ is the unit outward (from the region V) normal to the surface S. Furthermore, it is understood that for supersonic flow only those parts of V and S lying within the domain of dependence (Mach forecone) of the point $\bar{R}_1$ are to be included in the integration.

For source-free ($Q\equiv0$), irrotational ($\bar{w}\equiv0$) flow, equation (5) reduces to

$$\bar{v}\,(\bar{R}_1) = -\frac{1}{2\pi K}\oint_S \bar{n}\cdot\bar{w}\,(\bar{R})\,\nabla\frac{1}{R_\beta}\quad dS +\frac{\beta^2}{2\pi K}\oint_S\{\bar{n}\times\bar{w}(\bar{R})\}\frac{\bar{R}-\bar{R}_1}{R_\beta^3}\,dS \quad (6)$$

This is a relation between $\bar{v}$ inside S and the values of $\bar{n}\cdot\bar{w}$ and $\bar{n}\times\bar{v}$ on S, but these two quantities cannot be specified independently on S.

To determine the source-free, irrotational flow about an arbitrary body B by means of equation (6), assume that the surface S coincides with the wetted surface of the body, with any trailing wake that it may have, and with a sphere of infinite radius enclosing the body and the whole flow field about it, namely, $S = S_B + S_W + S_\infty$.

This surface S divides the space into two regions, V_e external to the body, and V_i internal to it. Applying equation (6) to both V_e and V_i, since the integrals over S_∞ converge to zero, the following expression is obtained:

$$\bar{v}(\bar{R}_1) = \frac{1}{2\pi K} \oint_{S_B + S_W} \bar{N} \cdot \Delta \bar{w}(\bar{R}) \nabla \frac{1}{R_\beta} \, dS - \frac{\beta^2}{2\pi K} \oint_{S_B + S_W} \{\bar{N} \times \Delta \bar{v}(\bar{R})\} \times \frac{\bar{R} - \bar{R}_1}{R^3_\beta} \, dS \quad (7)$$

where $\bar{N} = \bar{n}_1 = -\bar{n}_e$ is the unit normal to the body, or wake as the case may be, positive from the interior to the exterior of the body, $\Delta \bar{w} = \bar{w}_e - \bar{w}_1$, and $\Delta \bar{v} = \bar{v}_e - \bar{v}_1$. Here the subscripts designate the values of the quantities on the corresponding face of S. The first surface integral can be considered as representing the contribution of a source distribution of surface density $\bar{N} \cdot \Delta \bar{w}$, while the second surface integral gives the contribution of a vorticity distribution of surface density $\bar{N} \times \Delta \bar{v}$.

If the boundary condition of zero mass flux through the surface $S_B + S_W$ is applied to both external and internal flows

$$\bar{N} \cdot \rho \bar{u}_e = \bar{N} \cdot (\rho_\infty \bar{u}_\infty + \rho_\infty \bar{w}_e) = 0$$

$$\bar{N} \cdot \rho \bar{u}_1 = \bar{N} \cdot (\rho_\infty \bar{u}_\infty + \rho_\infty \bar{w}_1) = 0 \quad (8)$$

then the condition $\bar{N} \cdot \Delta \bar{w} = 0$ exists over $S_B + S_W$, and the flow field is uniquely determined by

$$\bar{v}(\bar{R}_1) = -\frac{\beta^2}{2\pi K} \oint_{S_B + S_W} \bar{\gamma}(\bar{R}) \times \frac{\bar{R} - \bar{R}_1}{R^3_\beta} \, dS \quad (9)$$

where $\bar{\gamma}(\bar{R}) = \bar{N} \times \Delta \bar{v}$ is the surface vorticity density.

EXTENSION TO SUPERSONIC FLOW

In order to extend the application of the vortex lattice method to supersonic flow, it is essential to consider the fundamental element of the method, the vortex filament, as a numerical approximation scheme to the integral expression (9) instead of a real physical entity. The velocity field generated by a vortex filament can be obtained by a straightforward limiting process, the result being

$$\bar{v}(\bar{R}_1) = \frac{-\beta^2}{2\pi K} \oint_C \bar{\Gamma} \times \frac{\bar{R} - \bar{R}_1}{R^3_\beta} \, d\ell \quad (10)$$

30

where $\bar{\Gamma} = \lim_{\substack{\bar{\gamma} \to \infty \\ \delta \to 0}} \bar{\gamma} \cdot \delta$

δ is a dimension normal to γ, and $d\ell$ is the distance element along γ. In the classical vortex lattice method, applicable only to subsonic flow, the vorticity distribution over the body and the wake, i.e., over the surface $S_B + S_W$, is replaced by a suitable arrangement of vortex filaments whose velocity fields are everywhere determined by equation (10). This procedure is no longer appropriate for supersonic flow. For this latter case, it is necessary to go back to equation (9) and to derive an approximation to it. This is done in the following.

If the surface $S_B + S_W$, which defines the body and its wake, is considered as being composed of a large number of discrete flat area elements τ over which the surface vorticity density $\bar{\gamma}$ can be assumed approximately constant, then equation (9) can be approximated by the following equation:

$$\bar{v}(\bar{R}_1) = -\frac{\beta^2}{2\pi K} \sum_{J=1}^{N} \oint_{\tau_J} \bar{\gamma}_J \times \frac{\bar{R} - \bar{R}_1}{R_\beta^3} \, dS \qquad (11)$$

where N is the total number of discrete area elements τ. When the point whose position vector is $\bar{R}_1$ is not part of τ_J, the integral over this discrete area can be approximated by the mean value theorem as follows:

$$\oint_{\tau_J} \bar{\gamma}_J \times \frac{\bar{R} - \bar{R}_1}{R_\beta^3} \, dS = \bar{\gamma}_J \, \delta_J \times \oint_{C_J} \frac{\bar{R} - \bar{R}_1}{R_\beta^3} \, d\ell \qquad (12)$$

where C_J is a line in τ_J parallel to the average direction of $\bar{\gamma}$ in τ_J, δ_J is a distance normal to C_J, and $d\ell$ is the arc length element along C_J. This means that the velocity field induced by a discrete vorticity patch τ_J can be approximated for points outside of τ_J by some mean discrete vortex line whose strength per unit length is $\gamma_J \delta_J$. But if the point $\bar{R}_1$ is part of the discrete area τ, the integral in equation (11) has an inherent singularity of the Cauchy type due to the fact that $\bar{R} = \bar{R}_1$ at some point within τ. In order to evaluate the integral expression for this case, consider a point close to $\bar{R}_1$ but located just above τ by a distance ϵ. As indicated in figure 1, the area of integration in τ is divided into two regions, $A_{\tau-\epsilon}$ and A_ϵ. Obviously, the integral over $A_{\tau-\epsilon}$ has no Cauchy-type singularity, Hadamard's finite part concept being sufficient to perform the indicated integration. Thus,

$$\oint_{\tau} \bar{\gamma} \times \frac{\bar{R}-\bar{R}_1}{R^3_\beta} \, dS = \lim_{\epsilon \to 0} \oint_{A_\epsilon} + \lim_{\epsilon \to 0} \oint_{A_{\tau-\epsilon}}$$

$$= \lim_{\epsilon \to 0} I(\epsilon) + \bar{\gamma} \wedge \times \oint_C \frac{\bar{R}-\bar{R}_1}{R^3_\beta} \, d\ell \qquad (13)$$

The last integral in equation (13) represents the conventional discrete vortex line contribution whose evaluation presents no difficulty. In order to determine the integration denoted by $I(\epsilon)$ assume that, for simplicity, the coordinate system is centered at the point $\bar{R}_1$, and that the x-y plane is determined by the discrete area τ. Then, if γ denotes the modulus of $\bar{\gamma}$,

$$I(\epsilon) = \gamma \oint_{A_\epsilon} \frac{y \sin \Lambda - x \cos \Lambda}{\{x^2 - B^2(y^2 + \epsilon^2)\}^{3/2}} \, dx \, dy \qquad (14)$$

where Λ is the angle between the y-axis and the direction of the vorticity in τ, and $B^2 = -\beta^2 > 0$ (supersonic flow). The components of the vector cross product $\bar{\gamma} \times (\bar{R}-\bar{R}_1) = \bar{\gamma} \times \bar{R}$ which are not normal to the plane of τ have been left out of equation (14) because, when the limit operation $\epsilon \to 0$ is carried out, they will vanish. The area A_ϵ is bounded by a line parallel to the vorticity direction going through $x -(1+B)\epsilon$ and by the intersection of the Mach forecone from the point $(0, 0, \epsilon)$ with the τ-plane, consequently, if the integration with respect to x is performed first,

$$I(\epsilon) = \gamma \cos \Lambda \oint_{\lambda_1}^{\lambda_2} \left\{ \int_{ty -(1+B)\epsilon}^{-B\sqrt{y^2 + \epsilon^2}} \frac{ty - x}{\{x^2 - B^2(y^2 + \epsilon^2)\}^{3/2}} \, dx \right\} dy \qquad (15)$$

where $t = \tan \Lambda$, and λ_1, λ_2 are the values of y corresponding to the intersection of the line $x = ty -(1+B)\epsilon$ with the hyperbola $x = -B\sqrt{y^2 + \epsilon^2}$. Let $\phi = \epsilon^2(1+2B)-2(1+B)\epsilon ty -(B^2-t^2) y^2$, then the finite part of the x-integration yields

$$I(\epsilon) = \gamma \cos \Lambda \oint_{\lambda_1}^{\lambda_2} \left\{ \frac{ty \, (ty-(1+B)\epsilon)}{B^2 (y^2 + \epsilon^2)\sqrt{\phi}} - \frac{1}{\sqrt{\phi}} \right\} dy$$

32

$$= \frac{Y \cos \Lambda}{B^2} \oint_{\lambda_1}^{\lambda_2} \left\{ \frac{B^2 \varepsilon - (1+B)\varepsilon t y - (B^2-t^2)y^2}{y^2 + \varepsilon^2} \right\} \frac{dy}{\sqrt{\phi}} \qquad (16)$$

Since ε is a very small quantity, the variation of y in the interval (λ_1, λ_2) is going to be equally small, and, therefore, the quantity within brackets in the last integrand of equation (16) can be replaced by a mean value and taken outside of the integral sign. The same is not true of the term $1/\sqrt{\phi}$ since it will vary from ∞ for $y = \lambda_1$, go through finite values in the integration interval, and then again increase to ∞ for $y = \lambda_2$. With this in mind, and if $\tilde{y}$ denotes a mean value of y, $I(\varepsilon)$ can be written as

$$I(\varepsilon) = \frac{Y \cos \Lambda}{B^2} \frac{B^2 \varepsilon - (1+B)\varepsilon t \tilde{y} - (B^2-t^2)\tilde{y}^2}{\tilde{y}^2 + \varepsilon^2} \oint_{\lambda_1}^{\lambda_2} \frac{dy}{\sqrt{\phi}} \qquad (17)$$

But λ_1, λ_2 are the roots of $ty - \varepsilon = -B\sqrt{y^2 + \varepsilon^2}$, i.e., they are the roots of the polynomial denoted by ϕ. Thus

$$\sqrt{\phi} = \sqrt{\varepsilon^2(1+2B) - 2(1+B)\varepsilon t y - (B^2-t^2)y^2} = \sqrt{B^2-t^2} \cdot \sqrt{(\lambda_1-y)(y-\lambda_2)} \qquad (18)$$

Introducing this expression for $\sqrt{\phi}$ into (17), and taking the limit $\varepsilon \to 0$, the following value for $I(\varepsilon)$ is obtained:

$$I(0) = \lim_{\varepsilon \to 0} I(\varepsilon) = -\frac{Y \cos \Lambda}{B^2} \sqrt{B^2-t^2} \oint_{\lambda_1}^{\lambda_2} \frac{dy}{\sqrt{(\lambda_1-y)(y-\lambda_2)}} \qquad (19)$$

The integral appearing in equation (19) can be easily evaluated by complex variable methods; its value is found to be

$$\oint_{\lambda_1}^{\lambda_2} \frac{dy}{\sqrt{(\lambda_1-y)(y-\lambda_2)}} = \pi \qquad (20)$$

The contribution of the inherent singularity to the velocity field induced by vorticity patch $\mathcal{T}$, within $\mathcal{T}$, denoted herein by w^*, is therefore given by

$$w^* = -\frac{\beta^2}{2\pi} \lim_{\epsilon \to 0} I(\epsilon) = -\frac{\gamma \cos \Lambda}{2} \sqrt{\beta^2 - t^2} \tag{21}$$

This contribution is perpendicular to the plane of $\mathcal{T}$, and it has only physical meaning when $\beta^2 > t^2$, i.e., when the vortex lines are swept in front of the Mach lines. It is expression (21), taken in conjunction with equation (12), that makes the vortex lattice method applicable to supersonic flow.

MODELING OF LIFTING SURFACES WITH THICKNESS

The method of quadrilateral vortex rings placed on the actual body surface (ref. 1) provides a way of computing the surface pressure distribution of arbitrary bodies using discrete vortex lines only. Numerical difficulties may occur when the above method is applied to the analysis of airfoils with sharp trailing edges due to the close proximity of two vortex surfaces of nearly parallel direction. An alternative approach, requiring somewhat less computer storage and easier to handle numerically, consists in using a double, or biplanar, sheet of swept horseshoe vortices to model a lifting surface with thickness, as shown schematically in figure 2. This constitutes an approximation to the true location of the singularities, similar in nature to the classical lifting surface theory approximation of a cambered sheet.

All the swept horseshoe vortices, and their boundary condition control points, corresponding to a given surface, upper or lower, are located in a same plane. The upper and lower surface lattice planes are separated by a gap which represents the chordwise average of the airfoil thickness distribution. The results are not too sensitive to the magnitude of this gap; any value between one half to the full maximum chordwise thickness of the airfoil has been found to be adequate, the preferred value being two thirds of the maximum thickness. Furthermore, the gap can vary in the direction normal to the x-axis to allow for spanwise thickness taper. On the other hand, the chordwise distribution, or spacing, of the transverse elements of the horseshoe vortices have a significant influence on the accuracy of the computed surface pressure distribution. For greater accuracy, for a given chordwise number of horseshoe vortices, the transverse legs have to be longitudinally spaced according to the 'cosine' distribution law

$$x_J^v - x_o = \frac{c}{2} \left[1 - \cos \left(\pi \frac{2J-1}{2N} \right) \right] \tag{22}$$

where $x_J^v - x_o$ represents the distance from the leading edge to the midpoint of the swept leg of the Jth horseshoe vortex, c is the length of the local chord running through the midpoints of a given chordwise strip, and N is the number of horseshoe vortices per strip. The chordwise control point location

corresponding to this distribution of vortex elements is given by

$$x_J^C - x_o = \frac{c}{2}\left[1 - \cos\left(\pi\frac{J}{N}\right)\right] \tag{23}$$

The control points are located along the centerl ne, or midpoint line, of the chordwise strip (fig. 3). Lan has shown (ref. 7) that the chordwise 'cosine' collocation of the lattice elements, defined by equations (22) and (23), greatly improve the accuracy of the computation of the effects due to lift. His results are directly extendable to the computation of surface pressure distributions of wings with thickness by the 'biplanar' lattice scheme presented herein.

The small perturbation boundary condition

$$\bar{v} \cdot \bar{n}' = -\bar{u}_\infty \cdot \bar{n} \tag{24}$$

is applied at the control points. In equation (24), $\bar{n} = l\bar{I} + m\bar{J} + n\bar{K}$, and $\bar{n}' = m\bar{J} + n\bar{K}$, where l, m, and n are the direction cosines of the normal to the actual airfoil surface. Equation (24) implies that $|lu| \ll |mv + nw|$. The use of the small perturbation boundary condition is consis ent with the present 'biplanar' approach to the simulation of thick wings.

MODELING OF FUSIFORM BODIES

The modeling of fusiform bodies with horseshoe vortices requires a special concentrical vortex lattice if the simulation of the volume displacement effects, and the computation of the surface pressure distribution, are to be carried out. To define this lattice, it is necessary to consider first an auxiliary body, identical in cross-sectional shape and longitudinal area distribution to the actual body, with a straight barycentric line, i.e., without camber. The cross-sectional shape of this auxiliary body is then approximated by a polygon whose sides determine the transverse legs of the horseshoe vortices. The vertices of the polygon and the axis of the auxiliary body (which by definition is rectilinear (zero camber) and internal to all possible cross sections of the body) define a set of radial planes in which the bound trailing legs of the horseshoe vortices lie parallel to the axis (fig. 4). As the body cross section changes shape along its length, the corresponding polygon is allowed to change accordingly, but with the constraint that the polygonal vertices must always lie in the same set of radial planes. The axial spacing of the cross-sectional planes that determine the transverse vortex elements, or polygonal rings, follows the 'cosine' law of equation (22). The boundary condition control points are located on the auxiliary body surface, and in the bisector radial planes, with their longitudinal spacing given by equation (23).

The boundary condition to be satisfied at these control points is the zero mass flux equation

$$\overline{w} \cdot \overline{n} = -\overline{u}_\infty \cdot \overline{n} \qquad (25)$$

where all the components of the scalar product $\overline{w} \cdot \overline{n} = \beta^2 \ell u + mv + nw$ are to be retained. Thus, equation (25) is a higher order condition than equation (24). The use of this higher order boundary condition, within the framework of a linearized theory, is not mathematically consistent. Therefore, it can only be justified by its results rather than by a strict mathematical derivation. In the present treatment of fusiform bodies, it has been found that the use of higher order, or 'exact' boundary conditions is a requisite for the accurate determination of the surface pressure distribution.

The fact that the vector $\overline{w}$, instead of $\overline{v}$, appears in the left hand member of equation (25) requires some elaboration. First, it should be pointed out that for small perturbations $\overline{w} \cdot \overline{n} \cong \overline{v} \cdot \overline{n}'$. Furthermore, for incompressible flow ($\beta = 1$), the vector $\overline{w}$ is identical to the perturbation velocity $\overline{v}$. Consequently, the boundary condition equation (24) is consistent with the continuity equation, $\nabla \cdot \overline{w} = 0$, to a first order for compressible flow, and to any higher order for incompressible flow. But when a higher order boundary condition is applied in compressible flow to a linearized solution, it should be remembered that this solution satisfies the conservation of $\overline{w}$, not of $\overline{v}$, i.e., $\nabla \cdot \overline{w} = 0$. Thus, the higher order boundary condition should involve the reduced current velocity, or perturbation mass flux, vector $\overline{w}$, as in equation (25), rather than the perturbation velocity vector $\overline{v}$.

The body camber, which was eliminated in the definition of the auxiliary body, is taken into account in the computation of the direction cosines $\ell, m,$ and n, which are implicit in equation (25). Therefore, the effect of camber is represented in the boundary condition but ignored in the spatial placement of the horseshoe elements. This scheme will give a fair approximation to cambered fusiform bodies provided that the amount of body camber is not too large.

THE GENERALIZED VORTEX LATTICE METHOD

Description of Method

The three features discussed above, i.e., the inclusion of the vorticity-induced residual term w^* for supersonic flow, the 'biplanar' scheme for representing thickness, and the use of a vortex grid of concentrical polygonal cylinders for the simulation of fusiform bodies, have been implemented in a computational procedure herein known as the Generalized Vortex Lattice (GVL) method. The GVL method has been codified in a Fortran IV computer program (VORLAX), which has been widely utilized throughout the Lockheed-California Company as an efficient aerodynamic design tool for advanced aircraft configurations in subsonic and supersonic flows.

36

The basic element of the method is the swept horseshoe vortex with 'bound' and 'free' legs. In the present version of the method, the free legs may trail to downstream infinity in any arbitrary, but predetermined, direction. The lattice formed by the bound legs of the horseshoe vortices is laid out on the proper cylindrical surfaces, the trailing legs being parallel to the x-axis. Figure 5 illustrates schematically the representation of a simple wing-body configuration within the context of the present method. The streamwise arrangement of the lattice follows the 'cosine' distribution law (eq. (22)), whereas the spanwise, or cross-flow, spacing of the trailing legs can be arbitrarily specified. To each horseshoe vortex there corresponds an associated control point, placed midway between the bound trailing legs of the horseshoe and longitudinally spaced according to equation (23).

The velocity field induced by the elementary horseshoe vortex is derived from equation (12), and it includes the contribution given by equation (21) when the velocity induced by a horseshoe at its own control point is evaluated at supersonic Mach numbers. This velocity field is used to generate the coefficients of a system of linear equations relating the unknown vortex strengths to the appropriate boundary condition at the control points. This linear system is solved by either a Gauss-Seidel iterative procedure (ref. 8), or by a vector orthogonalization technique (ref. 9).

The pressure coefficients are computed in terms of the perturbation velocity components. Force and moment coefficients are determined through a numerical integration process. Due account is taken of the leading edge suction through the application of Lan's procedure (ref. 7), which the GVL method directly extends to supersonic flow.

Numerical Considerations

At supersonic Mach numbers, the velocity induced by a discrete horseshoe vortex becomes very large in the very close proximity of the envelope of Mach cones generated by the transverse leg of the horseshoe. At the characteristic envelope surface itself, the induced velocity correctly vanishes, due to the finite part concept. This singular behavior of the velocity field occurs only for field points off the plane of the horseshoe. For the planar case, the velocity field is well behaved in the vicinity of the characteristic surface. A simple procedure to treat this numerical singularity consists of defining the characteristic surfaces by the equation

$$(x-x_1)^2 = C \ B^2 \left\{ (y-y_1)^2 + (z-z_1)^2 \right\} \tag{26}$$

where C is a numerical constant whose value is greater than, but close to, 1. It has been found that this procedure yields satisfactory results, and that these results are quite insensitive to reasonable variations of the parameter C.

Another numerical problem, peculiar to the supersonic horseshoe vortex, exists in the planar case (field point in the plane of the horseshoe) when the field point is close to a transverse vortex leg swept exactly parallel to the Mach lines (sonic vortex), while the vortex lines immediately in front of and behind this sonic vortex are subsonic and supersonic, respectively. This problem can be handled by replacing the boundary condition equation for such sonic vortex with the averaging equation

$$-\gamma_{I^*-1} + 2\,\gamma_{I^*} - \gamma_{I^*+1} = 0 \tag{27}$$

where γ_{I^*} is the circulation strength of the critical horseshoe vortex, and γ_{I^*-1} and γ_{I^*+1} are the respective circulation values for the fore-and-aft adjacent subsonic and supersonic vortices.

The axialwash induced velocity component (u) is needed for the computation of the surface pressure distribution, and for the formulation of the boundary condition for fusiform bodies. When the field point is not too close to the generating vorticity element, the axialwash is adequately described by the conventional discrete horseshoe vortex representation. But if this point is in the close vicinity of the generating element, as may occur in the biplanar and in the concentrical cylindrical lattices of the present method, the error in the computation of the axialwash due to the discretization of the vorticity becomes unacceptable. This problem is solved by resorting to a vortex-splitting technique, similar to the one presented in reference 10. Briefly, this technique consists of computing the axialwash induced by the transverse leg of a horseshoe as the summation of several transverse legs longitudinally redistributed, according to an interdigitation scheme, over the region that contains the vorticity represented by the single discrete vortex. This is done only if the point at which the axialwash value is required lies within a given near field region surrounding the original discrete vortex.

COMPARISON WITH OTHER THEORIES AND EXPERIMENTAL RESULTS

Conical flow theory provides a body of 'exact' results, within the context of linearized supersonic flow, for some simple three-dimensional configurations. These exact results can be used as bench mark cases to evaluate the accuracy of numerical techniques. This has been done rather extensively for the GVL method, and very good agreement between it and conical flow theory has been observed in the computed aerodynamic load distribution and all force and moment coefficients. Only some typical comparisons are presented in this paper, figures 6 through 9.

Finally, the capability of computing surface pressure distributions by the method of this paper is illustrated in figures 10 and 11.

CONCLUDING REMARKS

It has been shown that vortex lattice theory can be extended to super-sonic flow if due account is taken of the principal part of the surface vorti-city integral. Furthermore, special vortex lattice layouts, which allow the simulation of thickness and volume with horseshoe vortices, have been presented. All this greatly enhances the value of vortex lattice theory as a computationally efficient design and analysis tool, as exemplified by its extensive use at the Lockheed-California Company, discussion of which has been precluded by space limitations.

REFERENCES

1. Maskew, B.: Calculation of the Three-Dimensional Potential Flow Around Lifting Non-Planar Wings and Wing-Bodies Using a Surface Distribution of Quadrilateral Vortex-Rings. Loughborough University of Technology TT 7009, 1970.

2. Tulinius, J.; Clever, W.; Niemann, A.; Dunn, K.; and Gaither, B.: Theoretical Prediction of Airplane Stability Derivatives at Subcritical Speeds. North American Rockwell NA-72-803, 1973. (Available as NASA CR-132681.)

3. Ward, G. N.: Linearized Theory of Steady High-Speed Flow. Cambridge University Press, 1955.

4. Robinson, A.: On Source and Vortex Distributions in the Linearized Theory of Steady Supersonic Flow. Quart. J. Mech. Appl. Math. I, 1948.

5. Lomax, H.; Heaslet, M. A.; and Fuller, F. B.: Integrals and Integral Equations in Linearized Wing Theory. NACA Report 1054, 1951.

6. Hadamard, J.: Lectures on Cauchy's Problem in Linear Partial Differential Equations. Yale University Press, 1923.

7. Lan, E. C.: A Quasi-Vortex-Lattice Method in Thin Wing Theory. Journal of Aircraft, Sept. 1974.

8. Bratkovich, A.; and Marshall, F. J.: Iterative Techniques for the Solution of Large Linear Systems in Computational Aerodynamics. Journal of Aircraft, Feb. 1975.

9. Purcell, E. W.: The Vector Method of Solving Simultaneous Linear Equations. Journal of Mathematical Physics, Vol. 23, 1953.

10. Lan, E. C.; and Campbell, J. F.: Theoretical Aerodynamics of Upper-Surface-Blowing Jet-Wing Interaction. NASA TN D-7936, Nov. 1975.
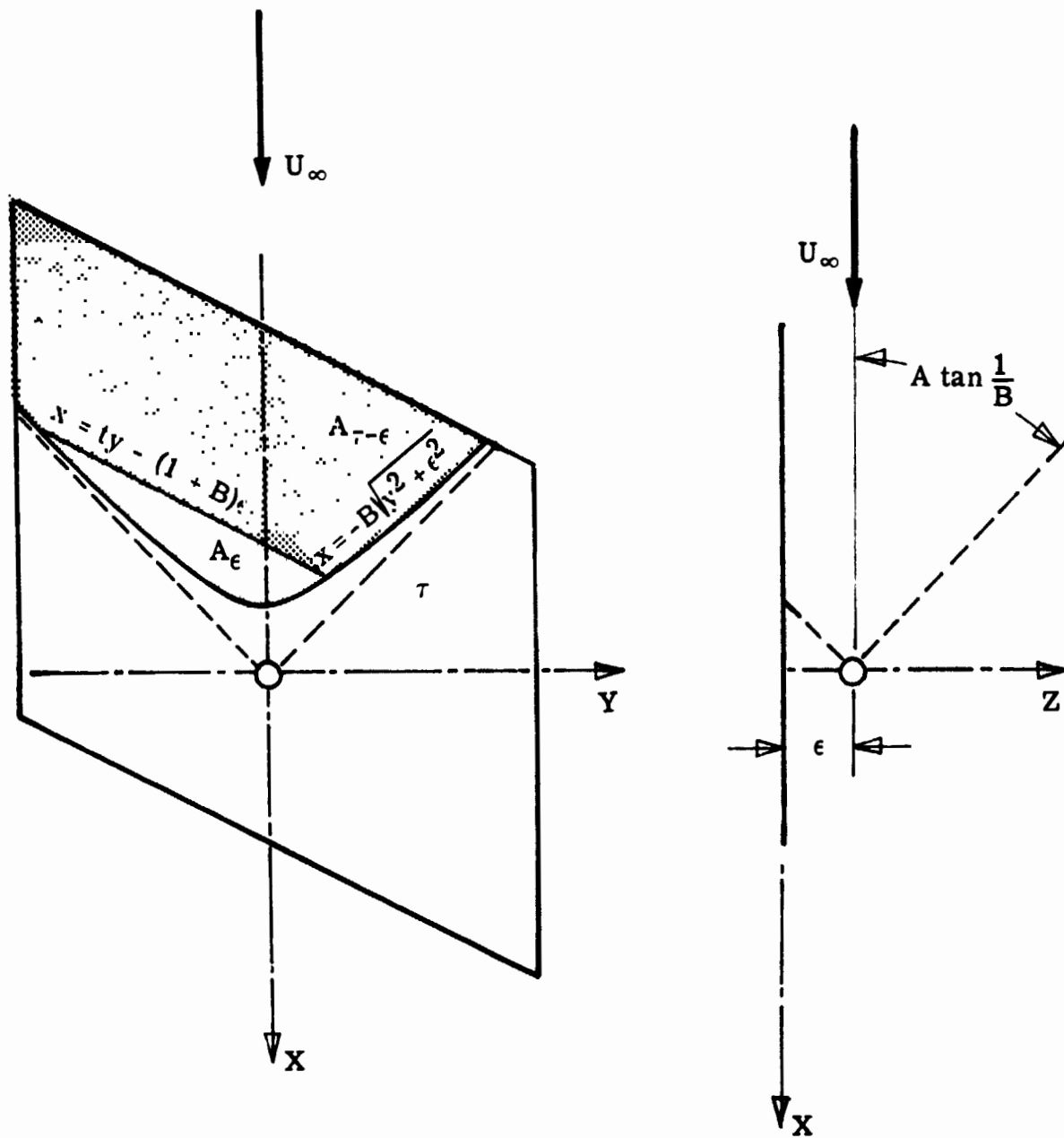
Figure 1.- Definition of integration regions for the
computation of principal part.

ACTUAL WING PANEL

BOUNDARY CONDITION: $\overline{w} \cdot \overline{n}' = \overline{v} \cdot \overline{n}' = -\overline{u}_{\infty} \cdot \overline{n}$; $\overline{n}' = m\overline{j} + n\overline{k}$

THIN PANEL LATTICE
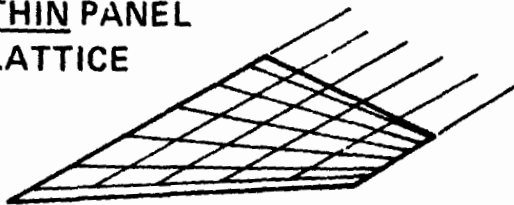
THICK PANEL LATTICE
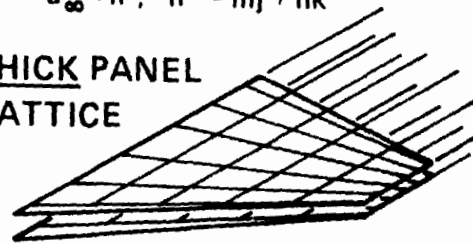
CHORDWISE DISTRIBUTION OF VORTEX LINES: $\dfrac{X_j^v \cdot X_0}{C} = \dfrac{1}{2} \left| 1 \cdot \cos\left(\pi \dfrac{2J \cdot 1}{2N}\right)\right|$

CHORDWISE DISTRIBUTION OF B.C. CONTROL POINTS: $\dfrac{X_j^c \cdot X_0}{C} = \dfrac{1}{2} \left| 1 \cdot \cos\left(\pi \dfrac{J}{N}\right)\right|$

Figure 2.- Modeling of thick wing with horseshoe vortices.
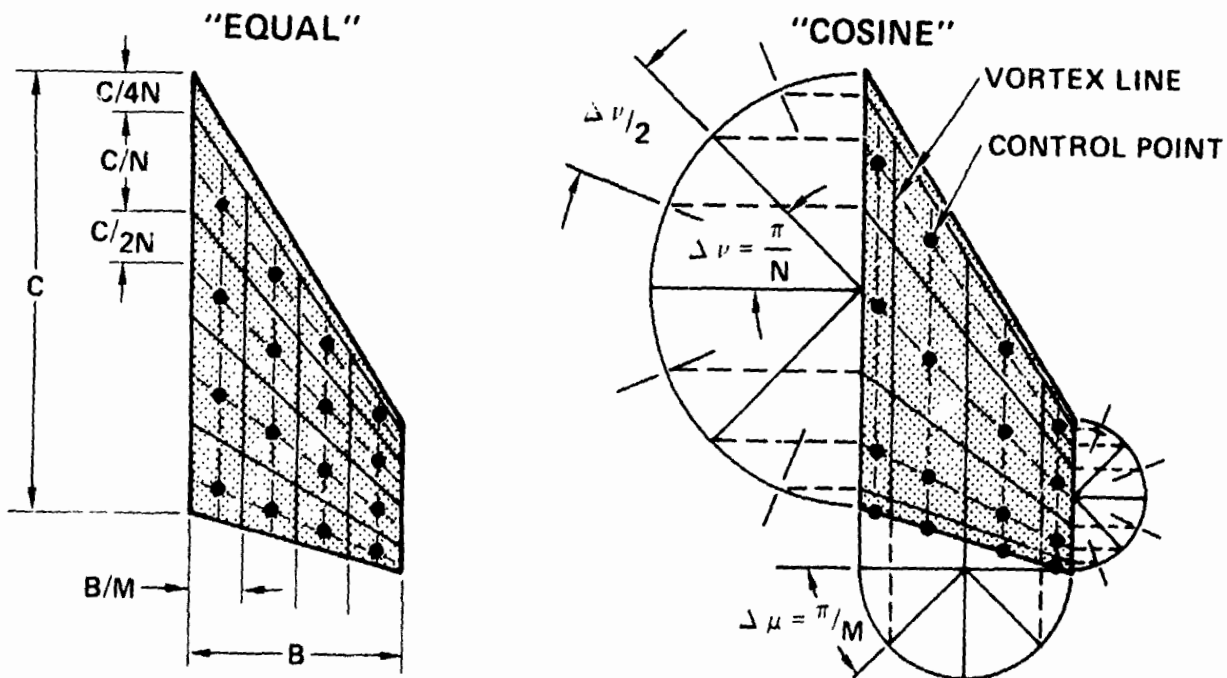
Figure 3.- Vortex lattice collocation.

BOUNDARY CONDITION: $\vec{w} \cdot \vec{n} = -\vec{u}_\infty \cdot \vec{n}$; $\vec{n} = \ell \vec{i} + m \vec{j} + n \vec{k}$

BOUNDARY CONDITION CONTROL POINT
(PLACED ON ACTUAL BODY SURFACE)

A

HORSESHOE VORTEX
TRANSVERSE LEG

PROFILE OF
SIMULATED BODY

A

HORSHOE VORTEX TRAILING LEGS

VIEW A-A
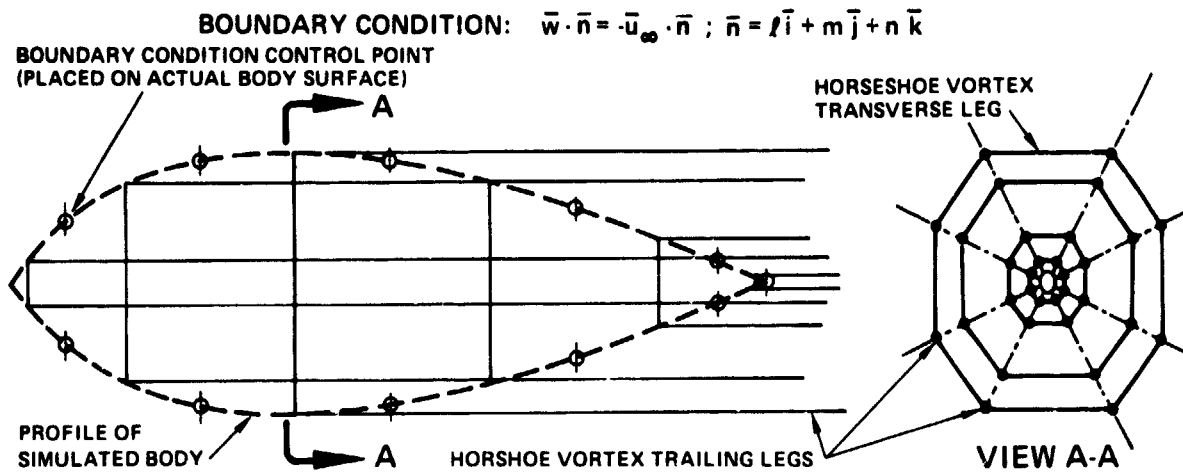
AXIAL DISTRIBUTION OF VORTEX LINES: $\dfrac{X_j^v - X_o}{L} = \dfrac{1}{2} \left| 1 \cdot \cos\left(\pi \, \dfrac{2J-1}{2N}\right) \right|$

AXIAL DISTRIBUTION OF B.C. CONTROL POINTS: $\dfrac{X_j^c - X_o}{L} = \dfrac{1}{2} \left| 1 \cdot \cos\left(\pi \, \dfrac{J}{N}\right) \right|$

Figure 4.- Modeling of fusiform body with horseshoe vortices.

HORSESHOE FREE LEGS

B.C. CONTROL POINT

α_v

β_v

HORSESHOE BOUND LEGS
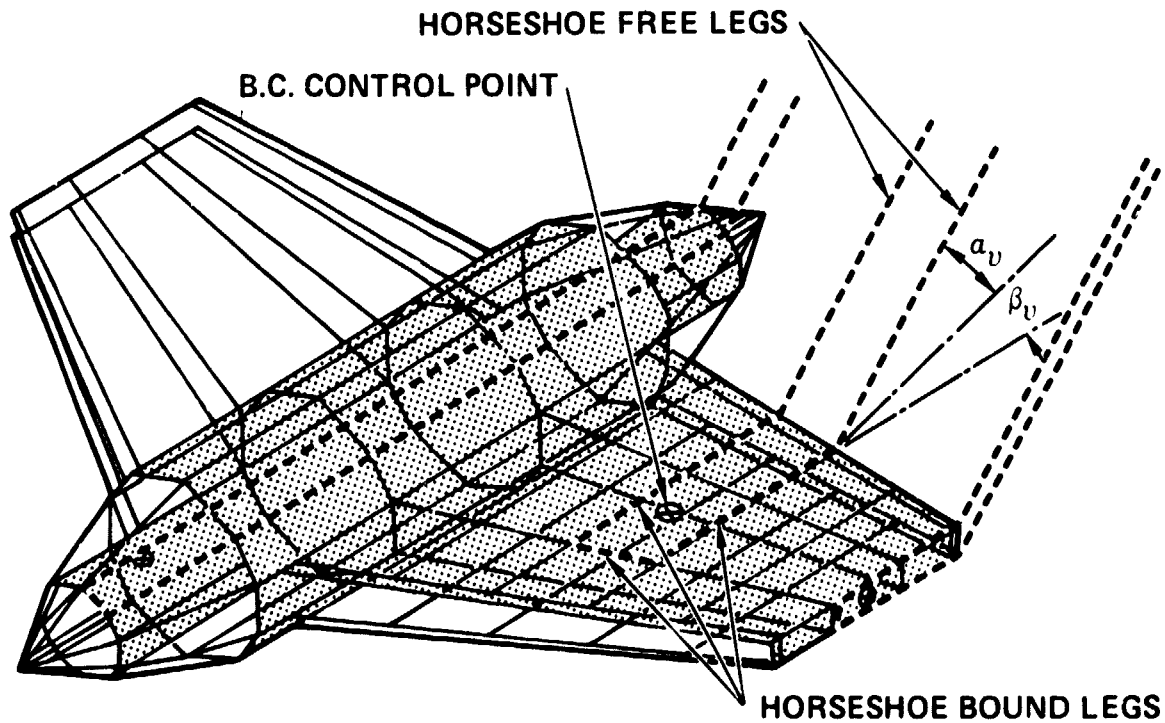
Figure 5.- Generalized vortex lattice model of wing-body configuration.

43
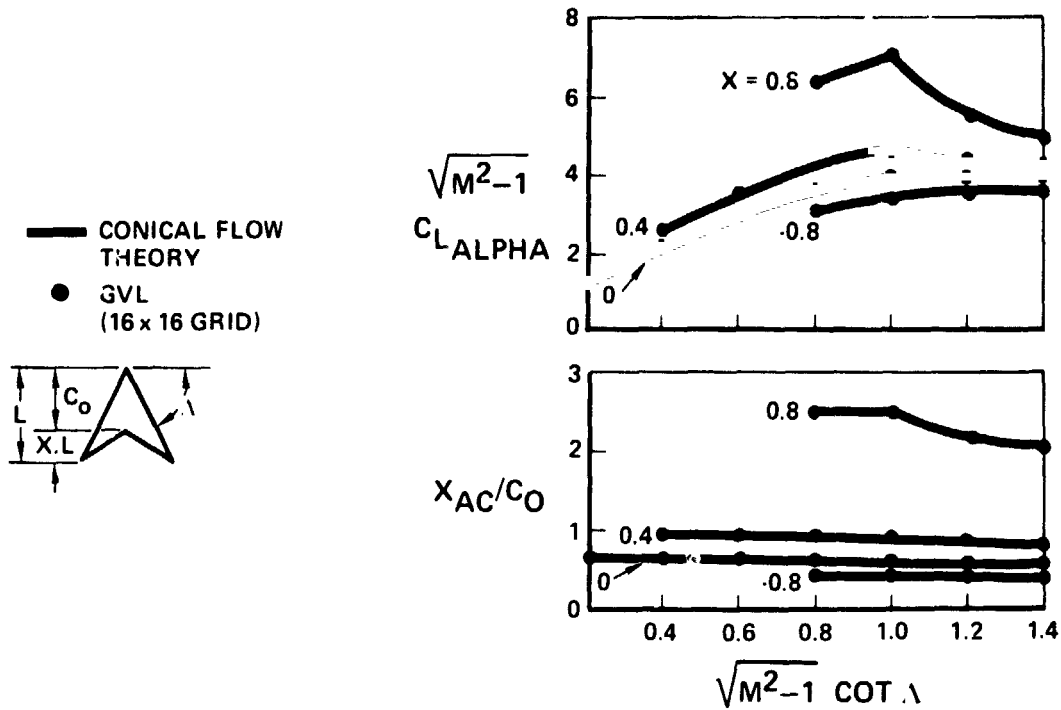
Figure 6.- Theoretical comparison of arrow wing lift slope
and aerodynamic center location.
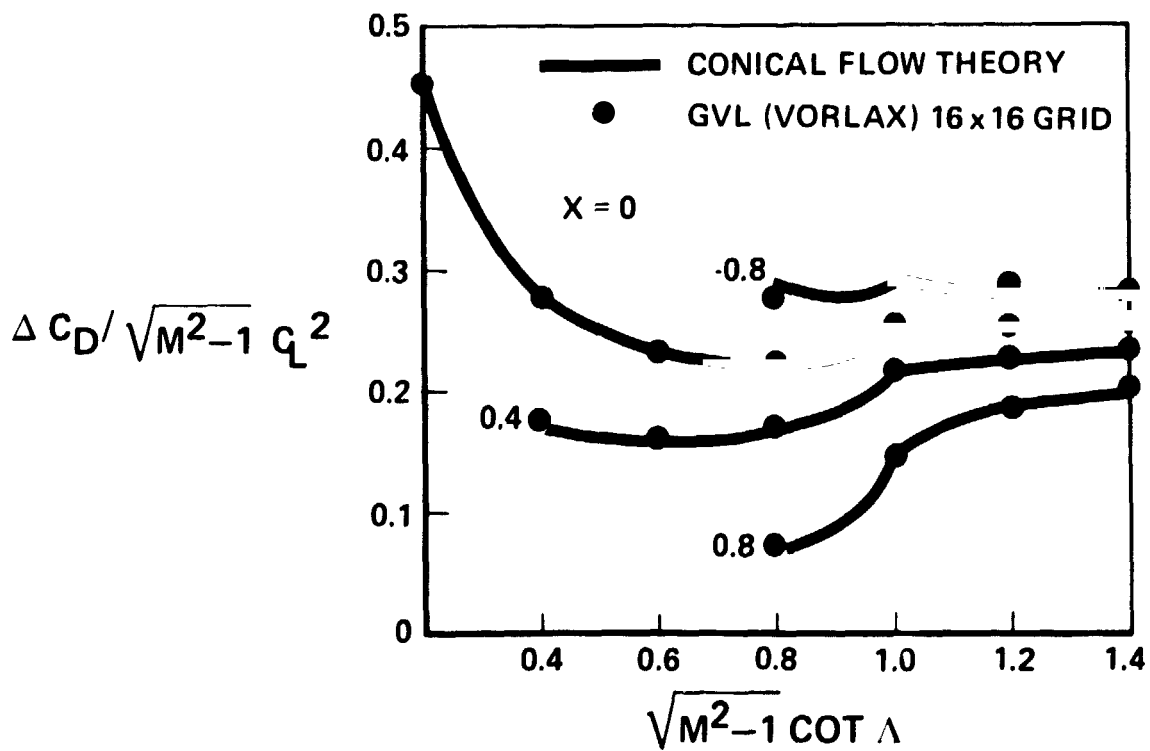
Figure 7.- Theoretical comparison of arrow wing drag-due-to-lift factor.
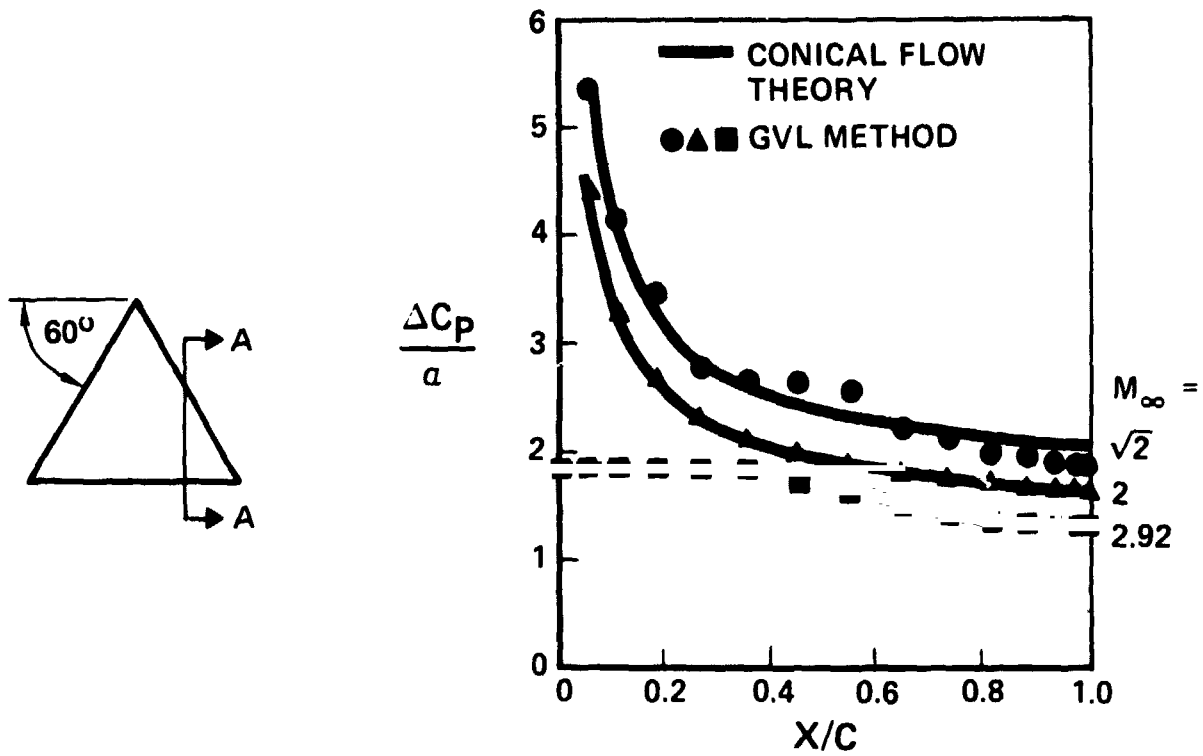
Figure 8.- Theoretical comparison of chordwise
loading for delta wing.

SWEEP=59°; ASPECT RATIO = 1.92 MACH NUMBER= $\sqrt{2}$
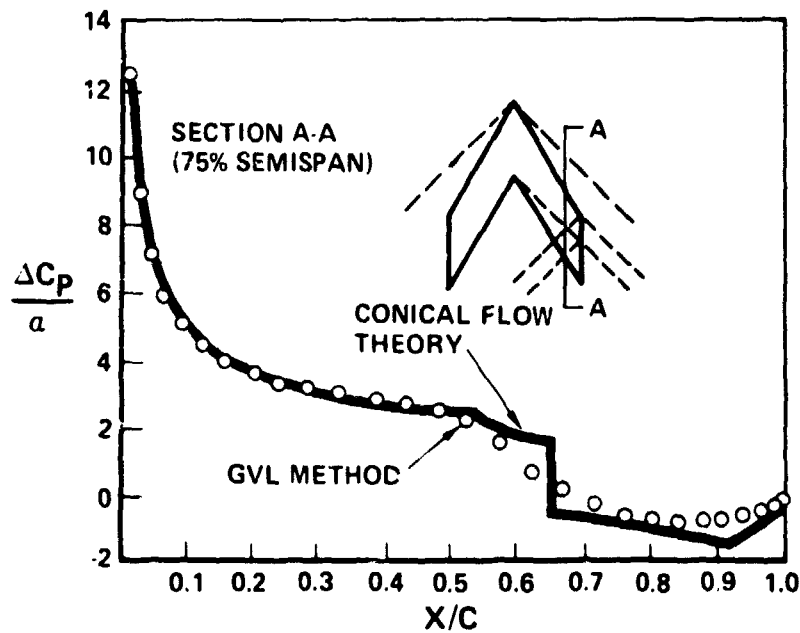
Figure 9.- Theoretical comparison of chordwise loading
for sweptback rectangular wing.
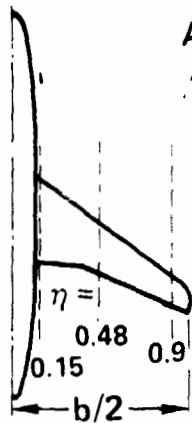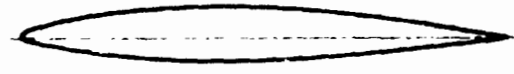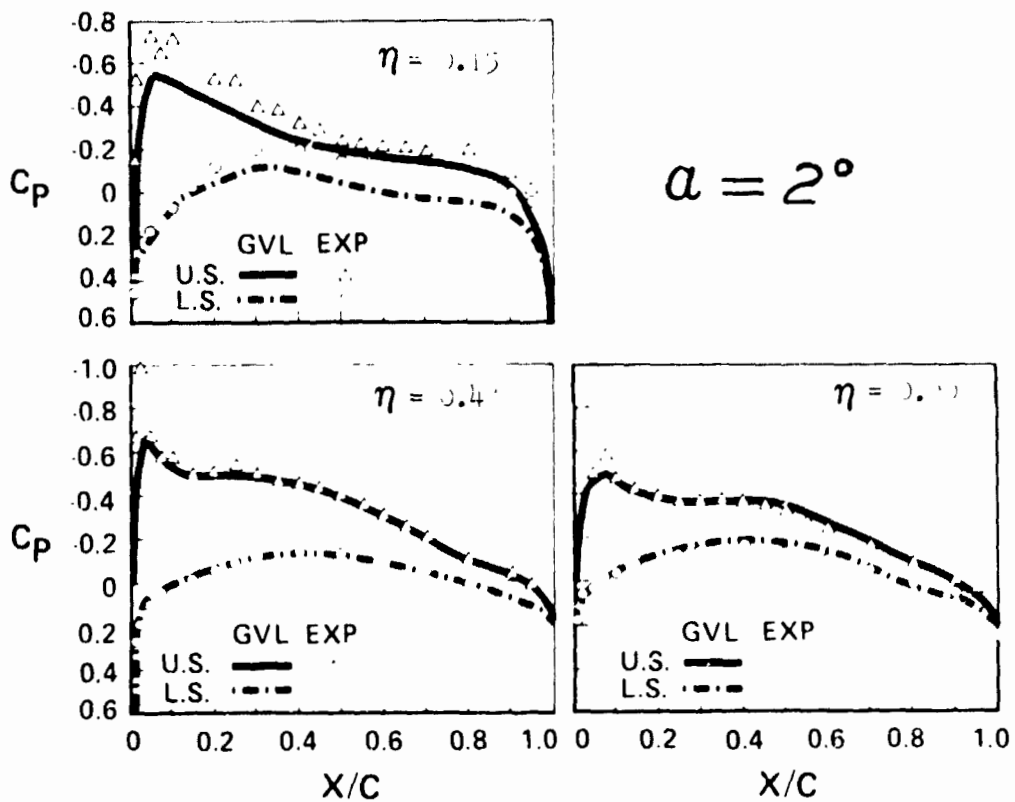
Figure 10.- Comparison with experimental pressure distribution
on wing-body model at Mach = 0.5.
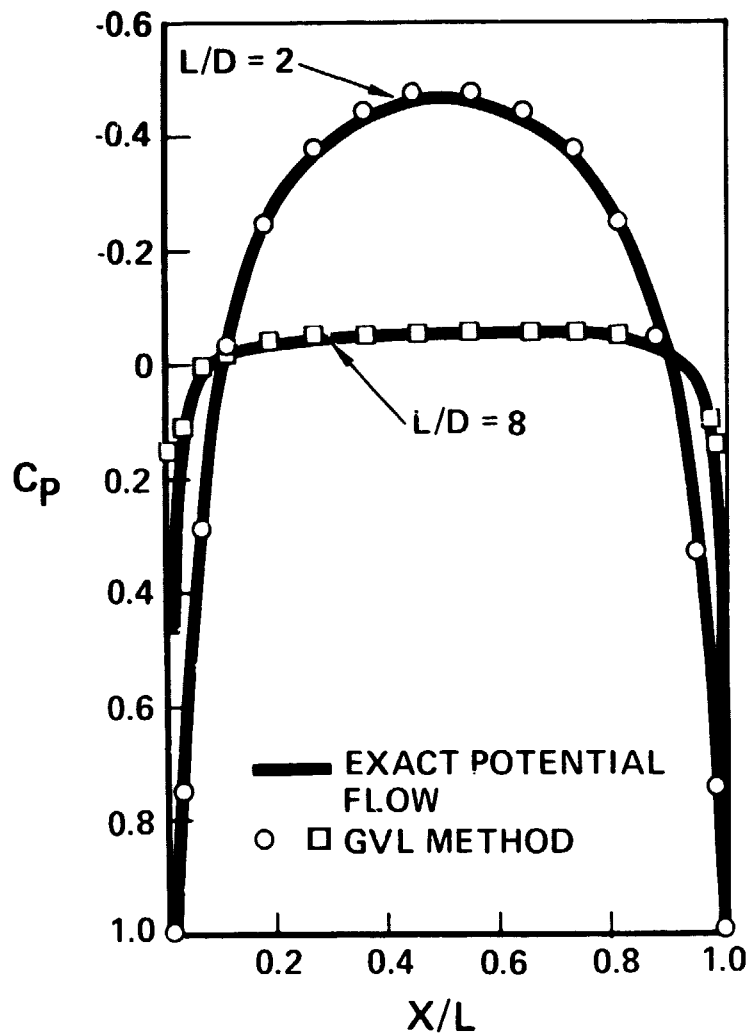
Figure 11.- Theoretical comparison of pressure distribution on ellipsoids at zero angle of attack in incompressible flow.

NUMERICAL METHOD TO CALCULATE THE INDUCED DRAG OR

OPTIMUM LOADING FOR ARBITRARY NON-PLANAR AIRCRAFT

James A. Blackwell, Jr.
Lockheed-Georgia Company

SUMMARY

A simple unified numerical method applicable to non-planar subsonic air-
craft has been developed for calculating either the induced drag for an arbi-
trary loading or the optimum aircraft loading which results in minimum induced
drag. The method utilizes a vortex lattice representation of the aircraft
lifting surfaces coupled with the classic equations and theorems for computing
and minimizing induced drag. Correlation of results from the numerical method
with non-planar solutions obtained from other more complex theories indicates
very good agreement. Comparison of the induced-drag computations using the
numerical method with experimental data for planar and non-planar configura-
tions was also very good.

INTRODUCTION

Over the past few years, increased attention has been focused on improving
aircraft performance. One method to improve performance is to lower the air-
craft induced drag. This can be accomplished by more efficient design of con-
ventional configurations or by developing new and unique designs whose intent
is to minimize induced drag. Typical of new configurations that have been
developed for this purpose are the Lockheed boxplane and the Whitcomb winglet
configuration.

The aircraft lifting surfaces for conventional aircraft as well as for new
configurations are generally non-planar in design. To achieve a minimum in-
duced drag, these non-planar surfaces must be designed to support the required
optimum loads as specified by classical theory (refs. 1 and 2). Unfortunately,
the use of classical theory to determine the design loads is quite cumbersome
since rather complex conformal transformations must be utilized. Thus, a
simple inexpensive method is required to determine what the "design to" loading
of a non-planar configuration should be to minimize the aircraft induced drag.
Furthermore, for conditions where the aircraft is not operating at design con-
ditions, an analysis method is required to quickly assess the magnitude of the
aircraft off-design induced drag. Also, methods of this type are of particular
importance in making configurational trade-offs.

The objective of this paper is to present a simple unified numerical
method applicable to subsonic non-planar aircraft for the rapid calculation of:

1. the induced drag for an arbitrary aircraft loading or

2. the optimum aircraft loading which results in minimum induced drag.

The paper will include a discussion of the fundamental theoretical concepts on which the method is based, followed by the theoretical formulation of the numerical calculation procedure. Computations will be made using the method and will be compared to existing theoretical solutions and to experimental data. This will be followed by an illustration of the utility of the method for making configurational trade-offs by comparing the loading and induced drag results for various types of wing additions such as winglets or wing-tip extensions.

SYMBOLS

A_{ij} geometric influence function

AR   aspect ratio, b^2/S

b   reference span

c   local chord of lifting surface

c_{AV} average chord (S/b)

c_n section load coefficient normal to load perimeter

C_L lift coefficient

C_{D_i} induced drag coefficient

C_{WB} bending-moment coefficient

D_i induced drag $(D_i = C_{D_i} qS)$

e   efficiency factor

F   resultant force of lifting surface

h   length of wing addition

$\bar{k}$ unit normal vector parallel to Z axis

ℓ length of load perimeter

L   lift force $(L = C_L qS)$

M   Mach number

50

m	number of lifting elements on load perimeter
$\bar{n}$	unit vector normal to load perimeter
N	section load normal to load perimeter ($N = q\ c_n\ c$)
q	free-stream dynamic pressure
s'	semi-width of vortex pair
s	nondimensional semi-width of vortex pair ($s = 2s'/b$)
S	reference area
S.F.	side force
u,v,w	induced velocities
V	resultant induced velocity
V_n	velocity normal to load perimeter
V_∞	free-stream velocity
Y', Z'	lifting element coordinate system
X, Y, Z	aircraft coordinate system
y_{cp}	aircraft spanwise center of pressure
Γ	circulation (eq. (10))
θ	rotation angle in the Y-Z plane

Superscript:

–	indicates vector quantity

Subscripts:

i	number designating a vortex pair that model a particular lifting element
j	number designating a control point on a particular lifting element
w	wing
wℓ	winglet

BASIC THEORETICAL CONCEPTS

Fundamental to the development of the present model is the representation of the aircraft non-planar lifting surfaces by a system of rectangular horseshoe vortices (ref. 3). The induced drag for a given loading or the optimum loading for minimum induced drag can be calculated for any arbitrary non-planar aircraft at subsonic speeds utilizing this vortex representation and the following basic law and theorems: Munk's Theorems I to III, Biot-Savart Law, and the Kutta-Joukowski Theorem.

Munk's first theorem (ref. 1) can be stated as follows:

> *The total induced drag of any multiplane system is unaltered if any of the lifting elements are moved in the direction of motion provided that the attitude of the elements is adjusted to maintain the same distribution of lif' among them.*

This theorem is commonly referred to as Munk's stagger theorem. An illustration of this theorem is shown in figure 1. Several practical applications can be deduced from this theorem. First, the chordwise distribution of pressure does not affect the theoretical induced drag of the aircraft if constant section lift is maintained. Second, wing sweep does not effect the theoretical induced drag as long as the spanwise distribution of lift is constant. A third application is that the load from a system of multi-surfaces (i.e. wing and horizontal tail) with the same projection in the Y-Z plane can be made equivalent to a single surface for the purpose of calculating induced drag.

In the following theoretical development, use will be made of Munk's first theorem to lump the chordwise distribution of vorticity into a single chordwise load and to translate all loads into the 0,Y,Z plane (fig. 1).

Munk's second theorem (ref. 1) is illustrated in figure 2 and can be stated as:

> *In calculating the total induced drag of a lifting system, once all the forces have been concentrated into the plane $0,Y,Z$, we may, instead of using the actual values of the velocity normal to the lifting elements $[V_n(x,y,z)]$ at the original points of application of the forces, use one-half the limiting value of the normal velocity $[V_n(\infty,y,z)]$ for the corresponding values at points $P(0,y,z)$.*

This theorem allows the computations to be done in the Trefftz plane (downstream infinity) rather than in the real plane. In the subsequent theoretical derivation, this fact will be utilized to make all the computations in the Trefftz plane, thereby greatly simplifying the calculations.

The third theorem given by Munk (ref. 1) is presented as follows:

> *When all the elements of a lifting system have been trans-*
> *lated longitudinally to a single plane, the induced drag*
> *will be a minimum when the component of the induced*
> *velocity normal to the lifting element at each point is*
> *proportional to the cosine of the angle of inclination of*
> *the lifting element at that point.*

This theorem is illustrated in figure 3 and can be summarized in equation form as:

$$V_n = w_o \cos\theta \tag{1}$$

For a horizontal lifting element it can be seen from equation (1) that the normal velocity (downwash) across the span is equal to a constant (fig. 3). For a vertical plane ($\theta = 90°$), the normal velocity (sidewash) must be equal to zero for minimum induced drag. The physical interpretation of this theorem will be further illustrated in a subsequent section.

Equation (1) will be utilized in the following theoretical development as the boundary condition necessary to achieve a minimum induced drag and hence an optimum aircraft loading.

The basic equation for calculating the aircraft-induced drag can be derived by applying the Kutta-Joukowski theorem in the drag direction. By virtue of Munk's theorems, the calculations can be accomplished in the Trefftz plane rather than the real plane. Thus, the equation for induced drag ex-pressed in terms of the Trefftz plane variables and using vector notation is:

$$D_i = \frac{1}{2V_\infty} \oint \bar{V} \cdot N\bar{n} \, d\ell \tag{2}$$

Equation (2) along with the induced velocities in the Trefftz plane de-rived from the vortex model of the lifting surfaces will comprise the basis for the induced drag computation.

PHYSICAL INTERPRETATION OF THEORETICAL CONCEPTS

To provide a better physical understanding of the computation of induced drag and the calculation of the optimum loading for minimum induced drag, the theoretical concepts discussed in the previous section will be illustrated using a wing-winglet configuration. In figure 4, the sources of induced drag for a wing-winglet combination are shown. These are:

    o Drag due to the induced flow by the wings on the wing

    o Drag due to the induced flow by the wings on the winglet

o Drag due to the induced flow by the winglets on the winglet

o Drag due to the induced flow by the winglets on the wing

For simplicity, the effects of symmetry are included in the sources of induced drag shown and are not delineated separately.

In figure 4(a), the effect of the wing induced flow is shown. The wing under positive load produces a downwash on itself which results in the wing force vector, $\bar{F}$, tilting rearward by an angle α_i. The wing force vector, $\bar{F}$, is perpendicular to the resultant, V, (Kutta-Joukowski theorem). The rearward rotation of the force vector results in a wing-induced drag. A sidewash is also produced by the wing at the winglet location. As can be seen in figure 4(b), the sidewash from the wing combined with the free-stream velocity produces a tilt forward of the winglet force resulting in a thrust component.

In figure 4(c), the induced drag resulting from the sidewash of the winglet on itself is presented. This results in a rearward tilting of the winglet force vector and an attendant induced drag. It should be noted that the direction of the winglet force vector is consistent with a positive (upload) or the wing. The winglet also induces an upwash on the wing. In figure 4(d), it can be seen that this upwash rotates the wing force vector forward producing a thrust force.

The results from figure 4 are summarized in figure 5, where all the induced velocities are combined. For minimum induced drag, equation (1) indicates that the velocity normal to the winglet must be equal to zero ($\theta = 90^\circ$). This can be seen to occur when the sidewash produced on the winglet by the wing exactly cancels the sidewash produced by the winglet on itself. In other words, the induced angle of attack (α_i) of the winglet is zero. The induced drag of the wing is also minimized by the presence of a winglet since the winglet causes a reduction in the net downwash at the wing; and, hence, the induced angle of attack is reduced.

DERIVATION OF NUMERICAL METHODS

Vortex Model

By virtue of Munk's theorems, the calculations for induced drag and the optimum loading can be accomplished in the Trefftz plane. This fact considerably simplifies the calculation problem since the method will not be a function of the longitudinal coordinate. The projection of the aircraft non-planar lifting surfaces in the Trefftz plane will be referred to as the load perimeter.

In the real plane, the aircraft lifting surfaces will be represented by a system of horseshoe vortices. The equations describing the induced velocities in the Trefftz plane at a control point $P(\infty, y_i, z_i)$ (fig. 6) due to a horseshoe

vortex located in the real plane at a point $P(x_j, y_j, z_j)$ are given below as derived from the Biot-Savart Law (ref. 3):

$$\frac{u_i}{V_\infty} = 0 \tag{3}$$

$$\frac{v_i}{V_\infty} = -\frac{1}{2\pi} \frac{\Gamma_i}{V_\infty} \left(\frac{z'}{R_1} - \frac{z'}{R_2} \right) \tag{4}$$

$$\frac{w_i}{V_\infty} = \frac{1}{2\pi} \frac{\Gamma_j}{V_\infty} \left(\frac{(y'-s')}{R_1} - \frac{(y'+s')}{R_2} \right) \tag{5}$$

where

$$R_1 = (z')^2 + (y'-s')^2 \tag{6}$$

$$R_2 = (z')^2 + (y'+s')^2 \tag{7}$$

$$y' = (y_i - y_j) \cos\theta_j + (z_i - z_j) \sin\theta_j \tag{8}$$

$$z' = -(y_i - y_j) \sin\theta_j + (z_i - z_j) \cos\theta_j \tag{9}$$

and the circulation by virtue of the Kutta-Joukowski theorem is given as

$$\frac{\Gamma_j}{V_\infty} = \frac{(c_n c)_j}{2} \tag{10}$$

Inspection of equations (3) to (5) indicates that there is no contribution from the horseshoe bound leg in the Trefftz plane and the induced velocities are not dependent on x. The resulting model then reduces to describing the load perimeter in the Trefftz plane (fig. 6) by lifting elements that are represented by a trailing vortex pair having a circulation of equal magnitude but of opposite rotation. For each lifting element there is an associated control point located midway between the pair of vortices.

Induced Drag Calculation

The basic equation for calculating the induced drag for an arbitrary non-planar lifting system was given in equation (2) as:

$$D_i = \frac{1}{2V_\infty} \oint \bar{V} \cdot N\bar{n} \; d\ell$$

The integral is a circuit integral taken around the perimeter of the projection of the lifting system in the Trefftz plane. The vector $\bar{V}$ is the resultant induced velocity vector in the Trefftz plane from all vortices on the load perimeter. The vector $\bar{n}$ is a unit vector, normal to the load perimeter.

Reducing equation (2) to coefficient form, nondimensionalizing the lifting element length (ℓ) by the reference semispan, and using the relationship for the average chord, the following result is obtained

$$C_{D_i} = \frac{1}{4} \oint \frac{\bar{V}}{V_\infty} \cdot \left(\frac{c_n \, c}{c_{AV}}\right) \bar{n} \, d \left(\frac{2\ell}{b}\right) \tag{11}$$

Writing the above in the form of a sum and assuming symmetry about the X-Z plane

$$C_{D_i} = \frac{1}{2} \sum_{i=1}^{m} \frac{(c_n \, c)_i}{c_{AV}} \frac{[V \cos(\bar{V},\bar{n})]_i}{V_\infty} \Delta(2\ell/b)_i \tag{12}$$

where m equals the number of elements that comprise the load perimeter. Writing equation (12) in terms of the nondimensional lifting element semi-width(s) and noting that

$$V_n = V\cos(\bar{V},\bar{n}) \tag{13}$$

the expression for induced drag can be written as

$$C_{D_i} = \sum_{i=1}^{m} \frac{V_{n_i}}{V_\infty} \frac{(c_n \, c)_i}{c_{AV}} s_i \tag{14}$$

The velocities normal to the lifting elements (V_n) can be determined by utilizing the expressions for the induced velocities in equations (4) and (5).

From the geometry of figure 6, the normal velocity at P_i due to a vortex pair at P_j can be expressed in terms of the induced velocities as:

$$\frac{V_{n_i}}{V_\infty} = \frac{w_i}{V_\infty} \cos(\theta_i - \theta_j) - \frac{v_i}{V_\infty} \sin(\theta_i - \theta_j) \tag{15}$$

Combining equations (4), (5), (10), and (15) yields the expression for the total normal velocity at the control point P_i due to vortices at all points P_j:

$$\frac{V_{n_i}}{V_\infty} = \sum_{j=1}^{m} \frac{(c_n \, c)_j}{c_{AV}} \left\{ \frac{c_{AV}}{4\pi} \left(\frac{(y'-s')}{R_1} - \frac{(y'+s')}{R_2}\right) \cos(\theta_i - \theta_j) \right.$$

$$\left. + \frac{c_{AV}}{4\pi} \left(\frac{z'}{R_1} - \frac{z'}{R_2}\right) \sin(\theta_i - \theta_j) \right\} \tag{16}$$

The portion contained in curvy brackets is only a function of the projected aircraft geometry in the Trefftz plane and will be denoted by A_{ij}. Thus, in terms of the geometric influence function A_{ij},

$$\frac{V_{n_i}}{V_\infty} = \sum_{j=1}^{m} \frac{(c_n c)_i}{c_{AV}} A_{ij} \qquad (17)$$

Substitution of equation (17) into equation (14) yields the final expression for the induced drag:

$$C_{D_i} = \sum_{i=1}^{m} \sum_{j=1}^{m} \left(\frac{(c_n c)_i}{c_{AV}}\right) \left(\frac{(c_n c)_i}{c_{AV}}\right) (s_i)(A_{ij}) \qquad (18)$$

The independent parameters in equation (18) are the loadings normal to the load perimeter, the lifting element semi-widths, and the geometric influence function. The loading normal to the load perimeter will be considered input to the present method. The normal loading can be determined from any available non-planar lifting surface calculation procedure such as in reference 3 or from experimental data. The lifting element semi-width is also considered as input. The geometric influence function (A_{ij}), as has been previously mentioned, is a function of the input aircraft geometry.

For an arbitrary applied load, the lift can be determined from the following expression

$$L = \oint N\bar{n} \cdot \bar{k} \, d\ell \qquad (19)$$

Expressing equation (19) in coefficient form and writing as a sum

$$C_L = 2 \sum_{j=1}^{m} \left(\frac{(c_n c)_i}{c_{AV}}\right) (s_j) \cos(\bar{n}_j, \bar{k}) \qquad (20)$$

Since

$$\cos(\bar{n}_j, \bar{k}) = \cos\theta_j \qquad (21)$$

the final expression for the lift coefficient is given by

$$C_L = 2 \sum_{j=1}^{m} \left(\frac{(c_n c)_i}{c_{AV}}\right) (s_j) \cos\theta_j \qquad (22)$$

The bending-moment coefficient at the X-axis can be expressed as

$$C_{WB} = \frac{1}{2} \sum_{j=1}^{m} \left(\frac{(c_n c)_i}{c_{AV}}\right) s_j \left(\frac{y_i}{b/2}\cos\theta_j + \frac{z_i}{b/2}\sin\theta_j\right) \qquad (23)$$

The spanwise center-of-pressure location can be determined from the following equation:

$$\frac{y_{cp}}{b/2} = \frac{4C_{WB}}{C_L} \tag{24}$$

The aircraft efficiency factor can be calculated from the following standard equation:

$$e = \frac{C_L^2}{\pi \, AR \, C_{D_i}} \tag{25}$$

Optimum Load Calculation

The expression for the total velocity normal to a lifting element was given in equation (17) as:

$$\frac{V_{n_i}}{V_\infty} = \sum_{j=1}^{m} \frac{(c_n \, c)_j}{c_{AV}} \, A_{ij}$$

According to Munk's theorem III, the loading for minimum induced drag is obtained when the distribution of normal velocity satisfies equation (1):

$$\frac{V_{n_i}}{V_\infty} = \frac{w_o}{V_\infty} \cos\theta_i$$

where w_o is a constant. Using equation (1) as a boundary condition and combining it with equation (17), there results:

$$\frac{w_o}{V_\infty} \cos\theta_i = \sum_{j=1}^{m} \frac{(c_n \, c)_j}{c_{AV}} \, A_{ij} \tag{26}$$

where the loading in equation (26) is the optimum loading. Using square brackets to indicate matrix notation, equation (26) can be written as:

$$\left[\cos\theta_i\right] = \frac{1}{w_o/V_\infty} \left[A_{ij}\right]\left[\frac{(c_n \, c)_j}{c_{AV}}\right] \tag{27}$$

Solving for the optimum loading

$$\left[\frac{(c_n \, c)_i}{c_{AV}}\right] = \frac{w_o}{V_\infty}\left[A_{ij}\right]^{-1}\left[\cos\theta_i\right] \tag{28}$$

The value of the arbitrary constant, w_o, can be determined from equation (22) by specifying the aircraft lift coefficient.

In summary, to determine the loading for minimum induced drag, only the lift coefficient and aircraft geometry are required for input. Once the

58

loading has been determined, the minimum induced drag, the spanwise center-of-pressure location, and efficiency can be determined in the manner previously presented (eqs. (18), (24), and (25)).

CORRELATION OF METHOD

The theory described in the previous section for calculating the aircraft induced drag for a given loading or the loading for a minimum induced drag has been coded for use on Lockheed computers. In this section, computations using the present method will be compared to other theoretical solutions and to experimental results.

Induced-Drag Correlations

Numerical solutions for the aircraft efficiency for a monoplane of aspect ratio eight are shown in figure 7 for various values of lifting element widths. For this example, the widths of the elements over the load perimeter were held constant. A more efficient result could have been obtained if, for instance, a cosine spacing of the elements had been used. The input loading on the monoplane was specified to be elliptical. The exact solution for the efficiency factor (ref. 1) on an elliptically loaded monoplane is, of course, 1.0. As can be seen, the numerical solution approaches the exact value as the width of the elements become smaller. For a lifting element width equal to .01 (b/2), the error was approximately 0.5% in efficiency.

A similar calculation was made for an aspect ratio eight biplane with wings of equal span and a height-to-span ratio of 0.5. The biplane was loaded optimally utilizing the loadings derived in reference 1, based on transformation theory. The numerical calculation for efficiency factor was 1.6307 (using constant elements of 0.0125(b/2) in width) compared to the value of 1.6260 given in reference 1. The resulting difference was approximately 0.3%.

In figure 8, induced-drag results calculated using the present method are compared to the experimental results for an advanced Lockheed transport designed to cruise at 0.95 Mach number and at a lift coefficient of 0.47. The spanwise loading for the aircraft was obtained from an available lifting surface program similar to that in reference 3. As can be seen, the agreement between theory and experiment is very good over a range near the design lift coefficient.

A further correlation example is presented in figure 9 where numerical results are compared with experimental data for a non-planar Lockheed boxplane configuration. Again, the loading was obtained from lifting-surface theory. As indicated, good agreement is obtained.

Optimum Load Correlations

In figure 10 the optimum loading is presented for an aspect ratio eight monoplane as calculated from equation (28) using constant elements of .01(b/2)

in width. Also shown is the classic optimum result for a monoplane – an elliptical loading. The correlation can be seen to be very good. The error in induced drag of the computed result was approximately 0.5%, which is consistent with the results in figure 7.

In reference 2, an optimum loading for a wing with a winglet is presented as derived from transformation theory. This solution is compared to the result calculated using the present method in figure 11. Good agreement between the two methods is obtained.

ILLUSTRATIVE USE OF METHOD

Taken together, the present numerical method provides a unique tool for understanding the sources of induced drag and making configuration trade-offs to achieve an overall aerodynamic as well as structurally optimum aircraft. An illustration of using the method to provide additional understanding into the basic sources and mechanisms of induced drag is presented in figure 12, where the magnitude of the induced-drag components for a wing-winglet configuration (fig. 4) with optimum load is presented. From the figure, it can be seen that the induced-drag contribution from the wing on the winglet and the winglet on the winglet are of the same magnitude and cancel each other. This is, of course, the result previously illustrated in figure 5.

As a result of design or structural constraints, the aircraft may not be able to achieve the op imum loading for minimum induced drag. The penalties that incur from the use of non-optimum loadings can be quickly assessed using the present method. This is illustrated in figure 13, where the winglet loading for a wing-winglet configuration is varied. As can be seen the induced drag is sensitive to certain types of changes (non-optimum 1) where it is not to others (non-optimum 2).

The present method can also be used to quickly make configuration trade-offs. This is illustrated in figures 14 and 15. In figure 14 the parametric effect of wing additions on induced drag and on the wing spanwise center-of-pressure location as calculated from the present method are presented. If, for instance, it was desired to find a configuration which would give the maximum induced drag reduction for a minimum outboard shift in wing center of pressure, this can quickly be determined by replotting the parametric data of figure 14 in the form of figure 15 and the result determined.

CONCLUDING REMARKS

A unified numerical method applicable to non-planar subsonic aircraft has been developed for the purpose of calculating the induced drag for an arbitrary loading or the optimum aircraft loading that gives minimum induced drag.

60

Use of the numerical method has indicated that:

(1) the method is simple and easy to use

(2) induced drag and optimum loading results from the numerical
     method correlate very well with non-planar solutions obtained
     from more complex theories

(3) numerical induced-drag predictions are in good agreement with
     experimental data for planar and non-planar configurations

(4) the numerical method provides both analysis and design capa-
     bility which allows the designer to make rapid configuration
     assessments and trade-offs for the purpose of achieving an
     overall aerodynamic as well as structurally optimum aircraft.

REFERENCES

1. Durand, W. F. (ed.): Aerodynamic Theory. Dover Publications, Inc.,
    New York, 1963, Volume II, Division E.

2. Lundry, J. L.: A Numerical Solution for the Minimum Induced Drag and the
    Corresponding Loading of Nonplanar Wings. NASA CR-1218, November 1968.

3. Blackwell, James A. Jr.: A Finite-Step Method for Calculation of Theo-
    retical Load Distributions for Arbitrary Lifting-Surface Arrangements at
    Subsonic Speeds. NAS TN D-5335, July 1969.

INDUCED DRAG $\big|_{\text{STAGGERED}}$ = INDUCED DRAG $\big|_{\text{UNSTAGGERED}}$
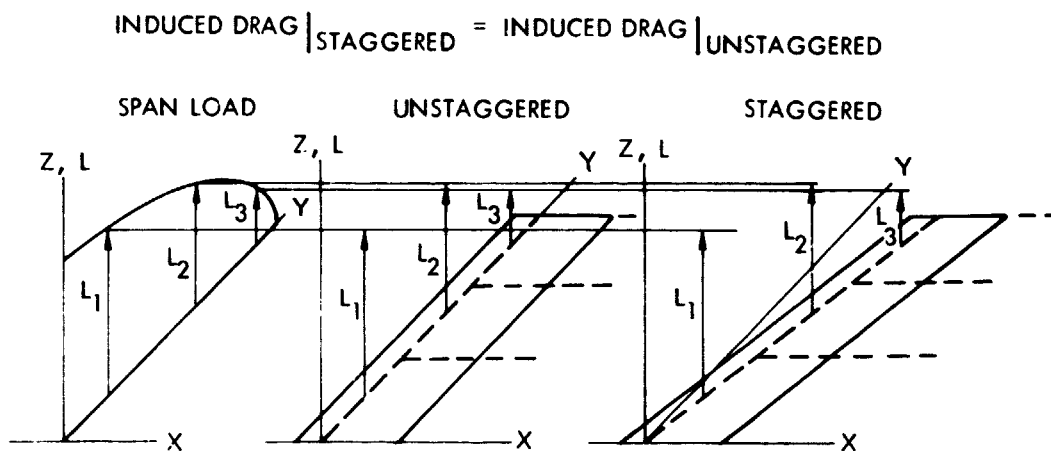
Figure 1.- Illustration of Munk's theorem 1.
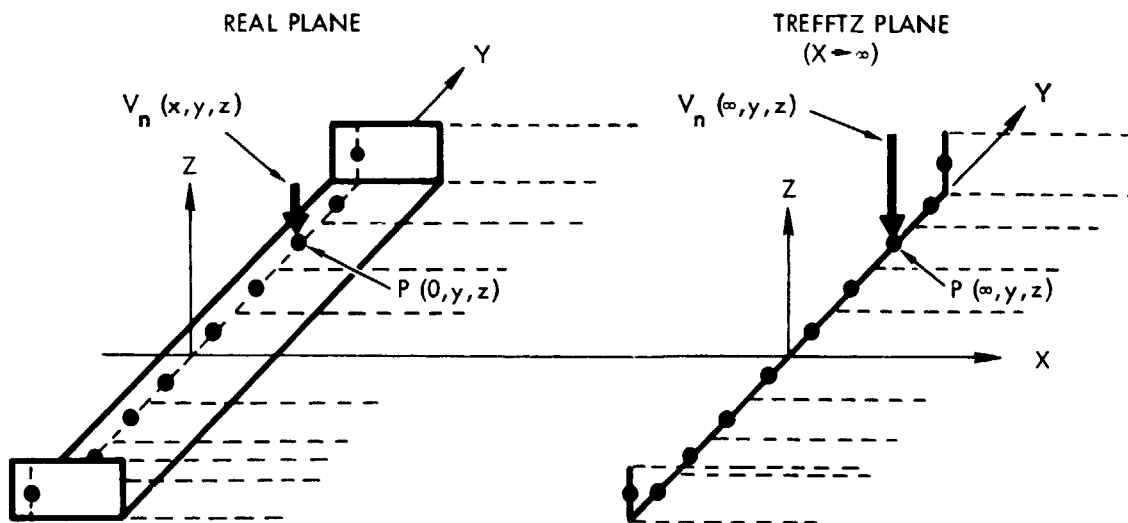
Figure 2.- Illustration of Munk's theorem II.

IN EQUATION FORM:

$$V_n = w_0 \cos\theta$$

WHERE

w_0 = CONSTANT

V_n = NORMAL VELOCITY
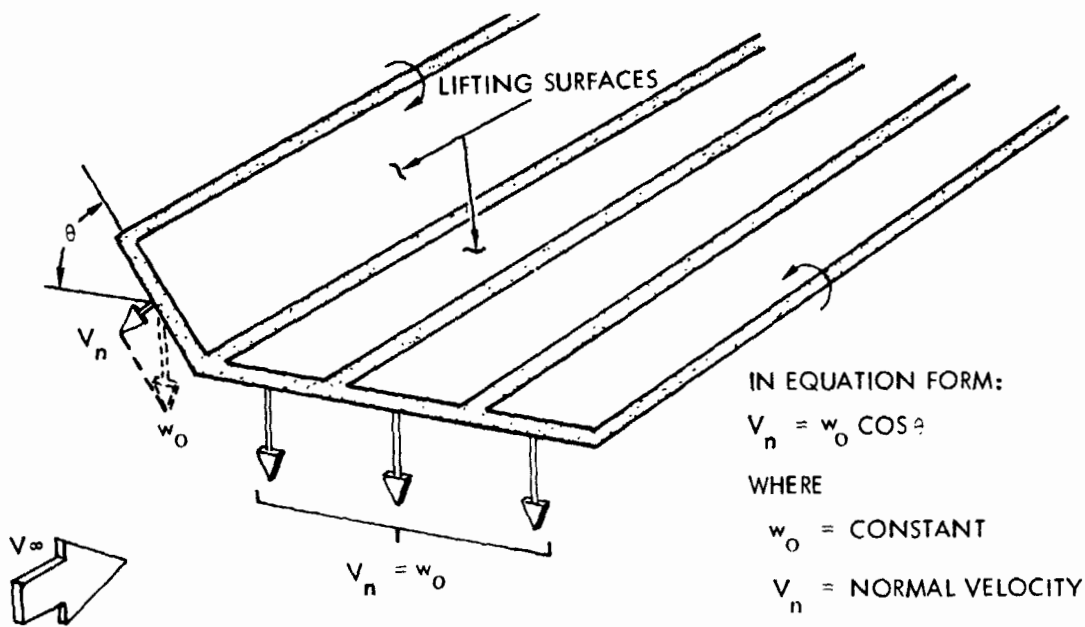
Figure 3.- Illustration of Munk's theorem III.

(a) Drag due to wing on wing $D_{i_{w,w}}$.

(b) Drag due to wing on winglet $D_{i_{w,w\ell}}$.

(c) Drag due to winglet on winglet $D_{i_{w\ell,w\ell}}$.

(d) Drag due to winglet on wing $D_{i_{w\ell,w}}$.

Figure 4.- Sources of induced drag for a wing/winglet configuration.

OPTIMUM SIDE LOAD
FOR VERTICAL SURFACE

$$v_{TOTAL} = v_{w\ell, w\ell} + v_{w, w\ell}$$

$$v_{TOTAL} = 0$$

OPTIMUM VERTICAL LOAD FOR
HORIZONTAL SURFACE

$$w_{TOTAL} = w_{w\ell, w} + w_{w, w}$$

$$w_{TOTAL} = CONSTANT$$
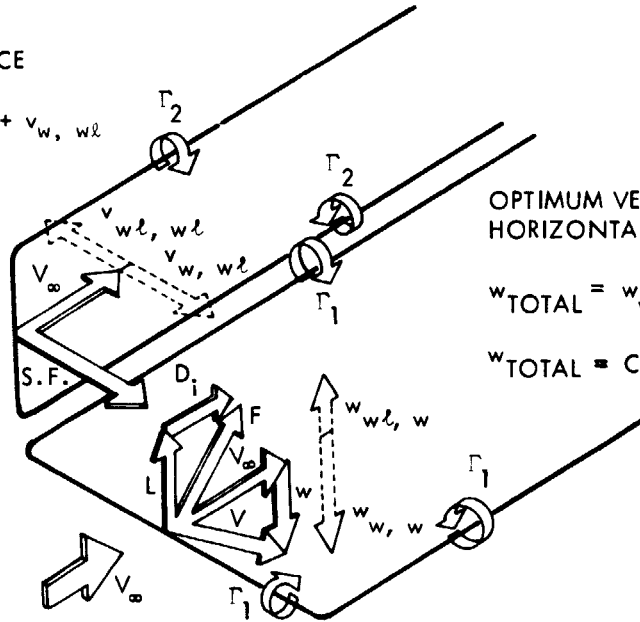
Figure 5.- Combined sources of induced drag for a wing/winglet configuration.
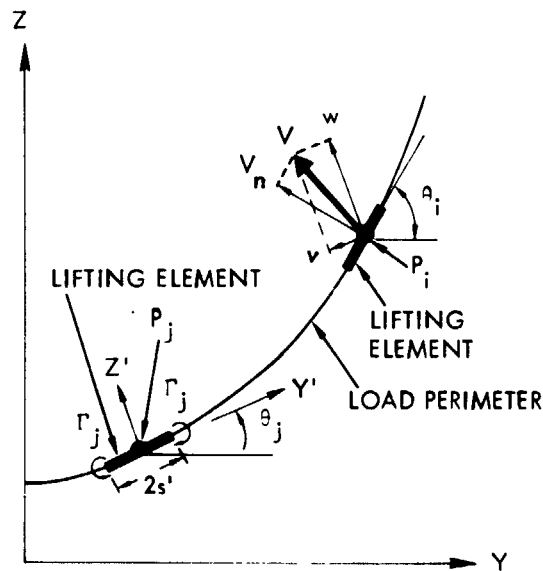
Figure 6.- Induced velocities in the
Trefftz plane.
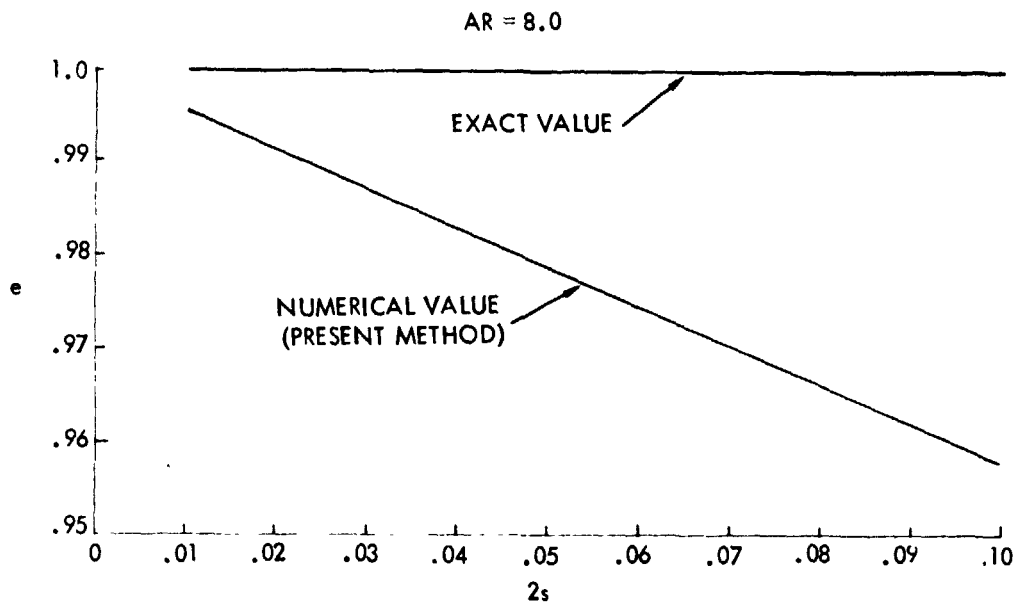
Figure 7.- Variation of efficiency for optimally loaded monoplane.
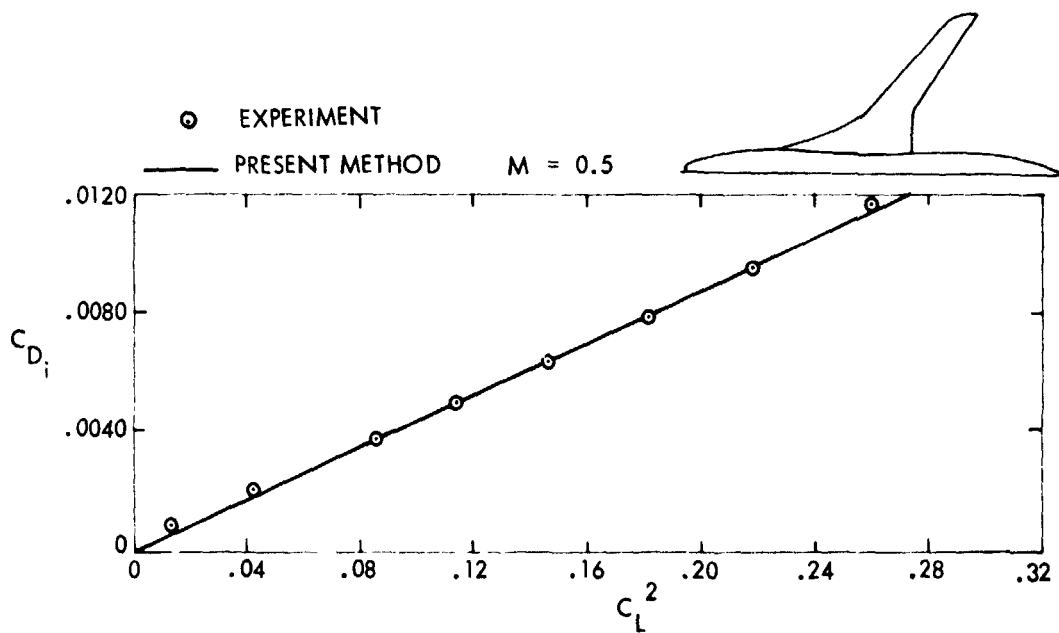
Figure 8.- Induced drag for Lockheed ATT-95 aircraft.
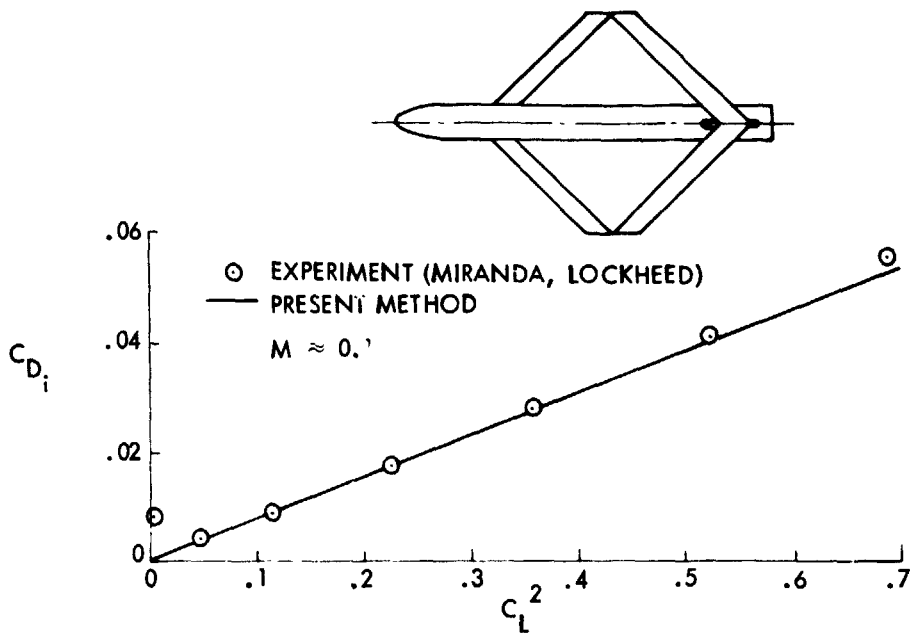
Figure 9.- Induced drag for a Lockheed boxplane.
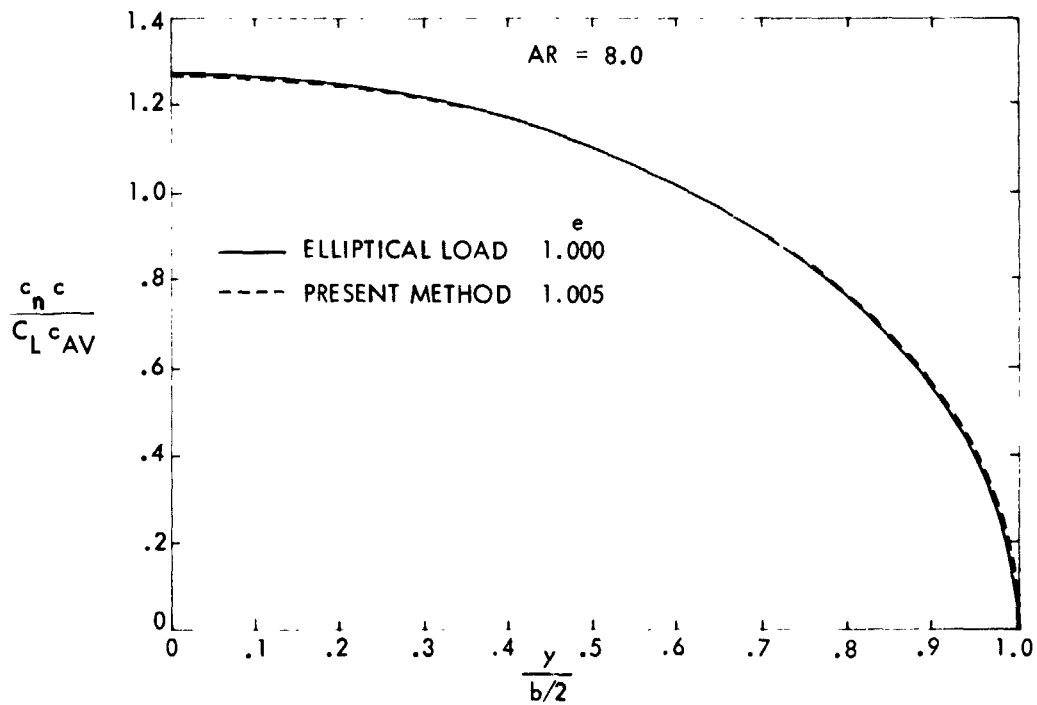
Figure 10.- Comparison of numerical and exact optimum
span loadings for a monoplane.
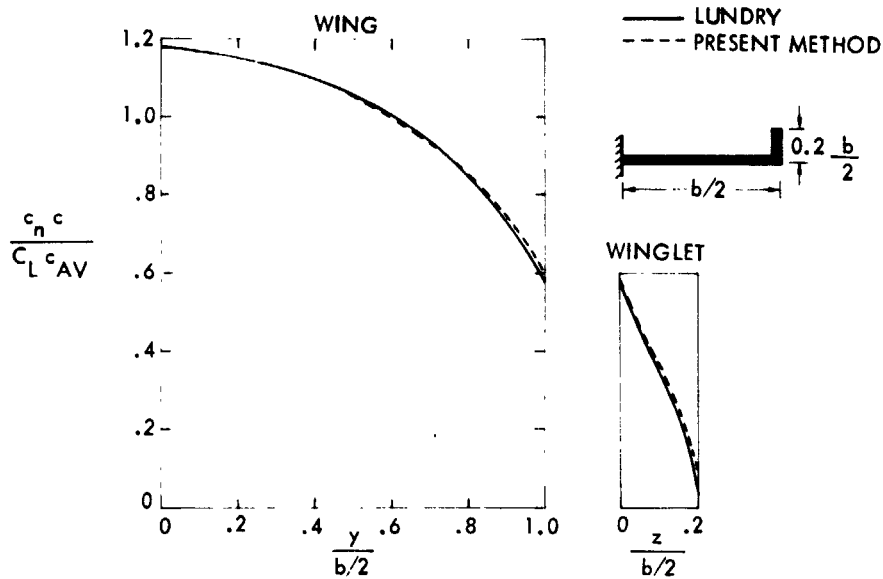
Figure 11.- Comparison of theoretical optimum loadings
for a wing/winglet configuration.

$C_L = 1.0$
$AR = 10.0$

WING - WINGLET

(1) $C_{D_{i_{w, w}}}$ = +.0369

(2) $C_{D_{i_{w, w\ell}}}$ = -.0110

(3) $C_{D_{i_{w\ell, w\ell}}}$ = +.0110

(4) $C_{D_{i_{w\ell, w}}}$ = -.0109

ΣC_{D_i} = +.0260

WING ALONE

C_{D_i} = +.0318
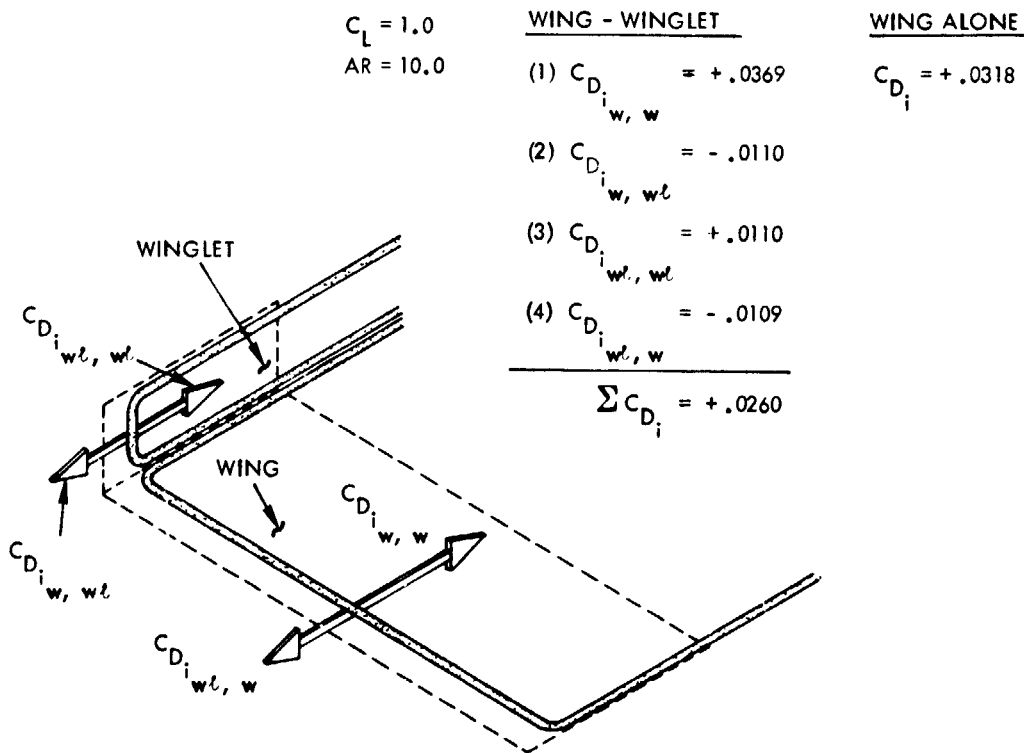
Figure 12.- Illustration of induced drag calculations for
a wing/winglet configuration.
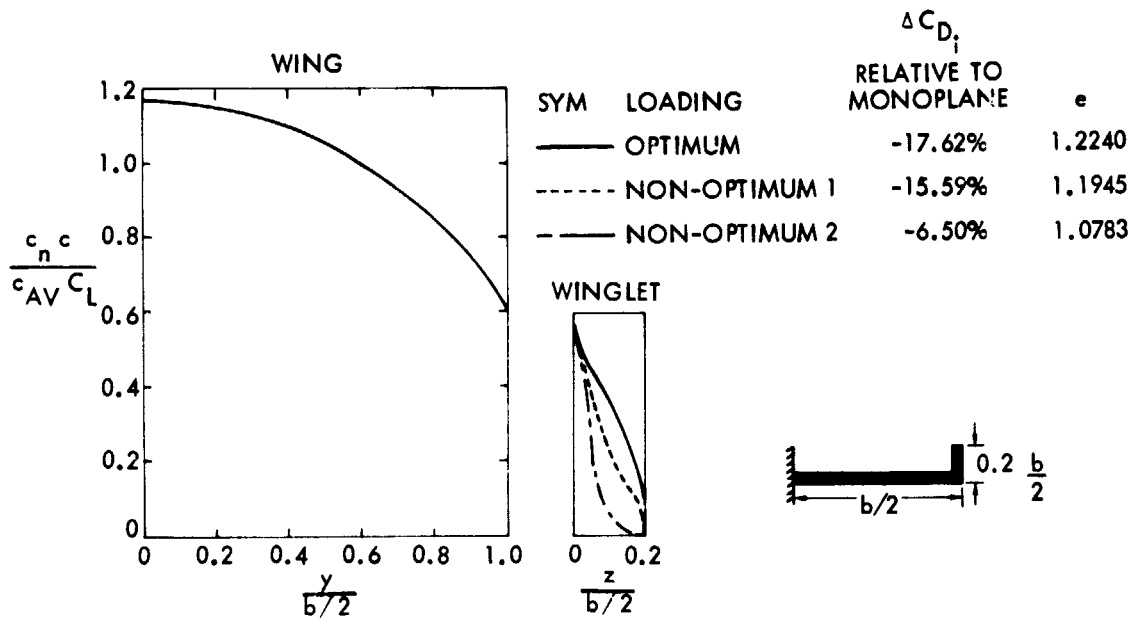
Figure 13.- Effect of changes in winglet loading on the ind·ied drag
of a wing/winglet configuration.
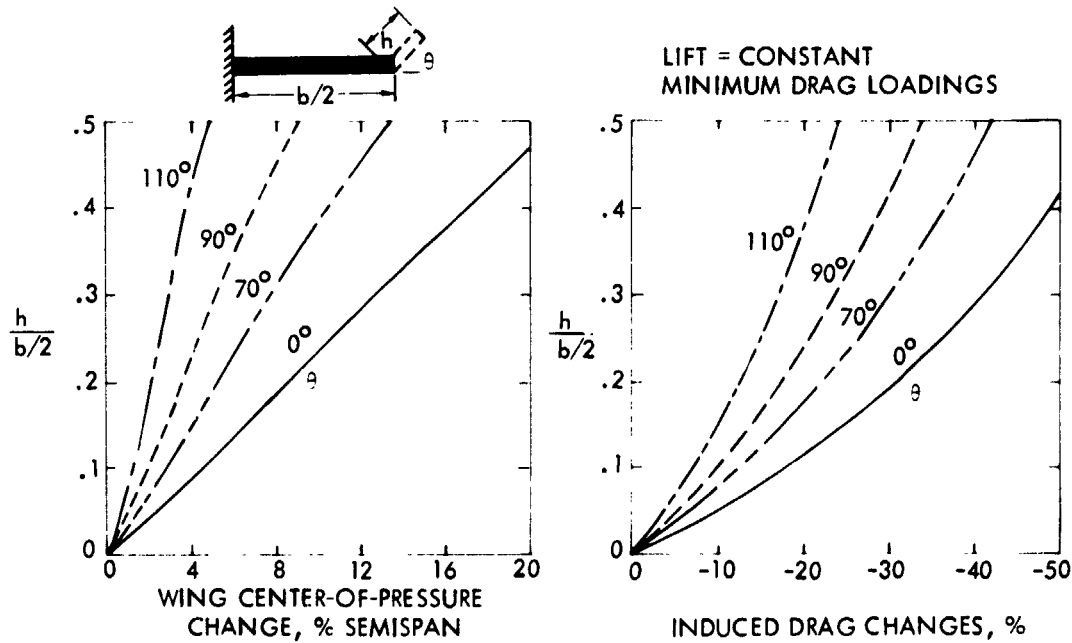
Figure 14.- Basic theoretical effects due to wing additions.

LIFT = CONSTANT
MINIMUM DRAG LOADING

INDUCED DRAG CHANGES, %

WING CENTER-OF-PRESSURE CHANGE
(% SEMISPAN)

Γ
0°
90°
110°
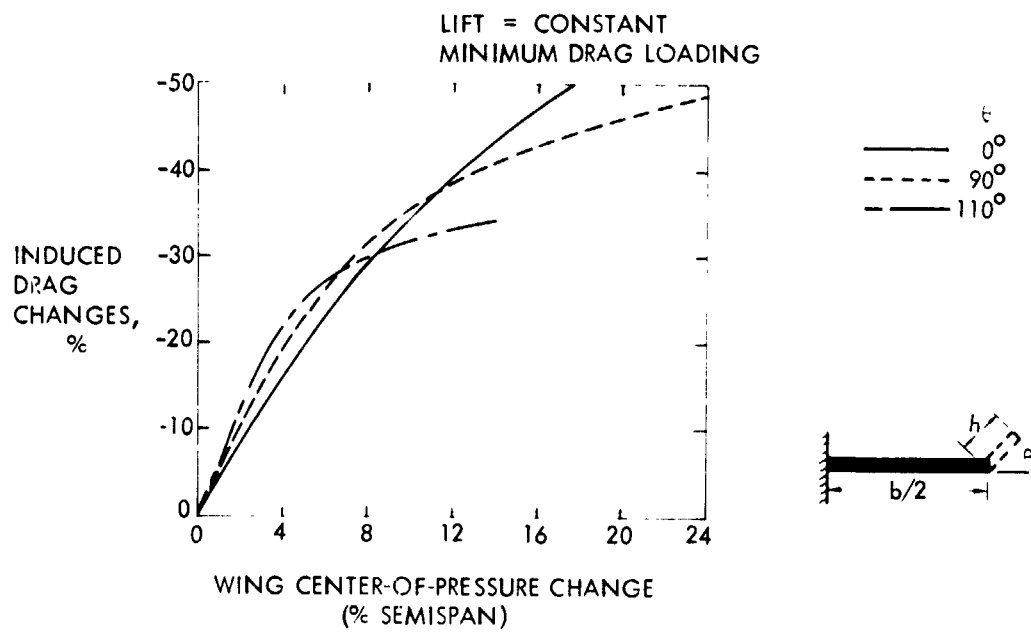
Figure 15.- Theoretical effect of wing additions
for various dihedral angles.

OPTIMIZATION AND DESIGN OF THREE-DIMENSIONAL AERODYNAMIC

CONFIGURATIONS OF ARBITRARY SHAPE

BY A VORTEX LATTICE METHOD

Winfried M. Feifel
The Boeing Company

SUMMARY

A new method based on vortex lattice theory has been developed which can be applied to the combined analysis, induced drag optimization, and aerodynamic design of three-dimensional configurations of arbitrary shape. Geometric and aerodynamic constraints can be imposed on both the optimization and the design process. The method is compared with several known analytical solutions and is applied to several different design and optimization problems, including formation flight and wingtip fins for the Boeing KC-135 tanker airplane. Good agreement has been observed between the theoretical predictions and the wind tunnel test results for the KC-135 modification.

INTRODUCTION

Falkner (ref. 1) has used vortex lattice networks as early as 1943 for the calculation of the aerodynamic forces on surfaces of arbitrary shape. With the advent of electronic digital computers, vortex lattice methods were the first powerful tools for three-dimensional potential flow analysis. In the past decade, vortex lattice computer codes were developed independently by several investigators, including Rubbert (ref. 2) and the author of this paper (ref. 3).

The vortex lattice approach is still favored for many engineering applications for several reasons, such as the ease of the problem description, the relatively small computational effort required and the "remarkable accuracy of the solution", as noted by James (ref. 4). One specific advantage of the vortex lattice idealization over the advanced panel methods is that the leading edge suction force is inherently included in the solution. This allows the computation of the configuration induced drag without resorting to the Trefftz-plane theorem.

Vortex lattice methods tend to slightly underpredict induced drag, as observed by Rubbert (ref. 2) and Kalman (ref. 5). However, as long as the paneling scheme is kept uniform, the induced drag computed by the vortex lattice method varies in a consistent fashion from known exact solutions. Therefore, it appears to be justifiable to utilize the vortex lattice near-field induced drag predictions for the optimization of the aerodynamic load distribution.

This paper presents a unified approach for the combined analysis, optimization, and design of three-dimensional aerodynamic configurations based on the vortex lattice technique. The new method will satisfy aerodynamic and geometric constraints while redesigning the contour of the configuration to yield minimum induced drag.

The new combined analysis-optimization-design method takes advantage of the vortex lattice near-field induced drag solution for the optimization process. When linearized boundary conditions with respect to the first guess of the configuration geometry are introduced, the new method can predict with good accuracy the changes in twist and camber required to achieve the load distribution for minimum induced drag and also satisfy additional design constraints.

PROBLEM FORMULATION

A good example of a complex design problem is the addition of wingtip fins to an existing airplane. For a given wing fin height and planform, the task is to determine the fin twist and camber, and the angle of attack of both the fin and the wing that will result in minimal induced drag for the airplane at a prescribed lift coefficient. To accomplish this, a mixed analysis/design problem must be solved. The problem can be stated as follows: Determine the twist and/or camber distribution required for portions or all of a three-dimensional system of wings with arbitrary planforms while a number of prescribed design requirements are satisfied. The design requirements could be any meaningful combination of the condition that the induced drag of the system (or of part of the system) be a minimum while at the same time a number of constraint conditions are imposed. Typical constraints would be, for example, that a given amount of lift be generated at a given pitching or rolling moment, or that the boundary conditions be satisfied on portions of the initial configuration.

72

Translated into the language of mathematics, the task described above amounts to finding the extremum of a function subject to a set of imposed constraints. Such a problem can be solved by Lagrange's method of multipliers.

SOLUTION

The configuration to be analyzed or designed is subdivided into a network of n panels spaced uniformly in spanwise and chordwise direction, as outlined in figure 1. Based on the theorem of Pistolesi (ref. 6) an unknown lifting vortex singularity γ is located along the 1/4-chord line of each panel. Helmoltz' law is satisfied by shedding a pair of trailing vortices along the panel edges downstream to infinity. It is a basic assumption for this horseshoe vortex model that these trailing vortices are aligned with the local flow direction; therefore, only the forces acting on the lifting vortex elements need to be computed. There are two points of special significance located on each panel: the lifting vortex midpoint and a boundary point at 3/4-chord.

Boundary Conditions

In the configuration analysis mode, the strength of the unknown singularities γ is determined such that the flow tangency condition is satisfied at all boundary points. In the configuration design mode, the boundary conditions need not necessarily be satisfied on the initial geometry, but there the angle formed between the panel surface and the velocity vector at the panel 3/4-chord point represents the unknown values $\Delta\alpha$, $\Delta\beta$ of the changes in panel orientation, which are necessary to yield the contour of the updated configuration.

The boundary condition for the panel j can be written in the generalized form

$$C(\gamma_1, \gamma_2 \ldots \gamma_n, \Delta\alpha_j, \Delta\beta_j) = \sum_{i=1}^{n} \gamma_i \, f_{ji} - \Delta\alpha_j a_j - \Delta\beta_j b_j - \vec{N}_j \cdot \vec{u}_\infty = 0 \quad (1)$$

where

f_{ji} =   boundary point influence coefficient indicating the velocity induced by a unit strength singularity i parallel to the surface normal vector $\vec{N}_j$ on panel j.

$\Delta\alpha_j, \Delta\beta_j$ = unknown pitch and yaw angles that may be required to reorient the panel j in order to satisfy the flow tangency at its boundary point.

a_j, b_j =   panel reorientation influence coefficients that indicate the change in $\vec{N}_j \cdot \vec{u}_\infty$ when the panel j is pitched or yawed by $\Delta\alpha = \Delta\beta = 1^\circ$.

$\vec{u}_\infty$ =   free stream velocity vector.

The panel reorientation influence coefficients are linearized with respect to the initial panel location. Therefore equation (1) can be considered accurate for orientation changes of approximately up to $\Delta\alpha_j = \Delta\beta_j = 20^\circ$. If the boundary condition has to be satisfied at the original position of the panel (analysis mode) then $\Delta\alpha_j$ and $\Delta\beta_j$ are zero.

Computation of Forces

The conditions at the 1/4-chord point (vortex midpoint) govern the forces acting on the panel. The velocity vector $\vec{v}_j$ at the 1/4-chord point is obtained as the sum of the free stream velocity vector $\vec{u}_\infty$ and the velocity induced according to Biot-Savert's law by all unknown vortex singularities in the flow field:

$$\vec{v}_j = \vec{u}_\infty + \sum_{i=1}^{n} \vec{w}_{ji} \, \gamma_i \tag{2}$$

where $\vec{w}_{ji}$ denotes the velocity induced at the midpoint of panel j by the unit strength horseshoe vortex of panel i. The velocity at the midpoint is assumed to represent the average value over the panel and is used to determine the force $\vec{F}_j$ acting on the panel by applying Kutta-Joukowsky's law for a fluid of unit density:

$$\vec{F}_j = \vec{v}_j \cdot \vec{S}_j \, \gamma_j \tag{3}$$

where $\vec{S}_j$ describes the length and orientation of the lifting vortex element.

The force vector $\vec{F}_j$ comprises the panel drag component D_j and the lift vector $\vec{L}_j$, which by definition is oriented normal to the free stream vector $\vec{u}_\infty$.

The induced drag of a whole configuration with n panels can be expressed as a quadratic function of all the panel vortex strengths γ in the form of the double sum:

$$D(\gamma_1 \cdots \gamma_n) = \sum_{j=1}^{n} \gamma_j \sum_{i=1}^{n} d_{ji} \, \gamma_j \tag{4}$$

74

The induced drag influence coefficients d_{ji} describe the drag force experienced by the panel j due to the panel i when their horseshoe vortices have unit strength. The drag influence coefficients contain only geometrical terms. In order to get a nontrivial minimum induced drag solution, at least one constraint must be introduced in addition to equation (4).

Constraint Conditions

There are a large number of different constraint conditions which can be imposed on the minimum induced drag problem. In the present method, any meaningful combination of the following constraints may be specified:

1) Boundary conditions: For each boundary condition to be satisfied, a new equation (1) is introduced.

2) Relationships between unknown singularities: The strength of certain horseshoe vortices or a relationship between groups of horseshoe vortices is introduced via an equation of the type:

$$C(\gamma_1, \gamma_2 \cdots \gamma_n) = \sum_{i=1}^{n} g_i \gamma_i + g_{n+1} = 0 \tag{5}$$

where the constants (g) are weighting functions describing the particular constraint condition.

3) Relationships between the panel reorientation parameters: The movements of panels or of groups of panels are controlled by the following constraint equations that establish relationships between the unknowns $\Delta\alpha$ and/or $\Delta\beta$:

$$C(\Delta\alpha_1 \cdots \Delta\alpha_n, \Delta\beta_1 \cdots \Delta\beta_n) = \sum_{i=1}^{n} g_i \Delta\alpha_i + \sum_{i=1}^{n} g_{n+1} \Delta\beta_i + g_{2n+1} = 0 \tag{6}$$

4) Force or moment relationships between groups of panels: Forces and moments due to individual panels or groups of panels are prescribed by equations of the following type:

$$C(\gamma_1, \cdots \gamma_n) = \sum_{i=1}^{n} g_i h_i \gamma_i + g_{n+1} \tag{7}$$

where the influence coefficient h_i indicates the force or the moment of the panel i for $\gamma_i = 1$.

The influence coefficients h_i are, in principle, described by equation (3). Equation (2) shows that for the computation of h_i, all vortex strengths γ need to be known. Equation (7) therefore is nonlinear. However, rather than solving the nonlinear problem directly, an iterative scheme is employed where the first solution of the vorticity distribution is found for $h_i^{(0)} = h_i(\vec{u}_\infty)$. Subsequent iterations use updated coefficients, $h_i^{(k)} = h_i(\vec{u}_\infty, \gamma_1^{(k-1)}, \ldots \gamma_n^{(k-1)})$ which are based on the vortex distribution of the previous solution. This process converges very rapidly, and in many cases the first solution is already sufficiently accurate.

Drag Minimization Under Constraint Conditions

The induced drag function (4) and the constraints C given by the expressions (1) and (5) through (7) may be combined in a new quadratic function:

$$G(\gamma_1 \cdots \gamma_n, \Delta\alpha_1 \cdots \Delta\alpha_n, \Delta\beta_1 \cdots \Delta\beta_n, \lambda_1 \cdots \lambda_m) = D(\gamma_1 \cdots \gamma_n) + \sum_{i=1}^{m} \lambda_i C_i \qquad (8)$$

where λ_i are the Lagrangian multipliers for m constraints imposed. A necessary requirement for the induced drag to be a minimum is that all the partial derivatives of equation (8) be zero. Differentiating the function G with respect to all its variables γ_1 through λ_m yields a system of simultaneous linear equations for the unknowns γ, $\Delta\alpha$, $\Delta\beta$, λ. Solution of this system of equations completes the configuration analysis-optimization-design process, unless an iteration is required to update the influence coefficients h of equation (7) or if the redesigned geometry deviates too much from the starting configuration.

VALIDATION OF THE TECHNIQUE

The vortex lattice analysis-optimization-design method has been programmed in FORTRAN IV on the CDC6600 computer. A series of data cases have been run to check the method against known analytical solutions.

Planar Wings

R. T. Jones (ref. 7) has given an analytical solution for the load distribution about wings of varying spans having the same prescribed lift and wing root bending moment. Some of his cases have been analysed by the present vortex lattice method using a single lifting line subdivided into 40 equal panels. The wingtip panel and its trailing vortex were inset by 1/4-panel span as proposed by Rubbert (ref. 2). The agreement between the vortex

lattice results and Jones' exact solution is excellent for both the shape and the spanwise load distribution (see figure 2) and the induced drag ratios shown in figure 3.

Nonplanar Configurations

Lundry (ref. 8) gives the induced drag factor, e, and the optimum spanwise circulation distribution obtained by a Trefftz-plane analysis of wings with a wingtip mounted end plate. Figure 4 shows the optimum circulation distribution on a wing with a 20% end plate compared to two vortex lattice results obtained with a single lifting line but using a different number of spanwise panels. The agreement with the exact solution is excellent, except in the corner between the wing and the tip fin. There the vortex lattice solution obtained with 25 panels per half-wing deviates slightly from the exact solution.

Some understanding of the source of the slight differences in span loading can be gained by comparing the downwash and sidewash computed at the midpoints of the lifting vortex elements with the known exact distribution. The Trefftz-plane analysis yields constant downwash along the span of the wing and zero sidewash along the span of the tip fin for the minimum induced drag load distribution. The present vortex lattice solution yields essentially the same results, but there are noticeable discrepancies in a small region of the wing-fin intersection, as shown in figure 5. This indicates that under certain conditions, the point selected for induced drag computation should not always be located exactly in the middle of each panel lifting vortex element. This error is, however, confined to a relatively small portion of the configuration and some of the downwash deviations are of oscillatory nature and therefore self-cancelling. The induced drag efficiency factors indicated by the vortex lattice method and by the exact solution are thus practically identical for this particular configuration, as shown in figure 6.

APPLICATION OF THE PRESENT VORTEX LATTICE DESIGN METHOD

The present method has been applied to a variety of problems, such as the design of wingtip fins, the modification of wings of a hydrofoil boat, and the optimum positioning of the leading-edge devices of the YC-14 military transport. The following two examples demonstrate some of the capabilities of the combined analysis-optimization-design vortex lattice method.

Formation Flight

Formation flying techniques have been proposed repeatedly as a means of reducing airplane drag. To get an estimate of the possible savings in induced drag, a group of five airplanes flying at the same altitude in an arrow formation illustrated in figure 7 were analyzed. The ideal (elliptic) load distribution, which yields minimum drag for the whole formation, is well known from the Trefftz-plane analysis. This optimum solution is, however, not practical since none of the airplanes off the centerline would be balanced in roll. In addition, a completely impractical wing twist distribution would be required to achieve such a load distribution. The induced drag savings indicated by this simple theory are, therefore, far too optimistic.

A more realistic picture is obtained by introducing the constraint that each airplane of the formation be trimmed in pitch and roll with respect to its own center of gravity. For this analysis, the airplanes are assumed to have swept, constant chord wings without wing twist. The left-hand and right-hand ailerons of each airplane are interconnected such that they deflect by equal but opposite angles. The horizontal tail is a simple flat plate. The unknown geometry variables are the angular deflections of every surface in the formation; ie, wing and horizontal tail incidences and aileron deflection angles. A lift coefficient of $C_L = 0.5$ is prescribed for the formation.

When only the lift for the whole airplane formation is prescribed, each of the airplanes carries a different amount of load, as seen in the top of figure 8. This distribution of the load between airplanes creates the minimum amount of induced drag for the whole formation flying at the conditions stated.

A more practical result is obtained when the constraint is introduced that each airplane in the formation flies at the same lift coefficient. Then the problem is fully defined, and only an analysis-design scheme has to be implemented. The load distribution and the induced drag values for the airplanes operating under this condition are shown in the center of figure 8.

As a third variant of the formation flight problem, the induced drag of only the No. 2 and No. 4 airplane has been minimized by allowing a redistribution of the formation weight among the other airplanes. The results are shown at the bottom of figure 8. The lift of the No. 2 and No. 4 airplanes is close to zero for minimum induced drag; the small residual lift stems from the condition that the planes are trimmed. This solution is only of academic interest, but it demonstrates the capability of the present method to minimize the induced drag of subsets of a configuration.

78

The analysis of this five-airplane formation using the vortex lattice method indicates that drag savings can be significant though much smaller than predicted by the idealizing Trefftz-plane assumptions. In addition, it is seen that the induced drag is unevenly distributed among the airplanes in the formation. Therefore, different formation arrangements should be used to obtain a more uniform drag level for all airplanes involved.

Wingtip Fins for the KC-135 Airplane

The present vortex lattice method has been used extensively by Ishimitsu, et al., (ref. 9) to evaluate and design tip fins for the KC-135 tanker airplane.

Figure 9 shows a typical vortex lattice representation of the KC-135 wing with the tip fins. Since the prime area of interest of this study was the region near the wingtip, the body of the airplane was not modeled in potential flow. The small loss in accuracy was believed to be outweighed by the savings in computer time. After a series of trades varying tip fin height and cant angle, the final planform was selected for the tip fin. For this given fin planform, the fin incidence angle and the profile camber shape were designed to yield minimum induced drag, while at the same time the boundary conditions were satisfied on the remainder of the airplane. As a first guess, the wing fin was input as a flat plate. The chordwise vorticity distribution on the fin was approximated by 10 lifting vortex elements, while 6 panels were used in the spanwise direction. Since the induced drag is independent of the shape of the chordwise load distribution (Munck's stagger theorem), the induced drag minimization problem is not fully defined unless a weighting function is introduced that prescribes how the vorticity is distributed among the 10 chordwise lifting elements. The vortex lattice program solves for the optimum total amount of lift carried by each chordwise column and for the orientation of the panels necessary to produce the prescribed chordwise load variation. The airfoil section camber line is obtained by integrating the panel slope changes calculated by the vortex lattice program. Thin airfoil theory has been used to superimpose a suitable thickness distribution and the fin camber lines. The results of this process are shown in figure 10.

The final tip fin configuration was tested in a wind tunnel. Figure 11 shows good agreement between the measured changes in a airplane drag and the predictions of the vortex lattice analysis. The experimental and theoretical loads on the wing and the tip fin are compared in figure 12. Considering that the incompressible vortex lattice analysis did not include the effects of the body and wing thickness, the agreement with the experiment is surprisingly good.

79

CONCLUSION

The vortex lattice method has been successfully applied to the design and optimization of three-dimensional configurations. The nonlinear analysis-design-optimization problem in which both the geometry or portions thereof and the optimum load distribution are unknown can be solved in a straightforward manner. The validity of the method has been demonstrated by application to several problems, previously not directly amenable to theoretical analysis. The new method has no serious dra...backs, but it must be applied with caution in regions of sudden geometric changes, such as intersecting wing surfaces, in which case additional work is required to determine the best paneling scheme and optimum location of the control points. Even though more advanced panel methods have been developed, the vortex lattice approach is still preferred in many applications for several reasons. The theory is simple and can be translated into fast numerical schemes. The vortex lattice approach, unlike many other methods, accounts for the leading edge suction force and therefore, yields an accurate near-field drag solution. These characteristics make the vortex lattice scheme a powerful tool in the hands of an experienced aerodynamicist for the analysis, modification, and optimization of three-dimensional configurations.

APPENDIX

SYMBOLS

|	
A	Wing area
AR	Wing aspect ratio
b	Wing span
c	Local chord length
$\bar{c}$	Mean chord length
C_D	Total airplane drag
C_{D_i}	Airplane induced drag
$C_{D_{i_{ell}}}$	Induced drag of elliptically loaded wing
C_L	Wing lift coefficient
C_ℓ	Local lift coefficient
e	Induced drag efficiency factor
h	Height of winglet
M_∞	Free stream Mach number
n	Number of panels
S	Wing half span
S_{ell}	Half span of elliptic wing
W	Downwash or sidewash at vortex midpoint
X, Y, Z	Cartesian coordinates
γ	Local vortex strength
η	Nondimensional spanwise station

81

REFERENCES

1. Falkner, V. M., "The Calculation of Aerodynamic Loading on Surfaces of Any Shape," R&M 1910, 1943, British Aeronautical Research Council.

2. Rubbert, P. E., "Theoretical Characteristics of Arbitrary Wings by a Nonplanar Vortex Lattice Method," Rept. D6-9244, 1964, The Boeing Company, Seattle, Wash.

3. Feifel, W. M., Fortran IV - Programm zur Berechnung von V-Leitwerken," Mitteilung im Institut für Aerodynamik und Gasdynamik der Technischen Universität, Stuttgart, Germany, 1966.

4. James, R. M., "On the Remarkable Accuracy of the Vortex-Lattice Discretization in Thin Wing Theory," Rept DAC-67211, McDonnell Douglas Corp, Long Beach, Calif., Feb. 1969.

5. Kalman, T. P., Giesing, J. P., Rodden, W. P., "Spanwise Distribution of Induced Drag in Subsonic Flow by the Vortex Lattice Method," J. Aircraft, Vol. 7, No. 6, 1970.

6. Pistolesi, E., "Betrachtungen über die gegenseitige Beeinflussung von Tragflügelsystemen." Gesammelte Vortrage der Hauptversammlung 1937 der Lilienthal-Gesellschaft (1937), S. 214-219.

7. Jones, R. T., "The Spanwise Distribution of Lift for Minimum Induced Drag or Wings Having a Given Lift and a Given Bending Moment," NACA Technical Note 2249, Ames Aeronautical Laboratory, Moffett Field, Calif., Dec. 1950.

8. Lundry, J. L., "A Numerical Solution for the Minimum Induced Drag, and the Corresponding Loading, of Nonplanar Wings," NASA CR-1218, issued by originator as Report DAC-66900, McDonnell Douglas Corp., Long Beach, Calif., 1968.

9. Ishimitsu, K. K., Van Devender, N., Dodson, R., "Design and Analysis of Winglets for Military Aircraft," Air Force Wright Aeronautical Laboratories, Wright-Patterson AFB, Ohio, Rpt No. AFFDL-TR-76-6, 1976.

82
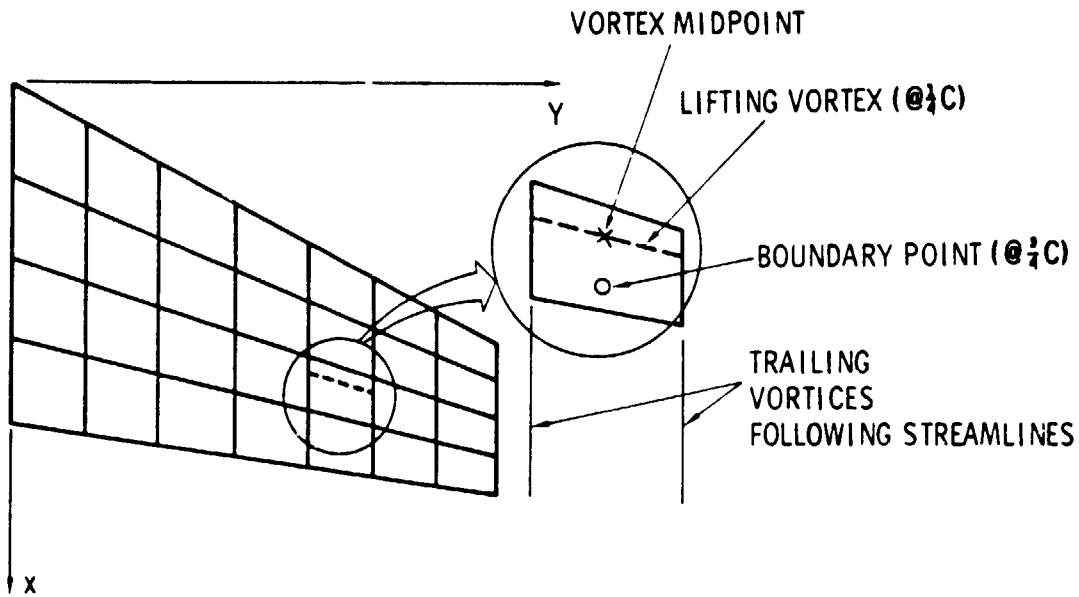
Figure 1.- Surface division into panels and location of
vortices and control points.
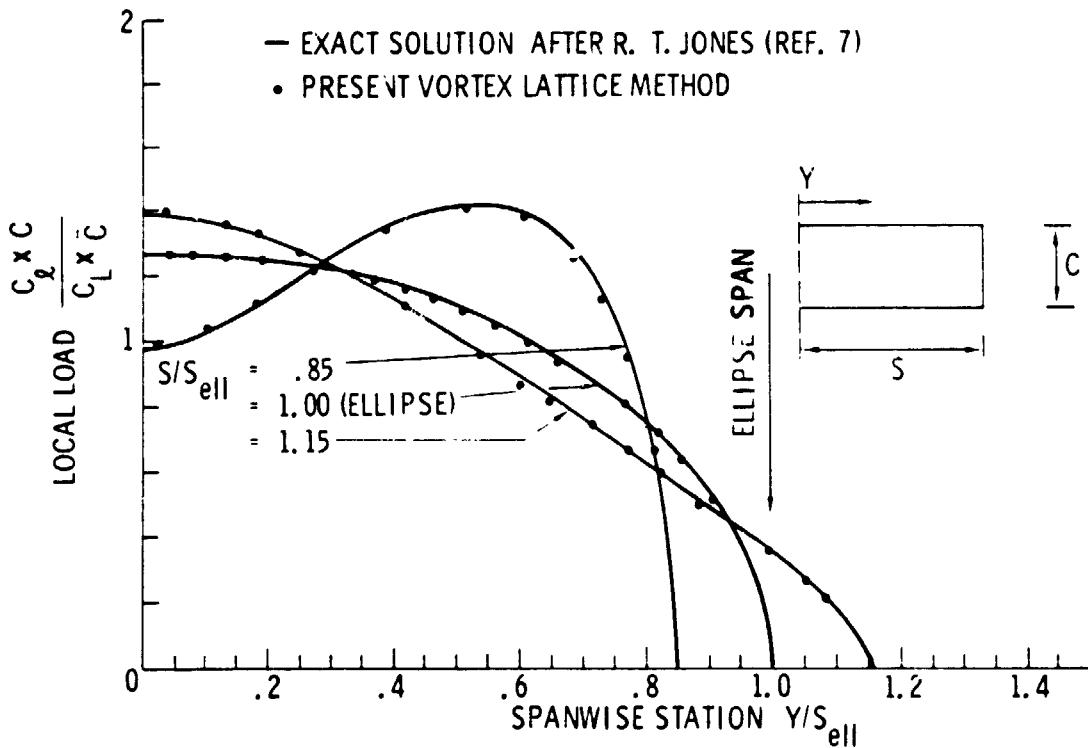
Figure 2.- Spanwise loading curve for minimum induced drag
of wings having a fixed total lift and a fixed root
bending moment.
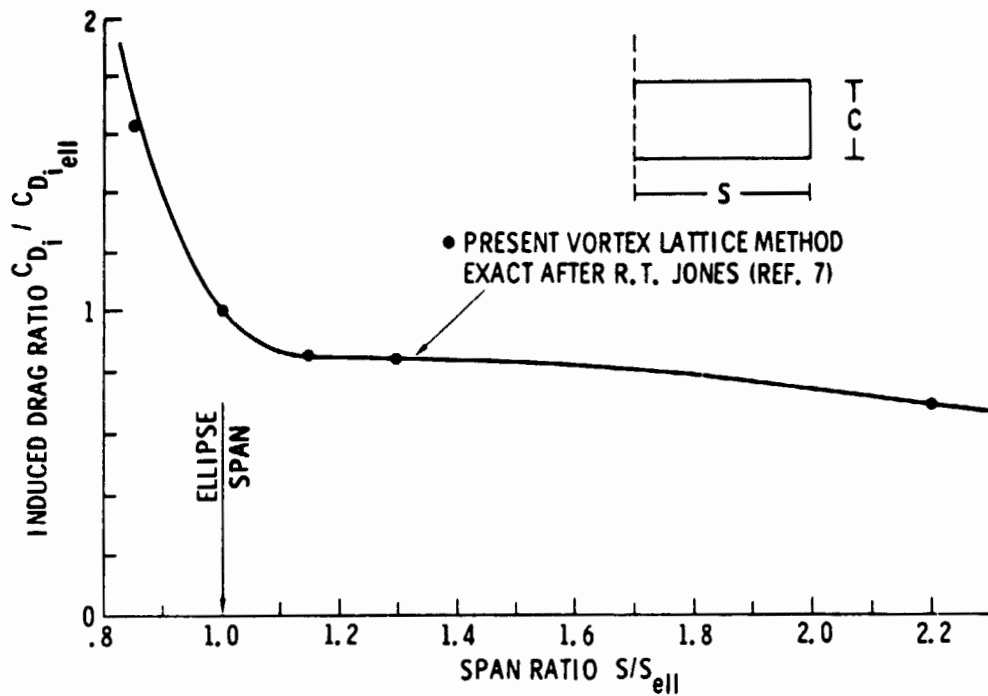
Figure 3.- Variation of minimum induced drag with span for
wings having a fixed total lift and a fixed root bending
moment.
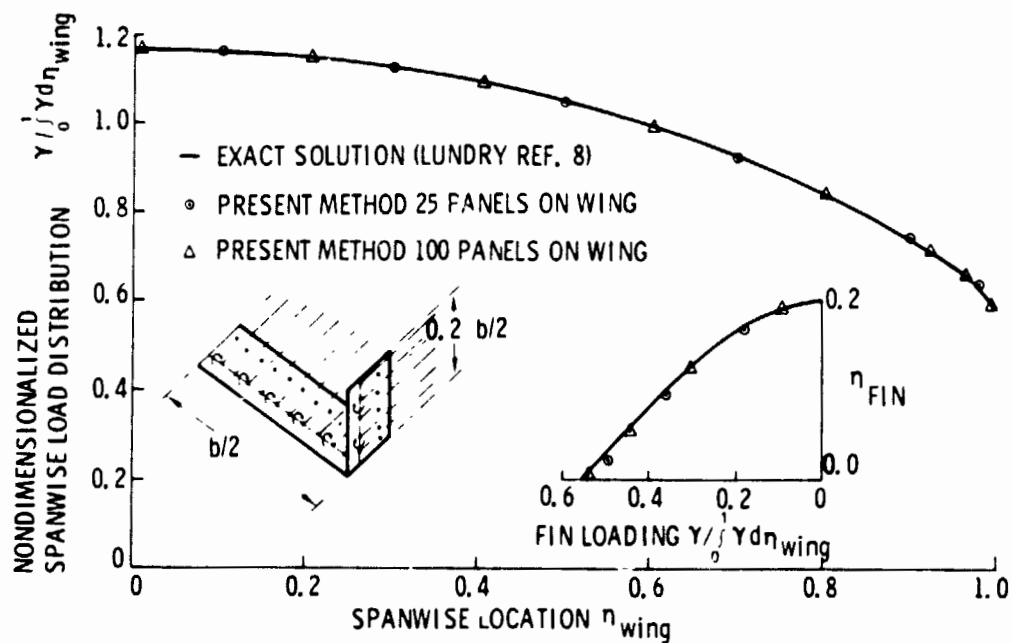
Figure 4.- Optimum load distribution about a wing with
an end plate.

84
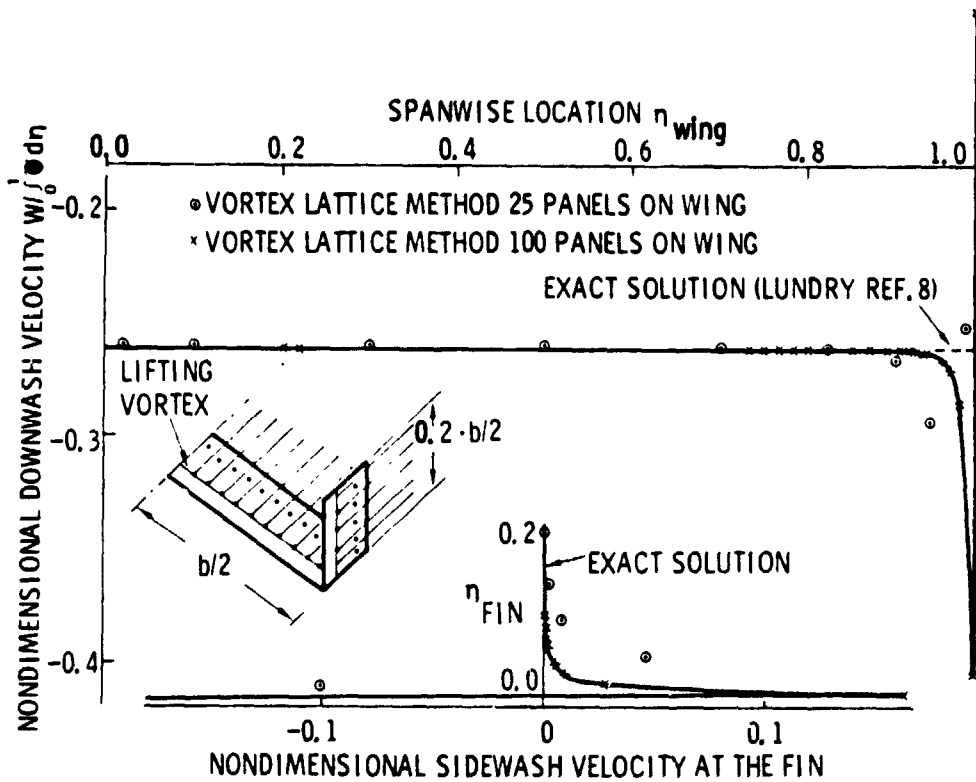
Figure 5.- Downwash and sidewash along the 1/4-chord line of a wing and end plate for the minimum induced drag load distribution.
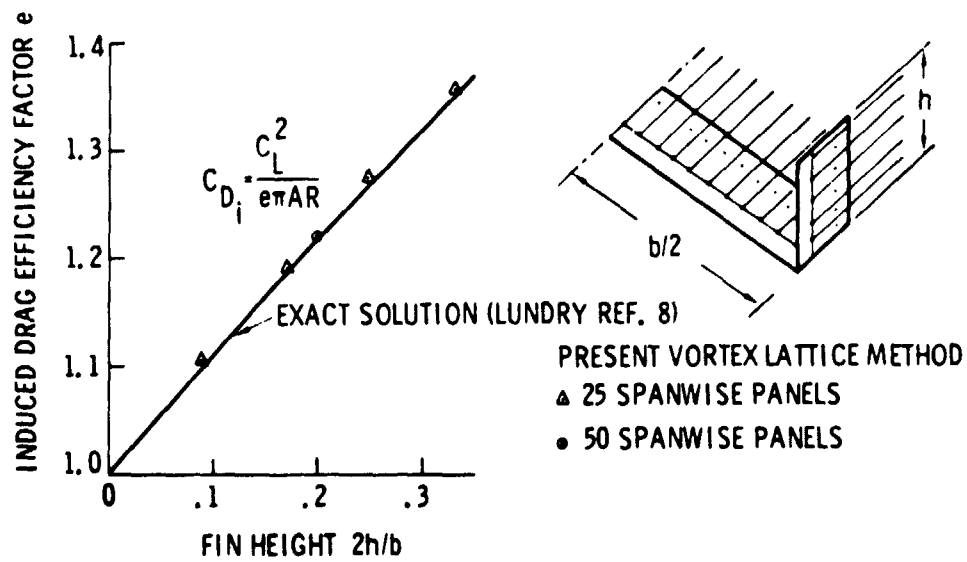
Figure 6.- Induced drag efficiency factor of wings with an end plate.

5 AIRPLANE ARROW FORMATION

AIRPLANE GEOMETRY:
- UNTWISTED SWEPT WING
- UNTWISTED HOR. TAIL
- LEFT-HAND AND RIGHT-HAND
  AILERONS INTERCONNECTED 1 1
- GIVEN LOCATION OF CENTER OF GRAVITY

PROBLEM SOLVED BY VORTEX LATTICE METHOD
- FIND WING & HOR. TAIL ANGLE OF ATTACK
  AND AILERON DEFLECTIONS REQUIRED
  TO TRIM EACH AIRPLANE IN PITCH AND
  ROLL AT A GIVEN
- a) FORMATION LIFT COEFF. & MIN. DRAG
- b) AIRPLANE LIFT COEFFICIENT
- c) MIN INDUCED DRAG FOR PLANE NO. 2 & 4
  AT GIVEN FORMATION LIFT COEFFICIENT

A_{ref} AIRPLANE = 6.0

A_{ref} FORMATION = 30.0

AR AIRPLANE = 6.0

AR FORMATION = 30.0
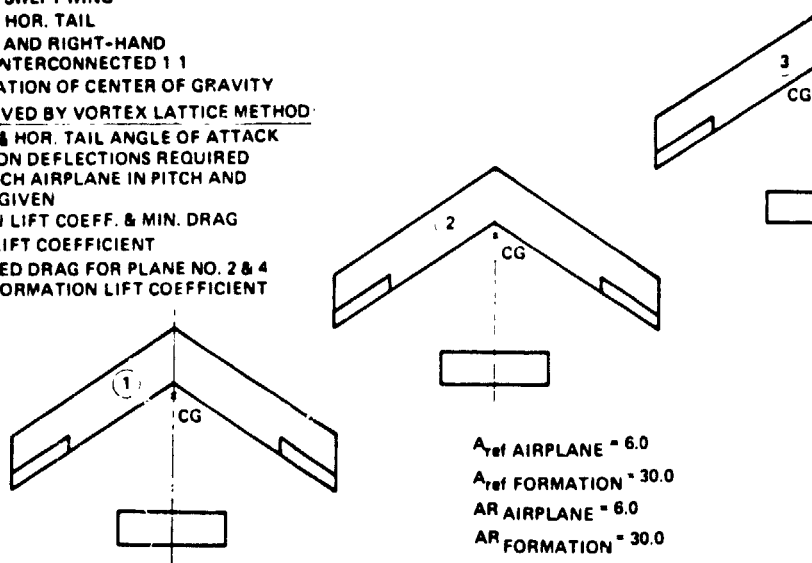
Figure 7.- Five-airplane arrow formation.

IDEAL (ELLIPTIC) LOAD
DISTRIBUTION FOR MINIMUM INDUCED
DRAG AT FORMATION C_L = .5
UNTRIMMED, UNCON-
STRAINED WING TWIST

a) FORMATION MINIMUM INDUCED DRAG SPANWISE LOAD DISTRIBUTION
   AIRPLANES TRIMMED AT OPTIMUM LIFT COEFFICIENT

b) SPANWISE LOAD DISTRIBUTION ABOUT FORMATION, ALL AIRPLANES
   TRIMMED AT C_L = .5

c) SPANWISE LOAD DISTRIBUTION FOR MINIMUM INDUCED DRAG OF THE NO 2
   AND NO. 4 AIRPLANES
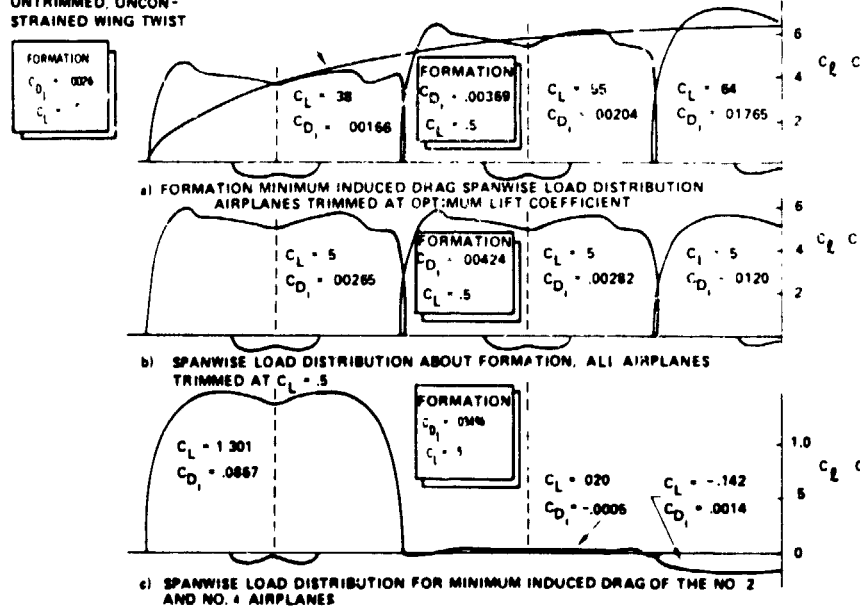
Figure 8.- Spanwise load distributions about five airplanes
flying in arrow formation at the same altitude.
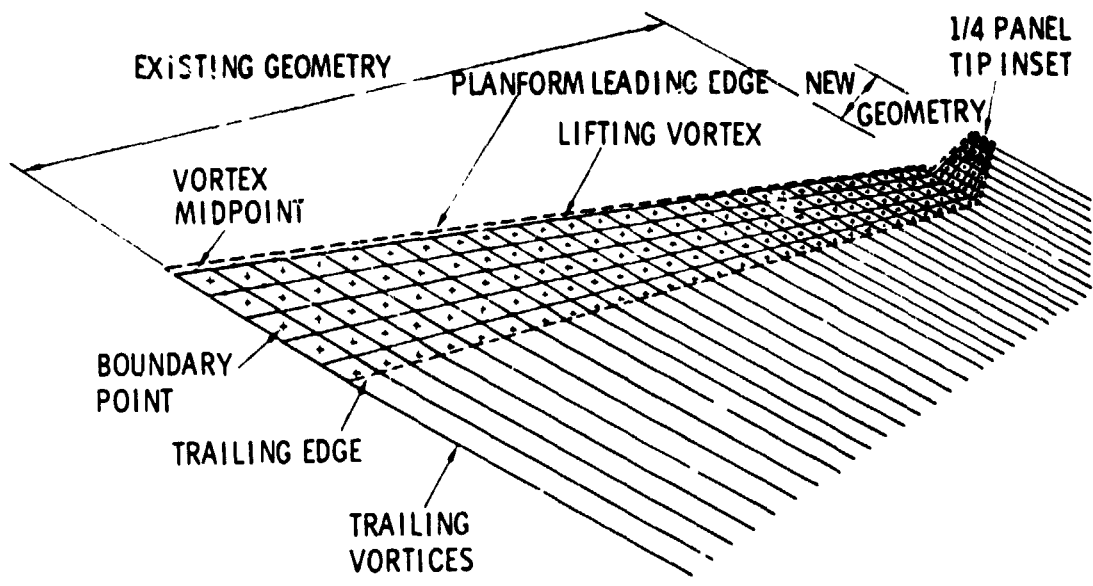
Figure 9.- Typical representation of wing and winglet by a multi-horseshoe vortex lattice system.
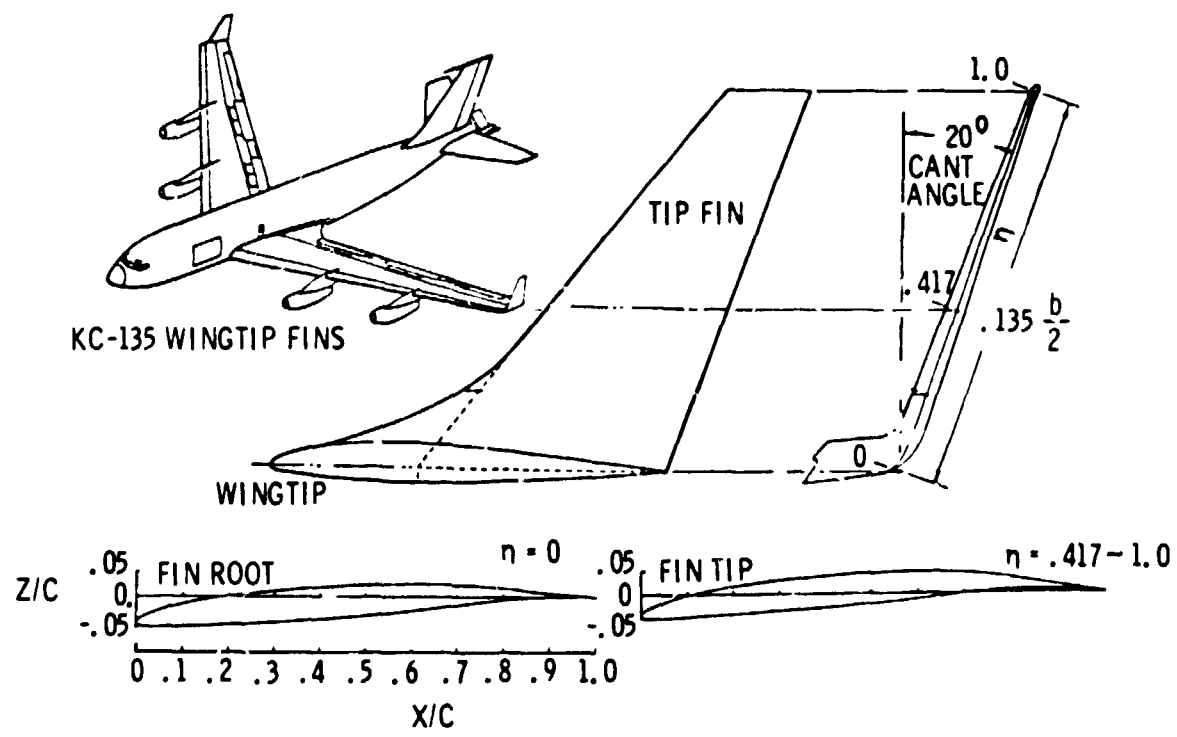
Figure 10.- Tip fin airfoil sections with camber line designed by vortex lattice optimizing method.
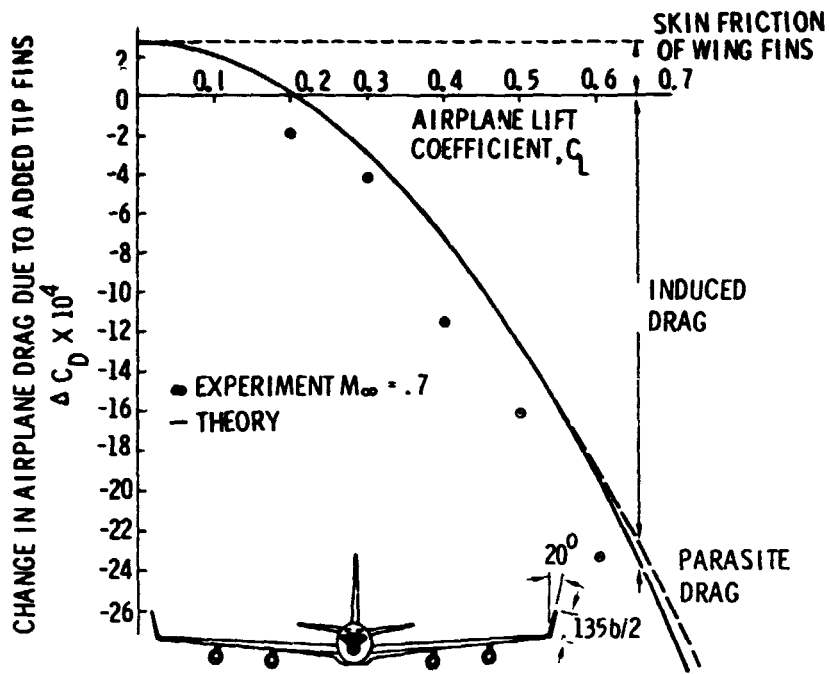
Figure 11.- Measured and predicted drag change of
Boeing KC-135 with tip fins.
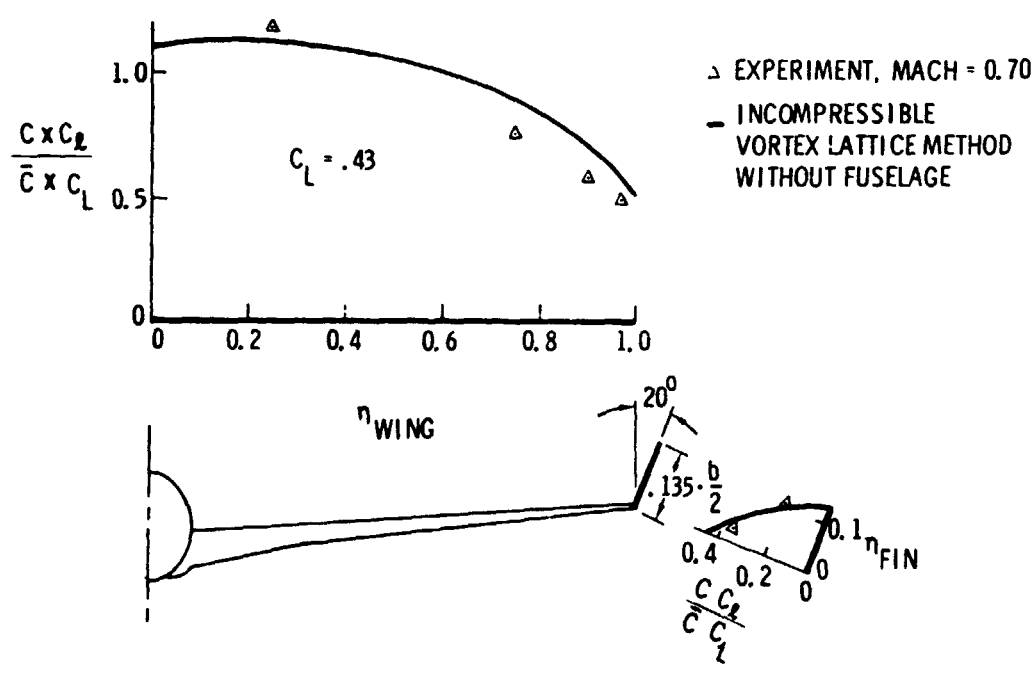
Figure 12.- Comparison between experimental and theoretical
span load distribution about KC-135 with tip fins.

MINIMUM TRIM DRAG DESIGN FOR INTERFERING LIFTING

SURFACES USING VORTEX-LATTICE METHODOLOGY

John E. Lamar
NASA Langley Research Center

SUMMARY

A new subsonic method has been developed by which the mean camber surface can be determined for trimmed noncoplanar planforms with minimum vortex drag. This method uses a vortex lattice and overcomes previous difficulties with chord loading specification. This method uses a Trefftz plane analysis to determine the optimum span loading for minimum drag, then solves for the mean camber surface of the wing, which will provide the required loading. Pitching-moment or root-bending-moment constraints can be employed as well at the design lift coefficient.

Sensitivity studies of vortex-lattice arrangement have been made with this method and are presented. Comparisons with other theories show generally good agreement. The versatility of the method is demonstrated by applying it to (1) isolated wings, (2) wing-canard configurations, (3) a tandem wing, and (4) a wing-winglet configuration.

INTRODUCTION

Configuration design for subsonic transports usually begins with the wing, after which the body and its effects are taken into account, and then the tails are sized and located by taking into account stability and control requirements. With the advent of highly maneuverable aircraft having closely coupled lifting surfaces, there has been an increased interest in changing the design order so that multiple surfaces could be designed together to yield a trimmed configuration with minimum induced drag at some specified lift coefficient. Such a combined design approach requires that the mutual interference of the lifting surfaces be considered initially.

Single planform design methods are available to optimize the mean camber surface, better called the local elevation surface, for wings flying at subsonic speeds (for example, ref. 1) and at supersonic speeds (for example, refs. 2 and 3). The design method presented in reference 1 was developed from an established analysis method (Multhopp type), also presented in reference 1, by using the same mathematical model, but the design method solves for the local mean slopes rather than the lifting pressures. In the usual implementation of reference 1, the design lifting pressures are taken to be linear chordwise, but must be represented in this solution by a sine series which oscillates about them. An example presented herein demonstrates that corresponding oscillations may appear in pressure distributions measured on wings which have been designed by the method of reference 1. The method developed herein overcomes this oscillatory lifting pressure behavior by specifying linear chord loadings at the outset.

The development approach used in the two-planform design problem will be similar to that used for a single planform. The analytic method employed, selected because of its geometric versatility, is the noncoplanar two-planform vortex-lattice method of reference 4.

The design procedure is essentially an optimization or extremization problem. Subsonic methods (for example, see refs. 5 and 6) are available for determining the span load distributions on bent lifting lines in the Trefftz plane, but they do not describe the necessary local elevation surface. This is one of the objectives of the present method which will utilize the Lagrange multiplier technique (also employed in refs. 2 and 3). The method of reference 4 is used to provide the needed geometrical relationships between the circulation and induced normal flow for complex planforms, as well as to compute the lift, drag, and pitching moment.

This paper presents limited results of precision studies and comparisons with other methods and data and is a condensed version of reference 7. Several examples of solutions for configurations of recent interest are also presented.

SYMBOLS

$A_{l,n}$ element of aerodynamic influence function matrix A which contains induced normal flow at lth point due to nth horseshoe vortex of unit strength; total number of elements is $\frac{N}{2} \times \frac{N}{2}$

AR   aspect ratio

a   fractional chord location where chord load changes from constant value to linearly varying value toward zero at trailing edge

a_i, b_i, c_i coefficients in spanwise scaling polynomial

b   wing span

C_D drag coefficient

$C_{D,o}$ drag coefficient at $C_L = 0$

$C_{D,v}$ vortex or induced drag coefficient, $\dfrac{\text{Vortex drag}}{q_\infty S_{ref}}$

C_L lift coefficient, $\dfrac{\text{Lift}}{q_\infty S_{ref}}$

C_m pitching-moment coefficient about $\bar{Y}$-axis, $\dfrac{\text{Pitching moment}}{q_\infty S_{ref} c_{ref}}$

ΔC_p lifting pressure coefficient

c   chord

90

c_l section lift coefficient

c_{ref} reference chord

I $\equiv \left[\bar{N}_c a + 0.75 \right]$ (brackets indicate "take the greatest integer")

K maximum number of spanwise scaling terms in solution technique for wings without dihedral

L lift

$M_{\bar{Y}}$ pitching moment about coordinate origin

M_∞ free-stream Mach number

m number of span stations where pressure modes are defined as used in reference 1

N maximum number of elemental panels on both sides of configuration; maximum number of chordal control points at each of m span stations as used in reference 1

$\bar{N}_c$ number of elemental panels from leading to trailing edge in chordwise row

$\bar{N}_s$ total number of (chordwise) rows in spanwise direction of elemental panels on configuration semispan

q_∞ free-stream dynamic pressure

S_{ref} reference area

s horseshoe vortex semiwidth in plane of horseshoe (see fig. 1)

U free-stream velocity

X,Y,Z axis system of given horseshoe vortex (see fig. 1)

$\bar{X},\bar{Y},\bar{Z}$ body-axis system for planform (see fig. 1)

$\hat{X},\hat{Y},\hat{Z}$ wind-axis system for planform (see sketch (a))

x,y,z distance along X-, Y-, and Z-axis, respectively

$\bar{x},\bar{y},\bar{z}$ distance along $\bar{X}$-, $\bar{Y}$-, and $\bar{Z}$-axis, respectively

$\Delta\bar{x}$ incremental movement of $\bar{X}$-$\bar{Y}$ coordinate origin in streamwise direction

y^*, z^* y and z distances from image vortices located on right half of plane of symmetry, as viewed from behind, to points on left panel

$\bar{z}_c$ canard height with respect to wing plane, positive down

$\bar{z}/c$ local elevation normalized by local chord, referenced to local trailing-edge height, positive down

$(\partial\bar{z}/\partial\bar{x})_l$ lth elemental local slope in vector $\{\partial\bar{z}/\partial\bar{x}\}$ of N/2 elements (see eq. (1))

α angle of attack, deg

Γ_n vortex strength of nth element in vector $\{\Gamma\}$ of N/2 elements

ε incidence angle, positive leading edge up, deg

δ independent variable in extremization process

η_l nondimensional spanwise coordinate based on local planform semispan

ξ distance along local chord normalized by local chord

ξ' fractional chordwise location of point where mean camber height is to be computed (see eq. (14))

σ, σ' dihedral angle from trailing vortex to point on left panel being influenced; σ measured from left panel, σ' measured from right panel

ϕ horseshoe vortex dihedral angle in $\bar{Y}\text{-}\bar{Z}$ plane on left wing panel, deg

ϕ' horseshoe vortex dihedral angle on right wing panel, $\phi' = -\phi$, deg

Subscripts:

c   canard

d   design

i,j,k   indices to vary over the range indicated

le   leading edge

l,n   associated with slope point and horseshoe vortex, respectively, ranging from 1 to N/2

L   left trailing leg

92

R   right trailing leg

ref   reference value

w   wing

Matrix notation:

{ }   column vector

[ ]   square matrix
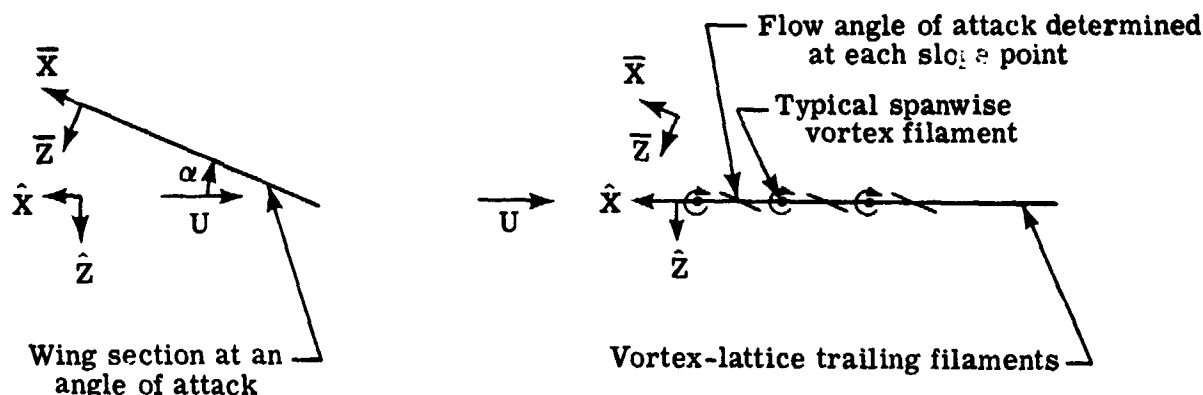
Sketch (a)

THEORETICAL DEVELOPMENT

This section presents the application of vortex-lattice methodology to the mean-camber-surface design of two lifting planforms which may be separated vertically and have dihedral. For a given planform, local vertical displacements of the surfaces with respect to their chord lines in the wing axis (see sketch (a)) are assumed to be negligible; however, vertical displacements of the solution surfaces due to planform separation or dihedral are included. The wakes of these bent lifting planforms are assumed to lie in their respective extended bent chord planes with no roll up. For a two-planform configuration the resulting local elevation surface solutions are those for which both the vortex drag is minimized at the design lift coefficient and the pitching moment is constrained to be zero about the origin. For an isolated planform no pitching-moment constraint is imposed. Thus, the solution is the local elevation surface yielding the minimum vortex drag at the design lift coefficient. Lagrange multipliers together with suitable interpolating and integrating procedures are used to obtain the solutions. The details of the solution are given in the following five subsections.

Relationship Between Local Slope and Circulation

From reference 4, the distributed circulation over a lifting system is related to the local slope by

$$\left\{ \frac{\partial \bar{z}}{\partial \bar{x}} \right\} = [A] \left\{ \frac{\Gamma}{U} \right\} \tag{1}$$

where the matrix $[A]$ is the aerodynamic influence coefficient matrix based on the paneling technique described in reference 4.

Circulation Specification

Once the surface slope matrix $\{\partial \bar{z}/\partial \bar{x}\}$ is known, chordwise integration can be performed to determine the local elevation surface $\bar{z}/c$, which contains the effects of camber, twist, and angle of attack. The major problem to be solved is determining the necessary circulation matrix $\{\Gamma/U\}$ to employ in equation (1). The problem is simplified somewhat by having the chordwise shape of the bound circulation remain unchanged across each span, although the chordwise shape may vary from one planform to another. The chordwise loadings allowable in the program range from rectangular to right triangular toward the leading edge and were selected because they are of known utility. An example is given in figure 2. Two different techniques are utilized to arrive at the spanwise scaling of the chordwise shapes. The particular technique to be employed depends on whether the configuration has dihedral.

For a configuration having dihedral, the spanwise scaling must be determined discretely because no finite polynomial representation of the scaling is known with certainty, even for an isolated wing. However, for configurations with no dihedral, the spanwise scaling can be written as a polynomial for each planform,

$$\sqrt{1 - \eta_l^2} \left(a_i + b_i \eta_l^2 + c_i \eta_l^4 \right)$$

(see fig. 2) with a maximum of three coefficients per planform being determined as part of the solution. It is possible to write this polynomial as a solution because the isolated wing solution is known to be of the elliptical form

$\sqrt{1 - \eta_l^2}$, and the presence of the other planform is assumed to generate a loading disturbance which can be represented by the other two terms in addition to adjusting a_i. Once the scaling is known from either technique, then $\{\Gamma/U\}$ is readily obtained by multiplication.

Lift, Pitching-Moment, and Drag Contributions

The contributions to C_L and to C_m, respectively, from the jth chordwise row of horseshoe vortices are

$$C_{L,j} = \frac{L_j}{q_\infty S_{ref}} = \frac{4 q_\infty s \cos \phi_j}{q_\infty S_{ref}} \sum_{i=1}^{\bar{N}_c} \left(\frac{\Gamma}{U} \right)_i \tag{2}$$

94

and

$$C_{m,j} = \frac{M_{\bar{Y},j}}{q_\infty S_{ref} c_{ref}} = \frac{4q_\infty s \cos \phi_j}{q_\infty S_{ref} c_{ref}} \sum_{i=1}^{\bar{N}_c} \left(\frac{\Gamma}{U}\right)_i \bar{x}_{j,i} \qquad (3)$$

where

$$\left(\frac{\Gamma}{U}\right)_i \equiv \begin{cases} 1 & \left(\xi_i \leq a\right) \\ \dfrac{1 - \xi_i}{1 - a} & \left(\xi_i > a\right) \end{cases} \qquad (4a)$$

$$\xi_i \equiv \frac{i - 0.75}{\bar{N}_c} \qquad (4b)$$

and

$$\bar{x}_{j,i} \equiv \left(\bar{x}_{1e}\right)_j - \left(\frac{i - 0.75}{\bar{N}_c}\right) c_j \qquad (5)$$

Even though $C_{L,j}$ and $C_{m,j}$ actually occur on the wing at the jth span-
wise location, they can be utilized in a Trefftz plane solution if the chordwise
summations are performed. This utilization is possible herein because the trail-
ing wake is assumed not to roll up, and the general configuration has specifiable
chord loading shapes. Summing the chordwise loadings at this point allows the
solution of the spanwise scaling to be performed on a bent lifting line located
in the Trefftz plane, which is, of course, ideally suited for the vortex drag
computation. In addition, the summation reduces the number of unknowns from the

product of $\bar{N}_c$ and $\bar{N}_s$ to only $\bar{N}_s$. Hence, a larger value of $\bar{N}_s$ can be used
in the Trefftz plane, which should yield improved accuracy in the spanwise scal-
ing factors without affecting the number of horseshoe vortices on the wing.
Then, when the circulations are needed on the wing for use in equation (1), the
well-defined variations of the spanwise scaling factors are interpolated to the
original spanwise positions of the wing vortex lattice which is used to generate
[A]. The procedure is implemented as follows:

The summation in the lift expression (eq. (2)) can be written as

$$\sum_{i=1}^{\bar{N}_c} \left(\frac{\Gamma}{U}\right)_i = \sum_{i=1}^{I} \left(\frac{\Gamma}{U}\right)_i + \sum_{i=I+1}^{\bar{N}_c} \left(\frac{\Gamma}{U}\right)_i \qquad (6)$$

where I is the last i value which satisfies $\xi_i \leq a$; that is,

$$I \equiv \left[\bar{N}_c a + 0.75\right] \tag{7}$$

where the brackets indicate "take the greatest integer." Hence,

$$\sum_{i=1}^{\bar{N}_c} \left(\frac{\Gamma}{U}\right)_i = I + \frac{\left(\bar{N}_c + 0.75\right)\left(\bar{N}_c - I\right)}{\bar{N}_c(1 - a)} - \frac{1}{\bar{N}_c(1 - a)} \sum_{i=I+1}^{\bar{N}_c} i \tag{8}$$

Similarly, the summation in the pitch expression (eq. (3)) can be written as

$$\sum_{i=1}^{\bar{N}_c} \left(\frac{\Gamma}{U}\right)_i \bar{x}_{j,i} = \left[\left(\bar{x}_{1e}\right)_j + \frac{0.75c_j}{\bar{N}_c}\right]\left[I + \frac{\left(\bar{N}_c + 0.75\right)\left(\bar{N}_c - I\right)}{\bar{N}_c(1 - a)}\right] - \frac{c_j}{\bar{N}_c} \sum_{i=1}^{I} i$$

$$- \frac{1}{\bar{N}_c(1 - a)}\left[\left(\bar{x}_{1e}\right)_j + c_j + \frac{1.5c_j}{\bar{N}_c}\right] \sum_{i=I+1}^{\bar{N}_c} i$$

$$+ \frac{c_j}{\bar{N}_c^2(1 - a)} \sum_{i=I+1}^{\bar{N}_c} i^2 \tag{9}$$

The contribution to the vortex drag coefficient at the ith chordwise row due to the jth chordwise row is obtained by using only half the trailing vortex induced normal wash from the Trefftz plane. The result is

$$C_{D,i,j} = \frac{s}{\pi S_{ref}} \left[\sum_{i=1}^{\bar{N}_c} \left(\frac{\Gamma}{U}\right)_i \sum_{j=1}^{\bar{N}_c} \left(\frac{\Gamma}{U}\right)_j \right] \left[\frac{\pm\cos\left(\sigma_{L,i,j} - \phi_i\right)}{\sqrt{\left(y_{i,j} + s\cos\phi_j\right)^2 + \left(z_{i,j} + s\sin\phi_j\right)^2}} \right.$$

$$- \frac{\pm\cos\left(\sigma_{R,i,j} - \phi_i\right)}{\sqrt{\left(y_{i,j} - s\cos\phi_j\right)^2 + \left(z_{i,j} - s\sin\phi_j\right)^2}}$$

$$- \frac{\cos\left(\sigma'_{L,i,j} - \phi_i\right)}{\sqrt{\left(y^*_{i,j} + s\cos\phi'_j\right)^2 + \left(z^*_{i,j} + s\sin\phi'_j\right)^2}}$$

$$\left. + \frac{\cos\left(\sigma'_{R,i,j} - \phi_i\right)}{\sqrt{\left(y^*_{i,j} - s\cos\phi'_j\right)^2 + \left(z^*_{i,j} - s\sin\phi'_j\right)^2}} \right] \tag{10}$$

In the $\pm$ sign, plus indicates that the trailing vortex filament is to the left of the influenced point; minus, to the right.

In using equations (2), (3), and (10), a new vortex system is set up in the Trefftz plane in which the bent chord plane is represented by a system of uniformly spaced trailing vortices (the quantity $2s$ in fig. 1). This uniformity of vortex spacing leads to a simplification in the equations and can be thought of as a discretization of the ideas of Munk (ref. 8) and Milne-Thomson (ref. 9) for a bound vortex of constant strength.

Spanwise Scaling Determination

To determine the spanwise scaling with either technique requires the combination of the contributions from each spanwise position for configurations with dihedral or the mode shape contributions for configurations without dihedral. These contributions must be employed in the appropriate total C_L and C_m constraint equations as well as in the $C_{D,v}$ extremization operation. Due to limited space only the solution for wings without dihedral will be discussed. The equations to be employed in the Lagrange extremization method are

$$C_L = 2 \sum_{k=1}^{K} \delta_k C_{L,k} \tag{11}$$

97

$$C_m = 2 \sum_{k=1}^{K} \delta_k C_{m,k} \tag{12}$$

and

$$C_{D,v} = 2 \sum_{i=1}^{K} \sum_{k=1}^{K} \delta_i C_{D,i,k} \delta_k \tag{13}$$

where $K \leq 6$ and $C_{L,k}$ and $C_{m,k}$ are the C_L and C_m contributions associated with the kth term in the polynomials

$$\sqrt{1 - \eta_1^2} \left(\delta_1 + \delta_2 \eta_1^2 + \delta_3 \eta_1^4 \right)$$

or

$$\sqrt{1 - \eta_1^2} \left(\delta_4 + \delta_5 \eta_1^2 + \delta_6 \eta_1^4 \right)$$

(Note that $k = 1, 2,$ and 3 are assigned to the first planform and 4, 5, and 6 to the second.) These contributions are computed by first assuming a unit value of scaling with each term in the polynomial, then multiplying each resulting spanwise scaling distribution by the $C_{L,j}$ and $C_{m,j}$ terms of equations (2) and (3), and finally summing spanwise over all the chordwise rows associated with each set of k values (or planform). The vortex drag coefficient associated with the ith and kth combination of spanwise scaling distributions $C_{D,i,k}$ is compared similarly. The δ_k terms are equivalent to the unknown coefficients in the polynomial and are the independent variables in the solution.

An application of the preceding process to a conventional wing-tail configuration is shown in figure 3. The resulting idealized loading set is of the type that would meet the constraints and extremization.

Determination of Local Elevation Curves

With δ_k known, then $\{\Gamma/U\}$, C_L, C_m, and $C_{D,v}$ can be determined. The results for $\{\Gamma/U\}$ are interpolated to the original spanwise positions of the paneling which is used in equation (1) and in the following equation to find the local elevation curves. The equation for the local elevation above the computational plane at a particular point $(\xi', \bar{y})$ is

$$\frac{\bar{z}}{c}(\xi', \bar{y}) = \int_1^{\xi'} \frac{\partial \bar{z}}{\partial \bar{x}}(\xi, \bar{y}) \, d\xi \tag{14}$$

RESULTS AND DISCUSSION

General

It is necessary to examine the sensitivity of the results of the present method to vortex-lattice arrangement. It is also important to compare results obtained with this method with those available in the literature. Unfortunately, the available solutions, whether exact or numerical, may not be for configurations which will exercise the constraint or extreminization capabilities of the present method. In fact, the available exact solutions are for configurations which are either two-dimensional sections or isolated three-dimensional wings with a nonelliptic span loading. The solutions for such configurations require program modifications to the span loading and involve no optimization.

Two-Dimensional Comparison

Various chordwise arrangements and number of vortices were investigated for several chordwise loading shapes, of which the $a = 0.6$ results are given in figure 4. Although difficult to see clearly from this figure, the agreement of the present method with analytic results (ref. 10) is good for both local slope and elevation. Examination of figure 4 leads to the following general conclusions concerning the chordwise arrangement: (1) Uniform spacing is preferred; (2) $\bar{N}_c = 20$ is a good compromise when considering both computational requirements and completely converged results. An additional conclusion is that the present method yields incidence angles near the leading edge which are slightly higher than the analytical ones.

Number of Rows Along Semispan $\left(\bar{N}_s\right)$

Various spanwise arrangements and number of vortices were studied for one planform and from these studies the following conclusions were drawn: (1) Uniform spacing is preferred; (2) for at least 10 spanwise rows per semispan, the local slopes and elevations were not too sensitive to increasing the number.

Three-Dimensional Comparisons

Two comparisons with available mean-camber-surface solutions will be made. The comparisons are for a high-aspect-ratio sweptback and tapered wing with a uniform area loading at $C_{L,d} = 1.0$ and $M_\infty = 0.90$ and a lower aspect-ratio trapezoidal wing with $a = 1.0$, spanwise elliptic loading at $C_{L,d} = 0.35$, and $M_\infty = 0.40$.

Figure 5 presents the predicted results from the present method for the sweptback wing and compares these results with those from references 1 and 11. A comparison of the three solutions indicates that they are all in generally good agreement with the exception of the results at $\frac{y}{b/2} = 0.05$. The surprising result is that the present method and the modified Multhopp method (ref. 1) agree as well as they do at this span station because of the known differences that exist between them near the plane of symmetry. The reason for the larger disagreement between the present method and that of reference 11 near $\frac{y}{b/2} = 0$

is not clear, but this disagreement may be caused by the different $\bar{N}_c$ values utilized by the two methods. Reference 11 effectively uses an infinite number since over each infinitesimal span strip across the wing the method locates a single quadrilateral vortex around the periphery of the enclosed area. This vortex extends from the leading edge to the trailing edge and includes segments of the edges as well. For a uniform area loading, the trailing leg parts of the quadrilateral vortices cancel with adjacent spanwise ones all across the wing. This leaves only the edge segments to contribute to the induced flow field. The present method utilizes a numerical rather than a graphical solution in order to provide a general capability; hence, $\bar{N}_c$ values are limited as discussed previously. Also, vortices are not placed around the leading and trailing edges in the present method.

A comparison of the present design method with that of reference 1 is shown in figure 6 for a lower aspect-ratio trapezoidal wing. The local slopes and elevations determined by the two methods are in reasonably close agreement at the three spanwise locations detailed; however, an oscillatory trend is evident in the local slopes obtained from the method of reference 1 (fig. 6(a)). These oscillations apparently originate in the truncated sine series used in reference 1 to represent a uniform chordwise distribution. Integration of the local slopes to obtain local elevations tends to suppress the oscillations (fig. 6(b)); however, the local pressures depend upon the slope rather than the elevation. Consequently, the measured chordwise pressure distribution will demonstrate the same oscillatory character. A model built according to the design of reference 1 was tested (ref. 12), and the measured pressure distributions for a typical spanwise location (fig. 6(c)) indicate that indeed the oscillations are present. Presumably, similar measurements on a model designed by the present method would not behave in this manner since the input loadings are truly linear.

Force tests (ref. 13) of an essentially identical model indicate that the measured drag polar was tangent to $C_D = C_{D,o} + \dfrac{C_L{}^2}{\pi AR}$; that is, the vortex drag was indeed a minimum at the design C_L (or 100 percent leading-edge suction was obtained). It is presumed from the small differences in local slope between the present method and the method of reference 1 that a similar result would be obtained for a design by the present method.

Application to a Wing-Canard Combination

The present method has been demonstrated by optimizing a wing-canard combination (fig. 7). To illustrate how the span load optimizing feature operates with the constraints, figure 8 presents individual and total span load distributions for various values of $\bar{a}_c$ and $\bar{a}_w$ with the moment trim point at $\dfrac{\Delta \bar{x}}{b/2} = 0.1$ and $\dfrac{\bar{z}_c}{b/2} = 0$. (This trim point is given with respect to the axis system shown in the sketch in figure 9.) From figure 8 there are three important observations to be made: (1) The individual span loadings change in the anticipated direction with the changing chord loadings in order to meet the same C_L and C_m constraints; (2) the total span loading does not change; (3) consequently, the vortex drag of the configuration is constant, as would be anticipated from Munk's stagger theorem.

100

The effects of varying the vertical separation and the moment trim point on the resulting drag and span loadings are also illustrated (figs. 9 and 10). All surfaces are designed for $C_{L,d} = 0.2$, $a_c = 0.6$, $a_w = 0.8$, and $M_\infty = 0.30$ and have $C_m = 0$ about the moment trim point. Figure 9 shows that for all vertical separations, moving the moment trim point forward increases the vortex drag over some range, and furthermore, increasing the out-of-plane vertical separation reduces the vortex drag. Of course, not all moment trim points utilized will produce a stable configuration. These variations illustrate the importance of balancing the lift between the two lifting surfaces so that for some reasonable moment trim point and vertical separation, the vortex drag will be at a minimum. The minimum point on each vortex drag curve occurs with the pitching-moment constraint not affecting the extremization.

Figure 10 presents the individual span loadings with increasing vertical separation $\left(\dfrac{\bar{z}_c}{b/2} < 0 \text{ above the wing plane}\right)$ with $a_c = 0.6$ and $a_w = 0.8$. There are three observations which can be made from these results for increasing vertical separation: (1) The individual span loadings tend to become more elliptical; (2) consequently, the vortex drag decreases; (3) the individual lift contributions show only a little sensitivity to separation distance once the canard is above the wing when compared with the coplanar results.

Application to Tandem Wing Design

This design method has been employed in the determination of the local elevation surfaces for a tandem wing. Figure 11 shows a sketch of a tandem wing configuration and selected results taken from the wind-tunnel tests made with a model based on this design at a Mach number of 0.30 (ref. 14). At $C_{L,d} = 0.35$ the vortex drag increment is correctly estimated. The measured C_m is slightly positive (0.02). Reference 14 states that a part of the C_m error $\left(C_m \text{ should be zero}\right)$ is a result of a difference in the fuselage length between the designed and constructed model.

Design of a Wing-Winglet Configuration

Figure 12 presents the wing-winglet combination of interest along with pertinent aerodynamic characteristics and local elevations obtained from the present method. For comparison these same items are calculated with a program modification that adds a root-bending-moment constraint to produce the same moment that would be obtained on the original wing extending to the plane of symmetry but without its basic wingtip. The assumed span loading is elliptical. The force and moment coefficients are based on the wing outside of a representative fuselage and without the basic wingtip.

The results of this comparison are as follows: (1) The root-bending-moment constraint increases the vortex drag slightly because of the changes in the $c_\ell c$ distribution required; (2) the differences in local elevations are confined primarily to the outer 50 percent semispan and result mainly from the differences in the incidence angles; (3) significant amounts of incidence are required in the winglet region with or without the root-bending-moment constraint.

CONCLUDING REMARKS

A new subsonic method has been developed by which the mean camber (local elevation) surface can be determined for trimmed noncoplanar planforms with minimum vortex drag. This method employs a vortex lattice and overcomes previous difficulties with chord loading specification. This method designs configurations to have their local midsurface elevations determined to yield the span load for minimum vortex drag while simultaneously controlling the pitching-moment or root-bending-moment constraint at the design lift coefficient. This method can be used for planforms which (1) are isolated, (2) are in pairs, (3) include a winglet, or (4) employ variable sweep, but only at a specified sweep position.

Results obtained with this method are comparable with those from other methods for appropriate planforms. The versatility of the present method has been demonstrated by application to (1) isolated wings, (2) wing-canard configurations, (3) a tandem wing, and (4) a wing-winglet configuration.

REFERENCES

1. Lamar, John E.: A Modified Multhopp Approach for Predicting Lifting Pressures and Camber Shape for Composite Planforms in Subsonic Flow. NASA TN D-4427, 1968.

2. Carlson, Harry W.; and Middleton, Wilbur D.: A Numerical Method for the Design of Camber Surfaces of Supersonic Wings With Arbitrary Planforms. NASA TN D-2341, 1964.

3. Sorrells, Russell B.; and Miller, David S.: Numerical Method for Design of Minimum-Drag Supersonic Wing Camber With Constraints on Pitching Moment and Surface Deformation. NASA TN D-7097, 1972.

4. Margason, Richard J.; and Lamar, John E.: Vortex-Lattice FORTRAN Program for Estimating Subsonic Aerodynamic Characteristics of Complex Planforms. NASA TN D-6142, 1971.

5. Lundry, J. L.: A Numerical Solution for the Minimum Induced Drag, and the Corresponding Loading, of Nonplanar Wings. NASA CR-1218, 1968.

6. Loth, John L.; and Boyle, Robert E.: Optimum Loading on Nonplanar Wings at Minimum Induced Drag. Aerosp. Eng. TR-19 (Contract N00014-68-A-1512), West Virginia Univ., Aug. 1969. (Available from DDC as AD 704 502.)

7. Lamar, John E.: A Vortex-Lattice Method for the Mean Camber Shapes of Trimmed Noncoplanar Planforms With Minimum Vortex Drag. NASA TN D-8090, 1976.

8. Munk, Max M.: The Minimum Induced Drag of Aerofoils. NACA Rep. 121, 1921.

9. Milne-Thomson, L. M.: Theoretical Aerodynamics. Second ed. D. Van Nostrand Co., Inc., 1952.

10. Abbott, Ira H.; Von Doenhoff, Albert E.; and Stivers, Louis S., Jr.: Summary of Airfoil Data. NACA Rep. 824, 1945. (Supersedes NACA WR L-560.)

11. Katzoff, S.; Faison, M. Frances; and DuBose, Hugh C.: Determination of Mean Camber Surfaces for Wings Having Uniform Chordwise Loading and Arbitrary Spanwise Loading in Subsonic Flow. NACA Rep. 1176, 1954. (Supersedes NACA TN 2908.)

12. Henderson, William P.: Pressure Distributions on a Cambered Wing-Body Configuration at Subsonic Mach Numbers. NASA TN D-7946, 1975.

13. Henderson, William P.; and Huffman, Jarrett K.: Effect of Wing Design on the Longitudinal Aerodynamic Characteristics of a Wing-Body Model at Subsonic Speeds. NASA TN D-7099, 1972.

14. Henderson, William P.; and Huffman, Jarrett K.: Aerodynamic Characteristics of a Tandem Wing Configuration at a Mach Number of 0.30. NASA TM X-72779, 1975.
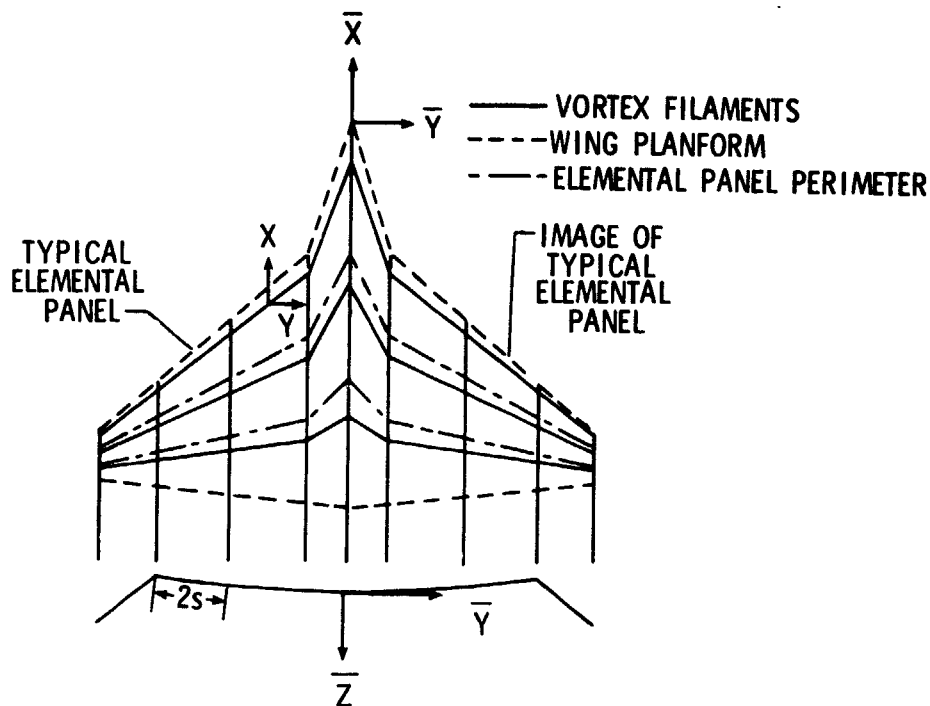
Figure 1.- Axis systems, elemental panels, and horseshoe vortices for typical wing planform.
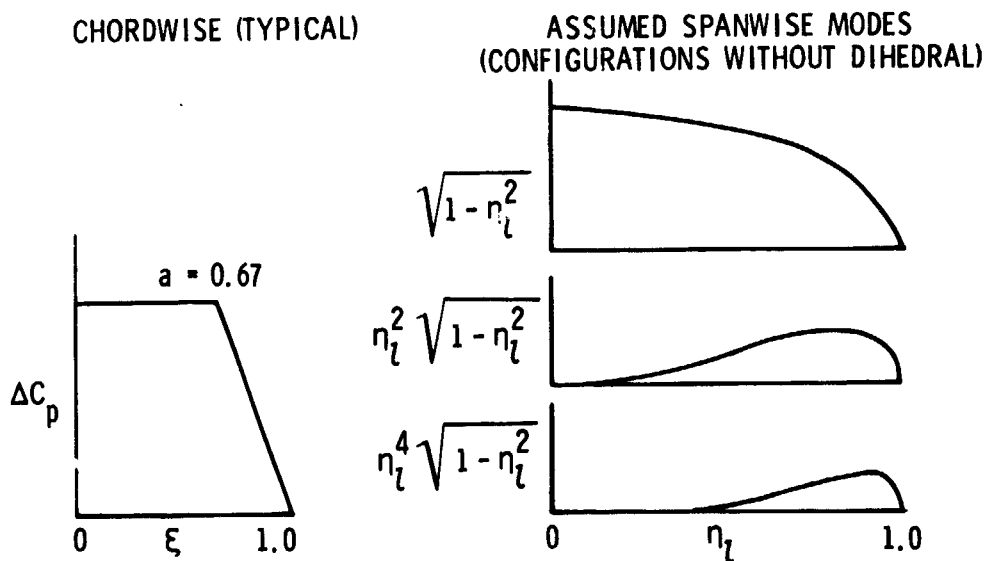

Figure 2.- Planform load distributions.
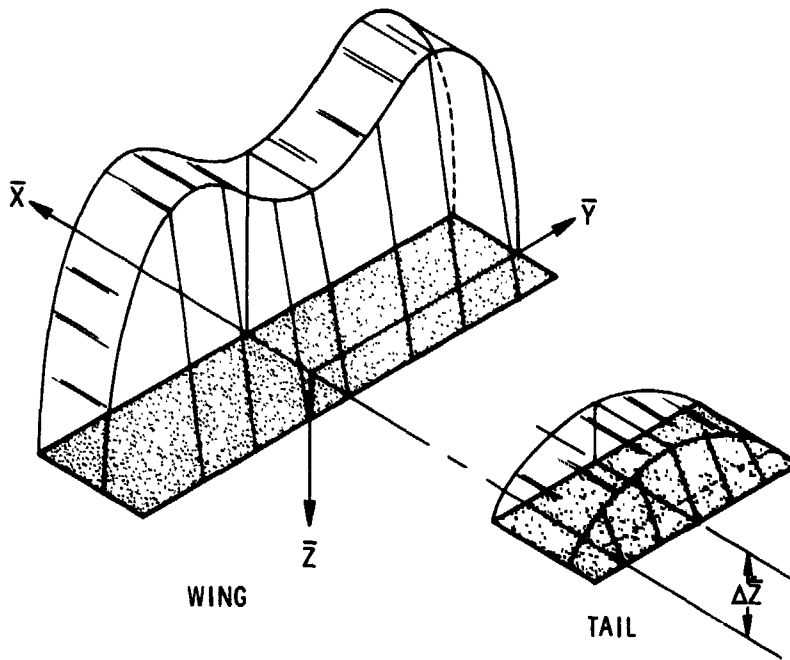
Figure 3.- Idealized loading set on trimmed configuration for minimum drag.

	$\bar{N}_c$	$\bar{N}_s$	CHORDWISE SPACING	EXTRAPOLATION
◯	10	25	UNIFORM	CONSTANT
☐	20	20	UNIFORM	CONSTANT
◇	20	20	UNIFORM	SPLINE
△	10	25	COSINE	SPLINE
——	ANALYTICAL			
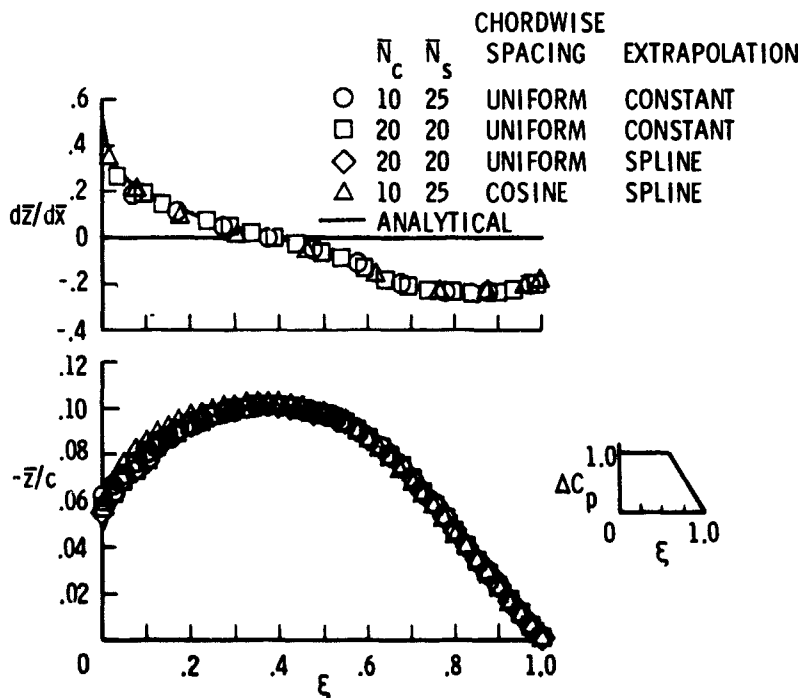
Figure 4.- Two-dimensional local slopes and elevations; a = 0.6.
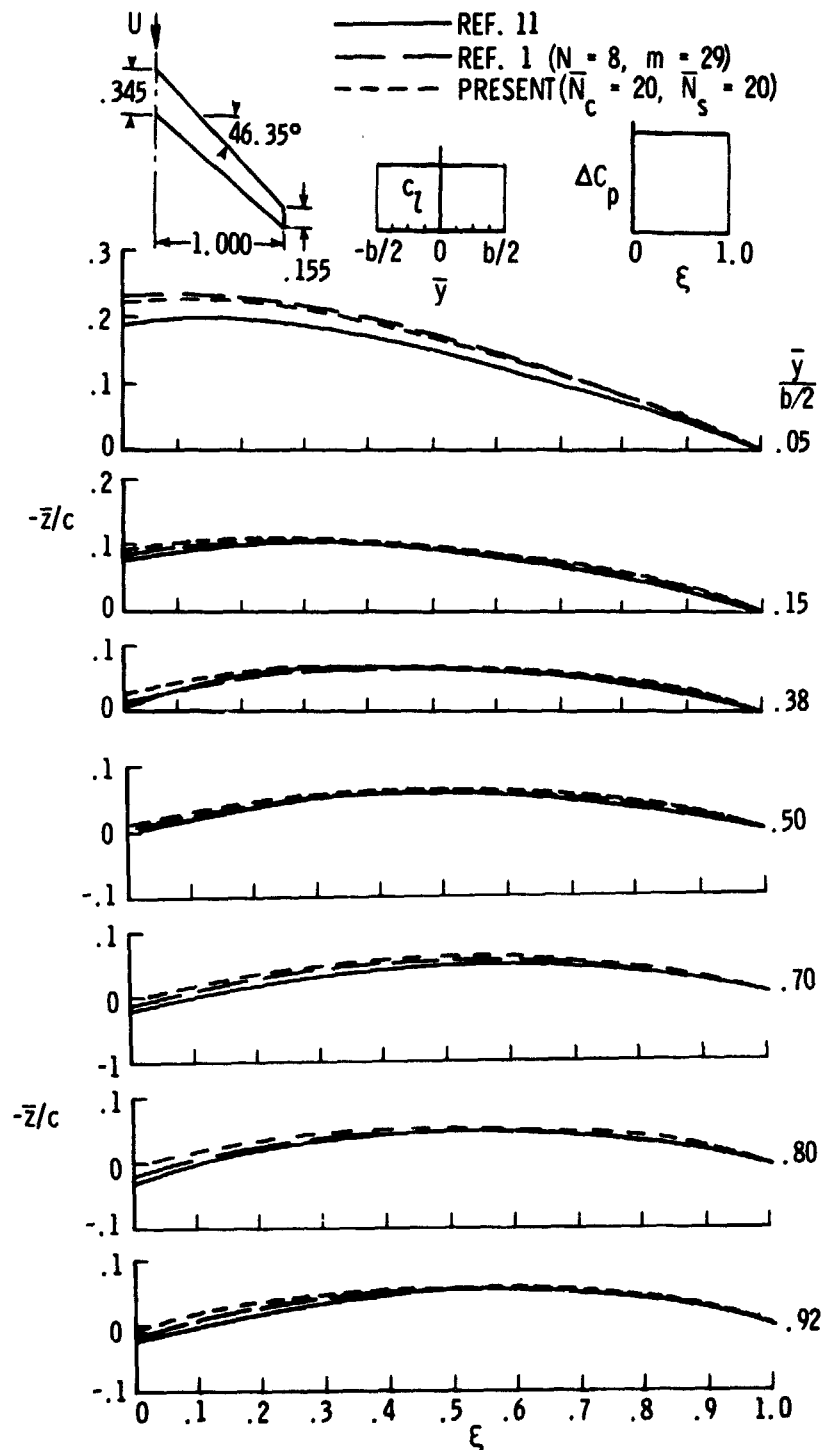
Figure 5.- Local elevation estimates for high-aspect-ratio wing; $C_{L,d} = 1.0$; $M_\infty = 0.90$.
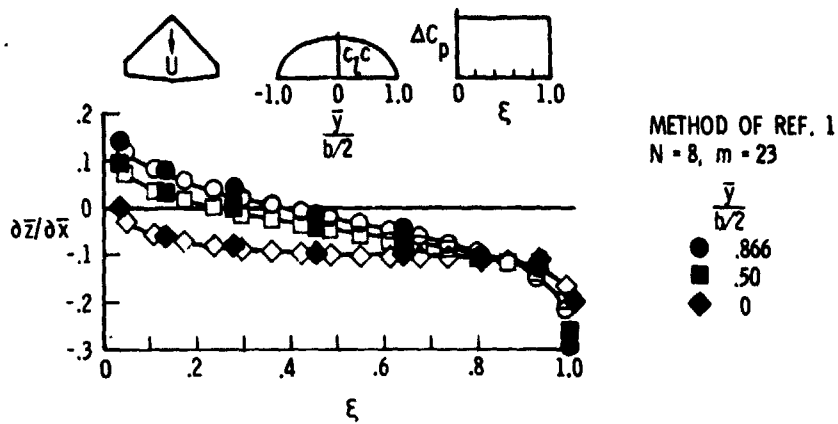
(a) Local slopes.
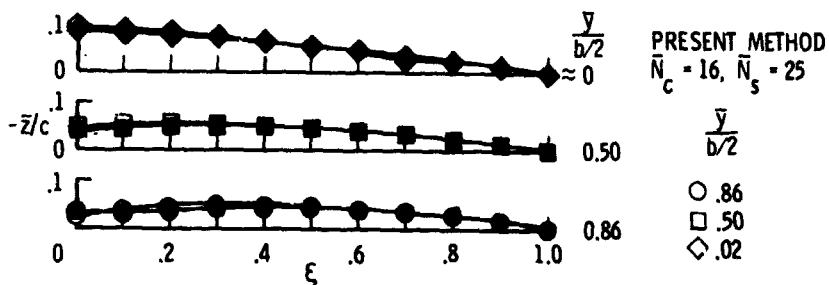
(b) Elevations.
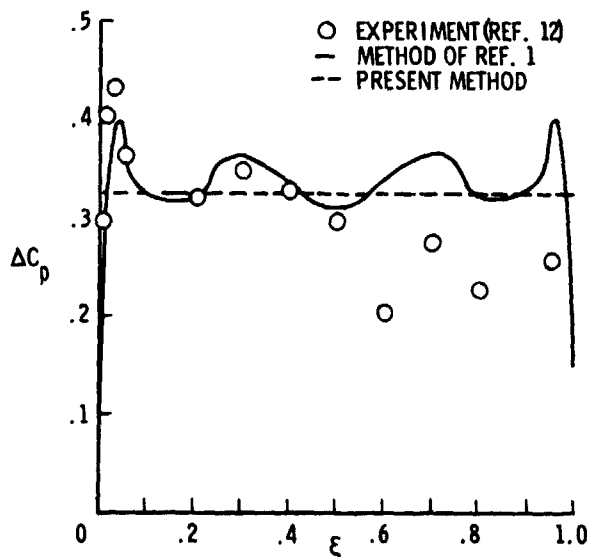
(c) Lifting pressure distributions; $\dfrac{\bar{y}}{b/2} = 0.259$.

Figure 6.- Local slopes, elevations, and lifting pressure distributions; $C_{L,d} = 0.35$; $M_\infty = 0.40$.

$\bar{Y}$

$\bar{X}$
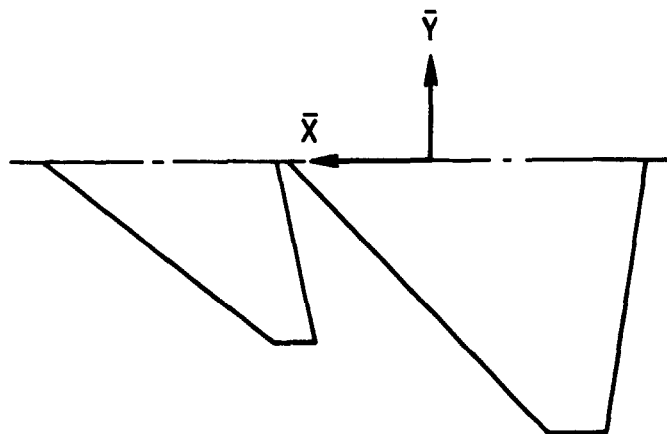
Figure 7.- Typical wing-canard combination.

LINE SYMBOL	a_c	a_w	$C_{L,c}$	$C_{L,w}$	$C_{D,v}$
-------	0	0	.0338	.1662	.00494
– – –	1	1	.0574	.1426	.00495
———	.6	.8	.0505	.1495	.00495

COMBINATION

$\dfrac{c_l c}{b/2}$

CANARD

WING

$\dfrac{\bar{y}}{b/2}$

$\dfrac{\bar{y}}{b/2}$
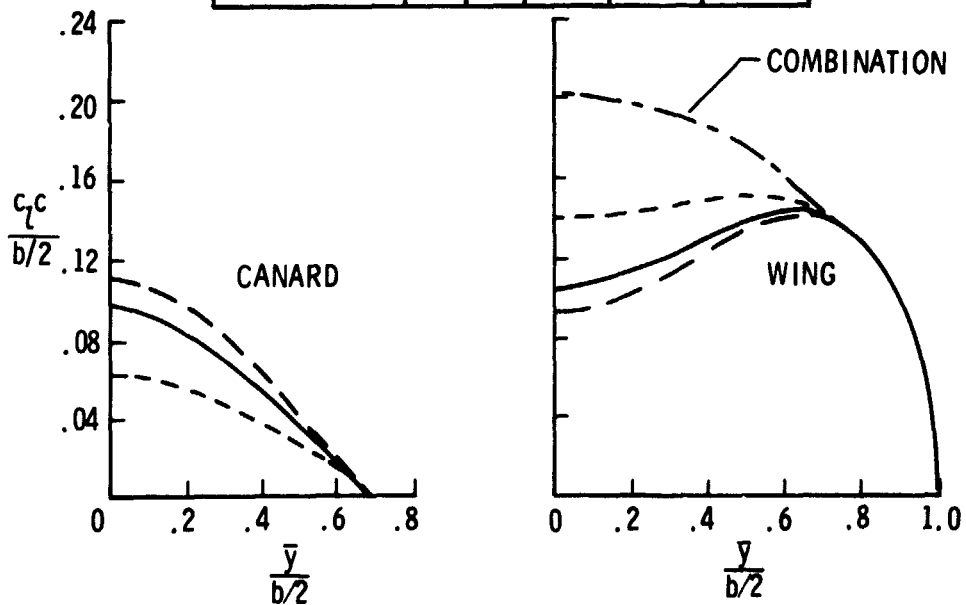
Figure 8.- Effect of chord loading on span loadings for trimmed coplanar wing-canard combination; $M_\infty = 0.30$.
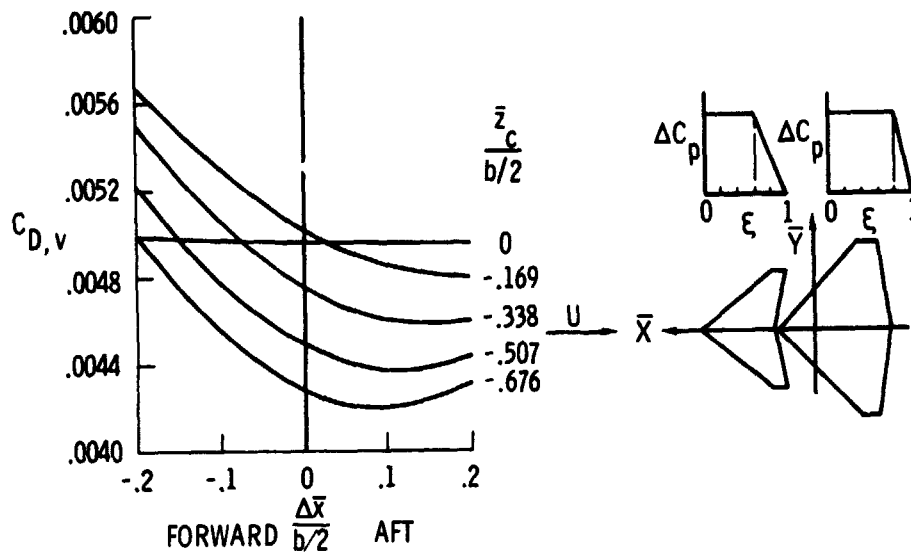
Figure 9.- Vortex drag for range of center-of-gravity positions and vertical separations; $C_{L,d} = 0.2$; $M_\infty = 0.30$.

| LINE SYMBOL	$2\bar{z}_c/b$	$C_{L,c}$	$C_{L,w}$	$C_{D,v}$
─ ─ ─ ─ ─	-.169	.0498	.1503	.00485
── ── ──	-.338	.0493	.1507	.00459
─·─·─·─	-.507	.0491	.1510	.00437
─── ───	-.676	.0489	.1512	.00419
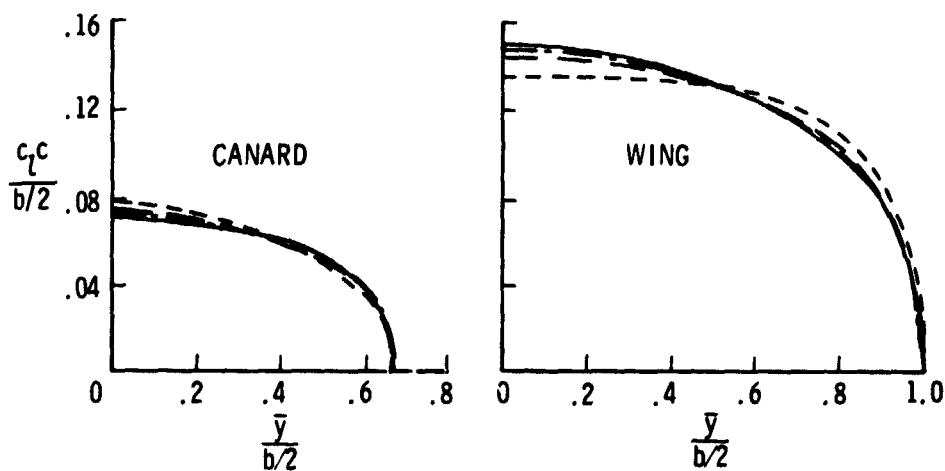
Figure 10.- Effect of vertical displacement of span loadings for trimmed wing-canard combination; $a_c = 0.6$; $a_w = 0.8$; $M_\infty = 0.30$; $\dfrac{\Delta\bar{x}}{b/2} = 0.10$.

109
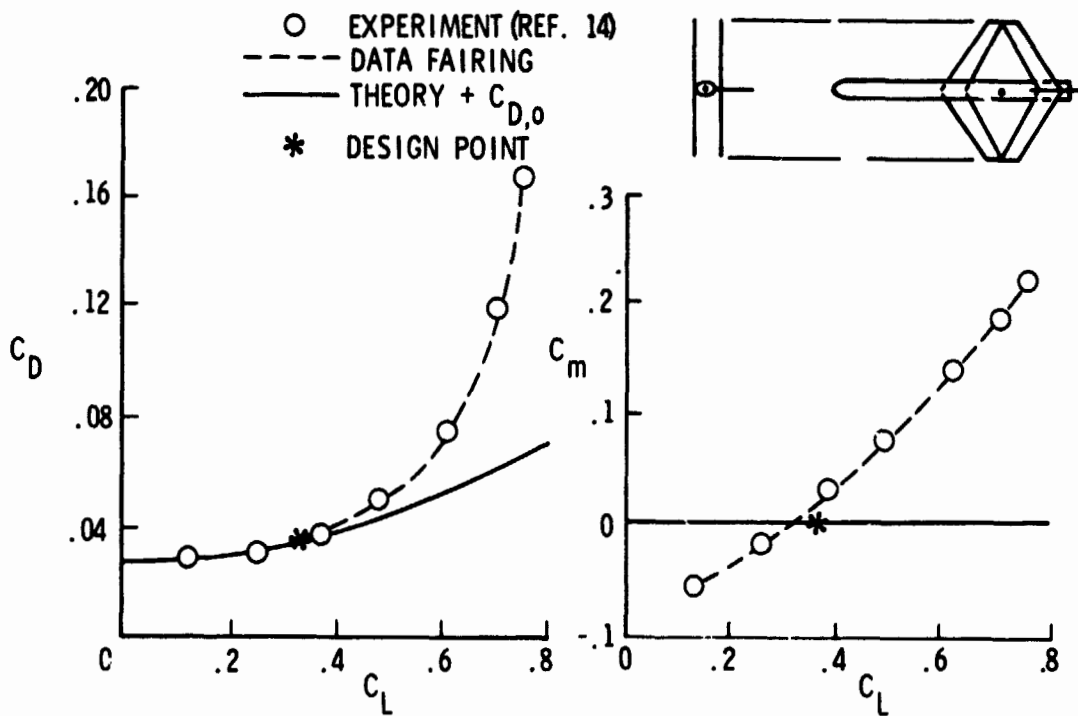
Figure 11.- Longitudinal aerodynamic characteristics of tandem wing;
$C_{L,d} = 0.35$; $M_\infty = 0.30$.
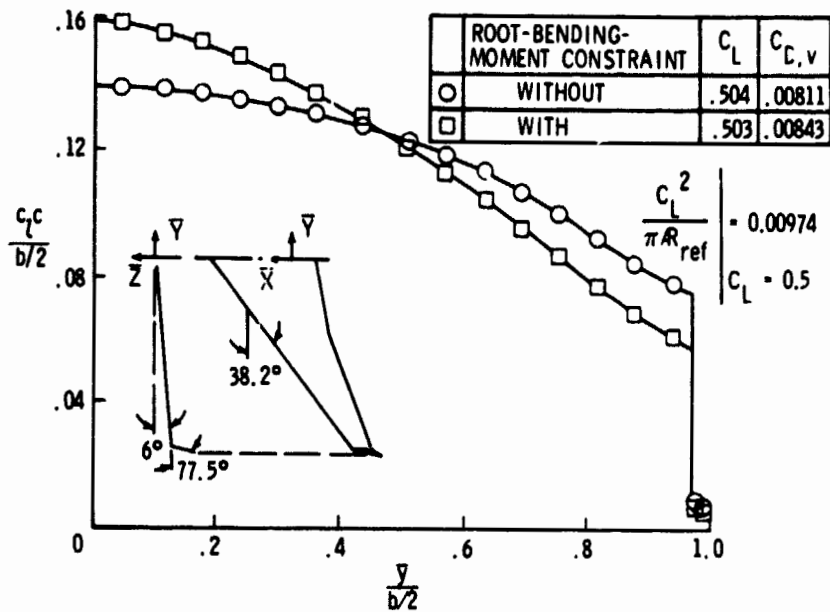
(a) Aerodynamic characteristics.
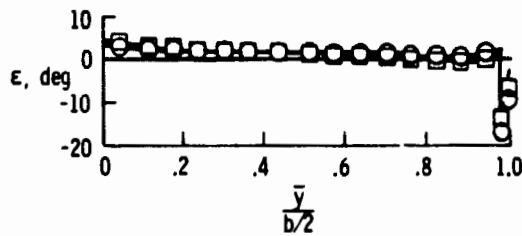
(b) Incidence angle distribution.
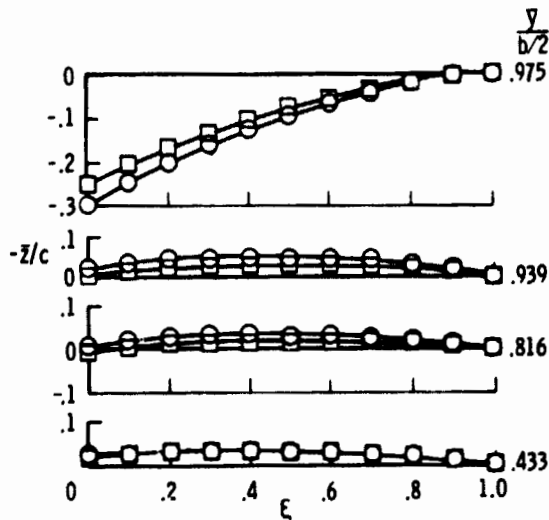
(c) Local elevations.

Figure 12.- Effect of root-bending-moment constraint on aerodynamic characteristics, local elevations, and incidence angle distribution of wing-winglet combination (AR = 6.67); $\bar{N}_c$ = 20; $\bar{N}_s$ = 17; M_∞ = 0.80.

111

APPLICATIONS OF VORTEX-LATTICE THEORY TO

PRELIMINARY AERODYNAMIC DESIGN

John W. Paulson, Jr.
NASA Langley Research Center

SUMMARY

This paper presents some applications of the vortex-lattice theory to the preliminary aerodynamic design and analysis of subsonic aircraft. These methods include the Rockwell-Tulinius vortex-lattice theory for estimating aerodynamic characteristics, a Trefftz plane optimization procedure for determining the span loads for minimum induced drag, and a modification of the Trefftz plane procedure to estimate the induced drag for specified span loads. The first two methods are used to aerodynamically design aircraft planforms, twists, and cambers, and the latter method is used to estimate the drag for components such as flaps and control surfaces.

Results from the theories for predicting lift and pitching moment, drag due to lift, and the drag of control surfaces are compared with experimental data. The data were obtained on a general aviation model with flaps and a close-coupled canard-wing model.

INTRODUCTION

In the preliminary stages of aircraft design, it is necessary that the designer have valid estimates of aircraft aerodynamics, particularly lift, drag, and pitching moments. Lift and pitching moment are required to size the planforms (wing, tail, and canard) and locate them with respect to a moment center, usually a desired aircraft center of gravity, for trimmed lift requirements and stability margins. Skin friction, form, and induced drags must be estimated and minimized for best performance. Many theoretical methods involving various levels of complexity have been developed which estimate these characteristics to varying degrees of accuracy. The preliminary designer, however, wants methods that are fast, reasonably accurate, and easy to use so that changes in aircraft configuration can be easily assessed. Once the overall configuration geometry is defined, he may wish to use some of the more highly sophisticated methods to refine his estimates before beginning experimental verification of the design. This paper will address applications of easy-to-use methods appropriate at the preliminary design stage; these methods include the Rockwell-Tulinius vortex-lattice theory for estimating aerodynamic characteristics, a Trefftz plane optimization procedure for determining the span loads for minimum induced drag, and a modification of the Trefftz plane procedure to estimate the induced drag for specified span loads.

SYMBOLS

A	aspect ratio, b^2/S
b	span
C_D	drag coefficient
$C_{D,i}$	induced drag coefficient
$C_{D,o}$	minimum drag coefficient
C_L	lift coefficient
C_{L_α}	lift-curve slope
C_m	pitching-moment coefficient
C_N	normal-force coefficient
c	chord
c_{avg}	average chord
$\bar{c}$	mean aerodynamic chord
c_l	section lift coefficient
c_n	section normal-force coefficient
E_v	y-component of influence function for pair of trailing vortex legs
E_w	z-component of influence function for pair of trailing vortex legs
e	induced-drag efficiency parameter, $C_L^2/C_{D,i}\pi A$
h	vertical separation ·between canard and wing
N_y	y-component of normal unit vector
N_z	z-component of normal unit vector
q	dynamic pressure
S	wing area
ΔS	incremental section width (from ref. 1)
T_y	tangent unit vector spanwise component

114

T_z	tangent unit vector vertical component
V_∞	free-stream velocity
w	downwash velocity
X,Y,Z	axis system
x,y	distance along X- and Y-axes
x_{mc}	moment-center location
α	angle of attack
Γ	section circulation
δ_f	flap deflection
η	fraction of semispan, $y/b/2$
ρ	density

Subscripts:

cp	center of pressure
d	design
j,k	indices
max	maximum

DISCUSSION

Prediction of Lift and Pitching Moment

The Rockwell-Tulinius unified vortex-lattice theory (refs. 1 and 2) can be used to predict static and rotary stability derivatives for configurations with multiple lifting surfaces of arbitrary shape. It can also compute the section and total configuration forces and moments for arbitrary planform geometries with twist and camber. This method, as programed, is fast, easy to use, and fairly accurate.

The agreement between this theory and experimental data for the lift of a simplified general aviation model is shown in figure 1. The model has a straight untapered wing using the NASA GA(W)-1 airfoil section (refs. 3 and 4) and had 2° of twist (washout) from the root to the tip. The model body was a flat-sided ellipse. For the theoretical calculations, the fuselage was modeled as a flat plate and the wing as a camber line with twist. Agreement between the estimated C_L and the experimental C_L was quite good at low angles of attack prior to flow separation which occurred at $\alpha = 4^\circ$.

Also shown in figure 1 are the theoretical drag polars for 0-percent and 100-percent leading-edge suction as given by the equations

$$C_D = C_{D,o} + \frac{C_L^2}{\pi A e}$$

for 100-percent leading-edge suction and

$$C_D = C_{D,o} + \frac{C_L^2}{C_{L_\alpha}}$$

for 0-percent leading-edge suction. The value for $C_{D,o}$ was obtained from the experimental data. These curves for 100-percent and 0-percent leading-edge suction represent the best and worst possible drag polars, respectively, for a given configuration. The leading-edge radius and/or camber design should produce data that are as close to the 100-percent suction polar as possible. Near-field analyses are required to minimize viscous and separated flow effects to approach the 100-percent suction polar. For this case, the data show that the design was close to the 100-percent suction polar up to $C_L = 1.2$.

Two-dimensional separation can be delayed and minimized for moderate angles of attack by proper planform shaping, camber design, and leading-edge-radius selection. However, at large angles of attack, the viscous form drag must be reduced by taking advantage of interfering flow fields of adjacent surfaces, vortex flows, or induced propulsion effects. Examples of applications of this approach for reducing viscous form drag due to lift are shown later in this paper.

Figure 2 is a sketch of a close-coupled canard model tested in the Langley V/STOL tunnel to investigate the effects of propulsion on stability at high angles of attack. A similar unpowered model was tested in the Langley high-speed 7- by 10-foot tunnel by Blair B. Gloss (ref. 5) to determine the effect of vortex lift on performance, especially $C_{L,max}$. The wings and canards of both models had symmetrical circular arc airfoil sections. Also, strakes were utilized in both tests to produce vortex lift at the higher angles of attack. The agreement between theory and data of Gloss (fig. 3) is good over the linear range of the data for the wing and the wing-canard configurations. The method does not predict the additional vortex lift and resulting pitching moment when the strake is present.

This method was used to establish a moment center for a wing-canard model to give a stability margin at low C_L of -5 percent $\left(\partial C_m / \partial C_L = 0.05\right)$ prior to testing in the V/STOL tunnel. The data, shown in figure 4, indicate a value of $\partial C_m / \partial C_L$ of about 0.06 to 0.05 at low C_L, which agrees well with the predicted value.

Prediction of Minimum Induced Drag

Once the pla..orms of a configuration have been sized and located to meet lift and stability requirements, it is necessary to compute the optimum span loads for minimum induced drag for the interfering planforms. The expression for the induced drag was developed by using an equivalent lifting-line Trefftz plane approach of reference 1 and is illustrated by the following sketch and equation:
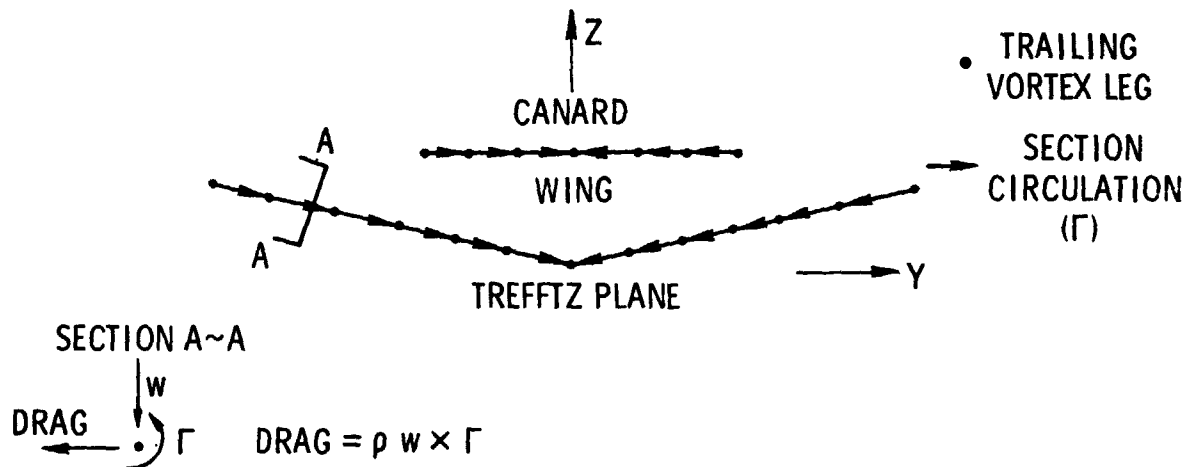
$$C_{D,i} = \frac{A}{2\pi b^2} \sum_{j=1}^{n} \sum_{k=1}^{n} \left(\frac{\Gamma}{V_\infty}\right)_j \left(\frac{\Gamma}{V_\infty}\right)_k \left[\left(E_{v,jk}T_{y,k} + E_{w,jk}N_{y,k}\right)T_{z,j}\right.$$

$$\left. - \left(E_{v,jk}T_{z,k} + E_{w,jk}N_{z,k}\right)T_{y,j}\right]\Delta S_j$$

By utilizing the method of Lagrangian multipliers with the induced-drag equation, the span loads for minimum $C_{D,i}$ may be calculated while constraining C_L and C_m to desired values. This procedure was programed by Tulinius and Gloss, and the results are given in reference 2. The input for this program consists of the basic planform geometry, as in the Rockwell-Tulinius method, along with the desired $(x/c)_{cp}$ distribution. The $(x/c)_{cp}$ distribution is required to locate the chordwise position of the net span load for constraining the pitching moment and is generally selected from a desired two-dimensional section loading.

The method was applied to the close-coupled wing-canard model of Gloss and the results with and without constraints on C_m are presented in figure 5.

The variation of the induced-drag efficiency parameter e is a function of wing-canard span ratio b_{canard}/b, wing-canard separation h/b, and wing-canard

117

lift ratio. The left side of figure 5 gives estimates of e when C_L is constrained and C_m is unconstrained. It can be seen that the estimated values of e increase as h/b and b_{canard}/b increase and are equal to or greater than 1.0. The right side of figure 5 gives estimates of e when both C_L and C_m are constrained to produce a trimmed configuration. It can be seen that the extra constraint lowers the values of e; however, e can still be greater than 1.0 if an upload on the canard is required for trim. When a canard or empennage download is required for trim, e is equal to or less than 1. In this figure, the location of the moment center was completely arbitrary and was chosen simply to give uploads and downloads on the canard.

A detailed study of the effect of moment-center location on e was performed for one configuration $\left(h/b = 0.09, \ b_{canard}/b = 0.68 \right)$ and is presented in figure 6. It can be seen that e is a maximum at a moment-center location of about 10 percent $\bar{c}$ due to the nearly elliptic span loads present for this case. As the moment center is moved away from 10 percent $\bar{c}$, the loads required on the wing and canard for trim become more nonelliptic and e decreases accordingly.

It should be noted that the wing and canard must be twisted and cambered to produce the span loads required to approach the minimum $C_{D,i}$. The data of Gloss (ref. 5) were obtained for both flat and cambered wings in the presence of a canard. The cambered wings were designed to lift coefficients of 0.35 and 0.70. These experimental data are compared with the theoretical minimum value of $\dfrac{C_D - C_{D,o}}{C_L^2}$ in figure 7. The uncambered wing alone does not approach the theoretical minimum at low C_L because the sharp leading edge does not carry any leading-edge thrust. This wing departs drastically from the minimum at higher C_L because of the flow separation from the sharp leading edge. The downwash and vortex from the canard and strake retard the two-dimensional type of separation on the wing and the data show large improvements over the wing alone at higher C_L. However, the flat wing-canard-strake combination still does not approach the theoretical minimum because of the zero leading-edge thrust associated with the sharp leading edge. The cambered wings for the wing-canard configuration do approach the theoretical minimum at the design C_L because the cambered airfoil carries thrust on the camber line and the leading edge is drooped into the local flow direction to reduce the leading-edge flow separation.

Prediction of Induced Drag Due to Control Deflections

In addition to using the theory to aerodynamically design a configuration to meet the primary mission requirements, it is also useful in examining the effects of deflecting control surfaces and high-lift devices on the induced drag. A modification was made by Paulson and Thomas to the induced drag mini-

mization program to calculate the induced drag for specified span loads. The input span loads may be obtained either theoretically or experimentally. An example of the variation in span load due to two different types of flaps is shown in figure 8. This analysis was done on the general aviation model shown in figure 1 without the fuselage. The span loads were calculated by using the Rockwell-Tulinius method for the plain wing and for the wing with either slotted flaps or Fowler flaps deflected. Figure 9 shows the experimental drag polars for the three configurations. At $C_L = 1.0$, the calculated differences in induced drag between the plain wing and the wing with slotted flaps or Fowler flaps were 0.0010 and 0.0126, respectively. (See table 1.) The corresponding differences in the experimental data were 0.0012 and 0.0165, respectively. The additional skin-friction drag for the deflected Fowler flap (ref. 6) was estimated to be 0.0024. When this is combined with the computed induced drag, a total theoretical increment in drag of 0.0150 is obtained for the Fowler flap. This agrees well with the experimentally measured increment of 0.0165.

CONCLUDING REMARKS

Three applications of theoretical methods for preliminary aerodynamic design have been discussed. These methods are used to estimate wing and empennage geometries and locations to meet performance and stability requirements, to estimate span loads for minimum trimmed induced drag, and to analyze the effects of control surface deflection on induced drag. The theories are, in general, easy to use, fast, and the agreement with experimental data shows that they give accurate results. These methods are being used to design complex multiple lifting-surface models for experimental investigations in the Langley V/STOL tunnel.

REFERENCES

1. Tulinius, J.; Clever, W.; Niemann, A.; Dunn, K.; and Gaither, B.: Theoretical Prediction of Airplane Stability Derivatives at Subcritical Speeds. NASA CR-132681, 1975.

2. Tulinius, Jan R.; and Margason, Richard J.: Aircraft Aerodynamic Design and Evaluation Methods. AIAA Paper 76-15, Jan. 1976.

3. McGhee, Robert J.; and Beasley, William D.: Low-Speed Aerodynamic Characteristics of a 17-Percent-Thick Airfoil Section Designed for General Aviation Applications. NASA TN D-7428, 1973.

4. Paulson, John W., Jr.: Wind-Tunnel Tests of a Conventional Flap and Aileron and a Fowler Flap and Slot-Lip Aileron for an Advanced General Aviation Wing. SAE Paper 750501, Apr. 1975.

5. Gloss, Blair B.: Effect of Wing Planform and Canard Location and Geometry on the Longitudinal Aerodynamic Characteristics of a Close-Coupled Canard Wing Model at Subsonic Speeds. NASA TN D-7910, 1975.

6. Peterson, John B., Jr.: A Comparison of Experimental and Theoretical Results for the Compressible Turbulent-Boundary-Layer Skin Friction With Zero Pressure Gradient. NASA TN D-1795, 1963.

TABLE 1.- ESTIMATION OF DRAG INCREMENT DUE TO FLAPS FOR GENERAL AVIATION MODEL

$$\left[\Delta C_{D,i} + \Delta C_{D,\text{skin friction}} = \Delta C_{D,\text{estimated}}\right]$$

	C_L	C_D	$\Delta C_{D,i}$	$\Delta C_{D,\text{skin friction}}$	$\Delta C_{D,\text{estimated}}$	$\Delta C_{D,\text{exp}}$
Plain wing	1.0	0.0695	------	------	------	------
Slotted flap	1.0	.0707	0.0010	------	0.0010	0.0012
Fowler flap	1.0	.0860	.0126	0.0024	.0150	.0165

121
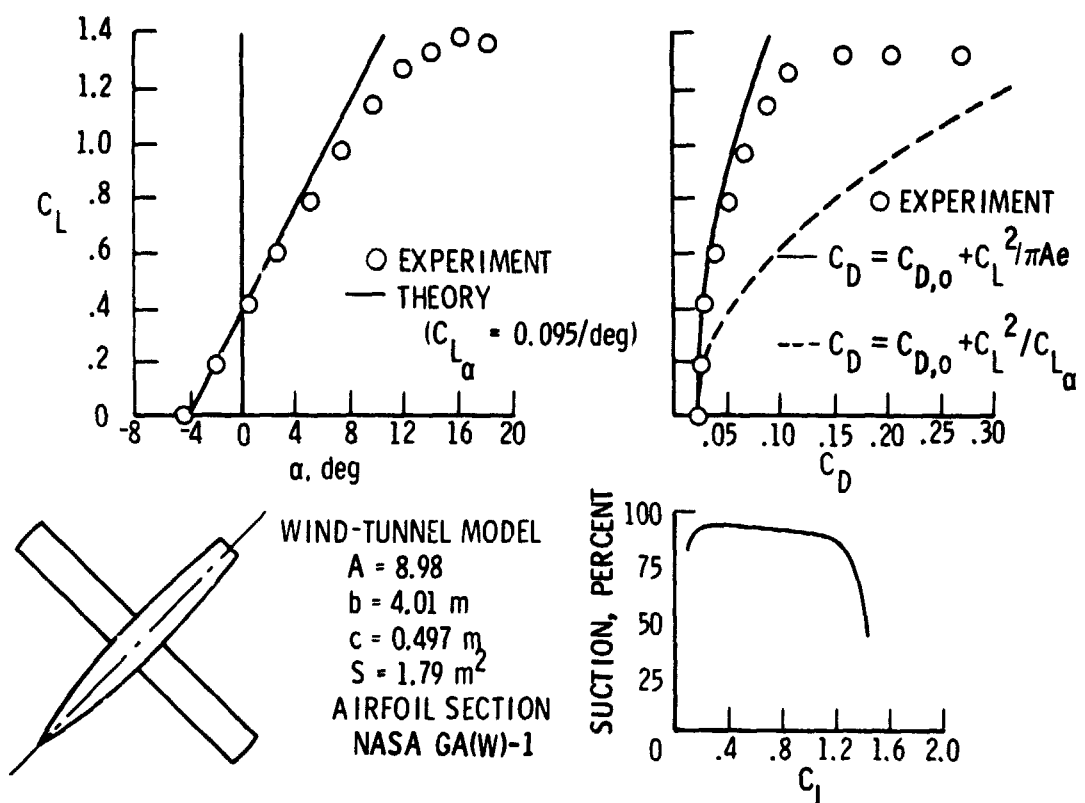
Figure 1.- Aerodynamic characteristics of general aviation model.

WIND-TUNNEL MODEL
A = 8.98
b = 4.01 m
c = 0.497 m
S = 1.79 m^2
AIRFOIL SECTION
NASA GA(W)-1

$C_D = C_{D,o} + C_L^2/\pi Ae$

$C_D = C_{D,o} + C_L^2/C_{L_\alpha}$

THEORY $(C_{L_\alpha} = 0.095/deg)$
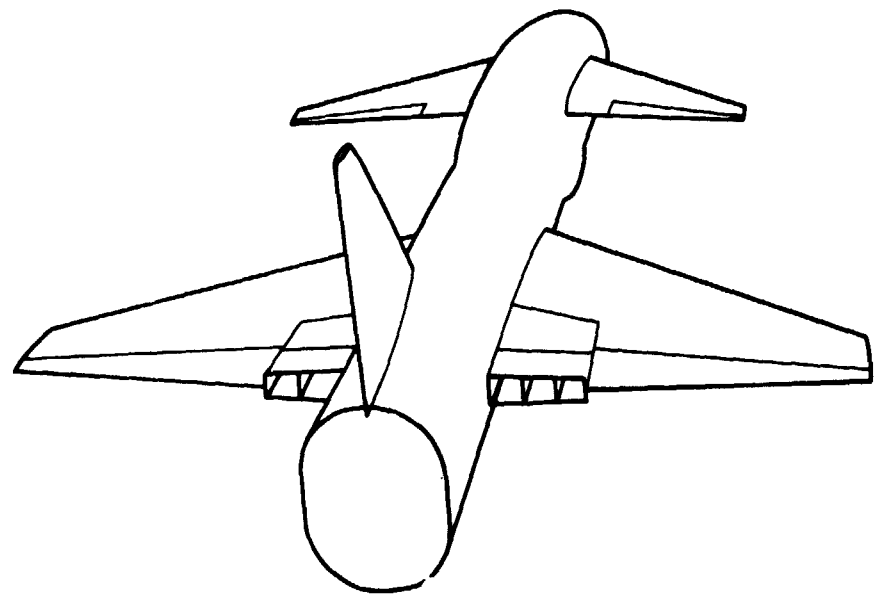
Figure 2.- Powered wing-canard research configuration.

122
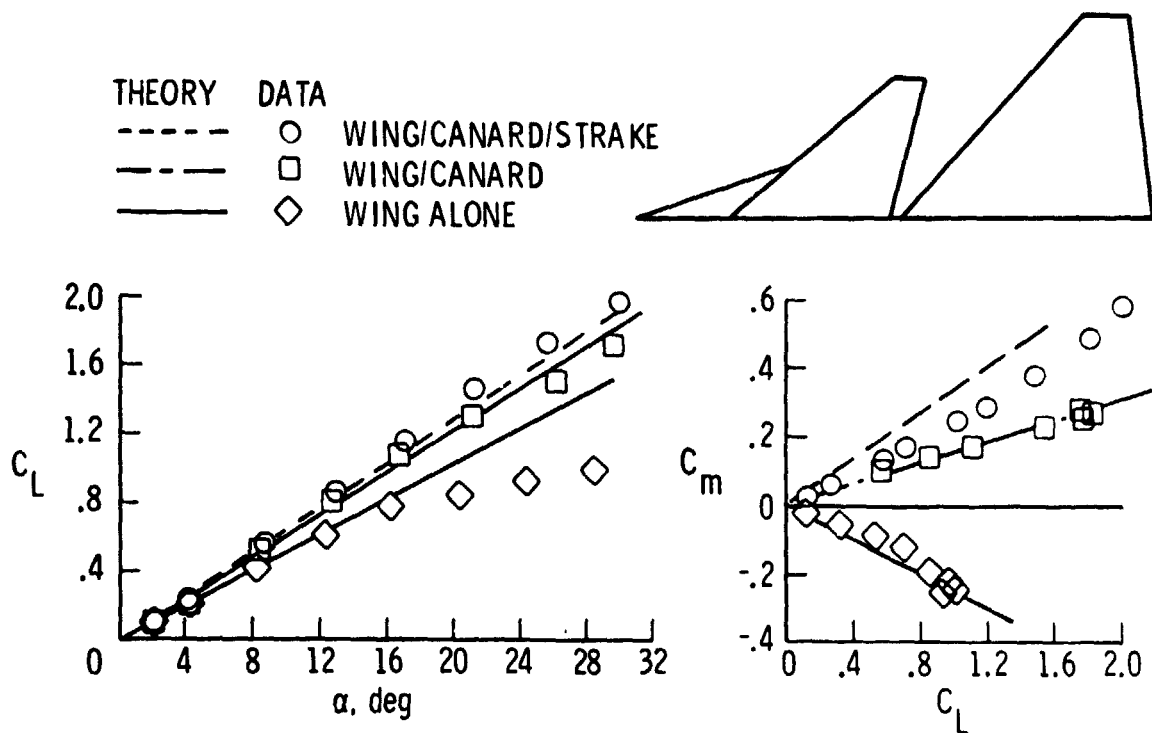
Figure 3,- Comparison between vortex-lattice theory and data. Theory from Rockwell-Tulinius vortex-lattice method; data from referebce 5.
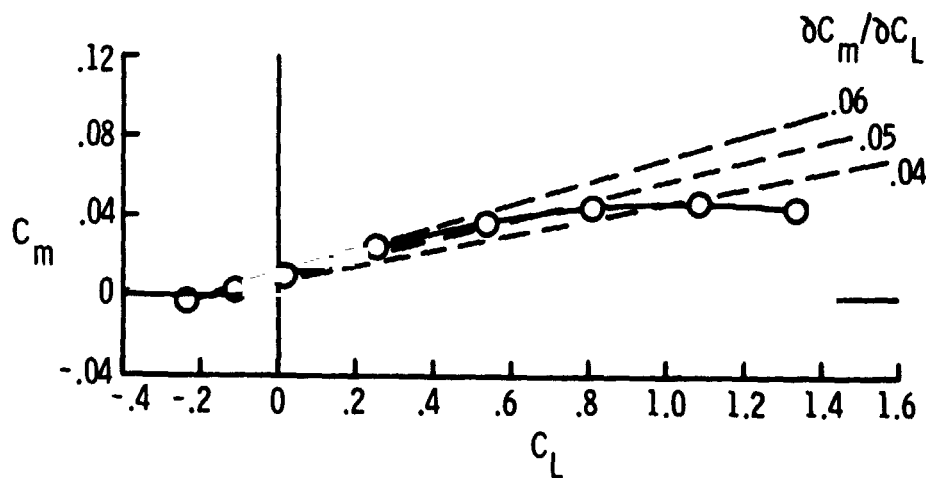
Figure 4.- Stability margin for model of figure 2.
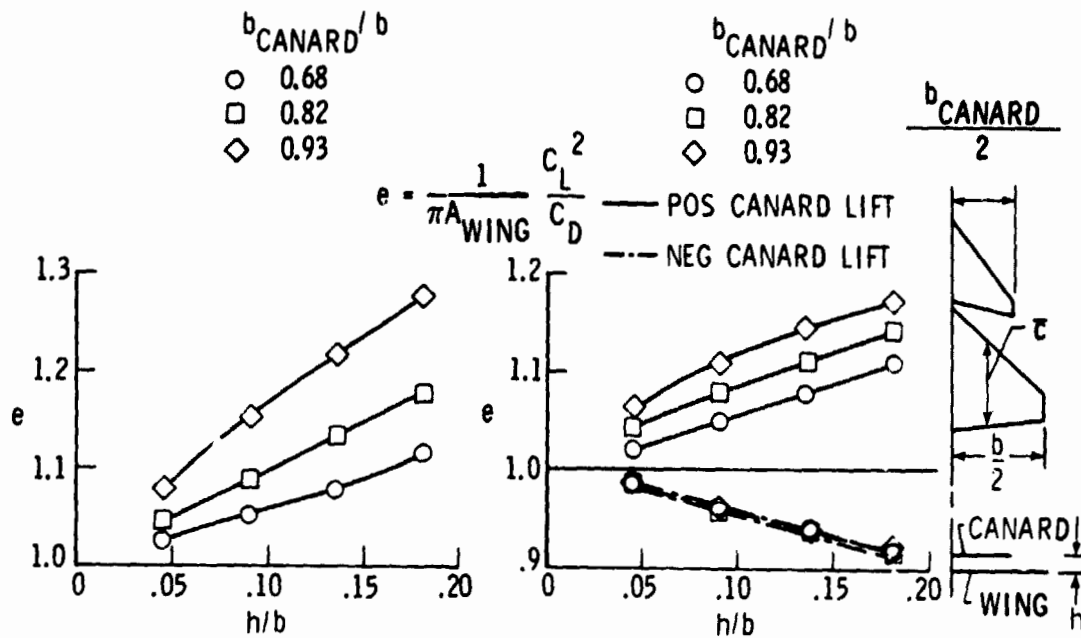
Figure 5.- Results from Trefftz plane vortex drag minimization
theory.   Equivalent lifting line approach.
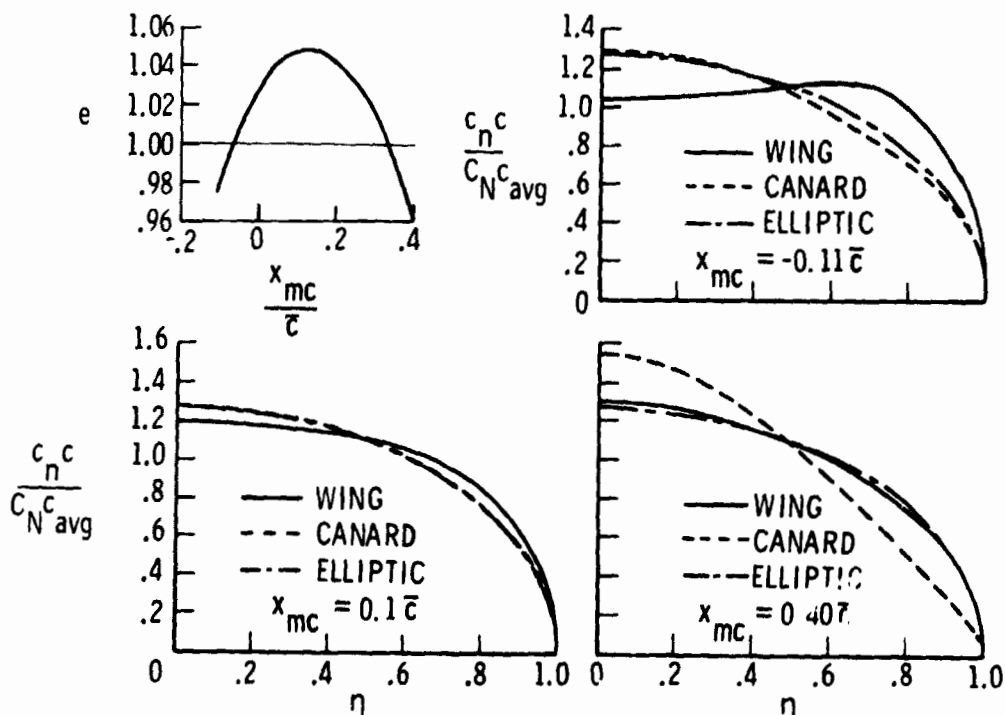
Figure 6.- Interference effects on optimum span load shape
of the wing and canard.
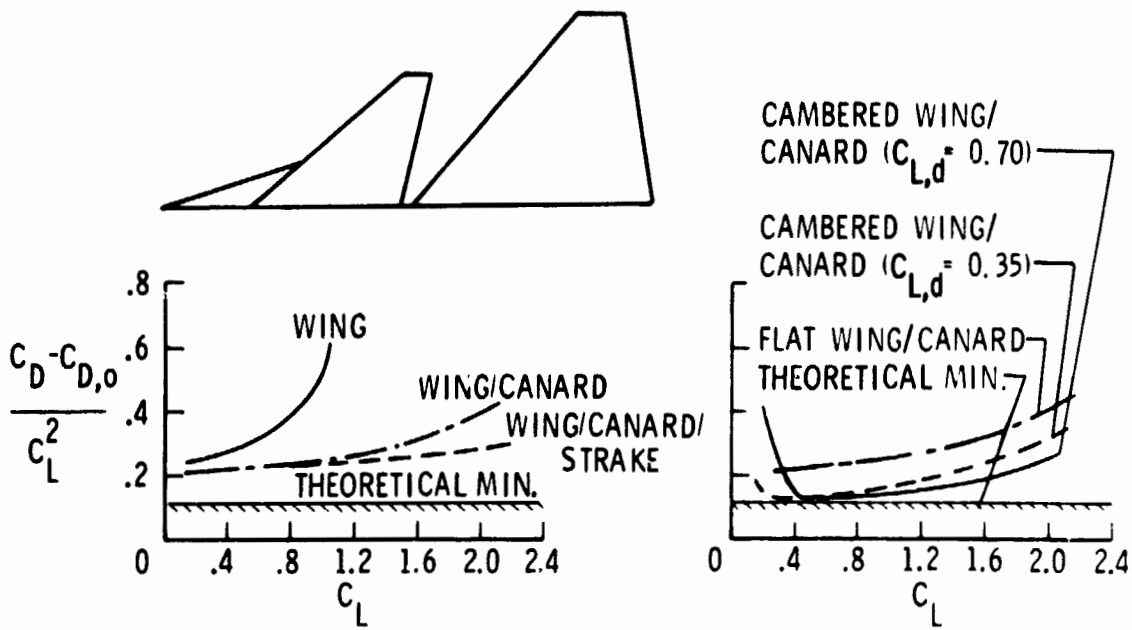
Figure 7.- Effects of canard, strake, and wing camber
on drag due to lift.
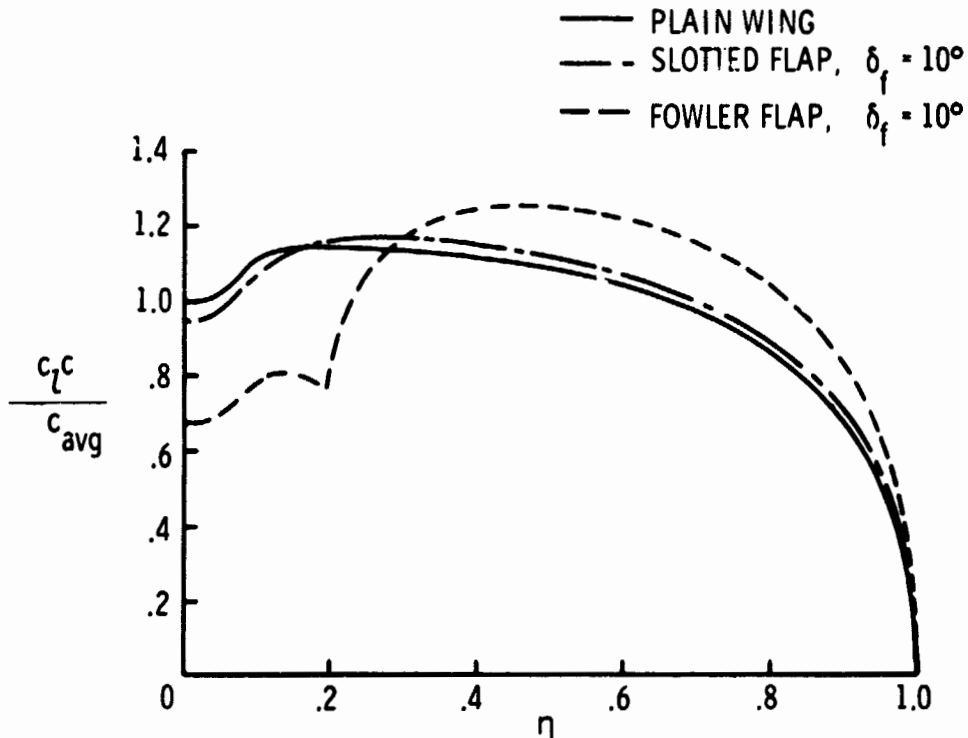
Figure 8.- Calculated span loads for general aviation
model at $C_L = 1.0$.
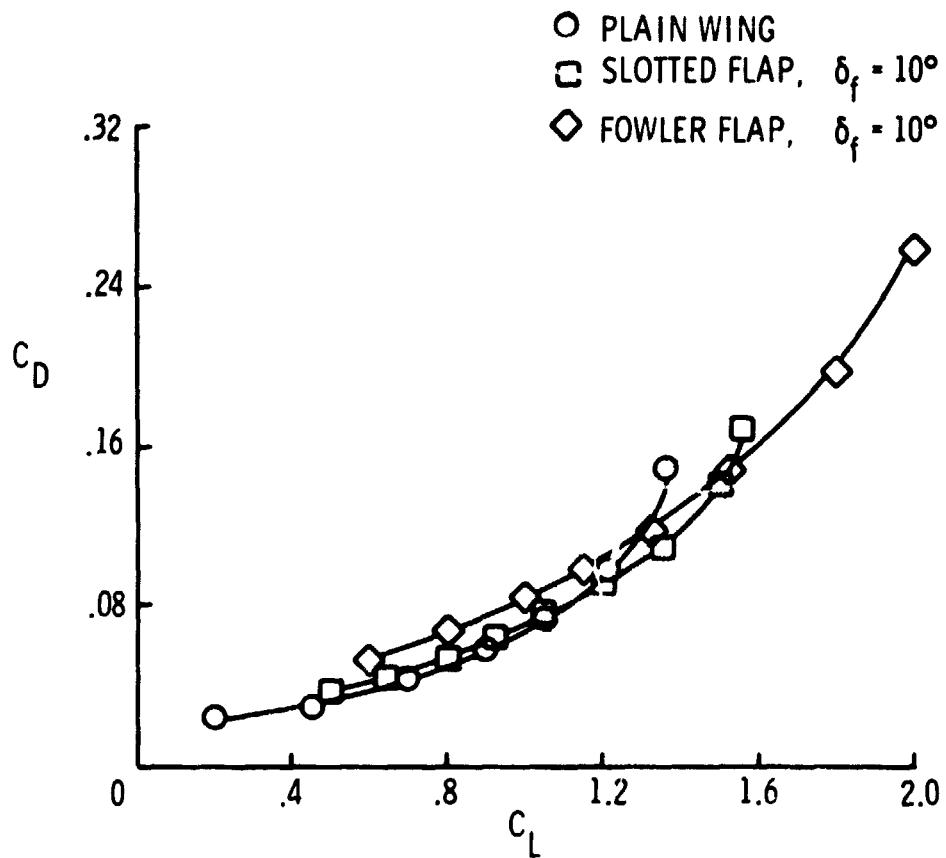
Figure 9.- Experimental drag polars for general aviation model.

UTILIZATION OF THE AEDC THREE-DIMENSIONAL

POTENTIAL FLOW COMPUTER PROGRAM*

Richard L. Palko
ARO, Inc.

SUMMARY

A potential flow computer program has been in use at the Arnold Engineering Development Center (AEDC) for several years. This program has been used primarily as a tool for flow-field analysis in support of test activities in the transonic wind tunnels of the Propulsion Wind Tunnel Facility (PWT). Analyses have been made over a Mach number range from 0 to 0.9 for a variety of configurations from aircraft to wind tunnels, with excellent agreement between calculated flow fields and measured wind tunnel data. Analytical and experimental data for seven different flow analysis problems are presented in this paper.

INTRODUCTION

The AEDC Three-Dimensional Potential Flow Computer Program (PFP) in the existing form was developed primarily as a result of the need to make calculations of the flow field in the vicinity of aircraft fuselages (typically at locations where aircraft inlets might be located). This need arose because of the support the theoretical flow-field calculations could lend to a research program carried out at AEDC to simulate the inlet flow fields in a wind-tunnel test of full/scale inlet/engine systems (refs. 1 and 2). Much of the computing capability that the PFP presently has resulted from these flow-field calculations which have as their primary variables the flow angularity (upwash and sidewash) over a y-z plane. After the initial solution of the velocity field for a given model attitude and Mach number is obtained, the upwash and sidewash can be determined for any given point or over any grid desired. A new solution is required for each model attitude or Mach number. In addition to computing the upwash and sidewash, the PFP also computes the local Mach number, C_p, and flow streamlines. A computer plotting program has been written to supplement the PFP, and computer plots can be

obtained for most of the above parameters. A streamline can be traced from any point in the stream either upstream or downstream (or both). The capability to make a plot of the mathematical representation of the model geometry before running the complete program allows corrections to be made, if needed, with only a slight loss of computer time. A two-volume report (ref. 3) that details the program, modeling techniques, application, and verification has been published.

This paper briefly outlines the PFP application to seven flow analysis problems in support of the transonic wind tunnels in the PWT at AEDC.

SYMBOLS

Values are given in both SI and U. S. Customary Units. The measurements and calculations were made in U. S. Customary Units.

A	angle of attack
C_L	lift coefficient
C_p	pressure coefficient
M_∞	free-stream Mach number
p/p_0	ratio of surface static pressure to free stream total pressure
X	coordinate along tunnel axis, positive downstream
Y	horizontal coordinate, sign as indicated
Z	vertical coordinate, sign as indicated
α	model angle of attack, deg, positive up
β	model angle of yaw, deg, sign as indicated
ϵ	upwash, deg, positive up
σ	sidewash, deg, positive as indicated

PFP APPLICATION AND UTILIZATION

The PFP at AEDC has been used primarily as a tool for analysis of the flow in the far field. (Far field refers to a distance away from the analysis model surface equal

to, or greater than, the vortex spacing in the direction of flow.) The modeling techniques required for this type of analysis are presented in volume II of reference 3. However, work is underway to develop the modeling technique to allow accurate analysis of the surface pressure. Results of some of this continuing effort are reported in reference 4. All the flow problems presented here are of the far-field type.

Flow Field Between Two Hollow Circular Cylinders

The analysis of these cylinders was part of a research program in which the objective was to create flow fields by some auxiliary method to simulate the flow entering a full-scale inlet/engine at high angles of attack and yaw. The device was to deflect (or induce) the flow upward as it passed between the inclined cylinders. A mathematical model of the cylinders is shown in figure 1. The last circumferential ray on each cylinder had trailing vortices that were trailed at an angle equal to one-half the cylinder pitch angle. A comparison between the theoretical and experimental flow angularity data is shown in figure 2. The theoretical results are shown as lines of constant flow angle (both upwash and sidewash), and the solid symbols show the relative location of experimental data with the magnitude of the measured angles indicated. The Mach number at which these data were taken was 0.9. It can be seen that the PFP overestimated the flow inclination angles by approximately 1°.

Flow Field Around an Aircraft Fuselage

Primary purpose of this analysis was to verify the results obtained from the PFP. Experimental flow-field data used for comparison with theory were available from wind-tunnel measurements made during the Tailor Mate test series. The objective of the wind-tunnel test was to determine the flow field (upwash and sidewash) at a typical engine inlet fuselage location. The mathematical model of the fuselage configuration is shown in figure 3. The comparison between the predictions from the PFP and the wind-tunnel data for a pitch angle of 25° and a free-stream Mach number of 0.9 are shown in figure 4. Here again, excellent agreement was obtained.

Flow Field Under a Fuselage-Wing Configuration

The purpose of this analysis was also for program verification; again experimental data obtained during the Tailor Mate studies were used. The fuselage-wing configuration was analyzed to compute the flow field under the wing at the wing-fuselage junction. The computer math model used in the analysis is shown in figure 5. A comparison between the upwash and sidewash predictions and the experimental data for a Mach number of 0.9 and an angle of attack of 10° is shown in figure 6. Analytical and experimental data trends show excellent agreement, although the predicted data show somewhat higher flow angularity gradients across the survey area than the measured data.

Streamtube Entering Inlet Behind Wing

The purpose of this analysis was to determine the origin of the streamtube entering the inlet in support of an inlet hot gas ingestion investigation. The comparison between experimental and theoretical data are shown in figure 7. These data were taken during a store separation study in an effort to verify the accuracy of the PFP to predict the correct flow field above and behind the wing. Data were taken at a Mach number of 0.3 with an angle of attack of 8°, and show excellent agreement between the experimental and theoretical values. The mathematical model and the predicted streamtube are shown in figure 8. The streamtube was determined by tracing streamlines from four locations beginning just upstream of the inlet and extending forward to just upstream of the aircraft nose. A Mach number of 0.3 and an angle of attack of 8° were also used for the streamtube analysis. This mathematical model is the largest analyzed to date, with 1559 loop vortices and 20 horseshoe vortices, and required approximately 4 hours run time on the AEDC IBM 370/165 computer.

Inlet/Engine in Crosswind

This analysis was made in support of a crosswind experiment conducted during an inlet study in the AEDC 16-ft (4.88-m) Transonic Wind Tunnel (PWT-16T). The objective of the analysis was to determine if a 0.91-m-diameter (3-ft-diameter) crosswind simulator would adequately simulate the crosswind when used in conjunction with the inlet model, and to determine the position for the simulator to give best results. The theoretical analysis was made with the inlet/engine in an infinite crosswind. The mathematical model included only a portion of the experimental model as shown in figure 9. A computer plot of the mathematical model is shown in figure 10. The engine ducts were closed on the downstream end and a negative source was located near the rear center of each engine duct to produce the correct inlet mass flow when that particular engine was in operation. Streamlines were traced upstream from near the four corners of the inlet, for each engine in operation, to determine the flow pattern of the airstream entering the inlet. By tracing the streamlines, a fan position was determined that would influence the inlet flow for all engine power settings and crosswind velocities required. A typical flow pattern for the analysis is shown in figure 11 for a crosswind velocity of 20.57 m/sec (67.5 ft/sec) with both engines operating.

Pressure Distribution in PWT-16T Contraction Section

The objective of this analysis was to determine the pressure distribution along the bottom and side walls of the PWT-16T contraction section. Pressure distributions were needed for use in a theoretical boundary-layer analysis of the wind-tunnel nozzle to support a test-section flow angularity study. Mathematical modeling used in the analysis is shown in figure 12. The flow in the test section area was specified to give the pressure ratio desired for Mach number 0.6. The analysis provided

streamline information at a distance of 0.305 m (1 ft) from the walls, and the calculated C_p was converted to p/p_o. Following the calculation of the theoretical pressure distribution, the pressure distribution was experimentally measured in the contraction section. A comparison between the theoretical and experimental pressure distribution is shown in figure 13, with excellent agreement indicated.

Strut Effects Analysis

The objective of this analysis was to determine the strut effect corrections to measured force and moment data for a slender winged vehicle with a mid-strut mount. The vehicle wing was located just forward of the strut. For this analysis the upwash angle was determined with the PFP for the body alone (fig. 14) and the body with strut (fig. 15). An incremental upwash angle was then determined at the wing location from these two sets of data. In this case the incremental values were negative because of the down flow around the strut. The incremental values along the wing location were averaged and the ΔC_L correction calculated from the average angle-of-attack change. A comparison of the calculated corrections and those measured with a subscale model are shown in figure 16. Excellent agreement is shown in both the trend with Mach number and the absolute values.

CONCLUDING REMARKS

The AEDC Potential Flow Program is used primarily as a tool for flow-field analysis in support of the test activities in the transonic wind tunnels of PWT. This paper has covered seven different problems that have utilized the PFP including both external and internal analysis. All but one of the examples have experimental data to verify the calculated flow fields, and all comparisons show excellent agreement. The PFP at AEDC has not been used as a tool to obtain absolute values, but rather as a tool to predict and verify flow fields in support of the test activities. In addition to the problems presented, the PFP has been used to predict the flow angularity at the model resulting from sting and support systems, to predict the flow around various types of support systems, and many other general flow analysis problems directly connected with wind-tunnel testing.

REFERENCES

1. Palko, R. L.: Full-Scale Inlet/Engine Testing at High Maneuvering Angles at Transonic Velocities. AIAA Paper No. 72-1026, Presented at the AIAA Seventh Aerodynamic Testing Conference, Palo Alto, California, September 13-15, 1972.

2. Palko, R. L.: A Method to Increase the Full-Scale Inlet/Engine System Testing Capability of the AEDC 16-Ft Transonic Wind Tunnel. AEDC-TR-73-9 (AD 762912), June 1973.

3. Todd, Donald C. and Palko, Richard L.: The AEDC Three-Dimensional, Potential Flow Computer Program. Vol. I and II. AEDC-TR 75-75, February 1976.

4. Heltsley, Fred L.: Report on the Status of a Slotted Wind-Tunnel Wall Representation Using the Vortex-Lattice Technique. Vortex-Lattice Utilization, NASA SP-405, 1976. (Paper no. 9 of this compilation.)

MACH NUMBER = 0.9

ε   EXPERIMENTAL DATA
σ
●   THEORETICAL UPWASH
--- THEORETICAL SIDEWASH

Ⓔ
⑩

CYLINDER DIAMETER = 1.42 m (56 in.) FULL SCALE
CYLINDERS SPACED 3.91 m (154 in.) CENTER-TO-
CENTER FULL SCALE (SCALED FOR PWT-16T)

Figure 2.- Experimental and theoretical comparison
of upwash and sidewash angles for the dual hollow
circular cylinders at a Mach number of 0.9.
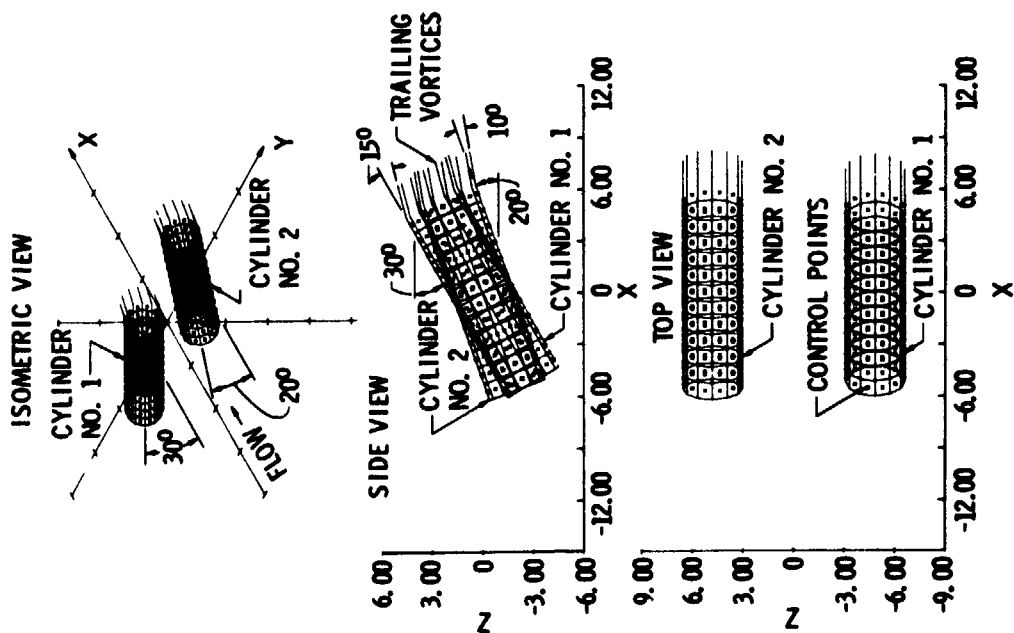
Figure 1.- Mathematical model of the
dual hollow circular cylinder
configuration.
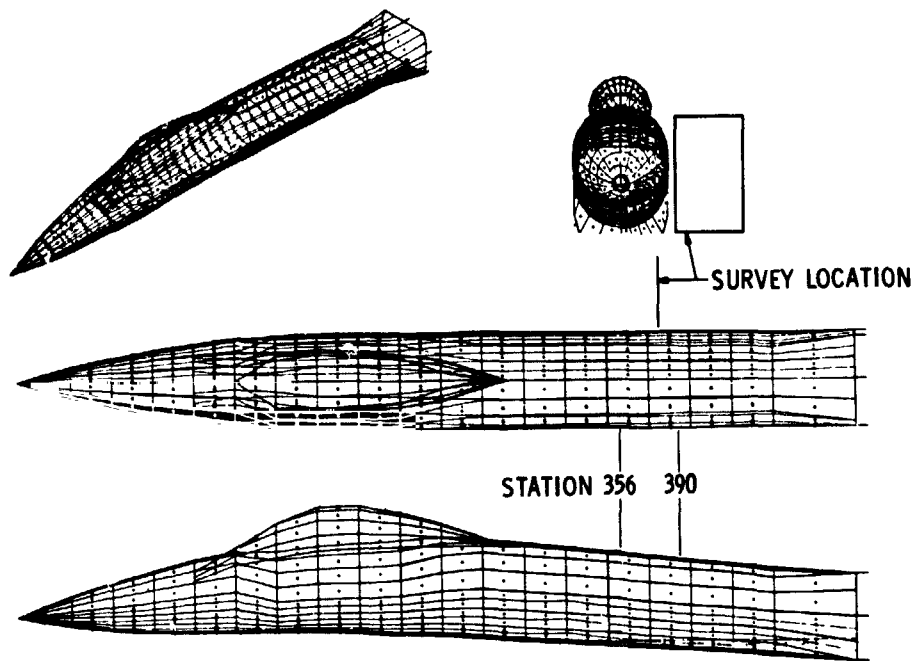
Figure 3.- Mathematical model of the fuselage configuration.
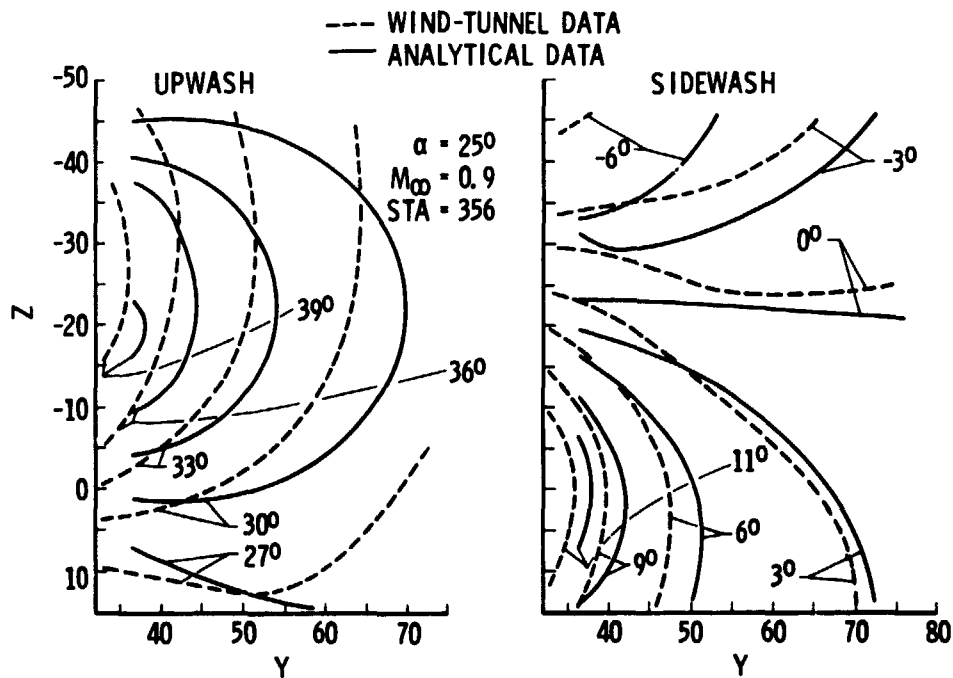
Figure 4.- Comparison between analytical and wind-tunnel data for
Mach number 0.9 at an angle of attack of 25°.

SURVEY LOCATION

SURVEY LOCATION
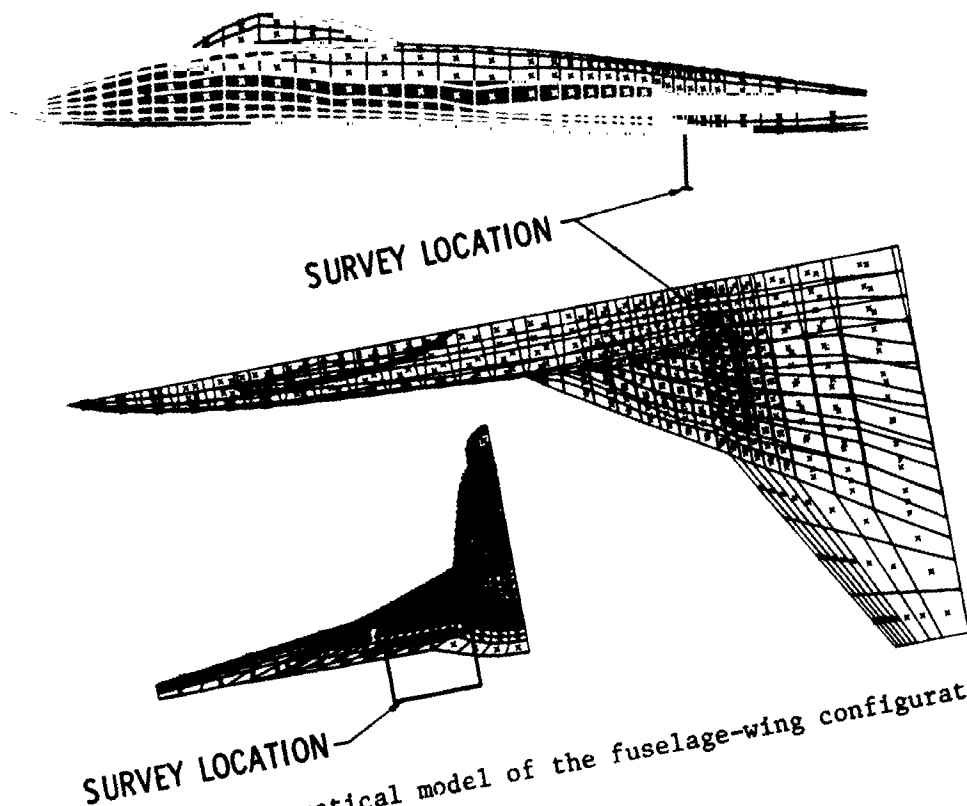
Figure 5.- Mathematical model of the fuselage-wing configuration.
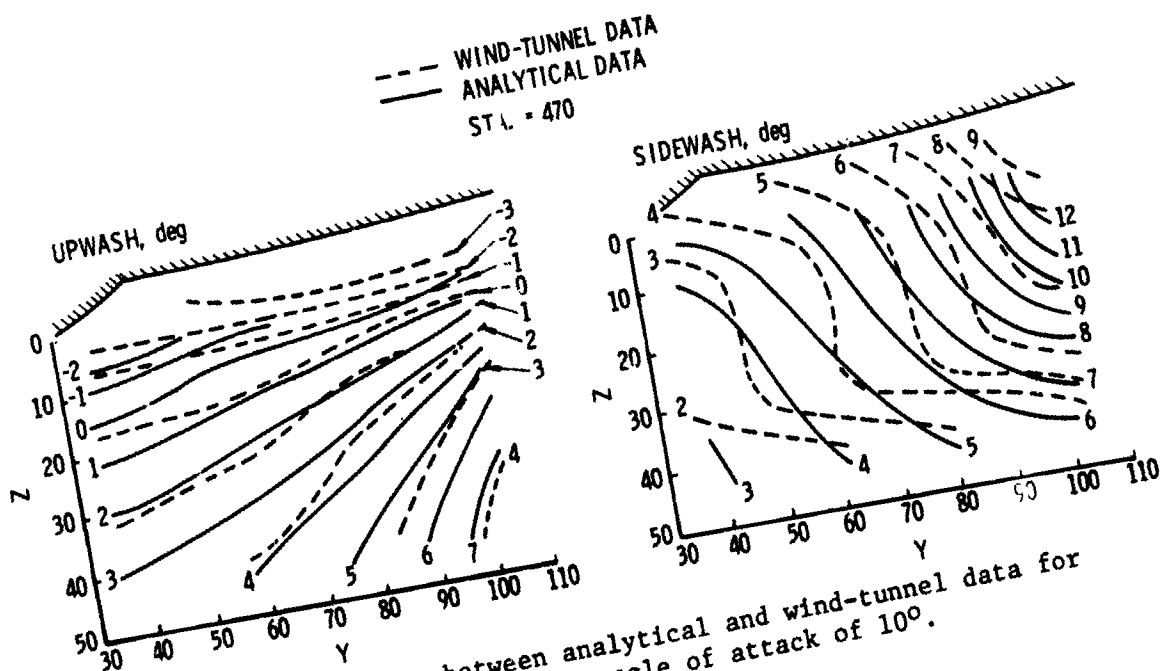
--- WIND-TUNNEL DATA
——— ANALYTICAL DATA

STA - 470

UPWASH, deg

SIDEWASH, deg

Figure 6.- Comparison between analytical and wind-tunnel data for
Mach number 0.9 at an angle of attack of 10°.

135

EXPERIMENTAL	THEORETICAL
$\epsilon = -6.15^0$	$\epsilon = -6.54^0$
$\sigma = 3.36^0$	$\sigma = 3.38^0$
$\epsilon = -13.47^0$	$\epsilon = -13.43^0$
$\sigma = 2.77^0$	$\sigma = 5.46^0$

EXPERIMENTAL	THEORETICAL
$\epsilon = -6.15^0$	$\epsilon = -6.54^0$
$\sigma = 3.36^0$	$\sigma = 3.38^0$
$\epsilon = -13.47^0$	$\epsilon = -13.43^0$
$\sigma = 2.77^0$	$\sigma = 5.46^0$
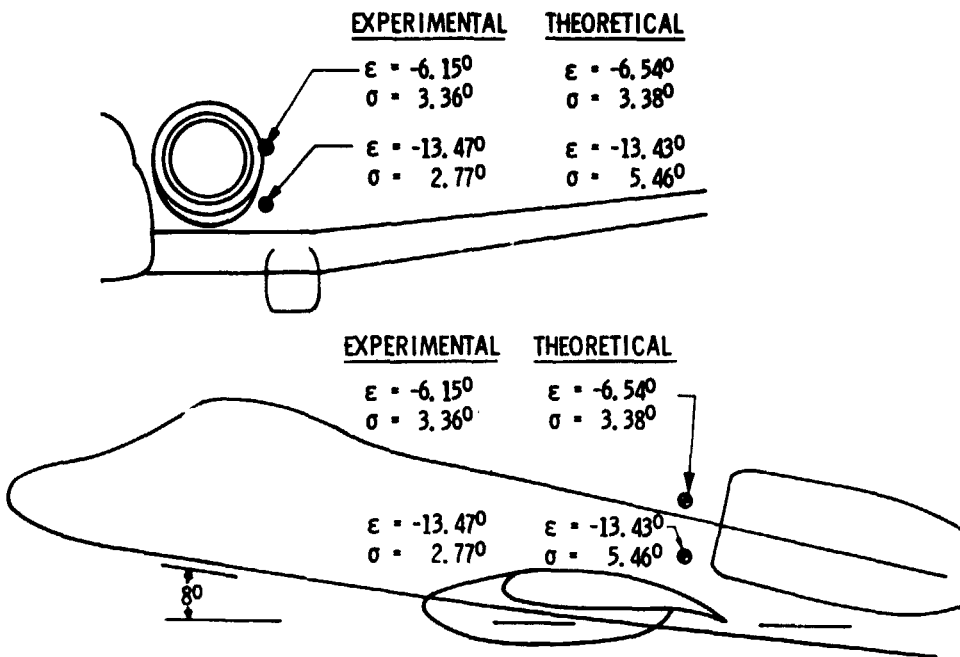
Figure 7.- Comparison between experimental and theoretical data for Mach number 0.3 at an angle of attack of 8^0.

SIDE VIEW

BOTTOM VIEW
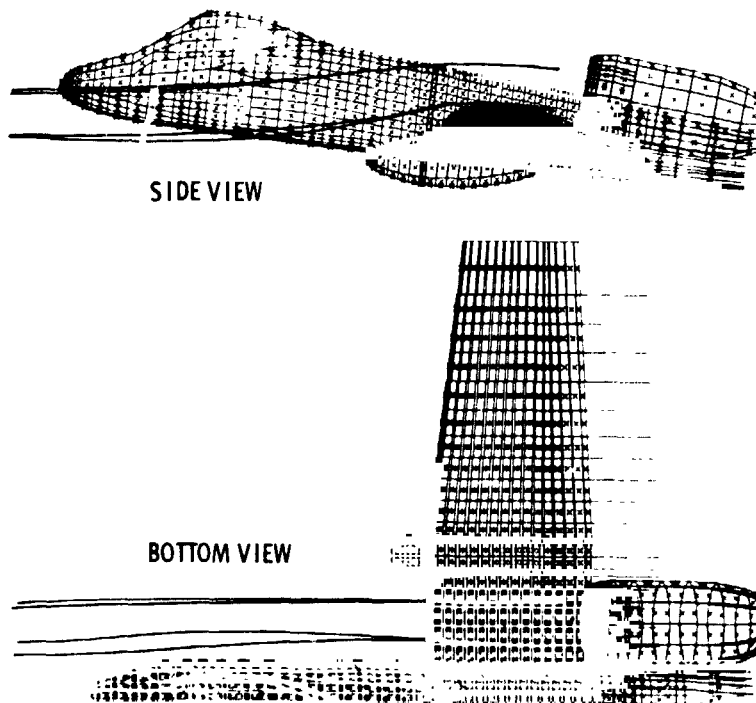
Figure 8.- Flow streamtube entering the inlet at Mach number 0.3 at an angle of attack of 8^0.
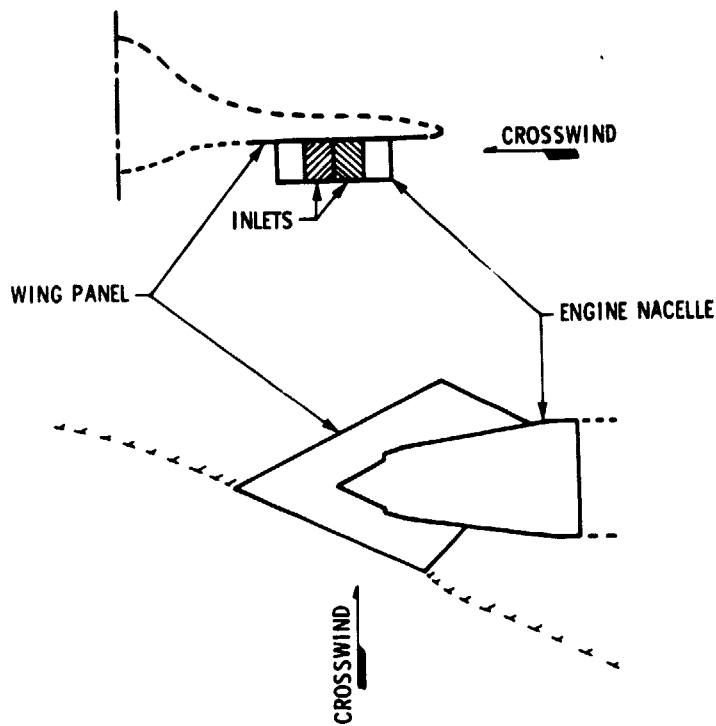
Figure 9.- Sketch of the section of the test model duplicated with the mathematical model.
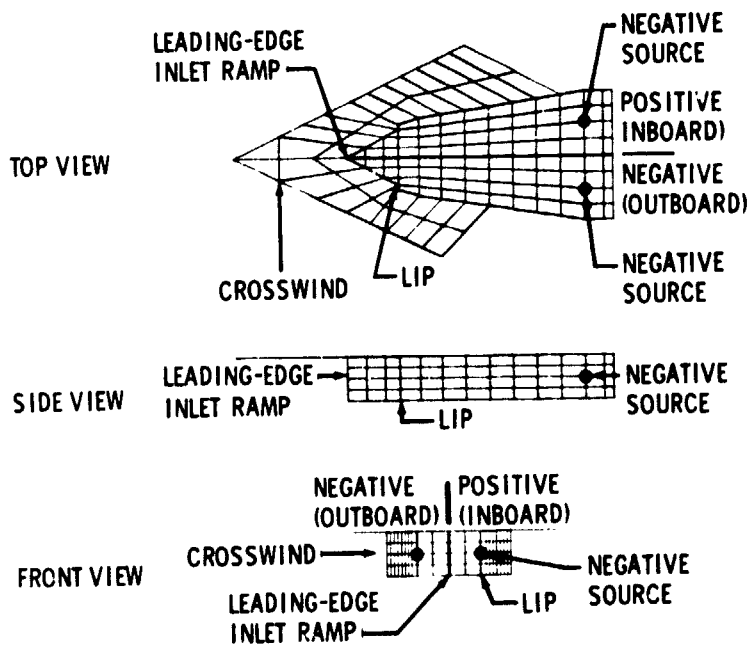
Figure 10.- Basic mathematical model for the inlet/engine crosswind analysis.
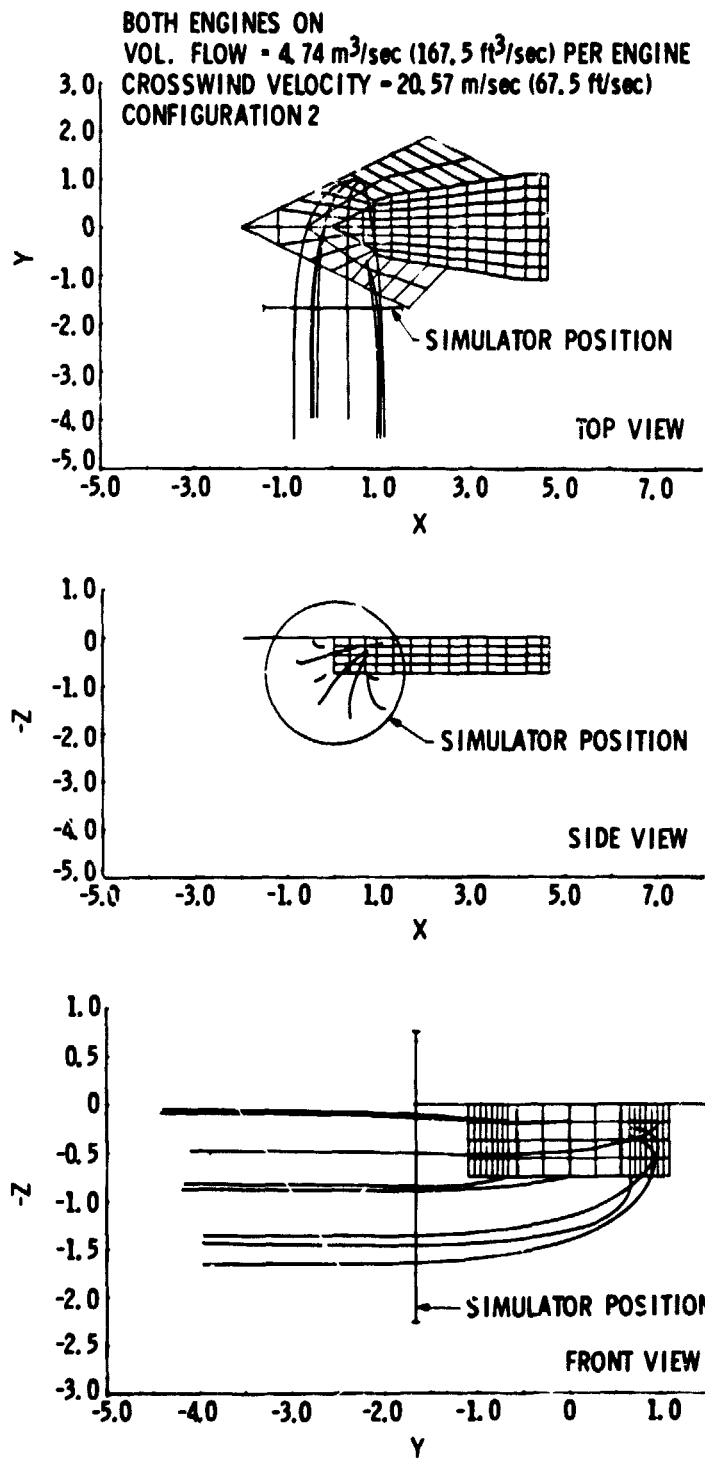
Figure 11.- Flow streamlines for both engines on with a
crosswind velocity of 20.57 m/sec (67.5 ft/sec).
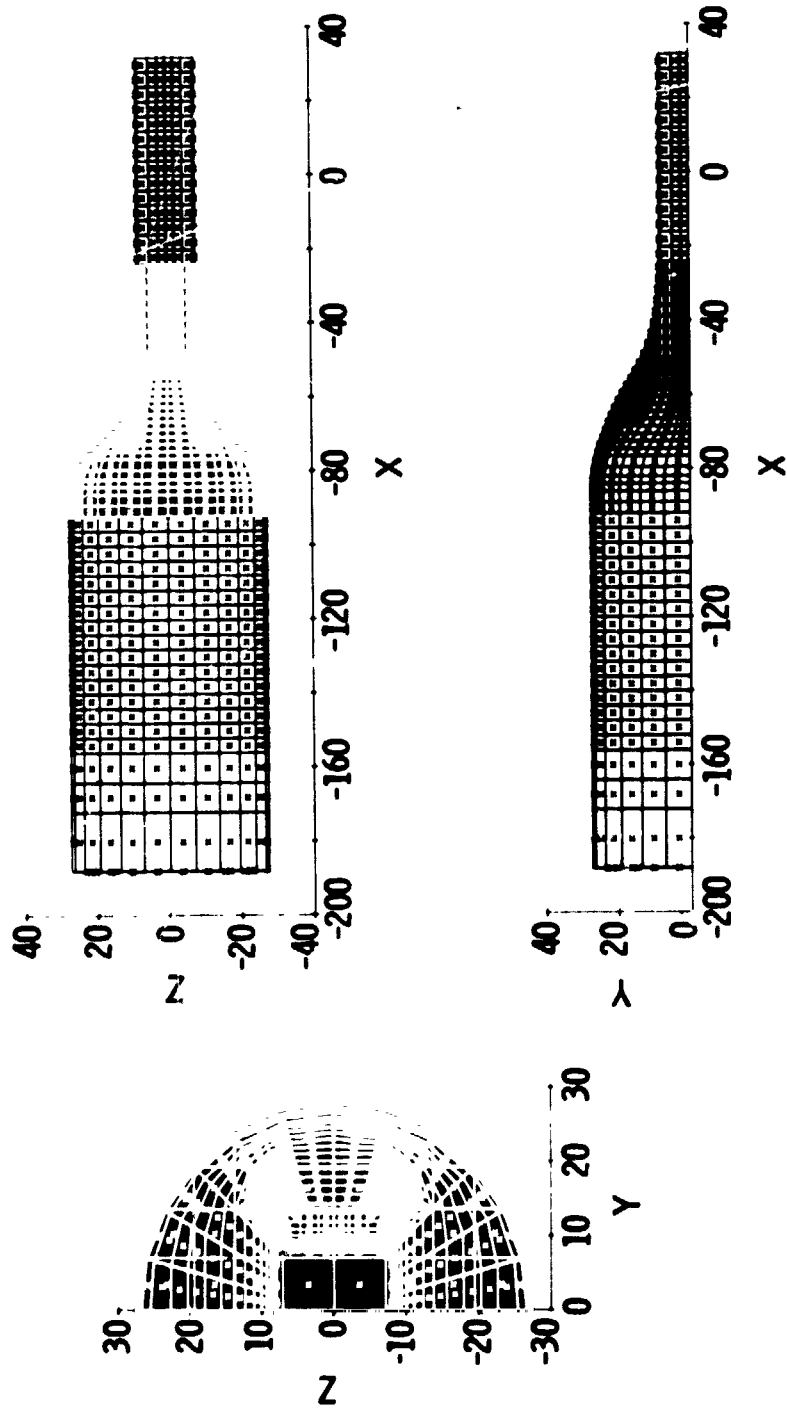
Figure 12.- Mathematical model of the PWT-16T contraction section.

SYM	LOCATION	SOURCE
—	BOTTOM WALL	PFP CALCULATED FOR 0.305 m
- - -	SIDE WALL	PFP (1 ft) OFF WALL
○	BOTTOM WALL	EXPERIMENTAL DATA
●	BOTTOM WALL	EXPERIMENTAL DATA (2/75)
▲	SIDE WALL	EXPERIMENTAL DATA (2/75)
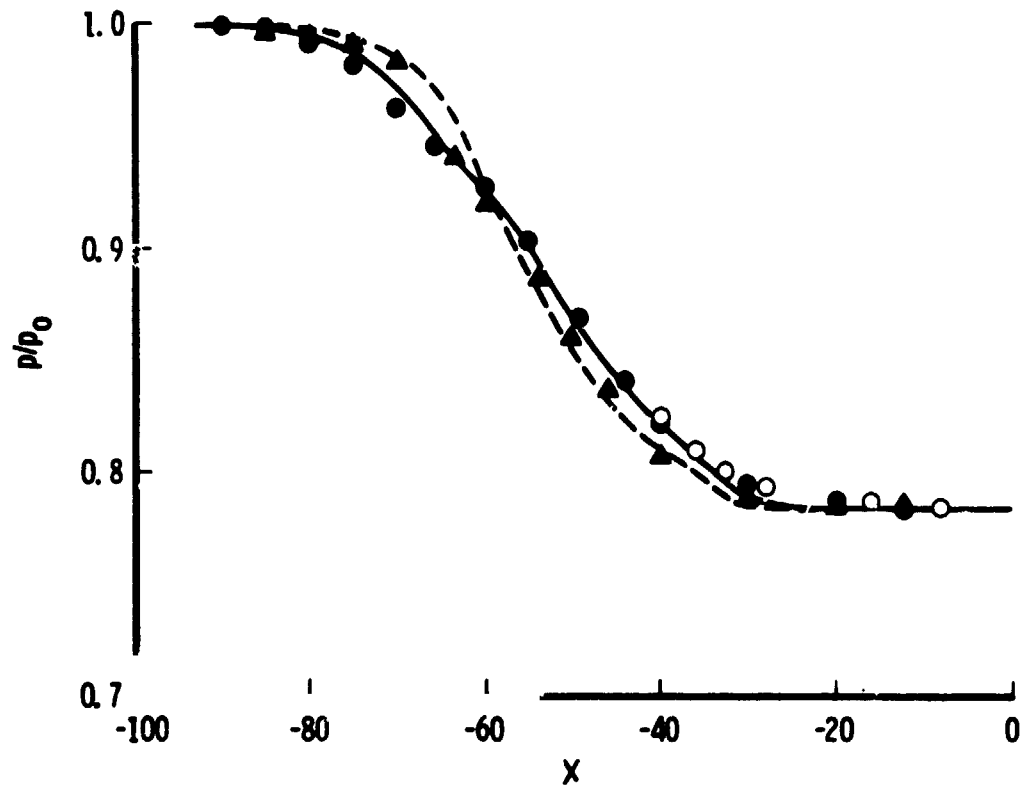
Figure 13.- Pressure distribution in PWT-16T for Mach number of 0.6.

140
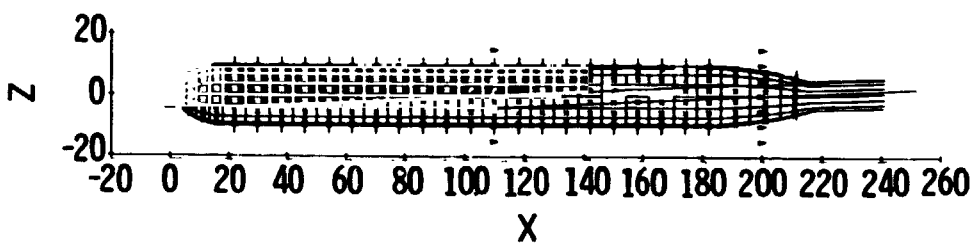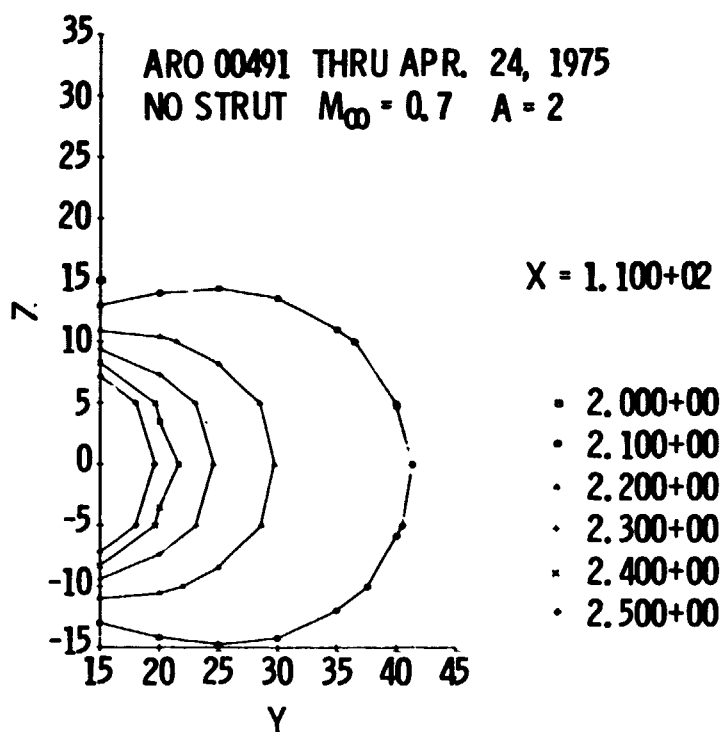
Figure 14.- Upwash about cylindrical model at $M_\infty = 0.7$ and $\alpha = 2°$.
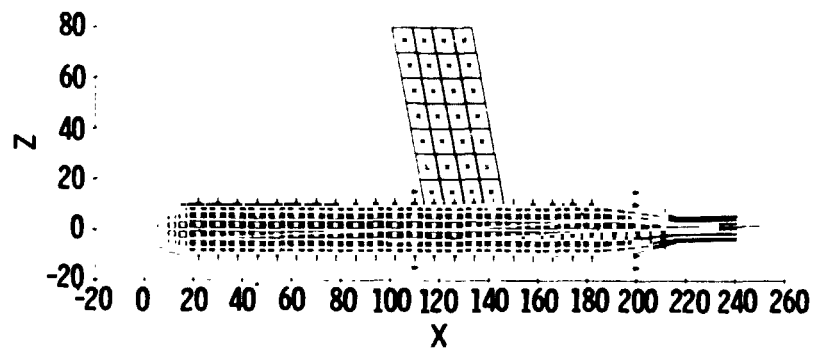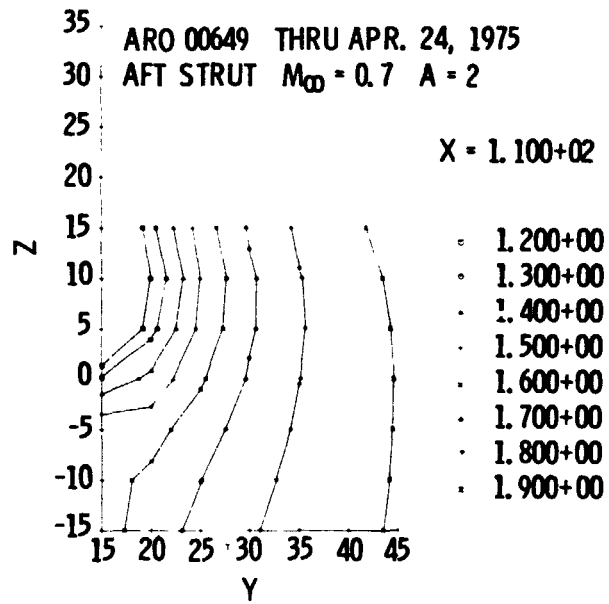
Figure 15.– Upwash about cylindrical model with strut at $M_\infty = 0.7$ and $\alpha = 2°$.
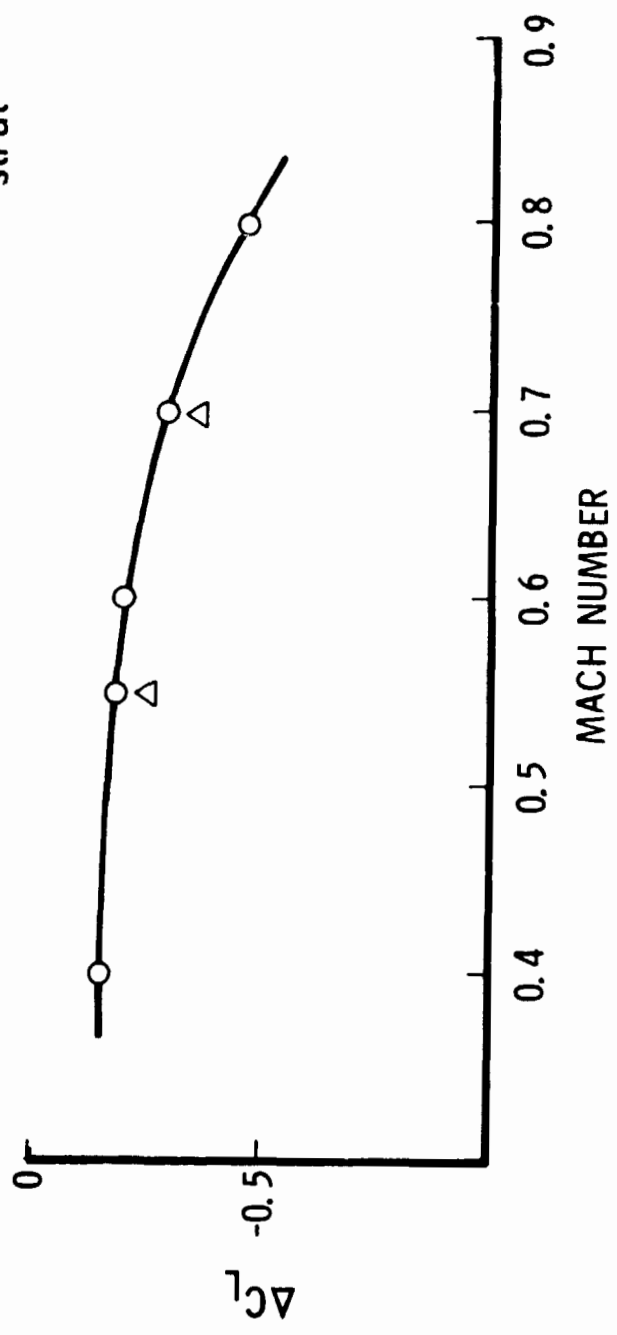
Figure 16.- Verification of strut effects of data.

143

REPORT ON THE STATUS OF A SLOTTED WIND-

TUNNEL WALL REPRESENTATION USING THE VORTEX-

LATTICE TECHNIQUE*

Fred L. Heltsley
ARO, Inc.

SUMMARY

A combined analytical/experimental program for development of an improved slotted wind-tunnel wall representation is described. The effort is presently being conducted at the Arnold Engineering Development Center (AEDC) and is scheduled for completion in 1977. The vortex-lattice technique which is being used as the primary analytical tool for representing both the wind-tunnel and the lifting model is discussed. Comparisons of results obtained to date with available data are presented. Included also is a brief description of the experimental effort to be conducted in conjunction with the analytical development.

INTRODUCTION

The literature contains numerous examples of the application of vortex-lattice theory to the modeling of closed wall wind tunnels (refs. 1 through 3). Interference factors provided by the vortex lattice method correlate well with values computed using various analytical techniques. Considerably less work, however, has been directed toward the vortex-lattice simulation of tunnels with partially open walls, in particular those with slots (refs. 2 and 3). In addition, comparisons of the resulting interference factors with those generated by analytical methods are limited to cases involving extremely simplified wall configurations and equally simple test vehicle geometries since analytical solutions are not available for the more complex models. This paper describes a program presently underway at the AEDC which is intended to provide a more useful vortex-lattice ventilated wind-tunnel model by accounting for the viscous effects

145

associated with flow through and/cr across the slots (ref. 4).
Similar studies have been conducted to develop representations of
several aerodynamic configurations (refs. 5 through 9). Many of
the resulting models are capable of generating the effects of
complex real flow phenomena such as separated wakes and jet
exhausts although most of the simulations are strongly dependent
upon empirical information. The intent of the present effort is
to develop an improved mathematical wind-tunnel wall formulation
by supplementing an in-depth analytical study with appropriate
experimentation.

SYMBOLS

$\hat{B}_i$ unit normal vector at the ith control point, negative
       away from the boundary on the inner surface

$\hat{b}_i$ unit normal vector at the ith control point

C   tunnel cross-sectional area

C^* reference tunnel area

$\vec{C}_{ij}$ influence of the jth singularity on the ith control
       point

C_L lift coefficient

C_p pressure coefficient

$d\ell$ length of a vortex line

$\vec{K}_i$ singularity density at the ith control point

N   number of singularities

P   wall

$\hat{p}_i$ unit vector parallel to the boundary at the ith
       control point

S   wing area

u_∞ free-stream velocity

$\vec{v}_i$ velocity induced at the ith control point in the vortex sheet

$\vec{v}_i^*$ velocity induced at the ith control point on the inner surface of the vortex sheet

$\vec{v}_i^{**}$ velocity induced at the ith control point on the outer surface of the vortex sheet

$\vec{v}_\infty$ free-stream velocity

Δv velocity jump across the vortex sheet

W local downwash velocity

X nondimensionalized distance from model along center line

x/c nondimensionalized chord length

α angle of attack

Γ_j strength of the jth singularity

δ lift interference factor

δ^* normalized lift interference factor

λ ratio of tunnel height to tunnel width

τ ratio of wing span to tunnel span

ANALYTICAL STUDY

Vortex-Lattice Technique

The analytical work has been directed toward representing both the wind-tunnel walls and the lifting model. The vortex-lattice technique was chosen as the primary tool since the

method can be extended to simulate extremely complex aerodynamic geometries without changing the basic solution scheme. Reference 10 describes a digital program (PFP) which has been developed at the Arnold Engineering Development Center for potential flow analysis using vortex-lattice theory. The computation procedure involves definition of the model geometry and boundary conditions, calculation of the influence coefficient matrix, and solution of the resulting set of linear equations for the strengths of the individual vortex filaments. Once the singularity strengths are known, velocities can be determined anywhere in the flow field, including the model surfaces. In addition, the program is capable of computirg lift forces, pressure coefficients, and streamlines. Routines are also available for generating three-view, isometric, and perspective plots of both the model input geometry and computed streamlines and velocity vectors.

Solid Surface Simulation

The PFP has been used extensively at the AEDC for aerodynamic analyses involving solid boundaries (refs. 5, 6, 8, and 10). These cases involved the classical form of the vortex lattice equation:

$$\vec{v}_i \cdot \hat{b}_i = \vec{v}_\infty \cdot \hat{b}_i + \sum_{j=1}^{N} \Gamma_j (\vec{C}_{ij} \cdot \hat{b}_i) \tag{1}$$

Application of the solid-wall boundary condition, $\vec{v}_i \cdot \hat{b}_i = 0$, forces the components of velocity perpendicular to the surface to vanish and permits solution of the resulting N linear homogeneous equations.

The technique has been used to compute lift interference in a closed wall wind tunnel. A simple example is illustrated in figure 1. The resulting interference levels averaged along the span at each axial location are shown in figure 2. Included also in the plot are interference distributions for several other tunnel cross sections along with corresponding analytical results due to Kraft (ref. 12).

Slotted Wall Simulation

Extension of the method to represent tunnels with partially open walls is somewhat more difficult due to the added complexity of applying the constant-pressure boundary condition in the slots. This requires that the tangential component of velocity on the interior surface of the vortex sheet which represents the free jet boundary must vanish. It can be shown that the continuity in the tangential component of velocity across the

vortex sheet is equal to the local vortex density, i.e.,
$K = d\Gamma/d\ell$. Since equation (1) is expressed in terms of the
velocity directly on the sheet, only half of the velocity jump
must be accounted for. Modification of equation (1) yields

$$\vec{v}_i^* \cdot \hat{p}_i = \vec{v} \cdot \hat{p}_i + \sum_{j=1}^{N} j \; (\vec{C}_{ij} \cdot \hat{p}_i) + (\tfrac{1}{2}\vec{K}_i \times \hat{B}_i) \cdot \hat{p}_i \quad (2)$$

The nomenclature used in equations (1) and (2) is illustrated in
figure 3.

A vortex-lattice model of a slotted wall tunnel is presented
in figure 4 to demonstrate the application of both types of
boundary conditions. The wall interference distribution computed
for the configuration show in figure 5. In addition, distribu-
tions for a closed tunnel and a tunnel with open upper and lower
walls and closed side walls are shown. Theoretical data due to
Kraft (ref. 12) and vortex-lattice results computed by Bhateley
(ref. 2) for similar configurations are included for comparison.
Two basic rules of thumb to be followed in the construction of a
model such as the one in figure 4 should be noted here. These
are (1) the edge of each slot should coincide with a vortex
filament and (2) the vortex grid and the control points should be
positioned by the same function. In the present case, the slot
configuration has been conveniently selected so that a uniform
spacing satisfies both rules. Situations in which the slots are
narrow relative to the width of the solid wall panels are some-
what more difficult to handle. Two primary alternatives exist. A
uniform spacing which is at least as narrow as the slots can be
used for both the slots and the solid wall panels. This may
result, however, in a prohibitive number of singularities. An
alternate solution is to select a nonuniform spacing. The use of
a cosine function has been found to yield good tip definition
when representing finite wings. A similar technique, illustrated
in figure 6, has been used by the author. In addition to reducing
the number of singularities required, the scheme provides excellent
mutual slot/panel edge definition.

Lifting Model

The experimental model used during this study to provide lift
interference measurements is shown in figure 7. The wing assembly
consists of a 32.0 in. (81.28 cm) span x 9.0 in. (22.86 cm) chord
NACA 63A006 airfoil with a minimum blockage circular centerbody.
A similar half-scale assembly is mounted aft of and above the
wing to provide tail surface measurements. A vortex-lattice
representation of the lifting model is presented in figure 8.
Since the PFP is capable of assuming symmetry, definition of only
one-half of the model is required. Pressure coefficient

distributions over a two-dimensional version of the wing model are shown in figures 9 and 10 to illustrate the effects of grid spacing and angle of attack, respectively. In all cases, a precisely computed cosine (cosine) function was used to determine both the vortex and the control point locations. An attempt to interpolate between previously obtained "as built" coordinates proved to be unsuccessful due to the extreme sensitivity to the lack of measurement precision. Finally, good results were achieved by generating slope continuous smoothing functions to define the surface.

Details of the leading and trailing edges of the lattice wing model are shown in figure 11. It should be noted that the trailing edge was not closed but was allowed to "leak" in both the two- and three-dimensional models since the tips of the three-dimensional wing were closed with lattice plates.

A less detailed vortex-lattice representation of the lifting model is under development which will require a significantly smaller number of singularities. The new model will be utilized in order to reduce the computer time required during the development of the tunnel wall model. Later, the detailed vortex lattice lifting model will be recalled to provide the necessary precision for correlation of analytical and experimental interference results.

EXPERIMENTAL PROGRAM

Wind-Tunnel Description

The AEDC Low Speed Wind Tunnel (V/STOL) shown in figure 12 will be used to provide experimental interference data. The tunnel has a test section 45.0 in. (114.3 cm) wide and 36.0 in. (91.44 cm) high and is capable of generating velocities from near zero to 250 ft/sec (76.2 m/sec). The solid test section walls can easily be replaced with selected slotted walls to provide wall flow relief. Figure 13 is a schematic of the lifting model installed in the V/STOL tunnel. The installation shown permits an angle-of-attack variation from 6° to 16° about the pitch center.

Interference Free Data

Only a limited amount of suitable interference free data are available for the lifting model since a majority of the previous tests has been conducted at high Mach numbers. Plans are presently underway to obtain the necessary additional interference free data for the lower Mach numbers.

CONCLUDING REMARKS

The vortex-lattice technique has been successfully used to represent solid surfaces for both the wind-tunnel walls and the lifting model. Correlation with available interference free experimental data and analytical results were excellent. In addition, the free jet boundary condition has been applied to simulate the flow in the tunnel wall slots. Good agreement was obtained with existing analytical predictions. Development of both vortex-lattice models is continuing.

Preparation for the experimental program is underway and testing will begin in the near future.

REFERENCES

1. Joppa, Robert G. "Wind Tunnel Interference Factors for High-Lift Wings in Closed Wind Tunnels." NASA CR-2191, February 1973.

2. Bhateley, I. C. "A Theoretical Optimization of the Test-Section Geometry for the Proposed Boeing Low-Speed Wind Tunnel." Boeing Report D6-15023, February 1967.

3. Wasserstrom, E., Borovik, Y., Hazandvsky, D., and Rom, J. "Calculation of Lift Interference Corrections Due to Wind-Tunnel Test-Section Boundaries by the Vortex-Lattice Method." T.A.E. Report No. 124, Technion-Israel Institute of Technology, Haifa, Israel, April 1971.

4. Keller, J. D. "Numerical Calculation of Boundary-Induced Interference in Slotted or Perforated Wind Tunnels Including Viscous Effects in Slots." NASA TN D-6871, August 1972.

5. Parker, R. L., Jr. and Heltsley, F. L. "Simulation of a High Disc Loading Free Propeller in a Cross Flow by the Vortex-Lattice Method." AEDC-TR-72-139, November 1972.

6. Heltsley, F. L. and Parker, R. L., Jr. "Application of the Vortex Lattice Method to Represent a Jet Exhausting from a Flat Plate Into a Crossflowing Stream." AEDC-TR-73-57, June 1973.

7. Rubbert, P. E., et al. "A General Method for Determining the Aerodynamic Characteristics of Fan-in-Wing Configurations." Vol. 1 and 2, USAAVLABS TR-67-61A, December 1967.

8. Palko, R. L. "Full-Scale Inlet/Engine Testing at High Maneuvering Angles at Transonic Velocities." AIAA Paper No. 72-1026, September 1972.

9. Maskew, B. "Calculation of the Three-Dimensional Potential Flow Around Lifting Non-Planar Wings and Wing-Bodies Using a Surface Distribution of Quadrilateral Vortex-Rings." Loughborough University of Technology, Report TT 7009, September 1970.

152

10. Todd, D. C. and Palko, R. L. "The AEDC Three-Dimensional, Potential Flow Computer Program, Vol. I and II." AEDC-TR-75-75.

11. Kraft, E. M. and Lo, C. F. "A General Solution for Lift Interference in Rectangular Ventilated Wind Tunels." AIAA Paper No. 73-209, January 1973.

12. Kraft, E. M. "Upwash Interference on a Symmetrical Wing in a Rectangular Wall Wind Tunnel: Part I - Development of Theory." AEDC-TR-72-187, March 1973.
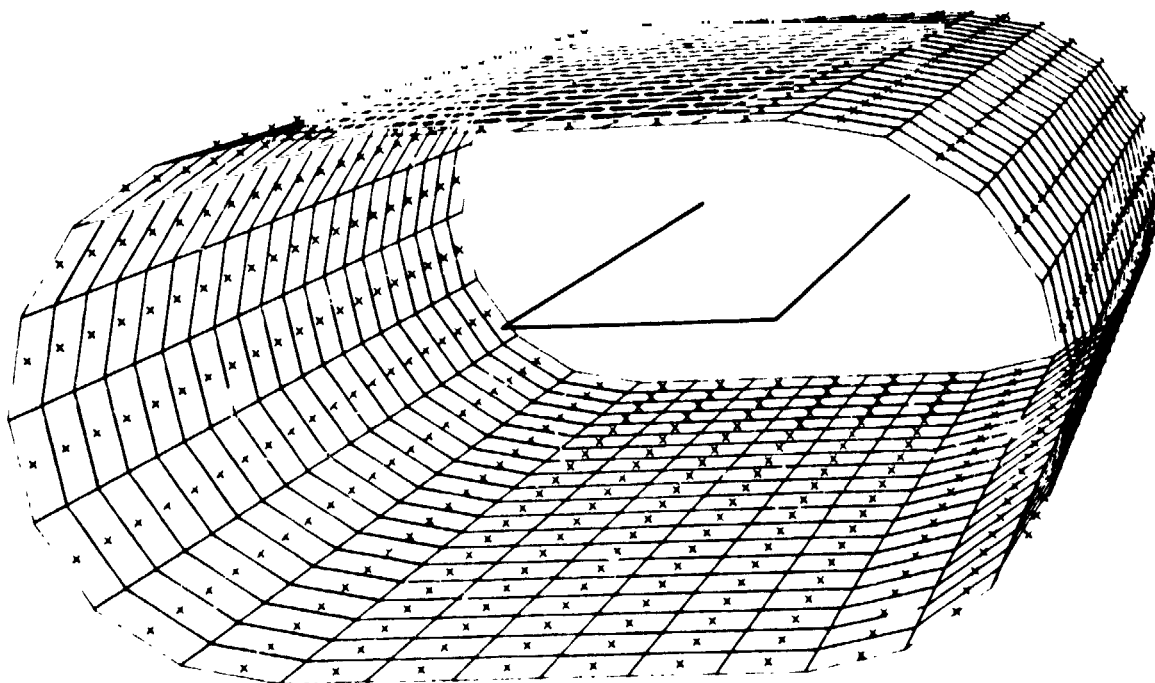
Figure 1.- Vortex-lattice representation of the
NASA Ames flat oval tunnel.
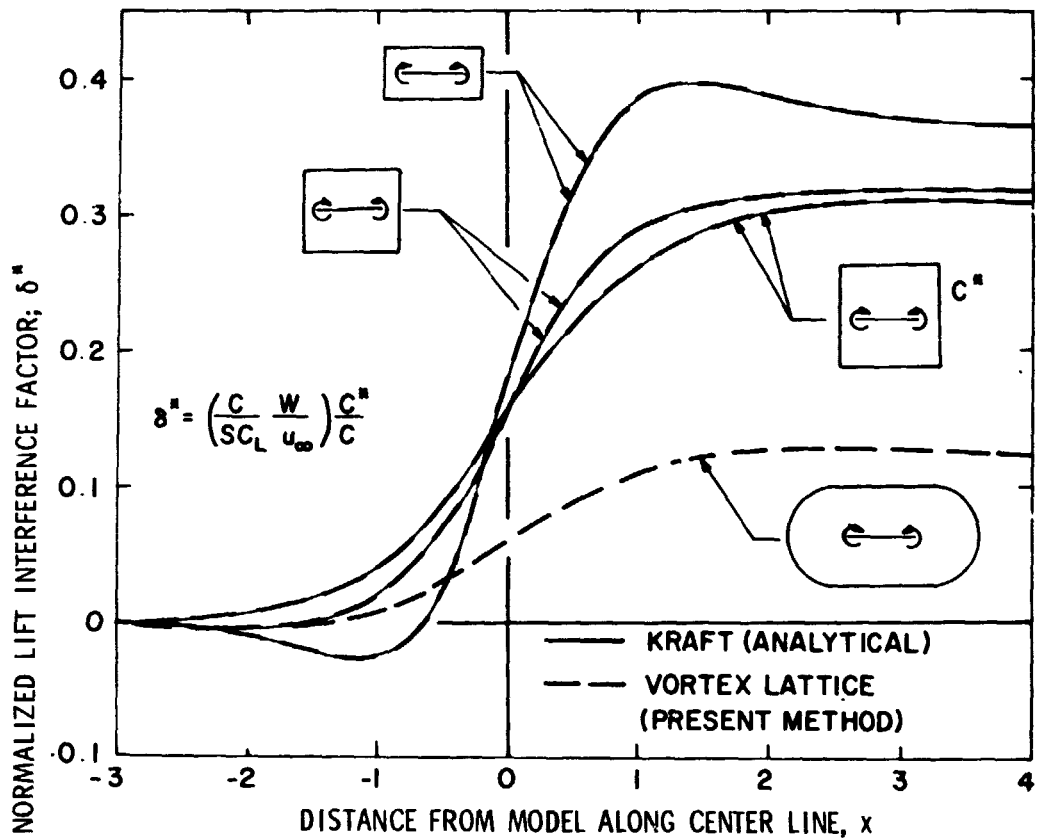
Figure 2.- Comparison of theoretical wall interference results for several tunnel cross sections.

$$\delta^{\text{x}} = \left(\frac{C}{SC_L}\frac{W}{u_{\infty}}\right)\frac{C^{\text{x}}}{C}$$

KRAFT (ANALYTICAL)

VORTEX LATTICE (PRESENT METHOD)

BOUNDARY CONDITION:

$$\vec{v}_i \cdot \hat{b}_i = 0$$
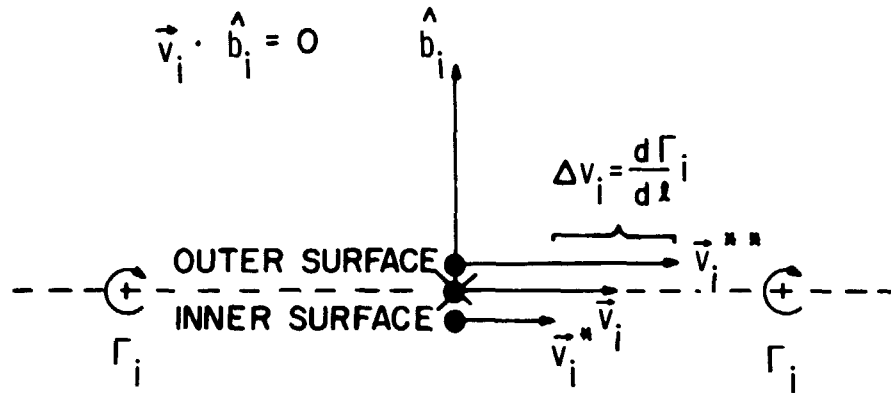
CLOSED WALL BOUNDARY

BOUNDARY CONDITION:

$$\vec{v}_i^* \cdot \hat{p}_i = 0$$
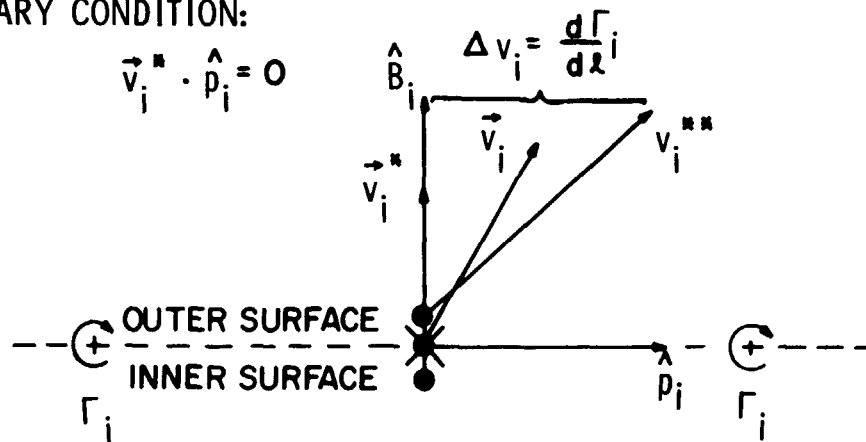
FREE JET BOUNDARY

Figure 3.- Vortex-lattice boundary condition nomenclature.

$$\underline{\text{OPEN SLOT}}$$
$$\vec{v}_i^* \cdot \hat{p}_i = 0$$

$$\underline{\text{SOLID WALL}}$$
$$\vec{v}_i \cdot \hat{b}_i = 0$$

$$\underline{\text{LIFT MODEL}}$$

$$\underline{\text{SOLID WALL}}$$

$$\underline{\text{OPEN SLOT}}$$
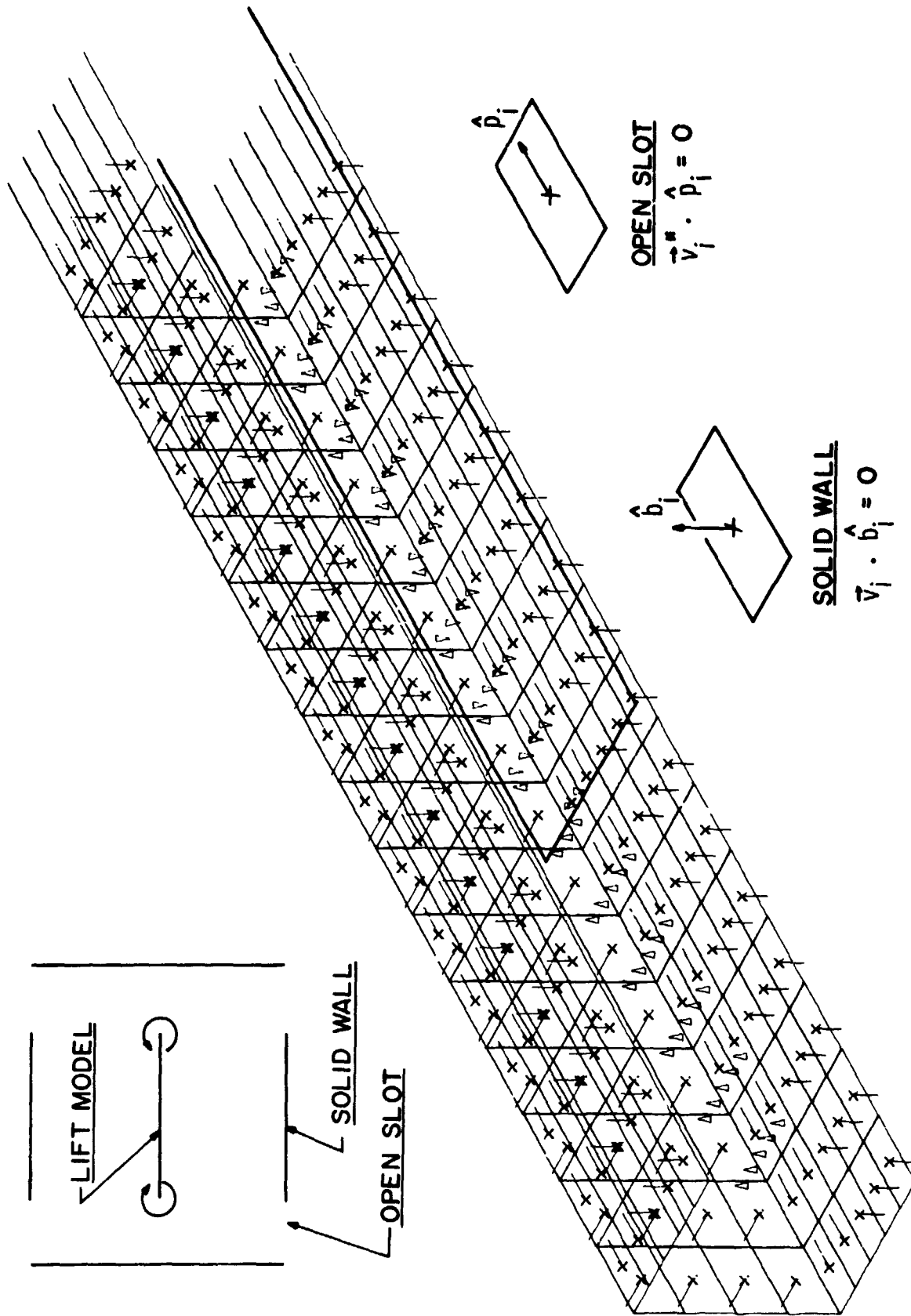
Figure 4.- Basic vortex-lattice wind tunnel model.
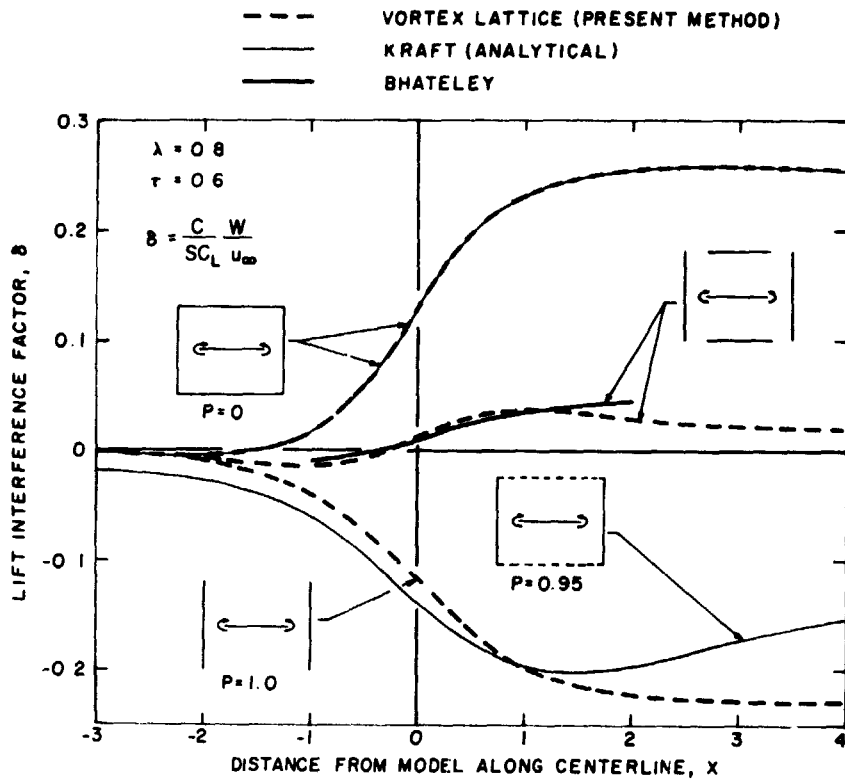
Figure 5.- Comparison of present data with other techniques for several tunnel configurations.
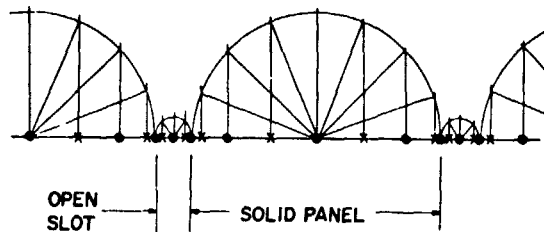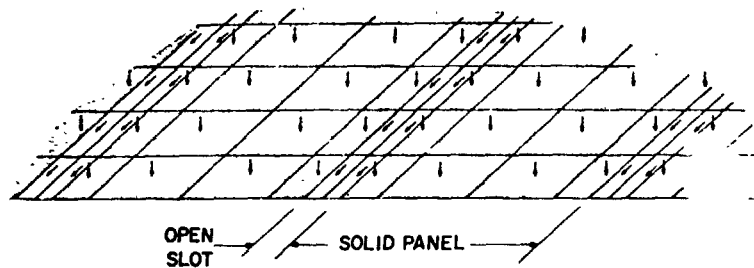
Figure 6.- Cosine spa 'ng details.
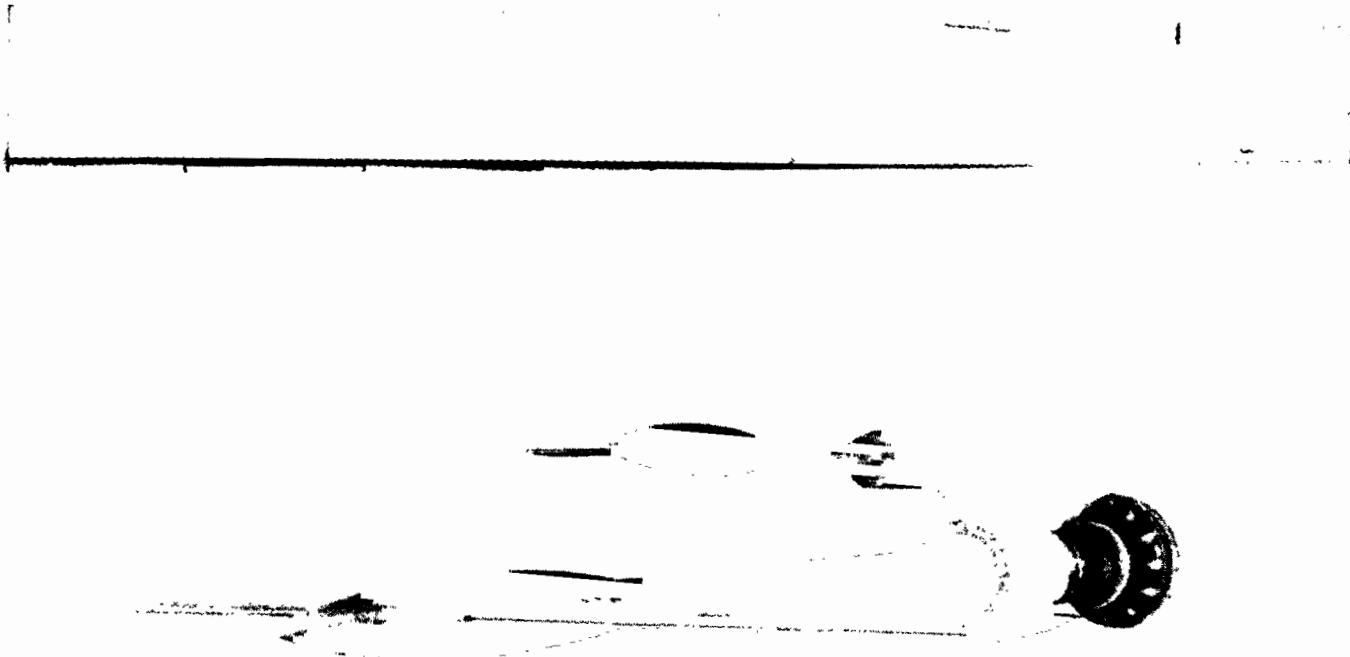
Figure 7.- Experimental lifting model.
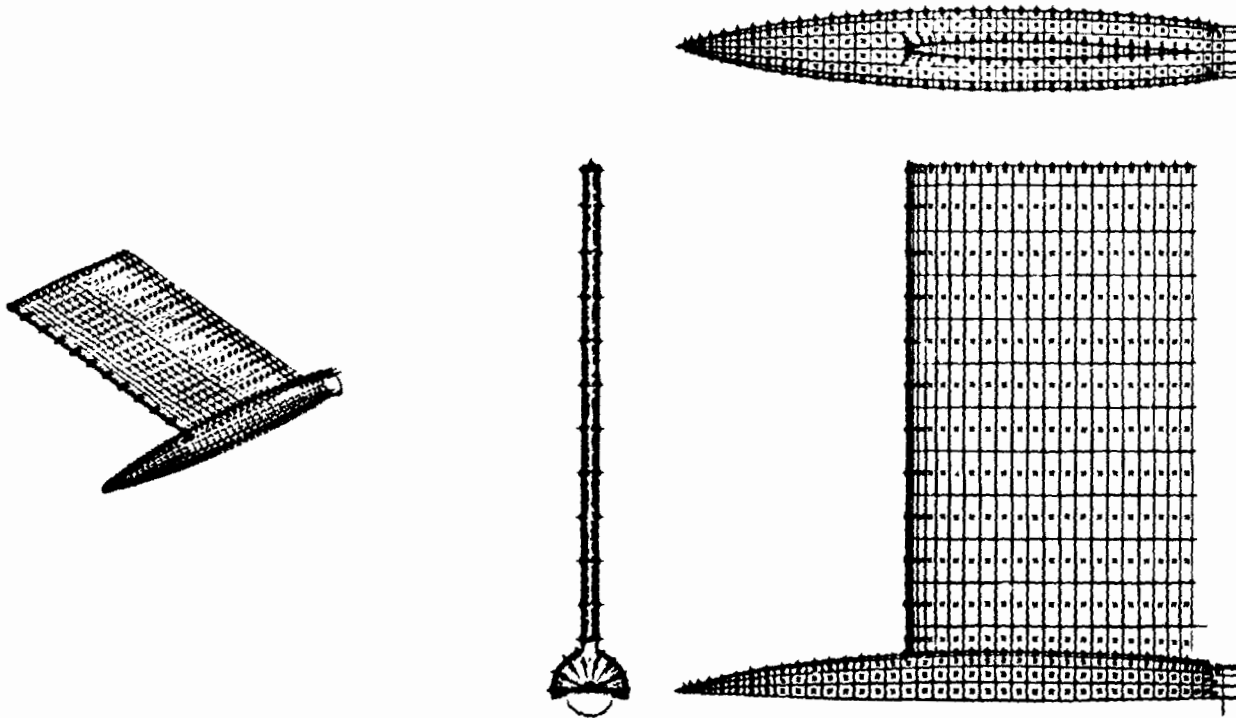
Figure 8.- Detailed vortex-lattice representation of the
lifting model.
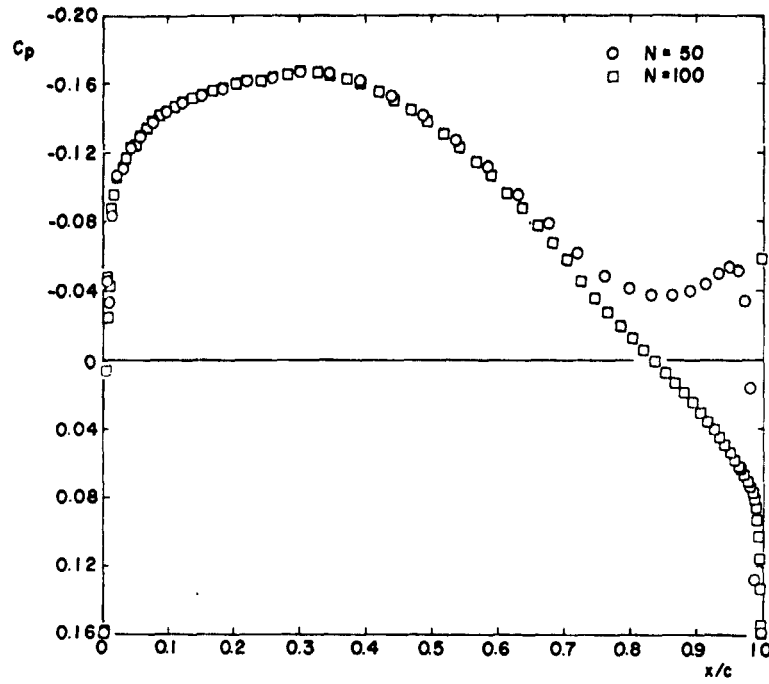
Figure 9.- Effect of vortex spacing.
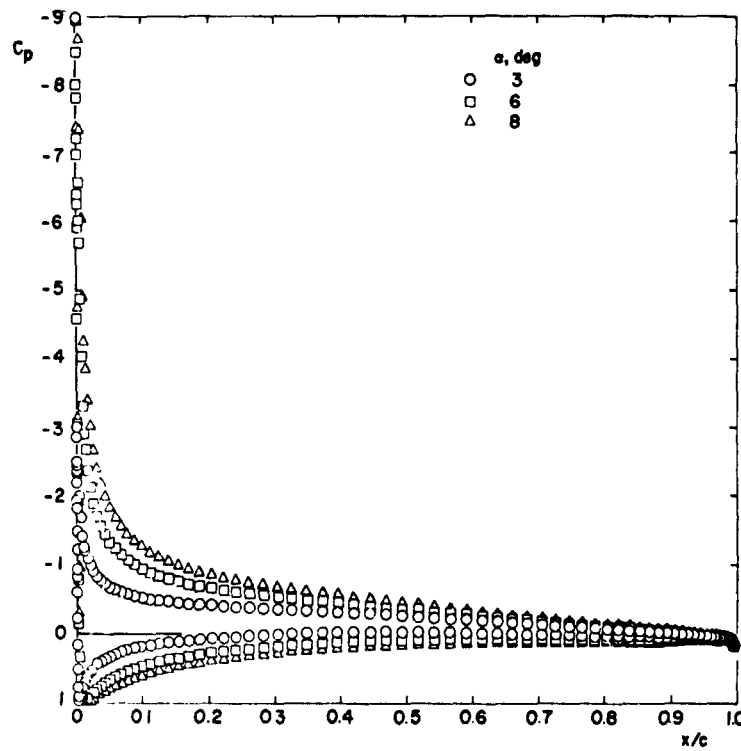
Figure 10.- Wing pressure coefficient versus
angle of attack.

160

LEGEND:
- — — REAL WING SURFACE
- —— CHORDWISE VORTEX
- ● SPANWISE VORTEX
- ↑ CONTROL POINT WITH UNIT NORMAL
- ✗

LEADING EDGE

TRAILING EDGE
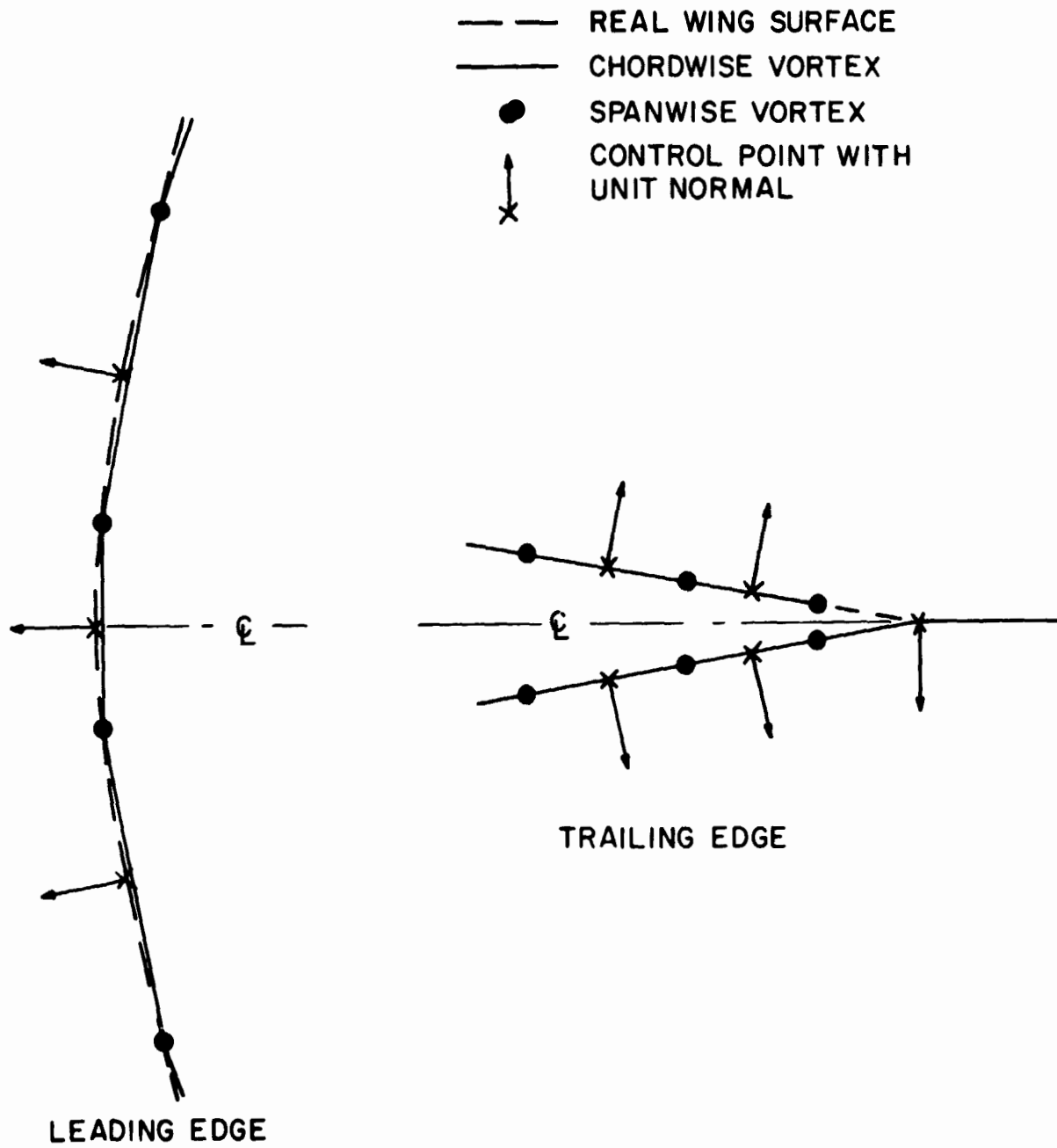
Figure 11.- Wing lattice details.
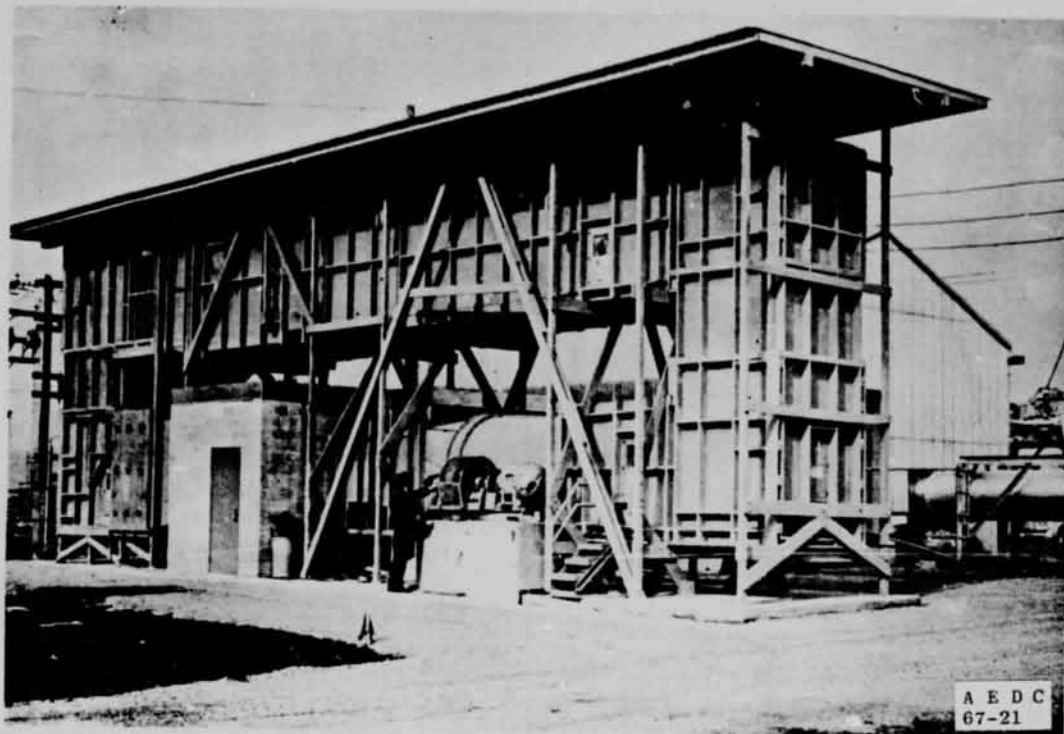
Figure 12.- AEDC low speed wind tunnel (V/STOL).

SLOTTED WALL

SOLID WALL

CENTER OF PITCH
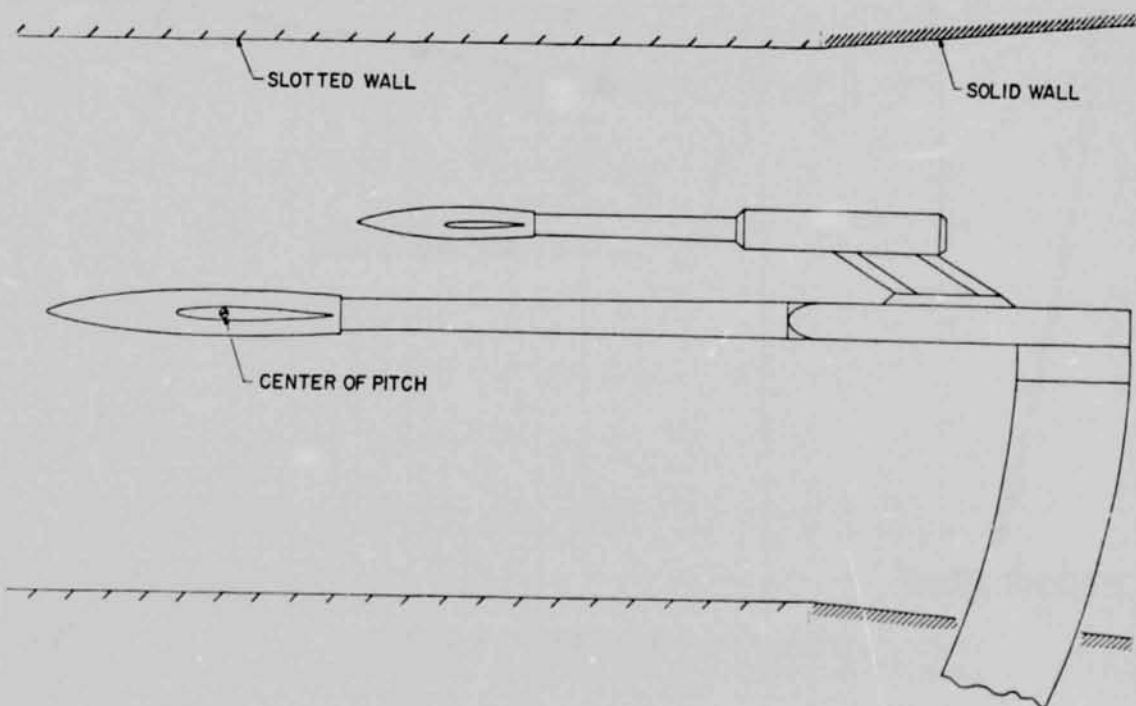
Figure 13.- Lifting model installed in the AEDC low speed
wind tunnel (V/STOL).

A QUADRILATERAL VORTEX METHOD

APPLIED TO CONFIGURATIONS WITH HIGH CIRCULATION

Brian Maskew
Analytical Methods, Inc.

SUMMARY

A quadrilateral vortex-lattice method is briefly described for calculating the potential flow aerodynamic characteristics of high-lift configurations. It incorporates an iterative scheme for calculating the deformation of force-free wakes, including wakes from side edges. The method is applicable to multiple lifting surfaces with part-span flaps deflected, and can include ground effect and wind-tunnel interference. Numerical results, presented for a number of high-lift configurations, demonstrate rapid convergence of the iterative technique. The results are in good agreement with available experimental data.

INTRODUCTION

The calculation of aerodynamic characteristics for three-dimensional configurations with high circulation, e.g., a wing with flap and tailplane can be misleading unless the trailing vortex wakes are represented correctly. In fact, initial applications of a quadrilateral vortex-lattice method with rigid non-planar wake (refs. 1 and 2) showed that results for a wing alone were sensitive to wake location at even moderate lift coefficients. The high circulation case, therefore, is non-linear, and requires a force-free wake representation.

The problem of calculating vortex sheet roll-up has recieved considerable attention in the past, (see review by Rossow (ref. 3)), but has been concerned mainly with the two-dimensional case. More recent work has included three-dimensional factors. Butter and Hancock (ref. 4) and also Hackett and Evans (ref. 5) included the influence of a bound vortex, and Belotserkovskii (ref. 6) incorporated a wake roll-up procedure with a vortex-lattice method. Mook and Maddox (ref. 7) developed a vortex-lattice method with leading-edge vortex roll-up. The roll-up procedure incorporated in the quadrilateral vertex method (ref. 2) differs slightly from the above methods, and is described here before discussing the high-lift applications.

α   incidence, in degrees

S   area

c   chord

$\overline{c}$ reference chord

A   aspect ratio

η   spanwise position normalised by wing semispan

C_L lift coefficient

C_M pitching moment coefficient (about the mid chord)

C_{D_i} induced drag coefficient

k   induced drag factor, $= \pi A\, C_{D_i}/C_L^2$

Subscripts:

W   wing

T   tailplane or wind tunnel

calc   calculated

exp   experimental

METHOD DESCRIPTION

   The method, which incorporates an iterative procedure for wake shape, is based on vortex-lattice theory (e.g., ref. 8), but the lattice is formed into quadrilateral vortices (fig. 1) instead of horse-shoe vortices. The quadrilateral form is equivalent to a piecewise constant doublet distribution and each vortex "panel" is self-contained. This makes it easier to apply to cambered surfaces. Another advantage is that only the quadrilaterals adjacent to trailing edges (and to side edges when edge separation is included) have trailing vortices, and so they are the only panels whose influence coefficients vary in the iterations for wake shape. The complete matrix of influence coefficients would be affected for the horse-shoe vortex model.

For the wake model, each trailing vortex is divided into straight segments (fig. 1), the number and length of which can be varied from vortex to vortex to allow more detailed representation in roll-up regions. The segmented part of each vortex ends in a semi-infinite vortex in the free-stream direction. In the iterative wake procedure, each trailing vortex segment is made approximately force-free by aligning it with the local mean velocity vector. The segment midpoint is the most appropriate position to apply this condition, yet most methods use the upstream end of the segment (following ref. 6). The present method calculates the mean velocity at 55% of the segment length (extrapolated from the previous segment) after examining a roll-up calculation (ref. 2) for a pair of equal strength, segmented vortices. Compared with the upstream end point, the 55% point gives faster convergence, and the results are less sensitive to segment length, (fig. 2).

Small Rankine vortex cores are placed on the vortices to avoid large velocities being calculated near the vortices; nevertheless, when calculating the velocity vectors for the wake relaxation, the local vortex contribution is excluded. To obtain the first vortex strength solution, the trailing vortices are assumed semi-infinite in the free-stream direction. A new vortex strength solution is obtained after each wake relaxation is completed.

RESULTS AND DISCUSSION

Wing-flap-tailplane

The wing-flap-tailplane configuration is a typical problem facing the aerodynamicist when calculating the behavior of an aircraft during landing and take-off. The present method enables the free-air and the ground-effect regimes to be evaluated. An illustrative calculation was performed for the part span flap configuration shown in figure 3(a). The geometric characteristics are presented in table 1.

Figure 3(a) shows the calculated vortex trajectories in free air after the fourth iteration. The vortex roll-up region from the flap edge passes close to the tailplane tip (outboard and below) and has clearly influenced the tailplane tip vortex trajectory (compare vortex (15) with vortex (10) from the wing tip, especially in the side view). The plan view shows wing inboard trailing vortices passing directly below the centers of tailplane quadrilaterals. If these vortices had been close to the tailplane surface, then the results would have diverged. In its present form, the method is not applicable to close approach problems unless the vortex trajectories are constrained to align with the local surface lattice. However, the close approach problem has been investigated, and a technique developed to overcome it (refs. 9 and 10) but, so far, this has not been incorporated in the main program.

The effect of iteration on the trajectory of vortex (7) from the flap edge region is given separately in figure 3(b). This vortex moved the most in the group; nevertheless, the figure shows little change between the third and fourth iterations. Sections through the calculated wakes in free air and in

ground effect are shown in figure 3(c). Compared with the free-air positions, the vortices move outwards in ground effect, and are deflected upwards. This movement will influence the ground-effect conditions at the tailplane.

Figure 4 shows the changes in wing and tailplane calculated lift and induced drag with iteration in free-air conditions. The wing lift is essentially converged by the second iteration and the induced drag factor, k, by the third. The tailplane lift and induced drag (in the presence of the wing) are essentially converged by the second iteration after a relatively big jump from the streamwise-wake value.

Table II gives the calculated values of lift and induced drag for free air and for ground-effect conditions, and includes values for wing and tailplane alone. These results imply (for the combined configuration) an average downwash angle at the tailplane of about 10.7° in free air and 1.7° in ground effect. The method, however, takes into account variations in downwash – and sidewash – across the span and chord of the tailplane. The presence of the tailplane causes small changes in the wing characteristics. In free air there is a small decrease in wing lift ($\approx 0.8\%$) and a small increase in induced drag factor (from 1.100 to 1.108), which result from a small downwash induced by the negative circulation on the tailplane. In ground effect, however, the tailplane – which now has positive lift – causes a small increase in wing lift and a decrease in its induced drag factor (from 0.613 to 0.581). Although the tailplane alone results show the expected increase in lift with ground effect, the wing-flap alone result shows a decrease. This apparent anomaly is in accordance with results found earlier in reference 11; with increasing camber and/or incidence, the initial increase in wing lift in ground effect decreases and eventually goes negative. This feature is made more apparent in the spanwise distribution.

The calculated spanwise load distribution, $C_L c/\bar{c}$, and center of pressure locus for the wing are shown in figures 5(a) and 5(b) for both free-air and ground-effect conditions. In ground effect (at the same incidence as in free-air) there is a relative <u>loss</u> in lift in the flapped region – evidently over the flap itself because the center of pressure moves forward there – while outboard there is a small <u>increase</u> in lift and a rearward shift in center of pressure (i.e., the normally accepted influences of ground effect). The net result, as already seen in table II, is a decrease in overall lift. Evidently, camber has a strong influence on the ground interference effect which must be taken into account when predicting aerodynamic characteristics near the ground (ref. 11).

As would be expected, the induced drag is concentrated over the flapped region in free air (fig. 5(c)), and in fact an induced thrust is calculated over the unflapped region – a plausible consequence of concentrating the load over the inboard part of a swept wing. In ground effect, the expected reduction in induced drag occurs mainly inboard of the flap edge region (i.e., in the upwash region from the flap edge trailing vortex image).

166

Wing-Flap in Wind Tunnel

Standard correction methods for wind-tunnel interference are largely based on image techniques, and assume the wing wake to be undeflected. When testing high-lift configurations, the trailing wake moves considerably from the basic wing plane, so unless the model is very small relative to the tunnel (with possible Reynolds Number problems), the real flow violates the assumptions. The present method calculates the wake shape in the presence of the model and the tunnel walls - the latter also being represented by a distribution of quadrilateral vortices. A calculation of this form would be particularly useful for wing-tailplane configurations, but sufficient elements were not available for a fair application to such a problem at this time (i.e., to cover wing, tailplane and wind tunnel). The results from a high-lift wing-flap calculation, therefore, are given here. The general arrangement is shown in figure 6, and the geometry is defined in table III. Lift values were available from unpublished wind-tunnel measurements on a blown-flap model.

Figure 7 shows the calculated vortex trajectories for $\alpha = 5^\circ$ in the wind tunnel. The lift coefficient is 2.14, and a correspondingly high rate of vortex roll-up is indicated. The tip vortex - which was allowed to separate from the flap hinge line to be more representative of the real flow conditions - moves steadily inboard as more vorticity is "entrained". The vortices just inboard of the tip have large "curvature" at the start, and ideally, should have had smaller segments there. A section through the calculated wake (fig. 7) is compared with that for free-stream conditions at approximately the same lift coefficient. This required a free-air incidence of 10° compared with 5° in the tunnel. In the tunnel, the roll-up region is squashed in a vertical sense and, on the whole, the vortex positions lie outboard relative to their positions in free air. In the tunnel, the vortices over the inboard region lie above the free-air position - a result of the reduced downwash in the tunnel.

Figure 8(a) shows the C_L characteristics calculated in the tunnel and in free air. The standard incidence correction (i.e., $\Delta\alpha = \delta C_L \, S_W/S_T$, with $\delta = 0.101$ here) applied to the in-tunnel values falls short of the free-air result by the order of 35%. Also shown are some values representing the experimental wind tunnel measurements with near critical blowing over the trailing-edge flap. These measurements were originally for a wing-body configuration, and have been modified to gross wing conditions. In view of this, they are included here only to indicate that the calculated in-tunnel $C_L \sim \alpha$ values are plausible. The modification for $C_{L_{gross}}$ applied to the measured net wing C_L was of the form:

$$\left(C_{L_{gross}} \right)_{exp} = \left(C_{L_{gross}} \middle/ C_{L_{net}} \right)_{theory} \left(C_{L_{net}} \right)_{exp}$$

The theoretical factor was obtained after applying the method first to the gross wing, and then to the net wing in the presence of a representative body. The factor was found to be a function of incidence, and varied from 1.145 at $\alpha = 0^\circ$ to 1.10 at $\alpha = 10^\circ$.

The calculated induced drag factor characteristics are shown in figure 8(b), and show a dependence on C_L in both free-air and in-tunnel conditions - the form of the dependence is not shown since only two points were calculated for each condition. The standard correction for drag $(\Delta C_{D_i} = C_L \times \Delta\alpha)$ added to the calculated in-tunnel induced drag gave k values which fell short of the free-air calculations; the difference in the increment in k -

i.e., $(\Delta k_{calc} - \Delta k_{standard})/\Delta k_{calc}$

varied from 11% at $C_L = 1.98$ to 18% at $C_L = 2.14$.

Small Aspect Ratio Wing

For an extreme test case for the wake roll-up calculation, a slender rectangular wing of aspect ratio 0.25 was considered at 20° incidence. Calculations were performed using an 8 x 6 vortex array and two iterations for two configurations:

(a) flat plate

(b) bent plate (20° deflection about the mid chord)

Flow visualization studies and wind-tunnel force and moment measurements have been carried out on these configurations by Wickens (ref. 12). The real flow for these cases is dominated by the tip-edge vorticity, and surfac viscous effects are relatively small; a comparison between the potential flow calculation and experiment is therefore practicable.

The side view and plan view of the calculated vortex trajectories from the flat and bent plates are presented in figures 9(a) and 9(b), respectively. Included in the side views are the approximate positions of the vortex cores from flow visualization (ref. 12) and the calculated centroid of vorticity locus. In the flat plate case, these lines are in excellent agreement, and in fact are inclined at approximately $\alpha/2$ to the surface - i.e., the theoretical angle for vanishingly small aspect ratio. In the bent plate case, two vortex cores appear in the experiment, one from the leading-edge tip and the other from the bend line tip - i.e., from the two peak vorticity regions. When calculating the centroid of vorticity locus for this case, the edge vortices were divided into two groups, the leading-edge vortex starting the first group, and the hinge-line vortex the second. The calculated centroid loci initially have fair agreement with the observed vortex cores, but later tend to diverge, indicating slower rate of roll-up in the calculation. Another iteration might have helped here, but the proximity of the end of the segment-represented region (the extent of which was limited by the number of segments available in the program) must have influenced the shape near the downstream end.

Although the principal objective here was to observe the behavior of the vortex roll-up calculation under extreme conditions, it is interesting to see (fig. 10) that the calculated lift, drag and pitching moment are in reasonable agreement with the experimental measurements from reference 12; the flat plate results are particularly good, while the indications are that the bent plate calculations are not fully converged. In the latter case, the changes in the characteristics from the initial (streamwise) wake values to those from the second iteration are particularly large (see table IV).

Tip-Edge Separation

Earlier applications (unpublished) of the method to wings at large incidence (8 to 16°) gave poor correlation with experimental spanwise load distributions and wake deformation. The differences were attributable to the presence, in the experiment, of tip-edge vortices of the type calculated on the small aspect ratio wing. These effects are demonstrated here for a rectangular wing of aspect ratio 5.33 and at 12° incidence. The vortex lattice is shown in figure 11, and includes tip-edge vortices. The calculated vortex trajectories are shown after two iterations. Figure 12(a) shows the spanwise load distribution with and without the tip-edge vortices present. The edge separation gives a higher loading level towards the tip and a local bulge near the tip when using a large number of spanwise intervals. The bulge, consistently calculated using lattices with 15 and 25 spanwise intervals, is also apparent in the experimental load distribution from reference 13. (The lower lift level in the experiment is caused by an inboard separation resulting from the interaction between the wing and wall boundary layer.) The calculated lift coefficient increases from 0.85 to 0.93 with the tip-edge vortices.

The calculations indicate that the extra loading near the tip is carried on the rear of the wing; the center of pressure locus, (fig. 12(b)), shows a marked rearward movement near the tip with the tip-edge vortices compared with the usual forward movement calculated with the "linear" method. The locus is consistently calculated using 8, 15 and 25 spanwise intervals.

These edge effects, which are present also at flap edges, etc., have marked implications for calculations at high lift, affecting boundary layer development, tip vortex formation and trailing vortex sheet shape. However, further evaluation of these effects (such as detailed surface pressure distributions) would require the previously mentioned problem of close interference between discretized vortex sheets to be removed. For such applications, the method would need extending to include a near-field technique such as that developed in references 9 and 10.

CONCLUDING REMARKS

The quadrilateral vortex lattice method with the iterative wake relaxation procedure has been applied to a number of configurations with high circulation. The iterative procedure shows rapid convergence, and the calculations

are in good agreement with available experimental results. Tip-edge separation effects have been shown to be important aspects of high-lift calculations. More detailed theoretical evaluation of these effects, e.g., in terms of surface pressure distributions, would require extensions of the method to incorporate recently developed near-field techniques. Such an extension would also allow other close interference effects to be studied.

REFERENCES

1. Maskew, B.: Calculation of the Three-Dimensional Potential Flow Around Lifting Non-Planar Wings and Wing-Bodies Using a Surface Distribution of Quadrilateral Vortex Rings. TT7009, Loughborough Univ. of Technology, England, Sept. 1970.

2. Maskew, B.: Numerical Lifting Surface Methods for Calculating the Potential Flow about Wings and Wing-Bodies of Arbitrary Geometry. Ph.D. Thesis, Loughborough Univ. of Technology, England, Oct. 1972.

3. Rossow, V.J.: Survey of Computational Methods for Lift-Generated Wakes. NASA SP-347, March 1975, pp. 897-923.

4. Butter, D.J.; and Hancock, G.J.: A Numerical Method for Calculating the Trailing Vortex System Behind a Swept Wing at Low Speed. The Aeronautical Journal, Vol. 75, No. 728, Aug. 1971, pp. 564-568.

5. Hackett, J.E.; and Evans, M.R.: Vortex Wakes Behind High-Lift Wings. J. Aircraft, Vol. 8, No. 5, May 1971, pp. 334-340.

6. Belotserkovskii, S.M.: Calculation of the Flow Around Wings of Arbitrary Planform over a Wide Range of Angles of Attack. NASA TTF-12, 291, May, 1971.

7. Mook, D.T.; and Maddox, S.A.: Extension of a Vortex Lattice Method to Include the Effects of Leading-Edge Separation. J. Aircraft, Vol. 11, No. 2, Feb. 1974, pp. 127-128.

8. Rubbert, P.E.: Theoretical Characteristics of Arbitrary Wings by a Non-Plaiar Vortex Lattice Method. D6-9244, The Boeing Co., 1964.

9. Maskew, B.: A Subvortex Technique for the Close Approach to a Discretized Vortex Sheet. NASA TM X-62, 487, Sept. 1975.

10. Maskew, B.: A Submerged Singularity Method for Calculating Potential Flow Velocities at Arbitrary Near-Field Points. NASA TM X-73,115, March, 1976.

11. Maskew, B.: On the Influence of Camber and Non-Planar Wake on the Airfoil Characteristics in Ground Effect. TT7112, Loughborough Univ. Of Technology, England, Oct. 1971, (See also ARC 33950, 1973, Aero. Res. Council, London).

170

12. Wickens, R.H.: The Vortex Wake and Aerodynamic Load Distribution of Slender Rectangular Wings. Canadian Aeronautics and Space Journal, June 1967, pp. 247-260.

13. Chigier, N.A.; and Corsiglia, V.R.: Tip Vortices - Velocity Distributions. NASA TM X-62,087, 1971.

TABLE I.   GEOMETRIC CHARACTERISTICS FOR THE
WING-FLAP-TAILPLANE CONFIGURATIONS

General:

    Incidence . . . . 10°

    Ground height (normalized by wing mean chord $\bar{c}$) 0.5

Wing:

    Aspect ratio 4

    Sweep back . . . . 45°

    Taper ratio 1

    Flap chord/$\bar{c}$ 0.25

    Flap span/semispan . . . . $0 \rightarrow 0.48$

    Flap deflection: normal to hinge line . . . . 36°

                 in vertical streamwise plane . . . . . 27°

    Vortex quadrilateral array: across chord 3

                       across semispan 7

Tailplane:

    Aspect ratio 2

    Sweep back . . . . 45°

    Taper ratio 1

    Span/wing span 0.4

    (Distance aft from wing)/$\bar{c}$ 2

    (Distance above wing plane)/$\bar{c}$ 0.2

    Angle to wing plane . . . . 0°

    Vortex quadrilateral array: across chord 3

                       across semispan 4

TABLE II.   CALCULATED WING-FLAP-TAILPLANE LIFT AND INDUCED DRAG
CHARACTERISTICS IN FREE AIR AND IN GROUND EFFECT
(SECOND ITERATION)

Configuration		Wing-Flap		Tailplane (based on wing area)	
		C_L	k	C_{L_T}	$C_{D_{i_T}}$
Free-air	together	0.9613	1.108	-0.0104	-0.00206
	alone	0.9691	1.100	0.1279	0.00761
Ground-Effect	together	0.9388	0.581	0.1067	0.01119
	alone	0.9385	0.613	0.1441	0.00757

TABLE III. BASIC CHARACTERISTICS FOR THE WING-FLAP IN WIND-TUNNEL CONFIGURATION

Theoretical Model

Wing:

    Aspect Ratio 2.9

    Taper Ratio 0.55

    Leading edge sweepback . . . . 31°

    Trailing-edge flap:
        Span/wing span 1.0
        Chord/wing chord 0.31
        Deflection (normal to hinge line) . . . . 40°
        Hinge-line sweepback . . . . 17°

    Vortex quadrilateral array (chordwise x spanwise) . . . . . . 3 x 10

Wind Tunnel:

    Wing span/tunnel width 0.56

    Wing area/tunnel cross section area (S_W/S_T) 0.256

    Tunnel 'length'/wing mean chord 6

    Vortex quadrilateral array (lengthwise x circumferential) . . 11 x 10

Experiment

Reynolds Number (based on wing mean chord) . . . . 1.2×10^{6}

Gross Wing:
    Basic details are the same as for theoretical model,
    but in addition:

    Leading edge flap:
        Full net span
        Chord/wing chord 0.15
        Deflection. . . . . 40°
        Hinge-line sweepback . . . . 28°

    Trailing-edge flap blowing momentum coefficient
    (critical value at $\alpha = 8^{\circ}$) 0.018

Body:
    Width 0.18*
    Depth 0.36*
    Length . . . . 1.834*+
    Length of fore and aft fairings 0.357*
    Wing position (above body center line). 0.096
    Section - rectangular with rounded corners

* Note: normalised by gross wing semispan   +(each)

TABLE IV.   CALCULATED CHARACTERISTICS FOR SLENDER RECTANGULAR

WINGS (ASPECT RATIO = 0.25)

Configuration	Wake	C_L	C_{D_i}	C_M
				($\frac{1}{2}$ chord)
Flat Plate $\alpha = 20^0$	Streamwise	0.7489	0.2633	0.1069
	First Iteration	0.5301	0.1725	0.1111
	Second Iteration	0.5301	0.1654	0.1116
Bent Plate $\alpha = 20^o$ Bend = 20°	Streamwise	1.9508	1.5405	-0.056
	First Iteration	1.0934	0.6174	0.078
	Second Iteration	1.1241	0.6381	0.075
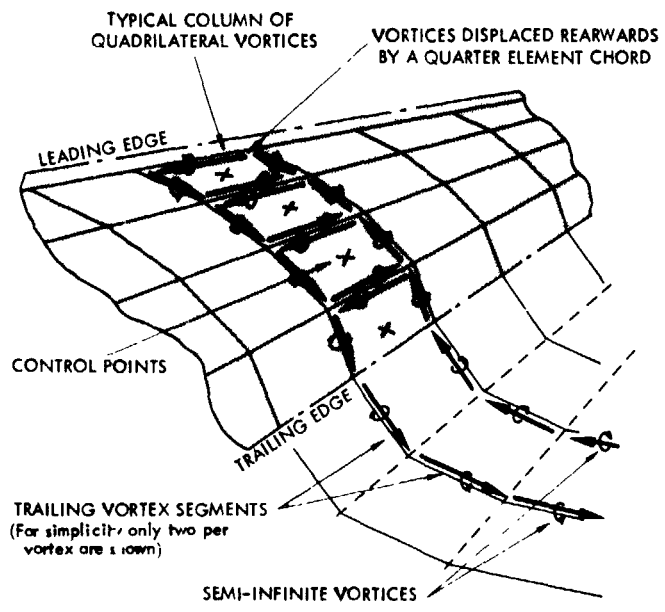
Figure 1.- Quadrilateral vortex model.
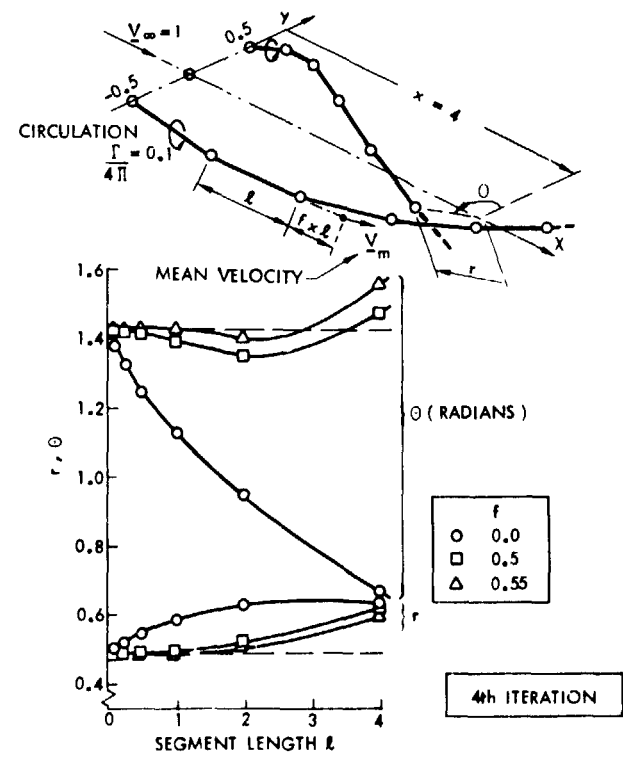
Figure 2.- Calculated roll-up of a pair of
segmented vortices.

176
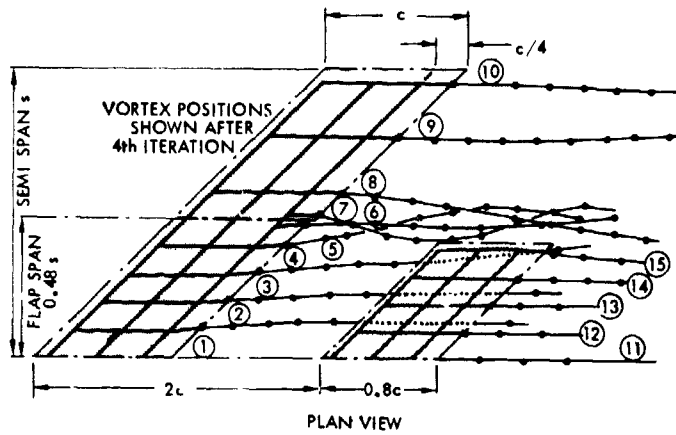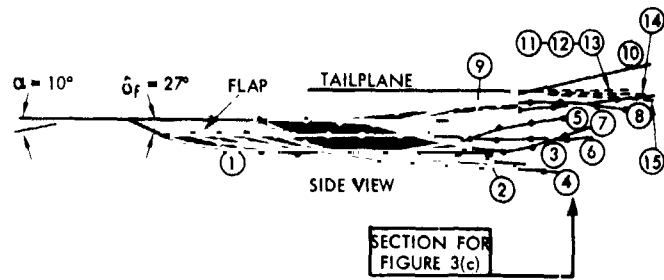
(a) Configuration and general views after four iterations.

(b) Effect of iteration on vortex (7) trajectory.

Figure 3.- Calculated vortex trajectories for a wing-flap-tailplane configuration in free air.

SPANWISE
LOCATION OF
FLAP EDGE

IN GROUND EFFECT
($\alpha = 10°$)

PLANE OF SYMMETRY

GROUND PLANE
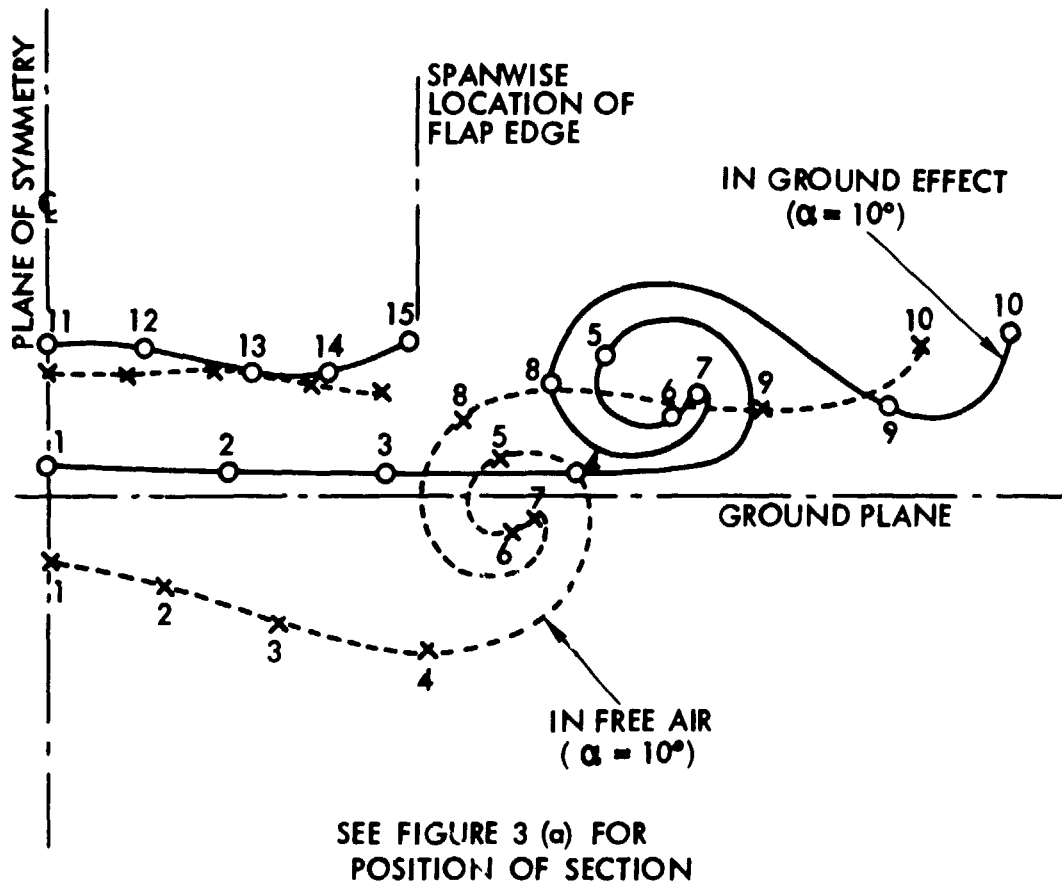
IN FREE AIR
($\alpha = 10°$)

SEE FIGURE 3 (a) FOR
POSITION OF SECTION

(c) Sections through the calculated wakes in
free air and in ground effect.

Figure 3.- Concluded.

178
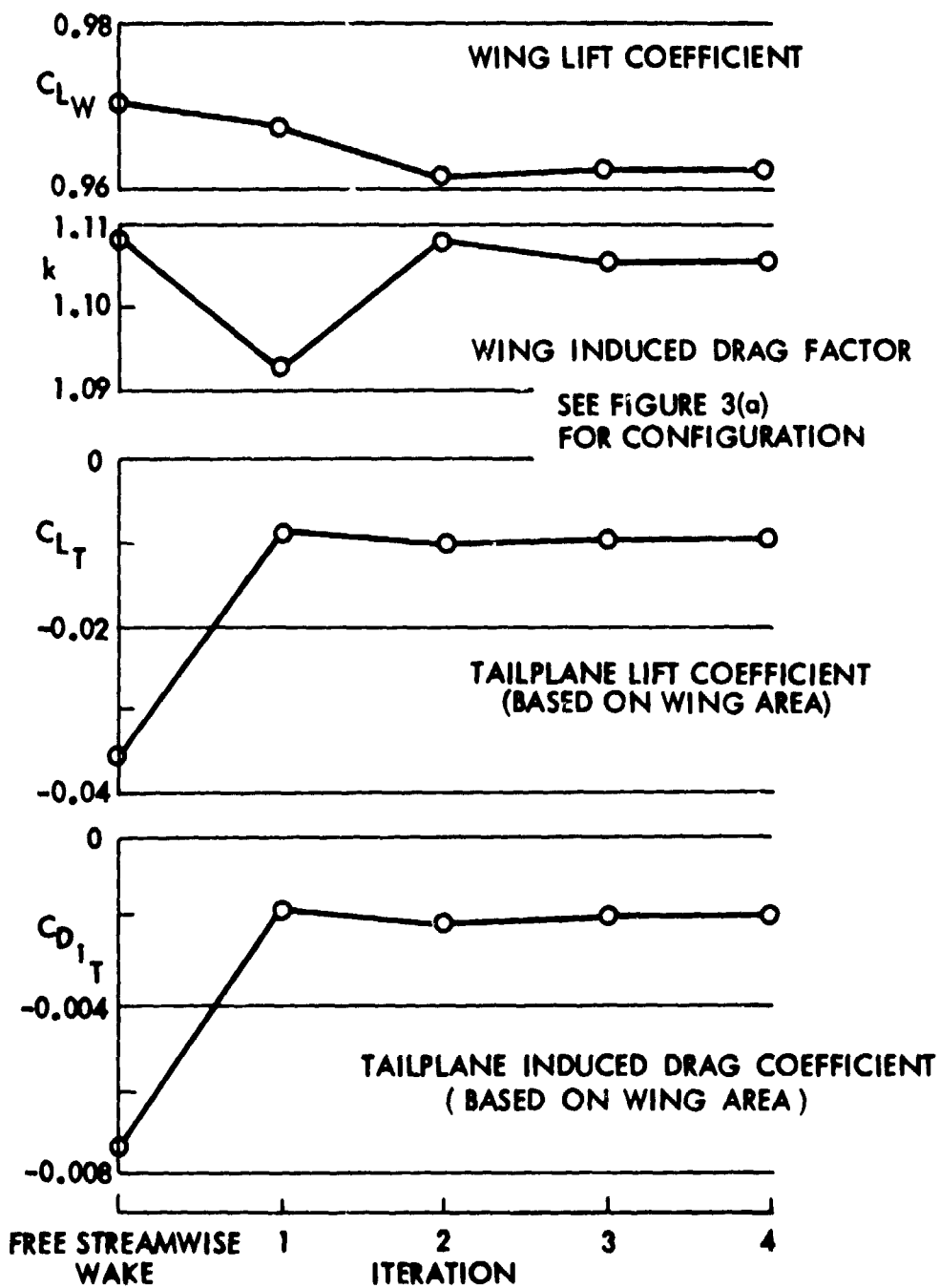
Figure 4.- Effect of iteration on the calculated lift and induced drag of the wing-flap-tailpiece configuration in free air.
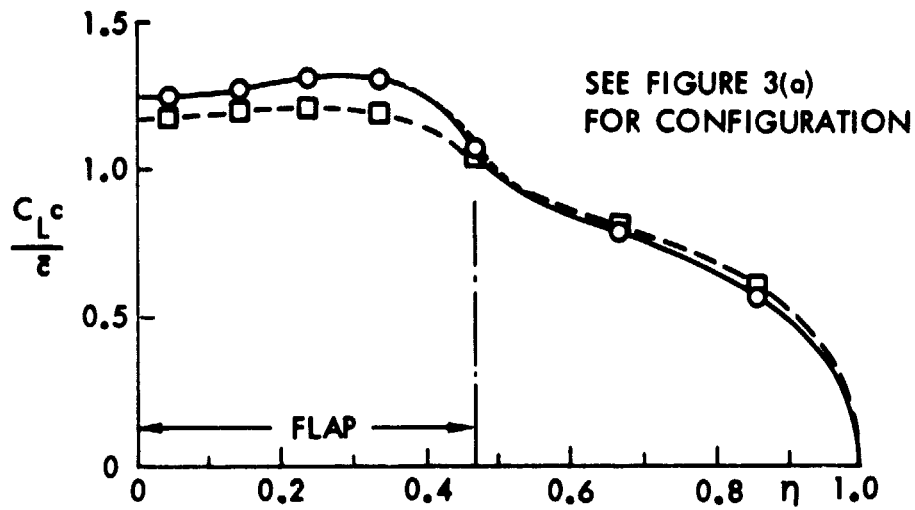
(a) Spanwise loading.
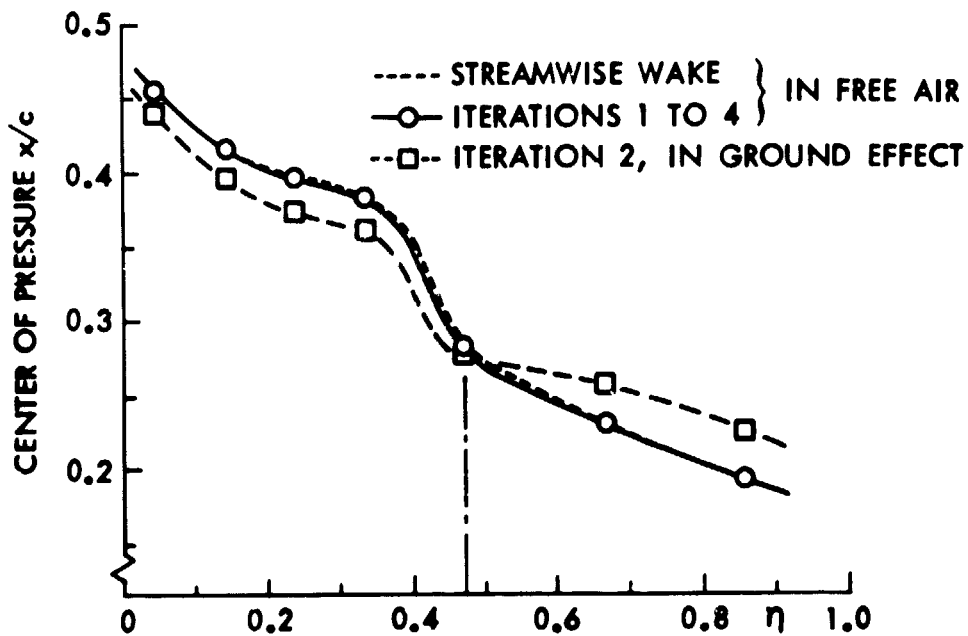
(b) Center of pressure locus.

Figure 5.- Calculated aerodynamic characteristics for the wing
and inboard flap in the wing-flap-tailplane configuration
in free air and in ground effect.

180

SEE FIGURE 3 (a)
FOR CONFIGURATION

--- STREAMWISE WAKE ⎱
—o— ITERATIONS 1 TO 4 ⎰ IN FREE AIR
--□-- ITERATION 2, IN GROUND EFFECT

$\dfrac{C_{d_i}}{C_L{}^2}$
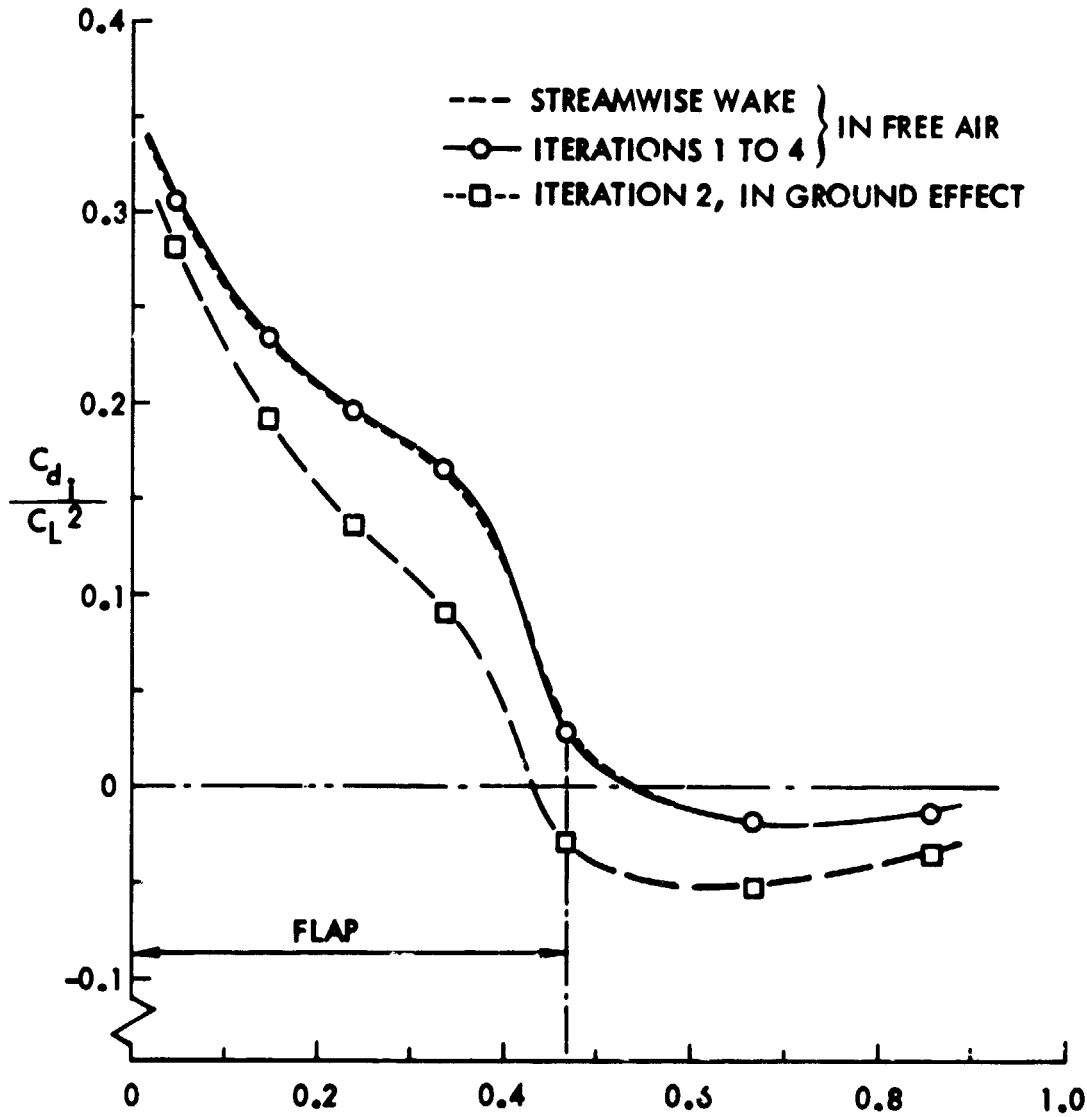
FLAP

(c) Induced drag distribution.

Figure 5.- Concluded.

VORTEX QUADRILATERALS REPRESENTING TUNNEL SURFACE

POSITION OF BODY IN EXPERIMENT

VIEW ON SECTION A-A

$$\frac{\text{WING AREA}}{\text{TUNNEL CROSS SECTION AREA}} = 0.256$$

$$\frac{\text{WING SPAN}}{\text{TUNNEL WIDTH}} = 0.56$$

$$\frac{\text{TUNNEL 'LENGTH'}}{\text{WING MEAN CHORD}} = 6$$

SEMI-INFINITE TRAILING VORTICES FROM TUNNEL

PLAN VIEW
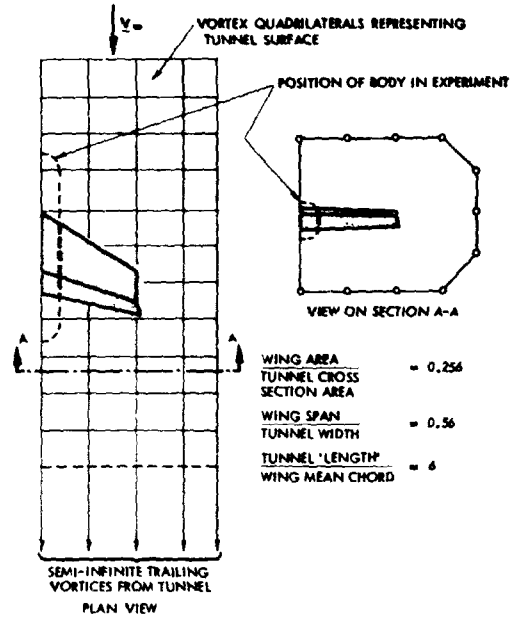
Figure 6.- Wing flap in wind tunnel – general arrangement of the theoretical model.

$a = 5°$

SIDE VIEW

TUNNEL FLOOR

END OF 'TUNNEL'

FLAP HINGE LINE

PLAN VIEW

IN FREE AIR ($C_L = 2.15$, $a = 10°$)

IN WIND TUNNEL ($C_L = 2.14$, $a = 5°$)

SECTION AT A-A
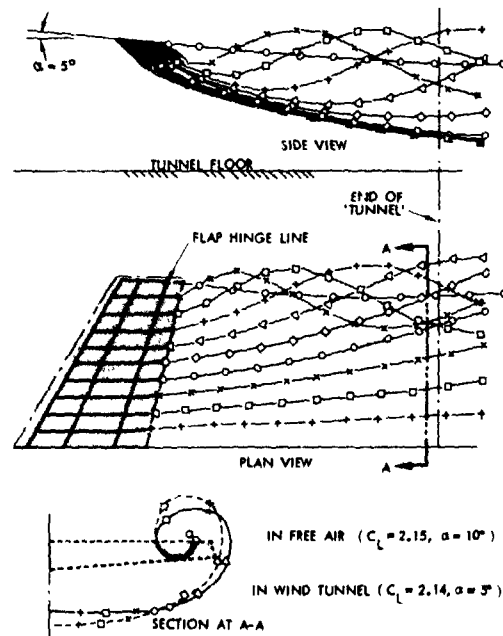
Figure 7.- Calculated vortex trajectories in wind tunnel.

STANDARD CORRECTION

$$\Delta\alpha = \delta \times \frac{S_W}{S_T} \times C_L$$
$$= 0.101 \times 0.256 \times C_L$$

△ EXPERIMENTAL VALUES – CORRECTED TO GROSS WING (SEE TEXT)

(a) Lift coefficient.

SEE FIGURE 7 FOR GENERAL ARRANGEMENT

STANDARD CORRECTION
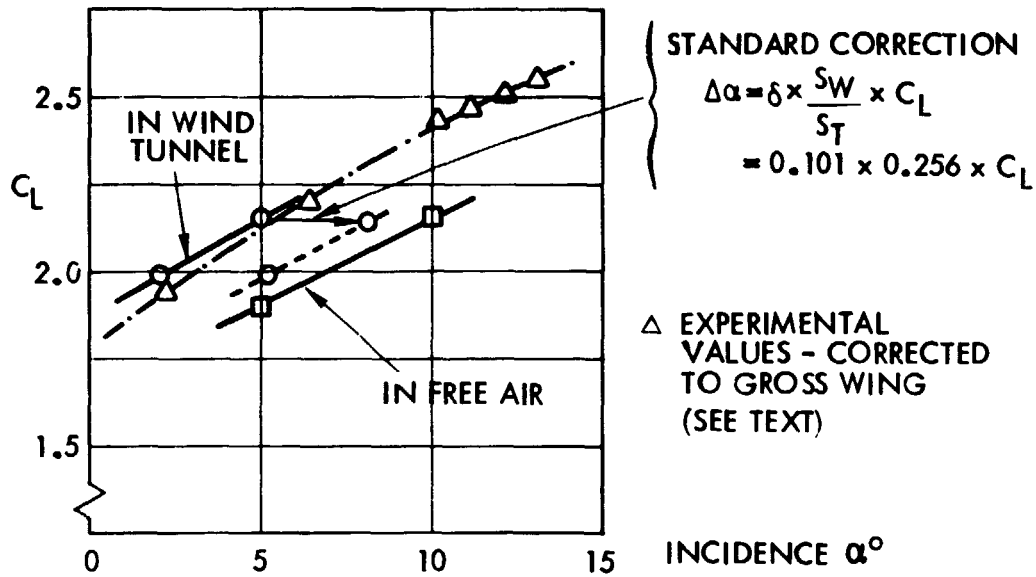
$$\Delta C_D = C_L \times \Delta\alpha$$
$$\text{or } \Delta k = \pi \times AR \times \delta \times \frac{S_W}{S_T}$$
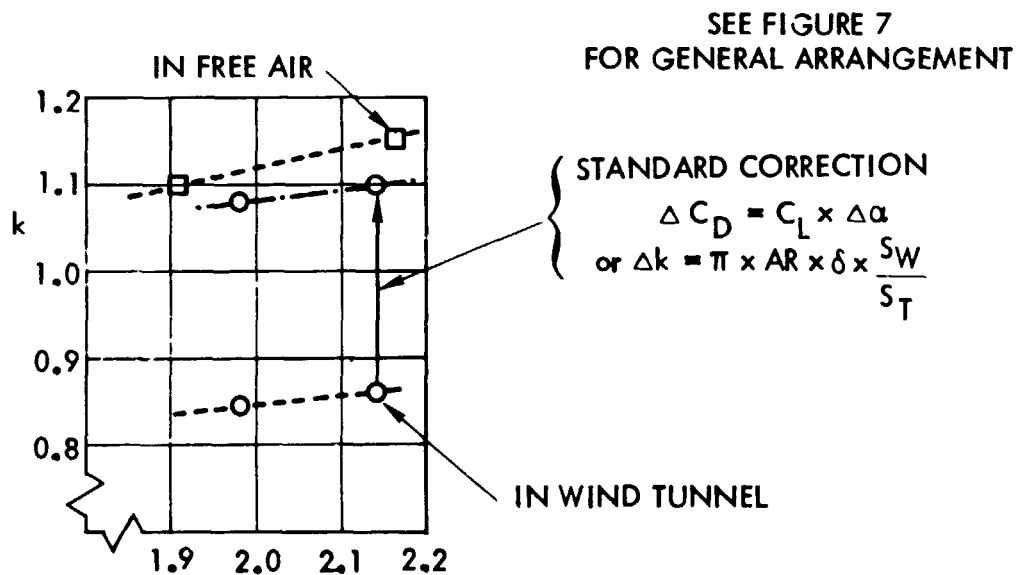
(b) Induced drag factor.

Figure 8.– Calculated aerodynamic characteristics of the wing-flap configuration in free air and in wind tunnel.

SIDE VIEW

L.E. T.E.

PLAN VIEW

———— VORTEX LINES
------- CALCULATED LOCUS OF VORTICITY CENTROID
—·—·— VORTEX CORES FROM SMOKE VISUALIZATION (ref. 12)

(a) Flat plate.

L.E.

20° BEND

SIDE VIEW

T.E.

PLAN VIEW
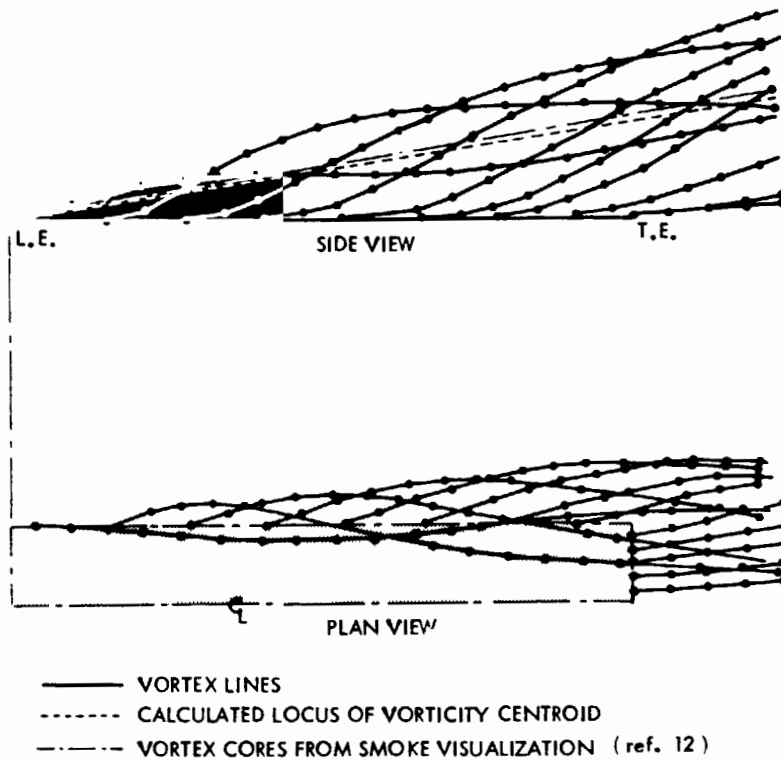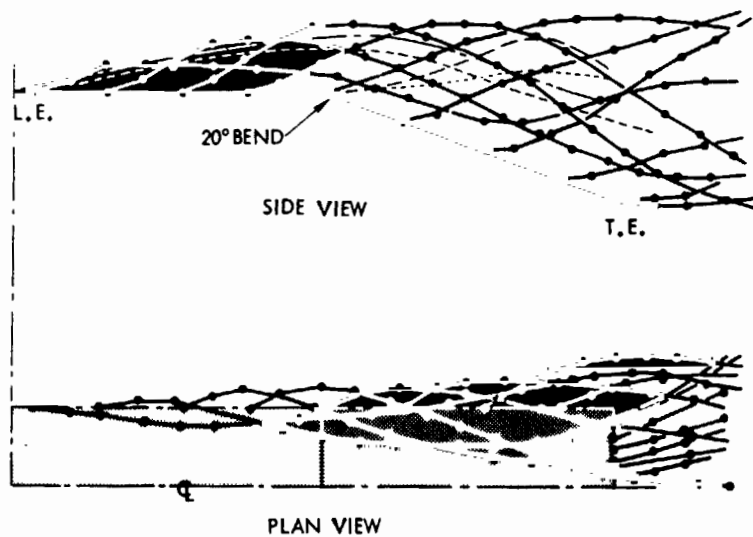
(b) Plate with 20° mid chord bend.

Figure 9.- Calculated vortex trajectories for aspect
ratio 0.25 wings at 20° incidence.
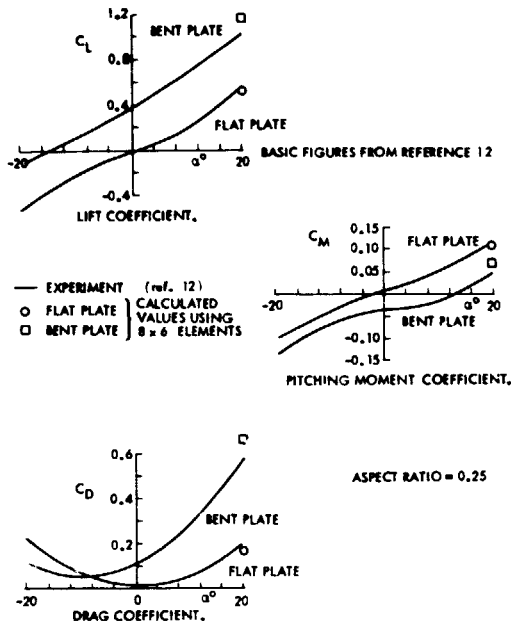
Figure 10.- Calculated aerodynamic characteristics
for the small aspect ratio wings compared with
experimental measurements.
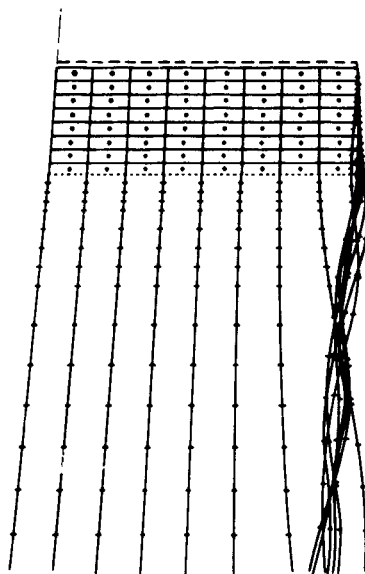
Figure 11.- Calculated vortex trajectories for
an aspect ratio 5.33 rectangular wing at
12° incidence after two iterations.

SYMBOL	VORTEX ARRAY	WAKE ITERATION	
▫----▫	7 x 15	FIRST	WITH TIP-EDGE VORTICES
○——○	7 x 15	SECOND	
△	8 x 8	SECOND	
✳——✳	5 x 25	SECOND	
+——+	5 x 25	FIRST	NO TIP-EDGE VORTICES
▽----▽	EXPERIMENT (REF. 13)		

(a) Lift distribution.

SYMBOL	VORTEX ARRAY	WAKE ITERATION	
▫——▫	7 x 15	FIRST	WITH TIP-EDGE VORTICES
○——○	7 x 15	SECOND	
△	8 x 8	SECOND	
✳——✳	5 x 25	SECOND	
+——+	5 x 25	FIRST	NO TIP-EDGE VORTICES
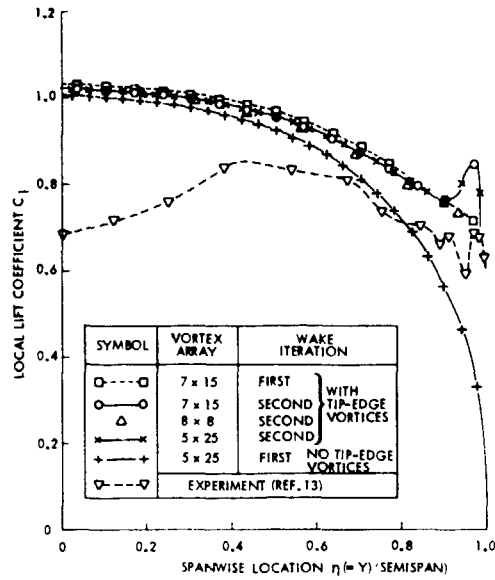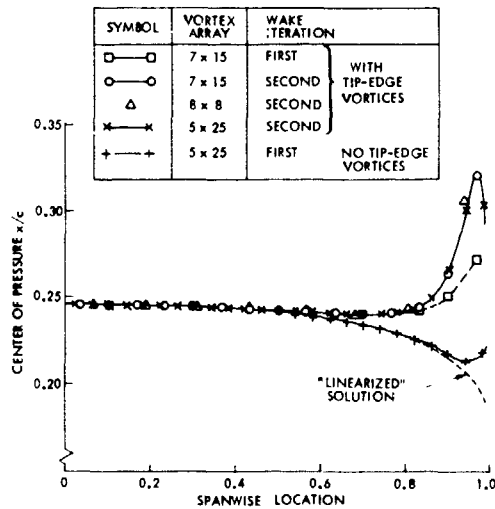
(b) Center of pressure locus.

Figure 12.- Calculated aerodynamic characteristics
   for the rectangular wing with and without tip
   edge vortices.

186

UPPER-SURFACE-BLOWING JET-WING INTERACTION[*]

C. Edward Lan
The University of Kansas

SUMMARY

A linear, inviscid, subsonic compressible flow theory is formulated for predicting the aerodynamic characteristics of upper-surface-blowing configurations. The effect of the thick jet is represented by a two-vortex-sheet model in order to account for the Mach number nonuniformity. The wing loading with the jet interaction effects is computed by satisfying boundary conditions on the wing and the jet surfaces. The vortex model is discussed in detail.

INTRODUCTION

In upper-surface-blowing (USB) configurations, the low-pressure-ratio jet from high by-pass ratio turbofan engines blows directly on the wing upper surface. As the jet is relatively thick, being of the order of 10% of the local chord, the conventional thin jet flap theory has been found to be inadequate to predict the high lift (ref. 1). This means that additional lift may come from the interaction between the wing flow and the thick jet which has higher dynamic pressure than the freestream. Of course, the jet entrainment will increase the lift also, mainly through producing the Coanda effect.

In this paper, a theoretical method will be described for predicting the interaction effects due to nonuniformity in Mach numbers and dynamic pressures in the flow field. The inviscid, linear, subsonic compressible flow theory is assumed.

SYMBOLS

C_L total lift coefficient (circulation lift plus jet reaction lift)

ΔC_L difference in lift coefficients with jet on and off

ΔC_{L_Γ} jet induced circulation lift coefficient

C_μ jet momentum coefficient

c   local chord length, m(ft)

C_j length of trailing jet included in the analysis, m(ft)

M   number of integration points or Mach number

N   number of chrodwise integration points

N_J number of streamwise vortices on the trailing jet

$\vec{n}$ unit vector normal to jet surface

R   radius of curvature, m(ft)

s   coordinate tangential to the jet surface

T $= \rho_o / \rho_j$

t_j jet thickness, m(ft)

u   nondimensional backwash

V   velocity, m/sec (ft/sec)

x,y,z   rectangular coordinates, with x positive downstream, y positive spanwise to the right and z positive upward

α angle of attack, deg.

γ nondimensional vortex density

δ_f flap angle, deg.

δ_j jet-deflection angle, deg.

μ $= V_o / V_j$

μ' $= \mu \cos \alpha$

ρ density, kg/m^3 (slugs/ft^3)

ϕ velocity potential, m^2/sec(ft^2/sec)

ψ nondimensional additional perturbation velocity potential

Subscripts:

c   chordwise

j   jet flow

o   outer flow

s   spanwise

w   wing

∞ freestream

METHOD OF ANALYSIS

Formulation of the Problem

The perturbation flow fields inside and outside the jet are assumed to be governed by the Prandtl-Glauert equations with M_j and M_o, respectively. The solutions of these equations must satisfy the boundary conditions that the jet surface is a stream surface and the static pressure must be continuous across it, in addition to the usual wing tangency condition. In the linear theory, these conditions can be written as (ref.1)

$$\frac{\partial \bar{\phi}_o}{\partial n} - \frac{\partial \bar{\phi}_j}{\partial n} = \frac{-\vec{V}_\infty \cdot \vec{n}(1-\mu')}{\vec{V}_\infty \cdot \vec{i}} \qquad \text{(jet stream surface condition)} \qquad (1)$$

$$\frac{\partial \bar{\phi}_j}{\partial s} - T(\mu')^2 \frac{\partial \bar{\phi}_o}{\partial s} = 0 \qquad \text{(jet static pressure continuity)} \qquad (2)$$

$$\frac{\partial \bar{\phi}_o}{\partial z} = \frac{\partial z_c}{\partial x} - \tan \alpha \qquad \text{(wing tangency)} \qquad (3)$$

where

$$T = \rho_o / \rho_j \qquad (4)$$

and $\bar{\phi}_o$ and $\bar{\phi}_j$ are related to the dimensional velocity potentials ϕ_o and ϕ_j as

$$\phi_o = \bar{\phi}_o \, V\infty \cos \alpha, \quad \phi_j = \bar{\phi}_j \, V_j \qquad (5)$$

Since the above problem is linear, it can be decomposed into a wing-alone case with potential $\bar{\phi}_w$ and the interaction case with additional potential ψ. Let

$$\bar{\phi}_o = \bar{\phi}_{wo} \, (M_o) + \psi_o \, (M_o) \qquad (6)$$

$$\bar{\phi}_j = \bar{\phi}_{wj} \, (M_j) + \psi_j \, (M_j) \qquad (7)$$

where $\bar{\phi}_{wo}$ and $\bar{\phi}_{wj}$ satisfy the Prandtl-Glauert equations with respective Mach numbers and the following boundary conditions

$$\frac{\partial \bar{\phi}_{wo}(M_o)}{\partial z} = \frac{\partial z_c}{\partial x} - \tan \alpha \qquad (8)$$

$$\frac{\partial \bar{\phi}_{wj}}{\partial z}(M_j) = \frac{\partial z_c}{\partial x} - \tan \alpha \qquad (9)$$

Substitution of equations (6)-(7) into equations (1)-(3) gives

$$\frac{\partial \psi_o}{\partial n} - \frac{\partial \psi_j}{\partial n} = - \frac{\vec{V}_\infty \cdot \vec{n}(1-\mu')}{\vec{V}_\infty \cdot \vec{i}} + \frac{\partial \bar{\phi}_{wj}}{\partial n}(M_j) - \frac{\partial \bar{\phi}_{wo}}{\partial n}(M_o) \qquad (10)$$

$$\frac{\partial \psi_j}{\partial s} - T(\mu')^2 \frac{\partial \psi_o}{\partial s} = - \frac{\partial \bar{\phi}_{wj}}{\partial s} + T(\mu')^2 \frac{\partial \bar{\phi}_{wo}}{\partial s} \qquad (11)$$

$$\frac{\partial \psi_o}{\partial z} = 0 \qquad (12)$$

The above equations indicate that there are jumps in normal velocities and tangential velocities across the jet surface. If there is no jet (i.e., $\mu'=1$, $M_o = M_j$ and $T = 1$), these equations show that the additional perturbation potentials will be automatically zero.

<center>Vortex Model</center>

In order to satisfy equations (10)-(11) simultaneously, two vortex sheets are introduced on the jet surface. These vortex distributions will induce normal and tangential velocities in the flow field. To evaluate these induced velocities on the boundaries so that boundary conditions,equations (10)-(12),can be satisfied, the induced velocity integrals are reduced to finite sums through the Quasi Vortex-Lattice Method (Quasi VLM) (ref. 2). The resulting discretized vortex arrangement is as shown in fig. 1. Note that the wing vortices directly below the jet surface are arranged so that they coincide with the jet vortices in location. Furthermore, the shaded region represents part of the nacelle. Since the present computer program does not include the nacelle model, special care must be exercised in this region. If vortex representation of the jet starts from the exit, instead of the leading edge, it has been found that the jet would induce a leading-edge type loading in the middle of the wing. Therefore, the vortex distribution must be extended to the wing leading edge, but with freestream conditions assumed in the nacelle region in the computation.

With the vortex arrangement made, the required induced velocities can be computed and substituted into equations (10)-(12) for the solution of unknown vortex strengths. These equations are satisfied only at a discrete number of control points which are chosen according to the "semi-circle method" as described in the Quasi VLM (ref. 2). These calculations are mostly straightforward, except in computing the induced tangential velocities (i.e., backwash) and representing the jet flap effect. These will be discussed below.

190

Computation of Induced Tangential Velocities

The induced tangential velocities on the jet surface are needed to satisfy equation (11). At any control point, the induced tangential velocity due to the jet vortex distribution in its neighborhood is simply equal to the vortex density at that control point. Since the vortex density at the control point does not appear in the formulation, it is necessary to express it in terms of those at the vortex points through interpolation, such as Lagrangian interpolation. However, the contribution from those vortices not on the same plane with the control point can not be accurately computed in the usual manner as in computing the induced normal velocities. To illustrate, consider the backwash expression in the two-dimensional flow:

$$u(x,z) = \frac{z}{2\pi} \int_0^1 \frac{\gamma(x')dx'}{(x-x')^2 + z^2} \tag{13}$$

As $z \to 0$, the integrand of equation (13) will have a second-order singularity. The usual method is not accurate in treating such singularity. Therefore, equation (13) should be rewritten as

$$u(x,z) = \frac{z}{2\pi} \int_0^1 \frac{\gamma(x') - \gamma(x)}{(x-x')^2 + z^2} dx' + \frac{\gamma(x)}{2\pi} z \int_0^1 \frac{dx'}{(x-x')^2 + z^2}$$

$$\approx \frac{z}{4\pi} \frac{\pi}{N} \sum_{k=1}^{N} \frac{\gamma(\theta_k)-\gamma(x)}{(x-x_k)^2 + z^2} \sin \theta_k + \frac{z\gamma(x)}{4\pi} \frac{\pi}{M} \sum_{j=1}^{M} \frac{\sin \theta_j}{(x-x_j)^2 + z^2} \tag{14a}$$

where

$$\left. \begin{array}{l} x_k = \tfrac{1}{2} (1 - \cos \theta_k), \quad \theta_k = \frac{2k - 1}{2N} \pi \\[2mm] x_j = \tfrac{1}{2} (1 - \cos \theta_j), \quad \theta_j = \frac{2j - 1}{2M} \pi \end{array} \right\} \tag{14b}$$

and

$$M = 2^P N \tag{14c}$$

for interdigitation between the control and integration points in the last summation and p is an arbitrary integer greater than 1.

In the implementation of equation (14a) in the present computer program, it is assumed that M=8N if N>6 and M=16N if N≤ 6. To compute the tangential velocity at a jet control point due to wing vortices, equation (14a) is applied to three wing vortex strips in the immediate neighborhood of the control point. This is indicated in fig. 2. On the other hand, if the control point is on the jet upper surface, the effect due to all vortices on the jet lower surface in the same streamwise section is computed with equation (14a). Similar principle is applicable if the control point is on the lower surface. This is illustrated in fig. 3. The accuracy of equation (14a) has been illustrated in ref. 3.

Incorporation of Jet Flap Effect in Thick Jet Theory

Due to Coanda effect, the USB jet will follow the wing surface and leave the wing trailing edge at an angle relative to the chord to produce the jet flap effect. This is to produce varying but unknown $\vec{V}_\infty \cdot \vec{n}$ in equation (10) along the trailing jet.

Since

$$\frac{\vec{V}_\infty \cdot \vec{n}}{\vec{V}_\infty \cdot \vec{i}} = -\frac{dz}{dx} + \tan \alpha ,\tag{15}$$

it is necessary to relate $\frac{dz}{dx}$ to the unknown jet vortex density. As shown in fig. 4, the irrotationality of the jet flow implies that

$$[V_j + V_j(\frac{\partial \bar{\phi}_j}{\partial s})_1](R - t_j/2) = [V_j + V_j(\frac{\partial \bar{\phi}_j}{\partial s})_2](R + t_j/2)$$

or

$$\frac{t_j}{R} = T(\mu')^2[(\frac{\partial \psi_o}{\partial s})_1 - (\frac{\partial \psi_o}{\partial s})_2 + (\frac{\partial \phi_{wo}}{\partial s})_1 - (\frac{\partial \bar{\phi}_{wo}}{\partial s})_2] = f(x,y)$$

$$\frac{1}{R} \approx \frac{d^2 z}{d_x^2}\tag{17}$$

where the subscripts 1 and 2 denote the upper and the lower jet surfaces, respectively, at the section under consideration. Equations (16)-(17) give the following initial value problem for determining $\frac{dz}{dx}$:

$$t_j \frac{d^2 z}{dx^2} = f(x,y)\tag{18}$$

$$z(t.e.) = 0$$

$$\frac{dz}{dx}(t.e.) = -\delta_j$$

To integrate the above problem for $\frac{dz}{dx}$, a finite jet length C_j is first chosen (It is not necessary to include infinite length of jet in the numerical

192

method as far as the wing loading is concerned). Then let

$$x = x_{t.e.} + \frac{c_j}{2} (1 - \cos \theta) \qquad (19)$$

It follows that

$$t_j \frac{d}{d\theta} \left(\frac{dz}{dx}\right) = \frac{c_j}{2} \sin \theta f(\theta, y)$$

and after integration once,

$$t_j \left(\frac{dz}{dx}\right)_i = -t_j \, \delta_j + \int_0^{\theta_i} \frac{c_j}{2} \sin \theta f(\theta, y) d\theta$$

$$\approx -t_j \, \delta_j + (\Delta\theta) \frac{c_j}{2} \left[\sum_{k=1}^{i-1} \sin \theta_k f(\theta_k, y) + \frac{1}{2}\sin \theta_i f(\theta_i, y) \right] \qquad (20)$$

by trapezoidal rule. With $\frac{dz}{dx}$ determined by equation (20) in terms of $f(\theta, y)$ and hence, $\frac{\partial \psi_0}{\partial s}$ through equation (16), it is possible to incorporate these terms with unknown vortex densities to the left hand side of equation (10) before equations (10)-(12) are solved.

Note that equations (10)-(12) are solved by the vector method of Purcell (ref. 4) which processes row by row of the augmented matrix in solving the equations. Since the tangential velocities are needed in equation (10) with the jet flap effect (see equation 16), equation (11) must be processed first with the tangential velocities computed there stored on file before equation (10) can be solved.

SOME NUMERICAL RESULTS

Before the method can be applied to any configurations, it is important to know how the discretized vortices should be arranged to produce reliable results. In the following, some convergence study with respect to the vortex arrangement for the configuration used by Phelps, et al. (ref. 5) will be presented. Fig. 5 shows the effects of number of vortices on the trailing jet with $C_j = 1c$ and $2c$. It is seen that 6 vortices (NJ = 6) with $C_j = 1c$ appear to be sufficient in applications. If C_j is increased to $2c$, more vortices would be needed to provide convergence. Fig. 6 indicates the rapid convergence of ΔC_{L_Γ} with respect to the number of wing spanwise vortex strips.

The above method is now applied to the configuration of ref. 5 with 30° full span flap. The jet-deflection angle is taken to be the angle of flap extension relative to the chord line. It is found to be 46.7°. The C_L values were computed by adding predicted ΔC_L to the experimental jet-off C_L. The results are shown in fig. 7. The predicted values are slightly higher possibly because the estimated jet angle was too high. On the other hand, the thin jet flap theory by the present method (ref. 1) would underestimate the lift.

To illustrate the importance of improved tangential velocity evaluation (see equation 14a), the configuration of ref. 6 with $\delta_f = 20^\circ$ and 40° is used in fig. 8. It is seen that without the improved integration technique, the predicted lift would be too high.

CONCLUDING REMARKS

A vortex model for the USB jet-wing interaction has been described. The model consists of using two vortex sheets on the jet surface to account for Mach number nonuniformity and differences in jet and freestream dynamic pressures. The rate of numerical convergence with respect to the number of vortices used appeared to be reasonably rapid. Comparison of the predicted results with some available data showed much better agreement than the thin jet flap theory.

REFERENCES

1. Lan, C. Edward; and Campbell, James F.: Theoretical Aerodynamics of Upper-Surface-Blowing Jet-Wing Interaction. NASA TN D-7936, 1975.

2. Lan, C. Edward: A Quasi Vortex-Lattice Method in Thin Wing Theory. Journal of Aircraft, Vol. 11, No. 9, Sept. 1974, pp. 518-527.

3. Lan, C. Edward: Some Applications of the Quasi Vortex-Lattice Method in Steady and Unsteady Aerodynamics. Vortex-Lattice Utilization, NASA SP-405, 1976. (Paper no. 21 of this compilation.)

4. Purcell, E. W.: The Vector Method of Solving Simultaneous Linear Equations. Journal of Math. and Phys., Vol. 32, July-Oct. 1953, pp. 180-183.

5. Phelps, Arthur E.; Letko, William; and Henderson, Robert L.: Low-Speed Wing-Tunnel Investigation of a Semispan STOL Jet Transport Wing-Body with an Upper-Surface Blown Jet Flap. NASA TN D-7183, 1973.

6. Smith, Charles C., Jr.; Phelps, Arthur E., III; and Copeland, W. Latham: Wind-Tunnel Investigation of a Large-Scale Semispan Model with an Unswept Wing and an Upper-Surface Blown Jet Flap. NASA TN D-7526, 1974.
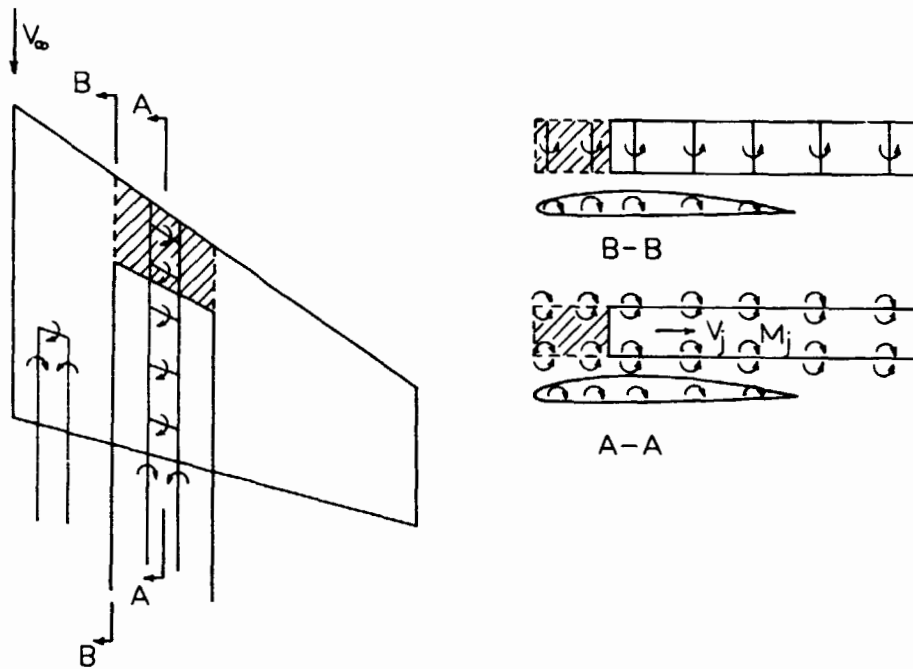
Figure 1.- Vortex model for computing jet-interaction effects.
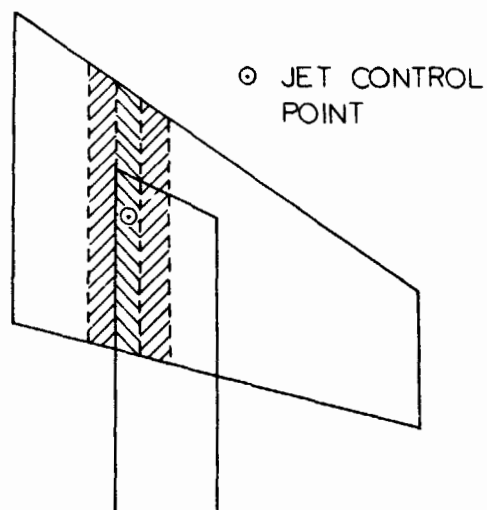
Figure 2.- Region (shaded area) of wing vortex strips subject to improved integration procedure of equation (14a) for computing u-velocity at a jet control point.
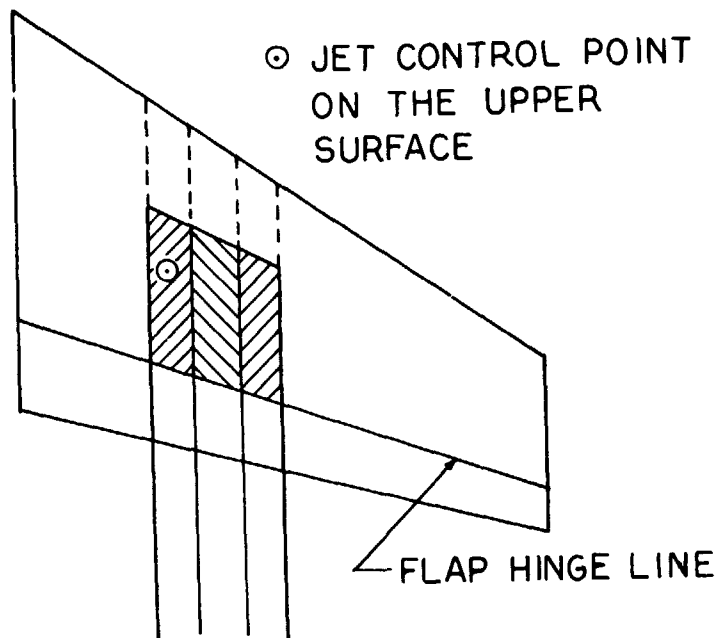
Figure 3.- Region (shaded area) of jet vortex strips on the lower surface subject to improved integration procedure of equation (14a) for computing u-velocity at a jet control point.

$$V_1 = V_j + V_j (\partial \bar{\phi}_j / \partial s)_1$$

$$V_2 = V_j + V_j (\partial \bar{\phi}_j / \partial s)_2$$
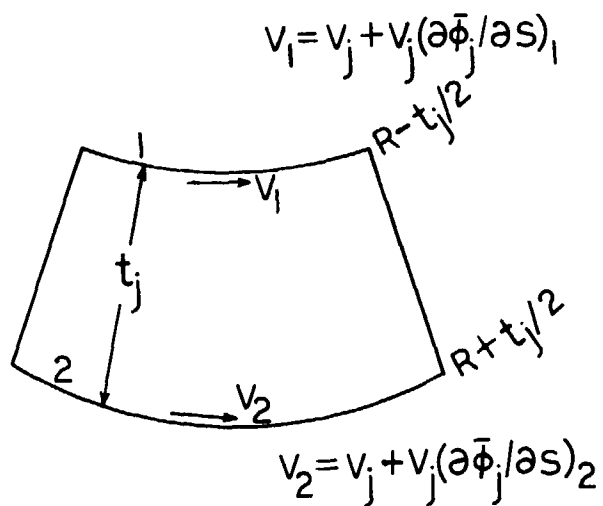
Figure 4.- Geometry of a jet cross section for formulating jet flow irrotationality condition.

196
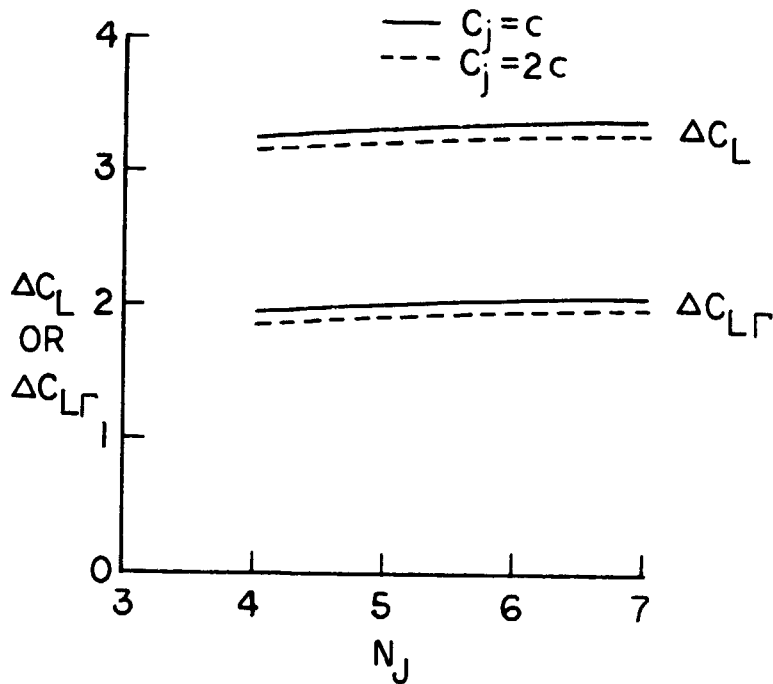
Figure 5.- Effect of number of trailing jet vortices on predicted lift. $C_\mu = 0.8 \times 2.095$; $\alpha = 5^o$; $\delta_f = 30^o$; $\delta_j = 46.7^o$; $N_c = 6$; $N_s = 9$.
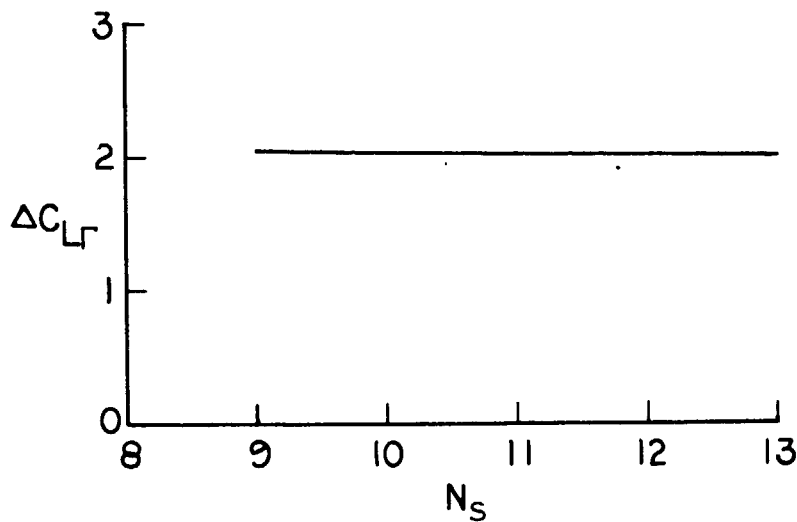
Figure 6.- Effect of number of wing vortex strips on predicted lift. $C_\mu = 0.8 \times 2.095$; $\alpha = 5^o$; $\delta_f = 30^o$; $\delta_j = 46.7^o$; $N_J = 6$; $C_j = 1c$.
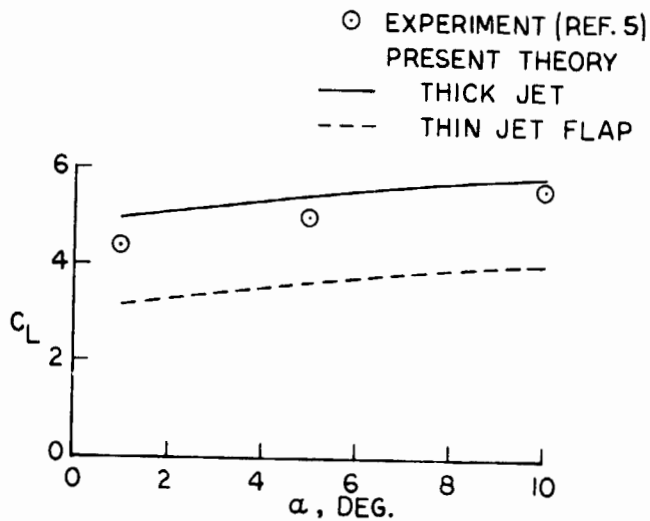
Figure 7.- Comparison of predicted lift curves with experimental data of ref. 4. $C_\mu = 0.8 \times 2.095$.
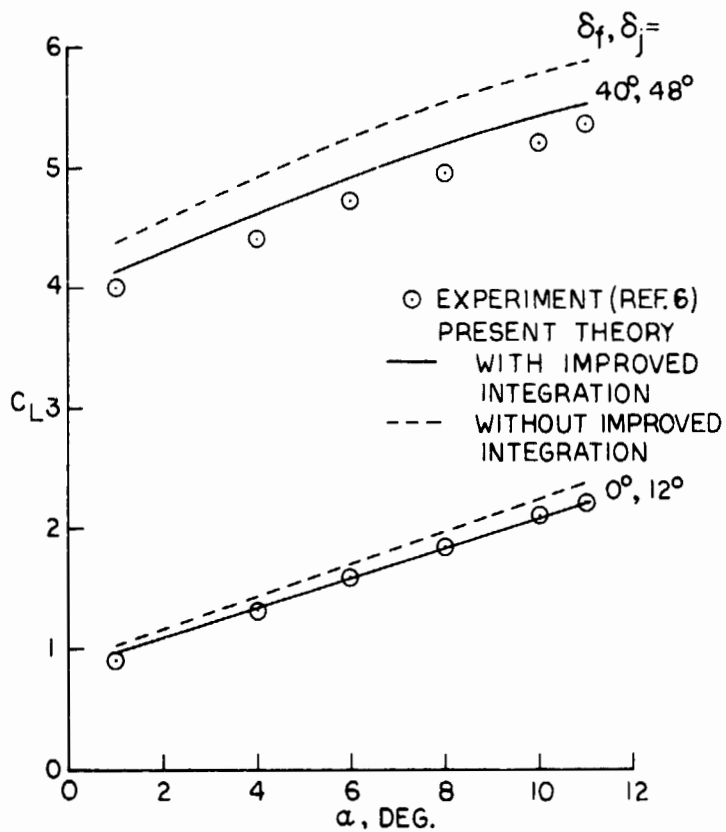
Figure 8.- Effect of backwash evaluation on predicted lift. $C_\mu = 2$.

CALCULATION OF THE LONGITUDINAL AERODYNAMIC

CHARACTERISTICS OF WING-FLAP CONFIGURATIONS

WITH EXTERNALLY BLOWN FLAPS[*]

Michael R. Mendenhall
Nielsen Engineering & Research, Inc.

SUMMARY

An analytical method for predicting the longitudinal aero-
dynamic characteristics of externally blown flap configurations
is described. Two potential flow models make up the prediction
method: a wing and flap lifting-surface model and a turbofan
engine wake model. A vortex-lattice lifting-surface method is
used to represent the wing and multiple-slotted trailing-edge
flaps. The jet wake is represented by a series of closely
spaced vortex rings normal to a centerline which is free to
move to conform to the local flow field. The two potential
models are combined in an iterative fashion to predict the jet
wake interference effects on a typical EBF configuration.
Comparisons of measured and predicted span-load distributions,
individual surface forces, forces and moments on the complete
configuration, and flow fields are included.

INTRODUCTION

The short take-off and landing requirements for STOL air-
craft necessitate a means of achieving very high lift coeffi-
cients on aircraft in take-off or landing configuration with
little sacrifice in cruise performance. The externally blown
jet-augmented flap (EBF) provides such a means. The jet efflux
from engines mounted beneath the wing is allowed to impinge
directly on the slotted flap system (fig. 1), thus producing a
large amount of additional lift through engine wake deflection
and mutual interference effects.

An analytical method for predicting the longitudinal aero-
dynamic characteristics of EBF configurations has been developed
(ref. 1). Potential flow models of the lifting surfaces and the
jet wake are combined in an iterative fashion to satisfy two
requirements. First, the tangency boundary condition must be
satisfied at selected points on each lifting surface, and second,
the centerline of each jet wake must lie along a streamline of
the total flow field. One goal of the EBF method is to predict

the total loads and distribution of loads on each component of
the wing-flap configuration under the influence of multiple jet
wakes. A second goal is that a minimum of empirical information
be required as input to the method.

This paper contains a discussion of the technical approach
to the prediction of EBF aerodynamic characteristics, a discussion
of the development of the potential flow models, and some
comparisons with data.

SYMBOLS

c_n section normal-force coefficient

C_D drag coefficient, positive aft

C_L lift coefficient

C_m pitching-moment coefficient, positive nose up

C_N normal-force coefficient

C_T thrust coefficient of a single jet

C_μ total thrust coefficient for a configuration with
multiple jets

R local radius of circular jet, m (ft.)

R_o initial radius of circular jet, m (ft.)

u axial velocity, m/sec (ft/sec)

V free-stream velocity, m/sec (ft/sec)

V_j initial jet wake velocity, m/sec (ft/sec)

x_j, y_j, z_j jet coordinate system with origin at the center of
the jet inlet

X, Y, Z wing coordinate system with origin at the wing root
chord leading edge

α angle of attack, degrees

γ jet wake vortex cylinder strength, m/sec (ft/sec)

δ_f flap deflection angle, degrees

Δ	convergence tolerance
Δs	jet model vortex ring spacing, m (ft.)
η	dimensionless spanwise coordinate
ϕ	dihedral angle, degrees

ANALYSIS

Wing-Flap Vortex-Lattice Model

The lifting surfaces of externally blown flap configurations consist of a wing and multiple-slotted trailing-edge flaps. The lifting-surface model needed to represent the typical EBF wing-flap configuration must be capable of handling individual lifting surfaces and predicting the spanwise and chordwise load distributions on each surface. Mutual interference between surfaces must be considered along with interference effects induced by some external source of disturbance, for example, the wake of a high bypass ratio turbojet engine. It is also essential that the lifting-surface model be capable of predicting the velocity field induced in the vicinity of the wing and flaps. The above requirements are best fulfilled through the use of a vortex-lattice model of the lifting surfaces.

The wing and flaps are divided into area elements, in each of which is placed a horseshoe vortex. Its bound leg is aligned with the element quarter chord and its trailing legs lie along the sides of the element as illustrated in figure 2. The trailing legs are positioned in the plane of their originating element, and they are deflected so that they lie in the plane of each surface downstream of the originating surface. The trailing legs extend to infinity in the plane of the last surface contacted.

The boundary conditions, expressing the flow tangency to the camber surface, are satisfied at a set of control points located at the midspan of the three-quarter chord line of each area element. The wing control points are all assumed to lie in the plane containing the root chord and making an angle ϕ with the $Z = 0$ plane. The control points on each flap are assumed to lie in the chord plane of the flap. The boundary condition equations (ref. 1) state that the total flow is tangent to the camber surfaces of the wing and flaps at each control point. The total velocity at each control point is made up of the free stream, the velocity induced by the vortex-lattice horseshoe vortex system, and additional velocities induced by an external source of disturbance. The solution of these equations provides the unknown value of the circulation of each horseshoe vortex.

201

Once the circulation strengths are determined, the flow field surrounding the lifting surface can be computed as well as the surface load distributions. The force on each area element is calculated as the product of density, local velocity normal to the element of vorticity, and circulation strength. The total force on each area element is made up of two contributions: that acting on the bound leg of the horseshoe vortex and the force acting on the trailing legs contained within the area element. There is only one bound leg associated with each area element, but numerous trailing legs may be present along each side of the area element, one for each area element upstream of the element being considered. All three components of force on each vortex leg are computed on each area element. These are resolved into normal and axial forces in each area element. The section characteristics of each lifting surface are computed from these elemental forces and finally the total individual surface forces are resolved into the gross aerodynamic characteristics relative to the aircraft axis system.

The vortex-lattice method is restricted to calculating longitudinal characteristics, and compressibility corrections are not included in the method. No small angle assumptions are used in the theoretical model.

Since the EBF model is to be used as a predictive technique, it is important that the vortex-lattice method be applicable to typical EBF configurations. The wing and flap configuration parameters are listed as follows:

Wing

Leading-edge shape: May have up to 30 breaks in sweep.

Trailing-edge shape: Same as leading edge.

Taper: Determined from leading-edge and trailing-edge specification.

Tip chord: Parallel to root chord.

Dihedral: Constant over the semispan.

Mean camber surface: May have both twist and camber.

Thickness: Neglected.

Flaps

Number: Up to ten individual flap segments.

Location: Only trailing-edge flaps are considered; gaps between surfaces are permitted.

Leading-edge shape: Straight.

Trailing-edge shape: Straight.

Taper: Linear.

202

Root chord: Must lie in a vertical plane parallel to the
              wing root chord.

Tip chord: Parallel to root chord.

Span: Full or partial span.

Deflection: Different for each flap.

Mean camber surface: Each flap may have both camber and
                       twist.

Thickness: Neglected.

The vortex-lattice arrangement on each lifting surface is
general enough to provide good flexibility in describing the
loading distribution. A maximum of thirty (30) spanwise rows of
vortices may be used, and each lifting-surface component can have
a maximum of ten (10) chordwise vortices. The area elements on
a lifting surface have the same chord at each spanwise station,
but the element chords need not be the same on adjacent surfaces.
Thus, the number of chordwise elements on each lifting surface
may be chosen according to the accuracy required in the predicted
chordwise loading distribution. In the spanwise direction, the
widths of the area elements may be varied to fit the loading
situations; that is, in regions of large spanwise loading
gradients, the element widths may be reduced to allow closer
spacing and more detailed load predictions. Convergence of
predicted results as a function of lattice arrangement on wings
and flaps is described in Appendix A of reference 2. One restric-
tion on the spanwise lattice arrangement on the wing and flaps is
the requirement that the lattice elements on the flaps be directly
aligned with those on the wing. This requirement is imposed be-
cause of the deflection of the vortex trailing legs and the neces-
sity for all trailing legs to lie along the edges of area elements.

When a wing-flap configuration has multiple spanwise flap
segments with different deflection angles like that shown in
figure 2, certain difficulties arise in calculating the loading
distributions on the flap segments, particularly near the flap
edges. The problem is caused by the deflected trailing legs from
the upstream area elements on the wing. The individual circula-
tion strengths can be large; but when the side edges of the area
elements coincide, the trailing vortex legs tend to cancel and
the net strength of the trailing vorticity on this side edge is
quite small. When the side edges do not coincide, as is the case
on adjacent flaps with different deflections, the net strength of
the trailing legs along these edges can be large. This has two
effects on the loading calculation. First, the unbalanced
trailing leg strengths can cause unrealistic circulations to be
computed near the flap edges; and because of the mutual inter-
ference between panels, this can be felt on surrounding panels.
Second, these circulation distributions on the flaps lead to
unusual force distributions. This particular problem is not

unique with this author as Rubbert presents an extensive investigation of the same type of difficulty in reference 3.

Since this problem has a large effect only on the flap loads on the area elements near the edges of the flaps, and the total effect on the gross loading on the configuration is small, the following approximate solution is applied to this area. The wing trailing vorticity at the semispan station corresponding to the flap side edges is not allowed to deflect along the flaps but is arbitrarily forced to move aft in the plane of the wing. It is relatively unimportant as to the exact position assigned to the wing trailing legs so long as they are combined; therefore, the choice was made to leave the wing trailing legs (at this one semispan station only) undeflected. There is still an imbalance in the trailing legs associated with the flap edges, but it generally has only a small effect on the resulting flap circulation distribution. In addition to the modification to the wing trailing leg positions, the imbalance in the trailing vortex strength on the flap edges produced some large forces on the flap edges. For this reason, it was necessary to neglect the normal-force component due to the trailing vortex leg at the free edge of each flap. These modifications smoothed the predicted load distribution on the flaps with negligible effect on the total loading on the configuration.

Vortex Ring Jet Model

A potential flow model of a high-bypass-ratio turbofan engine wake is needed which will provide a means for calculating the induced velocity field both inside and outside the boundary of the jet wake. The flow model should simulate the entrainment effect exhibited by jet wakes, the jet boundaries should behave according to observed spreading rates for jets in a coflowing stream, and the wake should be positioned under the influence of a lifting surface such that it lies along a streamline. Such a potential flow model of a jet wake with circular cross section is presented in reference 2, and the flow model is extended to elliptic cross-sectional jets in reference 1.

The flow model consists of a distribution of vorticity placed on the surface of an expanding cylinder with circular or elliptical cross section. The strength of the vorticity is determined by the jet thrust coefficient. The distribution of vorticity on the cylinder is modeled by a series of vortex rings coaxial with the jet centerline and having the same cross-sectional shape as the cylinder. Each ring represents a finite increment of length of the cylinder, and the vortex strength of each individual ring is equal to the net vorticity on the incremental length of cylinder which it replaces. The momentum inside the jet boundary remains constant; and if the expansion of the boundary is specified correctly, the mass flow inside the boundary is in good

204

agreement with actual jets. Thus, the model represents the momentum, mass, and entrainment characteristics of a turbulent, coflowing jet. While the velocity profile within the jet is approximated by a uniform profile (fig. 3), the induced velocities outside the jet boundary are accurate because they are related to the entrainment induced flow.

Measured velocity profiles in the wake of a JT15D-1 jet engine mounted beneath a wing are available in reference 4. The profiles were measured on both the wing side and the free side of the engine centerline at a point approximately two nozzle diameters downstream of the engine exit. These data are shown in figure 4 for $c_T = 0.56$. A circular vortex ring jet model was designed to expand at a rate that would produce the same mass flow at the measured profile station. The resulting pre ed velocity profile is also shown in figure 4. The jet mod as approximately 5 percent less momentum than the real jet; th re-fore, the vortex ring model can satisfactorily match both mass and momentum of an actual jet if the correct spreading rate is known. Any interference calculation taking place inside the jet boundaries will be reasonably accurate when averaged over the total wake area, but there may be certain inaccuracies locally due to differences in the shape of the velocity profile within the wake.

Use of the vortex ring jet model requires three items to determine completely the analytical description of the jet. The first item is the initial vortex ring strength which is related to the thrust and momentum in the jet. The remaining two items are the boundary of the jet and the position of the jet center-line. The jet centerline can either be located a priori, or it can be left free to move under the influences of the free-stream velocity, the wing and flap loading induced flow field, and the jet induced flow field. The objective in permitting the center-line to move freely is to be able to position it along the streamline of the wing-flap-jet flow which leaves the center of the exhaust. Iterations can be performed until convergence is attained between the jet centerline and the streamline position.

To complete the description of the jet wake, the boundary of the jet must be specified at all points along the jet. An analyt-ical method is available in reference 5 which gives the radius distributions for axisymmetric jets in a coflowing stream for various velocity ratios. Unfortunately, a similar series of curves is not available for noncircular cross-sectional jets. It is here that empirical evidence must be used to complete the specifications of the jet.

Little data exist on the cross-sectional shape of nonaxisym-metric jets in a coflowing stream. Jet wake extent and profiles measured aft of the last flap on a four-engine EBF configuration are presented in reference 6. These data illustrate that

initially circular jets tend to mix and become elliptical in cross section after interaction with the flaps. The expansion characteristics of these jets between the engine exit and the station aft of the wing is undetermined. Modeling of the jet in this region requires simply a good engineering estimate until more detailed measurements become available.

Interference Calculation

Calculation of the aerodynamic loading of a wing-flap configuration under the influence of the jet wake of a turbofan engine is done with the combination of the two potential flow models described above. The two flow models are combined by superposition (fig. 5). The jet model induces a velocity field on the wing and flap which produces an interference loading on the lifting surfaces. The wing and flap loadings induce a velocity field in the vicinity of the jet and tend to deflect the jet away from these surfaces. It is assumed that the engine thrust is unaffected by the presence of the wing-flap. Because of the mutual interaction between the jet and lifting surfaces, an iterative solution is required. The solution is carried out in the following manner.

Before any calculations are made, the jet centerline is positioned with respect to the wing and flap. The initial location of the centerline can be based on some a priori knowledge of the flow field beneath the wing and flap system, or it can be located in a strictly arbitrary fashion. For example, it is quite acceptable to choose the initial jet centerline to be a straight line aft from the engine exhaust as illustrated in figure 5.

The (expanding) jet boundary and cross-sectional shape distribution should be chosen according to whatever procedure seems most appropriate, and this distribution (which will be unchanged from this point on) is placed on the centerline to define an initial jet wake. The jet-induced velocity field is computed at selected control points on the lifting surfaces and the circulation distribution on the wing and flaps is obtained such that the tangency boundary condition is satisfied at each control point.

At this point in the solution, the boundary condition on the wing and flap surfaces is satisfied but the jet position has not been influenced by the presence of the wing and flap. The wing-flap influence consists of modifying the jet location to cause the jet centerline to lie along a streamline of the combined jet-wing-flap flow. The initial jet centerline is adjusted by computing the total flow field at a number of points on the centerline and moving the centerline to a new position such that it lies along the computed flow direction at the specified points.

206

This completes the first iteration. In this situation, the wing and flap loading is not compatible with the jet flow field corresponding to the new position of the jet. Thus, a second iteration is needed.

The flow field corresponding to the adjusted jet position is computed, and a new wing-flap loading distribution is obtained. The jet centerline is again moved to lie along the new flow directions. This procedure is continued until either the center-line position or the total wing and flap loading converges to within a desired tolerance. With a converged solution, the total flow is tangent to the wing and flap surfaces and the jet center-line lies along a streamline of the flow.

It is during the iteration procedure and the subsequent motion of the jet centerline that another bit of empiricism is used. The combination of the two potential flow models results in the deflection of the jet such that it passes beneath the wing and flap surfaces. A typical converged solution will show the maximum jet centerline deflection angle to be close to the maximum flap angle. Measurements indicate that the turning efficiency of a typical EBF configuration can drop as low as 0.75 at high flap angles. Consequently, a limit on jet deflec-tion angle is imposed during the iteration process to more realistically model jet deflection for high flap deflection angles.

RESULTS

The methods of analysis described in the previous section have been applied to a number of different EBF configurations under various flow conditions. Convergence characteristics of the iteration procedure are examined, and comparisons with experimental data are presented.

Convergence Characteristics

For purposes of examining the convergence characteristics of the prediction method, the four-engine EBF configuration of references 4 and 7 was chosen. This large-scale model has a 25° swept wing with an aspect ratio of 7.28 and a taper ratio of 0.4. The trailing-edge flap system considered for the calculations consists of three full-span, slotted flaps. Two JT15D-1 turbofan engines are pylon mounted beneath each wing at $\eta = 0.25$ and 0.42. The lattice arrangement for this configuration is shown in figure 6. The initial assumption for the jet centerline in all cases is a straight line coincident with the engine centerline. The convergence studies are carried out for the flaps in a take-off position ($\delta_f = 0°/20°/40°$) and a configuration angle of attack of 18.5°.

Convergence of the total wing-flap normal-force coefficient is shown in figure 7 for thrust coefficients of 2.3 and 4.0. At the end of the fourth iteration, both cases have converged to within 7 percent. This convergence pattern has been observed on the same configuration at other angles of attack and on other similar configurations.

The convergence of the normal-force coefficient on each component of the wing-flap configuration is shown in figure 8. Each component tends to converge according to its own pattern, but all components reach convergence at about the same time.

The convergence pattern of the spanwise distribution of section normal force on a single component, flap 2, of the configuration is shown in figure 9 through four iterations. The peak loadings are caused by direct jet interaction with the flap. The span loads on the other components have a similar convergence pattern and these are presented and discussed in reference 1.

The convergence results just described are typical of those observed on other EBF configurations over a wide range of flow conditions. The method has never failed to converge, but convergence is slower for high flap angles. Generally, calculations have been initiated with a straight jet centerline because of the simplicity in prescribing the input; however, the number of iterations required for convergence can be reduced if the initial centerline is located closer to the final position. On the basis of cases run, convergence is more rapid if the centerline approaches its final position from above rather than below, because the correcting velocities causing the centerline position to change are larger if the centerline starts too close to the wing and flaps.

EBF Data Comparisons

The overall EBF prediction method was evaluated by comparing predicted results with data on several EBF configurations. These comparisons are presented and discussed in detail in reference 1, and results presented herein are typical examples of those included in that reference.

The first configuration to be considered is the four-engine model of references 4 and 7 with take-off flap setting ($\delta_f = 0°/20°/40°$). The jet turning efficiency was assumed to be 85 percent which limited the jet downward deflection angle to $34°$ for all calculations. The predictions to follow have all converged to within an 8-percent tolerance. The convergence is not the same at all angles of attack, thus introducing some uncertainty in the slope of the predicted curves.

In figure 10, the predicted section normal-force coefficient on flaps 1, 2, and 3 are compared with experimental results at $C_\mu = 4$ and $\alpha = 18.5^\circ$ obtained from reference 7. Wing data are not available for this configuration. The predicted peak loadings on flaps 1 and 2 are greater than those measured and cover a smaller portion of the wing. This indicates that the chosen jet model has not expanded sufficiently at this station and perhaps should be expanded at a faster rate to produce better agreement with experiment. As noted on the figure, the predicted total normal-force coefficients on flaps 1 and 2 are larger than the value obtained by integrating the measured distribution. The comparison for flap 3 in this same figure shows good agreement between the predicted and measured loading distributions. The peak loadings, the width of the loading, and the total normal force on the flap are all in good agreement. Since this flap is nearest to the point at which the jet wake is specified, based on measurements in the wake of a similar EBF configuration (ref. 6), the jet model is probably in better agreement with the actual jet on this flap than on the previous two flaps.

The predicted and measured longitudinal aerodynamic coefficients on the four-engine EBF model with take-off flap configuration are compared in figure 11. The predicted curves include estimates for the force and moment contributions due to the fuselage and engines. No estimate of viscous drag is included in the predicted drag curve. The power-on results indicate that the method is converging on a lift coefficient that is too low at low angles of attack. This result may be caused by a poor estimate for the jet turning efficiency. The predicted pitching-moment coefficients are in reasonable agreement with experiment, but the moment curve slopes are in error. The predicted drag curves are in good agreement with experiment.

Comparisons of the measured and predicted section normal-force coefficients on the same wing with landing flap configuration ($\delta_f = 15^\circ/35^\circ/55^\circ$) are shown in figure 12 for $C_\mu = 4$ and $\alpha = 6.5^\circ$. The high loading peaks on the wing are caused by the jet being driven up against the aft portion of the wing by the induced upwash from the high loading on the flaps. The loading peaks are also narrow compared to the data, another indication that the real jet may be spreading faster than the assumed analytical model. The loading peaks and spanwise extent of the jet-induced loading on the flaps are in reasonable agreement as illustrated in the remainder of figure 12.

The measured and predicted longitudinal aerodynamic coefficients on the landing flap configuration are compared in figure 13. The overall results are very similar to those presented for the take-off configuration. These results were obtained assuming jet turning efficiency of approximately 0.70; thus, the jet turning angle was limited to a maximum downward deflection of 38.5°.

The predicted flow field aft of the trailing edge of the last flap at a spanwise station corresponding to the centerline of the inboard jet is shown in figure 14 for the take-off configuration ($\delta_f = 0°/20°/40°$) at $C_\mu = 2.3$ and $\alpha = 18.5°$. The uniformity of the jet flow characteristics of the vortex ring model is well illustrated. In the inset, the measured flow field aft of a similar EBF configuration under similar flow conditions is reproduced from reference 6. The measured flow field, also aligned with the centerline of the inboard jet, is very much like the predicted flow field.

The results presented thus far have all been obtained using a circular cross-sectional jet model because adequate information needed to specify an elliptic jet boundary are not available. Some results obtained using the elliptic jet model are described in reference 1. The elliptic jet used had the same initial momentum and cross-sectional area distribution along the centerline as the circular jet model. The elliptic jet was assumed to expand linearly from a circular cross section at the engine exit to a 2:1 ellipse aft of the last flap. The same jet turning efficiency used for the circular jet model was retained. The calculation was carried out for the landing flap configuration at $\alpha = 18.5°$ with the following results. The predicted loading is distributed differently over the wing and flap surfaces due to the different cross-sectional shape of the two jets, but the total normal force imparted to the wing-flap configuration by the elliptic jet model is only 2 percent different from that obtained from the circular jet model. It appears that the cross-sectional shape of the jet is important if loading distributions are important; but if gross aerodynamic forces are the goal of the calculation, the jet cross-sectional shape is relatively unimportant so long as the momentum in the jet is correct.

CONCLUDING REMARKS

An engineering prediction method developed to predict the loading distributions and longitudinal aerodynamic characteristics of externally blown flap configurations has been described. Comparisons of measured and predicted gross lift, drag, and pitching-moment coefficients on configurations with moderate flap angles ($\delta_f \leq 40°$) indicate generally good agreement for all thrust levels. This is due principally to the correct modeling of the entrainment and momentum characteristics of the engine wakes and to the proper treatment of the mutual interference between the jet wake and wing-flap. The interference model creates, on the wing-flap, both the momentum reaction due to jet deflection and the additional induced circulation characteristic of EBF systems.

210

As the flap angles increase beyond 40°, the predicted results agree less well with the data. The assumption that the wing-flap induced interference on the jet affects only its centerline and not its boundary becomes less accurate as the jet is more highly deformed, and it is possible that this is responsible for the poorer agreement at the higher flap angles.

Comparisons of measured and predicted spanwise loading distributions on the individual lifting surfaces indicate good quantitative agreement in some cases and poor agreement in others. Generally, the correct qualitative behavior is predicted in which large peak loadings occur locally on the flaps due to direct impingement of the jet wakes, but the magnitude of the peaks is not consistently in good agreement with the data. The differences are felt to be due primarily to the modeling of the velocity profile within the wake and the boundary of the wake.

REFERENCES

1. Mendenhall, M. R., Spangler, S. B., Nielsen, J. N., and Goodwin, F. K.: Calculation of the Longitudinal Aerodynamic Characteristics of Wing-Flap Configurations With Externally Blown Flaps. NEAR TR 97, Dec. 1975. NASA CR-2705, 1976.

2. Dillenius, M. F. E., Mendenhall, M. R., and Spangler, S. B.: Calculation of the Longitudinal Aerodynamic Characteristics of STOL Aircraft with Externally-Blown Jet-Augmented Flaps. NASA CR-2358, Feb. 1974.

3. Rubbert, P. E.: Theoretical Characteristics of Arbitrary Wings by a Non-Planar Vortex Lattice Method. Boeing Rept. D6-9244, Feb. 1964.

4. Aoyagi, K., Falarski, M. D., and Koenig, D. G.: Wind-Tunnel Investigation of a Large-Scale 25° Swept-Wing Jet Transport Model with an External Blowing Triple-Slotted Flap. NASA TM X-62,197, Nov. 1973.

5. Abramovich, G. N.: The Theory of Turbulent Jets. MIT Press, 1963.

6. Johnson, W. G., Jr. and Kardas, G. E.: A Wind-Tunnel Investigation of the Wake Near The Trailing Edge of a Deflected Externally Blown Flap. NASA TM X-3079, Oct. 1974.

7. Perry, B., III and Greene, G. C.: Wind-Tunnel Investigation of Aerodynamic Loads on a Large-Scale Externally Blown Flap Model and Comparison with Theory. NASA TN D-7863, Mar. 1975.
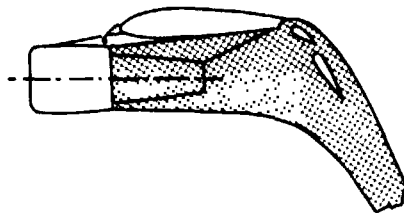
Figure 1.- EBF configuration.
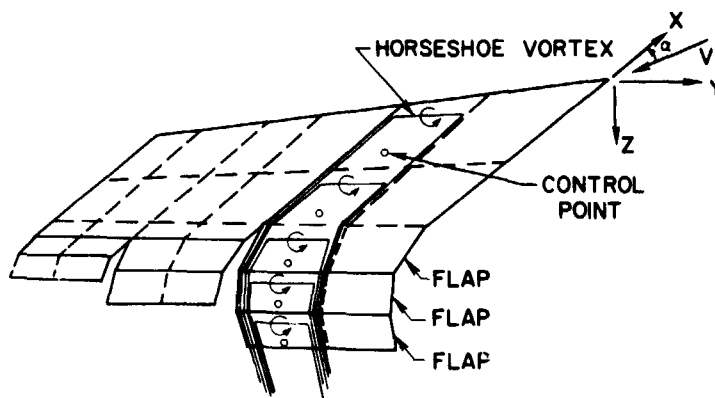
Figure 2.- Wing-flap vortex-lattice model.
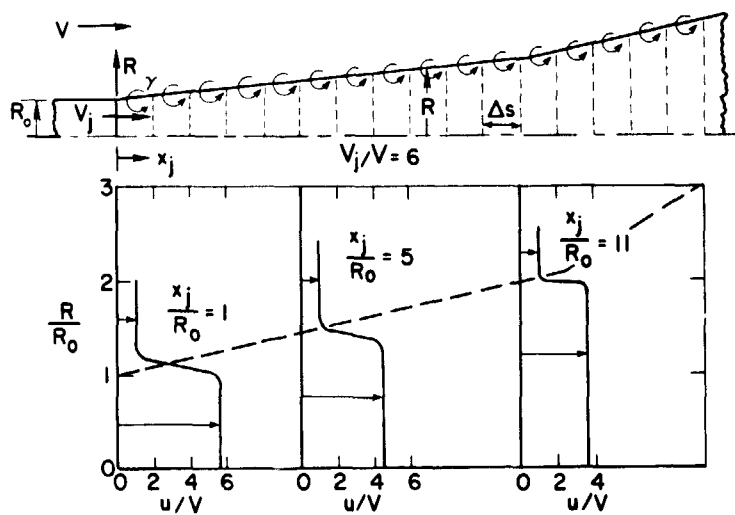
Figure 3.- Circular vortex ring wake model
and velocity profiles.
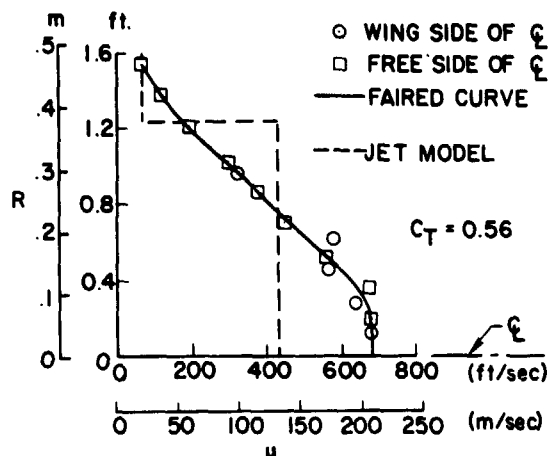
Figure 4.- Measured and predicted velocity profiles
in the wake of a JT15D-1 jet engine.

$\delta_f = 0°/20°/40°$

$C_\mu = 4.0$

$\alpha = 18.5°$
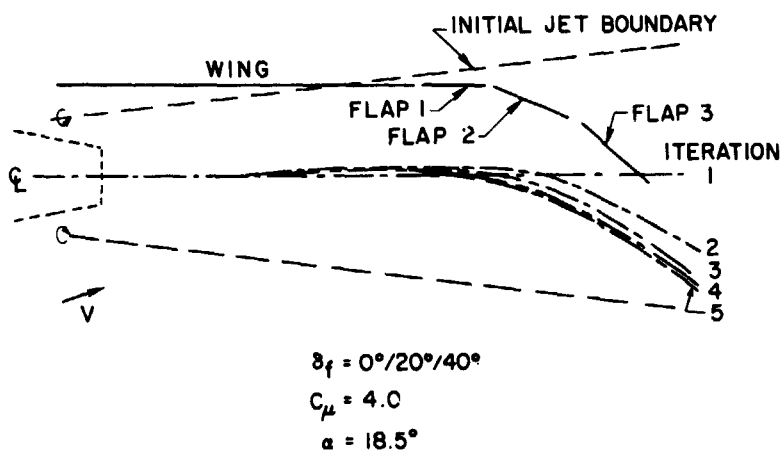
Figure 5.- Convergence of inboard jet centerline on
a four-engine EBF configuration.

213

WING
FLAP 1
FLAP 2
FLAP 3

ALL FLAPS SHOWN UNDEFLECTED
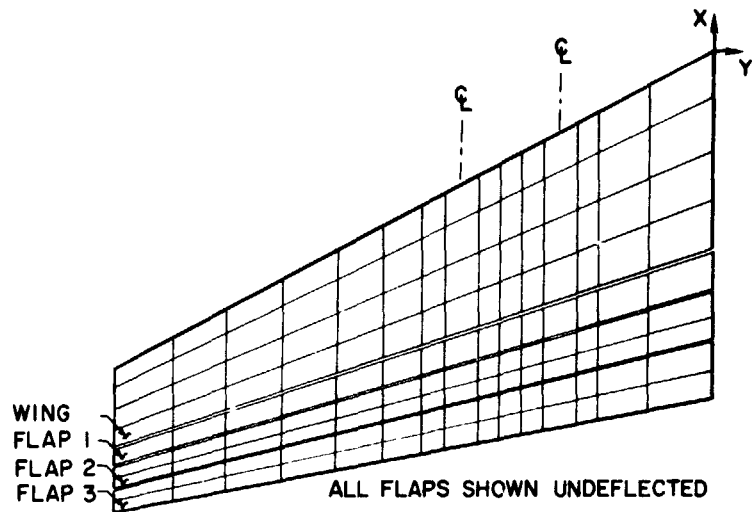
Figure 6.- Vortex-lattice arrangement for
EBF configuration.

$\delta_f = 0°/20°/40°$

$\alpha = 18.5°$

$C_\mu = 4.0$

$\Delta = 6.1\%$

2.3

$\Delta = 6.9\%$

C_N

ITERATION
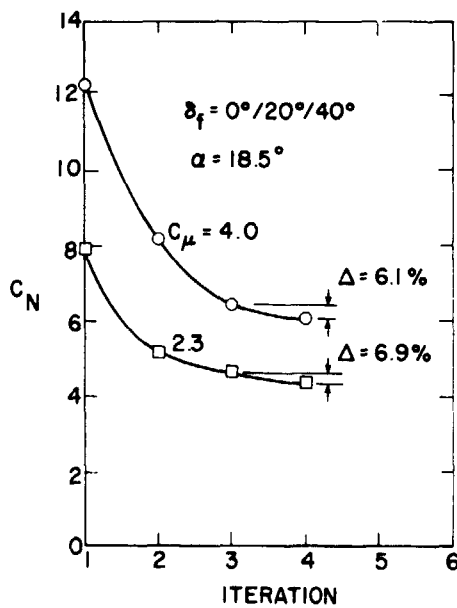
Figure 7.- Convergence of the total wing-flap
normal-force coefficient on a four-engine
EBF configuration.
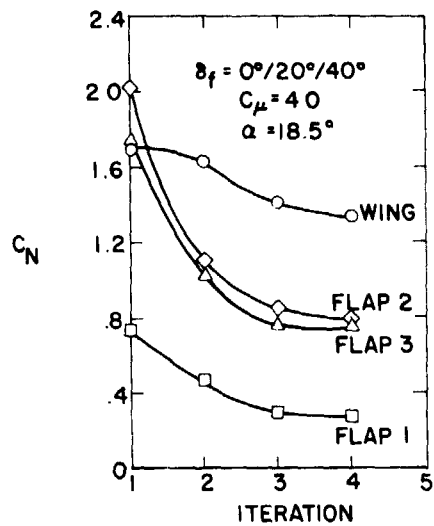
Figure 8.- Convergence of normal-force
coefficients on the wing and flaps of
a four-engine EBF configuration.
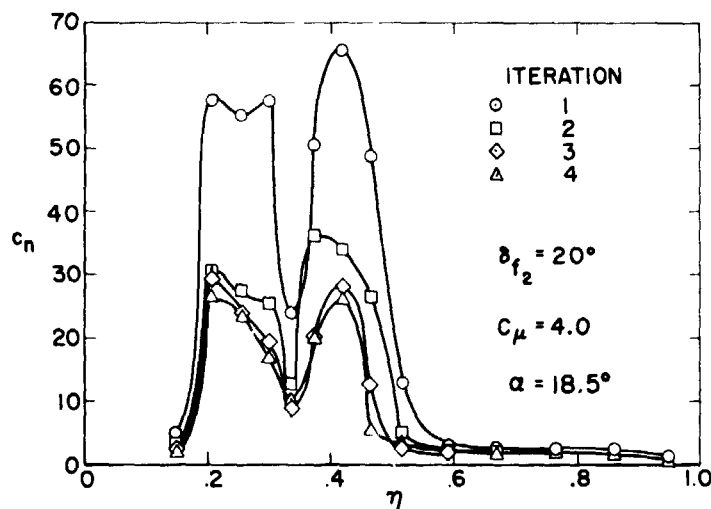
Figure 9.- Convergence of predicted spanwise
distribution of section normal-force
coefficients on flap 2 of a four-engine
EBF configuration.
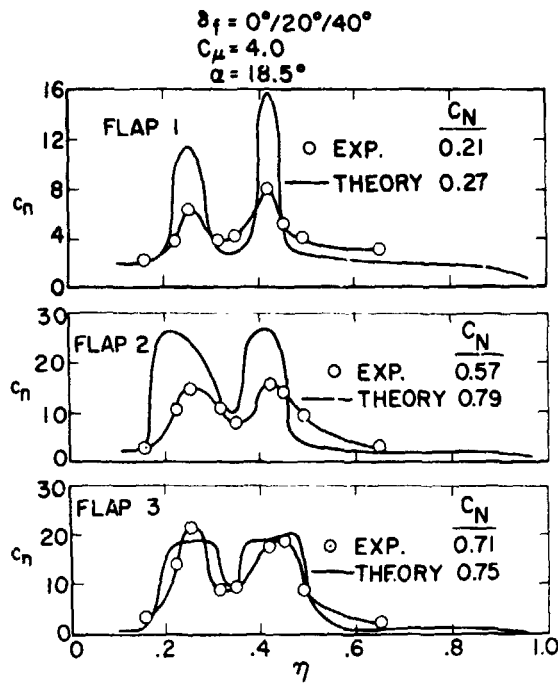
Figure 10.- Measured and predicted section normal-force coefficients on the lifting surfaces of a four-engine EBF model.
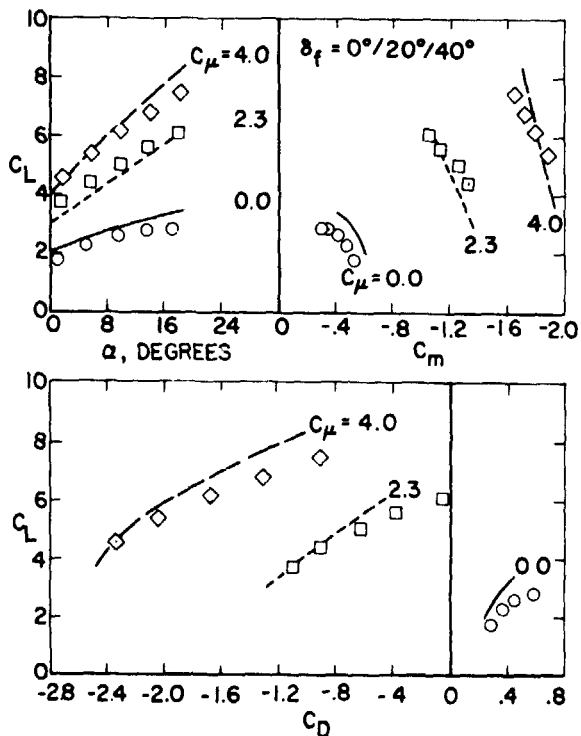
Figure 11.- Measured and predicted longitudinal aerodynamic characteristics of a four-engine EBF configuration.

216

$\delta_f = 15°/35°/55°$
$C_\mu = 4.0$
$\alpha = 6.5°$
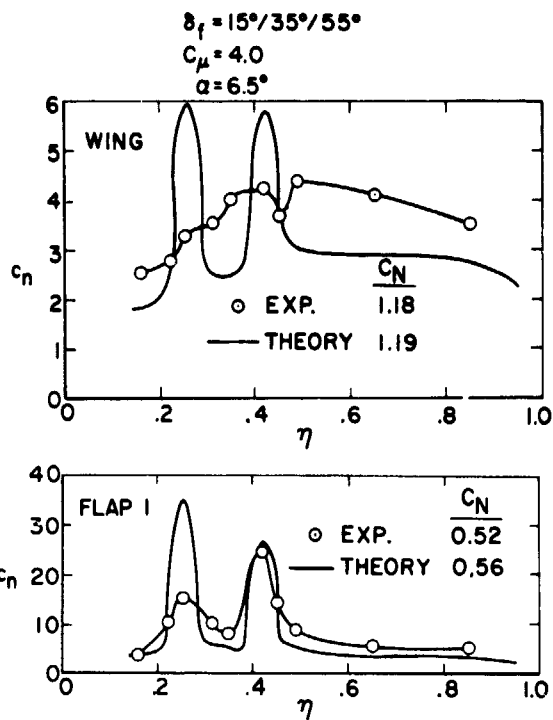
Figure 12.- Measured and predicted section normal-
force coefficients on the lifting surfaces of a
four-engine EBF configuration.
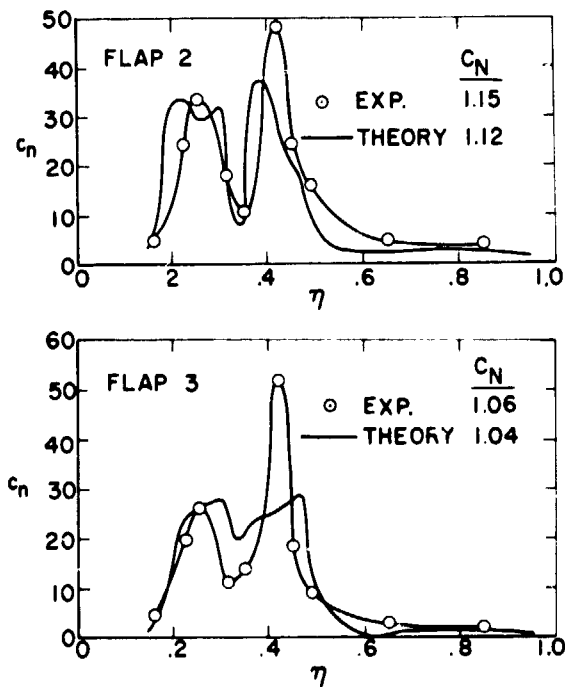
Figure 12.- Concluded.
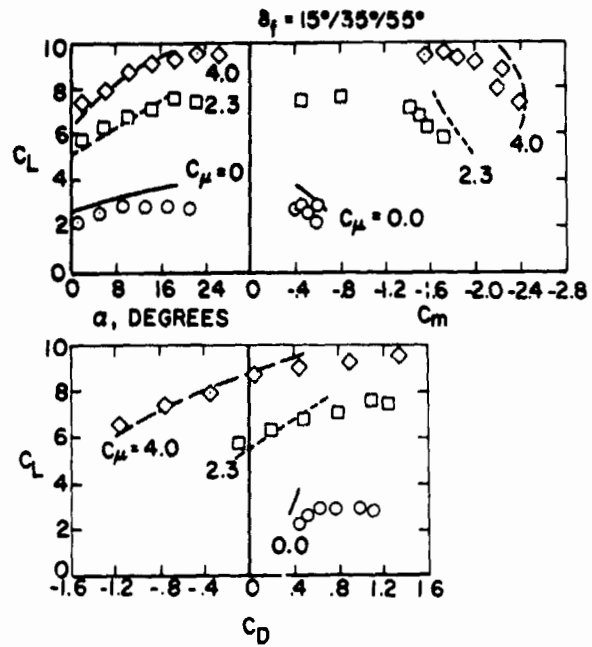
Figure 13.- Measured and predicted longitudinal
aerodynamic characteristics of a four-engine
EBF configuration.
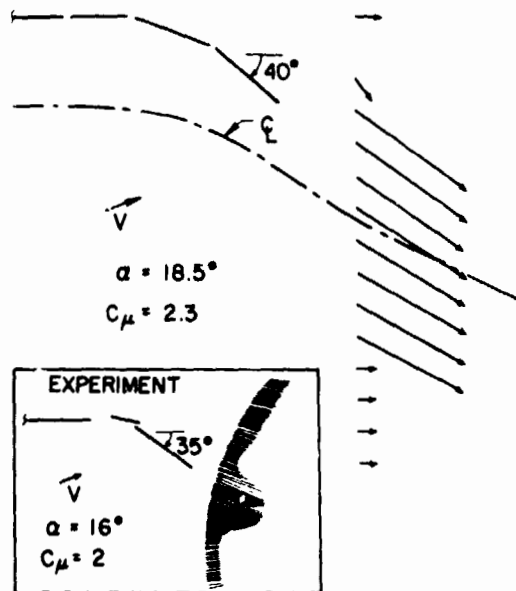
Figure 14.- Measured and predicted flow
fields aft of EBF configurations.

218

SOME RECENT APPLICATIONS OF THE SUCTION ANALOGY

TO ASYMMETRIC FLOW SITUATIONS

James M. Luckring
NASA Langley Research Center

SUMMARY

This paper reviews a recent extension of the suction analogy for estimation of vortex loads on asymmetric configurations. This extension includes asymmetric augmented vortex lift and the forward sweep effect on side edge suction. Application of this extension to a series of skewed wings has resulted in an improved estimating capability for a wide range of asymmetric flow situations. Hence, the suction analogy concept now has more general applicability for subsonic lifting surface analysis.

INTRODUCTION

For lifting surfaces having relatively sharp leading and side edges, the commensurate separation associated with the vortex-lift phenomena can have considerable impact on the performance of high-speed maneuvering aircraft. A detailed knowledge of these flow phenomena, which are referred to as vortex flows, is necessary for proper design and analysis of such aircraft.

For estimating the lift associated with these vortex flows, Polhamus introduced the concept of the leading-edge suction analogy (ref. 1). The suction analogy states that for the separated flows situation, the potential-flow leading-edge suction force becomes reoriented from acting in the chord plane to acting normal to the chord plane (a rotation of $90°$) by the local vortex action resulting in an additional normal force. (See insert on fig. 1.) The reasoning is that the force required to maintain the reattached flow is the same as that which had been required to maintain the potential flow around the leading edge.

An application of the suction analogy is shown in figure 1 for a $75°$ swept sharp-edge delta wing at a low subsonic Mach number taken from reference 2. Both lift as a function of angle of attack and drag due to lift are seen to be well estimated by the analogy. Since the original application, the suction analogy concept has been applied to more general planforms. (See refs. 3 and 4.)

In reference 5, Lamar demonstrated that the suction analogy was not limited to analysis of leading-edge vortex flows, but could be applied wherever singularities in the potential-flow induced velocities produce an edge force. Figure 2, taken from reference 5, illustrates that vortex lift may be expected along streamwise side edges due to the singularities in the sidewash.

Whereas the theories of references 1 to 5 have dealt with estimating the effects of separation-induced vortex flows on longitudinal aerodynamic characteristics for symmetrical configurations having symmetrical loads, it is desirable to have a method which allows for asymmetric configurations such as oblique

or skewed wings, for example, and asymmetric flight conditions such as those associated with sideslip or lateral control.

Accordingly, the present investigation deals with a recent extension of the suction analogy concept to include asymmetric flow situations. To accomplish this analysis, the computer program of references 6 and 7 has been generalized to account for asymmetry resulting in the asymmetric vortex-lattice (AVL) program. Although analysis with this program may be performed on many different types of asymmetric flow situations, as shown in figure 3, this paper will focus on the analysis of wings with geometric asymmetries and, in particular, on untapered skewed wings having separated vortex flows along leading and side edges. The effects of forward sweep on side-edge suction are introduced and the concept of augmented vortex lift as developed in reference 8 is applied to skewed wings.

Subsonic solutions can be obtained with the AVL program for configurations having matrix sizes up to 400×400. Operating in FORTRAN extended (FTN) version 4.4, the program requires 74000_8 storage and can solve a 200 singularity configuration in less than 2 minutes on the Control Data Corporation (CDC) 6600 system running under NOS 1.0. Compared with its symmetric progenitor, the program requires 13000_8 more storage, but executes roughly 20 percent faster for the same configuration.

SYMBOLS

A   aspect ratio

b   wing span

C_D drag coefficient, $\dfrac{\text{Drag}}{q_\infty S_{ref}}$

$C_{D,o}$ experimental value of drag coefficient at $C_L = 0$

C_L lift coefficient, $\dfrac{\text{Lift}}{q_\infty S_{ref}}$

$\Delta C_{L,v}$ C_L increment associated with augmented vortex lift

C_l rolling-moment coefficient about reference point, $\dfrac{\text{Rolling moment}}{q_\infty S_{ref} b}$

C_{l_β} $= \dfrac{\partial C_l}{\partial \beta}$

C_{l_p} $= \dfrac{\partial C_l}{\partial \left(\dfrac{pb}{2U}\right)}$

220

C_{l_r} $\qquad = \dfrac{\partial C_l}{\partial\left(\frac{rb}{2U}\right)}$

C_m $\qquad$ pitching-moment coefficient about reference point which is located at $\dfrac{c_{ref}}{4}$ unless otherwise stated, $\dfrac{\text{Pitching moment}}{q_\infty S_{ref} c_{ref}}$

C_N $\qquad$ normal-force coefficient, $\dfrac{\text{Normal force}}{q_\infty S_{ref}}$

C_n $\qquad$ yawing-moment coefficient about reference point, $\dfrac{\text{Yawing moment}}{q_\infty S_{ref} b}$

C_{n_β} $\qquad = \dfrac{\partial C_n}{\partial\beta}$

C_{n_p} $\qquad = \dfrac{\partial C_n}{\partial\left(\frac{pb}{2U}\right)}$

C_{n_r} $\qquad = \dfrac{\partial C_n}{\partial\left(\frac{rb}{2U}\right)}$

C_S $\qquad$ leading-edge suction-force coefficient, $K_{v,le}\left|\sin\alpha\right|\sin\alpha$

C_T $\qquad$ leading-edge thrust-force coefficient, $C_S\cos\Lambda$

C_Y $\qquad$ leading-edge side-force coefficient, $C_S\sin\Lambda$

$C_{Y,se}$ $\qquad$ side-edge side-force coefficient

c $\qquad$ streamwise chord

$\tilde{c}$ $\qquad$ characteristic length used in determination of $\bar{K}_{v,se}$

c_s $\qquad$ section suction-force coefficient, $\dfrac{\text{Section suction force}}{q_\infty c}$

c_t $\qquad$ section thrust-force coefficient, $\dfrac{\text{Section thrust force}}{q_\infty c}$

c_y section side-force coefficient, $\dfrac{\text{Section side force}}{q_\infty c}$

$f_{y,i}$ elemental side force

K_p potential-lift factor, $\dfrac{\partial\left(C_{N,p}\right)}{\partial(\sin \alpha \cos \alpha)}$

$K_{v,le}$ leading-edge-vortex lift factor,

$$\partial\left(\frac{\dfrac{\text{Leading-edge suction force from one edge}}{q_\infty S_{ref}}}{\partial \sin^2 \alpha}\right)$$

$K_{v,se}$ side-edge-vortex lift factor,

$$\partial\left(\frac{\dfrac{\text{Side-edge suction force from one edge}}{q_\infty S_{ref}}}{\partial \sin^2 \alpha}\right)$$

$\bar{K}_{v,se}$ augmented-vortex lift factor, $\dfrac{K_{v,le}}{(b)\ \sec \Lambda}\,\tilde{c}$

M free-stream Mach number

p roll rate, rad/sec

q_o free-stream dynamic pressure

r yaw rate, rad/sec

S surface area

U free-stream velocity

u induced velocity in x-direction at point (x,y)

v induced velocity in y-direction at point (x,y)

$\bar{x}$ centroid

α angle of attack

β angle of sideslip

γ distributed bound vorticity at point (x,y)

δ distributed trailing vorticity at point (x,y)

η spanwise location in percent semispan

Λ leading-edge sweep angle, positive for sweepback

Subscripts:

av   average

c   centroid

i   particular item of location

le   leading edge

p   potential or attached flow

r   root

ref   reference; for S, true wing area; for c, mean geometric chord

se   side edge

tot   total

vle   vortex effect at leading edge

vse   vortex effect at side edge

RESULTS AND DISCUSSION

Modified Vortex-Lattice Method

In the analysis of separation-induced vortex flow effects for symmetric configurations by the method of references 6 and 7, the following equations are used to compute C_L, C_D, C_m, and C_l:

$$C_{L,tot} = \underbrace{K_p \sin \alpha \cos^2 \alpha}_{C_{L,p}} + \underbrace{K_{v,le}|\sin \alpha| \sin \alpha \cos \alpha}_{C_{L,vle}} + \underbrace{K_{v,se}|\sin \alpha| \sin \alpha \cos \alpha}_{C_{L,vse}}$$

$$(1)$$

or

$$C_{L,tot} = K_p \sin \alpha \cos^2 \alpha + K_{v,tot}|\sin \alpha| \sin \alpha \cos \alpha \qquad (2)$$

$$C_D = C_{D,o} + C_L \tan \alpha = C_{D,o} + K_p \sin^2 \alpha \cos \alpha + K_{v,tot} \sin^3 \alpha \qquad (3)$$

$$C_{m,tot} = \overbrace{K_p \sin \alpha \cos \alpha \frac{\bar{x}_{c,p}}{c_{ref}}}^{C_{m,p}} + \overbrace{K_{v,le}|\sin \alpha| \sin \alpha \frac{\bar{x}_{c,le}}{c_{ref}}}^{C_{m,vle}}$$

$$+ \overbrace{K_{v,se}|\sin \alpha| \sin \alpha \frac{\bar{x}_{c,se}}{c_{ref}}}^{C_{m,vse}} \qquad (4)$$

$$C_{l,tot} = \overbrace{K_p \sin \alpha \cos \alpha \frac{\bar{y}_{c,p}}{b}}^{C_{l,p}} + \overbrace{K_{v,le}|\sin \alpha| \sin \alpha \frac{\bar{y}_{c,le}}{b}}^{C_{l,vle}}$$

$$+ \overbrace{K_{v,se}|\sin \alpha| \sin \alpha \frac{\bar{y}_{c,se}}{b}}^{C_{l,vse}} \qquad (5)$$

where the particular $\bar{x}$ terms represent the distance between the appropriate centroid and the reference point X_{ref} taken to be the quarter chord of the mean geometric chord. The potential flow lift term K_p is computed from the symmetric vortex lattice and the vortex lift terms, $K_{v,le}$ and $K_{v,se}$, are computed from the symmetric potential flow solution by using the suction analogy. The application of this technique is not limited, however, to symmetric conditions and should be applicable to asymmetric conditions providing the appropriate values of K_p and K_v can be obtained.

The asymmetric vortex-lattice computer program was developed from its symmetric progenitors (refs. 6 and 7) to compute potential flow solutions about arbitrary thin asymmetric configurations. Once the asymmetric potential-flow solution $\left(\text{and, hence, } K_p\right)$ is known, the suction analogy may be invoked to compute corresponding asymmetric vortex lift terms, $K_{v,le}$ and $K_{v,se}$. The analysis technique of equations (1) to (5) may now be employed by using the K_p and K_v quantities as computed from the asymmetric potential flow.

In applying this analysis to a series of sharp-edged skewed wings, some additional aerodynamic effects associated with these wings had to be considered. The following sections describe these effects and present the analysis.

Effects of Forward Sweep on Side-Edge Suction

In the computation of side-edge vortex lift by the method of reference 7, the portion of the wing inboard of the side edge is assumed to contribute to the side force acting on the side edge. For sweptback wings, this technique does not lead to complications with the leading-edge forces in that the leading-edge side force and the side-edge side force do not interact with one another. However, in the instance of forward sweep such as for a skewed wing as illustrated in the upper left part of figure 4, the leading-edge side force and the side-edge side force act in opposition to one another across an elemental spanwise strip. A more detailed illustration of the forward-swept semispan is presented in the upper right portion of figure 4. Here the leading-edge and side-edge section side forces are seen to oppose one another along a representative elemental spanwise strip; as a result, there is a region of positive elemental side force and a region of negative elemental side force. The distribution of elemental side force along the representative spanwise strip is shown in the lower right part of figure 4.

The change of sign of the elemental side force would tend to imply that the positive elemental side forces act on the side edge while the negative elemental side forces act on the leading edge. A comparison of the leading-edge side-force distribution computed by integrating the negative elemental side forces on the sweptforward semispan with the side-force component of the leading-edge thrust force on the sweptforward semispan is presented in the lower left part of figure 4. The agreement tends to substantiate the implication that the negative elemental side forces are in actuality the side-force component of the leading-edge thrust. This force has already been accounted for in the present method by computing the leading-edge thrust and using the secant relationship of the leading-edge sweep to compute the resultant leading-edge suction. Accordingly, to compute the side-edge force on the sweptforward semispan properly, only the positive elemental side forces inboard of the side edge are integrated.

Augmented Vortex Lift

In reference 8, Lamar introduced the concept of augmented vortex lift for estimation of loads rising from a vortex persisting downstream and passing over lifting surfaces such as the aft part of a wing or a tail. This persistence results in an additional vortex lift term $\Delta C_{L,v}$ unaccounted for by the suction analogy which deals only with the forces generated along a particular edge.

Figure 5 illustrates the concept of augmented vortex lift applied to a skewed wing. In applying the method of reference 8, the leading-edge vortex lift factor $K_{v,le}$ developed along the leading-edge length $b \sec \Lambda$ persists over a portion of the wing aft of the leading edge $\tilde{c}$ taken to be the tip chord. This condition results in the additional vortex lift factor

$$\bar{K}_{v,se} = \left(\frac{K_{v,le}}{b \sec \Lambda}\right)\tilde{c} \qquad\qquad (6)$$

which has the same angle-of-attack dependence as the other vortex terms. Since the chordwise centroid of side-edge vortex lift distributions is generally near the midpoint of the tip chord, the chordwise centroid of the augmented vortex lift factor is taken to be the midpoint of the tip chord. It should be noted that the augmented vortex lift occurs only on the downwind side edge.

As long as the leading-edge vortex remains in the vicinity of the leading edge, it will pass over a region of the wing aft of the leading edge that has a length roughly equal to the tip chord. The choice of the tip chord for $\tilde{c}$ is consistent with the assumption employed in this analysis that the vortex loads act along the edge from which they originate. This assumption is valid as long as a substantial amount of vortex growth and subsequent inboard movement of the vortex core is not encountered.

Skewed Wing Analysis

Figure 6 presents a comparison between a swept and a skewed wing of the span load and section suction distributions. Although in each case the total loads remain essentially the same for both wings, the distribution of the load is seen to shift for the skewed wing to the sweptback semispan. A comparison between the separated flow theory and experiment for these two wings is shown in figure 7. Data for the swept wing was obtained from reference 9. Although the lift is well predicted in both cases, the augmented pitching moment for the skewed wing is seen to predict the data well up to an angle of attack of approximately 6°; above this angle it overpredicts the data. The discrepancy between theory and data for the skewed wing pitching moment may partly be attributed to excessive vortex growth and subsequent movement of the vortex core inboard as the angle of attack is increased. This behavior is illustrated in figure 8. In the application of the suction analogy, the vortex loads are assumed to be edge forces and no angle-of-attack dependence of the centroids is computed. Moreover, as the vortex moves inboard, the amount of the wing over which the vortex passes giving rise to the augmented term decreases and may even become negative. Hence, the present application of augmentation for moment calculation may only be applicable for low to moderate angles of attack depending on how much variance $\tilde{c}$ will experience as a function of α.

Figures 9 to 11 present lift, pitching-moment, and rolling-moment characteristics of several skewed wings having an aspect ratio of one and varying leading-edge sweep. A configuration having a cylindrical fuselage 0.24b in diameter and $1.85c_r$ in length with a midwing is also presented.

In all cases, the lift was well estimated by including the edge-vortex and augmented-vortex contributions. Similarly, the nonlinear pitching-moment trends were well predicted by the edge-vortex contribution, the augmentation enhancing the prediction at low to moderate angles of attack. The potential-flow pitching-moment curve is seen to have a sign opposite from that of the data. Rolling moments were well predicted by the edge-vortex terms up to approximately 8° where the inboard vortex movement became significant; this condition caused a

226

sign reversal in the data except for the wing-fuselage configuration. The primary effect of the fuselage is to break the leading-edge vortex into two pieces, one emanating from the wing apex and bending downstream at the right-wing fuselage juncture and the other emanating from the left leading-edge fuselage juncture and bending downstream at the left wing tip. Regenerating the leading-edge vortex with the fuselage substantially decreases the extent of inboard movement of the vortex as exhibited by the agreement between theory and experiment for the pitching- and rolling-moment coefficients of figures 10 and 11.

Figures 12 to 14 present the lift, pitching-moment, and rolling-moment characteristics of several skewed wings of varying aspect ratio. As in the previous case, the lift was well predicted for the three wings. The experimental pitching moments are well predicted by including the augmented term but the experimental rolling moments still depart from the theory at approximately 6°. Hence, for these wings the chordwise distribution of the load is being well estimated whereas the spanwise distribution of the load can be estimated only as long as a substantial inboard movement of the vortex is not encountered.

CONCLUDING REMARKS

This paper has presented a recent extension of the suction analogy for the estimation of potential and vortex loads on asymmetric configurations. The analysis has been accomplished by the development and application of an asymmetric vortex-lattice computer program which may be used to compute the potential and vortex loads on asymmetric configurations. In applying this analysis to a series of sharp-edge skewed wings, the effects of forward sweep on side-edge suction and of a skewed geometry on augmented vortex lift have been accounted for. Total loads have been well predicted whereas pitching and rolling moments have been well predicted only as long as the assumption that the vortex loads act along the edge from which the vortex has originated is not violated. Hence, the suction analogy concept may now be applied to a wider range of isolated planforms resulting in an improved estimating capability of separation-induced vortex flow.

REFERENCES

1. Polhamus, Edward C.: A Concept of the Vortex Lift of Sharp-Edge Delta Wings Based on a Leading-Edge-Suction Analogy. NASA TN D-3767, 1966.

2. Wentz, William H., Jr.; and Kohlman, David L.: Wind Tunnel Investigations of Vortex Breakdown on Slender Sharp-Edged Wings. Rep. FRL 68-013 (Grant NGR-17-002-043), Univ. of Kansas Center for Research, Inc., Nov. 27, 1969. (Available as NASA CR-98737.)

3. Polhamus, Edward C.: Charts for Predicting the Subsonic Vortex-Lift Characteristics of Arrow, Delta, and Diamond Wings. NASA TN D-6243, 1971.

4. Polhamus, Edward C.: Predictions of Vortex-Lift Characteristics by a Leading-Edge Suction Analogy. J. Aircraft, vol. 8, no. 4, Apr. 1971, pp. 193-199.

5. Lamar, John E.: Extension of Leading-Edge-Suction Analogy to Wings With Separated Flow Around the Side Edges at Subsonic Speeds. NASA TR R-428, 1974.

6. Margason, Richard J; and Lamar, John E.: Vortex-Lattice FORTRAN Program for Estimating Subsonic Aerodynamic Characteristics of Complex Planforms. NASA TN D-6142, 1971.

7. Lamar, John E.; and Gloss, Blair B.: Subsonic Aerodynamic Characteristics on Interacting Lifting Surfaces With Separated Flow Around Sharp Edges Predicted by a Vortex-Lattice Method. NASA TN D-7921, 1975.

8. Lamar, John E.: Some Recent Applications of the Suction Analogy to Vortex-Lift Estimates. Aerodynamic Analyses Requiring Advanced Computers, Part II, NASA SP-347, 1975, pp. 985-1011.

9. Gersten, K.: Calculation of Non-Linear Aerodynamic Stability Derivatives of Aeroplanes. AGARD Rep. 342, Apr. 1961.
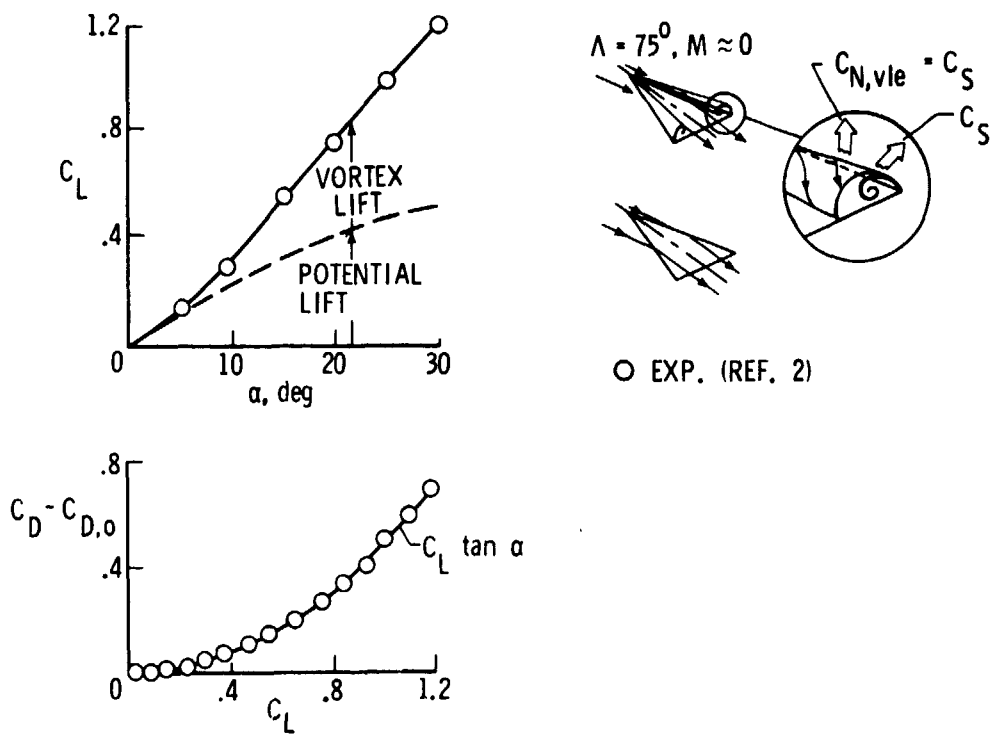
Figure 1.- Original application of leading-edge suction analogy.

$$C_L = K_p \sin \alpha \cos^2\alpha + (K_{v,le} + K_{v,se}) |\sin \alpha| \sin \alpha \cos \alpha$$
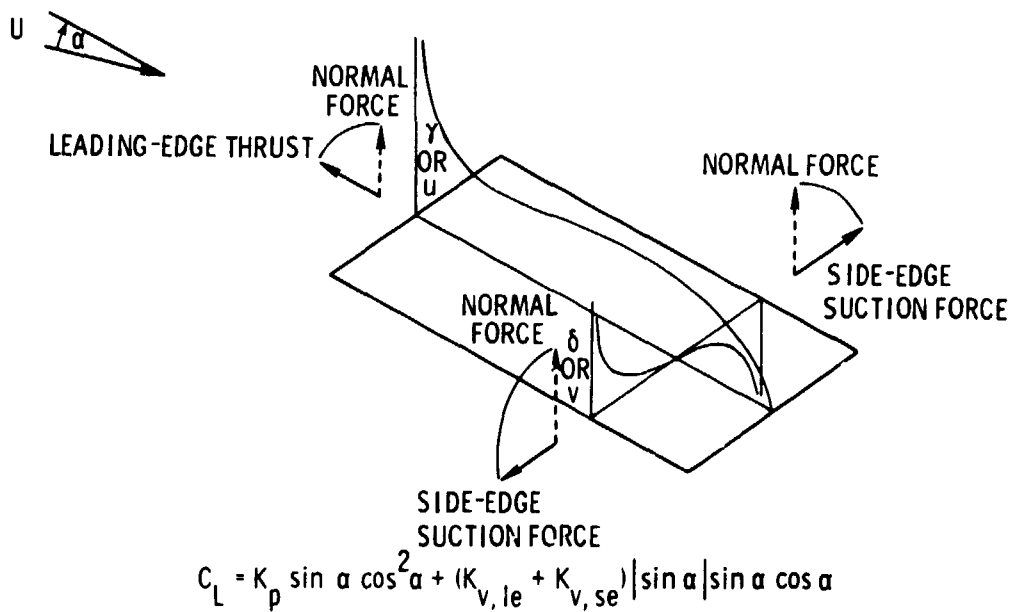
Figure 2.- Vortex-lift concept: suction analogy application
to leading edge and side edge.

GEOMETRIC ASYMMETRICS

- SINGLE PLANFORM
- SKEWED WINGS

- MULTIPLE PLANFORMS
- INTERACTION EFFECTS
- DIFFERENTIAL DEFLECTION

ONSETTING FLOW ASYMMETRICS

SIDESLIPPING

$\bullet C_{l_\beta}$
$\bullet C_{n_\beta}$

ROLLING

$\bullet C_{l_p}$
$\bullet C_{n_p}$

YAWING

$\bullet C_{l_r}$
$\bullet C_{n_r}$
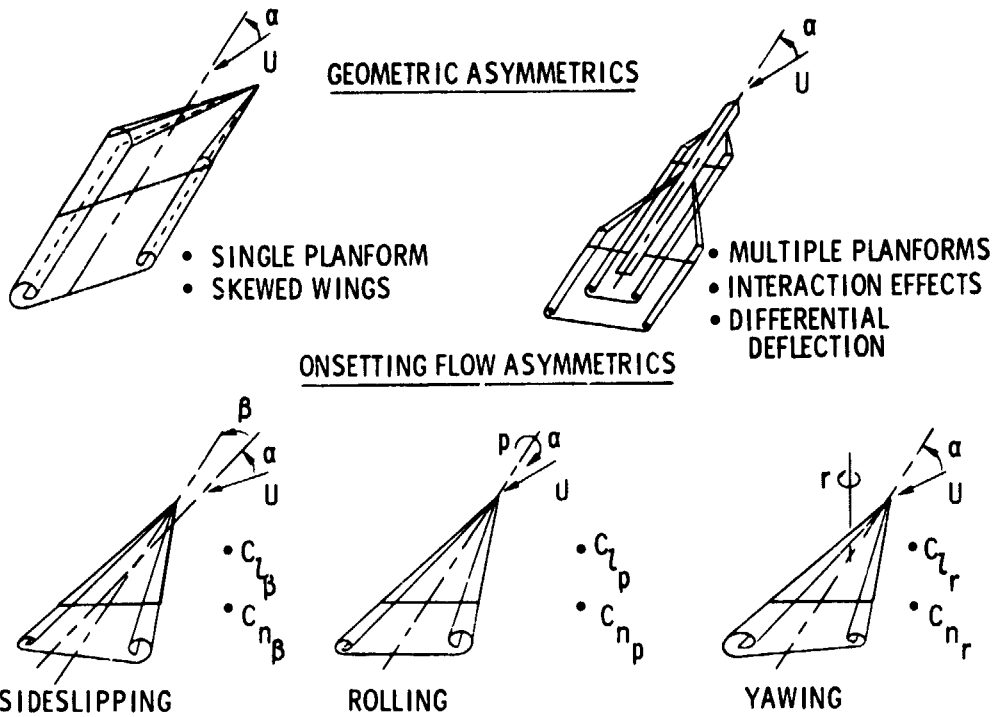
Figure 3.- Some recent applications of suction analogy to asymmetric vortex flow situations.

$M = 0$

C_S C_T

C_Y

$C_{Y, se}$

$C_{Y, se}$

NEGATIVE $f_{y,i}$

$c_s c$ $c_t c$

$c_y c$

$c_{y,se}$

POSITIVE $f_{y,i}$

$-.15$

$-.10$

$-.05$

0

$+.05$

$c_t c \tan \Lambda$ or $c_y c$

○ L.E. THRUST × TAN Λ
— L.E. SIDE FORCE

0   .2   .4   .6   .8   1.0   η

.10

.05

0

$-.05$

$f_{y,i}$
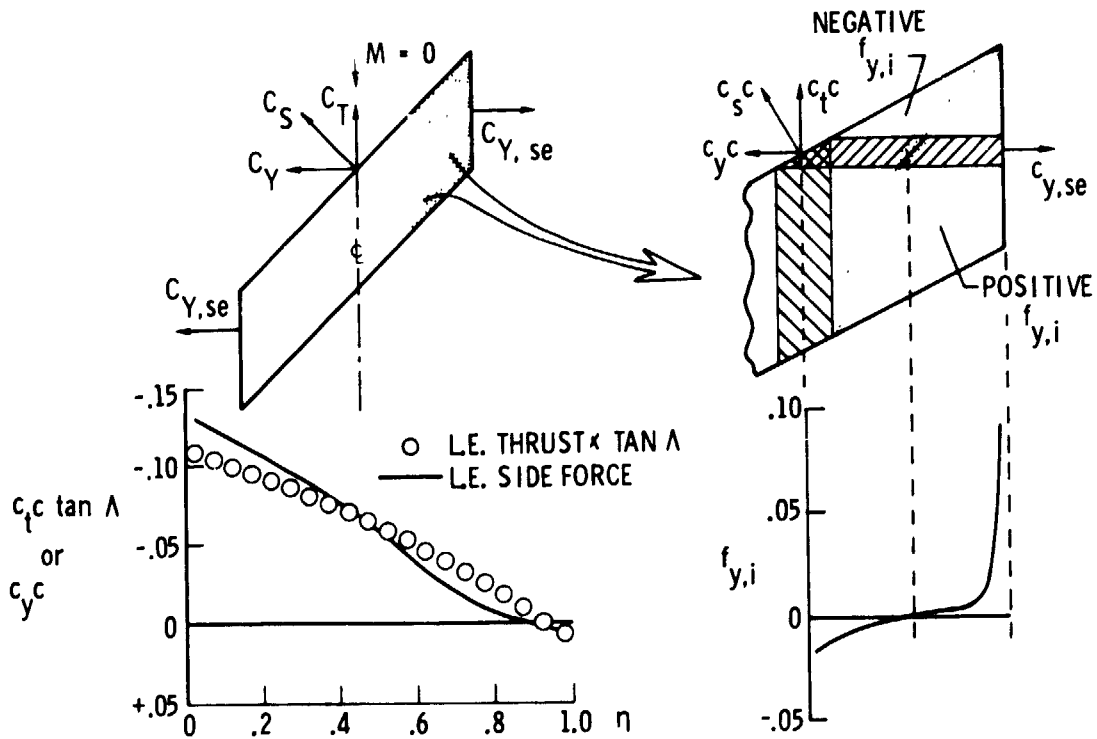
Figure 4.- Forward sweep effects on side-edge suction.
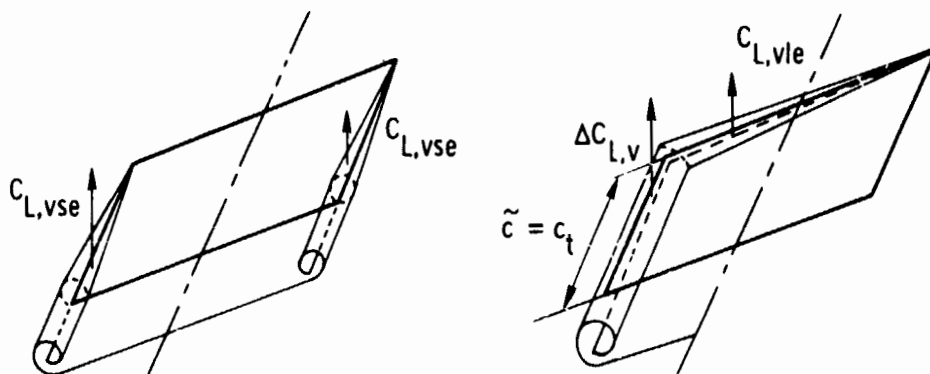
$$\bar{K}_{v,se} = \left(\frac{K_{v,le}}{b \, \sec \Lambda} \right) \tilde{c}$$

$$C_L = K_p \cos^2 \alpha \sin \alpha + (K_{v,le} + K_{v,se} + \bar{K}_{v,se}) \left| \sin \alpha \right| \sin \alpha \cos \alpha$$

Figure 5.- Concept of augmented vortex lift applied to a skewed wing.
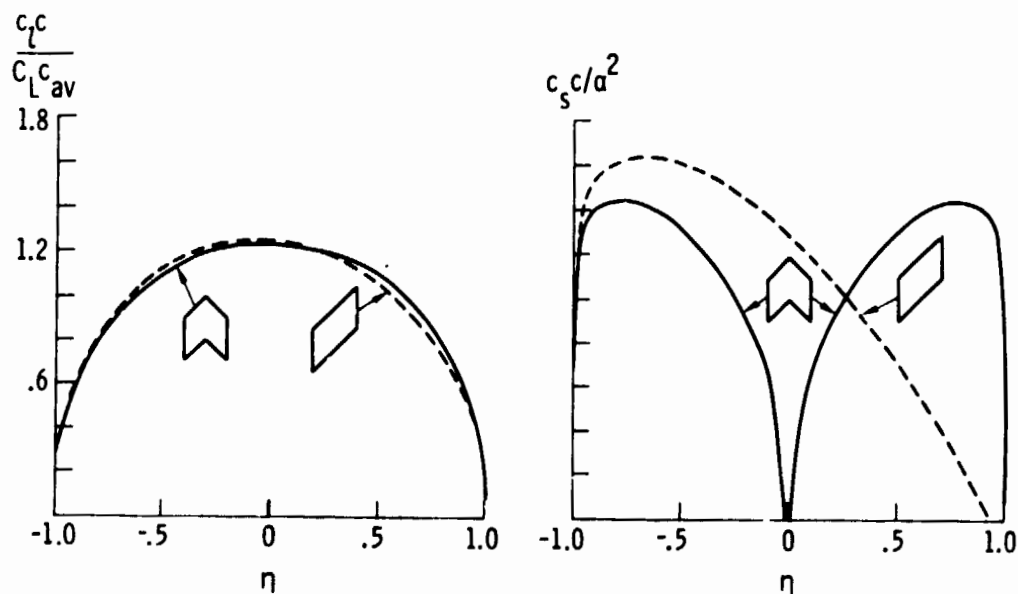
Figure 6.- Span load and section suction distributions on a swept and skewed wing. $\Lambda = 45°$; $A = 1$; $M = 0$.
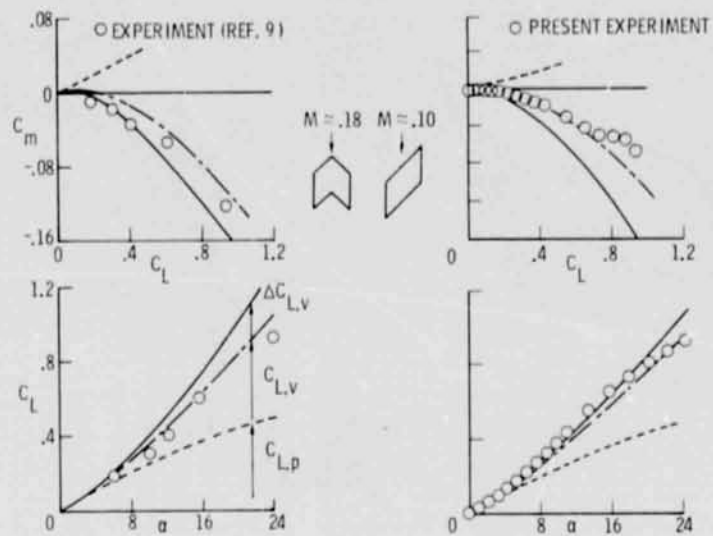
Figure 7.- Longitudinal characteristics of a swept and a skewed wing.
$\Lambda = 45$; $A = 1$.
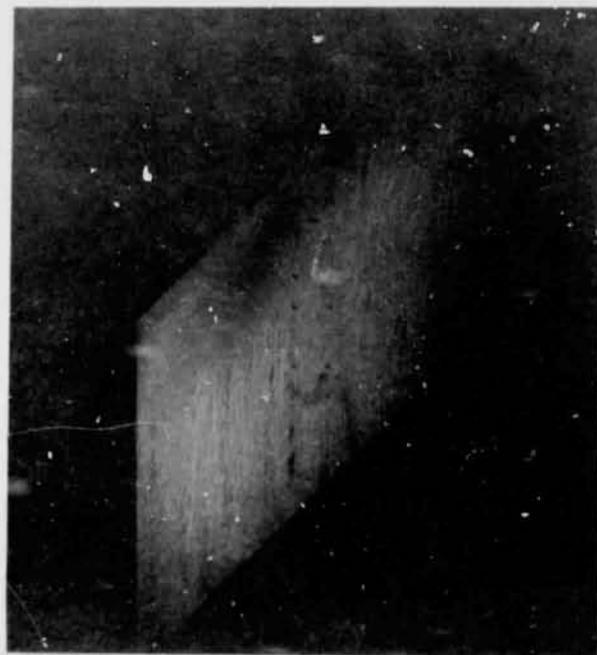
(a) $\Lambda = 45°$; $A = 1$; $\alpha = 5°$.

Figure 8.- Vortex flow on a skewed wing.
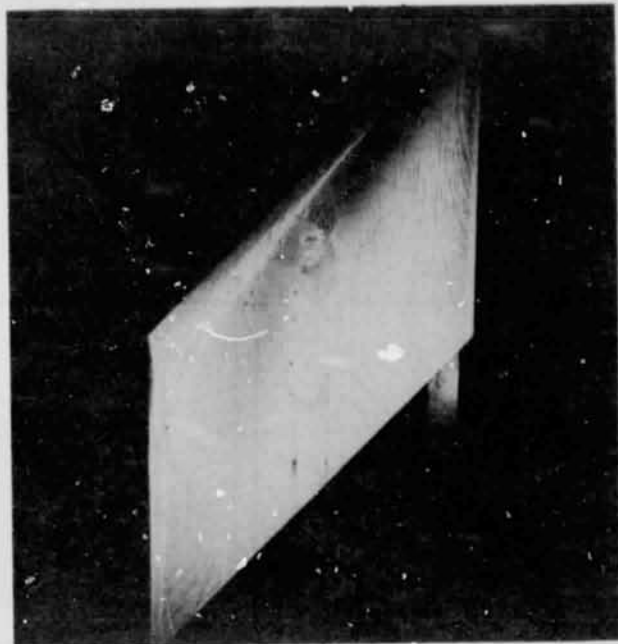
(b) $\Lambda = 45°$; $A = 1$; $\alpha = 10°$.
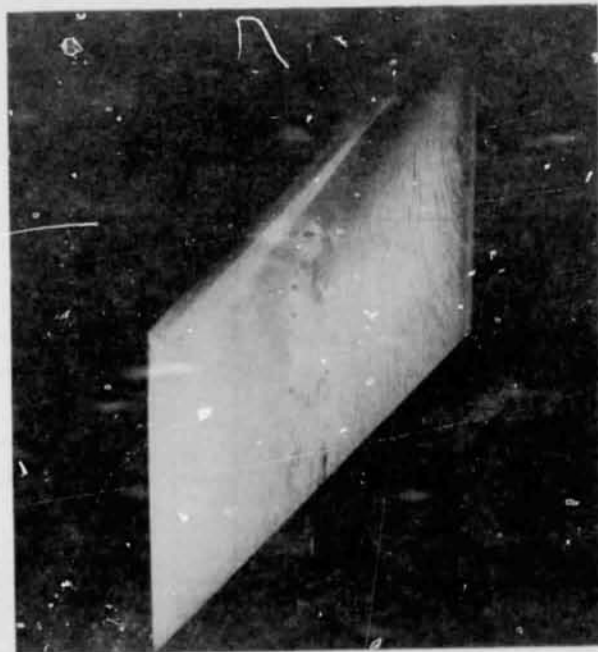
(c) $\Lambda = 45°$; $A = 1$; $\alpha = 15°$.

Figure 8.- Concluded.

233
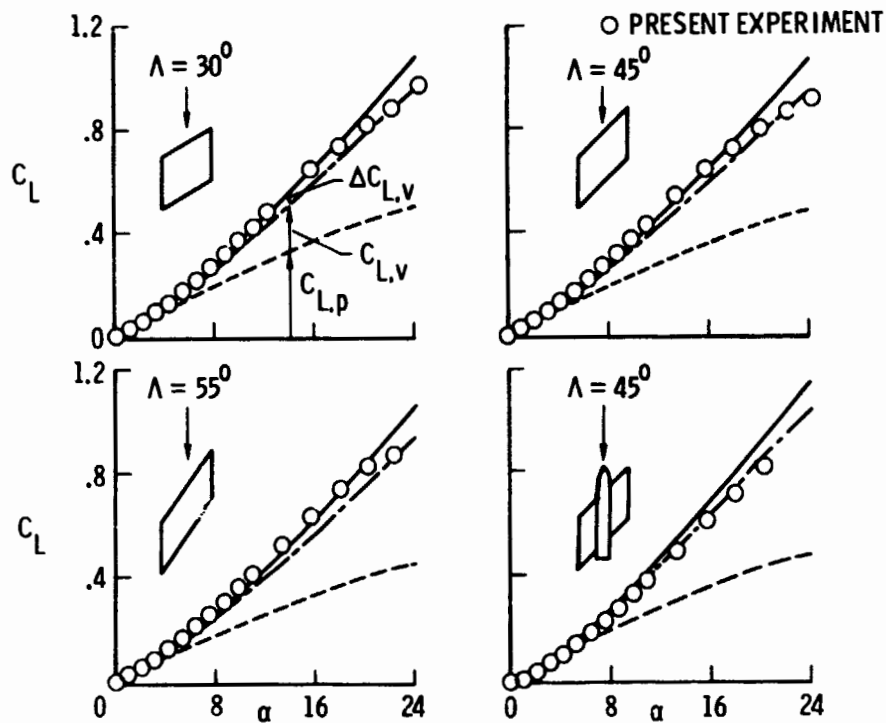
Figure 9.- Effect of leading-edge sweep on lift characteristics of several skewed wings. A = 1; M ≃ 0.10.
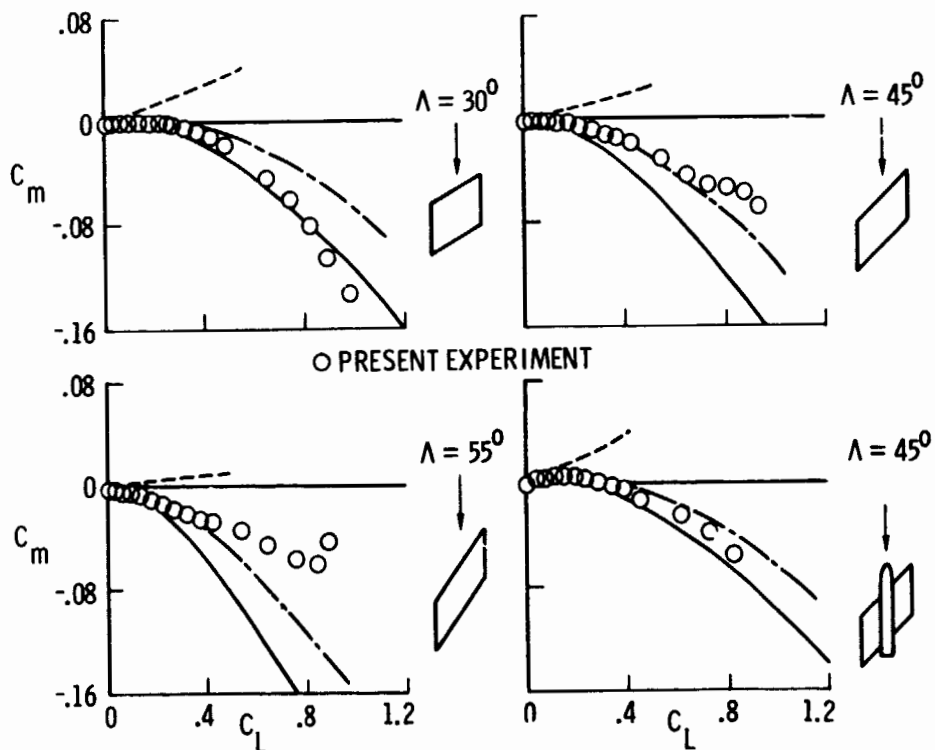
Figure 10.- Effect of leading-edge sweep on pitch characteristics of several skewed wings. A = 1; M ≃ 0.10.
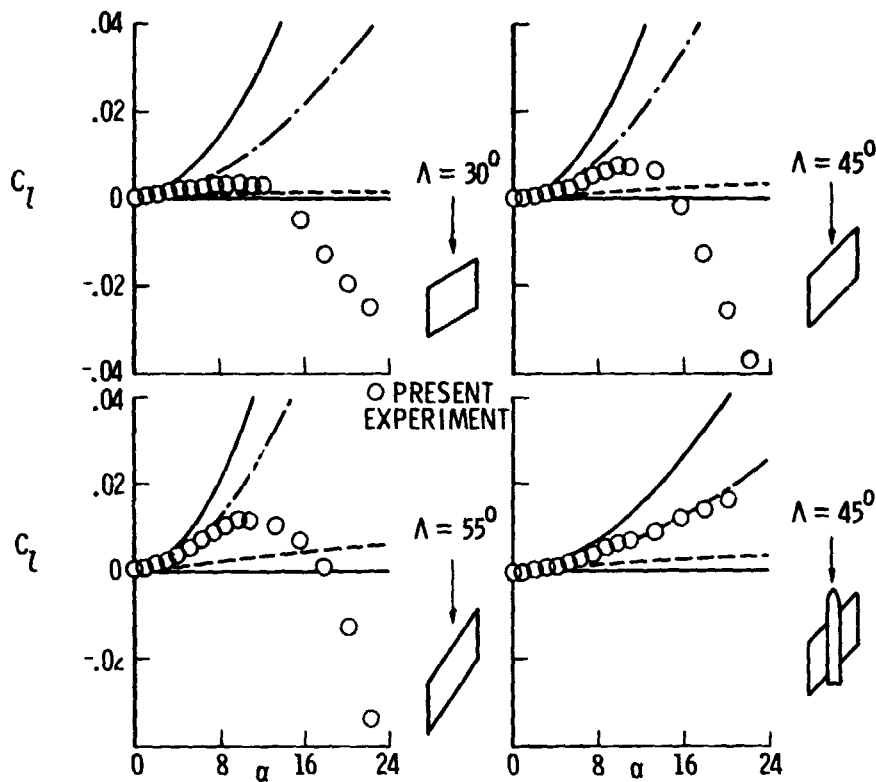
Figure 11.- Effect of leading-edge sweep on roll characteristics of several
skewed wings. A = 1; M ≈ 0.10.
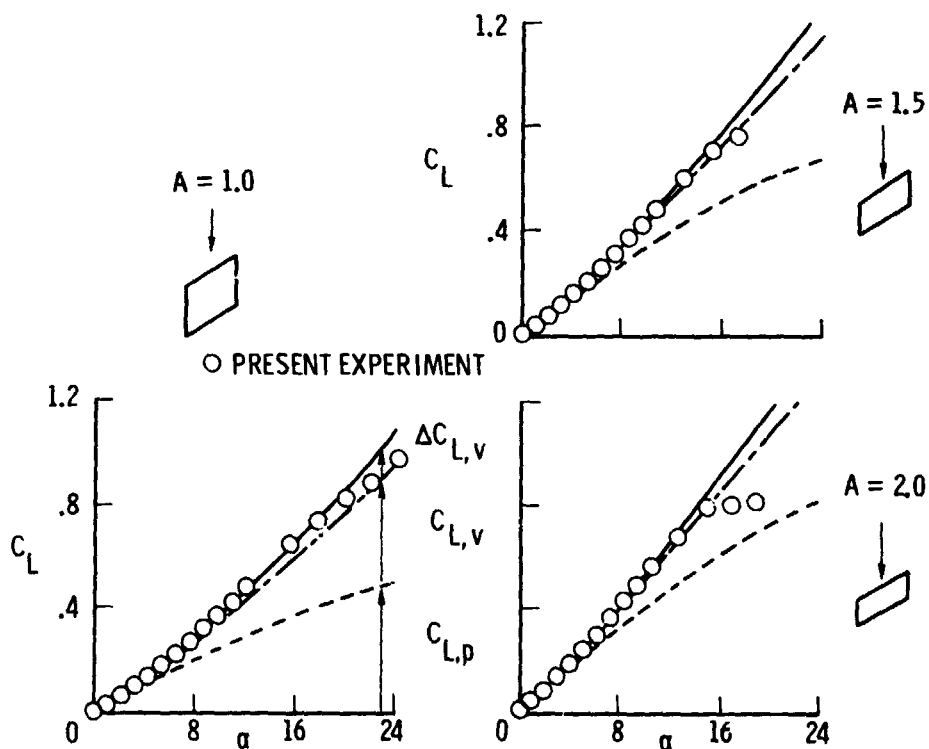
Figure 12.- Effect of aspect ratio on lift characteristics of several
skewed wings. Λ = 30°; M ≈ 0.10.
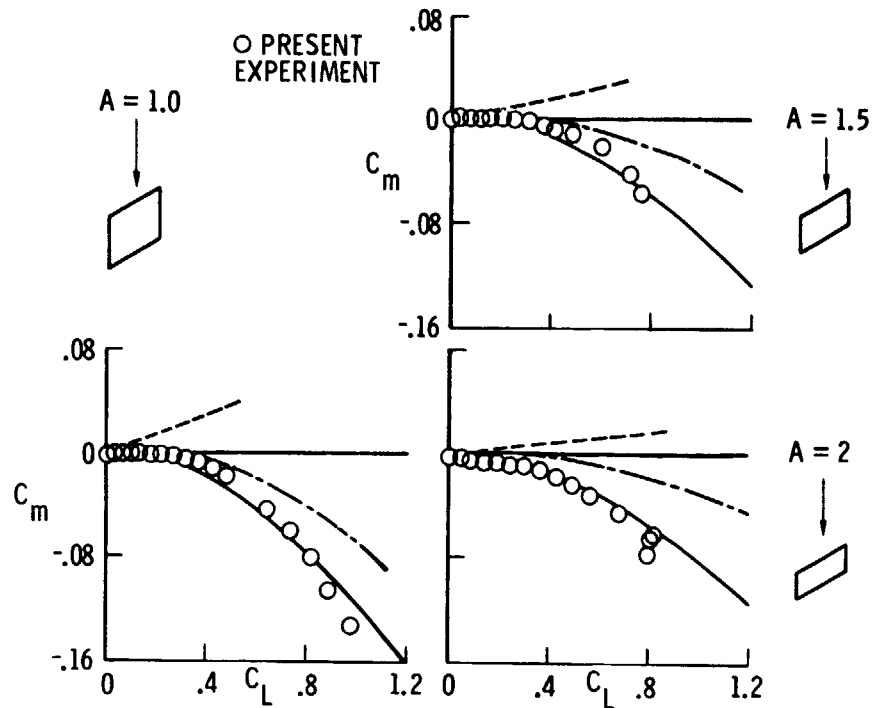
Figure 13.- Effect of aspect ratio on pitch characteristics of several skewed wings. $\Lambda = 30°$; $M \approx 0.10$.
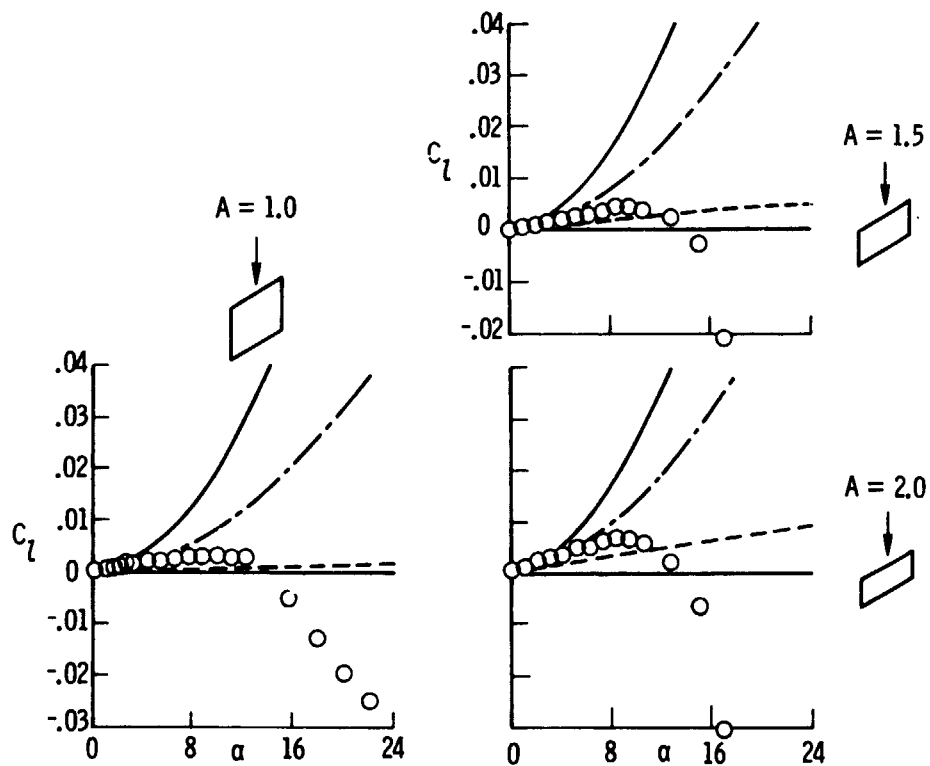
Figure 14.- Effect of aspect ratio on roll characteristics of several skewed wings. $\Lambda = 30°$; $M \approx 0.10$.

APPLICATION OF THE VORTEX-LATTICE TECHNIQUE TO THE ANALYSIS OF THIN WINGS WITH VORTEX SEPARATION AND THICK MULTI-ELEMENT WINGS

Charles W. Smith and Ishwar C. Bhateley
Fort Worth Division of General Dynamics

SUMMARY

Two techniques for extending the range of applicability of the basic vortex-lattice method are discussed. The first technique improves the computation of aerodynamic forces on thin, low-aspect-ratio wings of arbitrary planforms at subsonic Mach numbers by including the effects of leading-edge and tip vortex separation, characteristic of this type wing, through use of the well-known suction-analogy method of E. C. Polhamus. Comparisons with experimental data for a variety of planforms are presented.

The second technique consists of the use of the vortex-lattice method to predict pressure distributions over thick multi-element wings (wings with leading- and trailing-edge devices). A method of laying out the lattice is described which gives accurate pressures on the top and part of the bottom surface of the wing. Limited comparisons between the result predicted by this method, the conventional lattice arrangement method, experimental data, and 2-D potential flow analysis techniques are presented.

INTRODUCTION

Vortex-lattice methods are known to give reasonable results for thin wings of moderate to high aspect ratio. However, use of these methods to predict the aerodynamic forces on low-aspect-ratio wings has not been practical due to the significant vortex lift generated by these wings. The analysis and prediction of the nonlinearities associated with the vortex lift has received considerable attention in the literature for many years. Methods of solution based on complex mathematical models have generally failed. However, within the past several years, E. C. Polhamus of the NASA Langley Research Center has proposed and verified through comparison with experimental data an analytical method for sharp-leading-edge wings of zero taper ratio (reference 1). The

method is based on a leading-edge suction analogy proposed by Polhamus in reference 2. Extension of the suction analogy to plane rectangular rings has been accomplished by J. E. Lamar in reference 3. A method for calculating the lift, drag, and pitching moment of cambered, sharp-edged wings of arbitrary planform is presented here as a logical extension of the suction-analogy concept. A vortex-lattice program is utilized to provide the potential-flow force coefficients required by the suction-analogy concept and to provide the foundation for development of a computer procedure which incorporates the methods developed.

The accurate calculation of pressure distributions near the leading edge of thick multi-element wings is of considerable interest to the aerodynamicist. Vortex-lattice methods using the conventional vortex-lattice arrangement of distributing the vorticity on the camber surface yield pressure coefficients which approach infinity at the leading edge due to the singularity at the leading edge. An alternate method of laying out the lattice is described which circumvents this difficulty and gives reasonable predictions for the pressures on the top surface and a part of the bottom surface of wings.

SYMBOLS

Values are given in both SI and U.S. Customary Units. The measurements and calculations were made in U.S. Customary Units.

AR	aspect ratio
$\bar{c}$	mean aerodynamic chord, cm (in.)
C_A	axial-force coefficient
C_{D_L}	drag-due-to-lift coefficient
C_L	total lift coefficient ($C_{L_p} + C_{L_v}$)
C_{L_p}	zero-suction potential-flow lift coefficient
C_{L_v}	vortex-lift coefficient
C_m	total pitching-moment coefficient
C_{m_p}	zero-suction potential-flow pitching-moment coefficient for half-span wing

C_N	normal-force coefficient
C_{N_p}	potential-flow normal-force coefficient for half-span wing
C_P	pressure coefficient
C_S	potential-flow leading-edge suction coefficient for half-span wing
C_T	potential-flow leading-edge thrust coefficient for half-span wing
C_Y	potential-flow side-force coefficient for half-span wing
C_{Y_2}	potential-flow side-force-coefficient contribution from streamwise members of the vortex lattice for half-span wing
C_μ	nozzle momentum coefficient
K_p	potential-flow normal-force slope
$(K_p)_m$	potential-flow constant used in pitching-moment calculation
K_v	vortex-lift constant
$K_{v_{LE}}$	leading-edge vortex-lift constant used in lift calculation
$(K_{v_{LE}})_m$	leading-edge vortex-lift constant used in pitching-moment calculations
$K_{v_{TIP}}$	tip vortex-lift constant used in lift calculations
$(K_{v_{TIP}})_m$	tip vortex-lift constant used in pitching-moment calculations
M	Mach number
x_m	pitching-moment arm for tip vortex-lift contributions, cm (in.)
x_n	pitching-moment arm for leading-edge vortex-lift contributions, cm (in.)

x/c	nondimensionalized chordwise location
z_n	pitching-moment arm for leading-edge suction force, cm (in.)
α	angle of attack, degrees
λ	planform taper ratio
Λ	leading-edge sweep angle, degrees
$\emptyset$	slope of the mean line perpendicular to the planform leading edge, degrees

THEORETICAL DEVELOPMENT FOR THIN WINGS

The Polhamus Suction Analogy

The General Dynamics vortex-lattice method has been modified to incorporate the calculation of vortex separation effects.

The basis for this modification to the vortex-lattice procedure is the Polhamus leading-edge suction analogy, which is detailed in reference 2. Briefly, it is based on the postulate that the normal force on the upper surface is the same for attached vortex flow as the leading-edge suction force for attached potential flow. The total lift of sharp-edged, pointed-tip wings is given as

$$C_L = C_{L_p} + C_S \cos \alpha \tag{1}$$

where C_{L_p} is the potential-flow lift and C_S is the leading-edge suction force. Polhamus writes the lift in terms of K-factors, K_p and K_v, which are functions of planform and Mach number only. That is,

$$C_L = K_p \sin \alpha \cos^2 \alpha + K_{v_{LE}} \sin^2 \alpha \cos \alpha \tag{2}$$

where K_p is, by definition, the normal-force slope given by potential-flow theory,

$$K_p \equiv \frac{\partial C_{N_p}}{\partial \sin \alpha \cos \alpha} \tag{3}$$

and $K_{v_{LE}}$ is, by definition,

$$K_{v_{LE}} \equiv \frac{\partial C_S}{\partial \sin^2 \alpha} \tag{4}$$

J. E. Lamar extended the Polhamus concept to rectangular wings of low aspect ratio in work reported in reference 3. The equation is

$$C_L = C_{L_p} + C_S \cos \alpha + C_Y \cos \alpha \tag{5}$$

where C_Y is twice the potential-flow side force for the half-wing. In terms of K-factors,

$$C_L = K_p \sin \alpha \cos^2 \alpha + (K_{v_{LE}} + K_{v_{TIP}}) \sin^2 \alpha \cos \alpha$$

where, by definition,

$$K_{v_{TIP}} \equiv \frac{\partial C_Y}{\partial \sin^2 \alpha} \tag{6}$$

and K_p and $K_{v_{LE}}$ are given in equations (3) and (4).

Extension to Arbitrary
Flat-Plate Wings

The above equations have been extended (reference 4) to more complex planforms. For a trapezoidal planform, the finite tip effects are taken into account for defining the vortex-lift contribution as

$$C_{L_v} = \left[\frac{C_T}{\cos \Lambda} + C_Y - C_T \tan \Lambda \right] \cos \alpha \tag{7}$$

The above formulation recognizes that part of the total wing side force acts on the swept leading edge as part of the leading-edge suction vector ($C_T/\cos \Lambda$), and that the remainder ($C_Y - C_T \tan \Lambda$) acts on the wing tip, as shown in figure 1(a).

Generalization of the above result to wings of arbitrary planform results in the following equation for the lift:

$$C_L = C_{L_p} + \left[\sum_{n=1}^{N} \frac{C_{T_n}}{\cos \Lambda_n} + C_Y - \sum_{n=1}^{N} C_{T_n} \tan \Lambda_n \right] \cos \alpha \qquad (8)$$

The notation is illustrated in figure 1(b). In terms of K-factors, the total lift is given by

$$C_L = K_p \sin \alpha \cos^2 \alpha + (K_{v_{LE}} + K_{v_{TIP}}) \sin^2 \alpha \cos \alpha \qquad (9)$$

where

$$K_{v_{LE}} = \frac{\partial}{\partial \sin^2 \alpha} \left[\sum_{n=1}^{N} \frac{C_{T_n}}{\cos \Lambda_n} \right] \qquad (10)$$

and

$$K_{v_{TIP}} = \frac{\partial}{\partial \sin^2 \alpha} \left[C_Y - \sum_{n=1}^{N} C_{T_n} \tan \Lambda_n \right] \qquad (11)$$

The potential-flow in-plane force coefficients, C_T and C_Y, are those computed by any accurate lifting-surface theory. In this application, they are obtained from a vortex-lattice procedure. Compressibility effects are included through use of the Goethert transformation.

The zero-leading-edge-suction drag due to lift for sharp-edged, uncambered wings is defined by

$$C_{D_L} = C_L \tan \alpha \qquad (12)$$

where C_L is the total lift coefficient as given by equation (9).

Extension of the above formulations for the calculation of lift to the calculation of pitching moment logically follows. As in the lift case, the pitching moment is comprised of potential-

flow and vortex contributions. In general form, the resulting equation is

$$C_m = C_{m_p} + \frac{1}{c}\left[\sum_{n=1}^{N} (C_{T_n}/\cos\Lambda_n)(x_n) + \sum_{m=1}^{M}\left(\sum_{1}^{N+1} C_{Y_2}\right)_m (x_m)\right] \quad (13)$$

The notation is illustrated in figure 1(b). The potential-flow moment, C_{m_p}, is the moment resulting from the potential-flow normal forces on each member of the lattice.

The moment resulting from the vortex lift is comprised of a leading-edge and a tip component. To determine the leading-edge contribution, the leading-edge vortex lift, as determined by the suction analogy ($C_{T_n}/\cos\Lambda_n$), is assumed to act precisely at the leading edge of each chordwise strip. The moment is then the sum of the products of these forces and the moment arms (x_n), defined as the distance from the midpoint of the leading edge of each chordwise strip to the reference location. The leading-edge force includes a portion of the side force ($C_{T_n} \tan\Lambda_n$). The remainder of the side force, which is equal to the contribution of the streamwise members of the vortex lattice, is noted as

$$\left(\sum_{1}^{N+1} C_{Y_2}\right)_m$$

for each spanwise strip. The sum of this remainder constitutes the total tip vortex lift. Thus the tip-vortex-lift contribution to the moment is the sum of the products of these forces and the moment arms (x_m), defined as the distance from the midpoint of the tip of each spanwise strip to the reference location.

In terms of K-factors,

$$(K_p)_m \equiv \frac{\partial C_{m_p}}{\partial \sin\alpha \cos\alpha} \quad (14)$$

243

$$(K_{v_{LE}})_m \equiv \frac{\partial}{\partial \sin^2 \alpha} \left[\sum_{n=1}^{N} \frac{C_{T_n}}{\cos \Lambda_n} (x_n/\overline{c}) \right] \qquad (15)$$

and

$$(K_{v_{TIP}})_m \equiv \frac{\partial}{\partial \sin^2 \alpha} \left[\sum_{m=1}^{M} \left(\sum_{1}^{N+1} C_{Y_2} \right)_m (x_m/\overline{c}) \right] \qquad (16)$$

The total moment is given by

$$C_m = (K_p)_m \sin \alpha \cos \alpha + \left[(K_{v_{LE}})_m + (K_{v_{TIP}})_m \right] \sin^2 \alpha \qquad (17)$$

Extension to Cambered Wings

The basis for determining the force and moment coefficients for thin, cambered planforms is the hypothesis that the total suction force acts perpendicular to the slope of the mean line at the leading edge. This is a logical extension to the suction-analogy assumption that the suction force acts in the normal-force direction for flat-plate planforms. Thus for cambered planforms, contributions to both the normal force and the axial force (in the suction direction) are realized from the total suction force calculated by potential-flow theory.

The development that follows further assumes that the leading-edge vortex is positioned above the wing surface all along the wing span. Thus, extreme camber cases where the leading-edge vortex can be shed below the wing surface at low angle of attack and may even roll around the leading edge to the upper surface at some spanwise location are not allowed.

The general equation for lift as resolved from the normal, C_N, and axial, C_A, forces is

$$C_L = C_N \cos \alpha - C_A \sin \alpha \qquad (18)$$

244

Consistent with the current nomenclature, the total lift for the cambered planform (neglecting friction drag) then becomes

$$C_L = \left(C_{N_p} + \sum_{n=1}^{N} C_{T_n}\cos\phi_n/\cos\Lambda_n + C_Y - \sum_{n=1}^{N} C_{T_n}\tan\Lambda_n \right)\cos\alpha$$

$$+ \left(\sum_{n=1}^{N} C_{T_n}\sin\phi_n \right)\sin\alpha \qquad (19)$$

The angle ϕ is equal to the slope of the mean line perpendicular to the planform leading edge at the midpoint of the leading edge of each chordwise strip. Note that C_T is defined as a positive force in the upstream direction.

Similarly, the total drag due to lift (neglecting friction drag) is given by

$$C_{D_L} = C_N \sin\alpha + (C_A)_{\text{Suction}}\cos\alpha \qquad (20)$$

or, for the cambered planform,

$$C_{D_L} = \left(C_{N_p} + \sum_{n=1}^{N} C_{T_n}\cos\phi_n/\cos\Lambda_n + C_Y - \sum_{n=1}^{N} C_{T_n}\tan\Lambda_n \right)\sin\alpha$$

$$- \left(\sum_{n=1}^{N} C_{T_n}\sin\phi_n \right)\cos\alpha \qquad (21)$$

The pitching moment is determined in much the same manner as that described previously for the uncambered planform. An additional term is required to account for the moment contribution of the suction-force component in the axial-force direction. The moment arm, z_n, for this force is the vertical distance from the

reference to the midpoint of each chordwise segment. The re-
sulting equation is

$$C_m = C_{m_p} + \frac{1}{\bar{c}}\left[\sum_{n=1}^{N}(C_{T_n}\cos\phi_n/\cos\Lambda_n)(x_n) + \sum_{m=1}^{M}\left(\sum_{1}^{N+1}C_{Y_2}\right)_m(x_m)\right.$$

$$\left. + \sum_{n=1}^{N}(C_{T_n}\sin\phi_n)(z_n)\right] \tag{22}$$

where C_{m_p} is the potential-flow moment resulting from the
potential-flow normal forces only.

EVALUATION AND RESULTS FOR THIN WINGS

Verification of the aerodynamic coefficient calculations
for uncambered planforms has been accomplished through comparison
with test data for delta, arrow, diamond, double-delta, rectangular,
and ogee wings. Cambered wing calculations have been compared
with data for a moderately cambered delta planform.

Flat-Plate Wings

Data from reference 5 for delta and clipped delta planforms
of taper ratio 0.0 and 0.4 are presented in figures 2 and 3.
Results of the current method generally agree quite well with the
data. However, the test data for the delta wing begin to depart
significantly from the predictions when vortex breakdown reaches
the wing trailing edge. Reference 6 reports that vortex break-
down occurs at 14 degrees angle of attack for the wing of figure 2.
The delta wing (figure 2) exhibits little effect of vortex lift
on the pitching moment. Apparently the leading-edge vortex lift
is approximately equally distributed about the reference axis,
which is at the quarter-chord of the mean aerodynamic chord. On
the clipped delta wing of figure 3, the vortex-lift contribution
to the moment becomes much more pronounced. The potential-flow
results, considered alone, actually predict a moment in the wrong
direction.

246

Comparisons between the theoretical results and data from reference 7 for an aspect-ratio-2.0 rectangular wing are presented in figure 4. Even though the predicted total lift agrees well with the data up to an angle of attack of 12 degrees, the data depart from the predicted moment at 8 degrees. This is attributed to the progression of the vortex across the planform as angle of attack is increased.

Comparisons with reference 6 data for an 80-/65-degree double-delta planform and an ogee planform are presented in figures 5 and 6. Excellent agreement with the lift and drag predictions is apparent to the angle of attack for vortex breakdown. Good agreement with the pitching moment is obtained at the lower angles of attack, but the data break away from theory before the angle of attack for vortex breakdown is reached. This could be caused by a complex flow interaction resulting from the formation of multiple leading-edge vortices on this type planform.

Figures 7 and 8 present test-to-theory comparisons for two planforms (reference 3) which help investigate the ability of the method to evaluate the effects of trailing-edge sweep. The lift of the clipped arrow wing of figure 7 is predicted very well, however the lift of the clipped diamond wing of figure 8 is under-predicted. This is attributed to the induced lift effect of the shed vo tex on the additional surface area aft of the trailing edge of the diamond wing tip.

Test data from a model which employs spanwise blowing on the wing upper surface (reference 8) is presented in figure 9 for a 30-degree delta wing. Comparison with predictions illustrates the potential of this method as a tool for estimating the benefits which can be realized from vortex augmentation of this type. The ability of the spanwise blowing to extend the leading-edge vortex lift to higher angles of attack is most pronounced. Agreement with the predicted lift-curve slope is apparent to angles of attack much above the no-blowing vortex breakdown region. There is a blowing-induced camber effect which is, of course, not predicted by the theory.

Cambered Wings

The cambered-wing equations have been used to predict the characteristics of a moderately cambered (C_{ℓ_i} = 0.15) delta wing for which reference 5 presents test data. The comparisons of

lift, drag, and moment shown in figure 10 indicate good agreement.
The reference 5 data for the same wing with an uncambered section
have been included in figure 10 to illustrate the method's ability
to predict the incremental camber effect accurately. It is also
noteworthy that the incremental vortex-lift contribution due to
camber is very small. Thus, at least for small or moderate
amounts of camber, the potential flow increment due to camber
gives a good approximation for the incremental effects of camber.

VORTEX-LATTICE ARRANGEMENT FOR THICK WINGS

Vortex-lattice methods are best suited for the analysis of
thin wings with sharp leading edges which can be approximated
by camber surfaces. The predicted results in general for this
type of wing show good agreement with experimental data. How-
ever, when the vortex-lattice method is directly applied to thick
wings (including multi-element wings) the calculated results do
not agree with experimental data.

A typical conventional vortex-lattice layout for multi-
element wings is shown in figure 11. Each wing element is re-
presented by a network of horseshoe vortices lying on the camber
surface and trailing behind the surface. As can be seen from this
figure a bound vortex lies along the leading edge of each com-
ponent of the multi-element system. This causes infinite
velocities to be generated at the leading edge which produce very
large negative pressure coefficients (unrealistic) at points in
the immediate vicinity of the leading edge. This phenomenon is
acceptable for thin sharp-leading-edge wings but fails to give
acceptable predictions for thick wings. For example, the loads
calculated for the F-111 wing in the high-lift configuration at
angles of attack of 4 and 15 degrees are compared with experimental
data (reference 9) in figures 12(a) and 12(b), respectively. Large
discrepancies between experimental and theoretical loads are
evident near the leading edge of the wing and flaps.

A technique for laying out the lattice has been developed
at General Dynamics which greatly improves the pressure distri-
butions predicted by the vortex-lattice method for thick multi-
element wings. A typical example of this lattice is shown in
figure 13. Each element of the multi-element wing is represented
by a network of horseshoe vortices lying on and trailing behind
a surface which is composed of the top surface and part of the

bottom surface, and wraps around the leading edge of the wing. The surface on the bottom is extended downstream of the anticipated stagnation point. If the surface is extended to the trailing edge the problem becomes singular and meaningless results are obtained. No large differences in predicted pressures have been noted for variations in the extent of the vortex sheet on the lower surface.

A large-aspect-ratio, unswept, untapered wing having the same section as the F-111 wing section at BL 289 was analyzed using this wrapped lattice arrangement. The pressure distributions calculated at the centerline of this wing are shown in figures 14(a) and 14(b) for angles of attack of 4 and 12 degrees, respectively. The chordwise distribution of the vortex lines is also shown in these figures. Since the pressures at the centerline of a large-aspect-ratio wing are compatible with two-dimensional flow results they are compared with two-dimensional experimental data (reference 10) and two-dimensional theoretical results (reference 11) in these figures. The predictions show good agreement with both the experimental and theoretical results. The two-dimensional theoretical pressure distributions shown were obtained with a much denser chordwise distribution of points. A better prediction should be obtained with the vortex-lattice method if a denser chordwise portioning of the lattice is employed.

CONCLUDING REMARKS

A method has been formulated for determining the lift, zero-leading-edge-suction drag due to lift, and pitching moment of thin, sharp-edged, low-aspect-ratio wings with camber. This method utilizes a vortex-lattice procedure modified to include vortex-lift induced effects by including an extension of the Polhamus suction-analogy concept. Good agreement with experiment is obtained for simple highly swept planforms below the angle of attack at which vortex breakdown reaches the trailing edge of the wing and at somewhat lower angles of attack for wings with more complex flow patterns, such as double-delta and ogee planforms.

The method shows promise as a tool for evaluation of the potential of vortex augmentation systems.

To obtain more accurate predictions for the more complex planforms, it is necessary to include the effects of the

progression of the vortices away from the leading edge and tip of the planform and to include the vortex interactions on planforms which emanate multiple leading-edge vortices.

A method has also been developed for laying out the vortex lattice for thick multi-element wings which gives accurate pressure predictions on the top and part of the bottom surface of the wing. Comparison with experimental data and other theoretical methods substantiates the accuracy of the results.

REFERENCES

1. Poihamus, E. C.: Predictions of Vortex-Lift Characteristics by a Leading-Edge Suction Analogy. Journal of Aircraft, volume 8, no. 4, April 1971, pp. 193-199.

2. Polhamus, E. C.: A Concept of the Vortex Lift of Sharp-Edge Delta Wings Based on a Leading-Edge Suction Analogy. NASA TN D-3767, December 1966.

3. Lamar, J. E.: Extension of Leading-Edge-Suction Analogy to Wings with Separated Flow Around the Side Edges at Subsonic Speeds. NASA TR R-428, October 1974.

4. Bradley, R. G.; Smith, C. W.; and Bhateley, I. C.: Vortex-Lift Prediction for Complex Wing Planforms. Journal of Aircraft, volume 10, no. 6, June 1973, pp. 379-381.

5. Emerson, H. F.: Wind-Tunnel Investigation of the Effect of Clipping the Tips of Triangular Wings o' ifferent Thickness, Camber, and Aspect Ratio - Transonic Bum, Method. NACA TN 3671, June 1956.

6. Wentz, W. H., Jr.; and Kohlman, D. L.: Wind Tunnel Investigations of Vortex Breakdown on Slender Sharp-Edged Wings. NASA CR-98737, November 1968.

7. Nelson, W. H.; and McDevitt, J. B.: The Transonic Characteristics of 22 Rectangular, Symmetrical Wing Models of Varying Aspect Ratio and Thickness. NACA TN 3501, June 1955.

8. Bradley, R. G.; Wray, W. O.; Smith, C. W.: An Experimental Investigation of Leading-Edge Vortex Augmentation by Blowing. NASA CR-132415, 1 April 1974.

9. Goss, W. J.: Report of Fourth Series Wind Tunnel Tests of the 1/6-Scale F-111 Semi-Span Model. Grumman Aircraft Report GW.TT 184 (310-4), October 1963.

10. Goodwin, L. C.: Wind Tunnel Tests on a 2-D Model of a NACA 64A210 (Modified) Section with Various Leading and Trailing Edge Devices, Using the Canadair 2-D Blowing Walls, in the NAE 6x9-Ft Low-Speed Wind Tunnel, NAE Test 6x9/0/40, DIR Project All-Phase II, volumes 1, 2, and 3. Canadair Report ERR-CL-RAA-228-010, Sept. 1969.

11. Bhateley, I. C.: Investigation of Inviscid Incompressible Flow, Part IV: Potential Flow Analysis about Arbitrary Multiple Two-Dimensional Bodies by the Method of Distributed Singularities. General Dynamics Fort Worth Division Report ERR-FW-669, 31 March 1968.

(a) Trapezoidal.   (b) General.
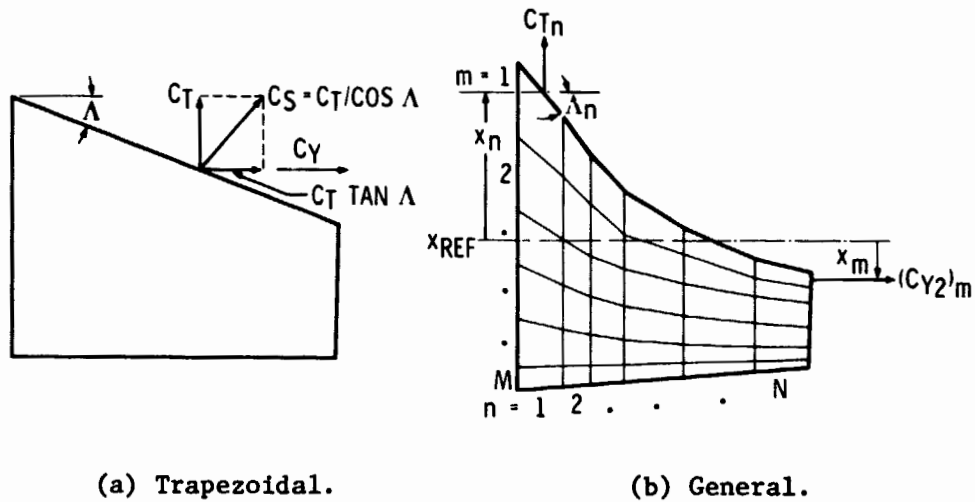
Figure 1.- Potential-flow force coefficients from the
vortex-lattice procedure.

M = 0.60

o   TEST DATA, 63A002 SECTION (REF. 5)
--- POTENTIAL
— POTENTIAL + VORTEX

VORTEX
BREAKDOWN
(REF. 6)
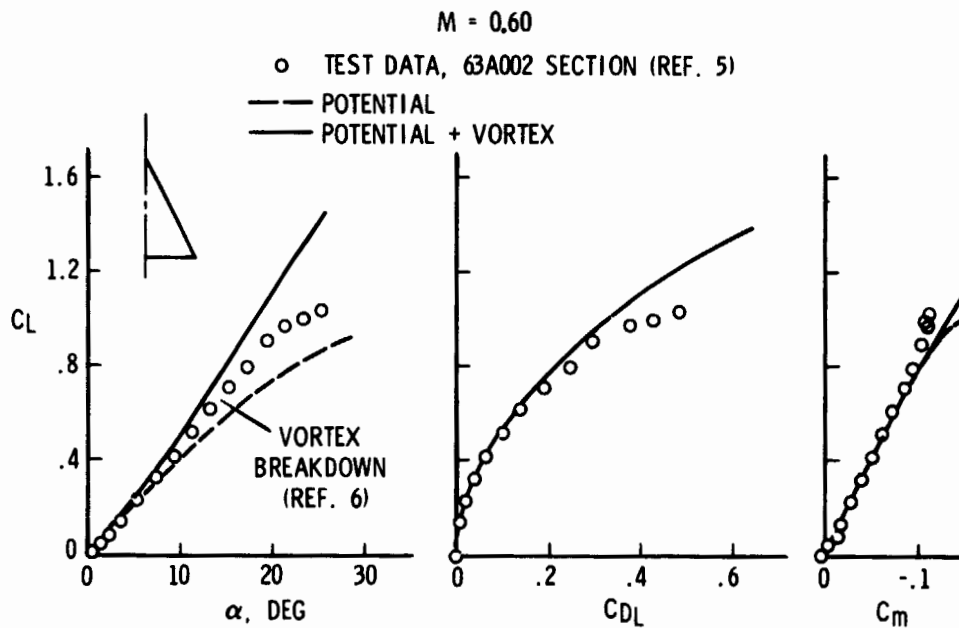
Figure 2.- Longitudinal aerodynamic characteristics
of a delta wing with $\Lambda = 63^{\circ}$.

M = 0.60

○ TEST DATA, 63A002 SECTION (REF. 5)
--- POTENTIAL
— POTENTIAL + VORTEX
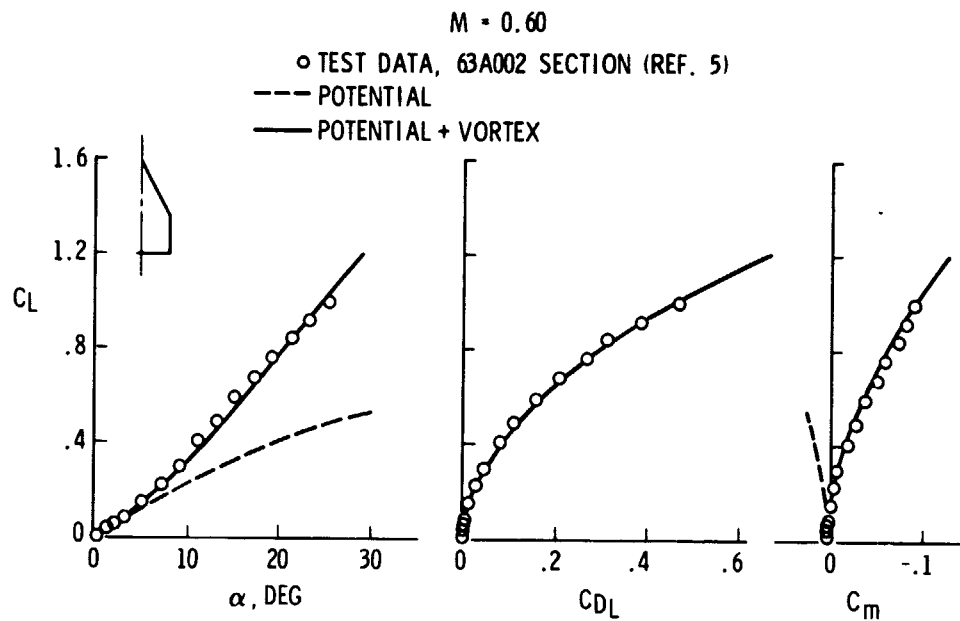
Figure 3.- Longitudinal aerodynamic characteristics of a
clipped delta wing with $\Lambda = 63^\circ$ and $\lambda = 0.4$.

M = 0.40

○ TEST DATA, 63A002 SECTION (REF. 7)
-- POTENTIAL
— POTENTIAL + VORTEX
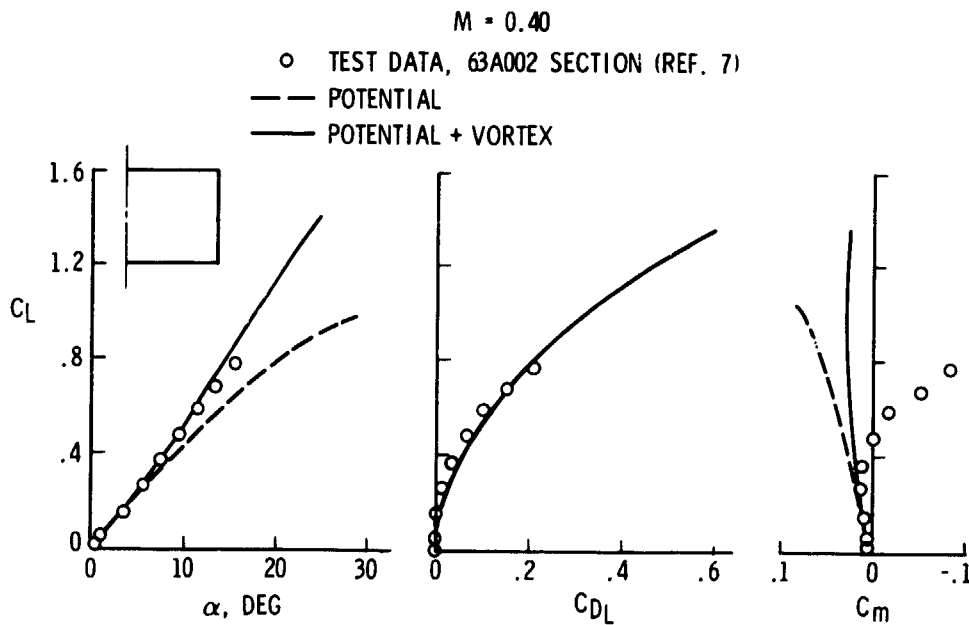
Figure 4.- Longitudinal aerodynamic characteristics of a
rectangular wing with AR = 2.0.
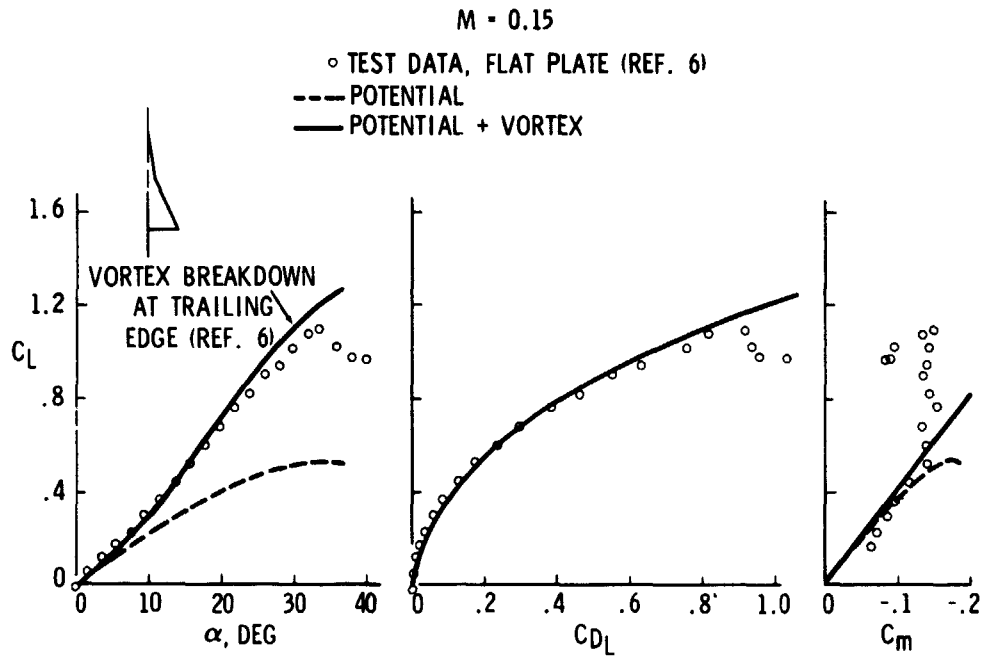
Figure 5.- Longitudinal aerodynamic characteristics of a
double-delta wing with $\Lambda = 80^{\circ}/65^{\circ}$.
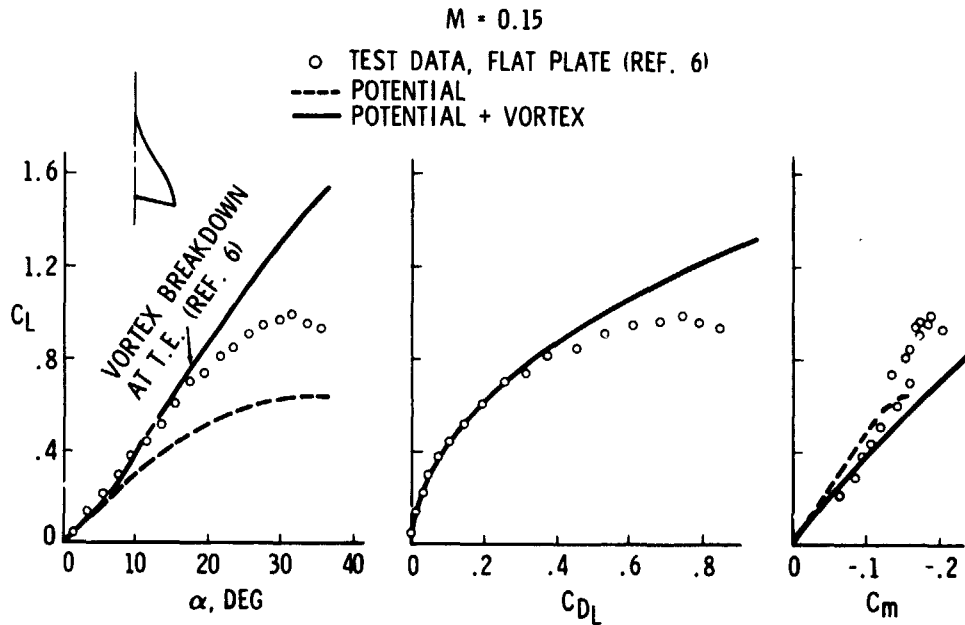
Figure 6.- Longitudinal aerodynamic characteristics of
an ogee wing with AR = 1.7.

M = 0.2

○ TEST DATA, FLAT PLATE (REF. 3)
--- POTENTIAL
— POTENTIAL + VORTEX
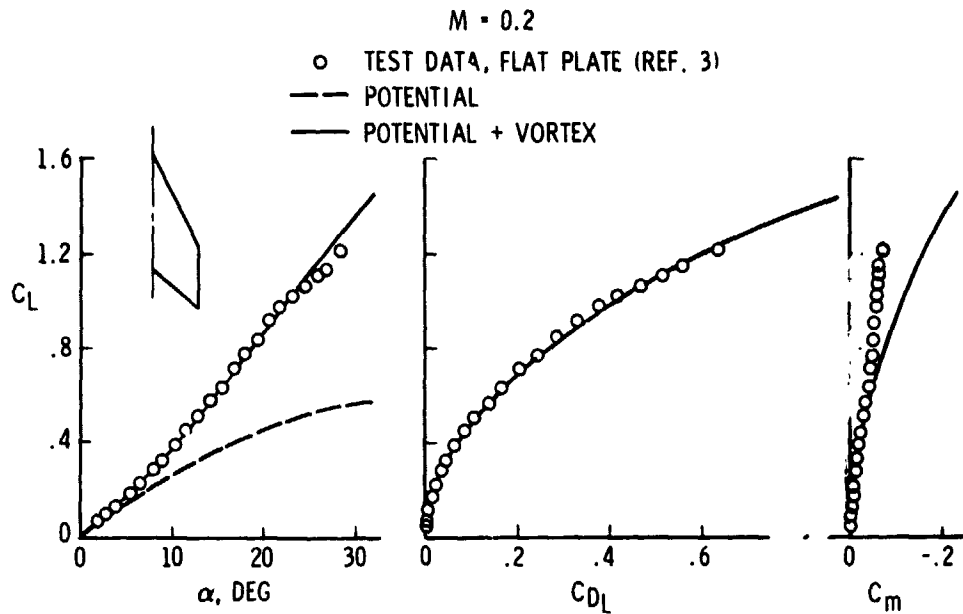
Figure 7.- Longitudinal aerodynamic characteris.ics of a
clipped arrow wing with $\Lambda = 63^{\circ}$.

M = 0.2

○ TEST DATA, FLAT PLATE (REF.3)
---- POTENTIAL
— POTENTIAL + VORTEX
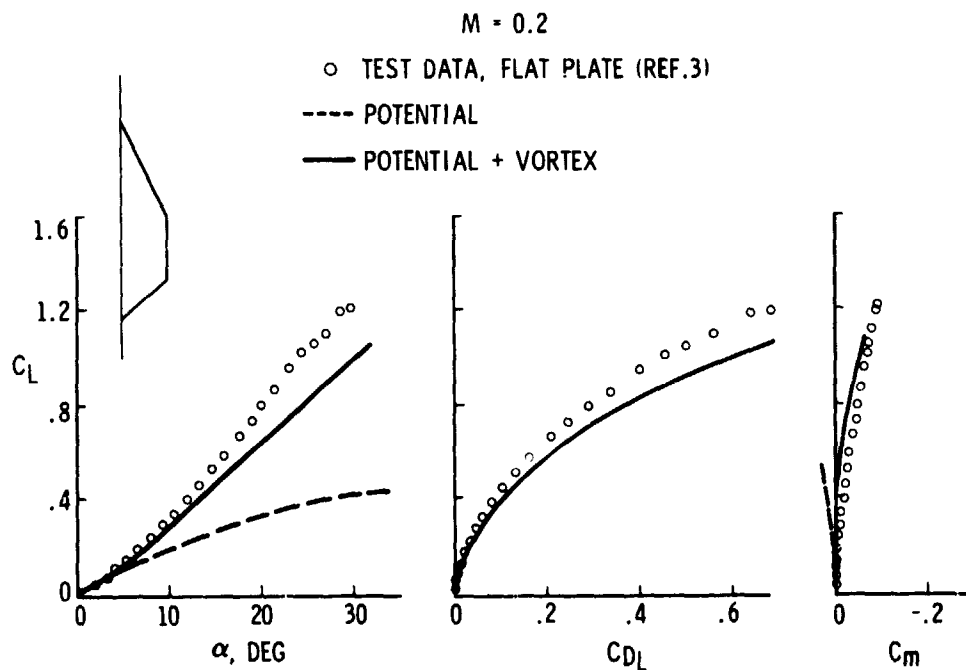
Figure 8.- Longitudinal aerodynamic characteristics of a
clipped diamond wing with $\Lambda = 63^{\circ}$.

255
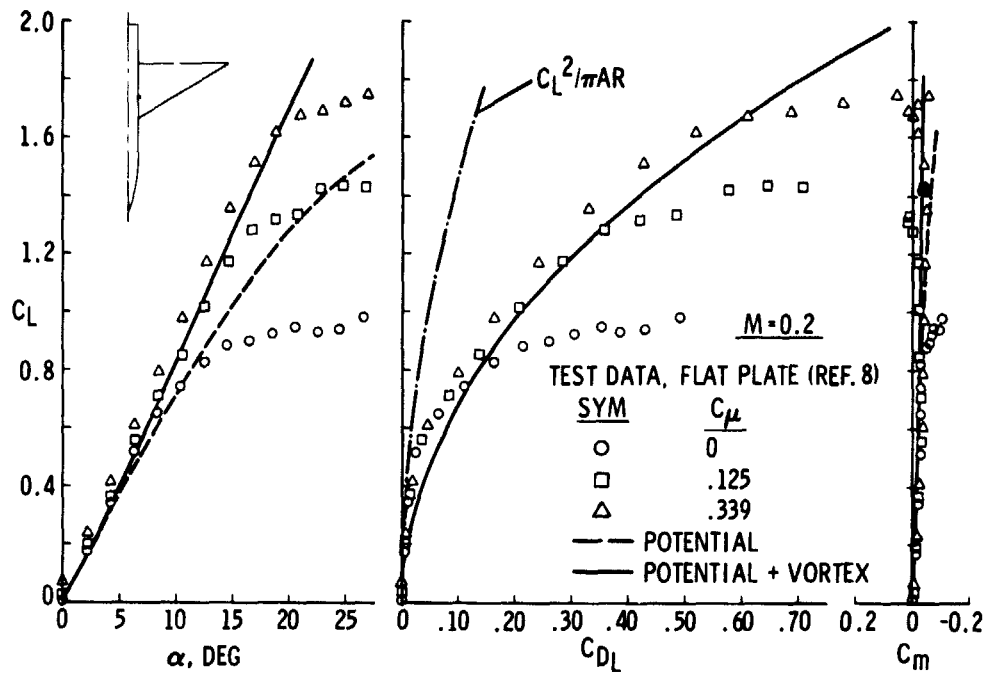
Figure 9.- Longitudinal aerodynamic characteristics of a
delta wing with $\Lambda = 30^\circ$ and spanwise blowing.

M = 0.6
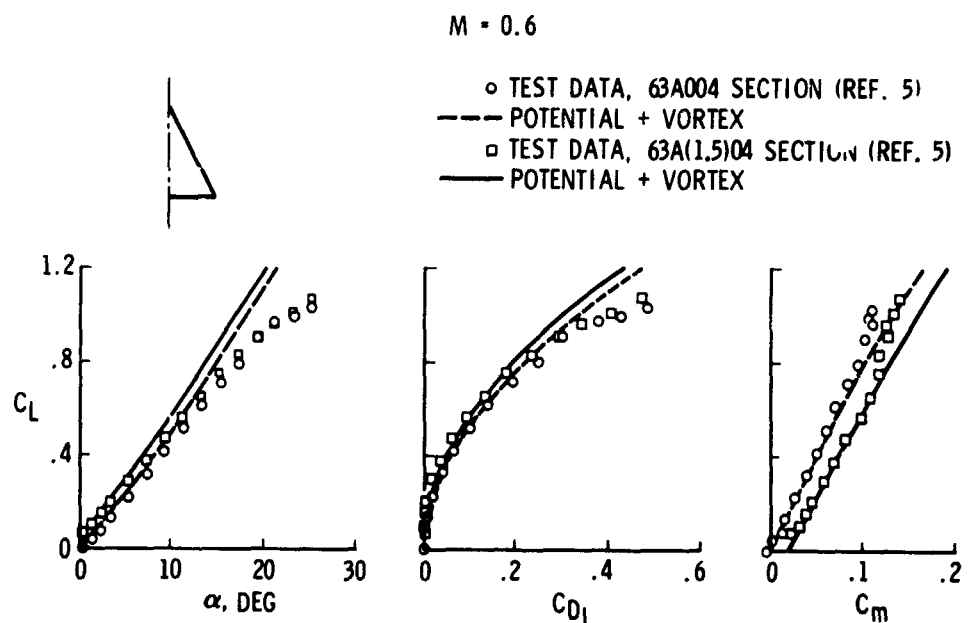
Figure 10.- Effect of camber on the longitudinal aerodynamic
characteristics of a delta wing with $\Lambda = 63^\circ$.
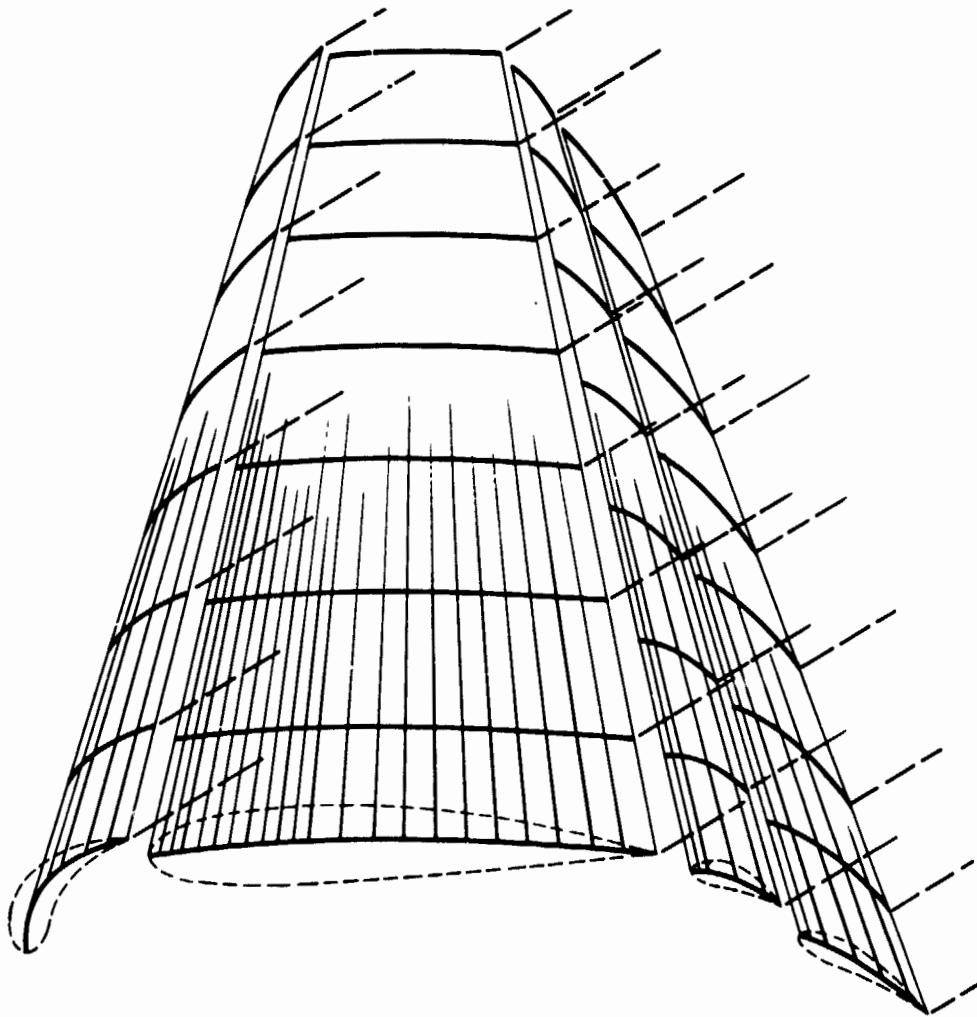
Figure 11.- Conventional vortex-lattice arrangement
on a thick multi-element wing.

(a) $\alpha = 4^o$.

(b) $\alpha = 15^o$.
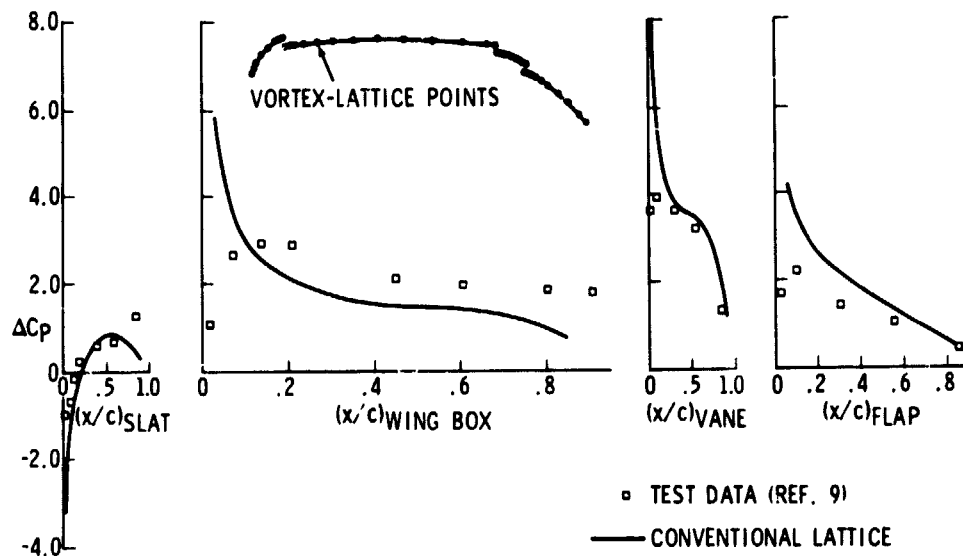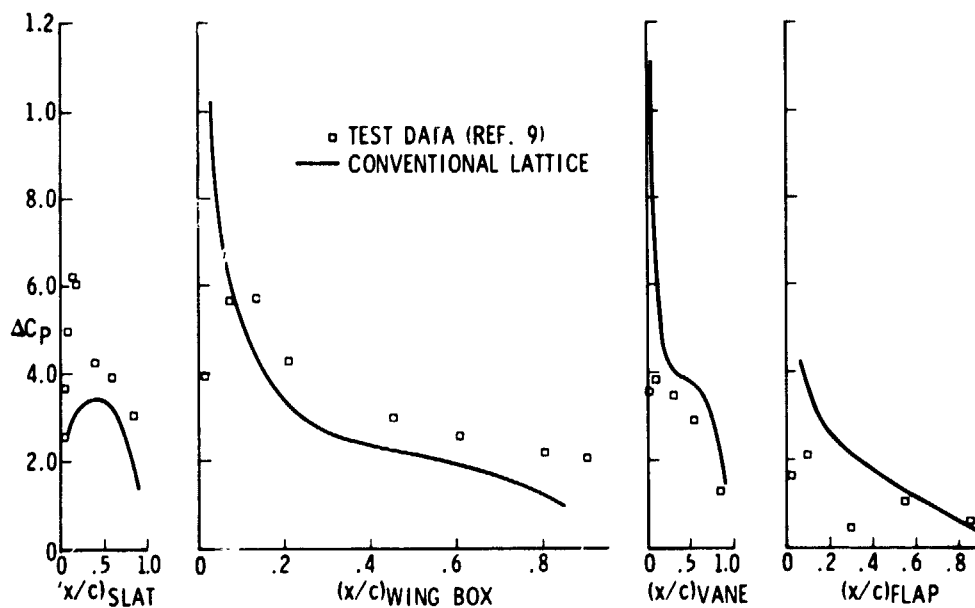
Figure 12.– Conventional vortex-lattice results compared with
experimental pressure data on a thick multi-element wing.
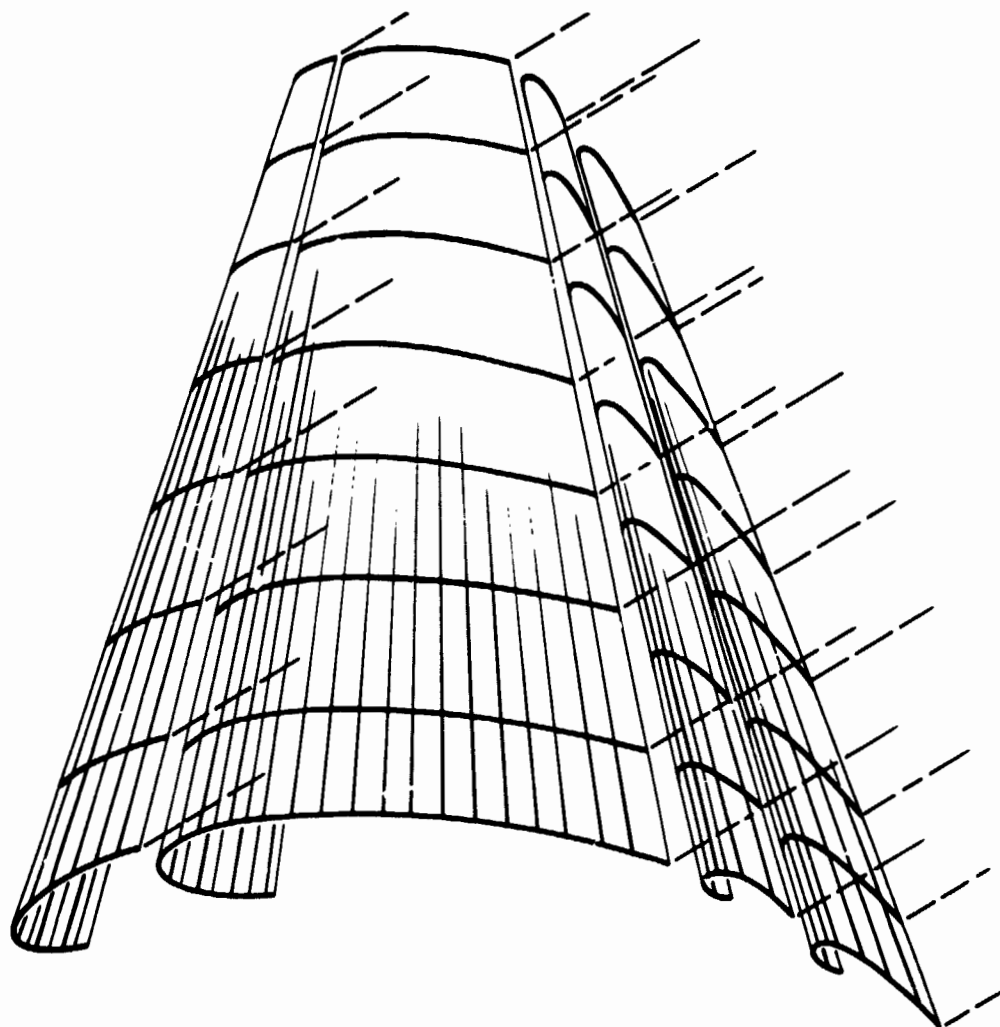
Figure 13.- Wrapped vortex-lattice arrangement on a
thick multi-element wing.

VORTEX-LATTICE POINTS

○□ TEST DATA (M = 0.2) (REF. 10)
—— 2-D POTENTIAL-FLOW THEORY
(INCOMPRESSIBLE) (REF. 11)
---- WRAPPED LATTICE METHOD
(INCOMPRESSIBLE)
(2-D SIMULATION)

(a) α = 4°.

○□ TEST DATA (M = 0.2) (REF. 10)
—— 2-D POTENTIAL-FLOW THEORY (INCOMPRESSIBLE) (REF. 11)
----- WRAPPED LATTICE METHOD (INCOMPRESSIBLE)
(2-D SIMULATION)

(b) α = 12°.
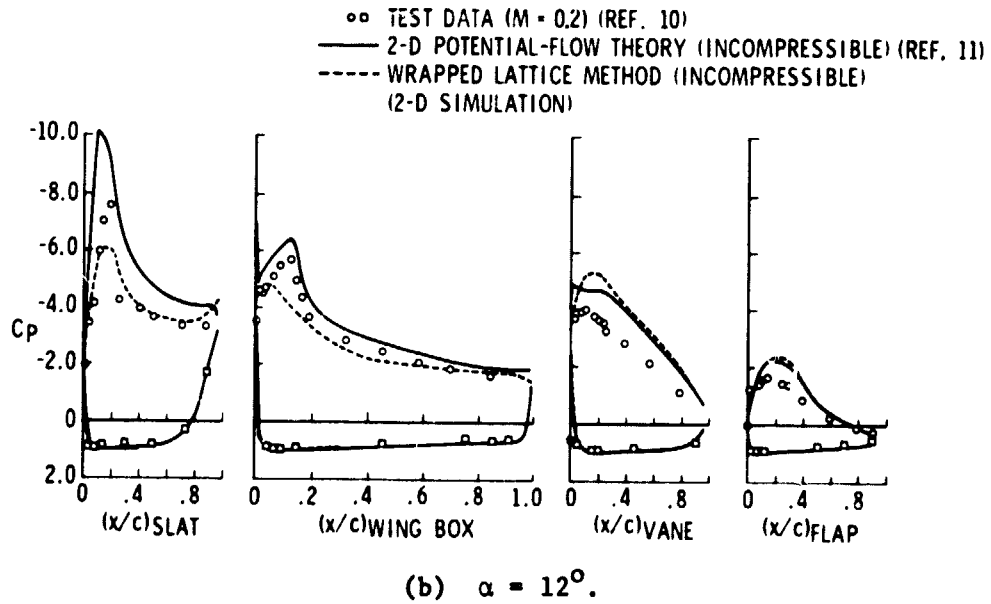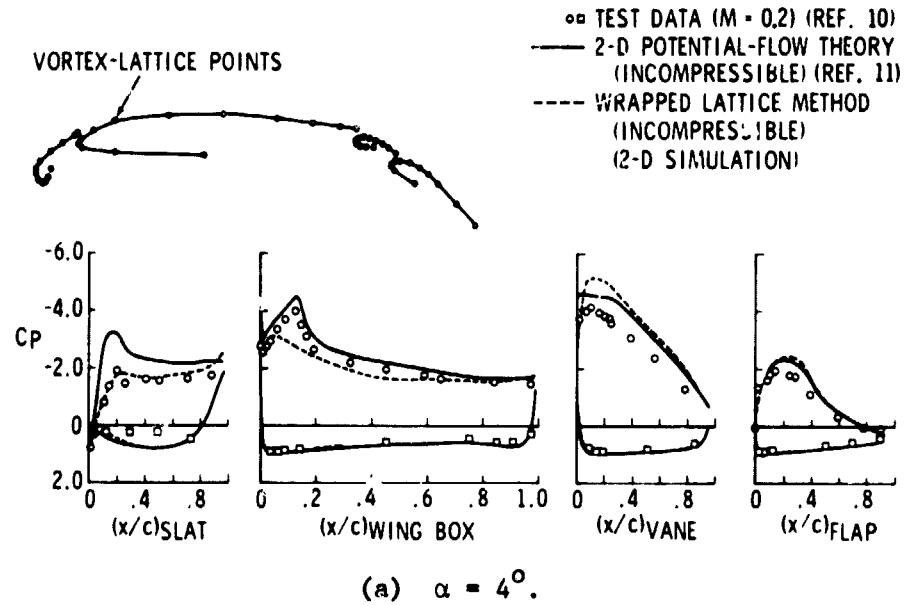
Figure 14.- Wrapped vortex-lattice results compared with experimental pressure data on a thick multi-element wing.

COMPARISON OF VORTEX LATTICE PREDICTED FORCES WITH

WIND TUNNEL EXPERIMENTS FOR THE F-4E(CCV) AIRPLANE

WITH A CLOSELY COUPLED CANARD

Lloyd W. Gross

McDonnell Aircraft Company

SUMMARY

The McDonnell Douglas F-4E (CCV) wind tunnel model with closely coupled canard control surfaces was analyzed by means of a version of a Vortex Lattice program that included the effects of nonlinear leading edge or side edge vortex lift on as many as four individual planforms. The results were compared with experimental data from wind tunnel tests of a 5-percent scale model tested at a Mach number M = 0.6. The comparison was facilitated by drawing the respective lift or thrust force vectors on the lift vs drag polar diagram. It indicated that nonlinear vortex lift developed on the side edges due to tip vortices, but did not appear to develop on the leading edges within the range of angles of attack that were studied. Instead, substantial leading edge thrust was developed on the lifting surfaces.

A configuration buildup illustrated the mutual interference between the wing and control surfaces. The effect of adding a lifting surface behind existing surfaces is to increase the loading on the forward surfaces. Similarly, adding a forward surface decreases the load on the following surfaces. On the configuration studied, addition of the wing increased the loading on the canard, but the additional load on the canard due to adding the stabilator was small. The effect of the wing on the stabilator was to reduce the static stability contribution of the stabilator. Then, when the canard was added, the stabilator suffered an additional loss of static stability contribution, in contrast to the effect on the canard of adding the stabilator.

This study verified the usefulness of the Vortex Lattice program as a predictive tool. It pointed up the need for a version capable of including vertical panels so that side forces and yawing moments can be included. Also, the ability to add independent planforms outboard of existing planforms, with a proper carry-over of lift, would facilitate the study of "all-movable" control surfaces.

INTRODUCTION

The McDonnell Aircraft Company has been using the Vortex Lattice program developed by Margason and Lamar of the NASA Langley Research Center (Reference 1) for the design and analysis of aircraft configurations having

single or multiple planforms with good results (unpublished studies similar to those of Reference 2). However, the available program was an early version of limited capability. The advent of versions having enhanced capability increases the potential for the use of the method as long as rules can be established to define the applicable ranges of the pertinent parameters. The version that currently has been made available by NASA (LRC Program No. A4737) includes the prediction of nonlinear leading edge and side edge vortex lift detailed in Reference 3 and has provision for as many as four planforms which can be arranged asymmetrically. This version of the Vortex Lattice program was developed by James Luckring of the NASA Langley Research Center.

A method of airplane control that is receiving new emphasis is the use of canards or control surfaces forward of the main lifting surface. This form of control has been made attractive by advances in active control technology that allow reduced or negative static stability. Also, it has been determined that the interference between the wing and canard is such that direct lift control and direct side force control can be achieved (Reference 4). These ideas have been explored by many agencies, among which are a series of wind tunnel tests conducted as part of the USAF Flight Dynamics Laboratory Fighter Control Configured Vehicle (CCV) programs. Various horizontal and vertical canard planforms were tested on several models of the McDonnell Douglas YF-4E airplane (e.g., Reference 5). The close-coupled, fully operable horizontal canards then were test-flown on an YF-4E under the MCAIR-sponsored Precision Aircraft Control Technology (PACT) program. These tests verified the use of canards for maneuverability enhancement and additional degrees of freedom of the flight path.

The use of canards on the YF-4E (PACT) airplane generated an interest in predicting all of their effects. The Vortex Lattice program has been shown to be useful in the prediction of the wing-canard interference (Ref. 2), but it had been limited by the restriction to two planforms. Once the four-planform version of the program became available, a more complex configuration could be studied. In particular, it was of interest to determine how well the Vortex Lattice program predicted the multiple lifting surface interactions and to what extent the various elements generated nonlinear vortex lift. Direct side force control could not be studied since there was no provision for vertical paneling. For a study of the longitudinal forces and moments, the wind tunnel model of Reference 5 was analyzed in order to provide a comparison with the experimental data. In addition to the analysis of the specific configurations for which experimental data was available, a complete configuration buildup was made to give an indication of the interference that existed between the components of the configuration.

SYMBOLS

b   wing span

c   wing or control surface chord

c_ℓ wing or control surface section lift coefficient

C_D total drag coefficient

C_{D_o} total drag coefficient at zero degrees angle of attack

C_L total lift coefficient

C_{L_o} total lift coefficient at zero degrees angle of attack

C_M total moment coefficient based on mean aerodynamic chord

C_N total normal force coefficient

C_{N_p} total normal force coefficient due to potential flow normal force on deflected control surface

C_{N_s} total normal force coefficient due to nonlinear leading edge thrust of deflected control surface

C_{N_r} total normal force coefficient due to nonlinear leading edge vortex lift of deflected control surface

C_S total leading edge suction force coefficient

C_T total leading edge thrust coefficient

C_{T_p} total leading edge thrust coefficient due to potential flow normal force on deflected control surface

C_{T_s} total leading edge thrust coefficient due to leading edge thrust of deflected control surface

C_{T_r} total leading edge thrust coefficient due to nonlinear vortex lift of deflected control surface

C_v total vortex force coefficient (Polhamus Effect)

C_Y total side force coefficient rotated to normal force direction (Polhamus Effect)

K_c constant

K_p kernel of potential flow normal force (defined in reference 3)

K_{p_a} kernel of potential flow normal force for undeflected portion of planform

K_{p_b} kernel of potential flow normal force for deflected control surface

$K_{V,LE}$	kernel of nonlinear leading edge suction force (defined in reference 3)
$K_{V,SE}$	kernel of nonlinear side edge thrust (defined in reference 3)
K_{V,LE_b}, K_{V,SE_b}	kernels of nonlinear forces for deflected control surface
MAC	mean aerodynamic chord
y	distance from aircraft centerline in wingtip direction
α	angle of attack
δ	control surface deflection
δ_c	canard deflection
δ_r	control surface deflection including rotation for Polhamus Effect

MODEL CONFIGURATION

The YF-4E (PACT) is equipped with a 1.86 m^2 auxiliary control surface and related fairing located just aft of and above the engine inlet on each side (Figure 1). The canard is an active control surface with the associated actuators and electronics. The wing includes leading edge slats on both inboard and outboard panels. The wind tunnel model, against which the analysis was checked, is of 5-percent scale and also includes the leading edge slats. The model was tested over a range of Mach numbers from M = 0.6 to M = 1.98, although the analysis is resticted to a Mach number M = 0.6. The configurations that were tested include the basic airplane, the basic airplane without stabilacor and the basic airplane with horizontal canard. The model was not tested with all of the configurations that normally would make up a full configuration buildup. In particular, the configuration with canard and wing but with the stabilator removed was not tested. Also, the design of this model precluded the removal of the wings.

The planform configurations used to represent the aircraft model are shown as Figure 2. The aft fuselage and stabilator configuration was changed from that of the model in order to keep the stabilator effective, but no attempt was made to determine whether this configuration change was necessary to match experiment. A list of the configurations that were analyzed is given as Table 1. The configurations for which experimental data are available also are noted.

RESULTS AND DISCUSSION

Control Surfaces Undeflected

The results of the analysis are compared with experiment in Figures 3 and 4. These figures show the usual presentation of the lift coefficient versus angle of attack and moment coefficient versus lift coefficient in Figures 3(a) through 3(c) for the three configurations for which experimental data are available. The lift coefficient versus drag coefficient polars are compared with experiment for these configurations in Figures 4(a) through 4(c). The three curves shown in each figure represent the end points of the force vectors identifiable by potential flow theory. The first curve is the sum of the lift and induced drag forces due to integration of the incremental vortex forces induced at right angles to the vortex lattice (potential flow normal forces). The second is the combination of the potential flow normal force and the non-linear thrust force induced in the direction of the vortex lattice (leading edge suction or thrust). The third is the combination of the potential flow normal force and the nonlinear forces normal to the vortex lattice induced by the presence of vorticity in the flow field near a sharp leading or side edge (vortex force). The magnitudes of the vortex forces are found by rotating the leading edge suction force or side edge force through ninety degrees (Polhamus Effect, Reference 6).

Conclusions might be drawn from Figures 3 and 4 but it is difficult to determine what percentage of leading edge thrust or vortex lift has been achieved. This becomes more obvious if the forces are drawn in vectorial form as in Figures 5(a) through 5(c). In this case the scales are not distorted as they are in Figure 4 so that the angular relationships can be appreciated. Since the drag direction is coincident with the freestream direction, the potential flow normal force is inclined to the lift force direction by the angle of attack. This vector is not drawn in order to reduce the number of lines but it locates the origin of the subsequent vectors. The side force vector is directed normal to the plane of the paper but appears in the direction of the potential flow normal force when rotated by the presence of the tip vortex. The leading edge suction force and the component of this vector in the thrust direction are at right angles to the potential flow normal force. The Polhamus Effect is illustrated by rotating the leading edge suction force to lie in the direction of the normal force.

The three examples for which experimental comparisons are available have had their force vectors for the midrange of angles of attack combined as Figure 6. It can be seen that there is a good agreement between experiment and analysis when the leading edge thrust effect is considered. Thus, at these angles of attack, there does not seem to be any leading edge vortex lift.

In order to evaluate the pitching moment predictions of the vortex lattice method, the longitudinal static stability was determined from Figures 3(a) through 3(c) and compared with experiment in Table II. Since the longitudinal static stability contribution of the vortex lift is zero at a lift coefficient of zero, its contribution was evaluated at the intermediate lift coefficient $C_L = 0.3$.

265

The distance to the centroid of lift from the normal reference center, expressed in terms of the wing mean aerodynamic chord, also is given in Table II. And since the centroid as calculated includes a portion of the fuselage lift, the distance from the model balance center to the quarter-chord of the mean aerodynamic chord for each lifting surface is included. It can be seen that in all three cases the analytical static stability is more negative than are the experimental values. Since the case without the stabilator shows good agreement and the cases with the stabilator show poorer agreement, it would appear that the stabilator as modeled is too effective. However, it was felt that additional studies to determine how best to model the tail in order to more closely match experiment were beyor: the scope of this investigation.

Effect of Control Surface Deflection

While vortex lift did not seem to form on the wing or control surfaces under standard flight conditions, it could form on thin control surfaces that had been deflected through an appreciable angle. But in order to isolate the effect of the deflected control surface, it was necessary to evaluate the force vectors in detail. To do this, a purely geometrical study was resorted to. The first assumption was that the leading edge sunction force vector of the control surface was in the direction of the twist angle of the leading edge panel. Thus, the single planform is made up of the untwisted part and the twisted part b (Figure 7) whose principle force directions are separated by the twist angle. It was further assumed that the total potential flow force as given by the program was determined by the integration of the force produced by the horseshoe vortices in the direction normal to the vortex lattice. In the same way, it was assumed that the total nonlinear force was determined by the integration of these vortex singularity forces in the direction of the vortex lattice. Then the forces of the individual panels can be written in terms of the given forces of the total planform (see Figure 7 for definition of the appropriate vectors).

Normal Forces:

$$K_p \sin\alpha \cos\alpha + C_{L_0} = K_{p_a} \sin\alpha \cos\alpha + K_{p_b} \sin(\alpha+\delta) \cos(\alpha+\delta) \cos\delta$$

Leading Edge Suction:

$$K_{V,LE} \sin^2\alpha + K_c = - K_{p_b} \sin(\alpha+\delta) \cos(\alpha+\delta) \sin\alpha + K_{V,LE_b} \sin^2(\alpha+\delta) \cos\delta$$

where δ is the twist angle of the control surface and K_p, $K_{V,LE}$, and C_{L_0} are known from the Vortex Lattice program solution.

At an angle of attack $\alpha = 0°$

$$C_{L_0} = K_{p_b} \sin\delta \cos^2\delta$$

$$K_c = - K_{p_b} \sin^2\delta \cos\delta + K_{V,LE_b} \sin^2\delta \cos\delta$$

These are two equations for the four unknowns K_c, K_{p_a}, K_{p_b}, and K_{V,LE_b}. To provide the other two equations, the solutions are matched at $\alpha = -\delta$ so that

$$-K_p \sin\delta \cos\delta + C_{L_o} = K_{p_a} \sin\delta \cos\delta$$

$$K_{V,LE} \sin^2\delta + K_c = 0$$

Then,

$$K_c = -K_{V,LE} \sin^2\delta \qquad\qquad K_{p_a} = -\frac{C_{L_o}}{\sin\delta \cos\delta} + K_p$$

$$K_{V,LE_b} = K_{p_b} - \frac{K_{V,LE}}{\cos\delta} \qquad\qquad K_{p_b} = \frac{C_{L_o}}{\sin\delta \cos^2\delta}$$

and $K_{V,SE_b} = K_{V,SE}$ since the integration of the side forces is unchanged by the fact that the control surface is rotated.

Resolving the forces on the control surface to the principal normal force and thrust force directions of the basic configuration:

Control Surface Potential Flow Force:

$$C_{N_p} = K_{p_b} \sin(\alpha+\delta) \cos(\alpha+\delta) \cos\delta$$

$$C_{T_p} = -K_{p_b} \sin(\alpha+\delta) \cos(\alpha+\delta) \sin\delta$$

Control Surface Leading Edge Suction Force:

$$C_{N_s} = K_{V,LE_b} \sin^2(\alpha+\delta) \sin\delta$$

$$C_{T_s} = K_{V,LE_b} \sin^2(\alpha+\delta) \cos\delta$$

Control Surface Suction Force with Polhamus Effect

$$C_{N_r} = (K_{V,LE_b} + K_{V,SE_b}) \sin^2(\alpha+\delta) \sin\delta_r$$

$$C_{T_r} = (K_{V,LE_b} + K_{V,SE_b}) \sin^2(\alpha+\delta) \cos\delta_r$$

where

$$\delta_r = \delta + \frac{\alpha+\delta}{|\alpha+\delta|} \frac{\pi}{2} \text{ to give the proper direction of rotation.}$$

The method of vectorial addition of the forces of the undeflected and deflected surfaces is illustrated in Figure 7. The lift vs drag polar for the complete configuration with the canard deflected 20° is shown in Figure 8. It can be seen that the vectorial representation gives a closer agreement with the experimental results than does the case where the force coefficient kernels K_p, $K_{V,LE}$ and $K_{V,SE}$ are all grouped together linearly. In this case, the agreement would appear to be enhanced if the side edge normal forces were

267

discounted as well.

Lifting Surface Effectiveness

One method of determining the interference between the components of a complete configuration would be an evaluation of the potential flow normal force coefficient kernels K_p. Another, more graphic, method is to look at the span loading for the individual components. In this case the span loadings are compared at a constant angle of attack $\alpha = 16.45°$. This angle of attack gives an overall lift coefficient $C_L = 1.0$ for the configuration including both canard and stabilator. Figure 9 shows the total span loading for the three cases with interfering flows. The integrated lift is approximately the same for all three cases; in fact, there is less than a 3% difference between the highest and the lowest total lift coefficient.

The span loadings on the individual components are given as Figures 10(a) through 10(c). The wing loadings are shown as Figure 10(a) and it can be seen that the presence of the canard decreases the total wing lift whereas the presence of the stabilator increases it. However, with the canard in place, the additional presence of the stabilator causes only a small increase of wing lift. The effect of the additional lifting surfaces on the canard is similar as can be seen in Figure 10(b). The total lift on the canard alone is increased by the presence of the wing and the additional presence of the stabilator causes only a very small additional lift.

However, the stabilator is much more sensitive to the presence of additional lifting elements as can be seen in Figure 10(c). As a surface acting alone, the stabilator can carry a good load. The presence of the wing substantially decreases the lift-curve slope so that the load carried at this angle of attack is much less than it would be if the stabilator were acting alone. The addition of the canard further decreases the static stability contribution of the stabilator. In this case the stabilator lift-curve slope is only one-tenth of the lift curve slope of the stabilator acting alone. This effect is analogous to the "cascading of lift" discussed in Reference 7 with respect to multi-element airfoils. In each case the addition of a lifting element causes the lift of forward elements to be increased and that of following elements to be decreased.

CONCLUSIONS

The Vortex Lattice program has been shown by comparison with wind tunnel tests to accurately calculate the normal forces of aircraft, even when multiple elements with strong interactions are present. This is true up to angles of attack where strong viscous-inviscid interactions become important. Calculation of the leading edge thrust also is good. These conclusions hold even for the case of deflected control surfaces as long as the force vectors are properly directed. Prediction of the longitudinal pitching moment was less satisfactory due to the stabilator paneling that was chosen.

The 5% scale model of the F-4E (CCV) aircraft apparently did not develop
leading edge vortex lift up to the angles of attack where the viscous inter-
actions predominate. Although the lifting surface leading edges are round,
their thickness to chord ratios are small enough that leading edge boundary
layer separation should occur. Unfortunately, the presence of the leading
edge slat clouds the comparison so that general conclusions can not be drawn.

Two possible improvements have suggested themselves during this study.
The first is the inclusion of vertical panels so that vertical control sur-
faces or fuselage surfaces can be modeled. This would allow the study of
phenomena such as direct side-force control due to differentially deflected
canards. The second is provision for the spanwise stacking of planforms (e.g.,
a canard and forward fuselage) with a proper carry-over of lift. In this way,
the effect of deflected control surfaces could be studied without having to
separate the contributions of the deflected and undeflected parts as was done
in this study.

REFERENCES

1. Margason, R. J. and Lamar, J. E., "Vortex-Lattice Fortran Program for Estimating Subsonic Aerodynamic Characteristics of Complex Planforms," NASA TN D-6142, February 1971.

2. Gloss, B. B., "Effect of Canard Location and Size on Canard-Wing Interference and Aerodynamic Center Shift Related to Maneuvering Aircraft at Transonic Speeds," NASA TN D-7505, June 1974.

3. Lamar, J. E. and Gloss, B. B., "Subsonic Aerodynamic Characteristics of Interacting Lifting Surfaces with Separated Flow Around Sharp Edges Predicted by a Vortex-Lattice Method," NASA TN D-7921, September 1975.

4. Stumpfl, S. C. and Whitmoyer, R. A., "Horizontal Canards for Two-Axis CCV Fighter Control," Presented to AGARD Symposium on "Impact of Active Control Technology in Airplane Design," AGARD CPP-157, October 1974.

5. Voda, J. J., "Summary of Results of Series II and III High Speed Wind Tunnel Tests of a 5-percent Scale Model F-4E (CCV), AEDC 4-foot Transonic Wind Tunnel Test No. 242," McDonnell Douglas Report MDC A2129, December 1972.

6. Polhamus, E. C., "A Concept of the Vortex Lift of Sharp-Edged Delta Wings Based on a Leading-Edge-Suction Analogy," NASA TN D-3767, 1966.

7. Smith, A. M. O., "High-Lift Aerodynamics," 37th Wright Brothers Lecture, Journal of Aircraft, V. 12, No. 6, June 1975.

TABLE I

CONFIGURATIONS STUDIED

1. Fuselage Alone

2. Fuselage + Canard

*3. Fuselage + Wing

4. Fuselage + Stabilator

5. Fuselage + Wing + Canard

*6. Fuselage + Wing + Stabilator

*7. Fuselage + Wing + Canard + Stabilator

*Experimental Comparison Available.

TABLE II

LONGITUDINAL PITCHING MOMENT PREDICTION

	Static Stability, $\left(\dfrac{dC_M}{dC_L}\right)$			Distance to Normal Force Centroid from Moment Center		
	Experimental	Predicted		Canard	Wing	Stabilator
		Linear ($C_L=0$)	Vortex ($C_L=0.3$)			
Fuselage + Wing	0.044	0.032	0.086		-0.0536	
Fuselage + Wing + Stabilator	0	-.133	-.143		0	-1.4046
Fuselage + Wing + Canard + Stabilator	.086	.054	.035	0.7836	-.1109	-1.6630
Distance to 1/4 MAC from Moment Center				.5790	.08	-1.4369
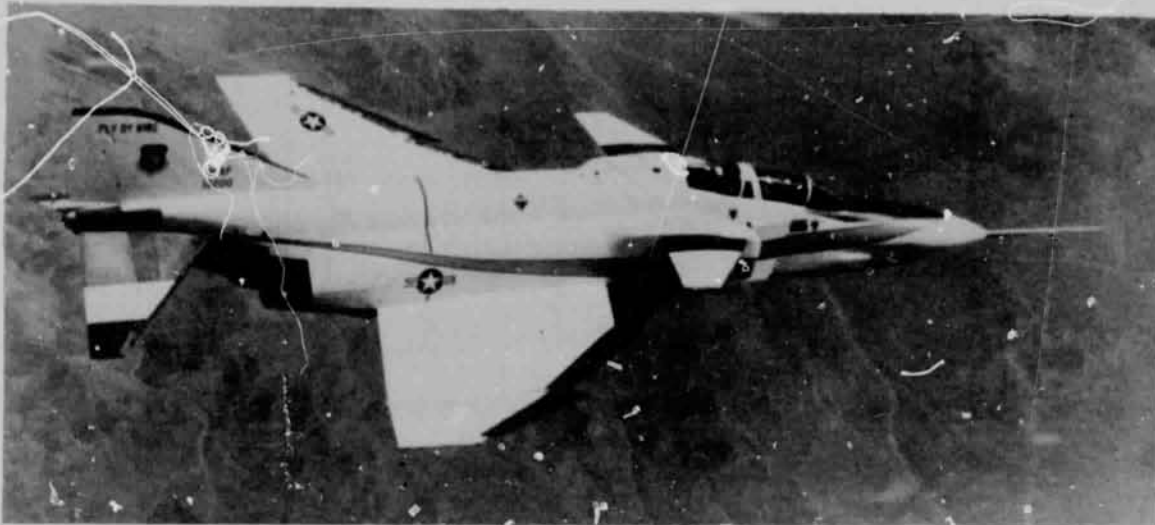
Figure 1.- McDonnell Douglas YF-4E (PACT) airplane.

FUSELAGE + CANARD

FUSELAGE + WING

FUSELAGE + STABILATOR

FUSELAGE + WING + CANARD

FUSELAGE + WING + STABILATOR

FUSELAGE + CANARD + WING
+ STABILATOR
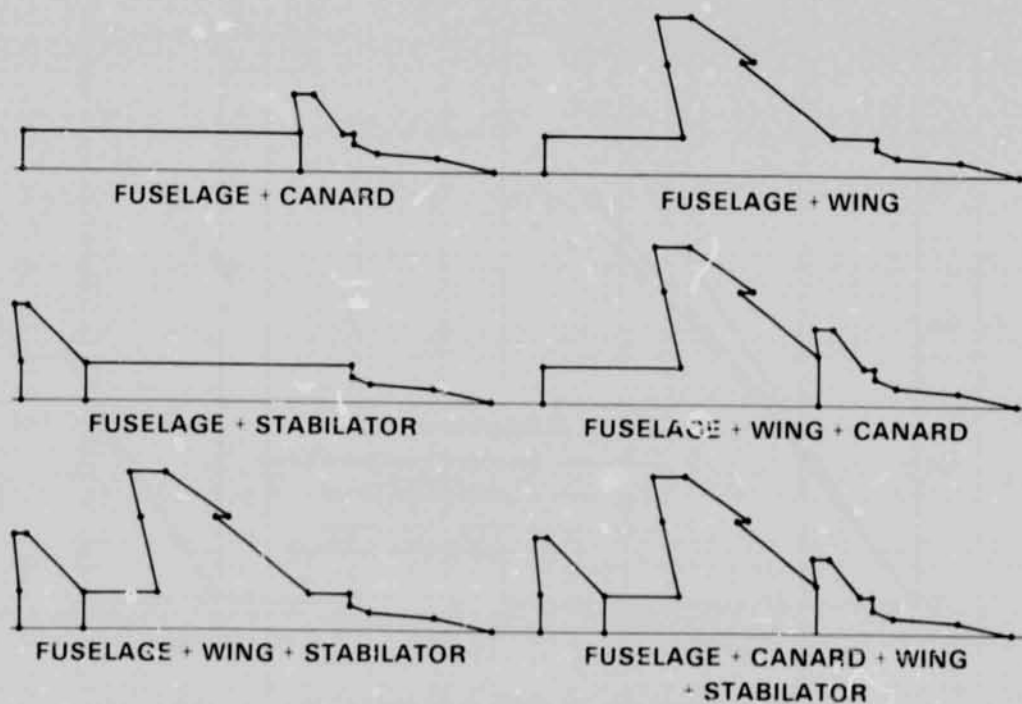
Figure 2.- Planform configurations of the McDonnell Douglas F-4E (CCV) studied.
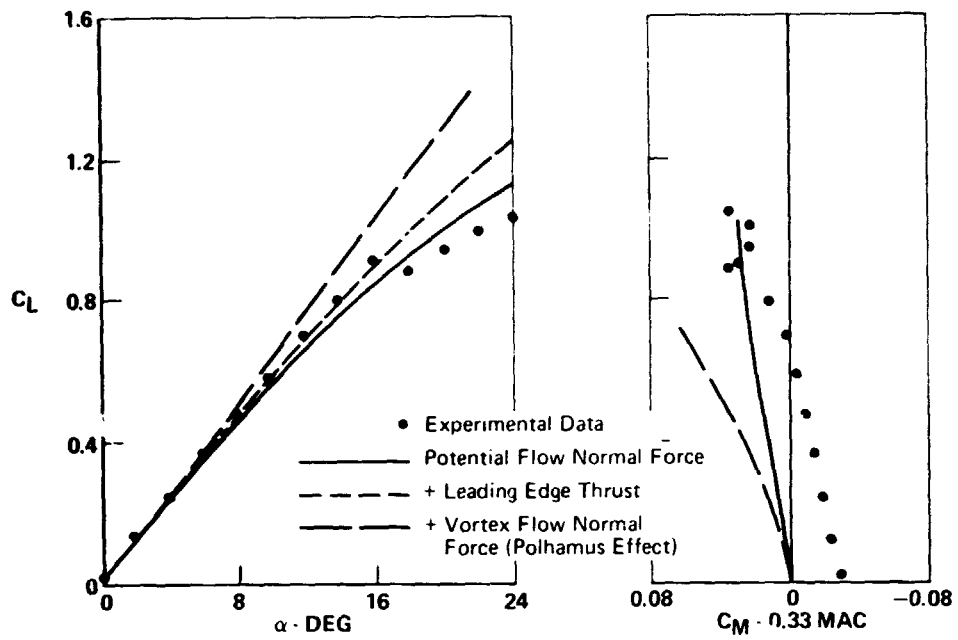
(a) Fuselage + wing.
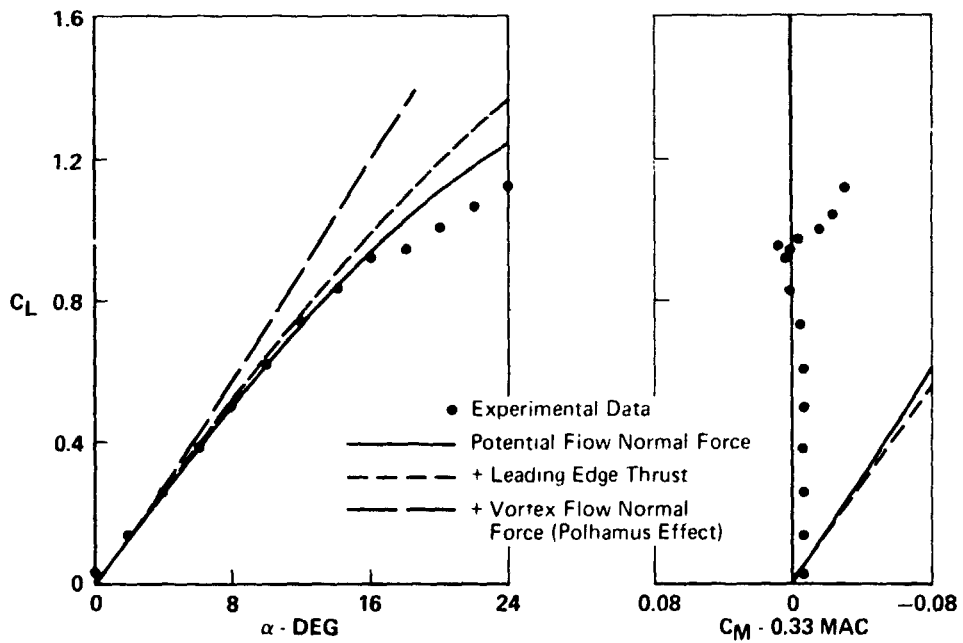
(b) Fuselage + wing + stabilator.

Figure 3.- Lift and moment polars for three configurations of the
F-4E (CCV); Mach number 0.6.

274

Experimental Data
Potential Flow Normal Force
+ Leading Edge Thrust
+ Vortex Flow Normal Force (Polhamus Effect)
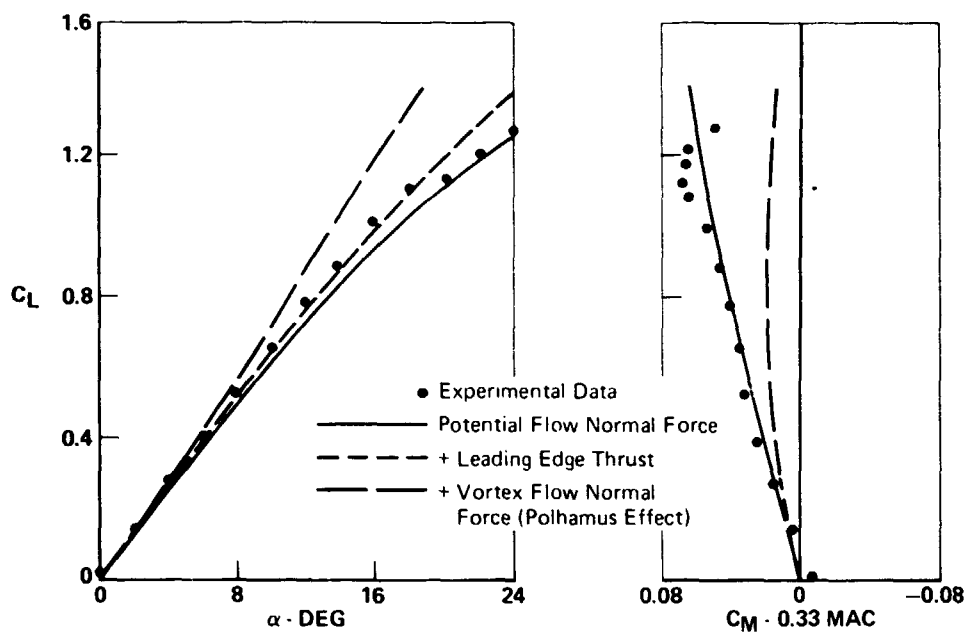
(c) Fuselage + wing + canard + stabilator.

Figure 3.- Concluded.
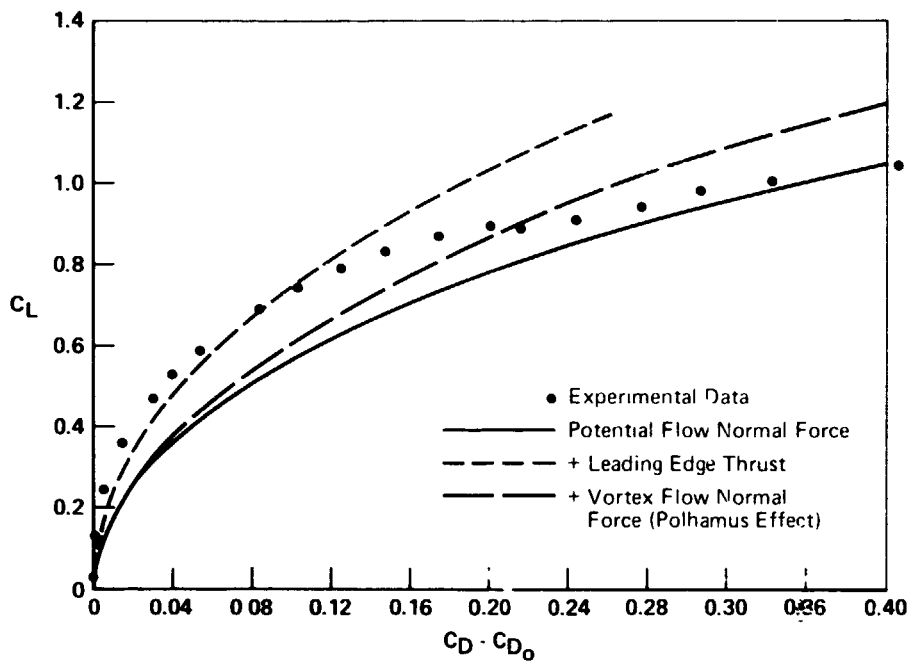
(a) Fuselage + wing.
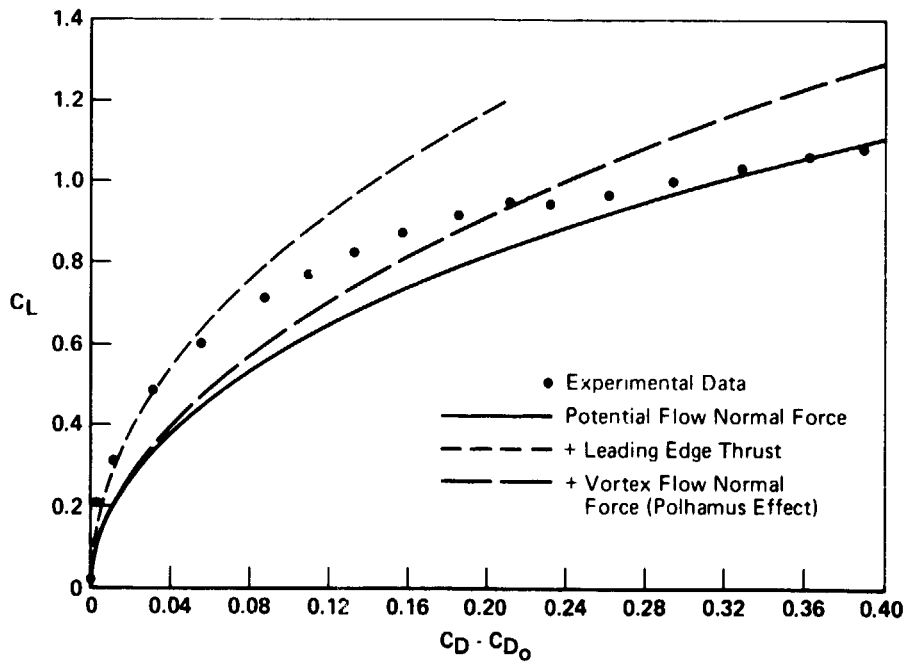
(b) Fuselage + wing + stabilator.

Figure 4.- Lift and drag polars for three configurations of the F-4E (CCV); Mach number 0.6.

276
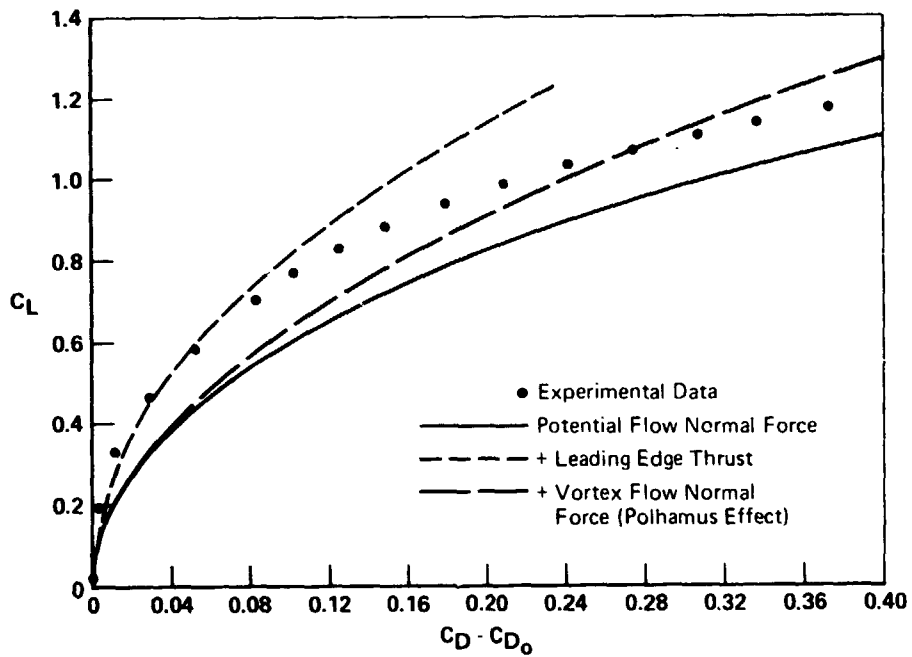
(c) Fuselage + wing + canard + stabilator.

Figure 4.- Concluded.
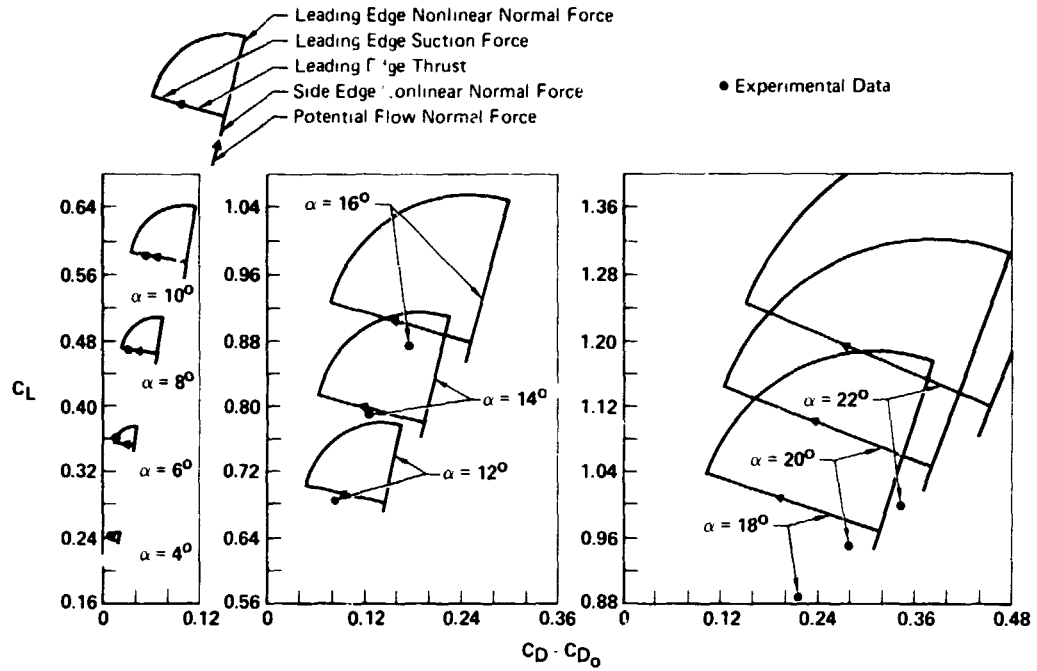
(a) Fuselage + wing.
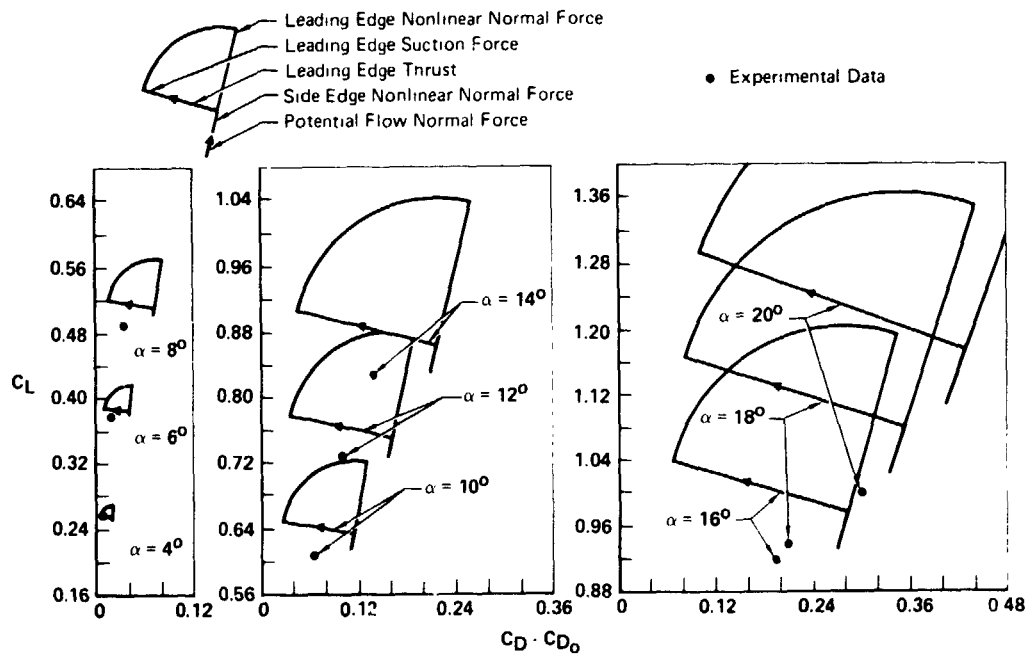
(b) Fuselage + wing + stabilator.

Figure 5.- Vectorial lift and drag polars for three configurations of the F-4E (CCV); Mach number 0.6.

Leading Edge Nonlinear Normal Force
Leading Edge Suction Force
Leading Edge Thrust
Side Edge Nonlinear Normal Force
Potential Flow Normal Force

●Experimental Data
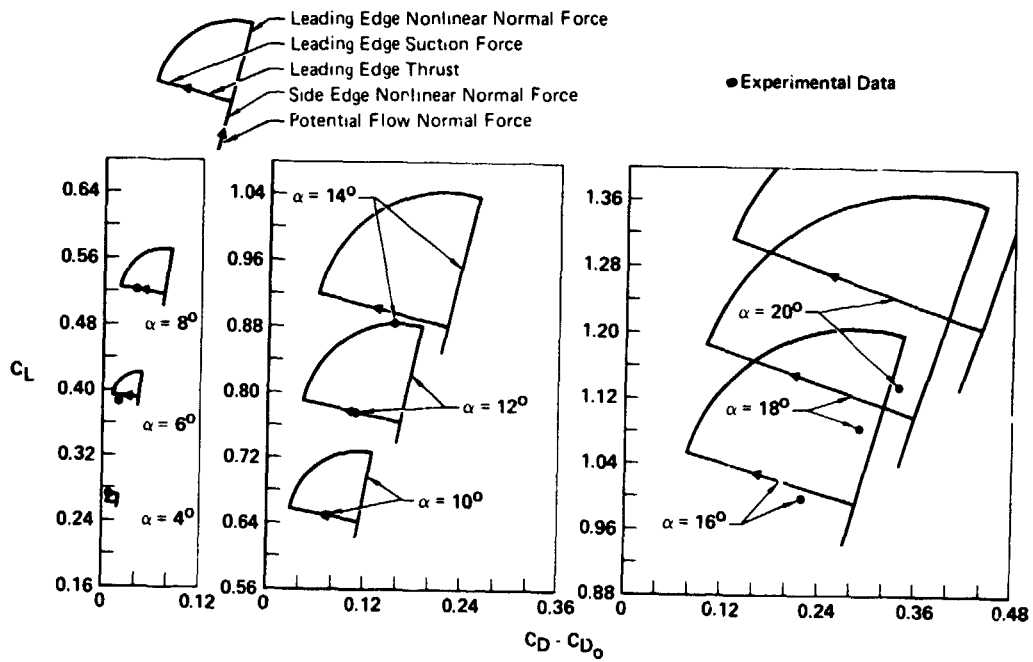
(c) Fuselage + wing + canard + stabilator.

Figure 5.- Concluded.
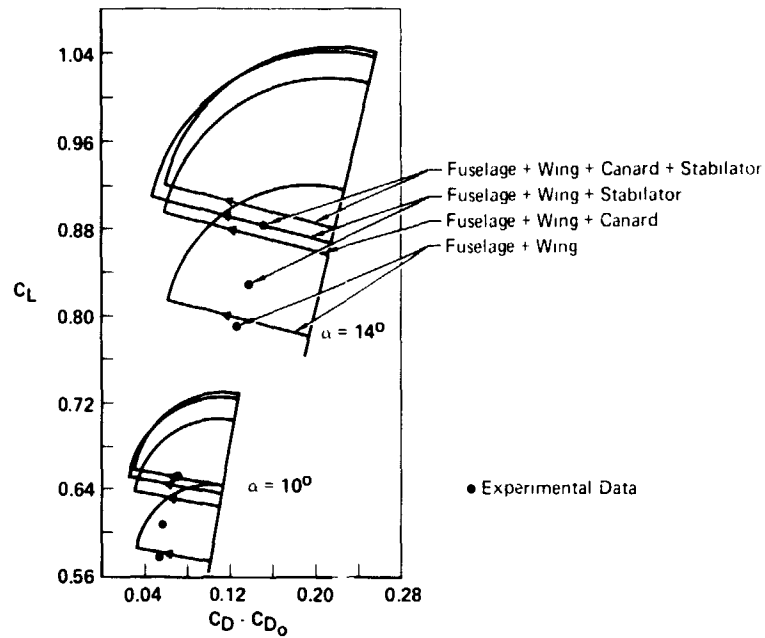
Figure 6.- Vectorial lift and drag polars at medium angles of attack for various configurations of the F-4E (CCV); Mach number 0.6.
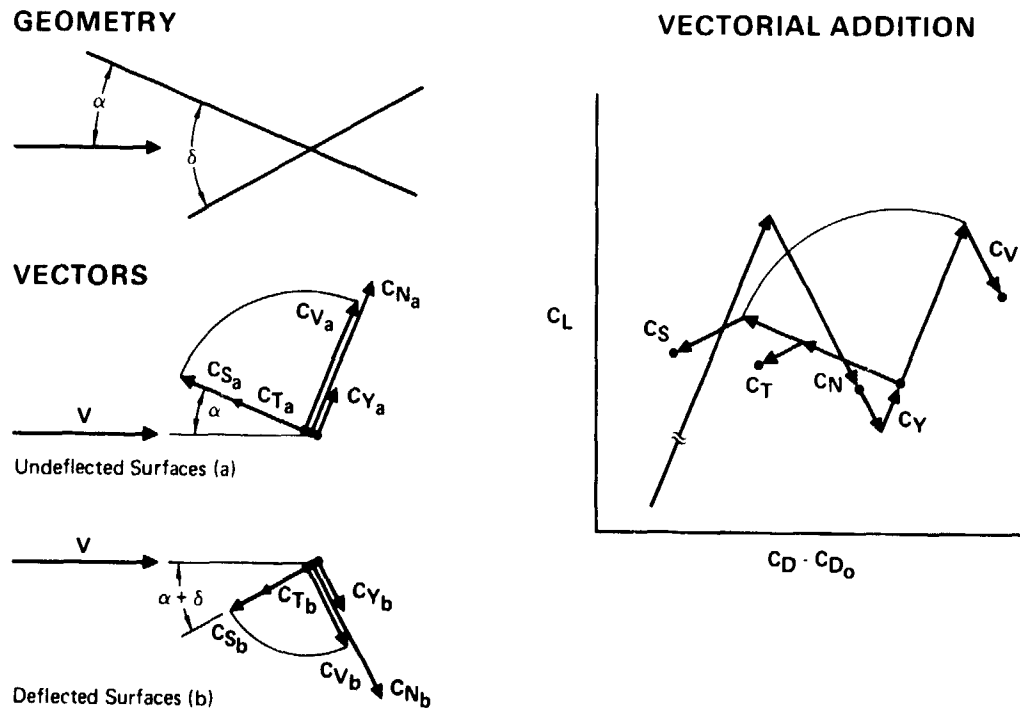
Figure 7.- Vectorial addition of lifting and control surface forces.
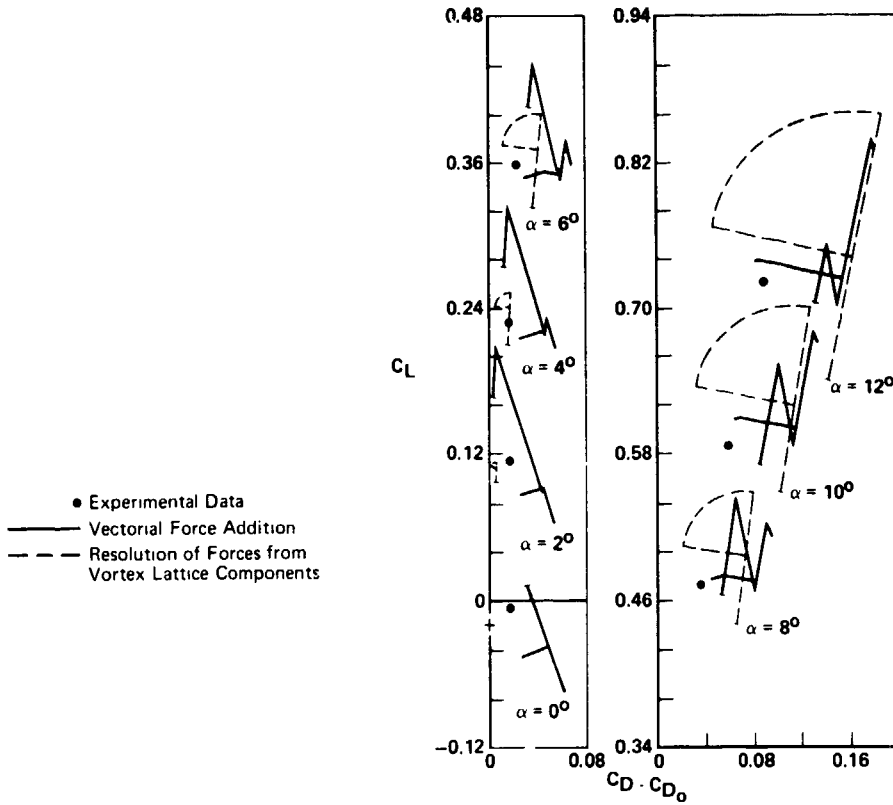
Figure 8.- Vectorial lift and drag polars for
   fuselage + wing + canard + stabilator;
   $\delta_c = -20°$.
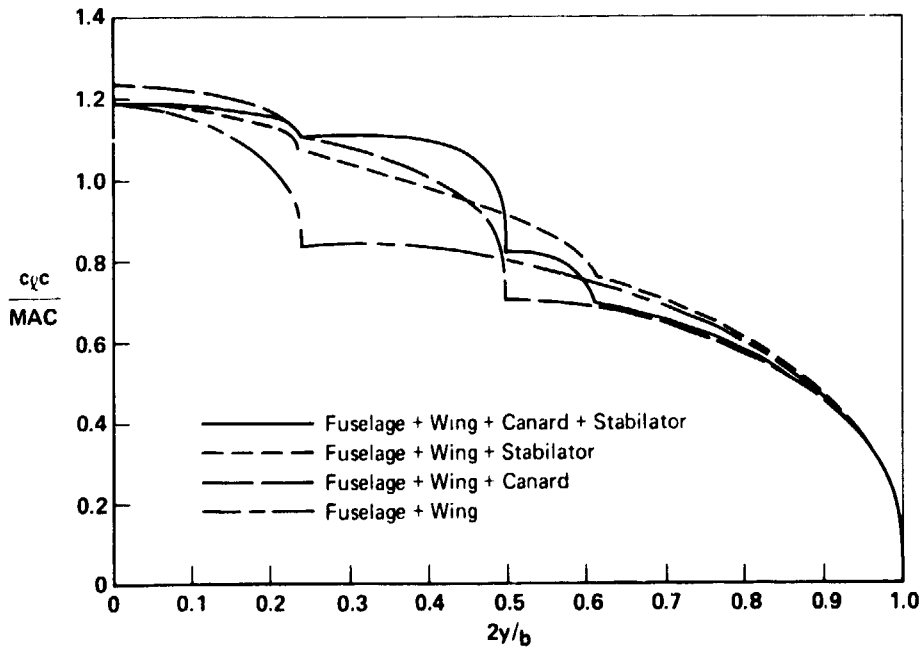
Figure 9.- Span loadings for complete configurations of the F-4E (CCV);
                       Mach number 0.6.
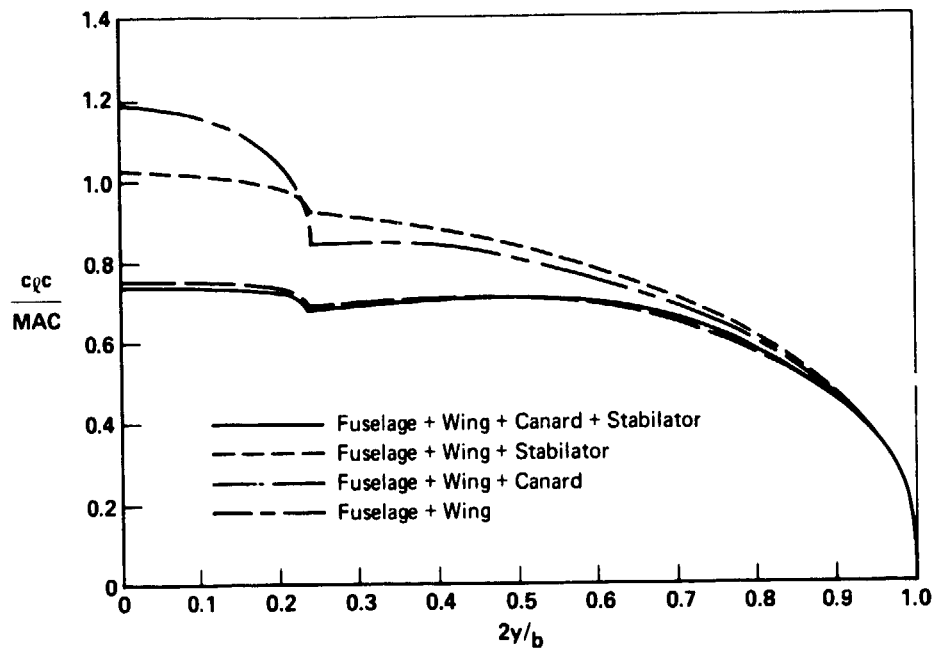
(a) Wing + partial fuselage.
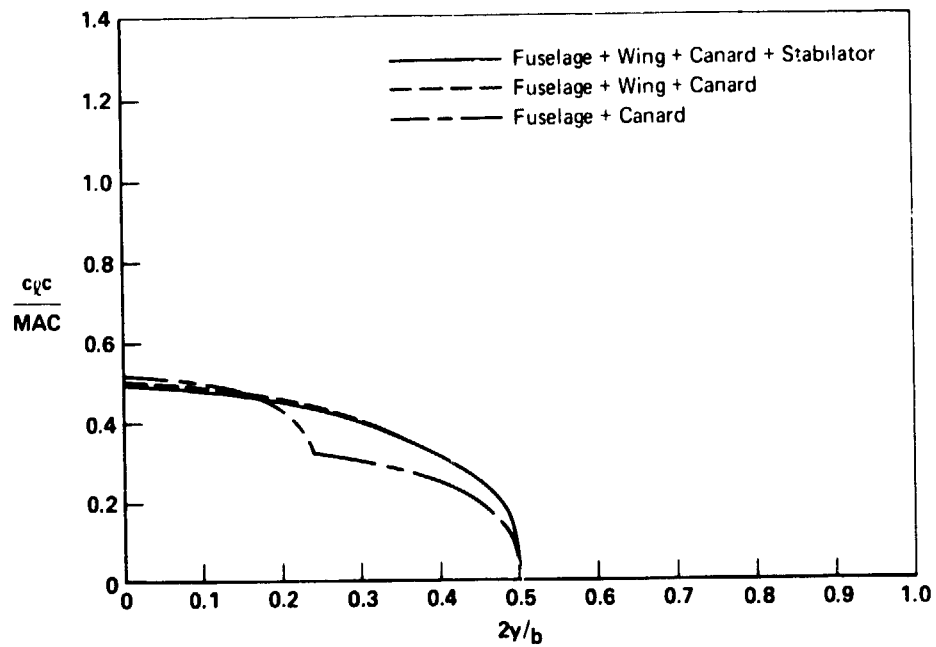
(b) Canard + partial fuselage.

Figure 10.- Span loadings for individual elements of various
configurations of the F-4E (CCV); Mach number 0.6.
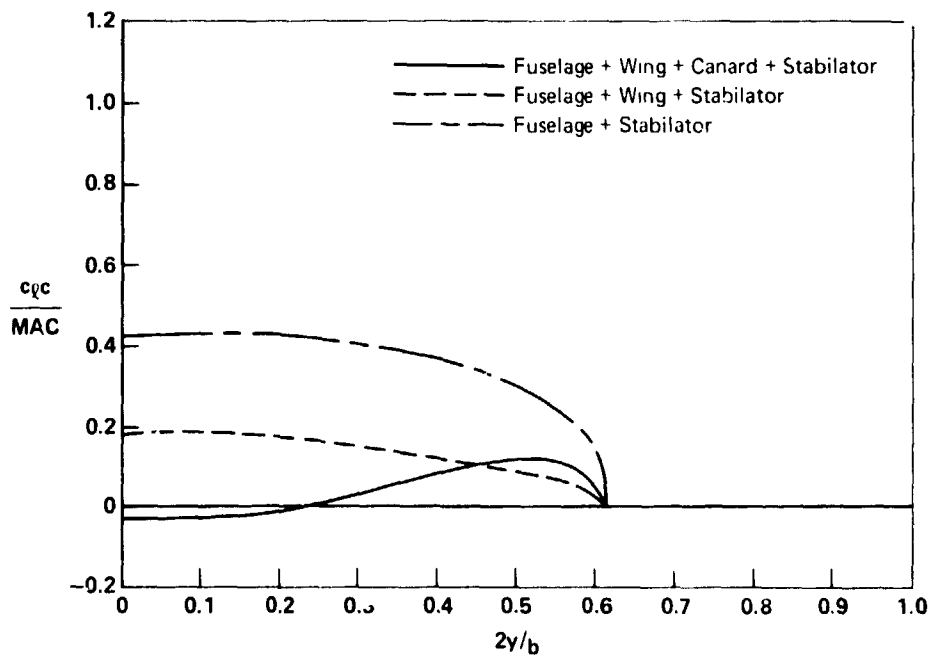
(c) Stabilator + partial fuselage.

Figure 10.- Concluded.

NEW CONVERGENCE CRITERIA FOR THE VORTEX-LATTICE MODELS
OF THE LEADING-EDGE SEPARATION*

Osama A. Kandil, Dean T. Mook, and Ali H. Nayfeh

Virginia Polytechnic Institute and State University

SUMMARY

The convergence criterion for the vortex-lattice technique which deals with delta wings exhibiting significant leading-edge separation has two requirements. First, the wake must converge to a force-free position for any given number of discrete vortex elements. Second, the distributed loads must converge as the number of elements increases. Replacing the vortex sheets representing the wakes by a system of discrete vortex lines whose positions are determined as part of the solution (first requirement), one finds that the total loads computed agree very well with experimental data. But the predicted pressure distributions have some irregularities which are the result of discrete vortex lines coming close to the lifting surface. Here it is shown that one can eliminate these irregularities and predict pressure distributions which agree fairly well with experimental data (which show some irregularities of their own) by replacing the system of discrete vortex lines with a single concentrated core. This core has a circulation equal to the algebraic sum of the circulations around the discrete lines and is located at the centroid of these lines. Moreover, the second requirement is replaced by the requirement that the position and strength of the core converge as the number of elements increases. Because the calculation of the position and strength of the core is much less involved than the calculation of the loads, this approach has the additional desirable feature of requiring less computational time.

INTRODUCTION

A characteristic feature of the flow over wings having highly swept, sharp leading edges is the formation of vortices above suction sides in the vicinity of the leading edges. These vortices roll up in a conical-like spiral with a concentrated core. This vortex spiral grows in size and strength as it approaches

---

the trailing edge. Below the angle of stall (i.e., the angle at which vortex bursting occurs), the effect of the leading-edge separation is to increase the velocity on the suction side of the lifting surface by adding a strong cross-flow component and hence to increase the aerodynamic loads. Experimental investigations, such as those described in refs. 1-7, and numerical investigations, such as those described in refs. 8 and 9, confirm these conclusions. Detailed descriptions of the flow field are als' given in these references.

Though the experimental results show that the pressure distribution is somewhat influenced by the character (laminar or turbulent) of the boundary layer, the lift and pitching-moment coefficients are independent of the Reynolds number. Thus, one expects an inviscid model of the flow to predict the total loads more reliably than the distributed loads. And such has turned out to be the case.

The early attempts to develop an inviscid model of these flows were based on assumptions of conical flow and/or slender-body theory. These assumptions are apparently discredited by the experimental observations; more discussion is given in references 8 and 9.

Subsequent attempts to develop inviscid models did not use these assumptions. Rehbach (ref. 10) developed a vortex-lattice technique which progressively shortens the leading edge of a rectangular wing until a delta wing is formed. Associated with this method are questions concerning the second convergence requirement and the undesirable feature of long computation times; more discussion is given in refs. 8 and 9. Weber et al (ref. 11) developed a technique which uses piecewise continuous, quadratic, doublet-sheet distributions. The second requirement apparently was not considered, and no results showing the computed shapes of the rolled-up wakes were given.

In a related effort, Suciu and Morino (ref. 12) developed a technique for modelling the region adjoining the trailing edge. However, numerical experiments, as described in refs. 8 and 9, show that the wake adjoining the trailing edge has very little influence on the aerodynamic loads.

In the present paper, the question of the convergence of the centroidal line as the number of discrete elements increases is considered; and this line, instead of the system of discrete vortex lines, is used to compute the pressure.

SYMBOLS

AR	aspect ratio
b	wing semi-span
C_{mz}	pitching-moment coefficient about the z-axis
C_n	normal-force coefficient
$c_n(x)$	local cross-normal-force coefficient
ΔC_p	pressure coefficient
c_r	root chord
$s(x)/b$	local semi-span/wing semi-span
t/c_r	thickness ratio
$\overline{U}_\infty$	free-stream velocity
x,y,z	body-fixed axes (z-axis is in spanwise direction)
x/c_r	dimensionless chord station
$z/s(x)$	dimensionless spanwise station
α	angle of attack
$\Gamma/c_r U_\infty$	dimensionless circulation
nel	number of elemental areas of the lattice

FORMULATION OF THE PROBLEM

The perturbation velocity potential, ϕ, of the inviscid, irrotational, incompressible flow past a wing is governed by Laplace's equation and satisfies the following boundary conditions: (a) the no-penetration condition on the wing surface given by

$$(\overline{U}_\infty + \nabla\phi) \cdot \overline{n} = 0 \quad \text{on } S(\overline{r}) = 0$$

where $\overline{n}$ is the unit normal to the wing surface S, (b) the no-pressure discontinuity condition across the wakes emanating from the leading and trailing edges of the wing given by

$$\Delta p = 0 \quad \text{across } w(\overline{r}) = 0$$

where Δp is the pressure jump across the wake surface w. This surface is an unknown of the problem and must be obtained as part of the solution, (c) the Kutta condition which requires that no-pressure jump exists across the wing surface along the leading and trailing edges where the wake surface is emanating, and (d) the disturbance velocity, $\nabla\phi$, diminishes far from the wing surface, S, and the wake surface, w. We note that the problem is nonlinear due to boundary condition (b).

287

DESCRIPTION OF THE METHOD OF SOLUTION

The solution of the problem posed above is constructed by modelling the lifting surface with a bound-vortex lattice and the wake with a system of discrete, nonintersecting vortex lines. Each vortex line in the wake is composed of a series of short, straight segments and one final semi-infinite segment. The unknowns here are the circulations around the vortex segments and the positions of the finite segments in the wake.

The disturbance velocity field produced by this model of the wing and wake is calculated according to the Biot-Savart law; thus, everywhere, except on the wing and the wake, Laplace's equation is satisfied. Moreover, the disturbance created by the wing dies out far from the wing and wake, boundary condition (d).

Associated with each elemental area of the lattice and with each finite segment in the wake is a control point. The lattice is arranged so that vortex segments leaving the sharp edges do so at right angles to the edge. Moreover, control points are placed between the last edgewise vortex segment of each row and column and the edge itself. This arrangement partially satisfies the Kutta condition (c).

The circulations and the positions of the finite segments in the wake are obtained by simultaneously requiring the normal component of velocity to vanish at the control points of the elemental areas of the lattice and the finite segments in the wake to be parallel to the velocities at their own control points. Boundary conditions (a) and (b) and the Kutta condition (c) are then satisfied, and the problem is solved for this lattice (i.e., the first requirement of the convergence criterion is met). More details, especially those regarding the iterative procedure used to effect the last step, are given in refs. 8 and 9.

Instead of calculating the aerodynamic loads and testing the second requirement of convergence at this point, with the present procedure we calculate the centroidal line of the system of free-vortex lines representing the leading-edge wake. To construct this centroidal line, we consider a series of cross-flow planes. Proceeding from the vertex toward the trailing edge, we calculate the centroids of the vortex lines penetrating these planes according to

$$\vec{r}_j = \frac{\sum\limits_{i=1}^{n_j} \Gamma_i \, \vec{r}_{ij}}{\Gamma_{cj}}$$

288

where Γ_{cj} is taken to be the circulation around the centroidal line between the jth and $(j+1)^{th}$ planes and it given by

$$\Gamma_{cj} = \sum_{i=1}^{n_j} \Gamma_i$$

$\vec{r}_j$ is the position of the centroid in the jth plane, $\vec{r}_{ij}$ is the position of the intersection of the ith vortex line with the jth plane, Γ_i is the circulation around the ith line, and n_j is the number of lines penetrating the jth plane. More lines penetrate the planes near the trailing edge than those near the vertex; thus, Γ_{cj} increases toward the trailing edge.

Now, the number of elements is increased and new centroidal lines are calculated until the changes in Γ_{cj} and $\vec{r}_j$ fall within prescribed tolerances. At this point, the second requirement of the convergence criterion is met.

Only when both requirements are met, do we calculate the aerodynamic loads and pressure distribution. The details for calculating the loads are given in ref. 8. The numerical results below show, for the examples being considered at least, that the centroidal lines converge to a position which is very close to the experimentally determined position of the core, that the total loads agree very well with the experimental data, and that the pressure distributions agree fairly well with the experimental data.

NUMERICAL EXAMPLES

Figures 1 and 2 show the actual calculated positions of the free-vortex lines for two delta wings. The plan view also shows the bound-vortex lattice. And the three dimensional view shows the free-vortex lines, their centroidal line, and the trace of the spiral vortex sheet. All the following results are associated with these two wings.

Figures 3 and 4 show the convergence of the circulations around the centroidal line. And figures 5-8 show the convergence of the position of the centroidal line and the close agreement between the position of the calculated line and the experimentally determined position of the vortex core.

Figures 9 and 10 show the convergence of the total loads calculated by using the system of discrete lines and by using the centroidal line as a function of the number of elements (nel). These results are compared with those obtained by the leading-edge-suction analogy (ref. 13) and with experimental data. We note

that there is a considerable difference in the experimentally determined normal-force coefficients in figure 10.

Figures 11 and 12 show comparisons of the predicted cross-load coefficients and experimental data. And figures 13-16 show comparisons of the predicted pressure distributions at several chordwise stations with those obtained by another method (ref. 11) and with experimental data. We note that the shape and size of the suction peak on the upper surface under the vortex differ from one experiment to another, depending on how thick the wing is and on whether the boundary layer is laminar or turbulent (refs. 5, 6, and 14).

CONCLUDING REMARKS

The second requirement of convergence is based on the centroidal line of the free-vortex lines representing the wake. Using this requirement greatly reduces the computational time. The position of the centroidal line compares very well with that of the vortex core. The centroidal line can also be used to calculate the total and distributed aerodynamic loads with good accuracy. This results in more reduction in the computational time and smoothing of the peaks produced by using many discrete lines.

290

REFERENCES

1. Peckham, D. H., "Low-Speed Wind-Tunnel Tests on a Series of Uncambered Slender Pointed Wings with Sharp Edges", R & M No. 3186, Brit. ARC, 1961.

2. Bergesen, A. J., and Porter, J. D., "An Investigation of the Flow Around Slender Delta Wings with Leading-Edge Separation", Princeton University, Department of Aeronautical Engineering, Report No. 510, May 1960.

3. Nangia, R. K., and Hancock, G. J., "Delta Wings with Longitudinal Camber at Low Speed", C.P. No. 1129, Brit. ARC, 1970.

4. Marsden, D. J., Simpson, R. W., and Rainbird, B. E., "An Investigation into the Flow over Delta Wings at Low Speeds with Leading-Edge Separation", The College of Aeronautics, Cranfield, Report No. 114, February 1958.

5. Hummel, D., "Study of the Flow Around Sharp-Edged Slender Delta Wings with Large Angles of Attack", NASA TT F-15,107, September 1973.

6. Hummel, D. and Redeker, G., "Experimental Determination of Bound Vortex Lines and Flow in the Vicinity of the Trailing Edge of a Slender Delta Wing", NASA TT F-15,012, August 1973.

7. Bartlett, G. E., and Vidal, R. K., "Experimental Investigation of Influence of Edge Shape on the Aerodynamic Characteristics of Low-Aspect-Ratio Wings at Low Speeds", Journal of Aeronautical Sciences, Vol. 22, No. 8, August 1955, pp. 517-533.

8. Kandil, O. A., "Prediction of the Steady Aerodynamic Loads on Lifting Surfaces having Sharp-Edge Separation", Ph.D. Dissertation, Engineering Science and Mechanics Department, Virginia Polytechnic Institute and State University, December 1974.

9. Kandil, O. A., Mook, D. T., and Nayfeh, A. H., "Nonlinear Prediction of the Aerodynamic Loads on Lifting Surfaces. AIAA Paper No. 74-503, June 1974. Also in Journal of Aircraft, Vol. 13, No. 1, January 1976, pp. 22-28.

10. Rehbach, C., "Numerical Investigation of Vortex Sheets Issuing from Separation Line near the Leading Edge", NASA TT F-15, 530, 1974.

11. Weber, J. A., Brune, G. W., Johnson, F. T., Lu, P., and Rubbert, P. E., "A Three-Dimensional Solution of Flows Over Wings with Leading-Edge-Vortex Separation", NASA SP-347, Part II, 1975, pp. 1013-1032.

12. Suciu, E. O., and Morino, L., "A Nonlinear Finite-Element Analysis of Wings in Steady Incompressible Flows with Wake Roll-Up", AIAA Paper No. 76-64, January 1976.

13. Polhamus, E. C., "A Concept of the Vortex Lift of Sharp-Edge Delta Wings Based on a Leading-Edge-Suction Analogy", NASA TN D-3767, December 1966.

14. Smith, J. H. B., "Improved Calculations of Leading-Edge Separation from Slender, Thin, Delta Wings", Proc. Roy. Soc. A. 306, 1968, pp. 67-90.
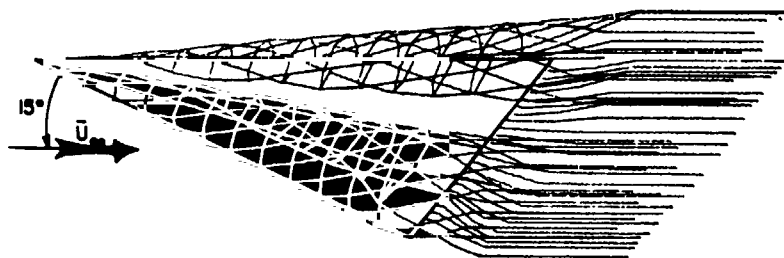
Figure 1.- A typical solution of the wake shape for a
delta wing with $\mathbb{R} = 1$. 12×12 lattice.
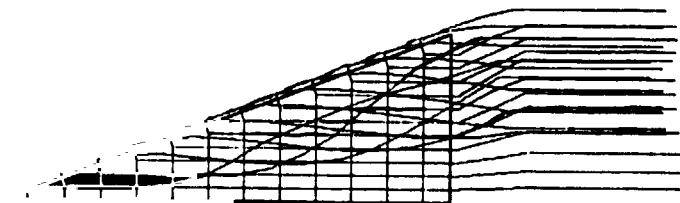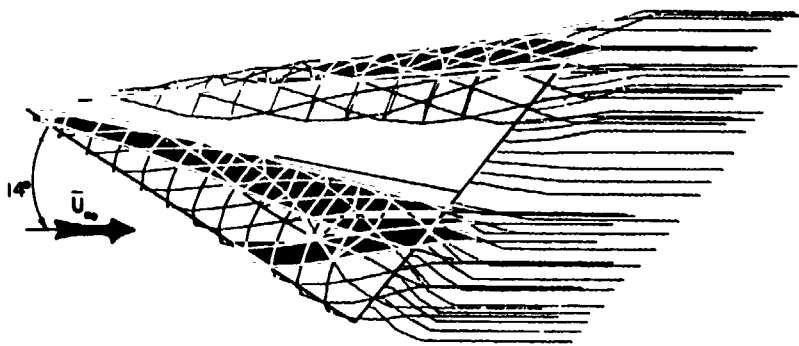
Figure 2.- A typical solution of the wake shape for a
delta wing with $\mathbb{R} = 1.46$. 12×12 lattice.

293
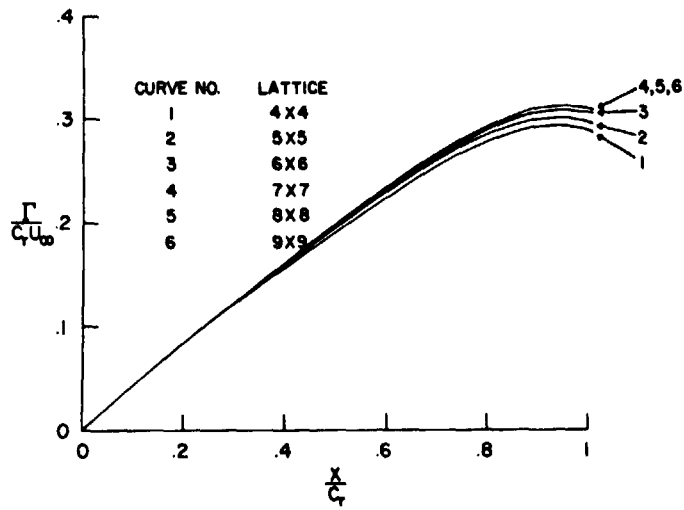
Figure 3.- Variation of circulation along the vortex core of a delta wing with $\mathbb{R} = 1.$ $\alpha = 15^{\circ}$.
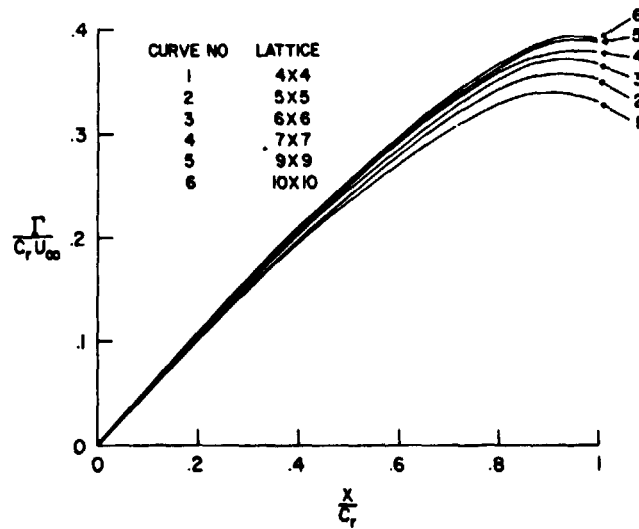
Figure 4.- Variation of circulation along the vortex core of a delta wing with $\mathbb{R} = 1.46.$ $\alpha = 14^{\circ}$.
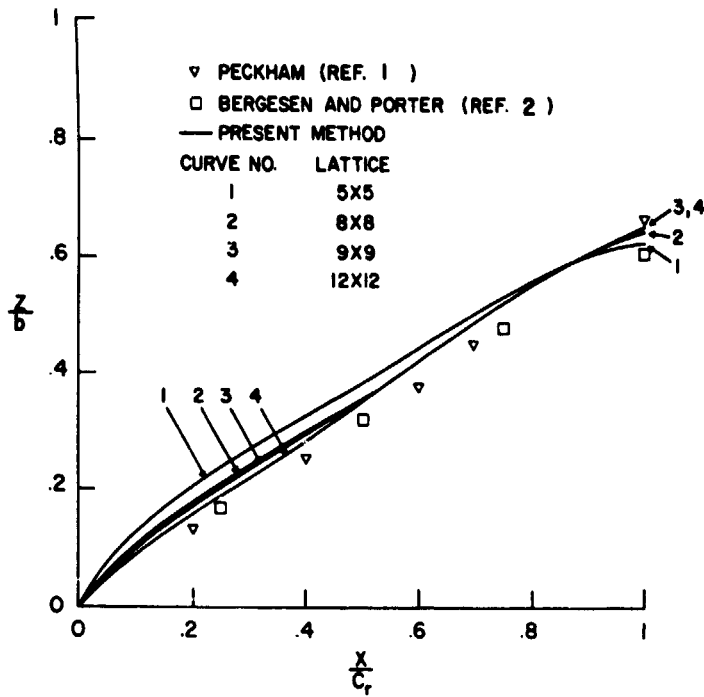
Figure 5.- Spanwise position of vortex-core path
on a delta wing with $R = 1$. $\alpha = 15^o$.
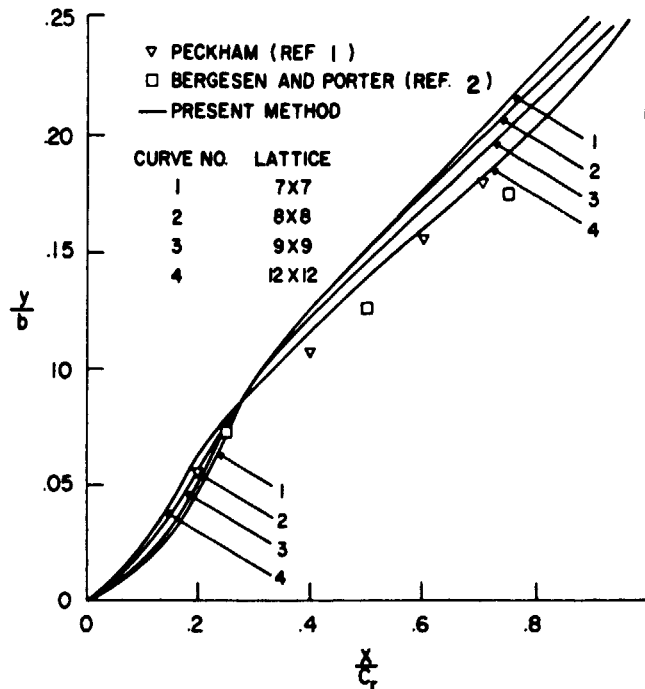
Figure 6.- Height of vortex-core path on a
delta wing with $R = 1$. $\alpha = 15^o$.
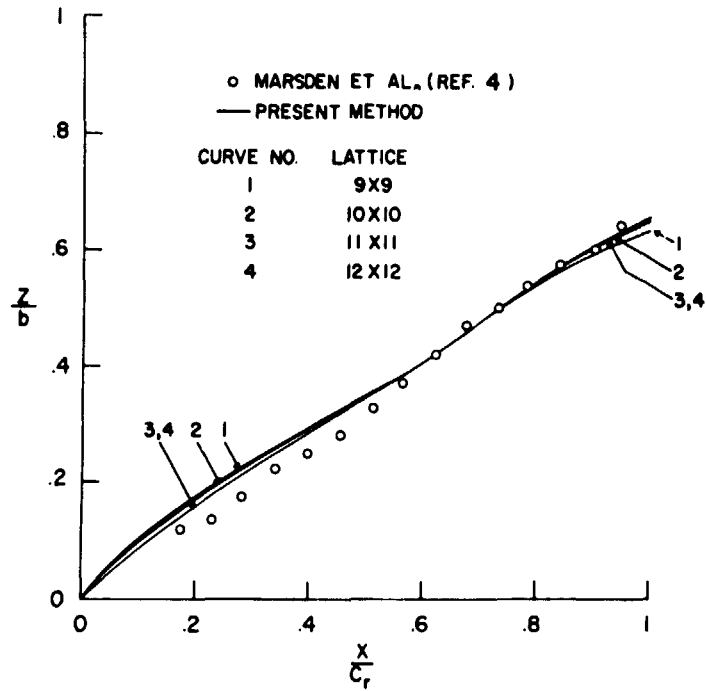
Figure 7.- Spanwise position of vortex-core path
on a delta wing with $R = 1.46$. $\alpha = 14°$.
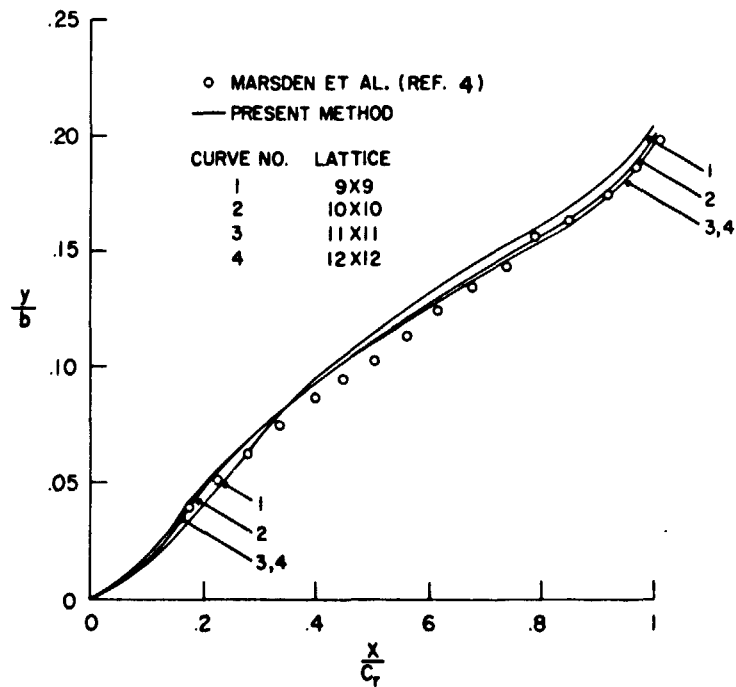
Figure 8.- Height of vortex-core path on a
delta wing with $R = 1.46$. $\alpha = 14°$.
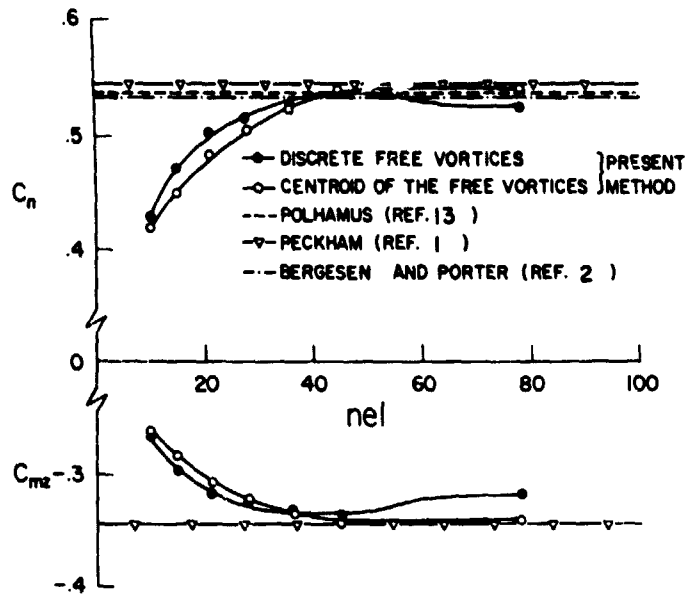
Figure 9.- Normal-force and pitching-moment
coefficients of a delta wing with $\mathcal{R} = 1$.
$\alpha = 15^o$.
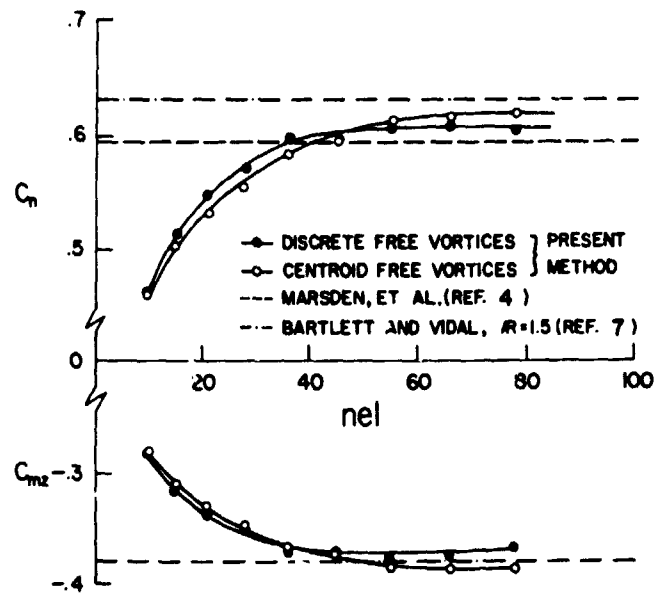
Figure 10.- Normal-force and pitching-moment
coefficients of a delta wing with $\mathcal{R} = 1.46$.
$\alpha = 14^o$.
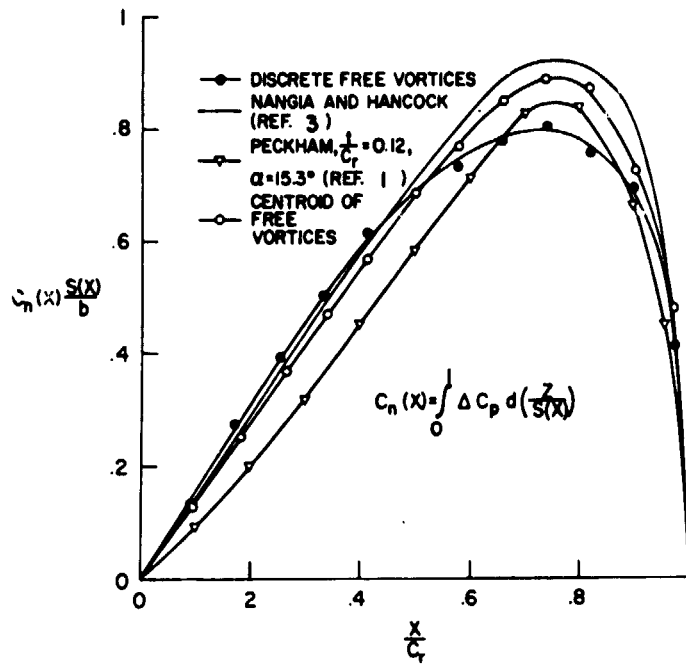
Figure 11.- Longitudinal distribution of cross load
for a delta wing with $R = 1$. 12×12 lattice;
$\alpha = 15^\circ$.
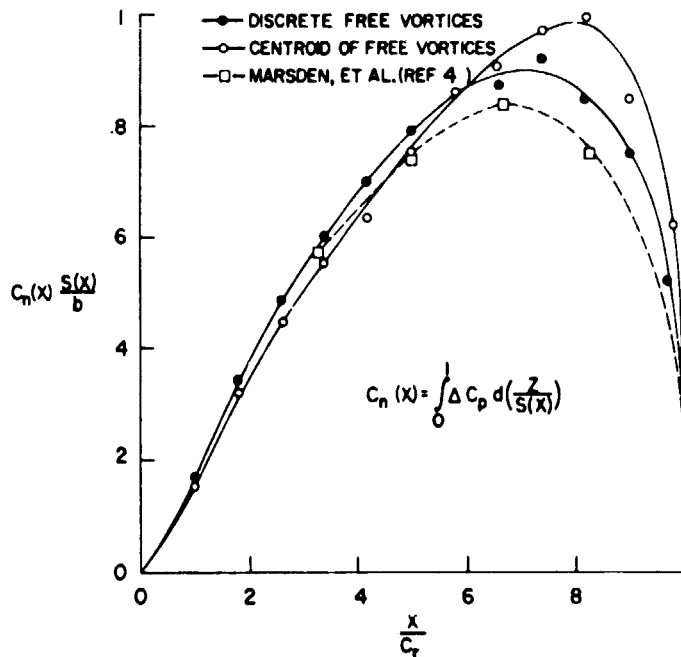
Figure 12.- Longitudinal distribution of cross load
for a delta wing with $R = 1.46$. 12×12 lattice;
$\alpha = 14^\circ$.
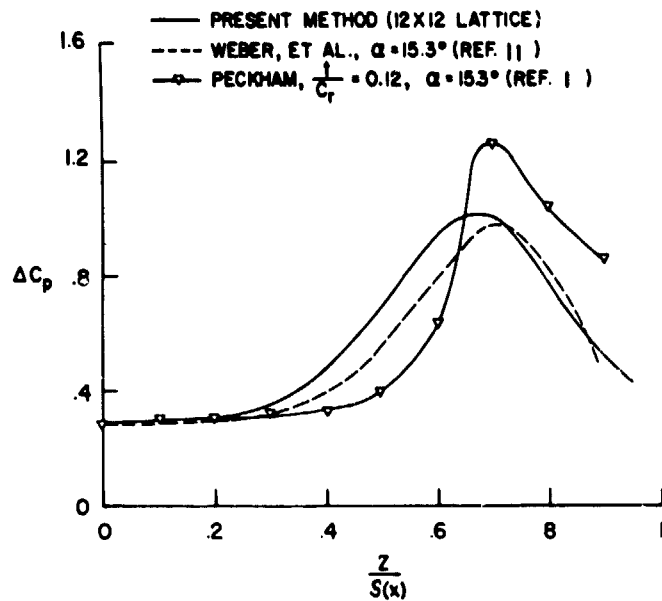
Figure 13.- Surface pressure distribution of a delta
wing at $\frac{x}{c_r} = 0.7$. $R = 1$; $\alpha = 15^o$.
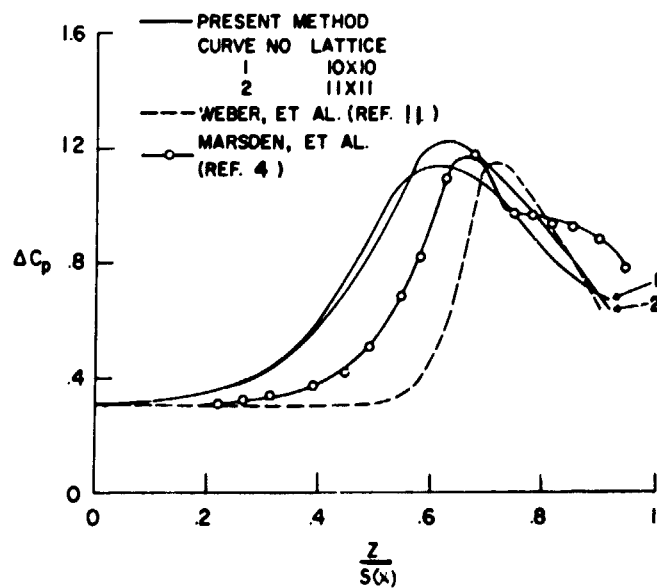
Figure 14.- Surface pressure distribution of a delta
wing at $\frac{x}{c_r} = 0.82$. $R = 1$; $\alpha = 15^o$.
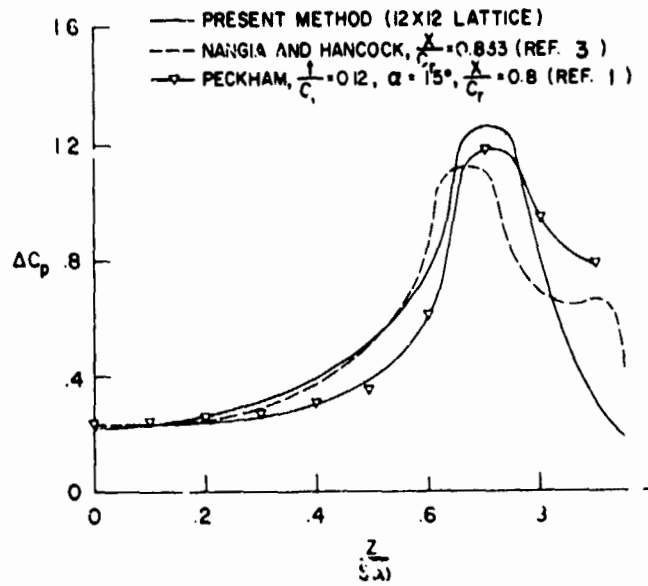
Figure 15.- Surface pressure distribution of a delta
wing at $\frac{x}{c_r} = 0.67$. $\mathcal{R} = 1.46$; $\alpha = 14^o$.
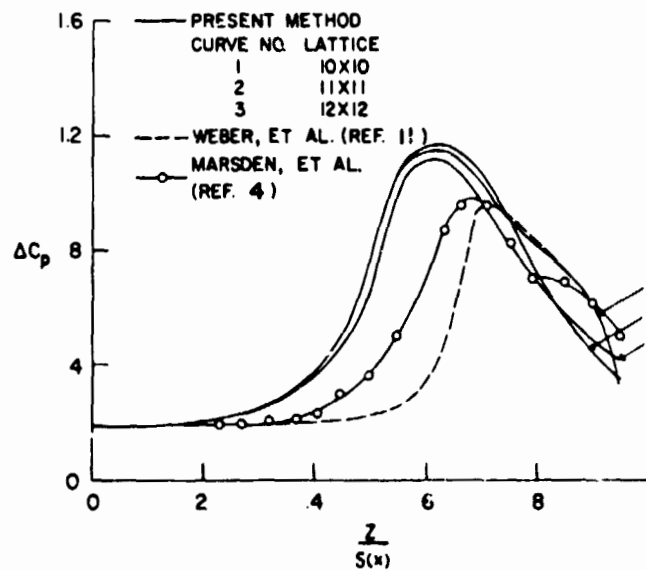
Figure 16.- Surface pressure distribution of a delta
wing at $\frac{x}{c_r} = 0.83$. $\mathcal{R} = 1.46$; $\alpha = 14^o$.

300

ARRANGEMENT OF VORTEX LATTICES

ON SUBSONIC WINGS*

Fred R. DeJarnette
North Carolina State University

SUMMARY

A new method is developed for solving the lifting-surface equation for thin wings. The solution requires the downwash equation to be in the form of Cauchy integrals which can be interpreted as a vortex lattice with the positions of the vortices and control points dictated by the finite sum used to approximate the integrals involved. Lan's continuous loading method is employed for the chordwise integral since it properly accounts for the leading-edge singularity, Cauchy singularity, and Kutta condition. Unlike Lan, the spanwise loading is also continuous and the Cauchy singularity in the spanwise integral is also properly accounted for by using the midpoint trapezoidal rule and the theory of Chebychev polynomials. This technique yields the exact classical solution to Prandtl's lifting-line equation. The solution to the lifting-surface equation for rectangular wings was found to compare well with other continuous loading methods, but with much smaller computational times, and it converges faster than other vortex lattice methods.

INTRODUCTION

The vortex lattice method has proven to be a useful technique for calculating the aerodynamic characteristics of complete configurations as well as wings. In the conventional vortex lattice method (VLM), the planform is divided into a number of elemental panels, and a horseshoe vortex is placed at the local quarter-chord of each panel. The boundary condition is satisfied at the local three-quarter chord of each elemental panel (called control points) by requiring the flow to be tangent to the surface there. The strengths of the horseshoe vortices are determined by solving the matrix equation formed from the tangent-flow boundary conditions. Then, the aerodynamic characteristics are calculated by summing the results from each elemental panel. A complete description of the conventional vortex lattice method is given by Margason and Lamar in reference 1.

Although reasonable results are obtained by the conventional VLM, Lan (ref. 2) listed the following deficiencies: 1) The method used to compute the induced drag implies that the leading-edge thrust is distributed over the chord

17

---

instead of being concentrated at the leading edge. 2) The predicted pressure distribution is not accurate near the leading edge. 3) The convergence of solutions is slow with respect to the number of panels used. In addition, the Kutta condition is not explicitly satisfied. Hough (ref. 3) found some improvement by using a 1/4 lattice width inset at the wing tips.

Lan (ref. 2) developed an ingenious method for thin, two-dimensional airfoils by using the midpoint trapezoidal rule and the theory of Chebychev polynomials to reduce the downwash integral to a finite sum. This method gives the exact lift, pitching moment, leading-edge suction, and pressure difference at a finite number of points; and the Kutta condition is satisfied at the trailing edge. A more detailed description is given below. Lan also developed a quasi-vortex lattice method for finite wings by using his two-dimensional method for the continuous chordwise vortex distribution but a stepwise constant vortex distribution in the spanwise direction. The results showed an improvement over those calculated by the conventional vortex lattice method.

This paper develops a new vortex lattice method which uses Lan's continuous chordwise vortex distribution but, unlike Lan, a continuous spanwise vortex distribution also. Although the vortex distributions are continuous, the method is easily interpreted as a vortex lattice method in which the arrangement of horseshoe vortices and control points are determined from the finite sum used to approximate the downwash integral of lifting-surface theory. In order to understand the development of the present method, Lan's two-dimensional theory is reviewed first, and then the present method is applied to Prandtl's lifting-line theory before developing the method for lifting-surface theory.

SYMBOLS

A	aspect ratio
b	wing span
c	wing chord
c_ℓ	sectional lift coefficient
c_m	sectional moment coefficient about leading edge
c_t	sectional leading-edge thrust coefficient
C_{D_i}	far-field induced drag coefficient
$C_{D_{ii}}$	near-field induced drag coefficient
C_L	wing lift coefficient

C_{L_α} lift-curve slope, per radian except when noted otherwise

C_M wing pitching moment coefficient about leading edge

C_{M_α} pitching-moment curve slope, per radian

C_S leading-edge suction parameter

C_T wing leading-edge thrust coefficient

e far-field spanwise efficiency factor, $C_L{}^2/C_{D_i} \pi A$

e_{nf} near-field efficiency factor, $C_L{}^2/C_{D_{ii}} \pi A$

$K_{ijk\ell}$ parameter defined by eq. (26)

M number of trailing vortices over whole wing span

$M-1$ number of spanwise control points over whole span

n summational integer

N number of chordwise vortices and control points

NLR   National Aerospace Laboratory, Netherlands

S wing planform area

VLM   vortex lattice method

V_∞ freestream velocity

w downwash velocity, referred to V_∞ and positive upwards

x chordwise coordinate measured from leading edge in direction of V_∞

x_{ac}, X_{ac} sectional and wing aerodynamic center locations, respectively

y spanwise coordinate, positive to the right

z_c vertical coordinate of mean camber line

α angle of attack

γ nondimensional circulation per unit chord

Γ circulation

ΔC_p difference between lower and upper pressure coefficients ($\Delta C_p = 2\gamma$)

θ transformed chordwise coordinate, see eq. (2)

ϕ transformed spanwise coordinate, see eq. (12)

Subscripts:

i chordwise control point, see eq. (7)

j spanwise control point, see eq. (15)

k chordwise vortex position, see eq. (6)

ℓ spanwise trailing vortex position, see eq. (14)

p evaluated at spanwise position $\phi_p = p\pi/M$

LAN'S TWO-DIMENSIONAL THEORY

For thin airfoils, the downwash equation is

$$w_i = -\frac{1}{2\pi} \int_0^c \frac{\gamma(x_1)\ dx_1}{x_i - x_1} \tag{1}$$

The integral on the right side is of the Cauchy type. Transform the x coordinate by

$$x/c = (1 - \cos\theta)/2 \tag{2}$$

and use the following result from airfoil theory (ref. 4)

$$\int_0^\pi \frac{d\theta_1}{\cos\theta_1 - \cos\theta} = 0 \tag{3}$$

to write eq. (1) as

$$w_i = -\frac{1}{2\pi} \int_0^{\pi} \frac{\gamma(\theta_1) \sin \theta_1 \, d\theta_1}{\cos \theta_1 - \cos \theta} = -\frac{1}{2\pi} \int_0^{\pi} \frac{[\gamma(\theta_1) \sin \theta_1 - \gamma(\theta) \sin \theta] d\theta_1}{\cos \theta_1 - \cos \theta} \qquad (4)$$

Lan (ref. 2) used the theory of Chebychev polynomials to show that

$$\sum_{k=1}^{N} \frac{1}{\cos \theta_k - \cos \theta_i} = \begin{cases} -N^2 & \text{for } i = 0 \\ 0 & \text{for } i \neq 0, N \\ N^2 & \text{for } i = N \end{cases} \qquad (5)$$

when the vortex positions are

$$\theta_k = \frac{(2k-1)\pi}{2N} \quad , \quad k = 1, \ldots, N \qquad (6)$$

and the control points are located at

$$\theta_i = \frac{i\pi}{N} \quad , \quad i = 0, 1, \ldots, N \qquad (7)$$

Then the integral in eq. (4) can be reduced to a finite sum by using the mid-point trapezoidal rule (ref. 5) and eq. (5) to obtain

$$w_i = -\frac{1}{2\pi} \frac{\pi}{N} \sum_{k=1}^{N} \frac{\gamma_k \sin \theta_k - \gamma_i \sin \theta_i}{\cos \theta_k - \cos \theta_i}$$

$$= -\frac{1}{2N} \sum_{k=1}^{N} \frac{\gamma_k \sin \theta_k}{\cos \theta_k - \cos \theta_i} + \begin{cases} -\frac{N}{2} \lim_{\theta \to 0} \gamma(\theta) \sin \theta & , \quad i = 0 \\ 0 & , \quad i \neq 0, N \\ \frac{N}{2} \lim_{\theta \to \pi} \gamma(\theta) \sin \theta & , \quad i = N \end{cases} \qquad (8)$$

However,

$$\lim_{\theta \to 0} \gamma(\theta) \sin \theta = 4 C_S \qquad (9)$$

where C_S is the leading-edge suction parameter and since the Kutta condition requires that $\gamma(\pi) = 0$,

$$\lim_{\theta \to \pi} \gamma(\theta) \sin \theta = 0 \qquad (10)$$

Unlike the conventional vortex lattice method, the Cauchy singularity, leading-edge square-root singularity and the Kutta condition are properly accounted for in this method. Equation (8) can be solved with $i \neq 0$ to obtain

the N values of γ_k, and then the leading-edge suction parameter can be computed by using eq. (8) with i = 0 (control point at the leading edge). Figure 1 illustrates the positions of the vortices and control points by the "semicircle method" for N = 2. With only one vortex (N = 1), the exact lift and leading-edge suction are obtained, and the Kutta condition is satisfied. With two or more vortices the exact pitching moment is obtained in addition to the above properties and the calculated values of γ_k are exact. It can be shown that the remarkable accuracy of this method is due to eq. (5), which is similar to the integral result given by eq. (3) and used in exact thin airfoil theory.

PRANDTL'S LIFTING-LINE THEORY

Before attacking the lifting-surface equation, the present method will be developed for Prandtl's lifting-line equation to compare the spanwise lift distribution with the classical solution (ref. 4). The lifting-line equation is given by ref. 6,

$$\Gamma = \pi \, V_\infty \, c \left[\alpha - \frac{1}{4\pi \, V_\infty} \int_{-b/2}^{b/2} \frac{d\Gamma}{dy_1} \frac{dy_1}{(y - y_1)} \right] \tag{11}$$

This equation also has a Cauchy integral on the right side, and thus Lan's airfoil technique is applicable. Transform the spanwise coordinate by

$$y = -\frac{b}{2} \cos \phi \tag{12}$$

and replace the downwash integral in eq. (11) with the midpoint trapezoidal-rule summation to get

$$w_j = -\frac{1}{4\pi \, V_\infty} \int_{-b/2}^{b/2} \frac{d\Gamma}{dy_1} \frac{dy_1}{(y_j - y_1)} \simeq -\frac{1}{4\pi \, V_\infty} \frac{\pi}{M} \frac{2}{b} \sum_{\ell=1}^{M} \frac{(d\Gamma/d\phi_1)_\ell}{\cos \phi_\ell - \cos \phi_j} \tag{13}$$

This equation represents the downwash due to M trailing vortices of strength $-(d\Gamma/d\phi_1)_\ell \, (\pi/M)$ located at

$$\phi_\ell = \frac{(2\ell - 1)\pi}{2M} \quad , \quad \ell = 1, \ldots, M \tag{14}$$

with control points located at

$$\phi_j = \frac{j\pi}{M} \quad , \quad j = 1, \ldots, M-1 \tag{15}$$

306

Now the conventional vortex lattice arrangement is shown in figure 2*, whereas the present arrangement is shown in figure 3. Note in particular that the tip vortices extend to the wing tip in the conventional method, whereas eq. (14) determines them to be inset (see fig. 3), which agrees with Hough's results (ref. 3).

Since $(d\Gamma/d\phi_1)_\ell$ is needed in eq. (13), it is convenient to represent the circulation by Multhopp's interpolation formula

$$\Gamma(\phi) = \frac{2}{M} \sum_{p=1}^{M-1} \Gamma_p \sum_{n=1}^{M-1} \sin n\phi_p \sin n\phi \tag{16}$$

where

$$\phi_p = \frac{p\pi}{M} \quad , \quad p = 1, \ldots, M-1 \tag{17}$$

Equation (16) is based on the following orthogonality property (ref. 7)

$$\frac{\pi}{M} \sum_{n=1}^{M-1} \sin n\phi_p \sin n\phi_j = \begin{cases} \frac{\pi}{2} & \text{for} \quad p = j \\ \\ 0 & \text{for} \quad p \neq j \end{cases} \tag{18}$$

Substitute eq. (16) into eq. (13) and then the downwash becomes

$$w_j \simeq - \frac{1}{V_\infty M^2 b} \sum_{\ell=1}^{M} \sum_{p=1}^{M-1} \Gamma_p \sum_{n=1}^{M-1} \frac{\sin n\phi_p \, n \cos n\phi_\ell}{\cos \phi_\ell - \cos \phi_j} \tag{19}$$

However, this result can be simplified by using eq. (5) to derive the important summation below

$$\frac{\pi}{M} \sum_{\ell=1}^{M} \frac{\cos n\phi_\ell}{\cos \phi_\ell - \cos \phi_j} = \frac{\pi \sin n\phi_j}{\sin \phi_j} \tag{20}$$

This equation is similar to the following integral result used in thin airfoil and lifting-line analyses (ref. 4)

$$\int_0^\pi \frac{\cos n\phi_1 \, d\phi_1}{\cos \phi_1 - \cos \phi} = \frac{\pi \sin n\phi}{\sin \phi} \tag{21}$$

When eq. (20) is used in eq. (19), the downwash reduces to

---

* In some conventional techniques the spanwise length of each vortex is uniform, but it is reported to have little effect on the results.

$$w_j \simeq - \frac{1}{V_\infty M b} \sum_{p=1}^{M-1} \Gamma_p \sum_{n=1}^{M-1} \frac{\sin n\phi_p \; n \sin n\phi_j}{\sin \phi_j} \tag{22}$$

Finally, substitute eq. (22) for the downwash in eq. (11) and apply the resulting equation at the spanwise locations $\phi_j (j = 1, \ldots, M-1)$ to obtain a matrix equation for the $(M-1)$ values of Γ_p. Then, the lift, pitching moment, and induced drag can be calculated by reducing the spanwise integrals to a finite sum through the midpoint trapezoidal rule. However, the midpoint trapezoidal rule gives exactly the same result for the spanwise integrals as the integral itself when eq. (16) is used for Γ. To prove this assertion, consider the spanwise integral for the lift. Using eq. (16), the exact integral result is

$$C_L \, V_\infty \frac{S}{b} = \frac{2}{b} \int_{-b/2}^{b/2} \Gamma dy = \frac{\pi}{M} \sum_{p=1}^{M-1} \Gamma_p \sin \phi_p$$

whereas the midpoint trapezoidal rule gives

$$\frac{2}{b} \int_{-b/2}^{b/2} \Gamma dy \simeq \frac{2\pi}{M^2} \sum_{\ell=1}^{M} \sum_{p=1}^{M-1} \Gamma_p \sum_{n=1}^{M-1} \sin n\phi_p \sin n\phi_\ell \sin \phi_\ell = \frac{\pi}{M} \sum_{p=1}^{M-1} \Gamma_p \sin \phi_p$$

which is the same as the exact integral result above. In obtaining this last result, the following orthogonality property was applied

$$\frac{\pi}{M} \sum_{\ell=1}^{M} \sin n\phi_\ell \sin \phi_\ell = \begin{cases} \dfrac{\pi}{2} & \text{for} \quad n = 1 \\[2ex] 0 & \text{for} \quad n \neq 1 \end{cases}$$

The integrals for the induced drag are handled in a similar fashion.

The remarkable feature of the present method is that the results are identical to the classical solution of Prandtl's lifting-line equation when a finite number of terms is used in the Fourier series for Γ (ref. 4). The success of the present method is attributed to the location of the spanwise vortices and control points, the summational result of eq. (20), and the accuracy of the midpoint trapezoidal rule for the spanwise integrals.

Figure 4 illustrates the convergence of this method compared with the conventional VLM for C_{L_α} of rectangular and elliptical planforms with an aspect ratio of 2π. Prandtl's lifting-line theory requires trailing vortices and spanwise control points, but no chordwise control points are needed because the theory assumes the downwash is constant in the chordwise direction. Therefore, the control points are placed on the "bound" vortex for both methods. In this way, the accuracy of the spanwise vortex arrangement can be tested without the influence of the location of chordwise control points. Figure 4 shows that the

conventional VLM converges slowly and C_{L_α} does not appear to approach the correct limit when the curve is extrapolated to an infinite number of trailing vortices, $M \to \infty$ $(1/M \to 0)$. On the other hand, the present method converges very quickly and approaches the correct limit. As in the classical solutions, only one horseshoe vortex ($M=2$) is needed to obtain the exact C_{L_α} for the elliptical planform in Prandtl's lifting-line theory. Figure 5 illustrates the effect of the number of trailing vortices on the spanwise efficiency factor used in the induced drag. Here again, the conventional VLM converges slowly and does not appear to approach the correct limit, whereas the present method converges quickly and approaches the correct limit.

LIFTING-SURFACE THEORY

For simplicity, the present method is developed here for rectangular wings. The downwash equation from lifting-surface theory is usually given by one of the two following integrals (ref. 6)

$$w(x,y) = \frac{1}{4\pi} \int \int_S \frac{\gamma(x_1, y_1)}{(y - y_1)^2} \left[1 + \frac{(x - x_1)}{\sqrt{(x - x_1)^2 + (y - y_1)^2}} \right] dx_1 \, dy_1 \qquad (23)$$

or

$$w(x,y) = -\frac{1}{4\pi} \int \int_S \frac{\partial \gamma}{\partial y_1} \frac{1}{(y - y_1)} \left[1 + \frac{\sqrt{(x - x_1)^2 + (y - y_1)^2}}{(x - x_1)} \right] dx_1 \, dy_1 \qquad (24)$$

Equation (23) contains the Mangler-type integral, and therefore, is not suitable for the present method. Equation (24), however, contains Cauchy-type integrals and is therefore in the form to apply a combination of Lan's two-dimensional method for the chordwise integration and the lifting-line method developed above for the spanwise integration. Note that the integrand of eq. (24) represents the downwash at (x,y) due to half of a horseshoe vortex as shown below.
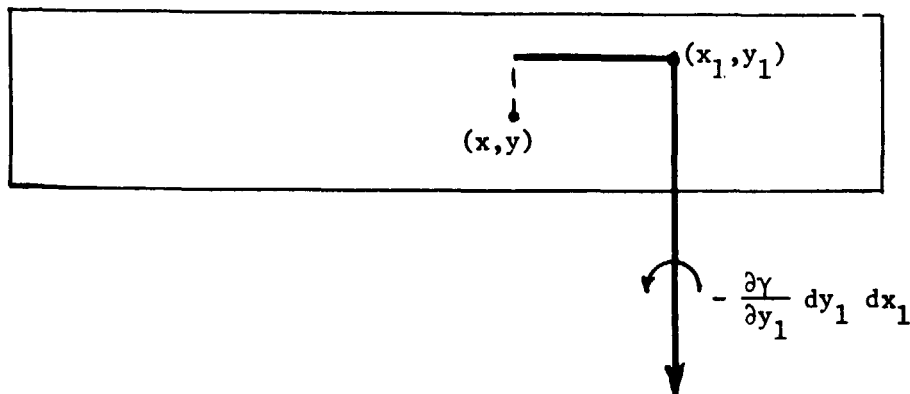
With $y = -b \cos \phi/2$ and $x/c = (1 - \cos \theta)/2$, replace both integrals in eq. (24) with the midpoint trapezoidal-rule sum to get

$$w_{i,j} \simeq - \frac{1}{4\pi} \frac{\pi}{M} \frac{\pi}{N} \frac{c}{b} \sum_{\ell=1}^{M} \sum_{k=1}^{N} \left(\frac{\partial \gamma}{\partial \phi_1}\right)_{k,\ell} \frac{K_{ijk\ell} \sin \theta_k}{(\cos \phi_\ell - \cos \phi_j)} + \begin{cases} -2NC_{S_j} & , \ i = 0 \\ \\ 0 & , \ i \neq 0 \end{cases} \tag{25}$$

where

$$K_{ijk\ell} \equiv 1 + \frac{\sqrt{(\cos \theta_k - \cos \theta_i)^2 + A^2(\cos \phi_\ell - \cos \phi_j)^2}}{\cos \theta_k - \cos \theta_i} \tag{26}$$

The control points are located at

$$\theta_i = \frac{i\pi}{N} , \ i = 1, \ldots, N \quad \text{(chordwise)} \tag{27}$$

and

$$\phi_j = \frac{j\pi}{M} , \ j = 1, \ldots, M-1 \quad \text{(spanwise)} \tag{28}$$

and the "joint" in the horseshoe vortices are located at

$$\theta_k = \frac{(2k - 1)\pi}{2N} , \ k = 1, \ldots, N \quad \text{(chordwise)} \tag{29}$$

and

$$\phi_\ell = \frac{(2\ell - 1)\pi}{2M} , \ \ell = 1, \ldots, M \quad \text{(spanwise)} \tag{30}$$

The positions of the horseshoe vortices and the control points are illustrated in figure 6 by the "semicircle method" for two chordwise vortices (N=2) and four trailing vortices (M=4). As in eq. (16), represent the spanwise variation of $\gamma_k(\phi)$, at the chordwise position θ_k, by Multhopp's interpolation formula,

$$\gamma_k(\phi) = \frac{2}{M} \sum_{p=1}^{M-1} \gamma_{p,k} \sum_{n=1}^{M-1} \sin n\phi_p \sin n\phi \tag{31}$$

where $\gamma_{p,k}$ represents the unknown circulations per unit chord at θ_k and $\phi_p = p\pi/M$. Substitute eq. (31) into eq. (25) to obtain the final form of the downwash as

$$w_{i,j} = \frac{-\pi c}{2bM^2 N} \sum_{\ell=1}^{M} \sum_{k=1}^{N} \sum_{p=1}^{M-1} \gamma_{p,k} \sum_{n=1}^{M-1} \frac{n \sin n\phi_p \cos n\phi_\ell \ K_{ijk\ell} \sin \theta_k}{(\cos \phi_\ell - \cos \phi_j)} + \begin{cases} -2NC_{S_j} & , \ i = 0 \\ \\ 0 & , \ i \neq 0 \end{cases} \tag{32}$$

310

The tangent-flow boundary condition for thin wings requires that

$$w_{i,j} = \left(\frac{\partial z_c}{\partial x}\right)_{i,j} - \alpha \tag{33}$$

where $z_c(x,y)$ is the shape of the mean camber line. The $N(M-1)$ values of $\gamma_{p,k}$ are calculated by solving the matrix equation formed by applying eq. (32) for $i \neq 0$ at the chordwise and spanwise control points given by eqs. (27) and (28). Then after $\gamma_{p,k}$ is calculated, the $(M-1)$ leading-edge suction parameters C_{S_j} can be computed by successively applying eq. (32) with $i = 0$ (control point at the leading edge) at the spanwise positions $j = 1, ..., M-1$. Regardless of the number (N) of chordwise vortices used, there is always a control point at the trailing edge which satisfies the Kutta condition, and another control point at the leading edge which gives the leading-edge suction parameter, if desired.

The sectional and wing aerodynamic characteristics may now be calculated by using the midpoint trapezoidal rule to reduce the integrals to finite sums, as shown below (for rectangular wings)

$$(c_\ell)_p = \frac{2\Gamma_p}{c\ V_\infty} = \frac{2}{c} \int_0^c \gamma_p(x_1)\ dx_1 \simeq \frac{\pi}{N} \sum_{k=1}^{N} \gamma_{p,k}\ \sin\ \theta_k \tag{34}$$

$$C_L = \int_{-b/2}^{b/2} c_\ell\ c\ dy \Big/ S \simeq \frac{\pi}{2M} \sum_{p=1}^{M-1} (c_\ell)_p\ \sin\ \phi_p \tag{35}$$

$$(c_m)_p = -\frac{2}{c^2} \int_0^c \gamma_p(x_1)\ x_1\ dx_1 \simeq -\frac{\pi}{2N} \sum_{k=1}^{N} \gamma_{p,k}\ (1 - \cos\ \theta_k)\ \sin\ \theta_k \tag{36}$$

$$C_M = \int_{-b/2}^{b/2} c_m\ c^2\ dy \Big/ Sc \simeq \frac{\pi}{2M} \sum_{p=1}^{M-1} (c_m)_p\ \sin\ \phi_p \tag{37}$$

$$(x_{ac}/c)_p = -(c_m/c_\ell)_p \tag{38}$$

$$X_{ac}/c = -C_M/C_L \tag{39}$$

$$C_{D_i} = \frac{C_L^2}{\pi A} \sum_{n=1}^{M-1} n \left[\sum_{p=1}^{M-1} \Gamma_p\ \sin\ n\phi_p\right]^2 \Bigg/ \left[\sum_{p=1}^{M-1} \Gamma_p\ \sin\ \phi_p\right]^2 \tag{40}$$

$$(c_t)_j = 2\pi \; c_{s_j}^2 \tag{41}$$

$$C_T = \int_{-b/2}^{b/2} c_t \; c \; dy / S \simeq \frac{\pi}{2M} \sum_{j=1}^{M-1} (c_t)_j \sin \phi_j \tag{42}$$

$$C_{D_{ii}} = C_L \; \alpha - C_T \tag{43}$$

The spanwise loading can be made continuous by eq. (31), and the chordwise loading can also be made cortinuous by fitting C_{s_j} and $\gamma_{j,k}$ to the chordwise loading functions for thin airfoil theory (ref. 4).

RESULTS FOR RECTANGULAR WINGS

For one horseshoe vortex and one control point (N=1, M=2), the present method yields

$$C_{L_\alpha} = \frac{\pi A}{1 + \sqrt{1 + A^2/7}} \quad \text{and} \quad C_{D_i} = \frac{C_L^2}{\pi A}$$

These results give the correct limit as $A \to 0$, but just as Lan found for airfoils, at least two chordwise vortices are needed to get an accurate pitching moment.

Table 1 gives a detailed comparison of the results of the present method with those of several other methods for a flat A = 2 rectangular wing. The methods chosen for comparison are the continuous loading method of the National Aerospace Laboratory of the Netherlands (NLR) presented in ref. 8, Lan's quasi-vortex lattice method (ref. 2), the conventional vortex lattice method of Margason and Lamar (ref. 1), and Wagner's continuous loading method (see ref. 2). In the NLR method (M-1) spanwise loading functions are applied but 8M spanwise integration points are used. Therefore, the results from this method are used as a base for comparison purposes. Table 1 shows that the present method yields more accurate overall aerodynamic characteristics than either the conventional VLM or Lan's quasi-vortex lattices. This table also shows that the spanwise variation of the sectional lift coefficient compares within four significant figures to those of the NLR method. The spanwise variation of the sectional aerodynamic center also compares well except near the wing tip. When the number of chordwise vortices was increased from N = 4 to N = 6 in the present method, these differences decreased considerably. Figure 7 compares the present method with the NLR method for the chordwise loading at midspan on this same A = 2 wing. Again, the results compare quite well.

The computational time required for the results in Table 1 was 22 minutes for the NLR method on a CDC 3300 computer; Lan's method required one minute on

the Honeywell 635 computer; Wagner's method used about three minutes; and the present method required less than ten seconds on an IBM 370/165. Therefore, the present method is as economical as the VLM for the same number of vortices, but it is generally more economical when one considers that a smaller number of vortices can be used to achieve the same accuracy as the VLM.

The effect of the vortex lattice arrangement on the convergence of the lift-curve slope is presented in figure 8 and compared with the conventional VLM for flat rectangular wings with A = 2, 4.5, and 7. This figure illustrates again the slow convergence of the conventional VLM and the rapid convergence of the present method. For all three wings, the present method gives good accuracy with only two chordwise vortices, but more spanwise vortices are needed for the A = 7 wing ($M/2 \simeq 10$) than the A = 4.5 wing ($M/2 \simeq 5$) or A = 2 wing ($M/2 \simeq 2$). Results for the pitching moment, aerodynamic center location, and induced drag were found to converge even faster than the lift-curve slope, therefore they are not presented.

The Prandtl-Glauert rule can be easily applied to the present method to include subsonic compressibility effects.

APPLICATIONS TO OTHER CONFIGURATIONS

Flaps and ailerons may be added to the wing by using an approach somewhat similar to that of Lan (ref. 2). For the chordwise integration, the interval from the leading edge of the wing to the flap leading edge is transformed into $[0,\pi]$ by the "semicircle method", and the interval from the flap leading edge to the trailing edge is also mapped into $[0,\pi]$ by another "semicircle". The same technique can also be applied in the spanwise direction.

Application of the present method to tapered and/or swept wings requires additional considerations. Care must be exercised so that the chordwise vortex and control points at one spanwise location match those at another spanwise position in order to evaluate the Cauchy integral properly. These configurations are presently being studied along with non-planar wings.

CONCLUDING REMARKS

A new method is developed for solving the lifting-surface equation for thin, subsonic wings. The downwash equation is written as Cauchy-type integrals for the chordwise and spanwise directions. They can be interpreted as a lattice of horseshoe vortices and the positions of the vortices and control points are determined by the finite sum used to approximate the integrals. Lan's two-dimensional method is used for the chordwise integral since it properly accounts for the leading-edge singularity, Cauchy singularity, and the Kutta condition. For the spanwise integral, Multhopp's interpolation formula is used in conjunction with the midpoint trapezoidal rule and the theory of Chebychev polynomials. This method properly accounts for the Cauchy singularity

313

and yields the classical solution to Prandtl's lifting-line equation. The numerical method for evaluating the chordwise and spanwise integrals is much simpler and quicker than other continuous loading methods.

The chordwise and spanwise methods are combined 'ᴗ obtain a continuous loading solution to the lifting-surface equation. The algorithm for the rectangular wing gives results which compare well with other continuous loading methods, but with much smaller computational times. In addition, it converges faster and is more accurate than other vortex lattice methods.

For rectangular wings, the vortex lattice arrangement dictated by the present method differs from the conventional VLM in that the chordwise positions of the vortices and control points do not follow the usual 1/4 - 3/4 rule. There is always a control point at the trailing edge, which allows the Kutta condition to be satisfied, and a control point at the leading edge which yields the leading-edge suction parameter. The spanwise vortices determined by the present method are not uniformly spaced, and the tip vortices are inset from the actual wing tip. This vortex lattice arrangement gives better results than other VLM's for rectangular wings. Other wing planforms require additional considerations, and they are presently being investigated.

REFERENCES

1. Margason, R. J.; and Lamar, J. E.: Vortex-Lattice Fortran Program for Estimating Subsonic Aerodynamic Characteristics of Complex Planforms. NASA TN D-6142, 1971.

2. Lan, C. E.: A Quasi-Vortex Lattice Method in Thin Wing Theory. J. Aircraft, vol. 11, no. 9, Sept. 1974, pp. 518-527.

3. Hough, G. R.: Remarks on Vortex-Lattice Methods. J. Aircraft, vol. 10, no. 5, May 1973, pp. 314-317.

4. Kuethe, A. M.; and Schetzer, J. D.: Foundations of Aerodynamics. John Wiley & Sons, Inc., N. Y., second edition, 1959.

5. Luke, Y. L.: The Special Functions and Their Approximations. Vol. II, Chap. XV, Academic Press, N. Y., 1969.

6. Ashley, Holt; and Landahl, M. T.: Aerodynamics of Wings and Bodies. Addison-Wesley Publishing Co., Inc., Mass., 1965.

7. Scheid, Francis: Theory and Problems of Numerical Analysis. Schaum's Outline Series, McGraw-Hill Book Co., N. Y., 1968.

8. Garner, H. C.; Hewitt, B. L.; and Labrujere, T. E.: Comparison of Three Methods for the Evaluation of Subsonic Lifting Surface Theory. Reports and Memoranda 3597, Aeronautical Research Council, London, England, June 1968.

TABLE 1. RESULTS FOR RECTANGULAR PLANFORM

A = 2

	Present N=4, M=16	NLR (ref. 8) N=4, M=16	Lan (ref. 2) N=8, M=30	VLM (ref. 1) N=6, M=40	Wagner from ref. 2
Overall Values					
C_{L_α}	2.4732	2.4744	2.4707	2.5239	2.4778
$-C_{M_\alpha}$	0.5187	0.5182	0.5173	0.5334	0.5180
X_{ac}/C	0.2097	0.2094	0.2094	0.2113	0.2091
$1/e$	1.0007	1.0007	1.0050	1.0018	1.0005
$1/e_{nf}$	0.9951	1.0108	1.0022	0.9764	1.0172

Values of c_ℓ/C_L

2y/b	Present	NLR
0	1.2543	1.2543
0.1951	1.2331	1.2331
0.3827	1.1692	1.1692
0.5556	1.0625	1.0625
0..071	0.9137	0.9137
0.8315	0.7257	0.7257
0.9239	0.5045	0.5044
0.9808	0.2588	0.2587

Values of x_{ac}/c

2y/b	Present	NLR
0	0.2200	0.2199
0.1951	0.2187	0.2187
0.3827	0.2150	0.2149
0.5556	0.2087	0.2085
0.7071	0.1999	0.1996
0.8315	0.1896	0.1886
0.9239	0.1798	0.1773
0.9808	0.1731	0.1685

$$x/c = (1 - \cos \theta)/2$$
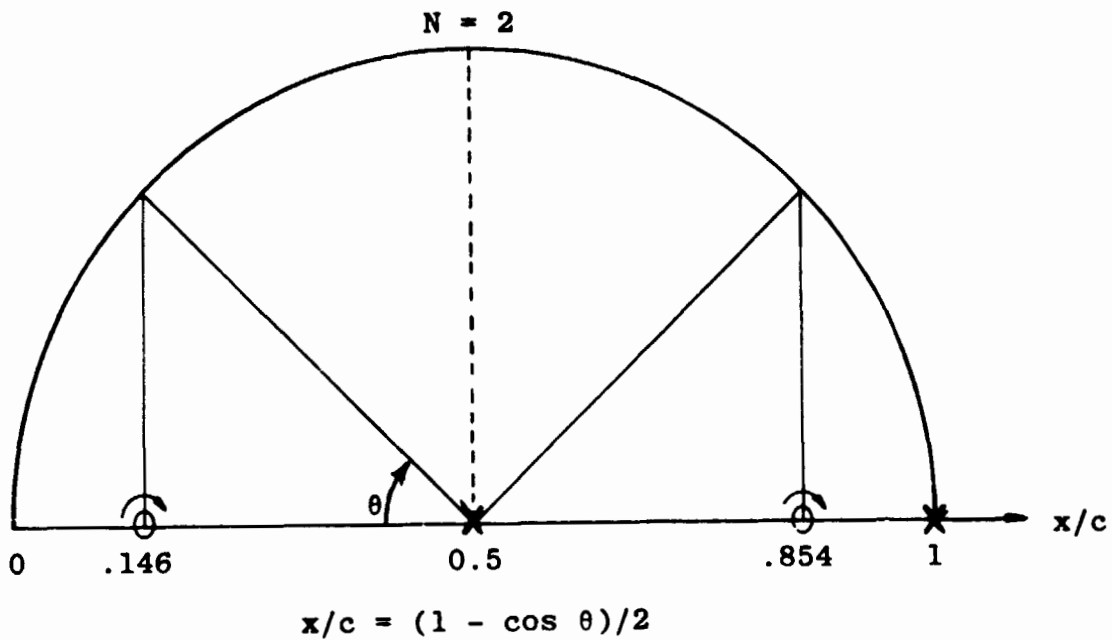
O Vortex Position: $\theta_k = \dfrac{(2k - 1)\pi}{2N}$ $(k = 1, \ldots, N)$

X Control Points : $\theta_i = \dfrac{i\pi}{N}$ $\qquad (i = 1, \ldots, N)$

Figure 1.- Lan's vortex arrangement for airfoils.
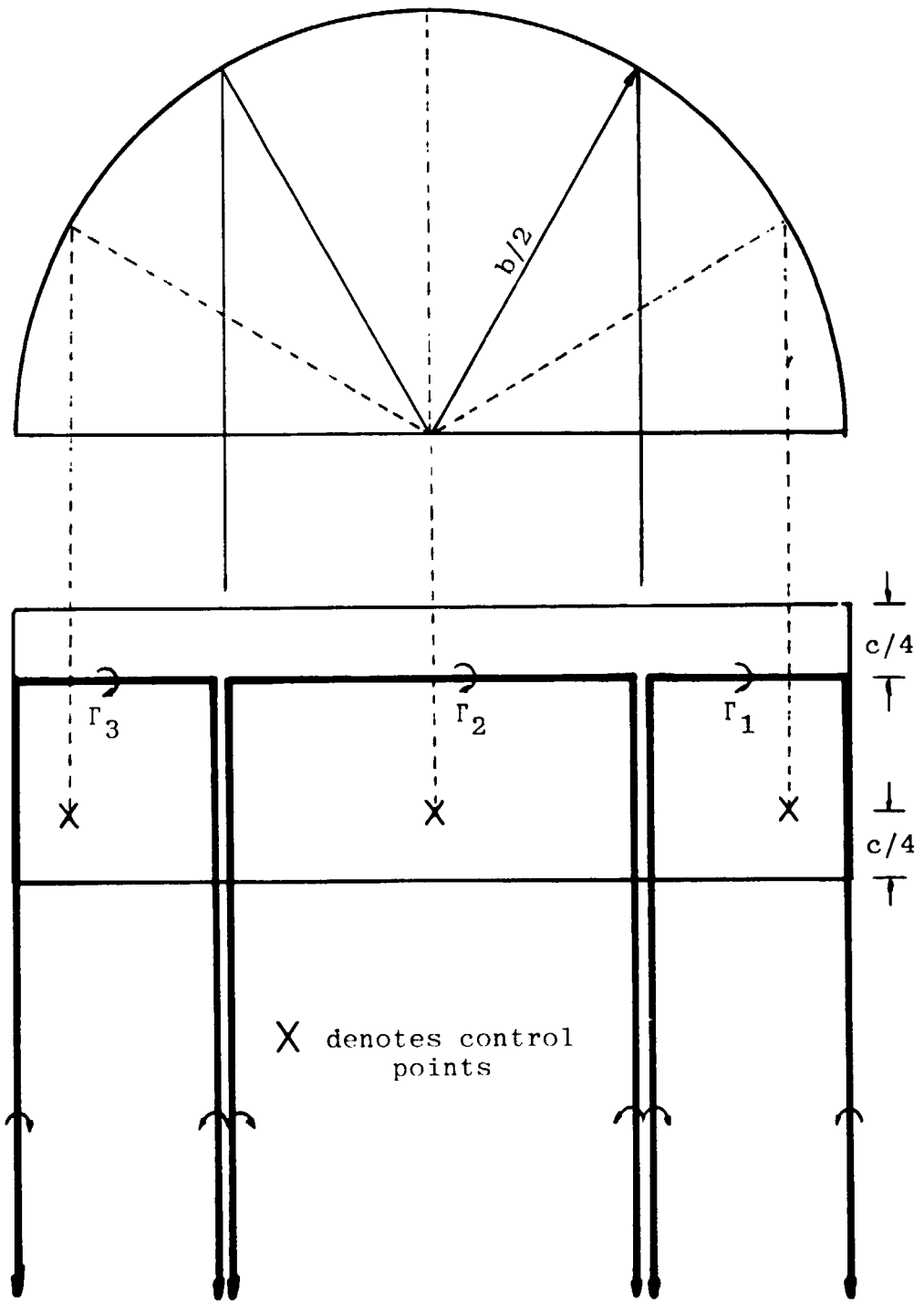
Figure 2.- Conventional arrangement of vortex lattice (illustrated for $N = 1$, $M = 4$).
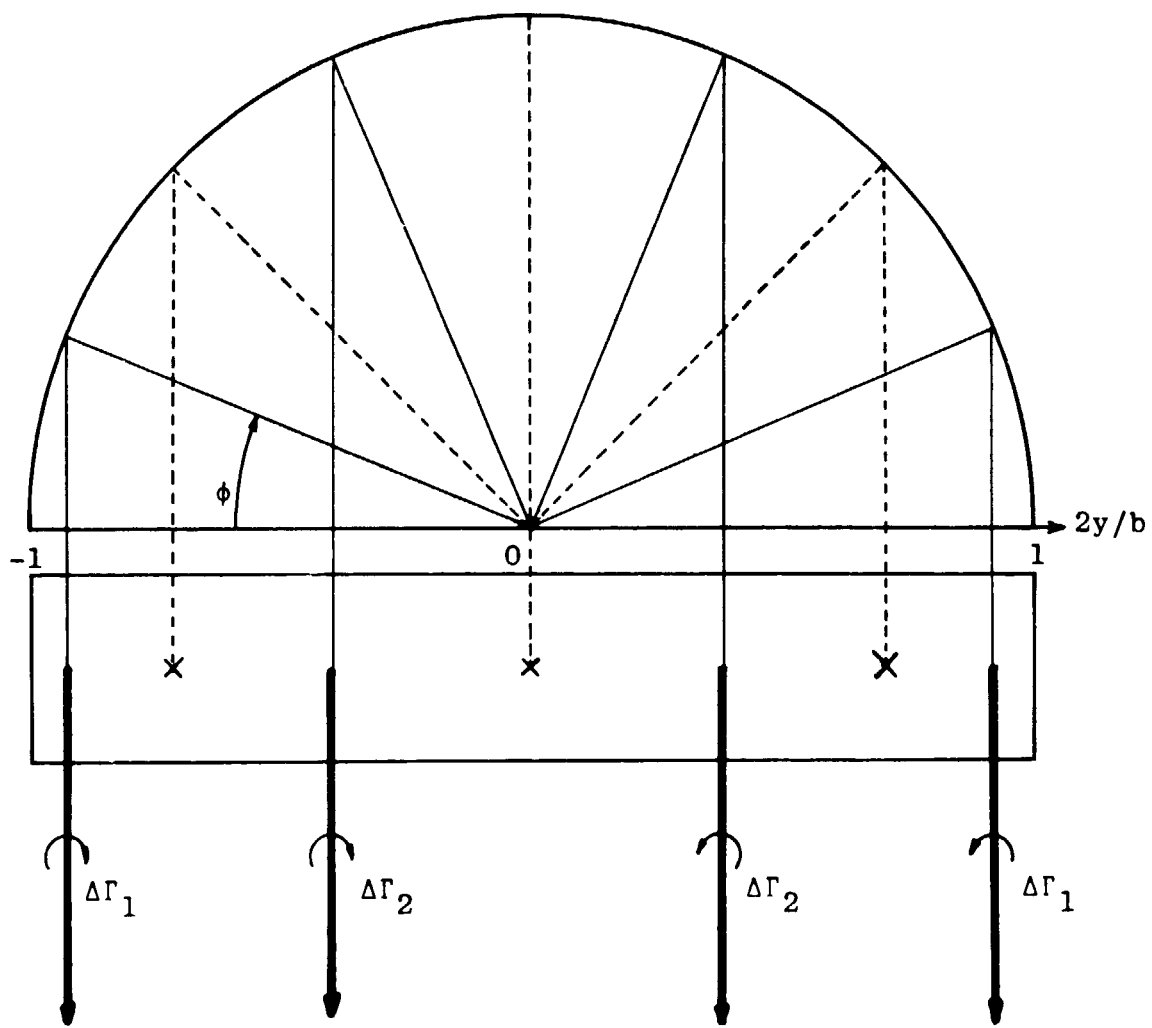
X = Spanwise Control Points   Rectangular Wing for M = 4

Figure 3.- Arrangement of trailing vortices for Prandtl's
lifting-line equation.
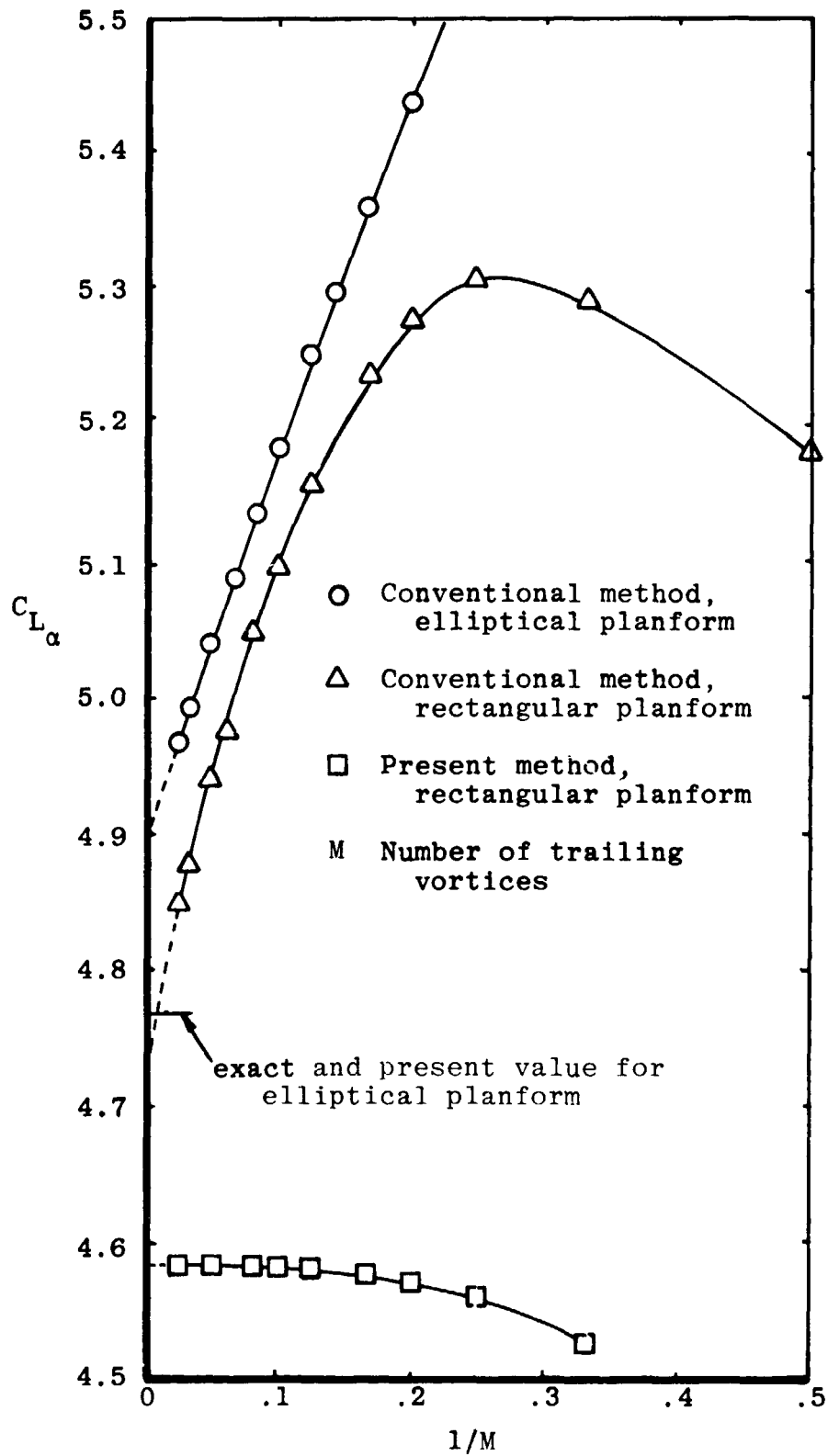
Figure 4.- Effect of number of trailing vortices on C_{L_α} from Prandtl's lifting-line theory, $A = 2\pi$.
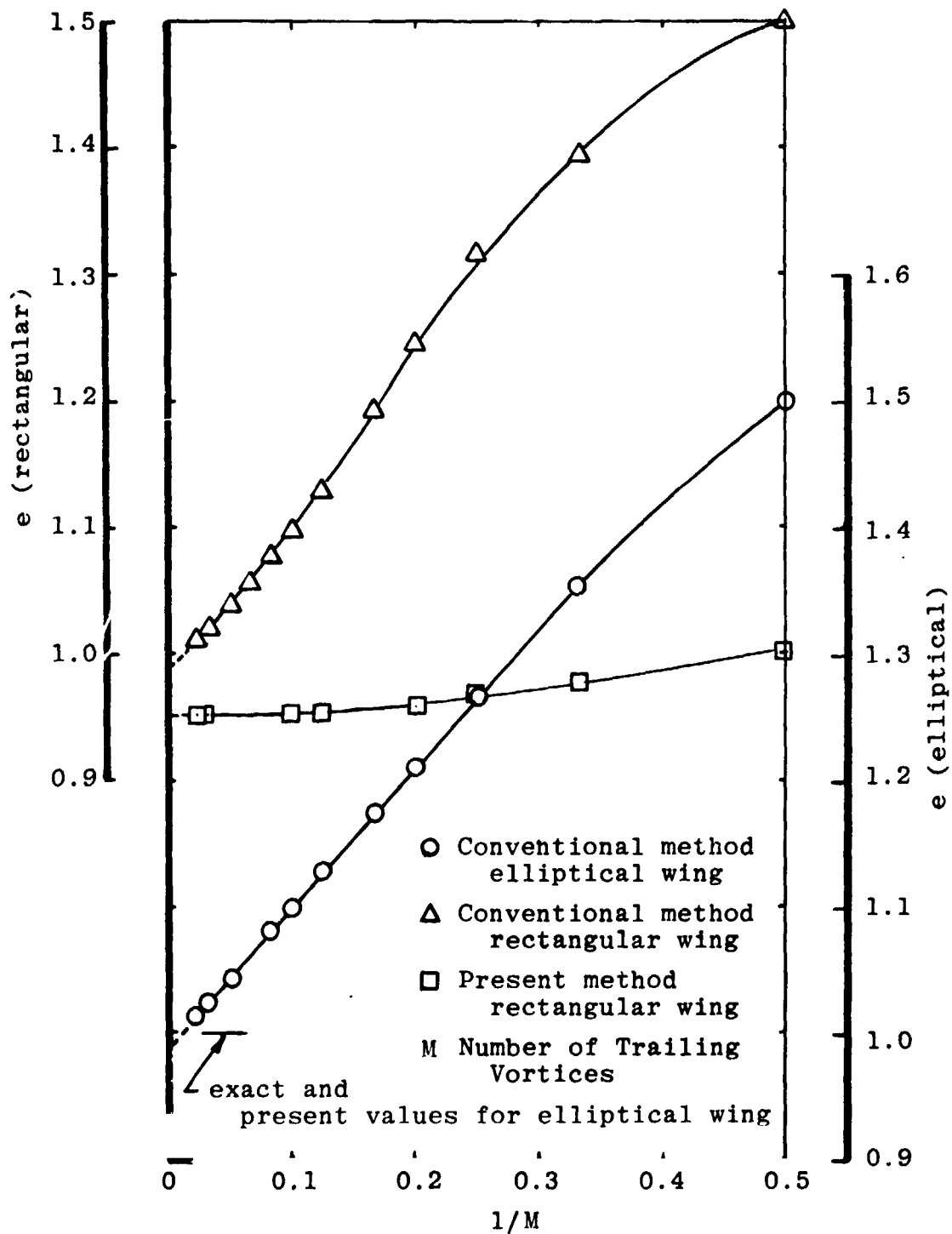
Figure 5.- Effect of number of trailing vortices on induced
drag from Prandtl's lifting-line theory, $A = 2\pi$.
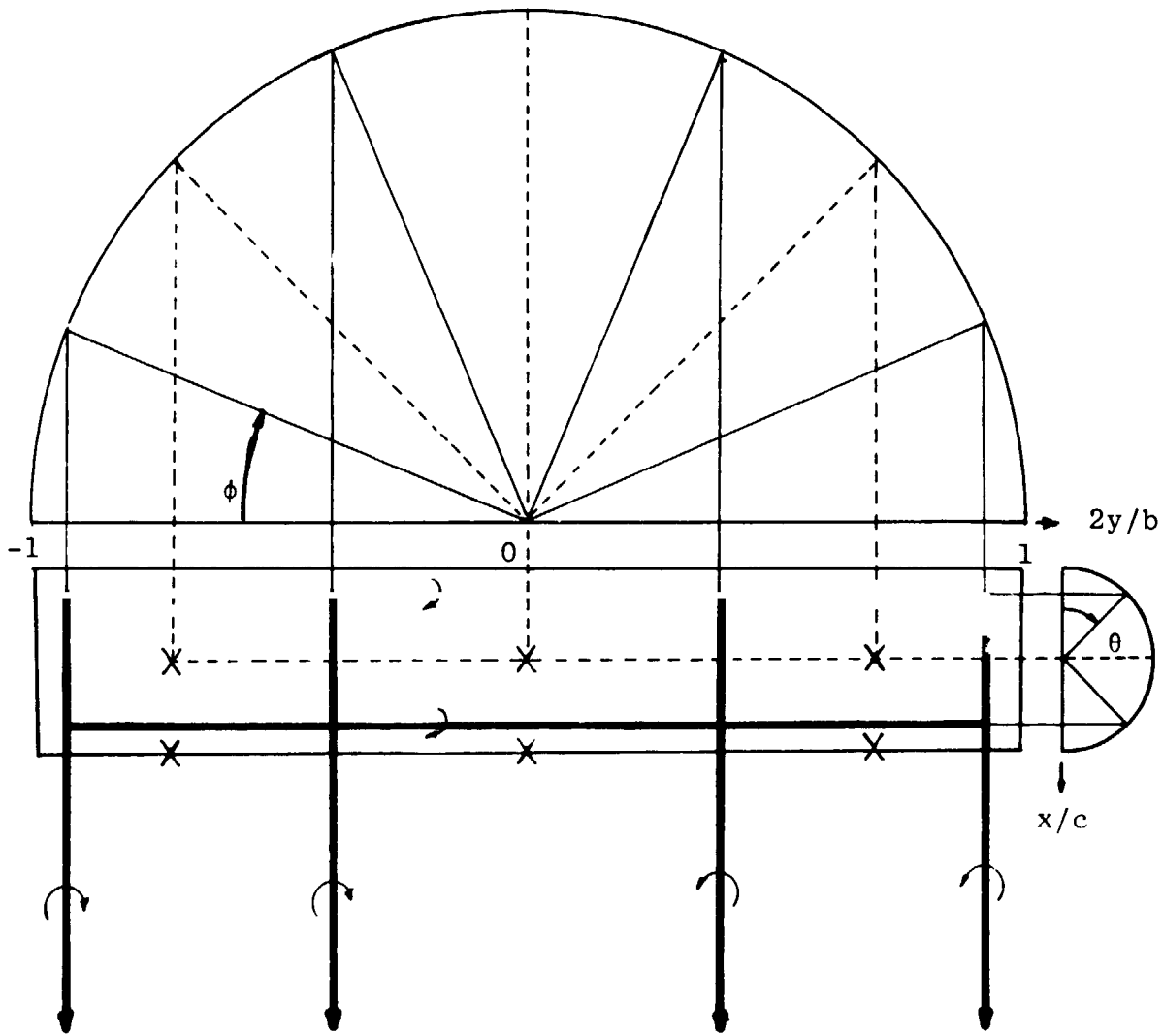
X = Control Points

Rectangular Wing for

N = 2, M = 4

Figure 6.- Arrangement of vortex lattice for lifting-surface equation.
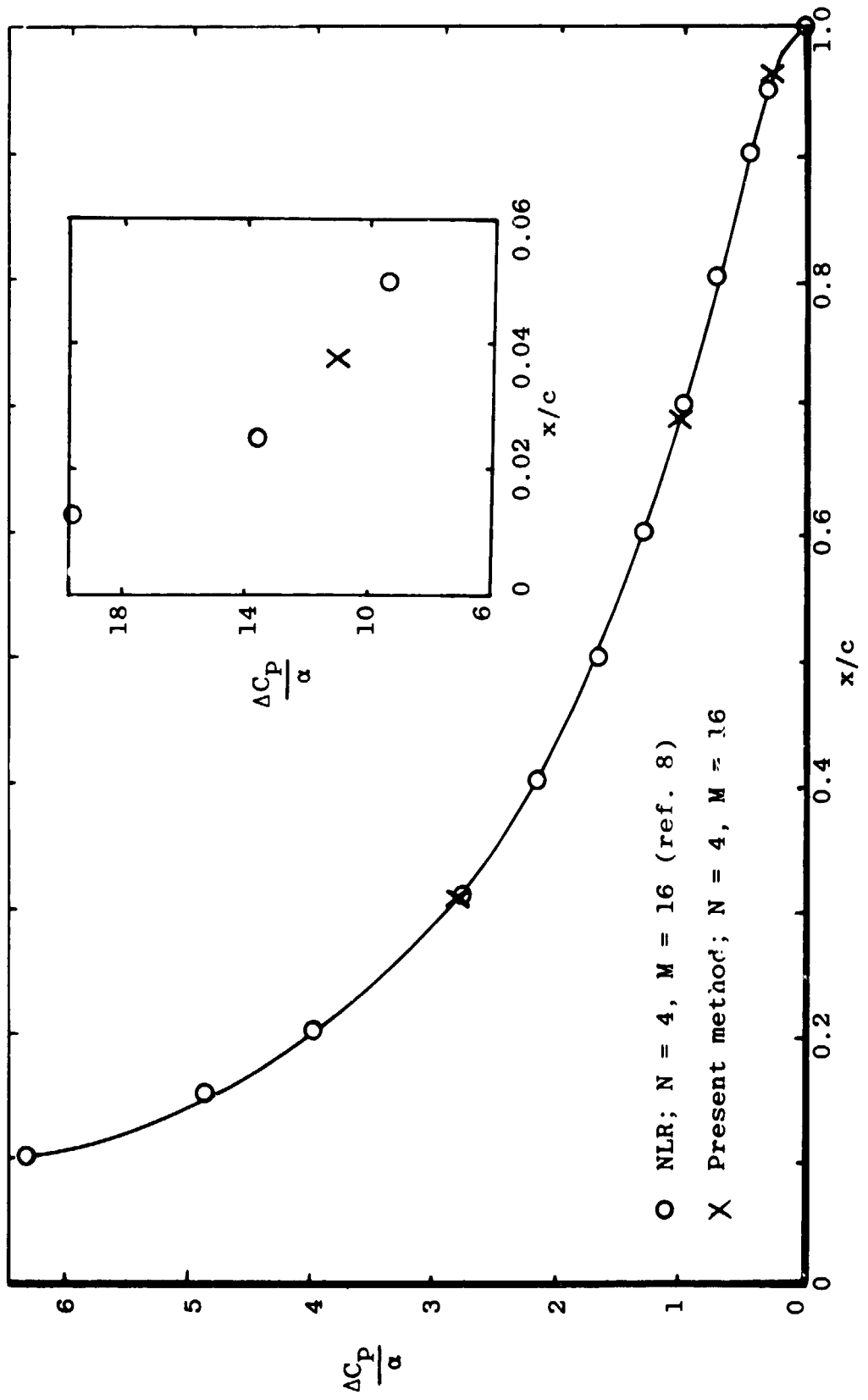
Figure 7.- Chordwise loading at midspan on rectangular wing, A = 2.
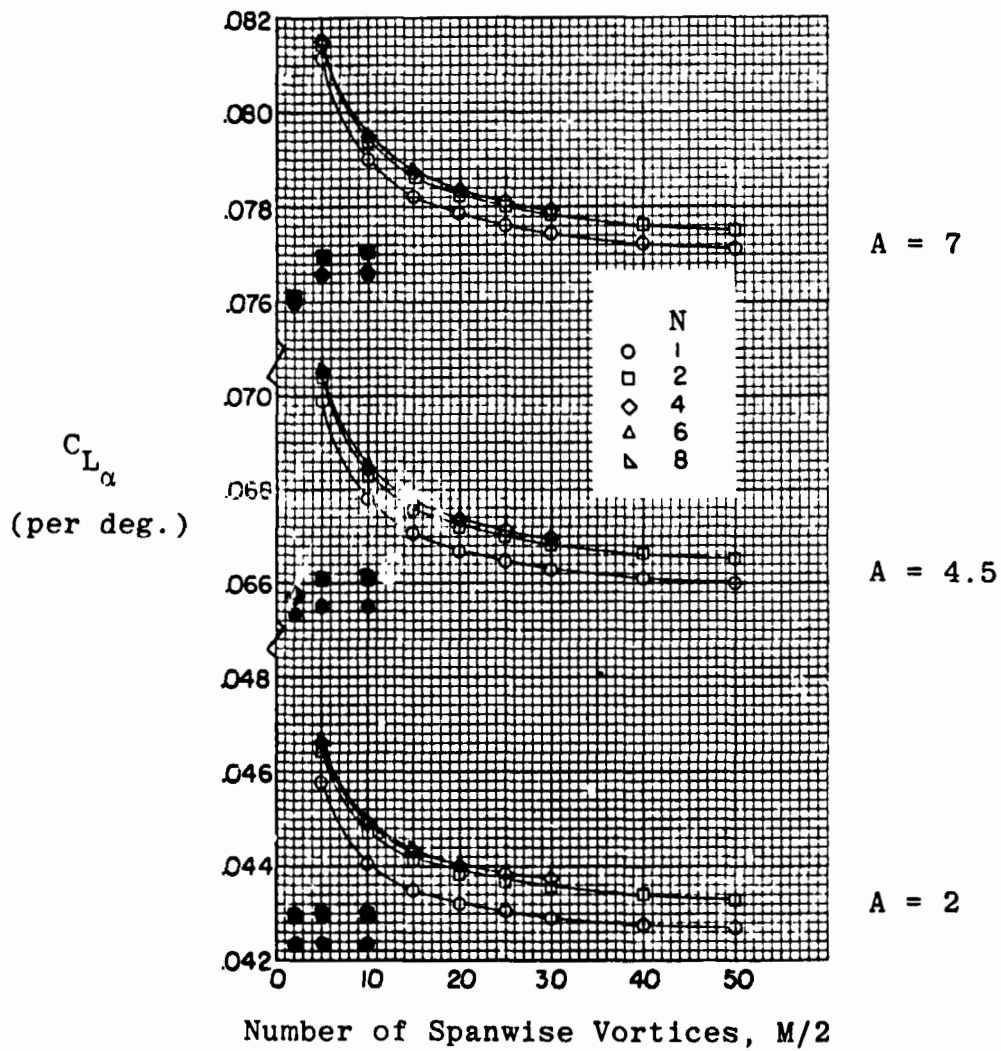
Figure 8.- Effect of vortex-lattice arrangement for
rectangular planforms.

LATTICE ARRANGEMENTS FOR RAPID CONVERGENCE

Gary R. Hough
Vought Corporation Advanced Technology Center

SUMMARY

A simple, systematic, optimized vortex-lattice approach is developed for application to lifting-surface problems. It affords a significant reduction in computational costs when compared to current methods. Extensive numerical experiments have been carried out on a wide variety of configurations, including wings with camber and single or multiple flaps, as well as high-lift jet-flap systems. Rapid convergence as the number of spanwise or chordwise lattices are increased is assured, along with accurate answers. The results from this model should be useful not only in preliminary aircraft design but also, for example, as input for wake vortex roll-up studies and transonic flow calculations.

INTRODUCTION

The vortex-lattice method (VLM) for the analysis of lifting-surface aerodynamics has become a widely used technique during the past decade. Although originally developed by Falkner in 1943 (ref. 1), it was not until the introduction of high-speed digital computers in the early 1960's that the method was reconsidered and extended, particularly by Rubbert (ref. 2). Since then, many applications of the VLM have been made to problems of aerodynamic design and analysis with considerable success.

The VLM represents a type of finite-element solution to lifting-surface theory problems. As opposed to the alternate kernel-function approach, it "seem(s) to possess none of the traditional values other than some approximation to the calculus of infinitesimals" (ref. 3). Nevertheless, a number of comparisons between the two methods have been favorable overall.

Criticisms of the VLM have continued though. These usually contend either that the lattices can be laid out in a preconceived manner to give some desired answer or that too many lattices are required for adequate convergence of the computed loadings. The present study was undertaken to derive systematically an optimized vortex-lattice layout which overcomes these objections and can be adapted to a wide variety of configurations.

The philosophy of the approach is outlined briefly and then the numerical results are presented.

PRECEDING PAGE BLANK NOT FILMED

SYMBOLS

All lengths are dimensionless with respect to the wing root chord.

A	aspect ratio
C_D	induced drag coefficient
C_L	lift coefficient
C_μ	jet momentum coefficient
c	local wing chord
d	tip lattice inset distance, fraction of lattice span
E	flap chord/wing chord
K	vortex drag factor, $\pi A C_D / C_L^2$
M	number of chordwise vortices
N	number of spanwise vortices on wing semispan
T	total number of vortices
x,y,z	right-handed Cartesian coordinates
x_{cp}	x-center of pressure
y_t	wing semispan
α	angle of attack, degrees
β	flap deflection angle, degrees
η	spanwise variable, y/y_t
τ	jet deflection angle, degrees

THE VORTEX-LATTICE APPROACH

The results presented here are based on the commonly used linearized analysis of thin lifting surfaces. The flow is considered to be steady, inviscid, and incompressible (although this latter assumption can readily be relaxed by using the Gothert transformation). While this strictly limits the study to attached flows with small deflections, the basic model has proved its usefulness in many extended applications because of its simplicity and the general agreement with experimental data.

The typical mechanics of the lattice layout, the mathematical details, and the computations of the resulting loads will not be discussed here, as they are assumed familiar or can be found in other reports (e.g., refs. 2,4,5). Rather, the focus of the analysis will be on deriving the optimized lattice structure which results in an accurate, cost-efficient approach to performance prediction for a wide variety of configurations, including wings with flaps and jet-flap systems.

Before proceeding with the details of the optimized VLM, a word about the "accuracy" (or lack of it) of these finite-element approaches is in order. It should be remembered that with the assumptions employed, we are in effect solving a particular boundary-value problem, and a unique solution exists. Hence, all properly formulated finite-element analyses (or assumed loading-function approaches) based on this model should give results which converge to this solution as the number of unknowns is increased indefinitely. There are of course some differences in the ease of application and computational effort involved in the various approaches, but what ultimately distinguishes their merits is how rapidly the results converge to the correct answer. This should be explored numerically for a number of configurations in order to give the ultimate user some degree of confidence in the particular prediction technique.

Since no exact solutions exist (except for the circular wing), determination of just what is the "correct" answer rests entirely upon comparison between two or more different theoretical approaches to the same problem. Thus, in this sense, a favorable comparison of analytical results with particular experimental data does not guarantee that the method is "accurate". Rather, once some degree of accuracy is established through numerical experimentation and agreement with other analyses, comparison with experiment should be used to verify the range of validity of the linearized thin-wing theory model. In cases where agreement is not good, it indicates that a better basic model is required.

NUMERICAL RESULTS

Rectangular Planforms

We first consider the case of an uncambered rectangular wing at angle of attack α, which will serve to illustrate some of the optimized lattice features. A right-handed xyz-coordinate system is chosen such that x is positive in the freestream direction and the origin is located at the wing root leading edge. For convenience, the wing root chord is normalized to unity, that is, all lengths are dimensionless with respect to the root chord. Then this wing geometry is completely described by y_t, the y-coordinate of the wing tip (or equivalently by the aspect ratio A).

The conventional lattice layout for this case (ref. 5) is to use uniformly spaced chordwise and spanwise panels which cover the whole wing. While the computed loads converge, they do so somewhat slowly with respect to the number of spanwise vortices. However, this can be accelerated by employing equally spaced lattices which are inset from the tip by a fraction d of the lattice span ($0 \leq d < 1$). (See fig. 1.) Such an idea was first suggested in reference 2 and was subsequently shown (ref. 6) to afford a marked improvement in spanwise convergence.

This is demonstrated in figure 2 where the percent error in the lift-curve slope per radian C_{L_α} is plotted as a function of the number of vortices on the semispan N for $A = 2$ and $A = 7$. The baseline data which are considered to be "exact" for these cases were taken from references 7 and 8, where careful calculations were carried out based on the kernel-function approach. It is seen that the use of $d = 1/4$ dramatically improves the convergence. In fact, for one

percent accuracy in C_{L_α}, only 5 spanwise vortices need to be used when $d = 1/4$ as opposed to about 35 when $d = 0$. Since the computational effort increases as between the square and cube of the number of unknowns, this represents possibly a two order of magnitude cost savings.

A key calculation which further reveals the advantages of spanwise lattice insetting is that of the lift-induced drag. This quantity may be computed by either a near or a far field approach. The latter is based on the work of Munk, in which a Trefftz-plane analysis is used to express the induced-drag coefficient C_D in terms of the Fourier coefficients of the spanwise lift distribution. This has the advantage of relative simplicity (assuming the lift distribution is accurate) but cannot be used to find the spanwise variation of C_D. On the other hand, the near field approach is more demanding of computer time, but does yield this spanwise variation. For the near field computation, we have found it best to use the direct method of summing the forces in the freestream direction on each bound vortex element, neglecting the influence of a bound element on itself. (See also ref. 9.)

In figure 3, the vortex drag factor $K = \pi A C_D / C_L^2$ by both the near and far field methods is shown for the $A = 2$ wing as a function of N with $d = 0$ and $d = 1/4$. The convergence as N is increased is displayed more clearly by plotting K against $1/N$. Again, the great improvement in using $d = 1/4$ is evident, along with the remarkable accuracy of the near field calculation. Further, for no insetting ($d = 0$), we see that to require very close agreement in the near and far field drags is doomed to failure unless an abnormally large number of spanwise vortices are used. The tendency of the VLM to "predict" low values of K (see ref. 9) is thus shown to be a consequence of not using the optimum lattice inset arrangement.

To illustrate the effect of varying the number of chordwise vortices M, the corresponding variation of K and the x-center of pressure x_{cp} are plotted in figure 4. Note that K is independent of M for $M>2$ (whether or not insetting is used), while x_{cp} is nearly linear in $1/M^2$ and tip insetting does not improve its convergence rate. For this $A = 2$ wing, the estimated converged values are $C_{L_\alpha} = 2.474$, $x_{cp} = 0.2094$, and $K = 1.001$, which are in excellent agreement with those obtained using the kernel-function approach (refs. 7 and 8) of $C_{L_\alpha} = 2.4744$ and $x_{cp} = 0.20939$.

These calculations have been made for an inset distance of one-quarter of a lattice span. A number of tests were made for other values of d, and it is found that $d = 1/4$ represents approximately the optimum value. As is usual in the VLM, the bound vortices are located at the local lattice quarter chord, and the tangential flow boundary condition satisfied at the local three-quarter chord midway between the trailing vortices. These positions were suggested by two-dimensional results and have been used by Falkner and all who followed. It can be shown that they are mandatory for the three-dimensional case as well (ref. 6).

Several other comments can be made regarding the overall lattice arrangement. First, the use of nonuniform chordwise spacings which bunch the lattices near the leading and/or trailing edges where the variation in vorticity is largest has been investigated. It is found for these uncambered wings that the

328

uniform chordwise spacing is just as good. Next, various types of nonuniform spanwise spacings (with and without insetting) were also tried, and again the equal span lattice arrangement with $d = 1/4$ is always superior. Finally, it has been suggested that the results from the VLM will be unreliable when individual lattice aspect ratios drop below a certain value, usually unity. However the calculations here have been carried out using lattice aspect ratios as low as 0.08 with no degredation in accuracy, thus destroying this myth.

Not only the overall loads, but also the spanwise distributions of lift, center of pressure, and induced drag are in excellent agreement with kernel-function results when the optimized layout is used. Regarding computational effort, we find that the execution time rises nearly as the square of the total number of lattices $T = MxN$ up to about $T = 80$, and then increases to become proportional to N^3 above about $T = 120$. Calculation of the near field drag increases the basic computational time by approximately 40%. Still, because of the very small number of lattices required (less than 30 for 1/2% convergence in C_{L_α}), computing costs are minimal.

For rectangular planforms, the only parametric study which can be made is on the effect of the aspect ratio A. This was carried out and several interesting features are observed. For example, the induced drag has a maximum at $A \simeq 3.5$, and the y-center of pressure on the half wing remains very nearly constant. Using a least squares analysis, an attempt to approximate the relationship between C_{L_α} and A along the lines of the classical high and low aspect ratio results yields the formula

$$C_{L_\alpha} = \frac{2\pi A}{A+3} \tag{1}$$

This is within 1% of the correct value for $16 \geqslant A \geqslant 2.5$ and agrees exactly with equation (7-52) of reference 10 for rectangular wings. A somewhat more accurate formula valid down to $A = 1$ was also found and is shown in figure 5.

Cambered Sections

Since most wing sections have some non-zero camber, it is worthwhile to look at the optimal lattice layout for this case. The study was restricted to rectangular wings with constant spanwise mean lines. However, the conclusions should be applicable to more complicated geometries. Generally, airfoil mean lines are characterized by large negative slopes near the leading edge, and we anticipate that the chordwise lattice spacing is crucial here.

As an example case, an $A = 5$ wing having an NACA 230 mean line was studied since some results for this case have already been presented (ref. 11). Calculations were made both for the uniform chordwise spacing and for a cosine-type spacing which concentrates the lattices near the leading edge where the change in slope is greatest. The results for C_L are shown in figure 6 as a function of $1/M^2$ for $\alpha = 0°$. It is seen that the cosine spacing converges more rapidly and so is preferable. The estimated converged value is $C_L = 0.077$ which agrees well with the Tulinius result reported in reference 11.

For cambered wings then, it is suggested that a nonuniform chordwise spacing be used for better accuracy. It should be remembered though, that the lift

due to angle of attack will generally be many times larger than the camber contribution and hence errors in computing the camber-induced lift will be somewhat submerged. Thus, for the example case considered at $\alpha = 8°$, the lift due to α is nearly 8 times that due to camber, and the total lift calculated using the uniform chordwise spacing for $M = 4$ differs by only 1.5% from the cosine spacing result.

Swept Tapered Planforms

The optimized VLM is readily extended to swept tapered wings by insuring that the bound portion of each horseshoe vortex is aligned with the local lattice quarter chord. As the example planform here, we choose the Warren-12 wing, which has been analyzed previously (refs. 7 and 12). It is defined by the x-coordinates of the tip leading and trailing edges of 1.27614 and 1.60947, respectively, and $y_t = 0.94281$. This gives a taper ratio of 1/3 and an aspect ratio of 2.8284. In figure 7 we show the convergence of the lift-curve slope C_{L_α} as a function of 1/N for several values of d. As before, it is seen that $d = 1/4$ provides about the fastest convergence rate. From this and other planform results, it turns out that the optimum value of d varies slightly with the aspect ratio and sweep angle, but that choosing $d = 1/4$ is the best compromise for all cases.

The variation of x_{cp} with M and N for this wing is similar to that for rectangular planforms, so that convergence is somewhat slower with respect to M. For the induced drag, both the near and far field calculations were made as before. This time, however, we find that the computed near field drag varies with both M and N, more especially with the former and that K is always less than unity. This poorer drag convergence for swept wings has been noted many times in the past, and arises from the discontinuity in the bound vortex slopes at the wing root. Tulinius (ref. 13) studied this problem and concluded that vortex-lattice approaches which use swept vortices always predict the downwash incorrectly in such regions (or near wing crank locations), but that the error is confined to the immediate neighborhood of the discontinuity. He also showed that the near and far field drag calculations should give identical answers when the bound vortex elements are all parallel.

There is a simple way to improve the near field convergence and accuracy. Suppose we have solved for the local bound vortex strengths using the appropriate swept horseshoe vortex elements. Then, to compute the drag, we must find the sum of the products of the local vortex strengths and the induced downwash at the bound vortex midpoints. Now, though, assume that the downwash is computed using rectangular horseshoe vortices whose strengths are the same as the swept elements which they replace. The results of such a calculation are shown in figure 8 where K is plotted against 1/M and compared with the result using fully swept vortices and also the far field calculation. It is evident that using rectangular elements for the drag calculation only is the answer to the problem. Not only is the dependence on M eliminated, but as it turns out, also the dependence on N. Further, the far field calculations for increasing N converge to this near field value.

While this approach has given a stable answer for the total induced drag, there is still some room for improvement in the convergence of the spanwise drag distribution, $cC_d/\bar{c}C_D$ (where C_d is the local drag coefficient and $\bar{c}$ is the

330

average chord). As shown in figure 9, the regions near the root and tip converge more slowly, and further study of this problem is needed. It is interesting to note that there is very little difference in the spanwise drag distribution curves for computations made with the rectangular or the swept vortex elements.

The kernel-function approaches also encounter similar difficulties for swept wings. In those analyses, the concept of artificial rounding at the root is often introduced, but only partially alleviates the problems (refs. 7 and 12).

The estimated converged values for this Warren-12 wing are $C_{L_\alpha} = 2.74$, $x_{cp} = 0.751$, and $K = 1.008$. The corresponding results from reference 7 are $C_{L_\alpha} = 2.75$ and $x_{cp} = 0.753$, while from reference 12, $C_{L_\alpha} = 2.74$ and $K = 1.010$. Again, the agreement is excellent. Here too, only a few lattices are required for accurate answers, e.g., a total of 30 lattices gives better than 1/2% agreement with the converged result.

This optimized layout has been used to study the properties of a number of different combinations of sweep and taper, including delta planforms. In all cases, rapid convergence and accurate results were obtained.

Other Planforms

A number of other wing planform arrangements have been studied to give further guidelines for the optimized lattice structure. Consider for example a cranked wing which has one or more discontinuities in the leading or trailing edge sweep angles. Here it is of interest to examine how the spanwise lattices should be laid out since in only a few very special cases will it be possible to use equally spaced lattices across the whole wing and keep $d = 1/4$. As a test case, a planform having both leading and trailing edge cranks located at the midspan $(0.5 \ y_t)$ with $A = 3.478$ was chosen. Then N_1 vortices were used inboard of the crank and N_2 outboard. The tip inset was set at 1/4 of the outboard lattice span. Figure 10 shows the convergence of C_{L_α} with $1/N$, $(N = N_1 + N_2)$, for $N_1 = 0.5N_2$, $N_1 = N_2$, and $N_1 = 2N_2$. Although all three arrangements appear to be converging to the same value, the fastest rate is realized with $N_1 = N_2$ or approximately equal inboard and outboard lattice spans.

Computations with other cranked wings have confirmed this finding; hence, N_1 and N_2 should be chosen to give as nearly equal lattice spans across the wing as possible. This rule is readily extended to wings with more then one spanwise crank location. Also, the induced drag should be calculated using the replacement rectangular vortices.

Other configurations which have been treated include skewed wings and planar interfering surfaces. In the former case, the symmetry with respect to y is destroyed and so the entire wing must be considered rather than just the semispan. While more vortices are required for a given accuracy, the concept of tip insetting with $d = 1/4$ still is needed for rapid convergence. Regarding the planar interfering surfaces, tip insetting is beneficial here also (on both of the wings), but an additional source of trouble is now present. This occurs if one or more trailing vortex lines from the forward surface pass sufficiently close to a control point on the aft surface where the local boundary condition is satisfied. Then, their influence becomes unduly magnified, with irrational

results. To overcome this instability, it is imperative to select the number of spanwise vortices on each wing carefully so that all the trailing vortices from the forward surface lie approximately on top of the trailing vortices from the aft surface. It is recommended that calculations for several combinations of spanwise vortices be carried out for each case to insure consistent answers.

Wings With Flaps

Although performance predictions for flapped wings using the VLM have received some attention, no detailed convergence studies are available. Indeed, from the results reported to date, it appears as if several hundred lattices are necessary to insure reasonable accuracy. The basic difficulty with flapped wings is that the loading is singular at the flap hingeline, and so a large number of chordwise vortices must be used to define the loading adequately in that region. Even the use of nonuniform cosine spacing about the hingeline does not improve the slow convergence with respect to M.

An optimized lattice arrangement has been developed which considerably reduces the number of unknowns required. For convenience in demonstrating the lattice layout, consider the simple case of a rectangular wing with a full-span trailing edge flap. The flap chord is taken as constant and equal to E, and the flap has a deflection angle β. As usual, the convergence with respect to N is accelerated by tip lattice insetting with d = 1/4. For the chordwise arrangement, we place bound vortex elements directly on the hingeline itself. This was apparently first proposed by Rubbert (ref. 2) but has not been widely used, possibly because few details or numerical results showing its benefits were given. As a result of placing bound vorticity on the hingeline, a finite loading is carried there, as opposed to the theoretically infinite value. However, the integrated loading on a non-zero chordwise element about the hingeline is finite in both cases.

The power of this hingeline-vortex approach was demonstrated initially in the two-dimensional case. There, convergence was greatly improved over the conventional approach, and the results are as good as those obtained using the quasi-continuous lifting-surface analysis of Lan (ref. 14). Calculations for the three-dimensional case are shown in figure 11, for a wing with A = 4 and E = 0.4. It is seen that the convergence of the lift-curve slope C_{L_β} is extremely good when vorticity is placed on the hingeline. From these and other computations, we conclude that less than 100 lattices are sufficient to achieve highly accurate results. This represents a substantial savings in computational effort.

Part-span flaps can be analyzed in a similar manner. That is, bound vorticity is placed along the flap hingeline and extended as necessary to the root and/or tip. The practice of insetting the vortices at the flap side edges was also recommended in reference 2, but numerical calculations here have shown that not only the local, but also the overall, loadings are highly sensitive to such an arrangement. Possibly the concept may be worthwhile in that nonlinear treatment, but it should be avoided when using the linearized approach.

This optimized VLM can be extended to treat wings with multiple flaps. These can be arranged in either chordwise or spanwise directions. For the

multiple chordwise flap case, it is necessary to place bound vortex segments on each of the flap hingelines to insure rapid convergence. The performance of leading edge high-lift devices can also be investigated using these layouts.

While there is a scarcity of good numerical results for comparison purposes, one kernel-function calculation should be mentioned. In reference 15, Garner analyzed a swept untapered wing of aspect ratio 4 with a 25% chord flap extending from the 45% spanwise station out to the tip. Using the kernel-function method, he predicted a value of $C_{L_\beta} = 0.758$ and $C_D = 0.179$. With the optimized VLM and 91 unknowns, $C_{L_\beta} = 0.757$ and $C_D = 0.180$. Here, 7 chordwise vortices (5 ahead of the hingeline and 1 behind) and 13 spanwise vortices (6 inboard and 7 on the flap) were employed. Also, the spanwise lift distribution compared very well for this case.

Finally, to show the versatility of this approach, the predicted spanwise lift distribution on a cranked tapered wing (approximating the Convair 990 planform) at 12° angle of attack with multiple spanwise flaps is plotted in figure 12. Here the seven flaps were deflected through various angles as shown in an attempt to produce a nearly linear dropoff in the loading over the outer half of the wing. Such loadings are of interest in wake vortex roll-up calculations.

Jet-Flap Wings

The optimized VLM has also been applied to predict jet-flap wing performance. The jet flap is basically an arrangement for integrating the propulsion system of an aircraft with its lift production by blowing a narrow jet of high-velocity air from a slot at the wing trailing edge. This deflected jet, besides supplying thrust, also increases the lift through an additional induced circulation as well as by a reaction to its vertical momentum. The additional circulation, or supercirculation as it is sometimes called, arises from the asymmetry induced in the main stream by the presence of the jet and can amount to a large fraction of the total lift on the wing under certain conditions.

Within the linearized theory framework, the trailing jet sheet can be represented by vortex lattices and the appropriate dynamic boundary condition satisfied at corresponding control points. We will consider only the so-called "singular blowing" configuration in which the jet leaves at an angle τ with respect to the slope of the camberline at the trailing edge. The jet strength is described by the parameter $C_\mu(y)$, the jet momentum coefficient. The following results are taken from reference 16 wherein a complete performance analysis was carried out. This work was sponsored by NASA ARC under Contract NAS2-8115.

As in the pure flapped wing, the jet-flap loading exhibits a singular behavior. Here, it is at the trailing edge where the streamline deflection changes abruptly. Thus, in analogy with the plain flap case, we try placing bound vorticity along the wing trailing edge. This was again verified to give good convergence characteristics in the limiting two-dimensional problem. In addition, it turns out to be necessary to use a nonuniform chordwise spacing which concentrates the lattices near the trailing edge. This does have the advantage that the infinite downstream extent of the jet sheet can be mapped into a finite region.

In figure 13, the convergence behavior of the lift-curve slope C_{L_T} is plotted for full-span blowing from a rectangular wing with A = 2 and C_μ = 1. The superiority of placing bound vorticity at the trailing edge is clear. Note that the lift on the wing is computed by adding the jet reaction component to the wing bound vortex, or circulation, lift. The numerical experiments indicate it is best to consider all of the trailing edge vortex lift applied to the wing, as shown in the figure. Overall, we must use a somewhat larger number of chordwise vortices for the jet flap, but again the total number required is considerably smaller than used in previous studies.

For the above wing, the estimated converged values are C_{L_T} = 2.00 and x_{cp} = 0.816. These can be compared with the results obtained in reference 17 by using an adaptation of Lawrence's improved low aspect ratio approximation, where it was calculated that C_{L_T} = 2.01 and x_{cp} = 0.810. Comparable agreement was found at other values of A and C_μ for these rectangular planforms.

Other planforms and blowing arrangements have also been treated. Thus, part-span blowing was analyzed and y-variations in C_μ (nonuniform blowing) were taken into account. An example calculation for nonuniform blowing over part of the wing span is illustrated in figure 14. In this case, the jet extended from the 25% to the 75% spanwise station, and C_μ varied quadratically in this region.

An interesting result of the nonuniform blowing calculations is that the wing circulation lift as well as its spanwise distribution is relatively unaffected by varying C_μ provided that the total, or integrated, jet momentum coefficient is the same for both cases. Thus, we can conclude that for most practical purposes, it will be sufficient to carry out nonuniform blowing calculations for the corresponding uniform blowing case with the same total jet coefficient, and then add in the true nonuniform jet reaction components to find the total lift, center of pressure, etc., at each spanwise location.

CONCLUSIONS

In conclusion, a simple, systematic optimized vortex-lattice layout has been developed for application to a wide variety of configurations. It results in a significant reduction in computational costs when compared to current methods. The key elements are:

(a) Use of tip lattice insetting to accelerate convergence as the number of spanwise lattices is increased.
(b) Placement of bound vortices at locations where discontinuities in streamline slope occur (flap hingeline, jet-flap trailing edge) to accelerate convergence as the number of chordwise vortices is increased.
(c) Use of nonuniform chordwise spacing for cambered sections and jet-flap wings to accelerate convergence for these cases.
(d) Use of rectangular horseshoe vortices to compute the near field drag.

Rapid convergence as the number of spanwise or chordwise lattices are increased is assured, along with accurate answers. The results from this model should be useful not only in preliminary aircraft design but also, for example, as input for wake vortex roll-up studies and transonic flow calculations.

REFERENCES

1. Falkner, V. M.: The Calculation of Aerodynamic Loading on Surfaces of Any Shape. Great Britain, ARC R&M 1910, August 1943.

2. Rubbert, P. E.: Theoretical Characteristics of Arbitrary Wings by a Non-planar Vortex Lattice Method. Boeing Co. Report D6-9244, 1964.

3. Ashley, H.; and Rodden, W. P.: Wing-Body Aerodynamic Interaction. Annual Review of Fluid Mechanics, Vol. 4, 1972, pp. 431-472.

4. Giesing, J. P.; Kalman, T. P.; and Rodden, W. P.: Subsonic Steady and Oscillat ry Aerodynamics for Multiple Interfering Wings and Bodies. J. Aircraft, Vol. 9, No. 10, 1972, pp. 693-702.

5. Margason, R. J.; and Lamar, J. E.: Vortex-Lattice Fortran Program for Estimating Subsonic Aerodynamic Characteristics of Complex Planforms. NASA TN D-6142, February 1971.

6. Hough, G. R.: Remarks on Vortex-Lattice Methods. J. Aircraft, Vol. 10, No. 5, 1973, pp. 314-317.

7. Medan, R. T.: Improvements to the Kernel-Function Method of Steady, Subsonic Lifting Surface Theory. NASA TM X-62,327, March 1974.

8. Labrujere, Th. E.; and Zandbergen, P. J.: On the Application of a New Version of Lifting Surface Theory to Non-Slender and Kinked Wings. J. Engineering Mathematics, Vol. 7, No. 1, 1973, pp. 85-96.

9. Kalman, T. P.; Giesing, J. P.; and Rodden, W. P.: Spanwise Distribution of Induced Drag in Subsonic Flow by the Vortex Lattice Method. J. Aircraft, Vol. 7, No. 6, 1970, pp. 574-576.

10. Jones, R. T.; and Cohen, D.: High Speed Wing Theory. Princeton University Press, 1960.

11. Wang, H. T.: Comprehensive Evaluation of Six Thin-Wing Lifting-Surface Computer Programs. NSRDC Report No. 4333, June 1974.

12. Garner, H. C.; Hewitt, B. L.; and Labrujere, Th. E.: Comparison of Three Methods for the Evaluation of Subsonic Lifting-Surface Theory. Great Britain, ARC R&M 3597, June 1968.

13. Tulinius, J.: Theoretical Prediction of Airplane Stability Derivatives at Subcritical Speeds. North American Rockwell Co. Report NA-72-803, 1972.

14. Lan, C. E.: A Quasi-Vortex-Lattice Method in Thin Wing Theory. J. Aircraft, Vol. 11, No. 9, 1974, pp. 518-527.

15. Garner, ". C.: The Vortex Drag of a Swept Wing with Part-Span Flaps. Great Britain, ARC R&M 3695, September 1970.

16. Hough, G. R.: Aerodynamic Performance of Jet-Flap Wings. NASA CR-137858, February 1976.

17. Erickson, J. C.; and Kaskel, A. L.: Theoretical Solutions and Numerical Results for Low-Aspect-Ratio Rectangular Jet-Flap Control Surfaces. Therm Advanced Research Report TAR-TR 6603, December 1966.

CONVENTIONAL ARRANGEMENT

$M\Delta x = 1$
$N\Delta y' = y_t$

TIP INSET ARRANGEMENT

$M\Delta x = 1$
$(N+d)\Delta y = y_t$

Figure 1.- Vortex-lattice layout.

RECTANGULAR PLANFORM

ASPECT RATIO

2 ———⊙———

7 — — — —

4 CHORDWISE VORTICES

PERCENT ERROR IN C_{L_a}

$d = 0$

INSET FRACTION

$d = \frac{1}{4}$

NUMBER OF SPANWISE VORTICES
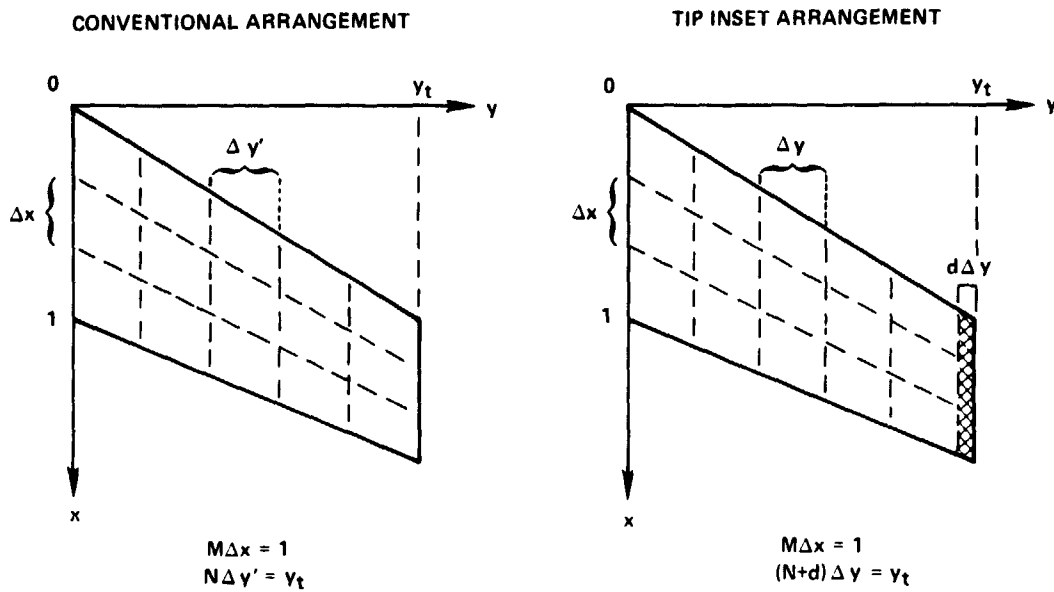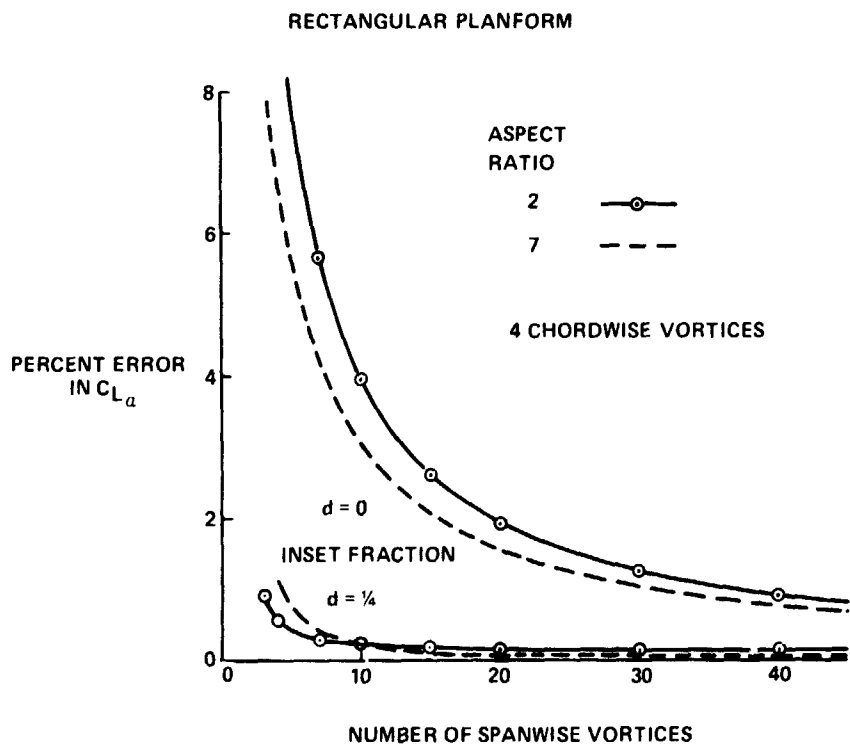
Figure 2.- Lift-curve slope convergence for rectangular wing.

RECTANGULAR PLANFORM, ASPECT RATIO = 2
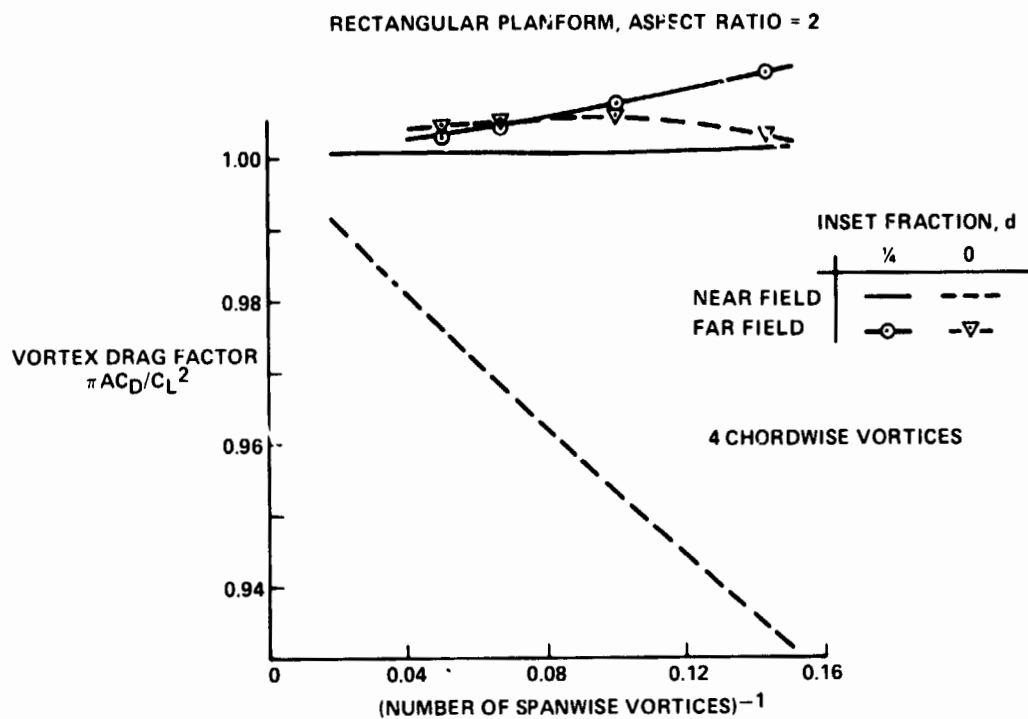
Figure 3.- Comparison of near and far field induced drag.

RECTANGULAR PLANFORM, ASPECT RATIO = 2
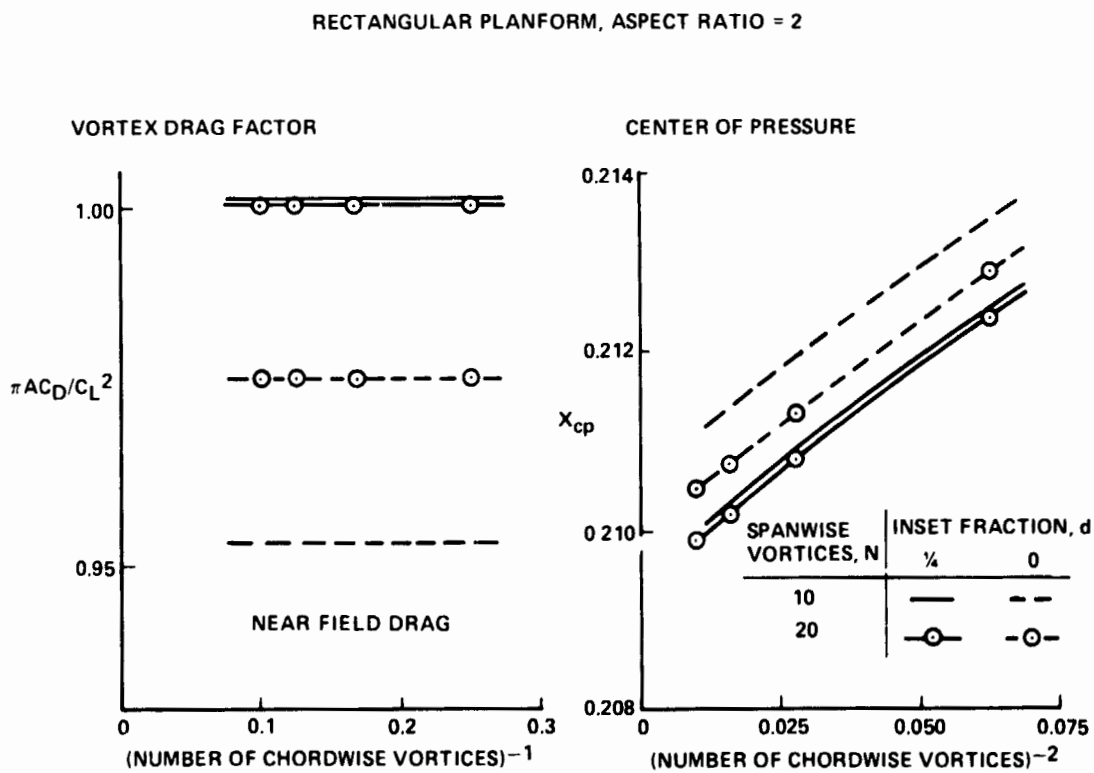
Figure 4.- Convergence behavior for rectangular wing.

337

● LIFTING-LINE THEORY (PRANDTL) – HIGH ASPECT RATIO, ELLIPTIC PLANFORM

$$C_{L_\alpha} = \frac{2\pi A}{A+2}$$

● LOW ASPECT RATIO THEORY (JONES)

$$C_{L_\alpha} = \frac{2\pi A}{A+4}$$

● NUMERICAL LIFTING-SURFACE THEORY (HOUGH) – RECTANGULAR PLANFORM

a. $C_{L_\alpha} = \dfrac{2\pi A}{A+3}$ (1% ACCURACY FOR $16 \geqslant A \geqslant 2.5$)

b. $C_{L_\alpha} = \dfrac{2\pi A}{A+2.903+\dfrac{0.377}{A}}$ (3/4% ACCURACY FOR $16 \geqslant A \geqslant 1$)

Figure 5.- Lift-curve slope formulas.

RECTANGULAR PLANFORM, ASPECT RATIO = 5
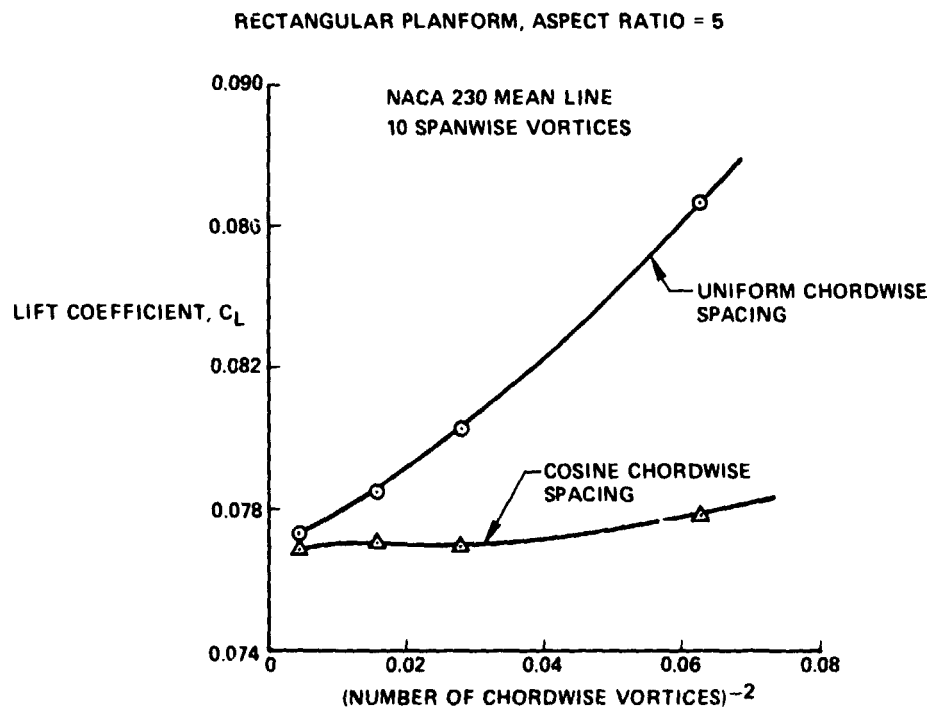
Figure 6.- Convergence for cambered wing.

WARREN-12 PLANFORM, ASPECT RATIO = $2\sqrt{2}$

d, INSET
DISTANCE

0	△
1/5	▢
1/4	⊙

LIFT-CURVE
SLOPE, C_{L_α}

2.85

2.80

2.75

2.70

0   0.04   0.08   0.12   0.16

(NUMBER OF SPANWISE VORTICES)$^{-1}$

4 CHORDWISE
VORTICES

U_∞
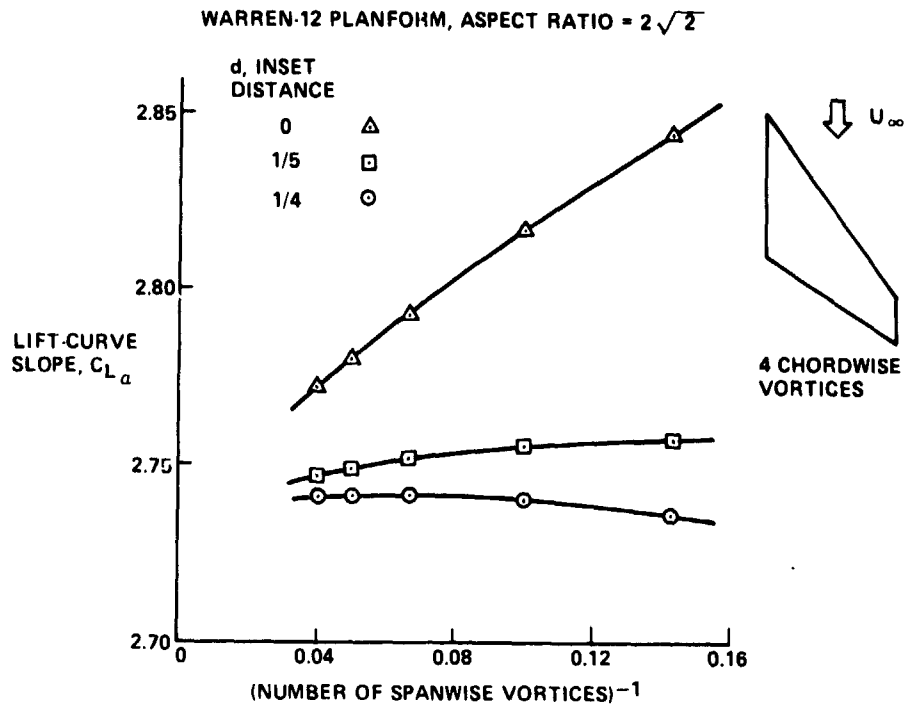
Figure 7.- Lift-curve slope convergence for tapered wing.

WARREN-12 PLANFORM, 10 SPANWISE VORTICES

FAR FIELD CALCULATION-

VORTEX DRAG FACTOR
$\pi A C_D/C_L^2$

1.02

1.00

0.98

0.96

0.94

0   0.1   0.2   0.3

(NUMBER OF CHORDWISE VORTICES)$^{-1}$

RECTANGULAR VORTICES
(FOR DRAG CALCULATION ONLY)

SWEPT VORTICES
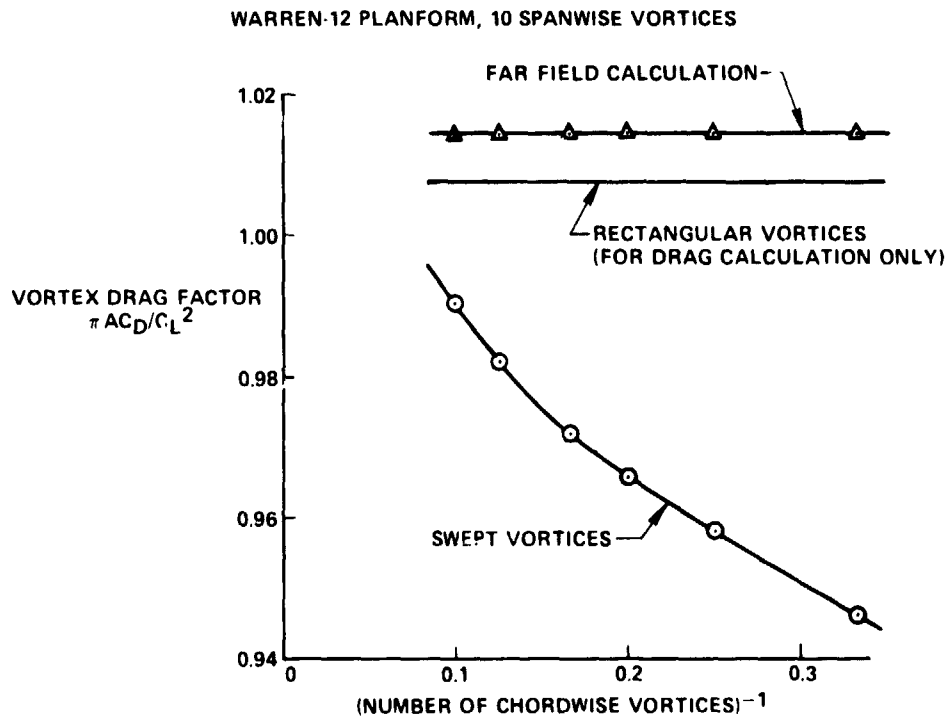
Figure 8.- Induced drag for tapered wing.

WARREN-12 PLANFORM
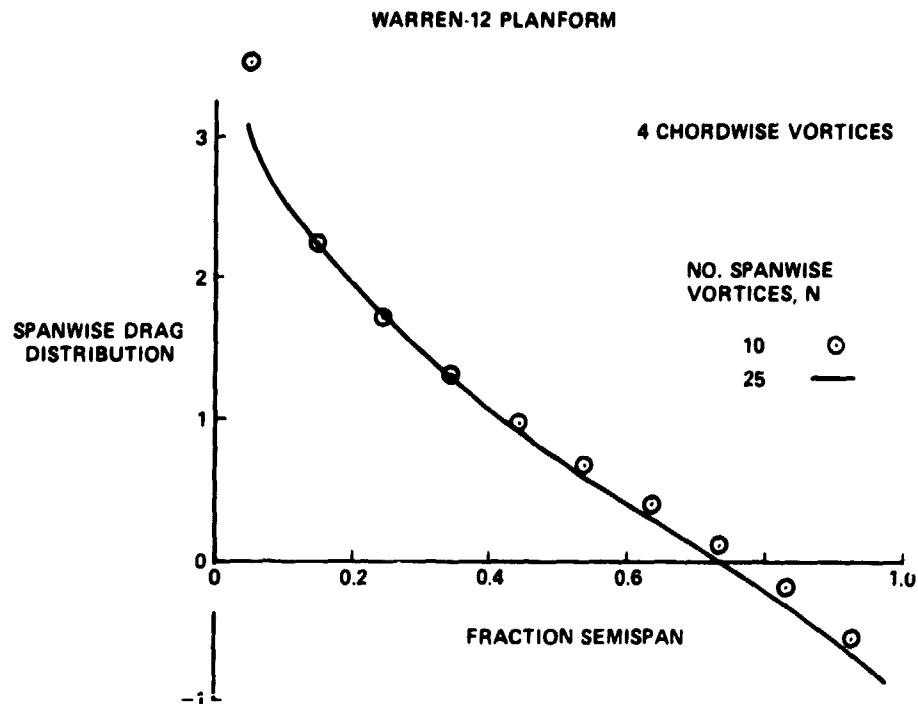
Figure 9.- Spanwise drag distribution for tapered wing.

5 CHORDWISE VORTICES
N_1 **SPANWISE VORTICES INBOARD OF CRANK**
N_2 **SPANWISE VORTICES OUTBOARD OF CRANK**
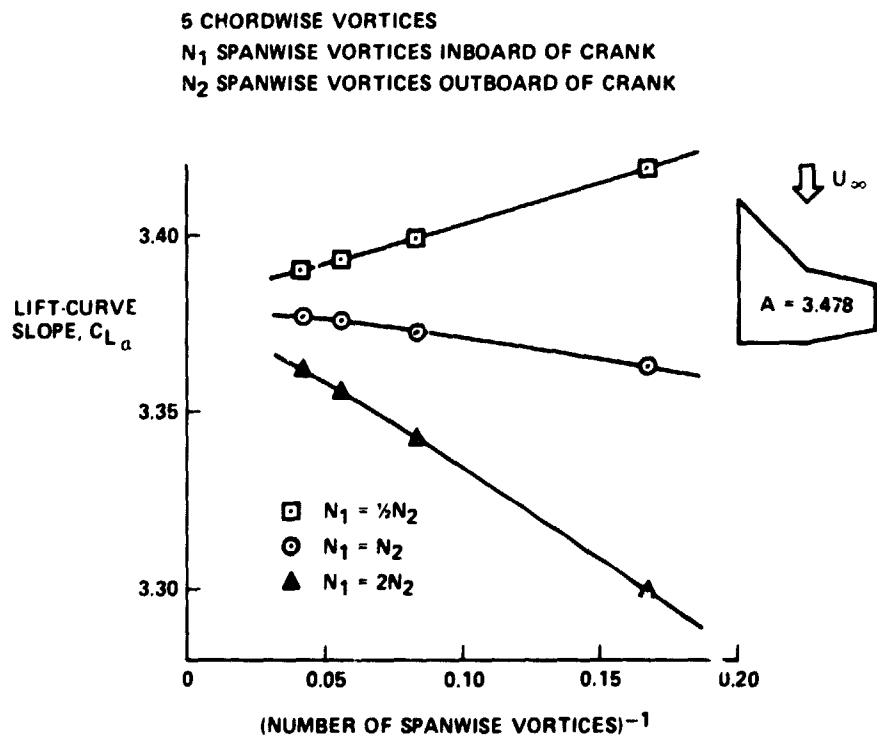
Figure 10.- Lift-curve slope convergence for cranked wing.

RECTANGULAR PLANFORM, ASPECT RATIO = 4
40% FLAP CHORD, DEFLECTION ANGLE β
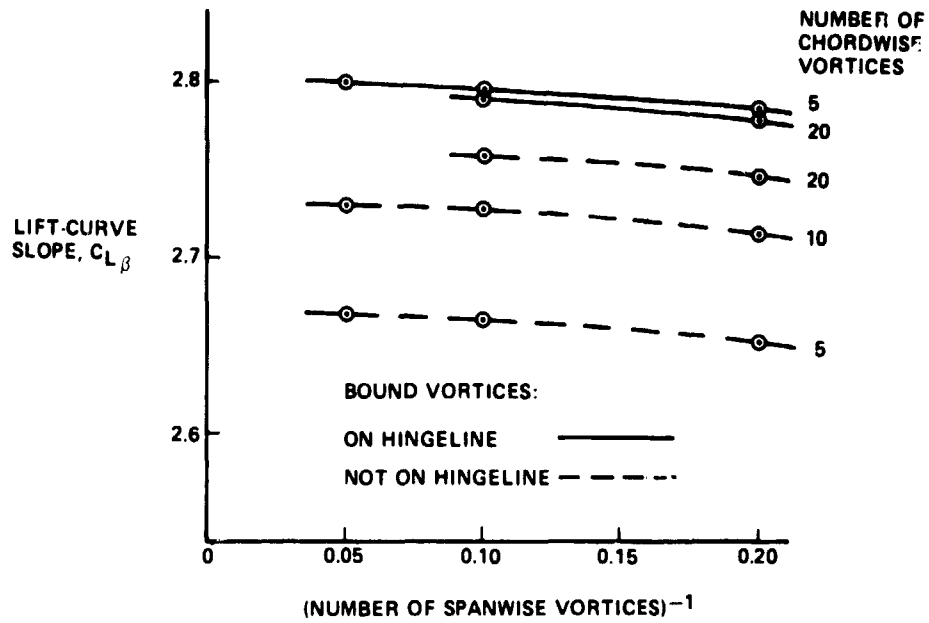
Figure 11.- Lift-curve slope convergence for flapped wing.
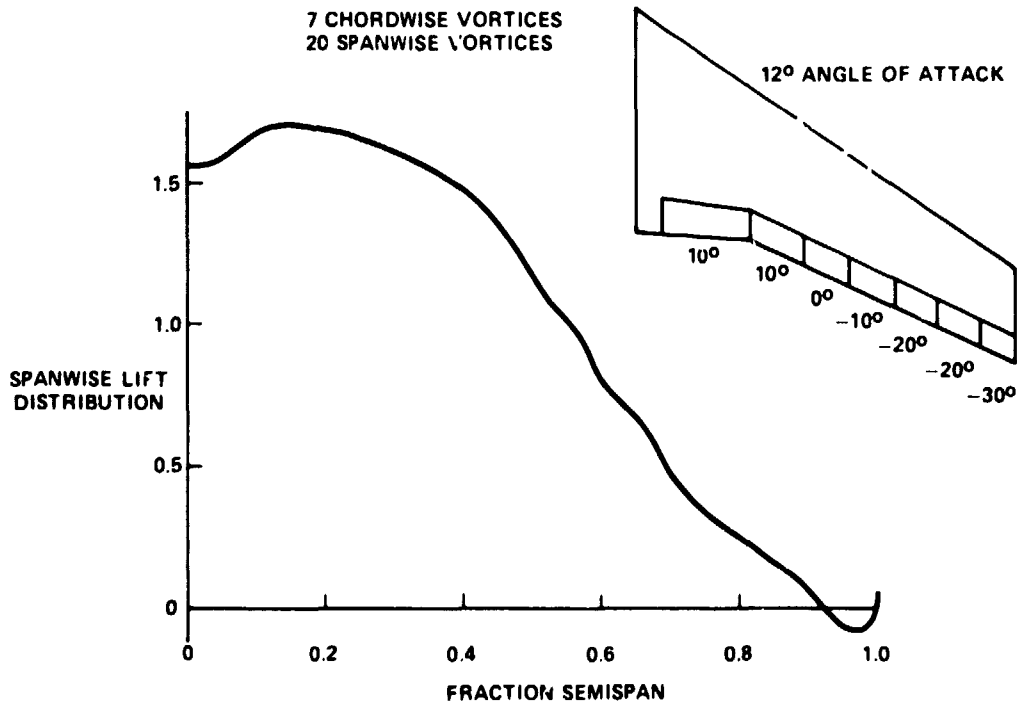
Figure 12.- Spanwise lift distribution for multiple flap configuration.

RECTANGULAR PLANFORM, ASPECT RATIO = 2
JET COEFFICIENT = 1, DEFLECTION ANGLE = τ
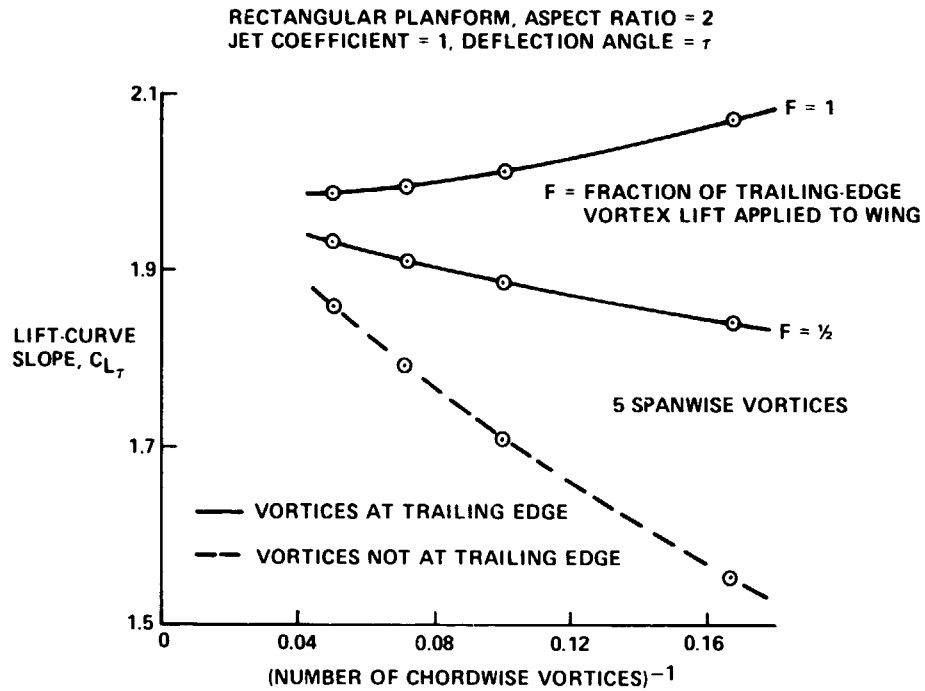
Figure 13.- Lift-curve slope convergence for jet-flap wing.

RECTANGULAR PLANFORM, ASPECT RATIO = 4.5
14 CHORDWISE VORTICES

$$C_\mu = -0.2 + 9.6\eta - 9.6\eta^2$$
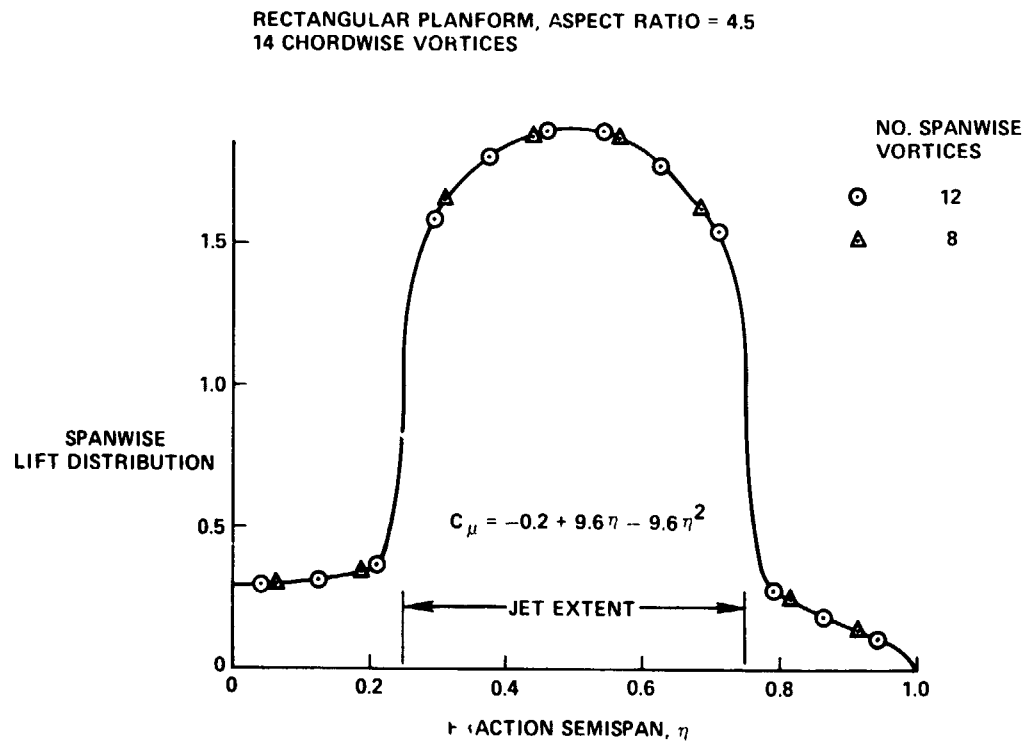
Figure 14.- Spanwise lift distribution for nonuniform blown, part-span jet flap.

OPTIMUM LATTICE ARRANGEMENT DEVELOPED FROM

A RIGOROUS ANALYTICAL BASIS*

John DeYoung
Vought Corporation Hampton Technical Center

SUMMARY

The spanwise vortex-lattice arrangement is mathematically established by lattice solutions of the slender wing which are shown to be analogous to the chordwise vortex-lattice thin wing solution. Solutions for any N number of panels to infinity are obtained. With the optimum lattice for any N value the slender wing theory lift and induced drag and thin wing theory lift and moment are predicted exactly. For $N \to \infty$, slender wing elliptic spanwise loading and thin wing cotangent chordwise loading are predicted, which proves there is mathematical convergence of the vortex-lattice method to the exact answer. Based on this $A \to 0$ and an $A \to \infty$ planform spanwise lattice arrangements, an A-vortex-lattice spanwise system is developed for arbitrary aspect ratio. This A-lattice has the optimum characteristic of predicting lift accurately for any N value.

INTRODUCTION

Growth of computer facilities has given the engineer a powerful tool for obtaining solutions to generalized problems. This is possible because with numerical or finite-difference methods the equations of a problem can be simplified readily to computer language. Vortex-lattice methods have been developed extensively for steady and unsteady pressure prediction and for planar and nonplanar configurations. Examples of some of the work and investigations in the vortex-lattice method and aspects and applications of this method are reported in references 1 through 20. A brief description of the typical vortex lattice is that the surfaces are divided in the spanwise and chordwise directions into panels which cover the surface with a lattice. The sides of the panels are parallel to the freestream and the chordwise panel boundaries follow the surface contour. The 1/4 chord line of each panel contains a bound or load vortex while the trailing vortices are at the sides of the panel. The boundary condition of no flow through the surface is fulfilled on every panel at one point located at the lateral center of the 3/4 chord line of the panel. These panels are distributed in a uniform, and thus geometrically simplest mesh, referred to as a planform lattice. However, in

1966 an application of the lattice method of reference 5 to a swept wing showed that the chord loading in the panel bordering the wing leading edge was too low, the spanwise loading near the wing tip was too high for engineering acceptability, and the net lift slightly too large. This was with 100 panels on the semispan, 10 chordwise times 10 spanwise. Investigation of a lattice mathematical model was made at that time of the chordwise panel distribution and later reported in reference 20. The results of this work showed that the loading at the leading edge panel needs a factor of about 1.128 which improved the loading value in that panel. However, the too high wing tip loading and lift was not explained. In early 1972 a mathematically rigorous spanwise vortex-lattice analysis was developed based on slender wing theory (part of ref. 19). This was mathematically analogous to the earlier chordwise solution but more complicated. This spanwise lattice arrangement is characterized by a 1/4 - 3/4 rule which locates the trailing vortices inboard 1/4 of the planform panel span and the no flow through points inboard 3/4 of planform panel span from the planform panel outboard edges. This inboard shift of the lattice leads to solutions with less loading near the wing tip and less lift, which improves the loading in the above example. This example supports the observation that accuracy depends on the position of the panels in the lattice as well as density of panels.

The objectives of the present study are to correlate and extend the work of references 19 and 20, to investigate the effect of three-dimensional planform on lattice arrangement, and to formulate a generalized vortex-lattice arrangement and method for three dimensional wings.

SYMBOLS

A $\qquad$ aspect ratio

A_e $\qquad$ swept panel aspect ratio [eq. (52)]

b, c $\qquad$ wing span, wing chord

C_L, C_{L_α} $\qquad$ lift coefficient, lift-curve slope

C_{D_i} $\qquad$ induced drag coefficient

c_ℓ, c_{ℓ_α} $\qquad$ section lift coefficient, section lift-curve slope

$c_{m\alpha_{LE}}$ $\qquad$ section pitching moment coefficient due to angle of attack

$e_{N_c n_c}$ $\qquad$ parameter of chordwise loading [eq. (38)]

$f_{N_c n_c}$ $\qquad$ chordwise loading factor [eq. (41) and table 5]

G $\qquad$ spanwise loading coefficient or dimensionless circulation [eq. (1)]

g_{Nn} $\qquad$ parameter of spanwise incremental circulation [eq. (7)]

h_{Nn} spanwise loading gradient factor [eq. (19) and table 2]

i_{Nn} spanwise loading factor [eq. (22) and table 3]

N, N_c integer number of panels on wing semispan, and wing chord respectively

n, m integers denoting spanwise position of vortex, and downwash point

n_c, m_c integers denoting chordwise position of vortex, and downwash point

V free stream velocity

α angle of attack

Γ circulation, also Gamma function

η lateral coordinate per wing semispan

$\Lambda_{1/2}$ sweep angle at 50% chord line

ξ longitudinal coordinate per wing section chord

Subscripts:

v vortex

w downwash point

LE   leading edge

SLENDER WING OPTIMUM VORTEX LATTICE

Physical Similarity of Trailing Vortex Sheet Flow with Chordwise Thin Wing Theory Flow

The objective of this study is to do a rigorous analytical derivation to determine the optimum spanwise distribution of panels analogous to the analysis done in reference 20 for the optimum chordwise distribution of panels. Optimum here defines the lattice which best duplicates exact solutions. A physical similarity does exist between the vorticity distribution of the chordwise loading with the trailing vortex sheet from a finite span wing. This can be seen graphically in figure 1 where thin airfoil theory chord-load vorticity is compared with the trailing vorticity which is predicted by slender wing theory (refs. 21 and 22). It has often been noted that the mathematics of thin wing and slender wing theories have a striking similarity.

From figure 1, it is noted that a similarity of vorticity is obtained when the wing tip at $\eta = 1$ correlates with the wing leading edge, and the

midspan point at $\eta = 0$ correlates with the wing trailing edge. Since this correlation makes the flow fields analogous, it follows that the optimum span-wise panel distribution is analogous to the optimum chordwise panel distribution given in reference 20. This is subject to the condition that the distribution start at the wing tip and proceed inboard. Applying this condition and using these distribution conditions, the spanwise panel distribution becomes that shown in figure 2. The determination of an optimum chordwise panel distribution is made by two-dimensionalizing the problem to planar flow and thus the spanwise extent of the panel is infinite. The optimum chordwise panel distribution is that which yields thin wing solutions which most accurately duplicate the results of exact thin airfoil theory. In the present work, the determination of an optimum spanwise panel distribution will be made by two-dimensionalizing the problem to cross-sectional flow and thus the chordwise extent of the panel is infinite. The optimum $A \to 0$ spanwise panel distribution is that which yields solution which most accurately duplicates the results of slender wing theory.

The objective of the present paper is to apply the analytical methodology of reference 20 to determine the optimum spanwise panel distribution. This distribution should result in an exact prediction of total lift for any number of spanwise panels and provide spanwise loading factors. The chordwise panel distribution analysis is correlated with thin airfoil theory for the determination of optimal accuracy. In an analogous procedure the spanwise panel distribution analysis here will be correlated with slender wing theory for the determination of optimal accuracy.

Formulation of Spanwise Lattice Matrix and Solution to Infinity which Satisfy All Boundary Points

Slender wing theory equations for additional loading (ref. 22) are

$$C_{L_\alpha} = \frac{\pi A}{2}; \quad G_\alpha(\eta) = (1 - \eta^2)^{1/2}; \quad \frac{dG_\alpha(\eta)}{d\eta} = \frac{-\eta}{(1 - \eta^2)^{1/2}} \tag{1}$$

where $G_\alpha(\eta) = \frac{\Gamma(\eta)}{bV\alpha} = \frac{c_\ell c}{2b\alpha}$

Also presented in reference 22 are solutions for flap, ailerons, and all spanwise loadings, which can be used to evaluate lattice accuracy when a problem involves these types of loadings.

By Biot-Savart law, the downwash at η_{wm} due to an infinite extent vortex at η_{vn} is (see fig. 2)

$$w_{mn} = \frac{\Delta\Gamma_n/b}{\pi(\eta_{vn} - \eta_{wm})} \tag{2}$$

with vortices located at

$$n_{vn} = \pm \frac{n - 1/4}{N} \tag{3}$$

boundary condition points at

$$n_{wm} = \pm \frac{m - 3/4}{N} \tag{4}$$

with equations (3) and (4) the downwash angle at n_{wm} is

$$\frac{\alpha_m}{\alpha} = \sum_{n=1}^{N} \left(\frac{1}{n_{vn} - n_{wm}} + \frac{1}{n_{vn} + n_{wm}} \right) \frac{g_{Nn}}{3N} \tag{5}$$

with equations (3), (4), and (5) for additional loading ($\alpha_m = \alpha$), equation (5) becomes

$$1 = \sum_{n=1}^{N} \frac{2}{3} \left(\frac{1}{2n - 2m + 1} + \frac{1}{2n + 2m - 2} \right) g_{Nn}; \quad m = 1, 2, \ldots N \tag{6}$$

where

$$g_{Nn} = \frac{3N\Delta\Gamma_{Nn}}{\pi bV\alpha} = \frac{3}{\pi} N\Delta G_{\alpha_{Nn}} \tag{7}$$

Generalized Inversion of g_{Nn} Equations

Equation (6) represents N unknowns, g_{Nn}, and N Equations. An inversion of equation (6) means a linear simultaneous solution of N equations. Solutions for N = 1, 2, . . . can be obtained readily for small N and from the resulted series formed of g_{Nn}, the general solution can be determined by induction. For N = 1, the solution is

$$g_{11} = 1$$

For N = 2, the linear simultaneous solution of two equations is

$$1 = g_{11} + \frac{7}{18} g_{22}; \qquad \text{then,} \qquad g_{21} = \frac{2}{5}$$

$$1 = -\frac{1}{2} g_{21} + \frac{7}{9} g_{22} \qquad\qquad\qquad g_{22} = \frac{54}{35} \tag{8}$$

These solutions are done for higher values of N until a sequence is formed. This sequence is presented in table 1. Examination of the 1st column in table 1 shows the sequence follows the general term of

347

for n = 1:

$$g_{N1} = \frac{3N(2N - 3)_{odd}!}{(2N + 1)_{odd}!} \tag{9}$$

In the second column, ratios of g_{N2}/g_{NL} gives the sequence

N =	2	3	4	5	6
$\frac{g_{N2}}{g_{N1}} =$	$\frac{3^2 \times 3}{1 \times 7}$	$\frac{3^2 \times 8}{3 \times 9}$	$\frac{3^2 \times 15}{5 \times 11}$	$\frac{3^2 \times 24}{7 \times 13}$	$\frac{3^2 \times 35}{9 \times 15}$

This shows the general term as [and using g_{N1} from eq. (9)]

for n = 2:

$$g_{N2} = \frac{3^2(N^2 - 1)\, g_{N1}}{(2N + 3)(2N - 3)} = \frac{3 \times 3^2(N+1)(N-1)(N)(2N-5)_{odd}!}{(2N+3)_{odd}!} \tag{10}$$

Similarly, ratios of g_{N3}/g_{N2} give the sequence

N =	3	4	5	6
$\frac{g_{N3}}{g_{N2}} =$	$\frac{5^2 \times 5}{11 \times 4}$	$\frac{5^2 \times 12}{3 \times 13 \times 4}$	$\frac{5^2 \times 21}{5 \times 15 \times 4}$	$\frac{5^2 \times 32}{7 \times 17 \times 4}$

This shows the general term as [using g_{N2} from eq. (10)]

for n = 3:

$$g_{N3} = \frac{5^2(N^2-2^2)g_{N2}}{2^2(2N-5)(2N+5)} = \frac{3 \times 3^2 \times 5^2(N+2)(N+1)(N)(N-1)(N-2)(2N-7)_{odd}!}{2^2(2N+5)_{odd}!} \tag{11}$$

These sequences of g_{N1}, g_{N2}, and g_{N3} show that

$$g_{N4} = \frac{7^2(N^2-3^2)g_{N3}}{3^2(2N-7)(2N+7)}$$

$$= \frac{3 \times 3^2 \times 5^2 \times 7^2(N+3)(N+2)(N+1)(N)(N-1)(N-2)(N-3)(2N-9)_{odd}!}{3^2 \times 2^2(2N+7)_{odd}!} \tag{12}$$

Then in general the recurrence is [from first equalities of eqs. (10), (11), and (12)]

$$g_{Nn} = \left(\frac{n-1/2}{n-1}\right)^2 \frac{N^2-(n-1)^2}{N^2-(n-1/2)^2} \; g_{N n-1} \tag{13}$$

The general term for net values of g_{Nn} is [from second equalities of eqs. (10), (11), and (12)]

$$g_{Nn} = \frac{3(N+n-1)! \, [(2n-1)_{odd}!]^2 \, (2N-2n-1)_{odd}!}{(n-1)! \, [(n-1)!]^2 \, (2N+2n-1)_{odd}!} \tag{14}$$

Equation (14) is an exact mathematical inversion of the matri . type represented in equation (6). The equation (14) solution is exact for a ' interger value of N, including N equal to infinity.

The odd factorial $(2n-1)_{odd}!$ can be converted to direct 'actorials by the relation

$$(2n-1)! = (2n-1)_{odd}! \; (2n-2)_{ev}!$$

where $(2n-2)_{ev}! = (2n-2)(2n-4)(2n-6) \dots = 2^{n-1}(n-1)(n-\ )(n-3)$

$$\dots = 2^{n-1} \, (n-1)!$$

then $\qquad (2n-1)_{odd}! = (2n-1)!/2^{n-1}(n-1)! \tag{15}$

Using equation (15) in equation (14), then g_{Nn} in terms of conventional factorials is

$$g_{Nn} = \frac{3n^2(2N-2n)!}{(N+n)(2N+2n)!} \left[\frac{(2n)!(N+n)!}{(n!)^2(N-n)!}\right]^2 \tag{16}$$

Factorials suggest Gamma functions. Extensive relations of Gamma functions and tables are presented in reference 23. In terms of Gamma functions equation (16) become:

$$g_{Nn} = \frac{3n^2}{\pi(N+n)} \frac{\Gamma(N-n+1/2)}{\Gamma(N-n+1)} \frac{\Gamma(N+n+1)}{\Gamma(N+n+1/2)} \left[\frac{\Gamma(n+1/2)}{\Gamma(n+1)}\right]^2 \tag{17}$$

The g_{Nn} function is thus expressed in three forms given by equations (14), (16), and (17) respectively.

Gradient of Spanwise Loading

The spanwise loading gradient is [using eqs. (3) and (7)]

then $\qquad G_\alpha{}'(\eta_{vn}) = -\frac{\pi}{3} \, g_{Nn} \tag{18}$

where g_{Nn} is given in equation (16). The spanwise position, η_{vn}, is given by equation (3). Comparable slender wing theory values of $G_\alpha'(\eta_{vn})$ are obtained by replacing η by η_{vn} in the gradient function given in equation (1). Comparison of equation (18) with the slender wing theory value of loading gradient shows that the lattice-method loading gradient requires a factor. This factor can be formulated accurately by this slender wing solution.

The loading gradient factor is defined as

$$h_{Nn} = \frac{G_\alpha'(\eta_{vn}) \text{ slender wing theory}}{G_\alpha'(\eta_{vn})} \tag{19}$$

Numerical values of h_{Nn} computed from equations (19) and (18) are presented in table 2. These factors are very near unity except at the wing tip region. Included are values for $N \to \infty$ determined in a following section.

Spanwise Loading

With the vortex position set by equation (3) the ΔG_{Nn} extends from $\eta_{vn} = (n - 1/4)/N$ to $(n - 1 - 1/4)/N$. The middle of this segment is at $\eta_n = (n - 3/4)/N$, that is at the same spanwise position as the boundary condition points given by equation (4). The spanwise station of the loading will be assumed to be at the middle of the segment, that is, at η_n. For symmetrical loading, the loading at wing center is constant in the range $-(1 - 3/4)/N \leq \eta \leq (1 - 3/4)/N$, and the middle of this segment is at $\eta_1 = 0$.

From equation (7) the loading at the n=N segment is

$$G_{\alpha NN} = \Delta G_{\alpha NN} = \frac{\pi}{3N} g_{NN}$$

At N-1 segment $\qquad G_{\alpha N,N-1} = \Delta G_{\alpha NN} + \Delta G_{\alpha N,N-1} = \frac{\pi}{3N}(g_{NN} + g_{N,N-1})$

Thus at the m segment $\qquad G_{\alpha Nn} = \frac{\pi}{3N} \sum_{m=n}^{N} g_{Nm} \tag{20}$

where g_{Nm} is given in equation (16) and in table 1, but with n=m numbers. These loadings are at the spanwise stations

$$\left. \begin{aligned} \eta_n &= \frac{n - 3/4}{N} \text{ ; for } n > 1 \\ &= \quad 0 \quad \text{ ; for } n = 1 \end{aligned} \right\} \tag{21}$$

Comparable slender wing theory values of $G_\alpha(\eta_n)$ are given by equation (1) with η_n of equation (21). Comparison of equation (20) with the slender wing theory value of spanwise loading shows that the lattice-method loading requires a

factor. This spanwise loading factor is defined as

$$i_{Nn} = \frac{G_\alpha(\eta_n) \text{ slender wing theory}}{G_\alpha(\eta_n)} \tag{22}$$

Numerical values of i_{Nm} computed from equation (22) are presented in table 3. These loading factors are very near to unity. Included are values for $N \to \infty$.

Lift-Curve Slope and Induced Drag

The lift coefficient is the integration of the loading coefficient, then

$$C_L = A \int_{-1}^{1} G(\eta) \, d\eta \tag{23}$$

Since ΔG_{Nn} is constant between η_{vn} and $-\eta_{vn}$, then the integration for lift is a summation of the pyramid layers of $2\eta_{vn} \Delta G_{Nn}$. Then by equation (23)

$$C_L = 2A \sum_{n=1}^{N} G_{Nn}\eta_{vn} \tag{24}$$

With the ΔG_{Nn} given in equation (7) and η_{vn} in equation (3), then equation (24) becomes C_{L_α}. The lift-curve slope is

$$C_{L_\alpha} = \frac{2\pi A}{3N^2} \sum_{n=1}^{N} (n - 1/4)g_{Nn} \tag{25}$$

where g_{Nn} is given in equation (16) and in table 1. With equation (16) inserted into (25) the lift-curve slope becomes $C_{L_\alpha} = \pi A/2$ for any value of N. This compares with the slender wing value given in equation (1).

In a following section for $N = \infty$ it is proven that $C_{L_\alpha} = \pi A/2$ for $N \to \infty$.

The induced drag coefficient is given by (for constant α_n)

$$C_{D_i} = \frac{A}{2} \int_{-1}^{1} \alpha_i G(\eta) d\eta = \frac{A}{2} \sum_{n=1}^{N} \alpha_n \Delta G_{Nn}\eta_{vn}$$

where α_n is that in equation (5) but with changed position of n and m. Since $\alpha_n = \alpha$ by the conditions of equation (6), and using equation (24), then $C_{D_i} = C_L\alpha/2$. It was shown by equation (25) that $C_L = \pi A\alpha/2$ for any value of N, then

351

$$C_{D_i} = \frac{\pi A}{4} \alpha^2$$

which is then also valid for any value of N. This is identical to slender wing induced drag. Therefore, it is concluded that this lattice and boundary point distribution results in exact integrations for lift and induced drag for any interger N. This exactness was not unexpected since the mathematics is similar to the chordwise solution (ref. 20) in which the first harmonic solution (elliptic chord loading) integrates exactly.

Solutions for N Approaching Infinity

Detailed mathematical derivations are developed in reference 19. Here the results are a digest of the mathematics in that study. The primary purpose for exploring solutions at $N \to \infty$ is to prove that a finite lattice-method solution does mathematically converge to the exact solution. In this problem the exact solution is elliptical spanwise loading evaluated from slender wing theory. Mathematical proof is needed that the integration for lift remains exact as $N \to \infty$. Asymptotic values of the factors h_{Nn} and i_{Nn} as $N \to \infty$ are useful in the tables of these factors. As $N \to \infty$ the functions become so unique and manageable the reader will find a mathematical exciting experience.

Equation (16) can be used to mathematically prove that spanwise distribution predicted from finite element loading methods do converge on the exact answer as the number of elements are increased.

Using the relation for large factorials

$$N! \xrightarrow{N \to \infty} (2\pi)^{1/2} N^{N+1/2} e^{-N} \tag{26}$$

then equation (16) becomes (except at the point n=N, i.e. at $\eta=1$ when $N=\infty$)

$$g_{Nn} = \frac{3n (N + n)^{1/2}}{\pi(N + n) (N - n)^{1/2}} = \frac{3\frac{n}{N}}{\pi(1 - \frac{n^2}{N^2})^{1/2}} \tag{27}$$

Combining equations (3), (18), and (27) results in

$$G_\alpha'(\eta_{vn}) = \frac{-\eta_{vn}}{(1-\eta_{vn}^2)^{1/2}} \tag{28}$$

Equation (28) is the same as the loading gradient given in equation(1) by slender wing theory. Thus it is proven that as lattice panels are increased, the solution converges to the exact loading.

With the relation that

$$\frac{\Gamma(N + 1/2)}{\Gamma(N + 1)} \xrightarrow{N \to \infty} \frac{1}{(N + 1/4)^{1/2}} \tag{29}$$

then equation (17) can be expressed in the forms

$$
\begin{array}{ll}
\begin{array}{l} N \to \infty \\ n = \text{finite} \end{array} & \begin{array}{l} N \to \infty \\ N-n = \text{finite} \end{array} \\
g_{N_N} = \frac{3n^2}{\pi N}\left[\frac{\Gamma(n + 1/2)}{\Gamma(n + 1)}\right]^2, & g_{N,N-n} = \frac{3N^{1/2}\,\Gamma(N - n + 1/2)}{\pi 2^{1/2}\,\Gamma(N - n + 1)}
\end{array} \tag{30}
$$

Then for $N \to \infty$ the spanwise loading gradient factor of equation (19) becomes

$$
\begin{array}{ll}
\begin{array}{l} N \to \infty \\ n = \text{finite} \end{array} & \begin{array}{l} N \to \infty \\ N-n = \text{finite} \end{array} \\
h_{Nn} = \frac{n - 1/4}{n}\left[\frac{\Gamma(n + 1)}{\Gamma(n + 1/2)}\right]^2, & h_{N,N-n} = \frac{\Gamma(N-n + 1)}{(N-n + 1/4)^{1/2}\Gamma(N-n + 1/2)}
\end{array} \tag{31}
$$

With the use of the series summation

$$\sum_{p=0}^{N-m} \frac{\Gamma(p + 1/2)}{\Gamma(p + 1)} = 2(N - m + 1/2)\frac{\Gamma(N - m + 1/2)}{\Gamma(N - m + 1)} \tag{32}$$

the spanwise loading factor of equation (22) for $N \to \infty$ becomes

$$
\begin{array}{l} N = \infty \end{array} \\
i_{N,N-n} = \frac{(N - n + 3/4)^{1/2}\,\Gamma(N - n + 1)}{(N - n + 1/2)\,\Gamma(N - n + 1/2)} \tag{33}
$$

Numerical values of equations (31) and (33) are listed in tables 2 and 3. Examination of these equations indicates simple relationships. These relationships extend to chordwise loading factors developed in a later section and can be expressed in one equation as follows:

for $N = N_c = \infty$

$$h_{N,N-n} = \frac{h_{Nn}^{1/2}}{(1-1/16n^2)^{1/2}} = \frac{i_{N,N-n+1}}{\left[1-1/16(N-n+1)^2\right]^{1/2}} = \frac{f_{N_c,N_c-n_c+1}}{\left[1-1/16(N_c-n_c-1)^2\right]^{1/2}} =$$

$$f_{N_c,n_c-1} \tag{34}$$

For the zero condition

$$h_{N,(N-n)=0} = f_{N_c,(n_c-1)=0} = \frac{2}{\pi^{1/2}} = 1.128379$$

For N-n = 1

$$h_{N,(N-n)=1} = f_{N_C,(n_C-1)=1} = \frac{4}{\sqrt{5}\pi} = 1.009253, \quad h_{N,n=1} = .954930, \quad i_{N,(N-n-+1)=1} =$$

$$f_{N_C,(N_C-n_C+1)=1} = .977205$$

For N = ∞ the expression for C_{L_α} develops into the following series summation:

$$C_{L_\alpha} = (\frac{A}{2}) \; 32\sqrt{2} \sum_{\Delta=0}^{\infty} \frac{(2\Delta)!}{2^{3\Delta}(\Delta!)^2(2\Delta+1)(2\Delta+3)(2\Delta+5)} \tag{35}$$

This factor of A/2 is π, thus $C_{L_\alpha} = \pi A/2$.

CHORDWISE VORTEX LATTICE

Formulation of Chordwise Lattice Matrix and Solution to Infinity

In reference 20 the lattice is distributed into equal length chord segments and the chord loading vortex is located at the 1/4 points of each of the chord segments; and boundary condition point at the 3/4 point of each of the chord segments. Then the load vortex chord station and the boundary condition chord station are respectively at

$$\xi_{m_C} = \frac{n_C-3/4}{N_C} \; ; \qquad \xi_{m_C} = \frac{m_C-1/4}{N_C} \tag{36}$$

where $\xi = x/c$.

The loading equations to be solved are given as,

$$\sum_{n_C=1}^{N_C} \frac{e_{N_C n_C}}{2m_C-2n_C+1} = 1; \; m_C = 1, 2, \ldots N_C \tag{37}$$

where

$$e_{N_C n_C} = \frac{N_C \Gamma_{n_C}}{\pi c V \alpha} = \frac{\gamma_{n_C}}{\pi V \alpha} = \frac{-\Delta c_{p n_C}}{2\pi\alpha} \tag{38}$$

The matrix inversion of equation (37) is obtained as a factorial function

$$e_{N_c n_c} = \frac{(2N_c - 2n_c + 1)_{odd}! \; (2n_c - 3)_{odd}!}{(2N_c - 2n_c)_{ev}! \; (2N_c - 2)_{ev}!} = \frac{(2N_c - 2n_c + 1)! \; (2n_c - 2)!}{2^{2N_c - 2} \left[(N_c - n_c)! (n_c - 1)! \right]^2}$$

In terms of Gamma functions

$$\left. e_{N_c n_c} = \frac{2n_c (2N_c - 2n_c + 1) \; \Gamma(n_c + 1/2) \; \Gamma(N_c - n_c + 1/2)}{\pi (2n_c - 1) \; \Gamma(n_c + 1) \; \Gamma(N_c - n_c + 1)} \right\} \quad (39)$$

Numerical values of equation (39) are presented in table 4.

Chordwise Loading Factor

The exact solution by thin wing theory gives the additional loading by the function [using ξ_{n_c} defined in eq. (36)]

$$e_{N_c n_c} = \frac{\gamma_{n_c}}{\pi V \alpha} = \frac{2}{\pi} \left(\frac{1 - \xi_{n_c}}{\xi_{n_c}} \right)^{1/2} = \frac{2}{\pi} \left(\frac{N_c}{n_c - 3/4} - 1 \right)^{1/2} \quad (40)$$

The chordwise loading factor is defined by the ratio of equation (40) to equation (39).

$$(41)$$

$$f_{N_c n_c} = \frac{e_{N_c n_c thin}}{e_{N_c n_c}} = \frac{\gamma_{n_c thin}}{\gamma_{n_c}} = \frac{(N_c - n_c + 3/4)^{1/2} \; (2n_c - 1) \; \Gamma(n_c + 1) \; \Gamma(N_c - n_c + 1)}{n_c (2N_c - 2n_c + 1) \; (n_c - 3/4)^{1/2} \; \Gamma(n_c + 1/2) \; \Gamma(N_c - n_c + 1/2)}$$

Numerical evaluation of equation (41) for a range of N_c are given in table 5.

Chordwise Lift-Curve Slope and Pitching Moment

Section wing lift is the integration of the chordwise loading and section moment is the integration of the product of chordwise loading and moment arm. In mathematical representation

$$c_\ell = 2 \int_0^1 \frac{\gamma}{Vc} \, d\xi \quad , \qquad\qquad c_{m_{LE}} = 2 \int_0^1 \frac{\gamma}{Vc} \, \xi d\xi \quad (42)$$

The lattice loading is constant with ξ over the interval

$$\Delta \xi_{n_c} = [n_c - (n_c - 1)]/N_c = 1/N_c$$ and the lattice load vortex is located at

$$\xi_{n_c} = (n_c - 3/4)/N_c$$ along the chord and the moment arm extends to this vortex.

Then with equation (38) equation (42) becomes

$$c_{\ell_\alpha} = \frac{2\pi}{N_C} \sum_{n_C=1}^{N_C} e_{N_C n_C} \quad , \qquad c_{m_{\alpha_{LE}}} = \frac{2\pi}{N_C^2} \sum_{n_C=1}^{N_C} (n_C - 3/4) \, e_{N_C n_C} \qquad (43)$$

The summation terms in equation (43) are listed in table 4 which when inserted into equation (43) show that the lift and moment for arbitrary N_C is the same as predicted by thin wing theory, that is

$$c_{\ell_\alpha} = 2\pi, \quad c_{m_{\alpha_{LE}}} = \frac{\pi}{2}, \quad a.c. = \frac{c_{m_{\alpha_{LE}}}}{c_{\ell_\alpha}} = 1/4 \qquad (44)$$

Proof that c_{ℓ_α} is Exact at All Values of N

Inserting equation (39) into (43) results in

$$c_{\ell_\alpha} = \frac{4}{N_C} \sum_{n_C=1}^{N_C} \frac{n_C(2N_C - 2n_C + 1) \, \Gamma(n_C + 1/2) \, \Gamma(N_C - n_C + 1/2)}{(2n_C - 1) \, \Gamma(n_C + 1) \, \Gamma(N_C - n_C + 1)} \qquad (45)$$

Now $\Gamma(n+1/2) = (n-1/2) \, \Gamma(n-1/2)$; $\Gamma(N-n-1/2) = \Gamma(N-n+1/2)/(N-n-1/2)$; and $\Gamma(n+1) = n\Gamma(n) = n!$, then

$$c_{\ell_\alpha} = 4 \sum_{n_C=0}^{N_C-1} \frac{N_C - n_C}{N_C} \frac{\Gamma(n_C + 1/2) \, \Gamma(N_C - n_C + 1/2)}{n_C! \, (N_C - n_C)!} \qquad (46)$$

The Gamma functions and factorials in equation (46) show that this product term is a symmetric function which is factored by an antisymmetric term $(N_C-n_C)/N_C$. Then some of the high n_C terms cancel the low n_C terms. By expanding the summation a new summation can be formed given by

$$c_{\ell_\alpha} = 2\pi \sum_{n_C=0}^{n_C \leq \frac{N_C}{2}} \frac{\varepsilon(\frac{N_C}{2} - n_C)}{\pi} \frac{\Gamma(n_C + 1/2) \, \Gamma(N_C - n_C + 1/2)}{n_C! \, (N_C - n_C)!} \qquad (47)$$

where
$$\varepsilon\left(\frac{N_C}{2} - n_c\right) = 1 \text{ for } n_c = \frac{N_C}{2} , = 2 \text{ for } n_c \neq \frac{N_C}{2}$$

The summation term in equation (47) is the Legendre polynomial of the first kind $P_{N_c}(\cos \Theta)_{\Theta=0}$ (see p. 36, ref. 24) and $P_N(1) = 1$ for any N_c. Thus the lift-curve slope is 2π for any N_C which is that predicted by thin wing theory.

Chordwise Solutions for $N \to \infty$

For $N_C \to \infty$ and n_c finite or $N_C - n_c$ finite then equation (39) becomes

$$
\left.
\begin{array}{l}
\begin{array}{c}
N_C \to \infty \\
n_c = \text{finite}
\end{array} \\[1em]
e_{N_c n_c} = \dfrac{4 N_C^{1/2} n_c \; \Gamma(n_c + 1/2)}{\pi(2n_c - 1) \; \Gamma(n_c + 1)} \\[2em]
\begin{array}{c}
N_C \to \infty \\
N_C - n_c = \text{finite}
\end{array} \\[1em]
e_{N_c, N_C - n_c} = \dfrac{2(N_C - n_c + 1/2) \; \Gamma(N_C - n_c + 1/2)}{\pi n_c^{1/2} \; \Gamma(N_C - n_c + 1)}
\end{array}
\right\}
\tag{48}
$$

For both N_C and n_c large [using eq. (29)], equation (39) becomes

$$
\begin{array}{c}
N \to \infty \\
n_c \to \infty
\end{array}
$$

$$e_{N_c n_c} = \frac{2(N_C - n_c)^{1/2}}{\pi n_c^{1/2}} = \frac{2}{\pi}\left(\frac{1-\xi}{\xi}\right)^{1/2} \tag{49}$$

Equation (49) is identical to the thin wing theory additional loading given in equation (40) and shows that a chord lattice solution converges to mathematical exactness as the lattice grid becomes infinite. With equations (48), (40), and (41) the chordwise loading factor at wing leading edge is given by (for $N_C \to \infty$)

$$f_{N_c n_c} = \frac{\Gamma(n_c - 1 + 1)}{(n_c - 1 + 1/4)^{1/2} \; \Gamma(n_c - 1 + 1/2)} \tag{50}$$

This function is identical to that of equation (31) when $n_c - 1 = N - n$, and is listed in equation (34). With equations (48), (40), and (41), the chordwise

loading factor at wing trailing edge is given by (for $N_c \to \infty$)

$$f_{N_c,N_c-n_c} = \frac{(N_c-n_c+3/4)^{1/2} \; \Gamma(N_c-n_c+1)}{(N_c-n_c+1/2) \; \Gamma(N_c-n_c+1/2)} \tag{51}$$

This function is identical to $i_{N,N-n}$ of equation (33) when $N_c-n_c = N-n$, and is listed in equation (34).

A_e-VORTEX LATTICE

Dependency of Spanwise Lattice on Effect of Aspect Ratio

As aspect ratio approaches zero the spanwise optimum lattice arrangement is that defined by equation (3), that is at $\eta_{vn} = (n-1/4)/N$. As aspect ratio approaches infinity the spanwise lattice arrangement is the planform lattice which positions the trailing vortices at $\eta_{vn} = n/N$, that is at the outside edge of the lattice panel including a vortex at the wingtip. This is because at $A = \infty$ the spanwise loading has the same distribution as the wing chord along the span. This high loading near the wing tip (when $A = \infty$) must be taken into account by the lattice trailing vortices. The objective here is to develop an aspect ratio function factor for the lateral panel positions which asymptotically approaches the correct values at $A_e \to 0$ and at $A_e \to \infty$. The subscript e denotes the effective swept panel aspect ratio given by

$$A_e = A/\cos\Lambda_{1/2} \tag{52}$$

The planform lattice ($\eta_{vn} = n/N$) is the lateral lattice arrangement that has been in general use in most vortex-lattice methods.

An aspect ratio equal to four is about an aerodynamic mean between $0 \le A_e \le \infty$. Loading values based on the $A_e \to 0$ lattice and on the $A_e \to \infty$ lattice will be computed for an $A_e = 4$ rectangular wing. Comparison with the loading predicted by an accurate analysis will establish the A-effect function that is needed. By Biot-Savart law the downwash due to an unskewed horseshoe vortex is

$$\frac{w}{V}\Big)_{m,m_c} = \frac{G_{nn_c}}{2\pi\xi_0} \left[\frac{\xi_0 + \sqrt{\xi_0^2+(\eta_{wm}-\eta_{\Delta n}+\eta_{vn})^2}}{\eta_{wm}-\eta_{\Delta n}+\eta_{vn}} - \frac{\xi_0 + \sqrt{\xi_0^2+(\eta_{wm}-\eta_{\Delta n}-\eta_{vn})^2}}{\eta_{wm}-\eta_{\Delta n}-\eta_{vn}} \right] \tag{53}$$

Where $\xi_0 = \xi_{wm_c} - \xi_{vn_c}$, and G_{nn_c} is the dimensionless vortex strength of the elemental horseshoe vortex. For $N_c = 1$ solution, ξ_0 remains constant equal to 1/4 for $A = 4$. $\eta_{\Delta n}$ is the lateral middle of the n panel. For the slender wing ($A_e \to 0$) lattice use

$$n_{vn} = \frac{n-1/4}{N} \quad , \quad n_{wm} = \frac{m-3/4}{N} \quad , \quad n_{\Delta n} = 0 \tag{54}$$

For the planform lattice use

$$n_{vn} = \frac{n}{N} \quad , \quad n_{wm} = \frac{m-1/2}{N} \quad , \quad n_{\Delta n} = 0 \tag{55}$$

The equation to be solved for additional loading for an $N_c = 1$ solution, $A = 4$ rectangular wing is

$$1 = \frac{2}{3N} \sum_{n=1}^{N} g_{Nn} \left[\frac{1/4 + \sqrt{1/16 + (n_{wm} + n_{vn})^2}}{n_{wm} + n_{vn}} - \frac{1/4 + \sqrt{1/16 + (n_{wm} - n_{vn})^2}}{n_{wm} - n_{vm}} \right] \tag{56}$$

Wing lift-curve slope is determined from equation (24) and wing loading by equation (20) with which

$$\frac{(c_\ell c)_n}{C_L c_{av}} = \frac{2A}{C_{L_\alpha}} \; i_{Nn} G_{\alpha Nn} \tag{57}$$

where for the A→0 lattice i_{Nn} values are given in table 3, while for the planform lattice i_{Nn} are all unity. Results of the solutions of equation (56) with the A_e→0 lattice of (54) and with the planform lattice of (55), for increasing N, are presented in tables 6 and 7. An accurate loading prediction of this $A = 4$ rectangular wing is made in reference 19. From reference 19

$$\left. \begin{array}{l} C_{L_\alpha} = 3.6623, \quad \eta = \cos\phi \\[1em] \dfrac{c_\ell}{C_L} = \dfrac{4}{\pi}(\sin\phi + .07879\sin3\phi + .01290\sin5\phi + .00350\sin7\phi + .00170\sin9\phi) \end{array} \right\} \tag{58}$$

Percent differences from the values of equation (58) are shown in tables 6 and 7. For this $A = 4$ wing the A→0 lattice has less than one-half the error of the planform lattice.

Spanwise A_e-Vortex Lattice

Since for the $A = 4$ wing the A→0 lattice prediction is too small and the planform (A→∞) lattice prediction too large then a factor can be developed between the two which forms the basis of spanwise A_e-lattice arrangement. This factor is $2/\sqrt{A_e+4}$, then for the A_e-lattice

$$
\eta_{vn} = \frac{1}{N}\left(n - \frac{1}{2\sqrt{A_e+4}}\right) \ , \ \eta_{wm} = \frac{1}{N}\left(m - \frac{1}{2} - \frac{1}{2\sqrt{A_e+4}}\right)
$$

$$
i_{ANn} = 1 - (1 - i_{Nn})\frac{2}{\sqrt{A_e+4}} \ , \ \eta_1 = \frac{1}{N}\left(\frac{1}{2} - \frac{1}{\sqrt{A+4}}\right) \ , \ \eta_n = \frac{1}{N}\left(n - \frac{1}{2} - \frac{1}{2\sqrt{A_e+4}}\right)
$$

(59)

where A_e is defined in equation (52) and η_n is the spanwise position of the
computed loading distribution. These spanwise lattice panel positions
asymptotically approach the A→0 lattice and the planform lattice as A→0 and ∞
respectively. With equation (59) the solutions of equation (56) for lift and
loading are listed in tables 6 and 7. With the A_e-lattice the predicted lift
and loading is accurate for all N's which was the basis for the term
optimum applied to the A→0 lattice and chordwise lattice. Equation (59) is
simply a mathematical statement that relative to the planform lattice all the
panels are shifted inboard by $1/2N\sqrt{A_e+4}$, and that the downwash point is at the
lateral center of each panel except in the wing root panel.

Application of the A_e-Vortex Lattice

For a uniform vortex lattice, the elemental skewed horseshoe vortex
lateral position at the trailing vortices is given by η_{vn} in equation (59) and
the chordwise position by ξ_{vn_c} in equation (36). The downwash points are
positioned laterally at η_{wm} in equation (59) and chordwise at ξ_{wm_c} in
equation (36). Let Γ_{nn_c} be the unknown circulation strength of the elemental
skewed horseshoe vortex. For symmetric wing loading Γ_{nn_c} is determined from
an NN_c matrix solution which satisfies NN_c downwash point boundary conditions.
The pressure coefficient at span station η_n in equation (59) and chord
station $\xi_{vn_c} = (n_c - 3/4)/N_c$ is given by

$$
\Delta C_{p_{nn_c}} = -2N_c \, i_{ANn} \, f_{N_c n_c} \frac{\Gamma_{nn_c}}{c_n V}
$$

(60)

where spanwise and chordwise loading factors are included [eq. (59), tables 3
and 5]. Now

$$
\Gamma_n = \sum_{n_c=1}^{N_c} \Gamma_{nn_c}
$$

(61)

then the spanwise loading at η_n of equation (59) is

$$\Gamma_n \Big)_{atn_n} = \frac{V}{2} c_\ell c \Big)_{atn_n} = i_{ANn} \Gamma_n \qquad (62)$$

which includes the spanwise loading factor [eq. (59), table 3]. The spanwise loading gradient at span station n_{vn} in equation (59) is

$$\frac{d\Gamma_n}{d\eta} = -h_{ANn} N(\Gamma_n - \Gamma_{n+1}) \qquad (63)$$

where Γ_n is given in equation (61) and where the spanwise loading gradient factor is given by

$$h_{ANn} = 1 - (1-h_{Nn})\frac{2}{\sqrt{A_e+4}} , \text{ with } h_{Nn} \text{ in table 2.}$$

The lift coefficient is [Γ_n from eq. (61)]

$$C_L = \frac{2A}{NbV}(\frac{3}{4}\Gamma_1 + \sum_{n=2}^{N} \Gamma_n) \qquad (64)$$

The induced drag is given by

$$\left.
\begin{aligned}
C_{D_i} &= \frac{A}{2bV}\int_{-1}^{1} \alpha_i \Gamma d\eta = \frac{A}{NbV}(\frac{3}{4}\alpha_1\Gamma_1 + \sum_{n=2}^{N} \alpha_n\Gamma_n) \\
\alpha_n &= \frac{N}{\pi bV}\left[(\frac{1}{N-n+1/2}+\frac{1}{N+n-1})\Gamma_N + \sum_{m=1}^{N-1} (\frac{1}{m-n+1/2}+\frac{1}{m+n+1})(\Gamma_m - \Gamma_{m+1})\right]
\end{aligned}
\right\} \qquad (65)$$

where Γ_n is given in equation (61). For spanwise loading distribution already known then equation (65) provides a convenient method for predicting induced drag. For this case $\Gamma_n)_{atn_n}$ is known then Γ_n is determined from equation (62) for application in (65).

CONCLUDING REMARKS

The application of the vortex-lattice method to the slender wing configuration has provided a rigorous analytical basis for the spanwise properties of the vortex-lattice method. Mathematical similarities are shown between the spanwise panel lattice solution and the chordwise solution which converge to thin wing theory results. As the number of chordwise panels approaches infinity, thin wing theory chordwise loading is predicted exactly except in the limit points exactly at the leading edge and at the trailing edge. At

these two points chordwise loading factors are mathematically evaluated which
are useful in finite panel solutions. Similarly, as the number of spanwise
panels becomes infinite, slender wing theory spanwise loading is predicted
exactly except at the point of the wing tip. At this point a spanwise loading
factor is mathematically determined from a limit solution. The presentation
in this paper is based on a planform uniform distribution of panels chordwise
and spanwise. In a discussion in 1972 Mr. W. B. Kemp, Jr. of NASA-Langley
said he had found that the chordwise vortex-lattice solution gave an accurate
integrated lift for an arbitrary planform panel distribution along the chord.
As part of the present work this was investigated and it was shown that using
the 1/4 - 3/4 rule for locating the vortex and downwash point in the planform
panel, the chordwise lift-curve slope of 2π and also the spanwise slender wing
value of $\pi A/2$ are predicted for any distribution of planform panels on the
wing and for any total number of panels. However, the loading distribution
factors are not as near unity. The aspect ratio effect on spanwise lattice
arrangement has a weak chordwise counterpart for a chordwise lattice
arrangement. An initial study of this effect indicates that the chordwise
lattice arrangement differs when aspect ratio is less than unity. In
conclusion, the A_e-vortex-lattice arrangement of the previous section provides
a uniform uncomplicated, accurate system. It leads to computations with a
high accuracy to work ratio.

REFERENCES

1. Falkner, V. M.: The Calculation of Aerodynamic Loading on Surfaces of Any Shape. A.R.C.R. & M. 1910, Aug. 1943, Aeronautical Research Council, England.

2. VanDorn, N. H.: and DeYoung, J.: A Comparison of Three Theoretical Methods of Calculating Span Load Distribution on Swept Wings. NASA TN 1491, 1947.

3. Runyan, H. L. and Woolston, D. C.: Method for Calculating the Aerodynamic Loading on an Oscillating Finite Wing in Subsonic and Sonic Flow. TR1322, 1957. NACA.

4. Rubbert, P. E.: Theoretical Characteristics of Arbitrary Wings by a Nonplanar Vortex Lattice Method. Report D6-9244, The Boeing Co., Seattle, Washington, 1964.

5. Dulmovits, J.: A lifting Surface Method for Calculating Load Distributions and the Aerodynamic Influence Coefficient Matrix for Wings in Subsonic Flow. Report ADR 01-02-64.1, 1964, Grumman Aerospace Corp., Bethpage, N.Y.

6. Hedman, S. G.: Vortex Lattice Method for Calculation of Quasi Steady State Loadings on Thin Elastic Wings In Subsonic Flow. Report 105, Oct. 1965. Aeronautical Research Institute of Sweden.

7. Belotserkovskii, S. M.: The Theory of Thin Wings in Subsonic Flow. Plenum Press, New York 1967.

8. Landahl, M. T. and Stark, V.J.E.: Numerical Lifting-Surface Theory-Problems and Progress. AIAA J., Vol. 6, No. 11, Nov. 1968, pp 2049-2060.

9. Woodward, F. A.: Analysis and Design of Wing-Body Combinations at Subsonic and Supersonic Speeds. J. of Aircraft, Vol. 5,No. 6, Nov.-Dec. 1968, pp. 528-534.

10. Albano E., and Rodden, W. P.: A Doublet-Lattice Method for Calculating Lift Distributions on Oscillating Surfaces in Subsonic Flow. AIAA J., Vol. 7, No.2, Feb. 1969, pp 279-285.

11. James, R. M.: On the Remarkable Accuracy of the Vortex Lattice Discretization in Thin Wing Theory. Report DAC-67211, Feb 1969, McDonnell Douglas Corp., Long Beach, California.

12. Houbolt, J. C.: Some New Concepts in Oscillatory Lifting Surface Theory. Report AFFDL-TR-69-2, June 1969, U. S. Air Force Flight Dynamics

Laboratory, Wright-Patterson Air Force Base, Ohio.

13. Margason, R. J. and Lamar, J. E.: Vortex-Lattice Fortran Program for Estimating Subsonic Aerodynamic Characteristics of Complex Planforms. NASA TN D-6142, Feb. 1971, 139 pp.

14. Kalman, T. P., Rodden, W. P., and Giesing, J. P.: Application of the Doublet-Lattice Method to Nonplanar Configurations in Subsonic Flow. J. of Aircraft, Vol 8, No. 6, June 1971, pp 406-413.

15. Lamar, J. E.: Nonplanar Method for Predicting Incompressible Aerodynamic Coefficients of Rectangular Wings with Circular-Arc Camber. Ph.D. Dissertation, Aerospace Engineering, Virginia Polytechnic Institute and State University, December 1971, 91 pp.

16. Seath, D. D. and DeYoung, J.: Generation of Finite-Difference Mesh Geometry Configurations. Convair Report ERR-FW-1240, Dec. 1971. General Dynamics, Fort Worth, Texas, 80 pp.

17. DeYoung, J. and Seath, D. D.: Examination of Mesh Geometry Generation Techniques. UTA Report No. AE 72-01, Dec 1971, University of Texas at Arlington, Arlington, Texas, 18 pp.

18. Lan, C. E.: A Quasi-Vortex-Lattice Method in Thin Wing Theory. J. of Aircraft, Vol. 11, No. 9, Sept. 1974, pp 518-527.

19. DeYoung, J.: Wing Loading Theory Satisfying All Boundary Points. Ph.D. Dissertation, The University of Texas at Arlington, Arlington, Texas, Dec. 1975, 180 pp.

20. DeYoung J.: Convergence-Proof of Discrete-Panel Wing Loading Theories. J. of Aircraft, Vol. 8, No.10, Oct. 1971, pp. 837-838.

21. Jones, R. T.: Properties of Low-Aspect Ratio Pointed Wings at Speeds Below and Above the Speed of Sound. NACA Report 835, 1946.

22. DeYoung, J.: Spanwise Loading for Wings and Control Surfaces of Low Aspect Ratio, NASA TN 2011, Jan. 1950, 36 pp.

23. Handbook of Mathematical Functions with Formulas, Graphs, and Mathematical Tables. Edited by Abramowitz, M. and Stegun, I.A., National Bureau of Standards, Applied Mathematics Series 55, U.S. Government Printing Office, 1965, 1046 pp.

24. Mangulis, V.: Handbook of Series for Scientists and Engineers. Academic Press, New York and London, 1965, 134 pp.

TABLE 1. - g_{Nn}, SPANWISE SOLUTIONS OF EQUATION (6)

N \ n	1	2	3	4	5	6
1	1					
2	$\dfrac{2\times3}{3\times5}$	$\dfrac{2\times3^4}{3\times5\times7}$				
3	$\dfrac{3^3}{3\times5\times7}$	$\dfrac{2^3\times3^4}{3\times5\times7\times9}$	$\dfrac{2\times3^4\times5^3}{11_{odd}!}$			
4	$\dfrac{2^2\times3^2\times5}{3\times5\times7\times9}$	$\dfrac{2^2\times3^5\times5}{11_{odd}!}$	$\dfrac{2^2\times3^5\times5^3}{13_{odd}!}$	$\dfrac{2^2\times3^3\times5^3\times7^3}{15_{odd}!}$		
5	$\dfrac{3^2\times5^2\times7}{11_{odd}!}$	$\dfrac{2^3\times3^5\times5^2}{13_{odd}!}$	$\dfrac{2\times3^6\times5^3\times7}{15_{odd}!}$	$\dfrac{2^5\times3^3\times5^3\times7^3}{17_{odd}!}$	$\dfrac{2\times3^3\times5^3\times7^3\times9^3}{19_{odd}!}$	
6	$\dfrac{2\times3^5\times5\times7}{13_{odd}!}$	$\dfrac{2\times3^5\times5^2\times7^2}{15_{odd}!}$	$\dfrac{2^4\times3^5\times5^4\times7}{17_{odd}!}$	$\dfrac{2^4\times3^6\times5^3\times7^3}{19_{odd}!}$	$\dfrac{2^2\times3^9\times5^4\times7^3}{21_{odd}!}$	$\dfrac{2^2\times3^9\times5^2\times7^3\times11^3}{23_{odd}!}$

$$N \quad \frac{3N(2N-3)_{odd}!}{(2N+1)_{odd}!} = \frac{3N}{4N^2-1} \qquad\qquad \frac{3\times2^{N-1}\left[(2N-1)_{odd}!\right]^3}{(N-1)!(4N-1)_{odd}!}$$

TABLE 2. - h_{Nn}, SPANWISE LOADING GRADIENT FACTOR

N \ n	1	2	3	4	5	6
1	1.082788					
2	.965721	1.118660				
3	.958851	1.000148	1.124345			
4	.956981	.993739	1.005515	1.126193		
5	.956199	.992082	.999207	1.007242	1.127013	
6	.955795	.991404	.997613	1.000965	1.008002	1.127446
∞ (n)	.954930	.990297	.995956	.997804	.998625	.999060
∞ (-N+n+6)	1.000564	1.000858	1.001459	1.003004	1.009253	1.128379

365

TABLE 3. - i_{Nn}, SPANWISE LOADING FACTOR

N \ n	1	2	3	4	5	6
	$\eta=0$					
1	.954930					
2	.983016	.966313				
3	.990965	.988798	.972705			
4	.994332	.993811	.992034	.974770		
5	.996085	.995935	.995712	.993301	.975684	
6	.997119	.997082	.997167	.996548	.993923	.976166
∞ ($-N+n+6$)	.999530	.999312	.998901	.997976	.995137	.977205

TABLE 4. - $e_{N_c n_c}$, CHORDWISE SOLUTIONS OF EQUATION (37)

N_c \ n_c	1	2	3	4	5	6	$\sum\limits_{n_c=1}^{N_c} e_{N_c n_c}$	$\sum\limits_{n_c=1}^{N_c} (n_c-\frac{3}{4})e_{N_c n_c}$
1	1						1	1/4
2	3/2	1/2					2	4/4
3	15/8	3/4	3/8				3	9/4
4	35/16	15/16	9/16	5/16			4	16/4
5	315/128	35/32	45/64	15/32	35/128		5	25/4
6	693/256	315/256	105/128	75/128	105/256	63/256	6	36/4
							‖	‖
							N	$N^2/4$

## TABLE 5. - $f_{N_c n_c}$, CHORDWISE LOADING FACTOR

N_c \ n_c	1	2	3	4	5	6
1	1.102658					
2	1.122892	.986247				
3	1.126095	1.004345	.980140			
4	1.127139	1.007210	.998126	.978631		
5	1.127603	1.008144	1.000974	.996589	.978043	
6	1.127848	1.008559	1.001902	.999433	.995991	.977756
$\frac{n_c}{\infty}$	1.128379	1.009253	1.003004	1.001459	1.000858	1.000564
$\frac{-N_c+n_c+6}{\infty}$	.999530	.999312	.998901	.997976	.995137	.977205

TABLE 6. - LATTICE COMPARISONS FOR PREDICTING C_{L_α}, A=4 RECTANGULAR WING

N	planform lattice C_{L_α}	ΔC_{L_α},%	A→0 lattice C_{L_α}	ΔC_{L_α},%	A_e-lattice C_{L_α}	ΔC_{L_α},%
1	4.4904	22.61	3.2513	-11.22	3.6176	-1.22
2	4.1267	12.68	3.4914	- 4.67	3.6787	.45
3	3.9629	8.21	3.5367	- 3.43	3.6622	0

TABLE 7. - LATTICE COMPARISONS FOR PREDICTING $\frac{c_\ell}{C_L}$, A= 4 RECTANGULAR WING

N		planform lattice η	$\frac{c_\ell}{C_L}$	$\frac{c_\ell}{C_L,19}$	$\Delta\frac{c_\ell}{C_L}$,%	A→0 lattice η	$\frac{c_\ell}{C_L}$	$\frac{c_\ell}{C_L,19}$	$\Delta\frac{c_\ell}{C_L}$,%	A_e-lattice η	$\frac{c_\ell}{C_L}$	$\frac{c_\ell}{C_L,19}$	$\Delta\frac{c_\ell}{C_L}$,%	i_{ANn}
1	.500	1		1.092	-8.45	0	1.273	1.187	7.25	.146	1.176	1.179	-. 29	.9681
2	.250	1.088		1.165	-6.62	0	1.230	1.187	3.65	.073	1.185	1.185	0	.9880
	.750	.912		.914	- .21	.625	1.026	1.024	.19	.662	.989	.995	- .67	.9762
3	.167	1.126		1.177	-4.33	0	1.224	1.187	3.09	.049	1.194	1.187	.58	.9936
	.500	1.049		1.092	-4.01	.417	1.145	1.124	1.87	.441	1.115	1.115	- .04	.9921
	.833	.826		.799	3.34	.750	.891	.914	-2.57	.77	.871	.883	-1.36	.9807

$$\frac{\sqrt{2}}{8}\frac{\gamma}{V\alpha} = \sqrt{\frac{1-\xi}{2\ \xi}}$$

$$\frac{\Gamma}{bV\alpha} = \sqrt{1-\eta^2}$$

$$-\frac{d\left(\frac{\Gamma}{bV\alpha}\right)}{d\eta} = \frac{\eta}{\sqrt{1-\eta^2}}$$

ROOT
T.E.

SEMISPAN
CHORD
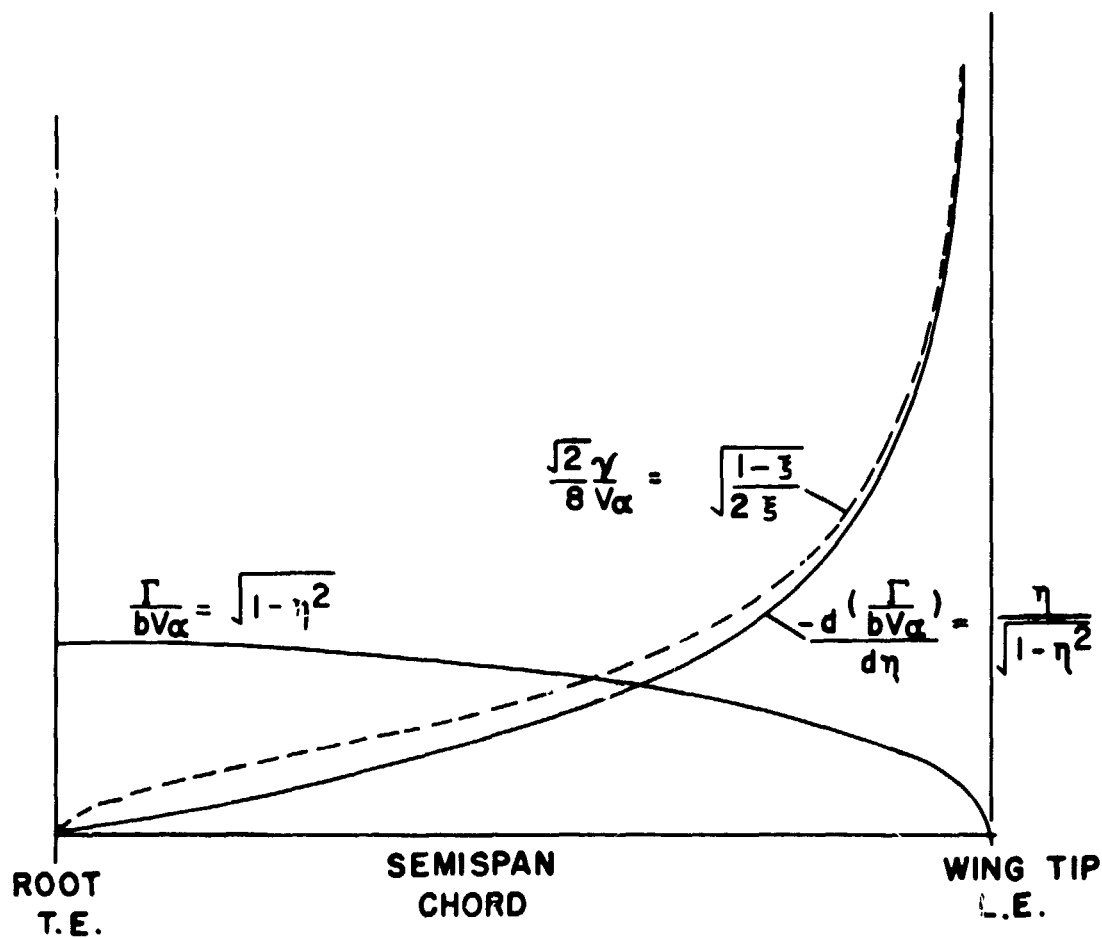
WING TIP
L.E.

Figure 1.- Comparison of chordwise loading with spanwise loading gradient.

$n = 1 \quad 2 \quad 3 \quad 4$

$\Delta\Gamma_1 \quad \Delta\Gamma_2 \quad \Delta\Gamma_3 \quad \Delta\Gamma_4$

$\eta_{vn} = \quad \eta_{v1} \quad \eta_{v2} \quad \eta_{v3} \quad \eta_{v4}$

$\eta_{wm} = \eta_{w1} \quad \eta_{w2} \quad \eta_{w3} \quad \eta_{w4}$

$0 \quad \eta \longrightarrow \quad 1$
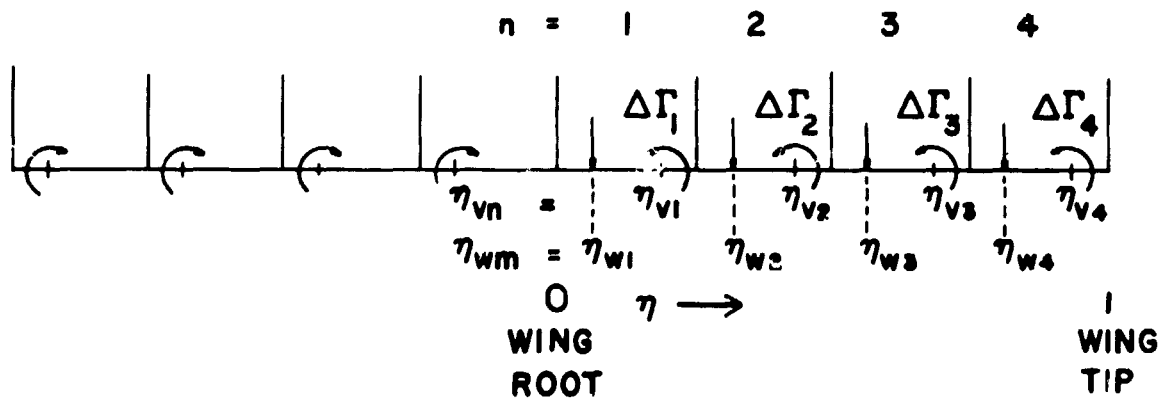
WING
ROOT

WING
TIP

Figure 2.- Spanwise panel distribution for N ≈ 4, and location of trailing
vortex of 1/4 panel width in from wing tip, and location of boundary
point at 3/4 panel width in from wing tip.

A SUBVORTEX TECHNIQUE FOR THE

CLOSE APPROACH TO A DISCRETIZED VORTEX SHEET[+]

Brian Maskew
Analytical Methods, In..

SUMMARY

The close-approach problem associated with vortex-lattice methods was examined numerically with the objective of calculating velocities at arbitrary points, not just at midpoints, between the vortices. The objective was achieved using a subvortex technique in which a vortex splits into an increasing number of subvortices as it is approached. The technique, incorporated in a two-dimensional potential flow method using "submerged" vortices and sources, was evaluated for a cambered Joukowski airfoil. The method could be extended to three dimensions, and should improve non-linear methods, which calculate interference effects between multiple wings and vortex wakes, and which include procedures for force-free wakes.

INTRODUCTION

A fundamental problem associated with vortex-lattice methods (e.g., ref. 1) is that appreciable errors can occur in velocities calculated close to the discretized vortex sheets because of the singular nature of the induced velocity expression. This problem has been circumvented in the past by calculating "near-field" velocities only at special points, e.g., midway between the vortices, and by employing interpolation for intermediate positions. For calculations involving multiple vortex sheets, (e.g., refs. 2 and 3), the near-field problem often requires that adjacent lattices be made to correspond across the gap between the sheets. However, such a solution is not practical in vortex-lattice methods which incorporate iterative procedures for force-free wakes, (refs. 3 through 11). Although these methods have proved very versatile in general, close-approach situations involving multiple discretized vortex sheets require careful treatment, and, ideally, the near-field problem should be removed.

The objective of this investigation was to develop a near-field modification for the discrete vortices which would allow velocities to be calculated anywhere in the flow field, not just at the special points. Such a capability would particularly benefit the analysis of high-lift configurations and the calculation of other close interference effects between wings and vortex sheets

---

(or vortices) such as occur in configurations with leading-edge or tip-edge vortices.

Although the present paper deals with the near-field problems in two-dimensional flow, the extension to three dimensions (particularly for methods having a force-free wake) is a major consideration throughout. The development of the technique described herein is presented in more detail in references 12 and 13.

EXTENT OF THE NEAR-FIELD REGION

To evaluate the extent of the near-field region, the velocity distribution was examined for a flat, two-dimensional vortex sheet with a parabolic vorticity distribution (ref. 12). This distribution was discretized using forty vortices with equal spacing, Δ. Velocity distributions were calculated over a region between two midpoints near the quarter position on the segment (fig. 1(a)) and compared with the analytic values. Error contours are shown in figure 1(b). The discretization gives negligible errors for both components of velocity in the region beyond 1Δ from the sheet. In effect, the "holes" in the representation are not sensed until we enter the 1Δ region. Inside the 1Δ region the errors increase rapidly except along special lines of approach to the sheet. For the normal velocity component, the zero-error lines follow approximately the normals to the sheet at the points midway between the vortices and also at the vortices. (Deviations from the normal lines occur because of the gradient in vorticity across the region.) Both sets of positions on the surface are used in the non-linear vortex-lattice method, (e.g., ref. 3), i.e., the midpoints are used as control points, as in the standard vortex-lattice theory, and the vortex points are used when applying the Kutta-Joukowski law for local forces and also when performing the trailing-vortex roll-up calculations. The zero-error lines for the tangential velocity component are less well known; these lines enter the near-field region above the quarter and three-quarter positions between the vortices, and approach the vortex locations along approximately elliptical paths. All the zero-error paths are situated on extreme "precipices" in the error contour map; small deviations from the paths result in large errors and lead to the near-field problems.

NEAR-FIELD MODELS

The previous section indicated that errors arising from the discretization of a vortex sheet become appreciable only within the 1Δ region. Clearly, if we wished to calculate velocities very close to the discretized vortex sheet, we could simply decrease the size of Δ by increasing the number of vortices; however, for three-dimensional problems the computing time could then become prohibitive. An alternative solution is to apply a near-field treatment to the vortices. This treatment would be applied only to those vortices that are within a specified near-field radius (e.g., 1Δ) from the point where the velocity is being calculated. A number of near-field models were considered.

A core model offers the simplest near-field treatment which removes the singular behavior of the velocity field. In such a model the velocity induced by the vortex is factored locally so as to remain bounded at the vortex center. The Rankine vortex and Lamb's viscous vortex are well known examples, but there are other possible forms. Core models have been used in the past to smooth the motions of vortices used in two-dimensional roll-up calculations (e.g. refs. 14 and 15). Several core models were tested using the discretized parabolic vorticity sheet, but none were found satisfactory for both components of velocity. For example, they fail to restore the tangential component of velocity near the vortex sheet. This can be seen in figure 2, which shows the error contours for a Rankine vortex model with a core diameter of Δ. Although the tangential velocity errors appear slightly worse than for the unmodified vortex (compare figs. 1(b) and 2), the normal component errors are improved, on the whole, within the core. But the error levels are still significant, and the zero-error lines no longer approach the vortex points. Other near-field models were, therefore, considered in which the vortex itself is modified, its strength being effectively distributed along a line representing the local position of the vortex sheet. This investigation led to the subvortex technique.

SUBVORTEX TECHNIQUE

A technique was developed in which the strength of a near-field vortex is distributed by splitting it into a number of small vortices, i.e., subvortices. These are distributed evenly along the vortex sheet joining the vortex to its two immediate neighbors. The joining sheet is not necessarily a straight line; the subvortices can be placed on an interpolated curve passing through the basic vortices, and this allows a close representation of curved vortex sheets. Half intervals separate the basic vortices from the nearest subvortices (fig. 3(a)), and so the basic vortex positions become midpoints in the subvortex system. This feature improves the accuracy of the calculated velocity at the basic vortices (see "error contours").

The subvortices must have a combined strength equal to that of the associated basic vortex. In the technique as used here, their strengths vary linearly with distance from the basic vortex position. When several neighboring basic vortices are treated in this way, the local effect approaches that of a piecewise linear vorticity distribution. Clearly, higher order distributions could be used, but would involve more than one basic vortex interval on each side.

The number of subvortices used is such that the point where the velocity is being calculated cannot "see the holes" in the discretized vortex sheet, i.e., the point is kept just outside the new local 1Δ region of the subvortex system. Figure 3(b) shows how this works using the following expression for the number of subvortices on one side of the basic vortex:

$$NSV = \text{integer-part-of } (1 + \Delta/H) \tag{1}$$

where H is the normal distance of the point from the segment. Use of this expression keeps the number of subvortices to a minimum and helps to keep compu-

371

ting costs down. When applied to the vortex-lattice methods, the midpoints between the vortices (i.e., the control points) should remain midpoints in the subvortex system; NSV must then be _even_, i.e., as shown dotted in fig. 3(b).

A maximum limit, NSV_{MAX}, is placed on the number of subvortices to avoid a runaway condition when the height H approaches zero. This limit controls the closest approach that can be made to the vortex sheet before the new local 1Δ region of the subvortices is entered. It can therefore be used to control the "accuracy" of the calculation in a trade-off with computing time, i.e., by increasing the limit the error region would decrease in size, but the computing time would increase, and vice-versa. To minimize calculation errors inside the 1Δ region of the subvortex system, each subvortex has been modified with a Rankine vortex core of diameter slightly less than the subvortex spacing. This smears out the tangential velocity discontinuity associated with the vortex sheet, but only over the new, diminished error-region. When representing free vortex sheets, this smeared region could be related to the thickness of the viscous wake in real flow.

Although the velocity errors become significant only within the 1Δ region, the near-field radius, within which the subvortex technique is applied, had to be increased to 5Δ to obtain the required accuracy ($\pm$ 0.5% error). The reason for this extension is that the induced velocity from the "distributed" model does not match that from the basic vortex until some distance away (ref. 12).

Error Contours

The technique was tested on the discretized parabolic vorticity distribution considered earlier. The error contours (fig. 4) are reduced to a very small region adjacent to the vortex sheet where the approach is closer than the subvortex spacing. The extent of this error region depends on the maximum limit placed on the number of subvortices. In these calculations NSV_{MAX} was 10.

The normal component of velocity calculated at the vortex locations has always been slightly less accurate than that calculated at points midway between the vortices. (The vortex points are effectively midpoints in a coarser discretization.) For the present discretized parabolic vorticity distribution, the error at the vortices in the region considered (see fig. 1(a)) is 2.8% compared with 0.03% at the midpoints. With the subvortex technique applied, the error at the vortices decreases to 0.2%; this reduction is helped by the fact that the basic vortex locations become midpoints in the subvortex system.

SUBMERGED SINGULARITIES

The subvortex technique was incorporated in a two-dimensional potential flow method (ref. 13) aimed at calculating pressures at arbitrary points on airfoil surfaces. For this purpose, the error region associated with the subvortex system was enclosed in the contour by "submerging" the vortices a small

distance below the surface (fig. 5). The basic vortices (before submerging) were positioned on the airfoil surface using equal angle increments in a cosine equation applied to distance along the contour. In this spacing system, half angles separate the initial vortex positions from the control points where the boundary condition of tangential flow is specified. This is an adaptation of Lan's work (ref. 16); it keeps the singularity strength distribution more uniform when passing through "difficult" regions such as leading and trailing edges and flap hinge lines. With this point distribution, the first control point is located at the trailing edge, and so the Kutta condition is applied by specifying the flow direction there, e.g., the direction along the mean line.

From their initial surface positions, the basic vortices are submerged along the local normals to the surface by a fraction of Δ, i.e., SDFΔ. The submerged depth factor, SDF, is constant over the whole contour except in the trailing-edge region where it automatically decreases along the single sheet (fig. 5). The control points remain on the airfoil contour except in the region very close to the trailing edge; here, corresponding upper and lower control points are combined and moved to the mean line. Hence, the model adjacent to the trailing edge resembles a camber line model. Because of this modelling, there are more control points than unknown singularities, and so the equations are solved in a least-squares sense.

The subvortices are placed on straight segments joining the basic vortices (see fig. 6). They are positioned in accordance with equal angle increments in the same system as the basic vortices (ref. 13).

For the three-dimensional case, quadrilateral vortices have been found convenient for modelling arbitrary geometry configurations (refs. 2,3 and 11). The present study, therefore, is based on the two-dimensional form of that model, viz., opposing vortex pairs, (fig. 6), which are equivalent to a piecewise uniform normal doublet distribution. Such a model, forming a closed surface, requires one doublet panel strength to be specified, otherwise the system is indeterminate. Accordingly, the upper panel adjacent to the crossover (fig. 6) is specified to have zero strength. The boundary condition equation associated with the control point above the specified panel is still included in the system of equations. The resultant vortex strengths are:

$$\Gamma_k = D_k - D_{k+1}; \ k = 1, \ 2, \ \ldots, \ N \tag{2}$$

where D_k are the doublet panel strengths, i.e., the strengths of the opposing vortex pairs. (Note that D_{N+1} has been assumed zero.)

Preliminary calculations using vortices alone (ref. 13) showed problems near the leading edge and near the crossover of the interior vortex "sheets". These problems were attributed to ill-conditioning of the boundary equations, particularly near the crossover, because the vortices were trying to provide thickness effects (as well as lifting effects) from a small base. Source singularities, which are more suitable for providing thickness effects, were therefore included in the model. The sources, coincident with the vortices and

receiving the same "subvortex" treatment, have a simple strength distribution which provides the basic thickness form symmetrically about the mean line (ref. 13). The sources particularly benefit the pressure calculations in the leading- and trailing-edge regions.

RESULTS AND DISCUSSION

Figure 7 shows the pressure distribution calculated at 120 surface points that are not related to the vortex/control point locations. The airfoil is a cambered Joukowski represented by 46 vortex/sources with a submerged depth of 0.1 and a near-field radius of 5 . Trapezoidal-rule integration of the pressure distribution yields the following lift, drag and moment coefficients: C_L = 1.7040 (0.4% error); C_D = -0.0069 (an error of 0.4% of C_L); and C_M = -0.5377 (0.26% error). The calculated pressure values show good agreement with the exact distribution, but they show a minor tendency to oscillate near the leading edge. The oscillations can be reduced (ref. 13) by increasing the density of the subvortex system, but the computing time increases (53% increase in time for a factor of 2 on the number of subvortices). Use of a higher order interpolation scheme for positioning the subvortices also reduces the oscillatory tendency (ref. 13). The oscillations can be eliminated by using a large number of basic singularities (e.g., 90). It is significant that the small oscillation disappears when there is no suction peak, e.g., figure 8 shows the pressure distribution for the same airfoil at zero incidence, the C_D error in this case being 0.0002 or 0.4% of C_L. (This case had the higher-order geometry routine for positioning the subvortices.) This implies that a higher-order strength variation for the subvortices might be useful when using only a small number of basic singularities; this would ensure that peaks in the pressure distribution are adequately represented. The higher-order routines would only be applied locally in the problem areas.

Figure 9 shows the pressures calculated at the same 120 arbitrary points as before, but with only 19 basic singularities; using so few vortex unknowns would clearly be an advantage in three dimensions. The distribution in figure 9 corresponds with figure 12 in reference 13, but the subvortex system for the present case was doubled. The higher-order geometry routine for positioning the subvortices was used, but the subvortex strength variation was linear. The calculated pressures are in good agreement with the exact solution except near the leading edge. A higher-order strength variation for the subvortices, as discussed above, should improve the calculations in the peak suction region.

Submerged Depth

The submerged depth has a significant effect on the solution. Typical variations in the errors in integrated C_L, C_M and C_D with submerged depth factor, SDF, are presented in figure 10. The errors in C_D and C_M decrease rapidly as the dpeth decreases, but the computing time increases because the

374

number of subvortices must increase; e.g., the time for SDF = 0.05 is 35% higher than that for SDF = 0.1. A submerged depth of about 0.1 seems a reasonable compromise.

Near-field Radius

The near-field radius factor, NRF, when multiplied by the Δ value of a basic vortex, defines a circle centered on that vortex. Whenever a velocity calculation point comes inside the circle, then that basic vortex is modified by the subvortex technique. Figure 11 shows the effect of NRF on the force and moment errors from the pressure integration. They show excellent convergence characteristics as NRF increases, although C_L appears to be converging towards an error of the order of 0.5%. The error in C_L based on circulation, however, converges towards zero. The calculated pressure distribution at the arbitrary points improves as NRF increases, but there is little visual change in the distributions from that shown in figure 7 (NRF = 5) for NRF values above about 3. Computing time decreases rapidly as NRF is reduced; a value of 3 instead of 5 for NRF gives a time saving of 30%.

CONCLUDING REMARKS

Discretization of a vortex sheet introduces significant velocity errors only within a distance from the sheet equal to the vortex spacing in the lattice. Core models applied to the vortices help to limit the size of errors but do not reduce them to a satisfactory level when the field of interest approaches close to the vortex sheet. The region where significant errors occur can be reduced to a small region of controllable width close to the vortex sheet by the use of the near-field model in which a discrete vortex splits into an increasing number of subvortices as it is approached. The combination of the subvortex technique with a concept that places the singularities inside the airfoil has resulted in a method by which accurate pressures (and velocities) can be calculated directly (i.e., without interpolation) at any arbitrary point on the airfoil surface. The method is essentially a numerical integration procedure, but, by developing it from the vortex-lattice model, a useful set of rules and automatic procedures has resulted, which makes the method accurate as well as efficient when moving from near to far-field regions. The calculations were enhanced by combining sources with the vortices.

The results obtained so far indicate that the number cf basic singularities used to represent an airfoil should be of the order of 40 to 50. However, the results also suggest that the use of a higher-order strength variation for the subvortices in regions of high pressure gradient might allow the number to be decreased -- possibly as low as 20. Bearing in mind accuracy and computing effort, the optimum values for the submerged depth and for the near-field radius would appear to be of the order of 0.1Δ and 3Δ, respectively. The method could be extended to the three-dimensional case for application to vortex-lattice methods, and should then allow close-approach situations associated with multiple components and force-free wake calculations.

REFERENCES

1. Rubbert, P.E.: Theoretical Characteristics of Arbitrary Wings by a Non-Planar Vortex Lattice Method. D6-9244, The Boeing Co., 1964.

2. Maskew, B.: Calculation of the Three-Dimensional Potential Flow Around Lifting Non-Planar Wings and Wing-Bodies Using a Surface Distribution of Quadrilateral Vortex Rings. TT7009, Loughborough Univ. of Technology, England, Sept. 1970.

3. Maskew, B.: Numerical Lifting Surface Methods for Calculating the Potential Flow about Wings and Wing-Bodies of Arbitrary Geometry. Ph.D. Thesis, Loughborough Univ. of Technology, England, Oct. 1972.

4. Belotserkovskii, S.M.: Calculation of the Flow Around Wings of Arbitrary Planform over a Wide Range of Angles of Attack. NASA TTF-12, 291, May 1971.

5. Butter, D.J.; and Hancock, G.J.: A Numerical Method for Calculating the Trailing Vortex System Behind a Swept Wing at Low Speed. The Aeronautical Journal, Vol. 75, No. 728, Aug. 1971, pp. 564-568.

6. Hackett, J.E.; and Evans, M.R.: Vortex Wakes Behind High-Lift Wings. J. Aircraft, Vol. 8, No. 5, May 1971, pp. 334-340.

7. Labrujere, Th.E.: A Numerical Method for the Determination of the Vortex Sheet Location Behind a Wing in Incompressible Flow. TR 72091 U, National Aerospace Laboratory (NLR), Amsterdam, the Netherlands, July 1972.

8. Lind, I.A.: A Non-Linear Vortex Lattice Method Applicable to Three-Dimensional Wing Systems with Rolled Up Vortex Wakes in Low Subsonic Flow. FI43, The Royal Institute of Tech., Stockholm, Sweden, 1973.

9. Rehbach, C.: Calculation of Flows around Zero Thickness Wings with Evolutive Vortex Sheets. NASA TTF-15, 183, 1973.

10. Mook, D.T.; and Maddox, S.A.: Extension of a Vortex Lattice Method to Include the Effects of Leading-Edge Separation. J. Aircraft, Vol. 11, No. 2, Feb. 1974, pp. 127-128.

11. Summa, J.M.: Potential Flow about Three-Dimensional Streamlined Lifting Configurations, with Application to Wings and Rotors. SUDAAR No. 485, Stanford University, California, Sept. 1974.

12. Maskew, B.: A Subvortex Technique for the Close Approach to a Discretized Vortex Sheet. NASA TM X-62, 487, Sept. 1975.

13. Maskew, B.: A Submerged Singularity Method for Calculating Potential Flow Velocities at Arbitrary Near-Field Points. NASA TM X-73, 115, March 1976.

376

14. Chorin, A.J.; and Bernard, P.S.: Discretization of a Vortex Sheet with an
    Example of Roll-up. FM-72-5, College of Engineering, Univ. of California,
    Berkeley, Calif., Nov. 1972.

15. Kuwahara, K.; and Takami, H.: Numerical Study of Two-Dimensional Vortex
    Motion by a System of Point Vortices. J. of the Physical Soc., Japan,
    Vol. 34, No. 1, Jan. 1973, pp. 247-253.

16. Lan, C.E.: A Quasi-Vortex Lattice Method in Thin Wing Theory. J. Aircraft,
    Vol. 11, No. 9, Sept. 1974, pp. 518-527.
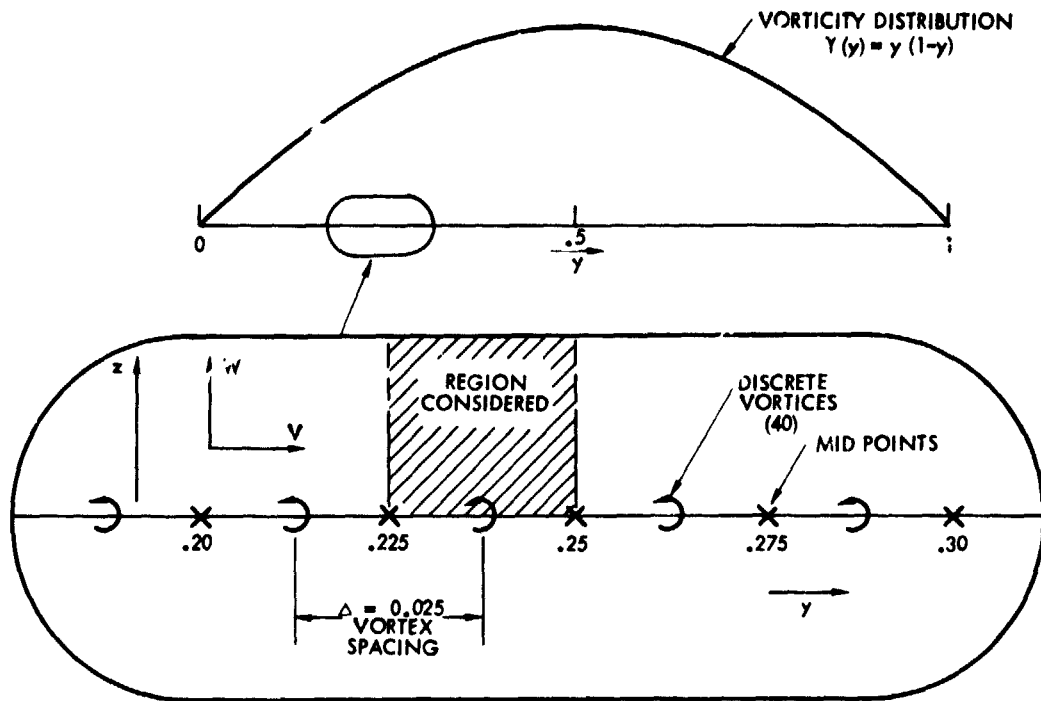
(a) Location of region considered.
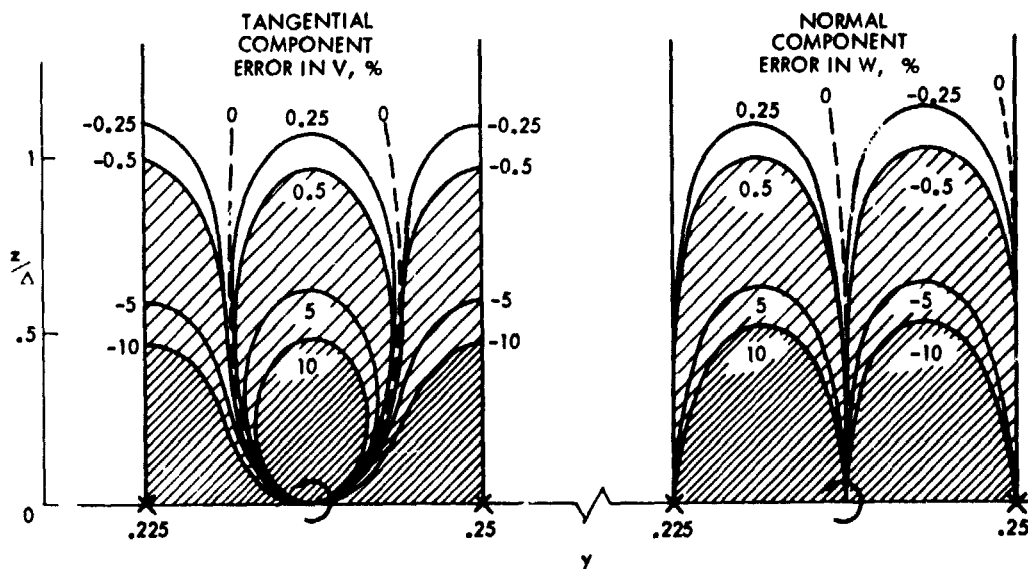
(b) Velocity error contours for the basic discretization.

Figure 1.- Velocity error calculations.

378
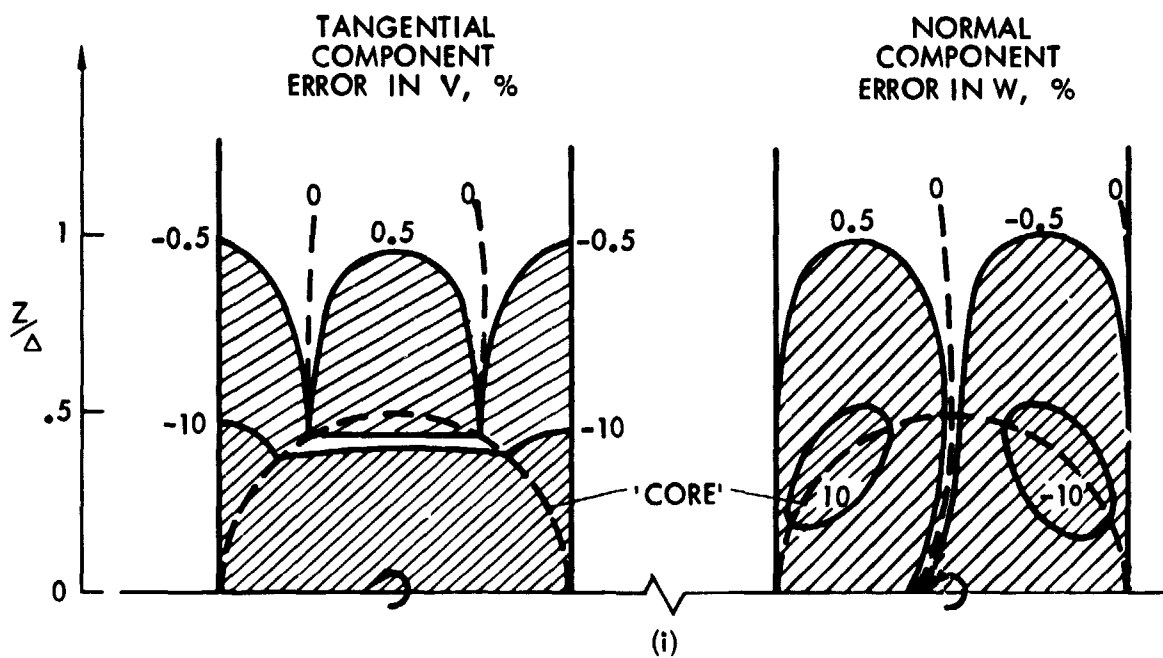
Figure 2.- Velocity error contours for a Rankine vortex core model. Core diameter = Δ.

BASIC VORTICES

SUBVORTICES

1=1   2   3   4 | 4   3   2   1

DISTANCE ALONG
SURFACE
$\longrightarrow$ S

S_V

Δ
VORTEX
SPACING
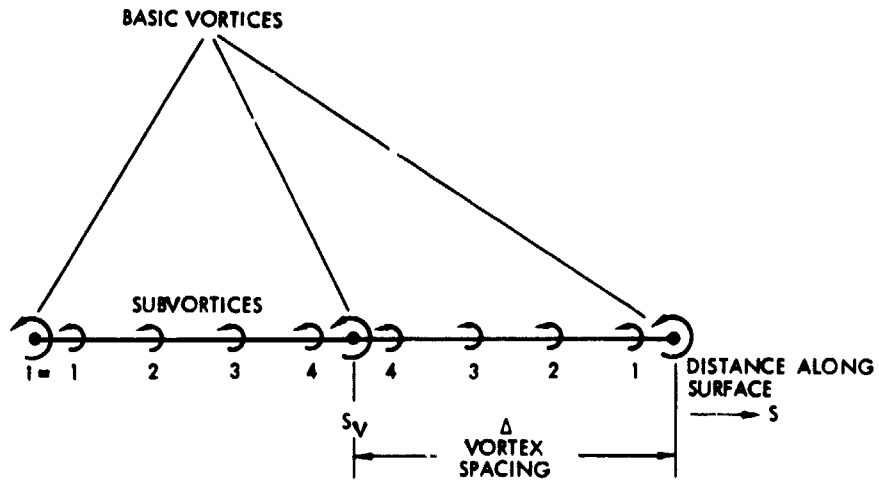
SUBVORTEX POSITIONS, $S_i = S_V \pm \{NSV + 0.5 - i\} \Delta / NSV$

(a) Arrangement of the subvortices for NSV = 4.

"BOUNDARY" FOR THE NEW 1Δ REGION
OF THE SUBVORTEX SYSTEM

FOR EVEN NSV IN A
VORTEX-LATTICE APPLICATION

EQ. 1

NUMBER OF SUBVORTICES PER SIDE, NSV

(HEIGHT ABOVE VORTEX "SHEET") / Δ
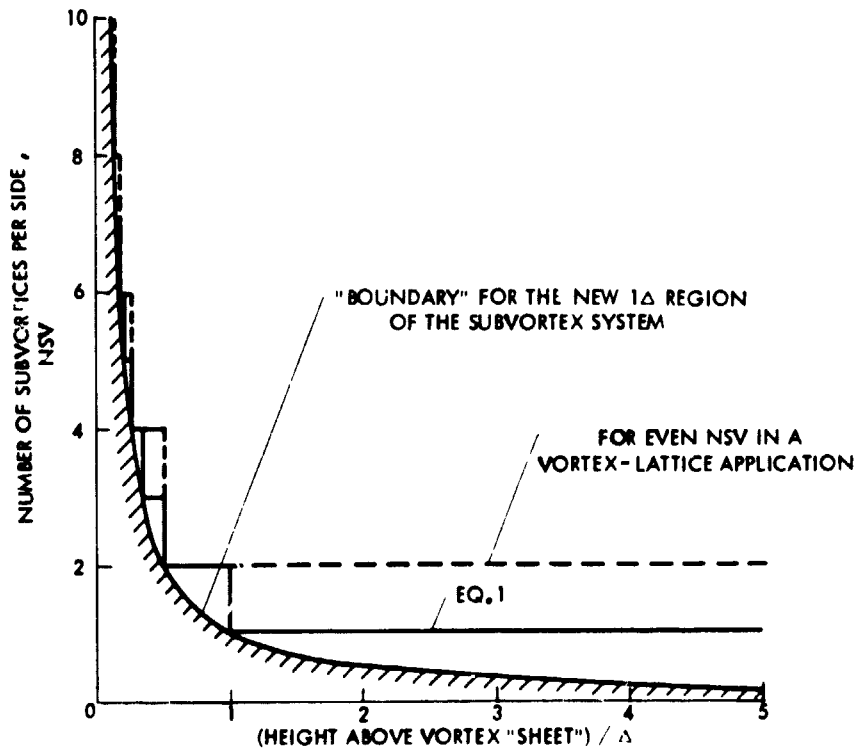
(b) Number of subvortices as a function of height
above the segment.

Figure 3.- The subvortex technique.
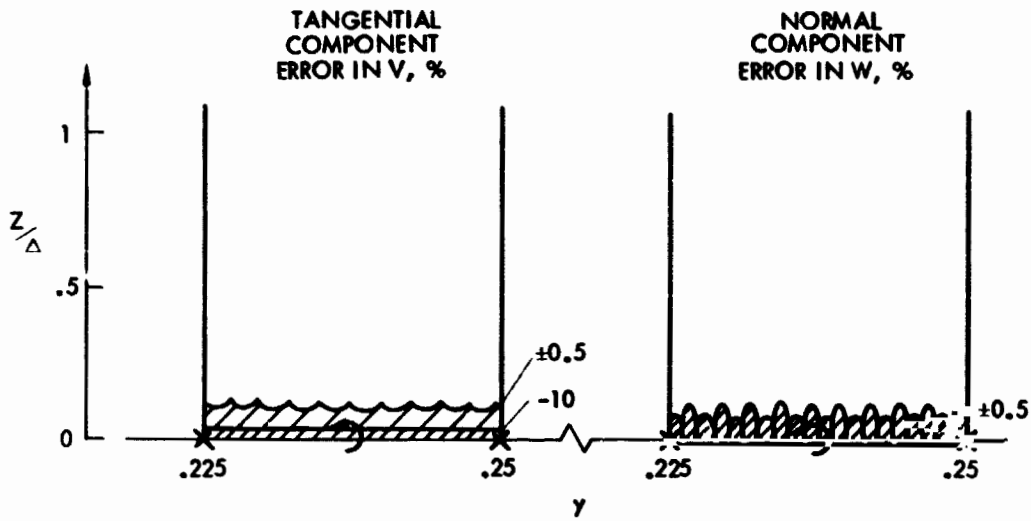
Figure 4.- Velocity error contours for the subvortex technique.
Near-field radius = 5Δ. NSV_{MAX} = 10.
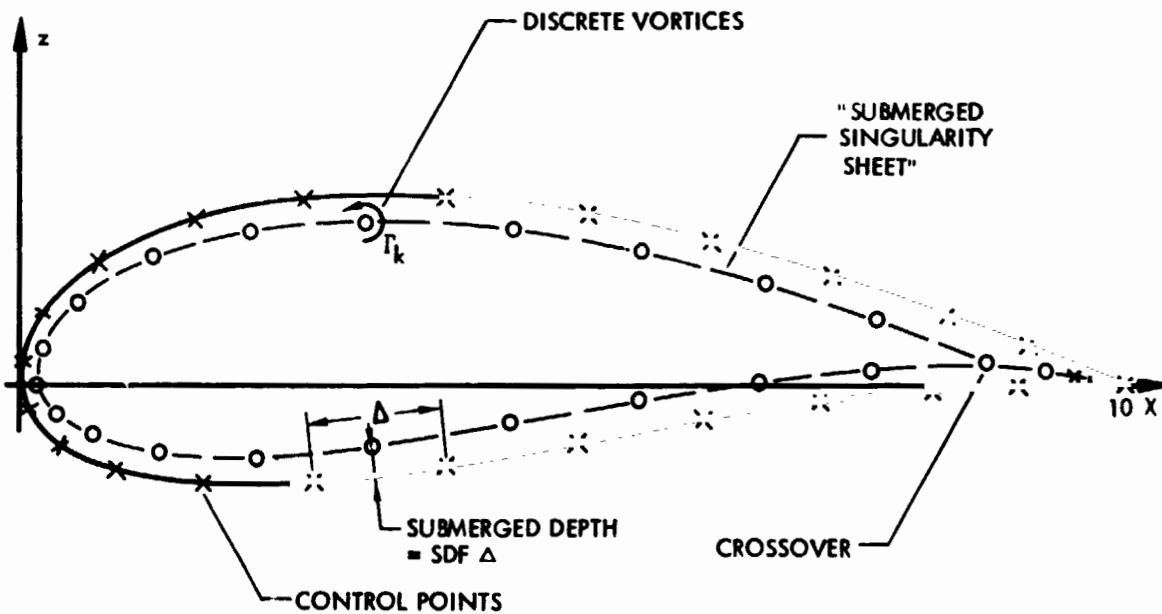
Figure 5.- Submerged singularity model with discrete vortices.
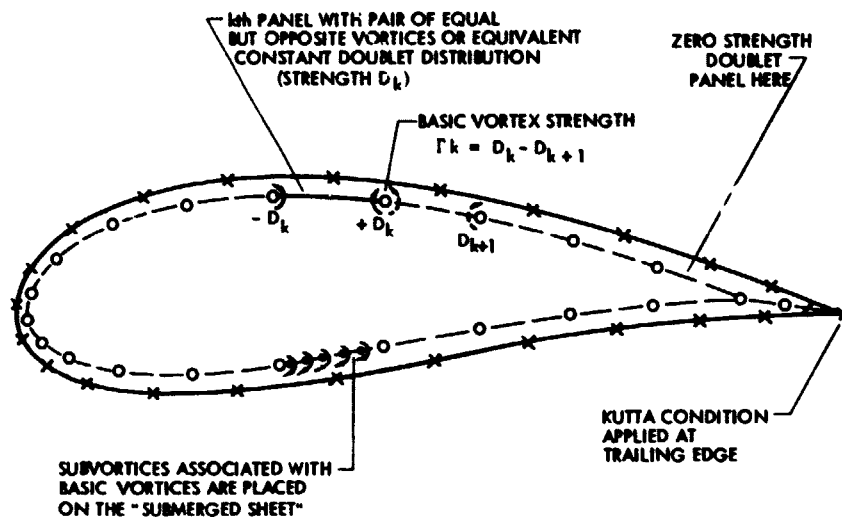
Figure 6.- Equivalent piecewise constant doublet model.
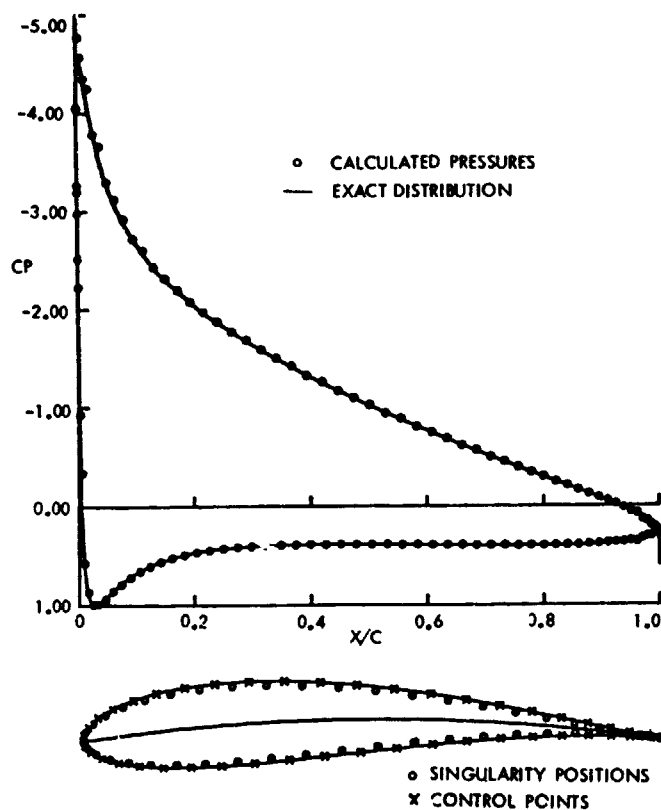
Figure 7.- Pressures calculated at arbitrary points on a
   Joukowski airfoil at 10° incidence. Model: submerged
   vortices and sources (coincident) with subvortex tech-
   nique applied (linear interpolation for position);
   46 basic singularities; submerged depth = 0.1Δ; near-
   field radius = 5Δ.
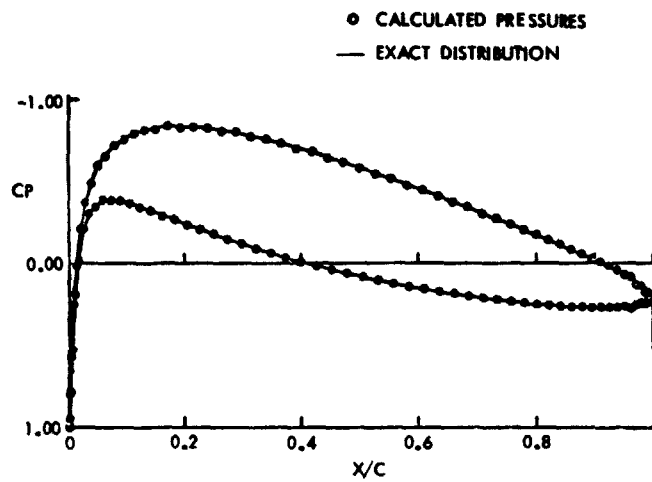
Figure 8.- Pressures calculated at arbitrary points on
a Joukowski airfoil at zero incidence. Model: as
in figure 7 but with higher-order interpolation for
subvortex positions.
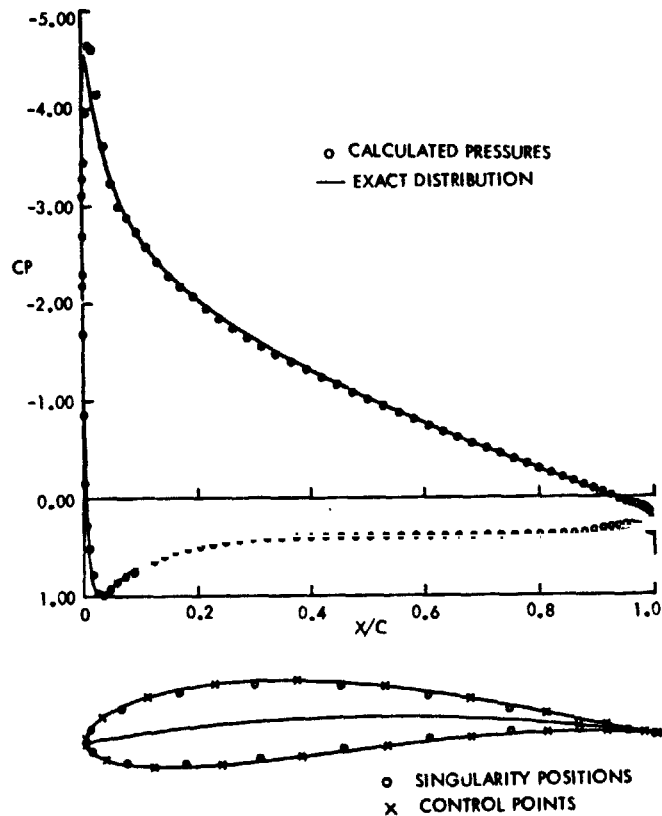
Figure 9.- Pressures calculated at arbitrary points
on a Joukowski airfoil at 10°. Model: as in
figure 7 but with 19 basic singularities.

383
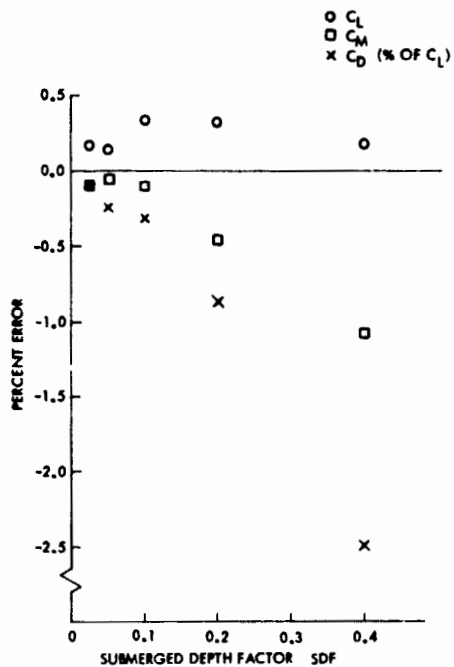
Figure 10.- Effect of submerged depth factor, SDF, on the errors in the integrated force and moment coefficients. Basic case as in figure 7.
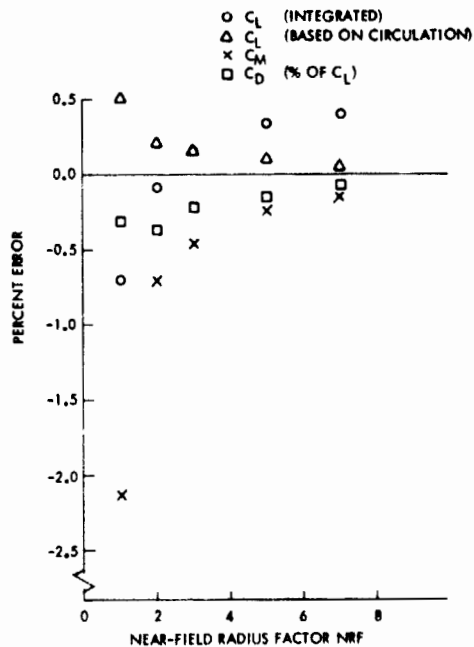
Figure 11.- Effect of near-field radius factor, NRF, on the errors in the integrated force and moment coefficients. Basic case as in figure 7.

SOME APPLICATIONS OF THE QUASI VORTEX-LATTICE METHOD

IN STEADY AND UNSTEADY AERODYNAMICS

C. Edward Lan
The University of Kansas

SUMMARY

The quasi vortex-lattice method is reviewed and applied to the evaluation of backwash, with applications in ground effect analysis. It is also extended to unsteady aerodynamics, with particular interest in the calculation of unsteady leading-edge suction. Some applications in ornithopter aerodynamics are given.

INTRODUCTION

The quasi vortex-lattice method (Quasi VLM) has been shown to produce good accuracy in lifting-surface problems not only for non-flapped but also flapped configurations (ref. 1). In these applications, the only induced velocity to be evaluated is the downwash. However, in some other applications such as ground effect analysis and wing-jet interaction (ref. 2), it is necessary to compute the u-induced velocity (i.e. backwash) in the flow field away from the wing plane. It is the purpose of this paper to assess the accuracy of such backwash computation.

One important feature of the Quasi VLM is the accurate prediction of the leading-edge suction without resorting to Kutta-Joukowsky relation. It is this feature that makes it possible to extend the method to the prediction of unsteady leading-edge suction in unsteady aerodynamics. This extension is also presented below.

SYMBOLS

AR   aspect ratio

c   chord length, m(ft), taken as unity.

C   leading-edge singularity parameter, defined in eq. (3c)

$C_{D,i}$ induced drag coefficient

c_ℓ sectional lift coefficient

$\bar{c}_\ell$ amplitude of sectional lift coefficient in unsteady flow

C_L total lift coefficient

C_{L_α} lift curve slope, per radian

C_m pitching moment coefficient

C_{m_α} pitching moment curve slope, per radian

ΔC_p pressure coefficient difference

$\bar{C}_T$ time-averaged leading-edge thrust coefficient

h, h_1 nondimensional height measured from the wing plane, referred to
            the chord length. See fig. 5.

$\bar{h}$ flapping amplitude

$\bar{h}_t$ flapping amplitude at the wing tip

k   reduced frequency, defined as $\omega c/2V$

M   number of integration points, or Mach number

N, N_c number of chordwise vortices

N_s number of spanwise vortex strips

S   leading-edge suction, N(lb), or wing area, $m^2(ft^2)$

386

$\bar{s}$	amplitude of unsteady leading-edge suction
u	nondimensional backwash, positive downstream
$\bar{u}$	amplitude of unsteady backwash on the wing plane
V	freestream velocity, m/sec (ft/sec)
w	nondimensional downwash, positive downward
x,y,z	rectangular coordinates, with x positive downstream, y positive spanwise to the right and z positive upward
dz_c/dx	camber slope
α	angle of attack, deg.
$\bar{\alpha}$	amplitude of pitching oscillation
β	$= \sqrt{1-M^2}$
$\bar{\eta}$	propulsive efficiency, percent
η	nondimensional spanwise coordinate
γ	nondimensional vortex density
ω	oscillation frequency, rad/sec
ρ	density, kg/m^3 (slugs/ft^3)
q_∞	freestream dynamic pressure, N/m^2 (lb/ft^2)
i	$= \sqrt{-1}$
$\bar{\delta}$	amplitude of flap angle
ℓ_∞	sectional lift coefficient in free air

Subscript:

f	flap

BASIC ANALYSIS IN QUASI VLM

For simplicity in presentation, consider the two-dimensional (2-D) downwash equation:

$$w(x) = \frac{1}{2\pi} \int_0^1 \frac{\gamma(x')dx'}{x-x'} \tag{1}$$

The integral is first transformed to a θ-integration and then reduced to a finite sum through the midpoint trapezoidal rule. It is obtained that

$$w(x_i) = \frac{-1}{2\pi}\int_0^\pi \frac{\gamma(\theta')\,\sin\theta'\,d\theta'}{\cos\theta - \cos\theta'} = \frac{-1}{2\pi}\int_0^\pi \frac{\gamma'\sin\theta' - \gamma\sin\theta}{\cos\theta - \cos\theta'}\,d\theta'$$

$$\approx \frac{-1}{2\pi}\frac{\pi}{N}\sum_{k=1}^N \frac{\gamma_k\sin\theta_k - \gamma_i\sin\theta_i}{\cos\theta_i - \cos\theta_k}$$

$$= \frac{1}{4N}\sum_{k=1}^N \frac{\gamma_k\sin\theta_k}{x_i-x_k} + \begin{cases} NC , & i=0 \\[6pt] 0 , & i\neq 0 \end{cases} \tag{2}$$

where

$$x_i = \frac{1}{2}(1 - \cos\theta_i) , \quad \theta_i = \frac{i\pi}{N} , \quad i = 0,1,\ldots,N \tag{3a}$$

$$x_k = \frac{1}{2}(1 - \cos\theta_k) , \quad \theta_k = \frac{(2k-1)\pi}{2N} , \quad k = 1,\ldots,N \tag{3b}$$

$$2C = \lim_{\theta\to 0} \gamma(\theta)\sin\theta \tag{3c}$$

Note that eq. (2) differs from the conventional VLM in that $\sin\theta$ in the formulation will eliminate the square-root singularities at the edges and the vortex densities are directly predicted, instead of the strengths of discrete vortices. Furthermore, the control and vortex points are defined by the so-called "semi-circle method." This is illustrated in fig. 1. By solving eq. (2) with $i\neq 0$, N γ_k-values can be obtained. Then the leading-edge singularity parameter C can be computed by taking $i=0$, i.e., by taking control point at the leading edge. The leading-edge suction is then

$$S = \pi\rho\frac{C^2}{4} \tag{4}$$

In three-dimensional cases, the above concept is also applicable by treating each chordwise vortex integral in a similar manner as in eq. (2). In this case, not only chordwise control and vortex locations are defined by the semicircle method, but also the spanwise vortex strips and control locations. See fig. 1. The detail is referred to in ref. 1. The rate of convergence of this method is indicated in figs. (2) and (3) for a 45°-sweep wing of AR=2 and constant chord. It is seen that the method converges reasonably fast.

BACKWASH EVALUATION AND GROUND EFFECT ANALYSIS

In ground effect analysis, it is known that the image vortex system may produce strong backwash to decrease the air velocity on the wing great enough to be significant. In fact, as a result the wing lift in ground effect may be less than the free air value. This unfavorable effect of backwash is particularly important in powered-lift aerodynamics and for wings under high lift conditions (ref. 3). Therefore, any formulation of ground-effect problem without backwash computation is applicable only to small loading conditions as analyzed in ref. 4.

To see the accuracy of backwash computation by VLM and Quasi VLM, consider the 2-D expressions for the backwash and downwash:

$$u(x,z) = \frac{z}{2\pi} \int_0^1 \frac{\gamma(x')dx'}{(x-x')^2+z^2} \tag{5}$$

$$w(x,z) = \frac{1}{2\pi} \int_0^1 \frac{(x-x')\gamma(x')dx'}{(x-x')^2+ z^2} \tag{6}$$

If $\gamma(x')= \sqrt{(1-x')/x'}$, the integration can be performed exactly. The results are shown in Appendix A. The downwash expression is included here for later comparison. In all computations shown below, equal-spacing elements are used for the VLM. For the Quasi VLM, again the θ-transformation is applied first before using the midpoint trapezoidal rule. Fig. 4 shows that the backwash along the chord evaluated by the VLM at both control and vortex points tend to be too high, in particular near the leading edge. On the other hand, the Quasi VLM gives quite accurate results everywhere at these not too small z-values. With these results in mind, both methods are now applied to the following 2-D linear ground-effect equations:

$$\frac{1}{2\pi} \int_0^1 \frac{\gamma(x')dx'}{x-x'} - \frac{1}{2\pi} \int_0^1 \gamma(x')\frac{(x-x')-2h_1\alpha}{(x-x')^2+4h_1^2} dx' = \alpha - \frac{dz_c}{dx} \tag{7}$$

$$c_\ell = 2 \int_0^1 \gamma(x)(1+u(x))dx \tag{8}$$

The corresponding geometry is given in fig. 5. The second integral in eq. (7) represents the normalwash due to the image vortex system. The "2hα" term is the backwash contribution. The results of computation are shown in fig. 6. Two points are of particular interest. Firstly, the linear vortex theory will give better results if the mean surface (as used in the mean surface approximation of the linear airfoil theory) is taken through the 3/4 chord point. Secondly, both the Quasi VLM and VLM predict approximately the same lift, despite the fact that the VLM gives higher backwash. This is because the VLM also produces higher downwash at a given z-value. This is shown in fig. 7. This means that the higher upwash from the image vortex system as predicted by the VLM tends to compensate the effect due to the higher predicted backwash. With flap deflected, the VLM predicts lower lift than the Quasi VLM does as shown in fig. 8.

The analysis with eqs. (7)-(8) becomes increasingly inaccurate at $h \leq 0.2$. As an extreme example, let $z=0.05$ in eq. (5). With $\gamma = \sqrt{(1-x)/x}$, the results are shown in figs. 9 and 10. It is seen that the backwash is underpredicted at the control points and overpredicted at the vortex points by both the VLM and the Quasi VLM. Depending on α, this would result in small or even negative c_ℓ in eq. (8). The backwash computation with small z has important applications in wing-jet interaction theory (ref. 2). Therefore, it is desirable to find a practical way to improve the accuracy of the computation. Even though increasing the number of vortex points (i.e. the number of integration points) can increase the accuracy, it is not a practical way because the number of unknowns to be solved would greatly increase, in particular, in 3-D applications. Since the inaccuracy is mainly due to the second-order singularity in eq. (5) as $z \to 0$, a practical method is described in ref. 6 to deal with this by weakening the singularity. According to this method, eq. (5) is evaluated as follows:

$$u(x,z) = \frac{z}{2\pi} \int_0^1 \frac{\gamma(x')-\gamma(x)}{(x-x')^2+z^2} dx' + \frac{z\gamma(x)}{2\pi} \int_0^1 \frac{dx'}{(x-x')^2+z^2} \tag{9}$$

$$\approx \frac{z}{4\pi} \frac{\pi}{N} \sum_{k=1}^N \frac{[\gamma(x_k)-\gamma(x)]}{(x-x_k)^2+z^2} \cdot \sin\theta_k + \frac{z\gamma(x)}{4\pi} \frac{\pi}{M} \sum_{j=1}^M \frac{\sin\theta_j}{(x-x_j)^2+z^2} \tag{10}$$

where x may be the control points (eq. 3a) or the vortex locations (eq. 3b) and

$$x_j = \frac{1}{2}(1-\cos\theta_j) \quad , \quad \theta_j = \frac{(2j-1)\pi}{2M} \quad , \quad j=1,\ldots,M \tag{11}$$

with M chosen to be $2^p N$ for interdigitation between control and vortex points, p being any integer. Note that the last integral in eq. (9) can be integrated exactly in 2-D case. However, the similar integral in 3-D would be too complicated to integrate. The accuracy of eq. (10) is also demonstrated with p=3 in figs. 9-10. Its application in a wing-jet interaction theory is discussed in ref. 7.

PREDICTION OF UNSTEADY LEADING-EDGE SUCTION

As mentioned earlier, the Quasi VLM predicts the leading-edge suction through the computation of the leading-edge singularity parameter. This feature can be easily extended to the unsteady aerodynamics if the downwash expression similar to that due to a steady horseshoe vortex can be derived for unsteady flow. This has been done recently by integrating the doublet potential by parts. The results are given in Appendix B for planar configurations. Note that if the oscillating frequency is zero, the expression is reduced to that for a steady horseshoe vortex. Using this expression, it is possible to extend the steady Quasi VLM to the unsteady case. In 2-D flow, this has been done in ref. 8. Some comparison with exact solutions of unsteady leading-edge suction (ref. 9) is made in Table I. It is seen that the accuracy of the Quasi VLM is quite good. Other aerodynamic characteristics at low or high subsonic Mach numbers can also be predicted accurately, including gust response (ref. 8).

In the 3-D method, note that the downwash expression given in Appendix B involves two types of integrals. The integration associated with I-integral, eqs. (B.15) and (B.18), can be performed by approximating the integrand, as has been done in ref. 10. On the other hand, the integrals, F_2 and F_4, can most conveniently be integrated by approximating the integrands by quadratic functions of the integration variable as has been done in ref. 10. The remaining aspects of the method follow closely the steady version.

To show the 3-D applications, the characteristics of a rectangular wing of aspect ratio 2 undergoing the first bending mode of oscillation (ref. 11) are computed. To indicate the rate of convergence of the method, the predicted complex lift coefficient is plotted in fig. 11 against the number of spanwise strips. It is seen that the method converges relatively fast for this planform. For instance, with $N_c=4$, C_L is changed by only 1% as N_s is increased from 10 to 20. Furthermore, the effect of N_c is seen to be small for this wing without chordwise deformation. The predicted pressure distributions at one spanwise station are compared with experimental data and those predicted by the Doublet-Lattice Method (DLM) (ref. 10) in fig. 12 with good agreement. The 3-D exact solution of unsteady leading-edge suction is not available. However, Bennett (ref. 12) has applied Reissner's high aspect-ratio theory to the computation of propulsive efficiency of ornithopters.

Here, the propulsive efficiency is defined as

$$\bar{\eta} = \frac{q_\infty S \bar{C}_T V}{\overline{q_\infty S C_L \dot{h}}} \tag{12}$$

$$\overline{C_L \dot{h}} = \frac{1}{2}\omega \int_{-1}^{1} \bar{h}(\eta)\bar{c}_\ell(\eta)d\eta \tag{13}$$

All quantities in eq. (12) have been averaged over one cycle. The results for two rectangular wings of aspect ratios of 6 and 12 performing linear apping $(\bar{h}(\bar{\eta}) = \bar{h}_t\eta)$ are shown in fig. 13. It appears that the high aspect ratio theory tends to predict higher thrust than the present method. The agreement of the predicted efficiency by both methods is good for AR=12. But for AR=6, the high aspect-ratio theory predicts lower efficiency, presumably because it would predict much higher input power which depends on the wing loading.

CONCLUDING REMARKS

The quasi vortex-lattice method was shown to possess good convergence characteristics in steady wing theory. Its application to the computation of downwash and backwash away from the wing plane in 2-D flow showed better accuracy than the conventional VLM with z not too small. When z is small, both methods become inaccurate in backwash computation. An improved method for the Quasi VLM was presented. The Quasi VLM was also extended to the unsteady aerodynamics, with the calculation of unsteady leading-edge suction being of particular interest.

APPENDIX A

Exact Integration for Eqs. (5) and (6)

(1)   Eq. (5)

$$u(x,z) = \frac{z}{2\pi} \int_0^1 \sqrt{\frac{1-x'}{x'}} \; \frac{dx'}{(x-x')^2+z^2} = \frac{az}{2\pi} \frac{b(1-x)-a^2}{a^4+b^2z^2} \left\{ \frac{\pi}{2} \, \text{sign}[b(1-x)-a^2] \right.$$

$$\left. + \frac{\pi}{2} \, \text{sign}[bx+a^2] \right\}$$
(A.1)

where

$$b = \frac{1}{2}(1-2x)$$
(A.2)

$$a^2 = \frac{\sqrt{[z^2+x(1-x)]^2+(1-2x)^2z^2} - [z^2+x(1-x)]}{2}$$
(A.3)

(2)   Eq. (6)

$$w(x,z) = \frac{1}{2\pi} \int_0^1 \frac{(x-x')\sqrt{\frac{1-x'}{x'}}}{(x-x')^2+z^2} \, dx' = \frac{(D-D^{-1})\cos\theta_1 + D^2 - \cos2\theta_1}{D^2+D^{-2}-2\cos2\theta_1}$$

where

$$D = \sqrt{2} \, / \, \left\{ [2+Z'+(Z'^2+16z^2)^{\frac{1}{2}}]^{\frac{1}{2}} + [Z'+(Z'^2+16z^2)^{\frac{1}{2}}]^{\frac{1}{2}} \right\}$$
(A.4)

$$\theta_1 = \cos^{-1} \left\{ [\frac{2}{2+Z' + (Z'^2+16z^2)^{\frac{1}{2}}}]^{\frac{1}{2}} \cos\theta \right\}$$
(A.5)

$$Z' = 4z^2-\sin^2\theta$$
(A.6)

$$\cos\theta = 1-2x$$
(A.7)

APPENDIX B

Downwash due to an Oscillating Horseshoe Vortex

The downwash produced by an "oscillating horseshoe vortex" for a planar configuration can be written as

$$\frac{\partial \phi}{\partial z} = \frac{\partial \phi_1}{\partial z} + \frac{\partial \phi_2}{\partial z} \tag{B.1}$$

where

$$\frac{\partial \phi_1}{\partial z} = F_1 + F_2 \tag{B.2}$$

$$\frac{\partial \phi_2}{\partial z} = F_3 + F_4 \tag{B.3}$$

$$
F_1 = \frac{\Delta C_p}{8\pi} \left\{ -\frac{1}{v'-y} + \frac{1}{\sqrt{(x-x')^2+\beta^2(y-y')^2}} \right.
$$

$$
\times \left[\frac{x'-x}{y'-y} + \frac{(x'-x)(x_2-x_1)+\beta^2(y_2-y_1)(y'-y)}{Q} \right] \right\}
$$

$$
\left. \times \exp \left\{ -i\frac{\omega}{V} \frac{M\sqrt{(x-x')^2+\beta^2(y-y')^2} - M^2(x-x')}{\beta^2} \right\} \right|
\begin{array}{l} x'=x_2 \\ y'=y_2 \\ \\ x'=x_1 \\ y'=y_1 \end{array}
\tag{B.4}
$$

$$F_2 = -i\frac{\omega}{V}\frac{\Delta C_p}{8\pi} \int_0^1 \left\{ -\frac{1}{\eta-y} + \frac{1}{(y_2-y_1)R}\left[\frac{(x_2-x_1)(\eta-y)+Q}{\eta-y}\right.\right.$$

$$\left.+ \frac{((x_2-x_1)(\eta-y)+Q)(x_2-x_1) + \beta^2(y_2-y_1)^2(\eta-y)}{Q}\right]\right\}$$

$$\times \left[\frac{M(y-\eta)}{R} + \left(\frac{M}{\beta^2}\frac{x_0}{R} - \frac{M^2}{\beta^2}\right)\frac{x_2-x_1}{y_2-y_1}\right] \exp\left[-i\frac{\omega}{V}\frac{MR-M^2 x_0}{\beta^2}\right] (y_2-y_1)d\tau \qquad (B.5)$$

$$R = \sqrt{A\tau^2+B\tau+C} \qquad (B.6)$$

$$A = (x_2-x_1)^2 + \beta^2(y_2-y_1)^2 \qquad (B.7)$$

$$B = -2[(x-x_1)(x_2-x_1) + \beta^2(y-y_1)(y_2-y_1)] \qquad (B.8)$$

$$C = (x-x_1)^2 + \beta^2(y-y_1)^2 \qquad (B.9)$$

$$\eta-y = (y_2-y_1)\tau-(y-y_1) \qquad (B.10)$$

$$Q = (x_2-x_1)(y-y_1) - (x-x_1)(y_2-y_1) \qquad (B.11)$$

$$x_0 = x-x_1 - \tau(x_2-x_1) \qquad (B.12)$$

$$F_3 = -i\frac{\omega}{V}\frac{\Delta C_p}{8\pi}\left\{ -\frac{1}{y_2-y} I_2 + \frac{1}{y_1-y} I_1\right\} \qquad (B.13)$$

$$F_4 = -i\frac{\omega}{V}\frac{\Delta C_p}{8\pi} \int_0^1 \frac{1}{\eta-y}\frac{\partial I}{\partial \eta} (y_2-y_1)d\tau \qquad (B.14)$$

$$I(\tau) = \int_{\tau_1 r_1}^{\infty} (1 - \frac{\tau'}{\sqrt{\tau'^2 + r_1^2}}) e^{-i\frac{\omega}{V}(\tau' + x_0)} d\tau' \tag{B.15}$$

$$\tau_1 r_1 = \frac{-x_0 + MR}{\beta^2} \tag{B.16}$$

$$r_1^2 = (y - \eta)^2 \tag{B.17}$$

$$(\tau_1 r_1)_1 = \tau_1 r_1 \text{ at } \tau = 0$$

$$(\tau_1 r_1)_2 = \tau_1 r_1 \text{ at } \tau = 1$$

$$r_{11}^2 = r_1^2 \text{ at } \tau = 0$$

$$r_{12}^2 = r_1^2 \text{ at } \tau = 1$$

$$x_{01} = x_0 \text{ at } \tau = 0$$

$$x_{02} = x_o \text{ at } \tau = 1$$

$$\frac{\partial I}{\partial \eta} = \frac{M(y-\eta)}{R}(1 - \frac{\tau_1}{\sqrt{1 + \tau_1^2}}) e^{-i\frac{\omega}{V}(\tau_1 r_1 + x_0)} + i\frac{\omega}{V} I(\tau) \frac{x_2 - x_1}{y_2 - y_1}$$

$$+ (1 - \frac{\tau_1}{\sqrt{1 + \tau_1^2}}) e^{-i\frac{\omega}{V}(\tau_1 r_1 + x_0)} (\frac{Mx_0}{\beta^2 R} - \frac{1}{\beta^2}) \frac{x_2 - x_1}{y_2 - y_1}$$

$$- (y - \eta) \int_{\tau_1 r_1}^{\infty} \frac{\tau'}{(\tau'^2 + r_1^2)^{3/2}} e^{-i\frac{\omega}{V}(\tau' + x_0)} d\tau' \tag{B.18}$$

In the above expressions, (x_1, y_1) and (x_2, y_2) represent inboard and outboard endpoints of the "bounded element," respectively.

396

REFERENCES

1. Lan, C. Edward: A Quasi Vortex-Lattice Method in Thin Wing Theory. Journal of Aircraft, Vol. 11, No. 9, Sept. 1974, pp. 518-527.

2. Lan, C. Edward and Campbell, James F.: Theoretical Aerodynamics of Upper-Surface-Blowing Jet-Wing Interaction. NASA TN D-7936, 1975.

3. Gratzer, L.B. and Mahal, A.S.: Ground Effects in STOL Operation. Journal of Aircraft, Vol. 9, No. 3, March 1972, pp. 236-242.

4. Saunders, G.H.: Aerodynamic Characteristics of Wings in Ground Proximity. Canadian Aeronautics and Space Journal, Vol. 11, No. 6, June 1965, pp. 185-192.

5. Thwaites, B.: Incompressible Aerodynamics. Oxford-Clarendon Press, 1960.

6. Lan, C. Edward: An Analytical Investigation of Wing-Jet Interaction. Section 6. NASA CR-138140, April 1974.

7. Lan, C. Edward: Upper-Surface-Blowing Jet-Wing Interaction. Vortex-Lattice Utilization, NASA SP-405, 1976. (Paper no. 11 of this compilation.)

8. Lan, C. Edward: The Induced Drag of Oscillating Airfoils in Linear Subsonic Compressible Flow. KU-FRL-400, June 1975, The Flight Research Laboratory, The University of Kansas Center for Research, Inc.

9. Garrick, I. E.: Propulsion of a Flapping and Oscillating Airfoil. NACA Report No. 567, 1936.

10. Albano, Edward and Rodden, William P.: A Doublet-Lattice Method for Calculating Lift Distributions on Oscillating Surfaces in Subsonic Flows. AIAA Journal, Vol. 7, No. 2, Feb. 1969. pp. 279-285.

11. Lessing, H.C.; Troutman, J.L.; and Menees, G.P.: Experimental Determination of the Pressure Distribution on a Rectangular Wing Oscillating in the First Bending Mode for Mach Numbers from 0.24 to 1.30. NASA TN D-344, 1960.

12. Bennett, Albert George, Jr.: A Preliminary Study of Ornithopter Aerodynamics. Ph.D. dissertation, 1970. University of Illinois.

Table I. — Comparison of Predicted Leading-Edge Suction Parameter with Exact Solutions in 2-D Incompressible Flow.

$$\bar{s} = \lim_{x \to -1} \bar{u}(x)\sqrt{1+x}$$

$$\bar{s}_{\alpha} = \partial\bar{s}/\partial\bar{\alpha} \quad , \quad \bar{s}_{\bar{\delta}} = \partial\bar{s}/\partial\bar{\delta}$$

(A) Pitching motion about midchord

$\underline{k}$	$\underline{N}$	Present Method $\bar{s}_{\bar{\alpha}}$	Exact, Ref. 9
0.1	10	1.18870-0.25555i	1.18870-0.25556i
0.5	15	0.89889-0.35527i	0.89889-0.35529i
1.0	15	0.83374-0.46737i	0.83378-0.46748i

(B) Flap Rotation with flap-chord ratio = 0.3

$\underline{k}$	(N_1, N_2)	Present Method $\bar{s}_{\bar{\delta}}$	Exact, Ref. 9
0.1	(12, 7)	0.37115-0.14696i	0.37139-0.14705i
0.5	(12, 7)	0.17483-0.11565i	0.17496-0.11576i
1.0	(12, 7)	0.12972-0.06580i	0.12982-0.065921i

Note: N_1 = number of doublet elements on the airfoil.

N_2 = number of doublet elements on the flap.
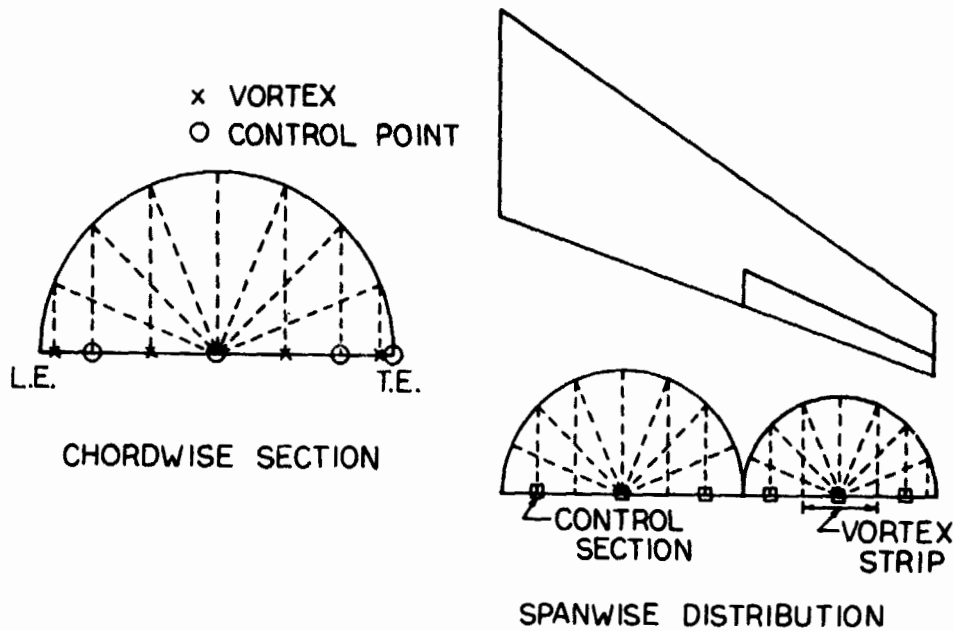
Figure 1.- Illustration of chordwise and spanwise control
and vortex locations.
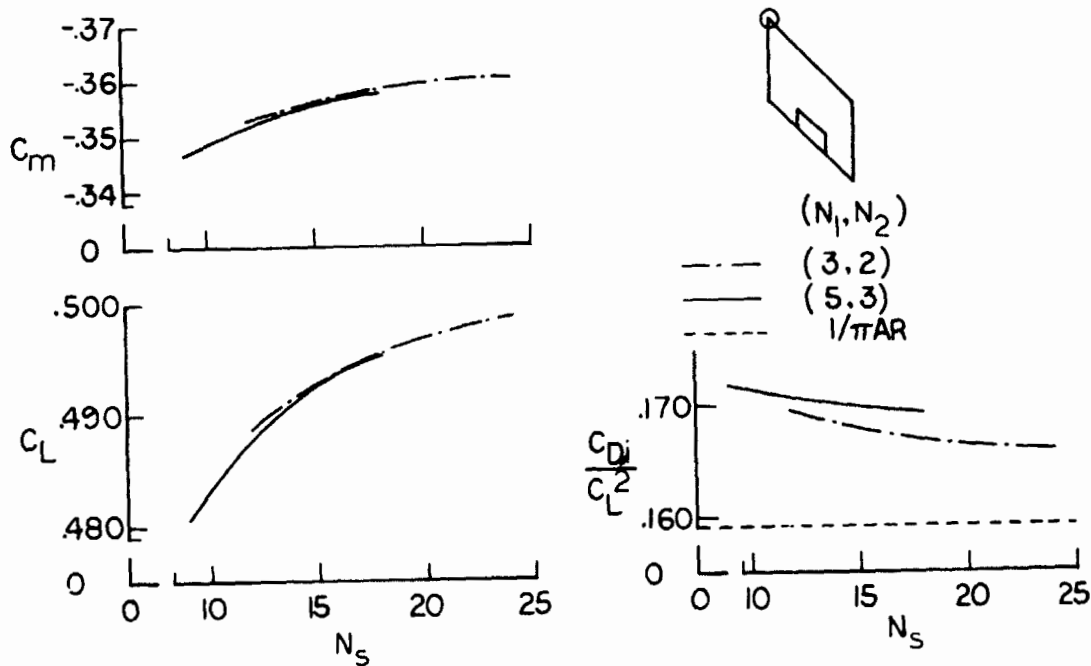
Figure 2.- Effect of vortex-lattice arrangement on aerodynamic
characteristics of a 45°-sweep wing of AR = 2. $\delta_f = 0°$;
M = 0.
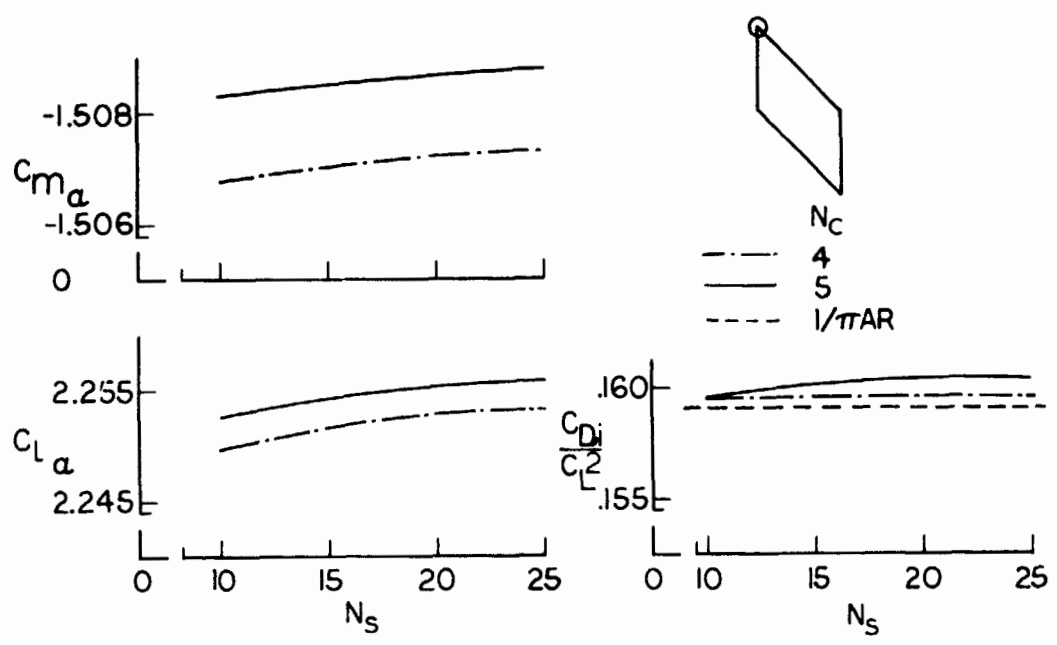
Figure 3.- Effect of vortex-lattice arrangement on aerodynamic characteristics of a 45°-sweep wing of AR = 2. $\delta_f = 10°$; $\alpha = 10°$; and M = 0.5.
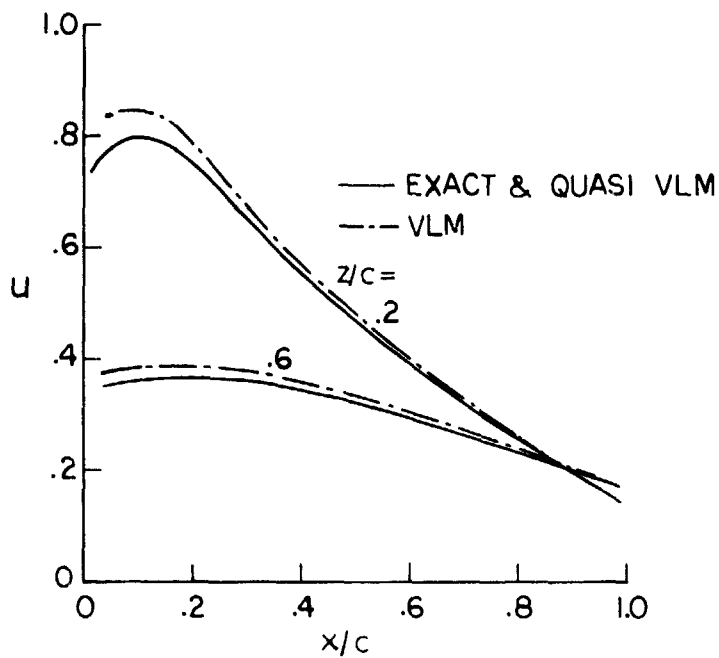
(a) At vortex points.
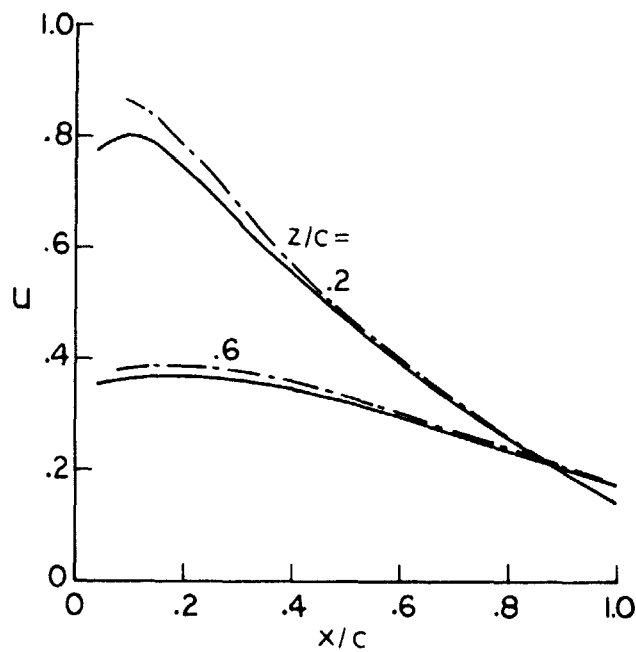
(b) At control points.

Figure 4.- Comparison of backwash evaluations (eq. 5) by different
methods. $\gamma(x) = \sqrt{(1 - x)/x}$; $N = 8$.
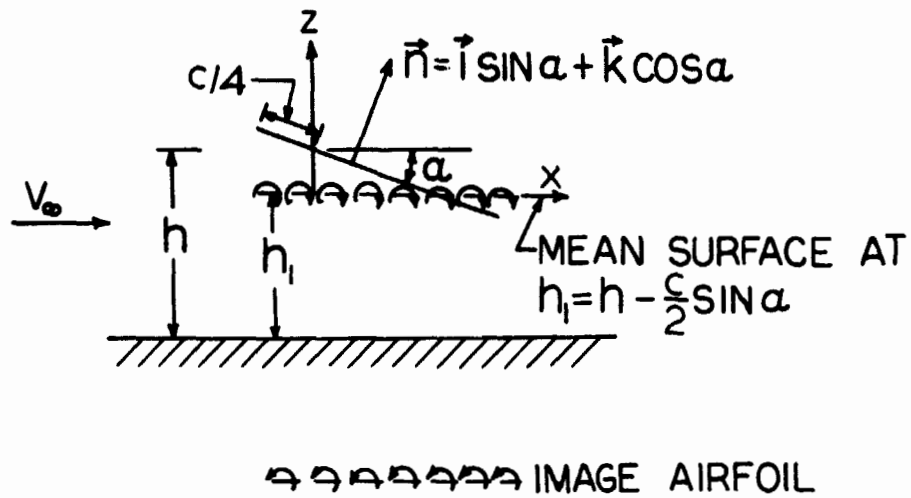
Figure 5.- Geometry for the ground-effect equation.
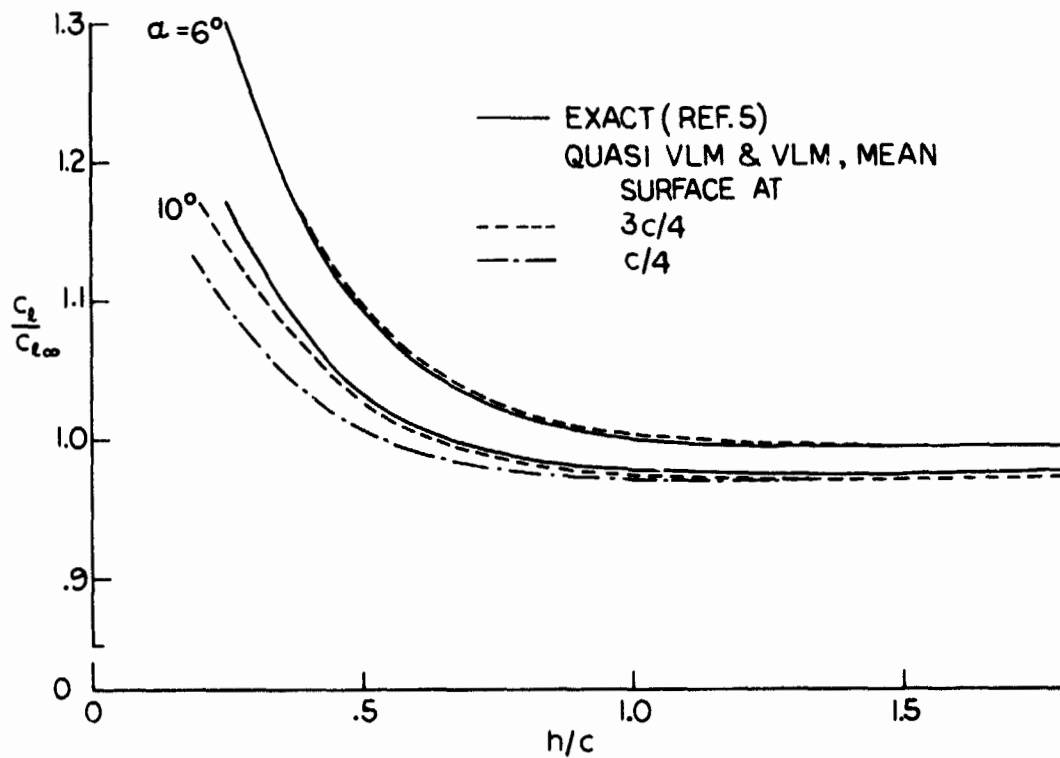
Figure 6.- Comparison of computed airfoil lift in ground effect by different methods. $c_{\ell_\infty} = 2\pi\alpha$; h measured from c/4.
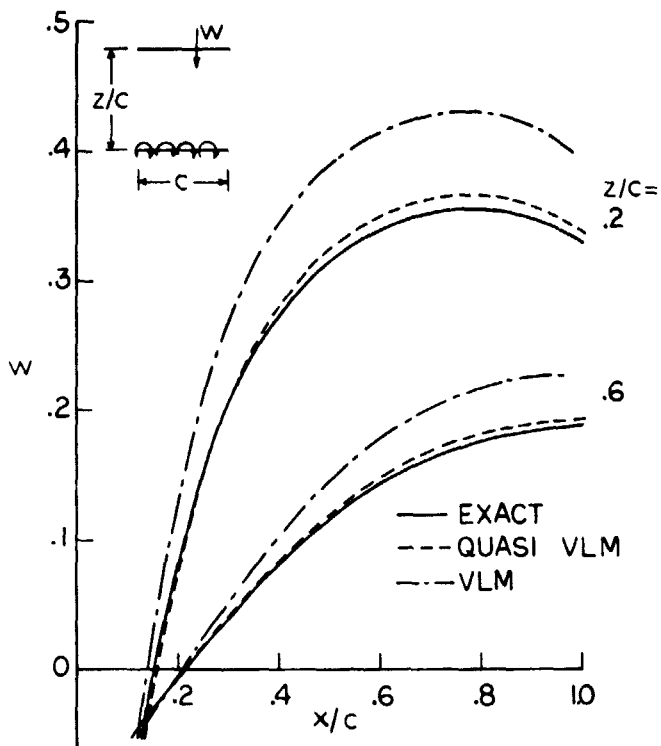
Figure 7.- Comparison of downwash evaluations (eq. 6) at control points by different methods. $\gamma(x) = \sqrt{(1 - x)/x}$; $N = 8$.
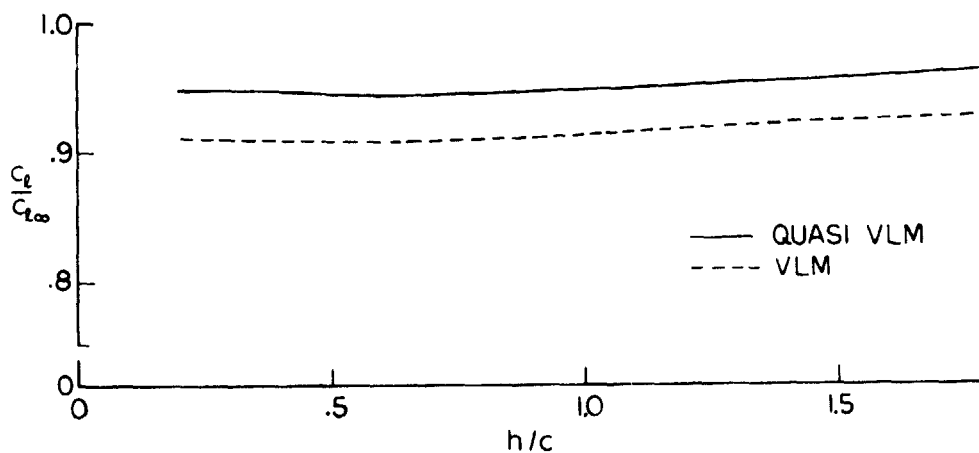

Figure 8.- Comparison of computed airfoil lift in ground effect by different methods. $c_f/c = 0.3$; $\delta_f = 20^\circ$; $\alpha = 2^\circ$; $c_{\ell_\infty} = 1.6685$; h measured from $c/4$.
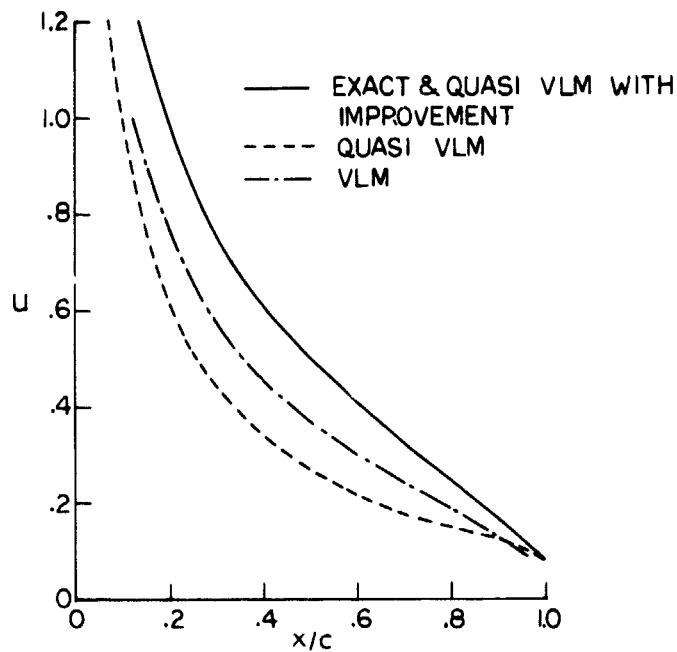
Figure 9.- Comparison of backwash evaluations at control points by different methods. $\gamma(x) = \sqrt{(1 - x)/x}$; $z/c = 0.05$; $N = 6$.
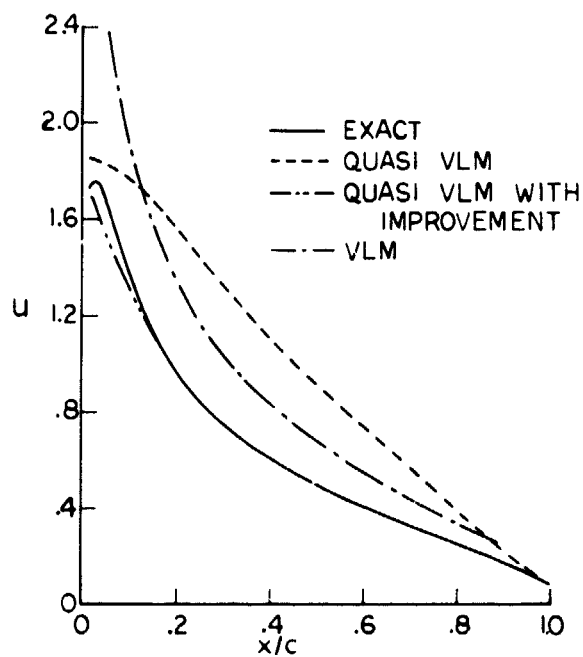
Figure 10.- Comparison of backwash evaluations at vortex points by different methods. $\gamma(x) = \sqrt{(1 - x)/x}$; $z/c = 0.05$; $N = 6$.

.90

N_C
——— 5
- - - - 4

C_L

.89

.88

IMAGINARY PART

0

10   15   20

N_S

REAL PART

-.30

-.31
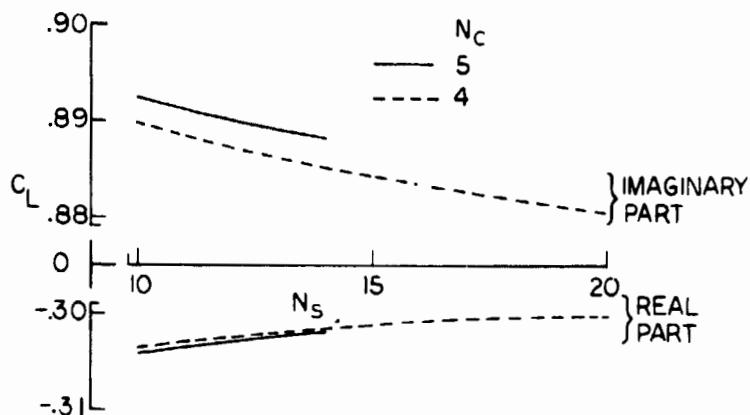
Figure 11.- Convergence of computed lift coefficient for a rectangular wing of AR = 2 oscillating in first bending mode.   M = 0.24; k = 0.47.

5

4

EXPERIMENT (REF.11)
⊙   REAL
⊡   IMAGINARY
——— QUASI VLM
- - - DLM (REF. 10)

$\dfrac{\Delta C_p}{\omega \bar{h}_t / V}$ 3

2

1

0

-1

0   .2   .4   .6   .8   1.0

x/c
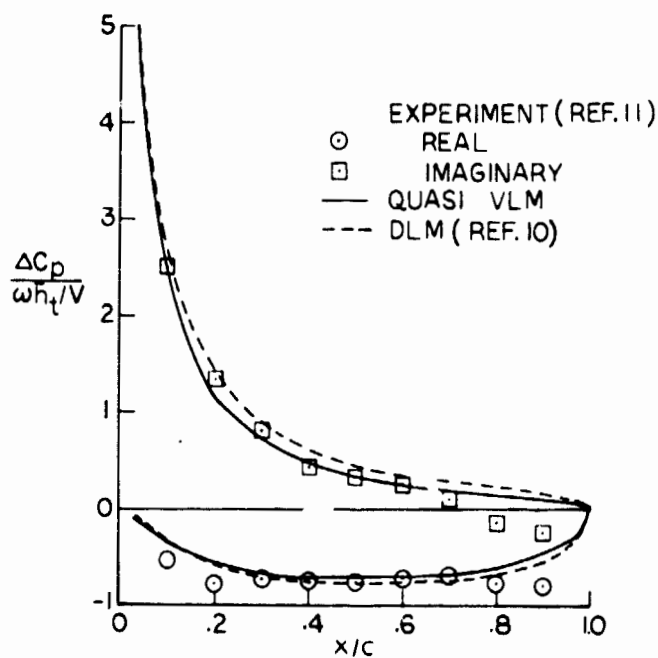
Figure 12.- Comparison of computed pressure distributions with experimental data for a rectangular wing of AR = 2 oscillating in first bending mode. M = 0.24; k = 0.47.

405
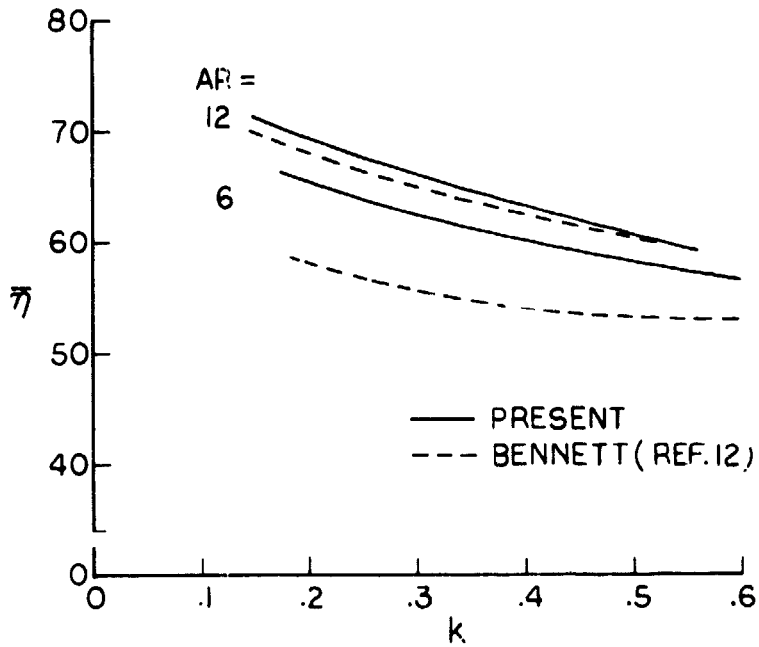
(a) Propulsive efficiency.
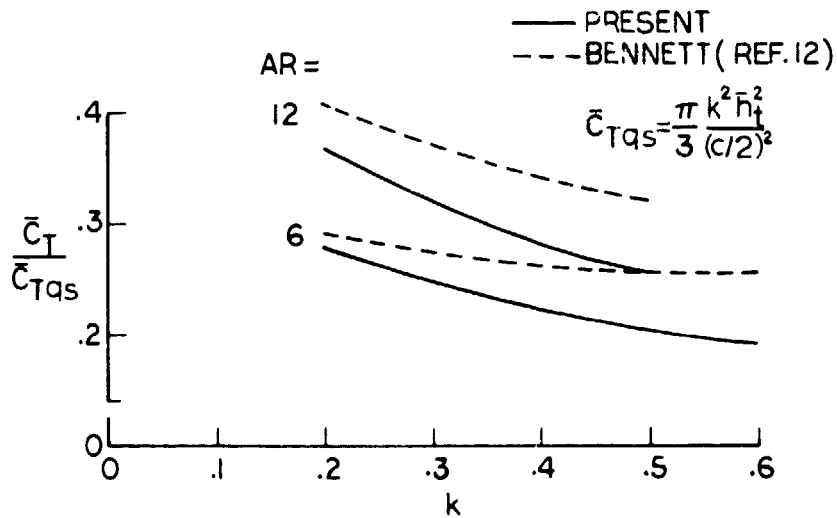
(b) Thrust.

Figure 13.- Theoretical propulsive efficiency and thrust for rectangular wings in linear flapping.

UNSTEADY FLOW PAST WINGS HAVING SHARP-EDGE SEPARATION*

E. H. Atta, O. A. Kandil, D. T. Mook, A. H. Nayfeh

Virginia Polytechnic Institute and State University

SUMMARY

A vortex-lattice technique is developed to model unsteady, incompressible flow past thin wings. This technique predicts the shape of the wake as a function of time; thus, it is not restricted by planform, aspect ratio, or angle of attack as long as vortex bursting does not occur and the flow does not separate from the wing surface. Moreover, the technique can be applied to wings of arbitrary curvature undergoing general motion; thus, it can treat rigid-body motion, arbitrary wing deformation, gusts in the freestream, and periodic motions.

Numerical results are presented for low-aspect rectangular wings undergoing a constant-rate, rigid-body rotation about the trailing edge. The results for the unsteady motion are compared with those predicted by assuming quasi-steady motion. The present results exhibit hysteretic behavior.

INTRODUCTION

For steady flows there is ample experimental evidence indicating that flows past thin wings, even those exhibiting significant leading-edge and wing-tip separation, can be described by a velocity potential. We assume that the same is true for unsteady flow.

The velocity potential for incompressible unsteady flow is governed by Laplace's equation and is subject to the following boundary conditions:

  (1) the fluid cannot penetrate the lifting surface,

  (2) the disturbance created by the lifting surface must die out away
       from the surface and its wake,

  (3) there must not be a discontinuity in the pressure in the wake, and

  (4) the Kutta condition must be satisfied along the sharp edges when
       the flow is steady.

The present technique is an improvement over the previously developed techniques for treating this problem. For example, Morino and Kuo (ref. 1) developed a technique in which the integral equation governing the velocity potential

---

is solved numerically. Ashley and Rodden (ref. 2), Rodden, Giesing and Kalman (ref. 3), Giesing, Kalman, and Rodden (ref. 4), and Albano and Rodden (ref. 5) developed techniques employing combinations of horseshoe-vortex lattice and doublets. However, these methods can treat small harmonic motions, and because none is capable of determining the geometry of the wake, the small harmonic motions must be about small angles of attack. Belotserkovskii (ref. 6) developed a technique for treating general unsteady motion, but because it is not capable of determining the geometry of the wake, it too is limited to small angles of attack. Djojodihardjo and Widnall (ref. 7) also developed a general technique in which the integral equation governing the velocity potential is solved numerically. Though they determined the geometry of the wake adjoining the trailing edge, they ignored the wing-tip vortex system; thus, their technique at best is limited to large angles of attack for moderately swept, high-aspect wings. With the present technique, the geometry of the wakes adjoining all sharp edges is determined as part of the solution, and there are no restrictions on the type of motion. The essential difference between the techniques of Belotserkovskii, Djojodihardjo and Widnall, and the present paper are illustrated in figure 1.

SYMBOLS

AR	aspect ratio
b	wing semi-span
C_n, C_m	normal-force, pitching-moment coefficients, respectively
C_p	pressure coefficient
C_r	root chord
$\vec{F}$	force vector
ℓ	length of vortex segment
$\vec{r}$	position vector
t	nondimensional time
Δt	time increment
$\vec{v}$	nondimensional velocity vector
X,Y,Z	wing-fixed coordinate system
α	angle of attack
α_0, α_f	initial and final angles of attack
Γ	nondimensional circulation
$\dot{\alpha}$	rate of change of angle of attack

THE PRESENT TECHNIQUE

For completeness, the vortex-lattice technique for steady flows is briefly discussed. Then the modifications needed to model unsteady flows are described.

Steady Flows

The wing surface is represented by a lattice of discrete vortex lines, while the wake is represented by a series of discrete nonintersecting vortex lines. Each vortex segment of the lattice is straight (the elemental areas are not necessarily planar), and each line in the wake is composed of a series of short straight segments and one semi-infinite segment. Control points are associated with each elemental area of the lattice and with each finite segment of the wake.

The desired velocity potential is the sum of the known freestream potential and the potentials of all the discrete vortex lines. The velocities generated by the latter are calculated in terms of the circulations around these segments according to the Biot-Savart law. These circulations are the primary unknowns.

To satisfy the no-penetration boundary condition, the normal component of the velocity is forced to vanish at each control point of the lattice. The velocity field generated by the vortex segments is calculated according to the Biot-Savart law; thus, the disturbance dies out far from the wing and its wake. The finite segments in the wake are aligned with the velocity at their control points in order to render the pressure continuous. Finally, no vortex segments on the lattice are placed between the last row and column of control points and the edge where the Kutta condition is imposed.

The problem is solved by the following iterative scheme:

(1) a direction is assigned to each segment in the wake,

(2) the circulations around each of the vortex segments are determined by simultaneously satisfying the no-penetration condition and spatial conservation of circulation,

(3) the segments in the wake are rendered force-free while the circulations are held constant,

(4) steps (2) and (3) are repeated until the shape of the wake doesn't change.

An example of a steady solution is shown in figure 2.

More details and results are given by Kandil, Mook and Nayfeh (ref. 8) and by Kandil (ref. 9).

Unsteady Flows

The initial condition can be a steady flow such as one obtained by the method described above or no flow at all. Here we consider the former. When conditions change with time, starting vortices form along the sharp edges; then they are shed and convected downstream with the local particle velocity. Thus, an ever-growing portion of the wake must also be represented by a lattice, not a series of nonintersecting lines as in the steady case. This is the essential difference between the steady and the unsteady model.

The continuous variation with time is approximated by considering the motion to be a series of impulsive changes occuring at evenly spaced time intervals; thus, the motion becomes smoother as the time intervals become smaller.

In figure 3, the wake adjoining the wing tip and trailing edge is spread out to illustrate how the lattice forms in the wake. The first arrangement shows the initial conditions; this corresponds to a steady solution such as the one shown in figure 2. The next arrangement corresponds to time = 1; hence, there is one shed vortex line in the wake. The last arrangement shown corresponds to time = 2. An actual solution is shown in figure 4; this picture corresponds to time = 4.

With an incompressible model of the flow, the instant the angle of attack changes, the vorticity on the wing and the position of the entire wake (i.e., the direction of the vorticity in the wake) change. A starting vortex forms along the sharp edges and subsequently is shed. But the strength of the vorticity in the wake does not change because the vorticity is convected downstream with the fluid particles. Such a model of the flow is realistic only when the particle velocity is small compared with the speed of sound (i.e., when the Mach number is small).

In terms of the present discrete-line representation, the instant the angle of attack changes, the circulations in the lattice representing the surface and the directions of the finite segments representing the wake change. But the circulations around the finite segments in the wake do not.

One cannot, simultaneously, render the wake force-free, satisfy the no-penetration condition on the surface, and spatially conserve circulation unless one adds a new vortex line which essentially parallels the sharp edges. Thus, the Kutta condition cannot be imposed during unsteady motion. This new vortex

line represents the shed vorticity which is convected downstream causing a lattice to form in the wake. One new vortex line is formed for each time interval. When the wing stops rotating, lines continue to be shed; however, the strengths of these lines decrease and the steady-state results are approached rapidly. This is illustrated in figures 5 - 7. The sequence of events leading up to figures 5 - 7 is as follows: Initially the angle of attack was eleven degrees and the flow was steady. Then the angle of attack was increased at the rate of one degree per nondimensional time unit until the angle of attack reached fifteen degrees. At this point the angle of attack stopped changing. The general unsteady program was allowed to run for twelve time units. This allowed the strength of the shed vortices to vanish, those of appreciable strength to be convected far downstream, and the flow to achieve a steady state.

In all three cases, the lift and moment produced by the unsteady flow are lower than those produced by a steady flow at the same angle of attack. The steady-flow results are shown by the dotted lines.

At each time step, the solution is obtained in essentially the same way that the steady problem is solved. But now there is the added complication of convecting the shed vorticity downstream with the particle velocity. This is accomplished by moving the ends of the segments of the shed line according to

$$\vec{r}(t + \Delta t) = \vec{r}(t) + \vec{v}\Delta t$$

where $\vec{v}$ is the particle velocity and Δt is the time interval.

The nondimensional loads are calculated according to

$$\vec{F} = 2\ell\vec{\Gamma} \times \vec{v}$$

where ℓ is the nondimensional length of the segment on which the force $\vec{F}$ acts, $\vec{\Gamma}$ is the circulation around this segment multiplied by a unit vector parallel to the segment and $\vec{v}$ is the velocity at the midpoint of the segment. The resultant force is obtained by adding the forces on the bound segments. The pressures are calculated by averaging one-half the forces on the segments along the edges of an elemental area over the elemental area, exceptions being those elements along the leading edge for which the entire force acting on the forward segment is averaged.

Figure 8 shows the convergence as the number of elements is increased. Comparing figures 9 and 10 with figures 5 and 6 shows that the unsteady results approach the steady results as the rate of changing the angle of attack decreases.

Figures 11 and 12, which show hysteretic behavior, compare the results for

increasing angle of attack, decreasing angle of attack, and the steady state. The initial conditions are the steady-state solutions at eleven and fifteen degrees.

More details and results are given by Atta (ref. 10).

CONCLUDING REMARKS

The method presented here is general. It can be used to treat arbitrary motions, including harmonic oscillations. And it can be used to treat leading-edge separation.

REFERENCES

1. Morino, L. and Kuo, C.C., "Unsteady Subsonic Flow Around Finite-Thickness Wings," Dept. of Aerospace Engineering, Boston Univ., TR-73-03, Feb. 1973.

2. Ashley, H. and Rodden, W. P., "Wing-Body Aerodynamic Interaction," Annual Review of Fluid Mechanics, pp. 431-472, 1972.

3. Rodden, W. P., Giesing, S. P. and Kalman, T. P., "Refinement of the Nonplanar Aspects of the Subsonic Doublet-Lattice Lifting Surface Mechod," J. of Aircraft, Vol. 9, pp. 59-73, Jan. 1972.

4. Giesing, J.P., Kalman, T.P. and Rodden, W.P., "Subsonic Steady and Oscillatory Aerodynamics for Multiple Interfering Wings and Bodies," J. of Aircraft, Vol. 9, No. 10, Oct. 1972.

5. Albano, E. and Rodden, W.P., "A Doublet-Lattice Method for Calculating Lift Distributions on Oscillating Surfaces in Subsonic Flows," AIAA J., Vol. 7, pp. 279-285, 1969.

6. Belotserkovskii, S.M., "Calculating the Effect on an Arbitrary Thin Wing," Fluid Dynamics, Vol. 1, No. 1, 1967.

7. Djojodihardjo, R.H. and Widnall, S.E., "A Numerical Method for Calculation of Nonlinear Unsteady Lifting Potential Flow Problems," AIAA J., Vol. 7, No. 10, pp. 2001-2009, Oct. 1969.

8. Kandil, O.A., Mook, D.T. and Nayfeh, A.H., "Nonlinear Prediction of the Aerodynamic Loads on Lifting Surfaces," AIAA Paper No. 74-503, June 1974 (also in J. of Aicraft, Vol. 13, No. 1, pp. 22-28).

9. Kandil, O.A., "Prediction of the Steady Aerodynamic Loads on Lifting Surfaces Having Sharp-Edge Separation," Ph.D. Thesis, Dept. Engr. Sci. & Mech., VPI&SU, Blacksburg, Va. Dec. 1974.

10. Atta, E.H., "Unsteady Flow Over Arbitrary Wing-Planforms, Including Tip Separation" MS. Thesis, Dept. Sci. & Mech., VPI&SU, Blacksburg, Va., Mar. 1976.

BELOTSERKOVSKII   DJOJODIHARDJO   PRESENT METHOD

(1966)   (1969)
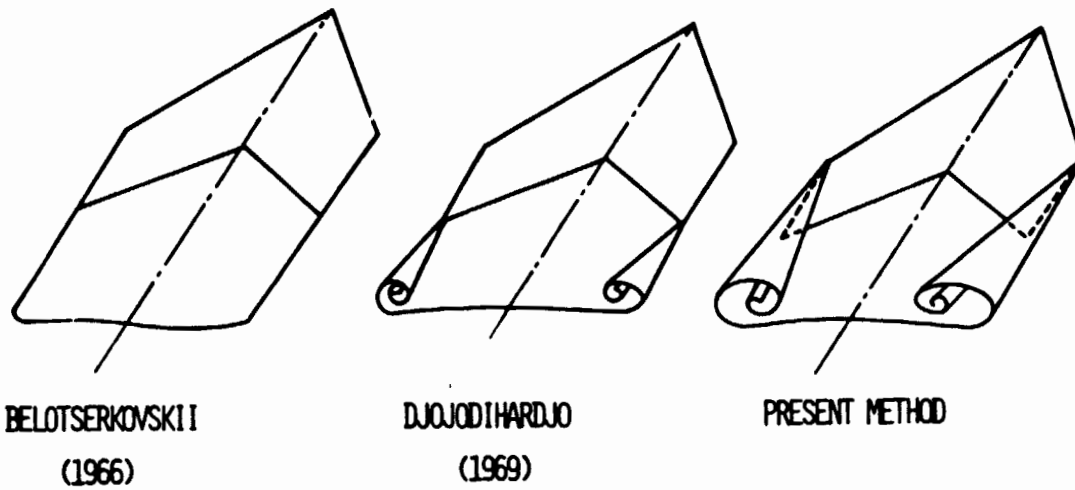
Figure 1.- Comparison of different methods.

FREE STREAM
11°

– – – BOUND-VORTEX LATTICE
——— FREE-VORTEX LINES
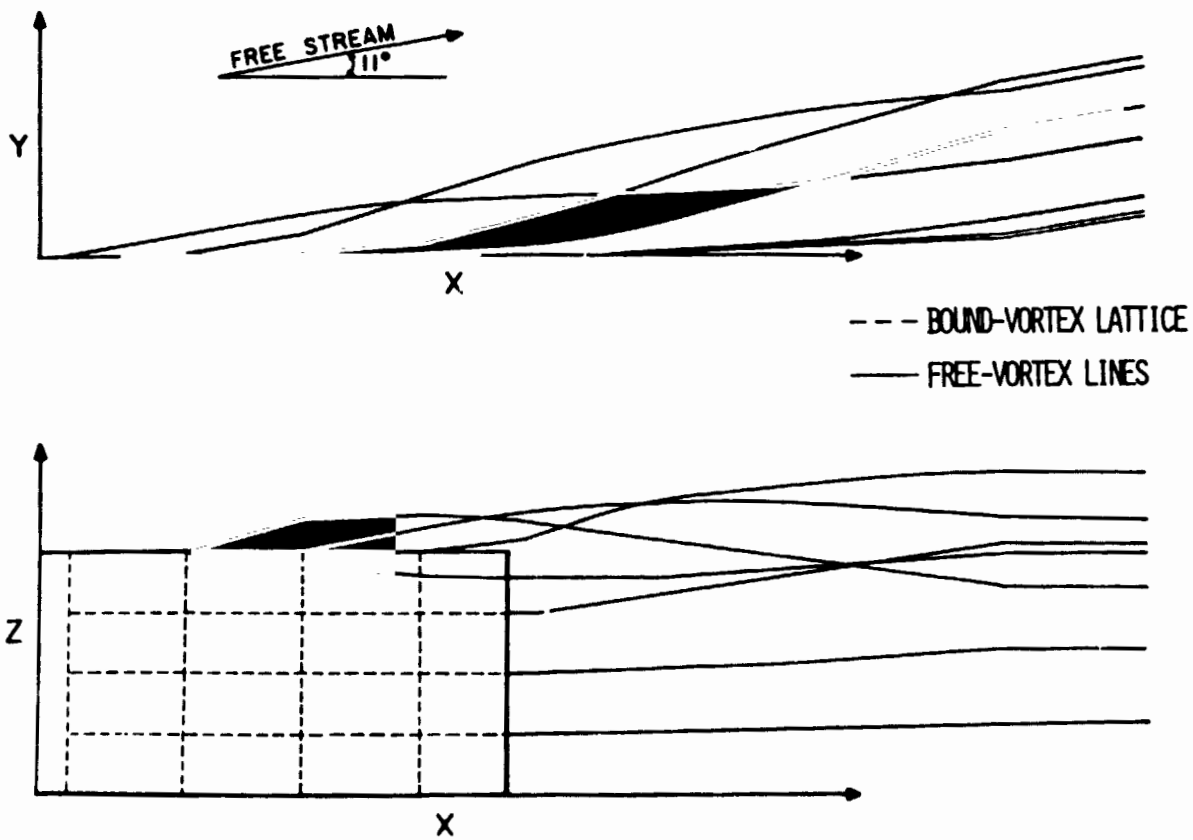
Figure 2.- Wake shape in a steady flow. $\alpha = 11^o$; $AR = 1$.

413

(WING-TIP VORTICES ARE ROTATED 90° FOR DEMONSTRATION)
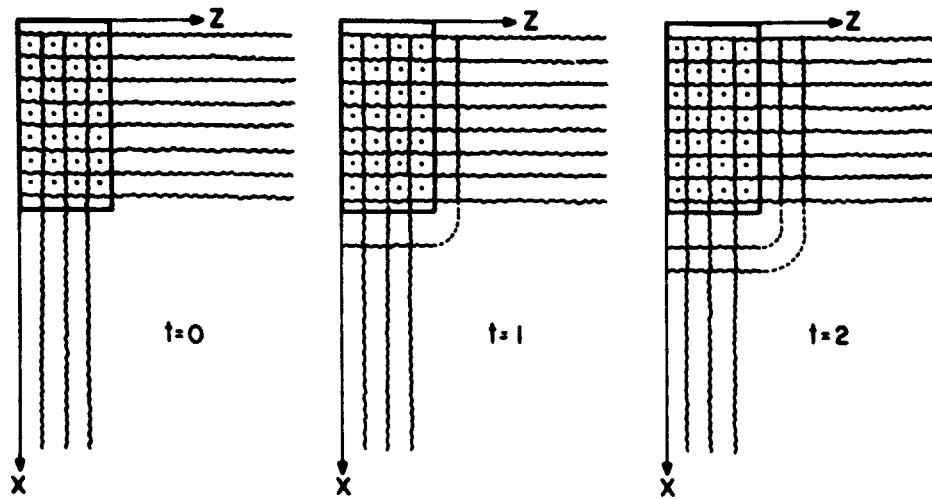
Figure 3.- Shed-vortex lines.

--- BOUND-VORTEX LINES
—— FREE-VORTEX LINES
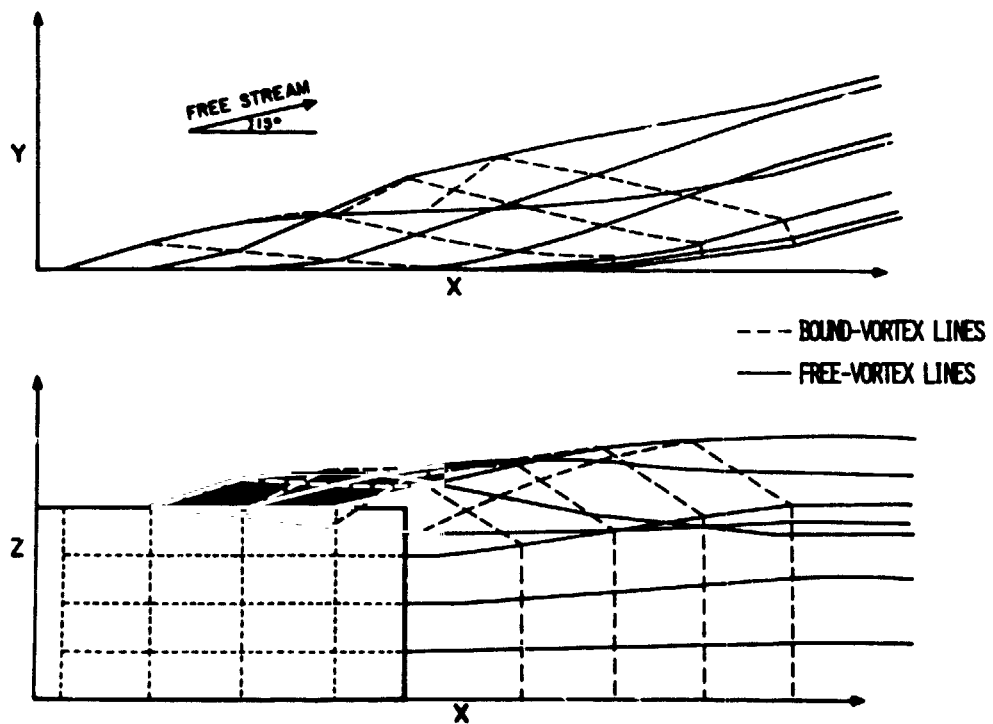
Figure 4.- Wake shape in an unsteady flow. $\alpha_o = 11°$; $\alpha_f = 15°$; $\dot{\alpha} = 1$; AR = 1; t = 4.

Figure 5.- Variation of the normal-force coefficient.
$\alpha_o = 11^o$; $\alpha_f = 15^o$; $\dot{\alpha} = 1$; $\Delta t = 1$.

Figure 6.- Variation of the pitching-moment coefficient.
$\alpha_o = 11^o$; $\alpha_f = 15^o$; $\dot{\alpha} = 1$; $\Delta t = 1$.
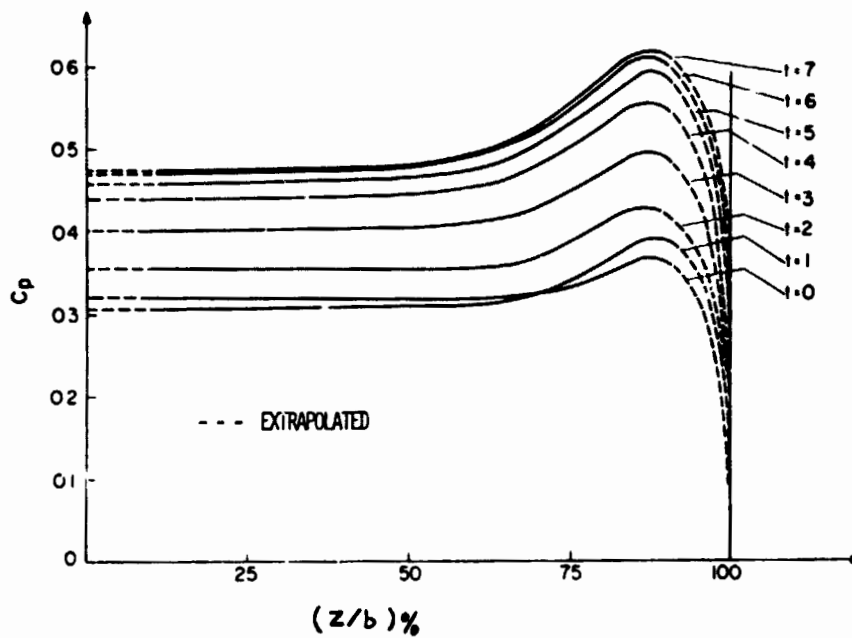
Figure 7.- Pressure coefficient variation. $\alpha_o = 11^o$; $\alpha_f = 15^o$; $\dot{\alpha} = 1$; AR = 1; $\Delta t = 1$; $X/C_r = 43.75\%$.
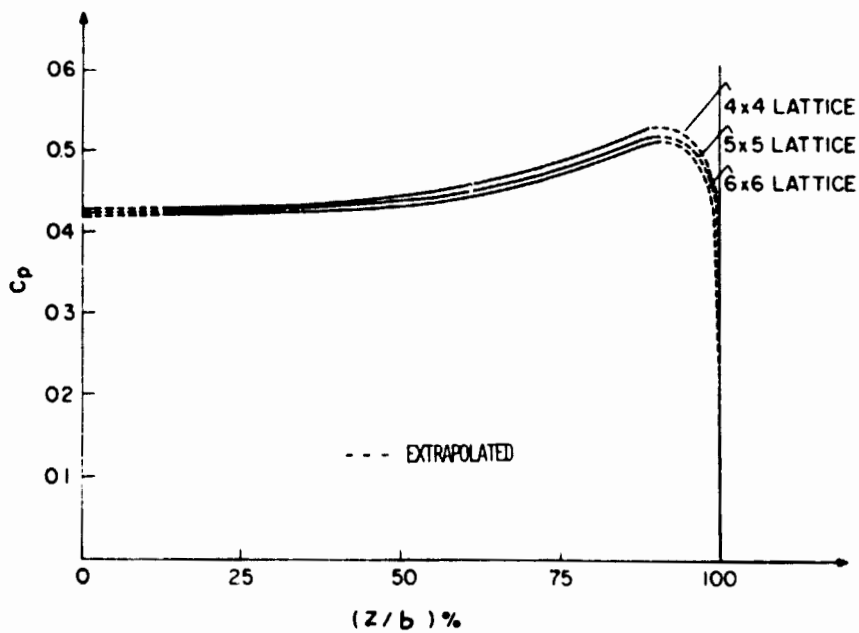

Figure 8.- Pressure coefficient for different lattices. $\alpha_o = 11^o$; $\alpha_f = 15^o$; $\dot{\alpha} = 1$; AR = 1; $\Delta t = 1$; $X/C_r = 43.75\%$; t = 5.

416
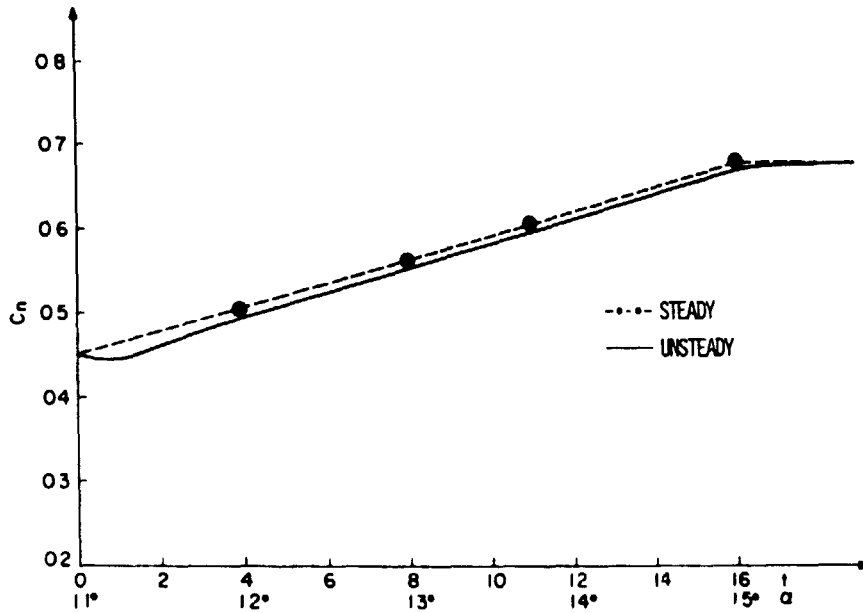
Figure 9.- Quasi-steady variation of the normal-force coefficient.
$\alpha_o = 11°$; $\alpha_f = 15°$; $\dot{\alpha} = 0.25$, $\Delta t = 1$; AR = 1.
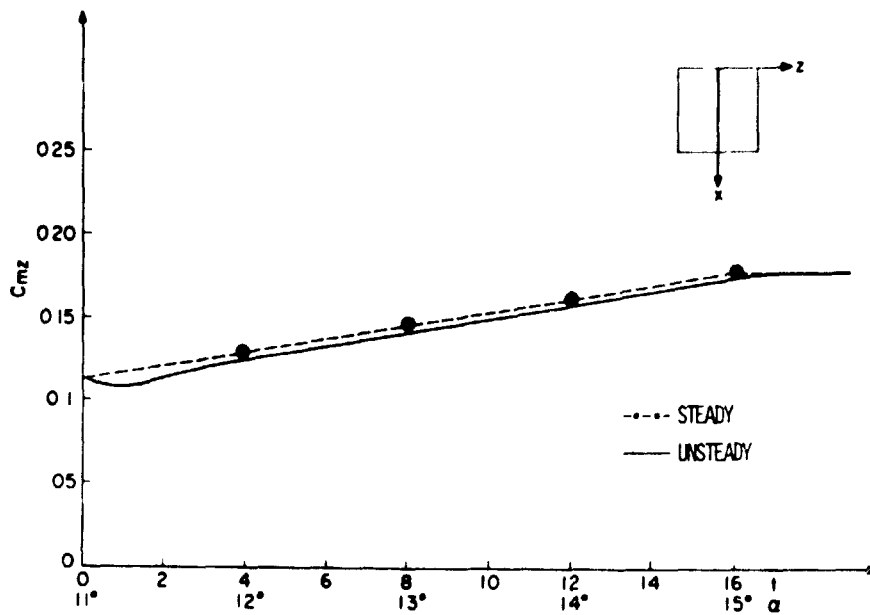
Figure 10.- Quasi-steady variation of the pitching-moment
coefficient. $\alpha_o = 11°$; $\alpha_f = 15°$; $\dot{\alpha} = 0.25$; $\Delta t = 1$;
AR = 1.
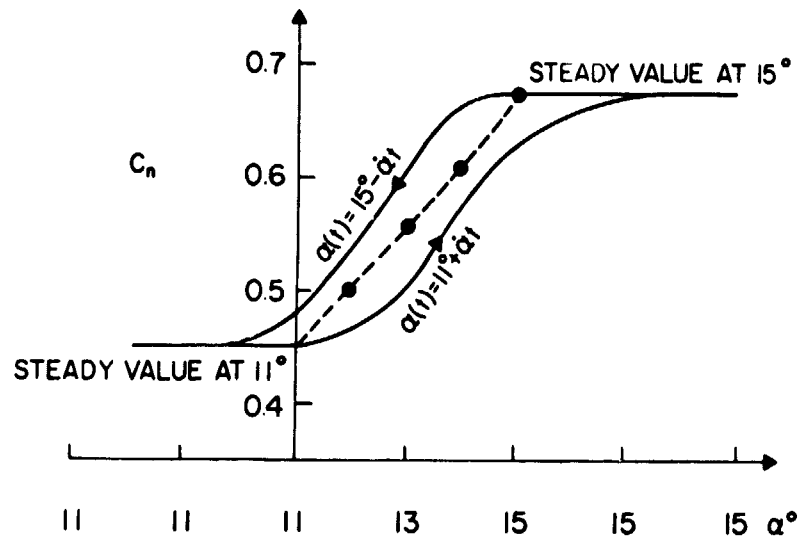
Figure 11.- Normal-force coefficient.
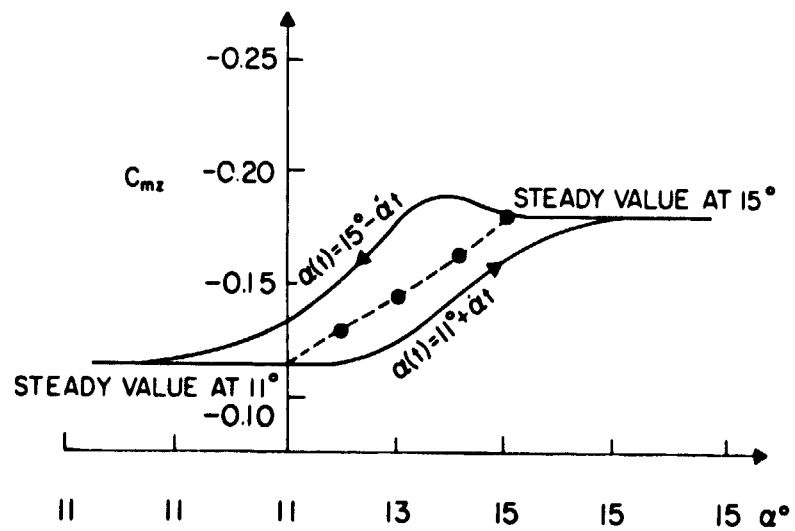
Figure 12.- Pitching-moment coefficient.

SUMMARY OF OPEN DISCUSSION ON FUTURE VORTEX-LATTICE UTILIZATION

John C. Houbolt
NASA Langley Research Center

The response of the attendees during the open discussion on vortex-lattice utilization was excellent. The intent of this summary is not to evaluate the comments made but simply to indicate the topics discussed. Essentially, the discussion focused on the following general topics: grid layout, drag calculations, bodies in combination, vortex lift, and separated flow effects.

In order to stimulate and initiate the discussion, a panel was set up on a spur-of-the-moment basis. Members were Jan Tulinius of NASA Langley Research Center, Joseph Giesing of McDonnell Aircraft Company, Winfried Feifel of The Boeing Company, and Brian Maskew of Analytical Methods, Inc. The subjects covered by each of these members are essentially as follows:

Tulinius, in effect, gave a very good impromptu paper. He covered two-dimensional and three-dimensional drag effects and discussed the equivalence of near- and far-field drag estimates. He mentioned supersonic vortex-lattice methods and pointed out problems associated with Mach cone and sonic line singularities, with natural edge conditions, and with nonplanar effects. He also discussed the use of distributed singularities versus the use of lattice constraint functions. Also covered was the topic of free vortices, whether of the leading-edge variety for arbitrary planforms or as associated with trailing-edge and tip wakes.

Giesing's remarks also constituted a very good impromptu paper. He discussed areas for numerical improvement of the lattice method with topic coverage as follows:

Supersonic flow

    Infinite velocity on Mach cones
    Smearing of loads - loads wandering out of Mach cone
    Instability of solutions

Convecting singularities (jets, wakes, leading-edge vortices)

    Infinite velocity when vortex contacts control point
    Force or pressure calculation inconvenient on yawed elements
    Wake next to fuselage
    Low lift for jet flaps

Subsonic flow

Discontinuity in Δx causes disturbance in pressures
Collocating points on body surfaces, while using axial singularities can
  cause instabilities
High frequency lattice method expensive and/or inaccurate
Computing time and accuracy trade-off for wing-bodies

Areas where Giesing felt there was need for basic improvement in the
lattice methods are as follows:

Transonic flow

Empirical corrections

Viscous corrections

Steady
Unsteady

Oscillatory flow

Nonplanar flaps down, etc.
Wing-jet interaction (compressible)
Leading-edge vortex

Lateral-directional forces

Feifel emphasized the need for practical considerations and input sim-
plicity. He discussed problems related to the treatment of cambered wings. He
also felt more attention should be given to grid system layout, especially with
respect to the simulation of bodies or other complex configurations. The treat-
ment of high lift configurations, such as constant chord flaps on tapered wings,
and the situation of wings with cutouts also represent problem areas.

Maskew's comments are summarized as follows. He referred to the use of
constraint functions discussed by Tulinius as a possible alternative to the
subvortex technique for keeping the number of unknowns down while effectively
using a large number of vortices. Maskew mentioned that he had used constraint
functions with a subvortex model, as reported in NASA TM X-73115 (ref. 1). The
number of unknowns was halved without spoiling the pressure calculations at the
arbitrary points. With the small number of unknowns, i.e., 46, the savings in
solution time was about the same as the time required to manipulate the matrix.
For a larger number of unknowns, there should be a savings in computer time.
On the question posed by Houbolt on separated flow modeling, Maskew felt the
answer might be found in Giesing's comments, namely, that the multienergy
modeling developed by Shollenberger for jet flow interference might also be
adapted for the low energy region associated with separated flows. Maskew
mentioned that certain problems arise in wake rollup calculations of compli-
cated flap systems. For the 747 flap system, with edge vortices on each flap,
he found that the two opposing regions from the flap edges adjacent to the high-

speed aileron pose a problem in that the calculations predict an orbiting motion which does not appear in real flow. The two vortices in fact soon cancel each other, leaving a single wake vortex. This merging problem needs further investigation so that it can be modeled correctly. Another problem he discussed deals with the near-field calculation of forces using the Kutta-Joukowski law applied to vortex segments. He pointed out that in most cases the forces are calculated only on the bound vortex segments, and with the assumption that the chordwise segments are alined with the local mean velocity and therefore carry no load. In some configurations this assumption is not valid. He brought out the example of a yawed wing which has been paneled for symmetrical flow and raised the question, does the wing need repaneling before calculating the yawed condition. The problem also appears on wings with deflected flaps. Large mean spanwise flow components exist on the flaps, particularly near the tip, and if the forces on the chordwise segments are computed in this case, the Kutta trailing-edge condition appears violated. Maskew pointed out that this problem requires further attention and that perhaps the chordwise segments should always be alined with the mean flow direction.

In summary, the following items appear to be of chief concern in continuing and future development of the vortex-lattice methods:

1. Grid layout, especially with respect to the use of the 1/4-point, 3/4-point rule, or the approach which employs equal angular spacing within a semicircle

2. Drag calculation techniques

3. Bodies in combination

4. Separated flow effects including wake rollup

5. Supersonic flow applications

6. Treatment of lateral flow or of combined pitch and yaw displacement

REFERENCE

1. Maskew, B.: A Submerged Singularity Method for Calculating Potential Flow Velocities at Arbitrary Near-Field Points. NASA TM X-73115, 1976.

SAMPLE WINGS FOR STUDY

John E. Lamar
NASA Langley Research Center

During the Vortex-Lattice Utilization Workshop, the proposal was made that the same sample wings be studied by all those interested in order to gain an appreciation for the accuracy of the various implementations - both old and new - of the vortex-lattice method. Therefore, two simple wings have been selected for which force, moment, and pressure data are available and they are presented in figures 1 and 2.
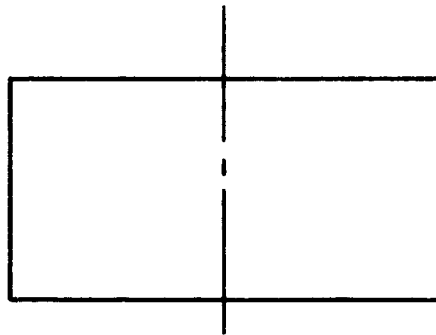
Figure 1.- Aspect-ratio-2 rectangular wing.
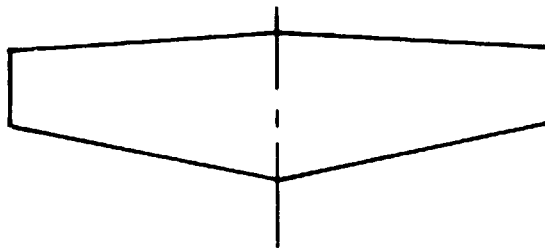
Figure 2.- Aspect-ratio-5 tapered wing. Leading-edge sweep, 3.317°; trailing-edge sweep, -11.308°; taper ratio, 0.5.

Data for the aspect-ratio-2 rectangular wing are found in references 1 and 2, and for the aspect-ratio-5 tapered wing in references 3 and 4.

REFERENCES

1. Fischel, Jack; Naeseth, Rodger L.; Hagerman, John R.; and O'Hara, William M.: Effect of Aspect Ratio on the Low-Speed Lateral Control Characteristics of Untapered Low-Aspect-Ratio Wings Equipped With Flap and With Retractable Ailerons. NACA Rep. 1091, 1952. (Supersedes NACA TN 2347 by Fischel and Hagerman and NACA TN 2348 by Naeseth and O'Hara.)

2. Holme, Olof A. M.: Measurements of the Pressure Distribution on Rectangular Wings of Different Aspect Ratios. FFA Rep. 37, Aeronaut. Res. Inst. of Sweden, 1950.

3. Thiel, G.; and Weissinger, F.: Six-Component Measurements on a Straight and a 35° Swept-Back Trapezoidal Wing With and Without Split Flap. NACA TM 1107, 1947.

4. Thiel, A.; and Weissinger, J.: Pressure-Distribution Measurements on a Straight and on a 35° Swept-Back Tapered Wing. NACA TM 1126, 1947.